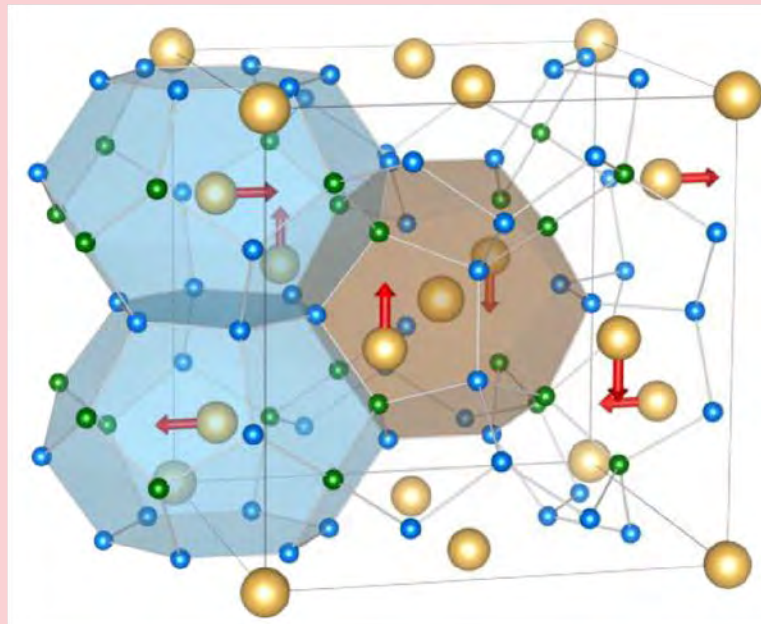




MATERIALS DESIGN AND
CHARACTERIZATION LABORATORY
SUPERCOMPUTER CENTER

ACTIVITY REPORT 2019



INSTITUTE FOR SOLID STATE PHYSICS
THE UNIVERSITY OF TOKYO

Materials Design and Characterization Laboratory (MDCL)

The MDCL was established as the third research facility of the Institute for Solid State Physics (ISSP) when the latter was reorganized in May 1996. Its aim is to promote material science with an emphasis on the “DSC cycle”, where DSC stands for design, synthesis and characterization, three processes for developing new materials.

The MDCL consists of two sections, Materials Design (MD) section and Materials Synthesis and Characterization (MSC) section. The Supercomputer Center of the ISSP (SCC-ISSP) is placed in the MD section, while in the MSC section there are seven laboratories for joint use; Materials Synthesis Laboratory, Chemical Analysis Laboratory, X-ray Diffraction Laboratory, Electron Microscope Laboratory, Electromagnetic Measurement Laboratory, Spectroscopy Laboratory, and High-Pressure Synthesis Laboratory.

Almost all the facilities of the MDCL are open to scientists in Japan through the User Programs conducted by two steering committees of the MDCL. One is the steering committee of the SCC-ISSP, under which the Supercomputer Project Advisory Committee is placed for reviewing proposals. The other is the steering committee of the MSC facilities. More than half of the members of these committees are from the outside of ISSP.

COVER FIGURE

Crystal structures and phonon properties of thermoelectric clathrate $\text{Ba}_8\text{Ga}_{16}\text{Ge}_{30}$. Adopted from T. Tadano and S. Tsuneyuki: Phys. Rev. Lett. 120 (2018) 105901. See T. Tadano, Page 15–24, “First-principles calculation of thermophysical properties of solids with strong phonon anharmonicity”.

PREFACE

The Supercomputer Center (SCC) is a part of the Materials Design and Characterization Laboratory (MDCL) of ISSP. Its mission is to serve the whole community of computational condensed-matter physics of Japan providing it with high performance computing environment. In particular, the SCC selectively promotes and supports large-scale computations. For this purpose, the SCC invites proposals for supercomputer-aided research projects and hosts the Steering Committee, as mentioned below, that evaluates the proposals.

The ISSP supercomputer system consists of two subsystems: System B, which is intended for more nodes with relatively loose connections. In July, 2015, the SCC replaced the two supercomputer subsystems (SGI Altix ICE 8400EX and NEC SX-9) to one new system (System B, SGI ICE XA/UV hybrid system). The system B consists of 1584 CPU nodes, 288 ACC nodes, and 19 FAT nodes. The CPU node has 2 CPUs (Intel Xeon). The ACC node has 2 CPUs (Intel Xeon) and 2 GPUs (NVIDIA Tesla K40). The FAT node has 4 CPUs (Intel Xeon) and large memory (1TB). The system B has totally 2.6 PFlops theoretical peak performance. The new system C (HPE SGI 8600) was installed in January, 2018. It consists of 252 nodes, and each node has 2 CPUs (Intel Xeon) and 192 GB of memory. The system C has totally 774 TFlops.

The hardware administration is not the only function of the SCC. Since 2015, the SCC has started “Project for advancement of software usability in materials science”. In this project, for enhancing the usability of the ISSP supercomputer system, we perform some software-advancement activities such as implementing a new function to an existing code, releasing a private code on Web, and writing manuals. Two target programs were selected in school year 2019 and developed software were released as abICS (proposal made by S. Kasamatsu (Yamagata Univ.)) and TeNeS (proposal made by N. Kawashima (ISSP)). The SCC has also started a service for porting users’ materials science software to General Purpose GPUs (GPGPU) since 2015. One program was selected for the GPGPU porting in school year 2019.

All staff members of university faculties or public research institutes in Japan are invited to propose research projects (called User Program). The proposals are evaluated by the Steering Committee of SCC. Pre-reviewing is done by the Supercomputer Project Advisory Committee. In school year 2019, totally 309 projects were approved. The total points applied and approved are listed on Table. 1 below. Additionally, we supported post-K and other computational materials science projects through Supercomputing Consortium for Computational Materials Science (SCCMS).

The research projects are roughly classified into the following three (the number of projects approved):

- First-Principles Calculation of Materials Properties (145)
- Strongly Correlated Quantum Systems (36)
- Cooperative Phenomena in Complex, Macroscopic Systems (128)

All the three involve both methodology of computation and its applications. The results of the projects are reported in 'Activity Report 2019' of the SCC. Every year 3-4 projects are selected for “invited papers” and published at the beginning of the Activity Report. In the Activity Report 2019, the following three invited papers are included:

"First-Principles Calculation of Thermophysical Properties of Solids with Strong Phonon Anharmonicity",
Terumasa TADANO

"Development of Open-Source Parallelized Tensor Network Softwares: mptensor and TeNeS",
Satoshi MORITA and Naoki KAWASHIMA

"Disorder-Free Glass Transitions of Spins and Orbitals in a Frustrated Pyrochlore Magnet",
Kota MITSUMOTO, Chisa HOTTA, and Hajime YOSHINO

June 1, 2020

Naoki Kawashima
(Chairman of the steering committee, SCC, ISSP)

CONTENTS

PREFACE

1 OUTLINE	1
1.1 Supercomputer System	1
1.2 Project Proposals	1
1.3 Committees	3
1.4 Staff	7
2 STATISTICS (SCHOOL YEAR 2019)	7
2.1 System and User Statistics	7
2.2 Queue and Job Statistics	8
2.3 Project for Advancement of Software Usability in Materials Science	10
2.4 GPGPU Support Service	10
3 RESEARCH REPORTS	14
3.1 Invited Articles	14
3.2 First-Principles Calculation of Material Properties	43
3.3 Strongly Correlated Quantum Systems	196
3.4 Cooperative Phenomena in Complex Macroscopic Systems	238
3.5 SCCMS Projects	359
3.6 Software Advancement Projects, GPGPU Implementation, and Workshop Support	385
4 PUBLICATION LIST	391
ISSP Joint Research Projects	392
SCCMS Projects	433
Doctor Theses	440
Master Theses	442

1 OUTLINE

1.1 Supercomputer System

In SY2019, the ISSP supercomputer center provided users with System B - SGI ICE XA/UV hybrid system and System C - HPE SGI 8600 system. System B is a massively-parallel supercomputer with three types of compute nodes: 19 “Fat” nodes, 1584 “CPU” nodes, and 288 “ACC” nodes. “Fat” nodes are each comprised of four Intel Xeon E5-4627v3 CPUs (10 cores/CPU) and 1 TB of memory. “CPU” nodes have two Intel Xeon E5-2680v3 CPUs (12 cores/CPU) and 128 GB of memory. “ACC” nodes have two nVIDIA Tesla K40 GPUs in addition to two Xeon E5-2680v3 CPUs and 128 GB of memory. System B achieves 2.6 PFLOPS in theoretical peak performance with high power efficiency. The subsystem comprised of only CPU nodes ranks 61st on the November 2015 Top 500 List, which is a ranking based on total performance measured by the HPL benchmark. The subsystem of ACC nodes ranks 104th on the Top 500 List, and it also ranks 23rd on the Green 500 List, which is a ranking based on performance per watt of electrical power consumption. The compute nodes communicate to each other through FDR Infiniband. The Fat nodes are interconnected in fat tree topology, while the CPU and ACC nodes are connected in enhanced hypercube topology. System B entered official operation on Aug. 21, 2015. SY2019 was the fifth year of the operation of the current System B. System C is a massively-parallel supercomputer with 252 “CPU” nodes, which have two Intel Xeon Gold 6148 CPUs (20 cores/CPU) and 192 GB of memory. System C achieves 774 TFLOPS in theoretical peak performance. SY2019 was the second year of the operation of the current System C. For further details, please contact ISSP Supercomputer Center (SCC-ISSP).

[Correspondence: center@issp.u-tokyo.ac.jp]

1.2 Project Proposals

The ISSP supercomputer system provides computation resources for scientists working on condensed matter sciences in Japan. All scientific staff members (including post-docs) at universities or public research institutes in Japan can submit proposals for projects related to research activities on materials and condensed matter sciences. These proposals are peer-reviewed by the Advisory Committee members (see Sec. 1.3), and then the computation resources are allocated based on the review reports. The leader of an approved project can set up user accounts for collaborators. Other types of scientists, including graduate students, may also be added. Proposal submissions, peer-review processes, and user registration are all managed via a web system.

The computation resources are distributed in a unit called “point”, determined as a function of available CPU utilization time and consumed disk resources. There were calls for six classes of research projects in SY 2019. The number of projects and the total number of points that were applied for and approved in this school year are listed in Table 1.

Table 1: Classes of research projects in SY 2019

Class	Maximum Points		Application	# of Proj.	Total points			
	Sys-B	Sys-C			Applied		Approved	
					Sys-B	Sys-C	Sys-B	Sys-C
A	100	100	any time	17	1.7k	0.9k	1.7k	0.9k
B	1k	500	twice a year	88	83.8k	4.7k	58.3k	4.1k
C	10k	2.5k	twice a year	182	1416.2k	88.2k	608.0k	63.0k
D	10k	2.5k	any time	5	26.9k	2.0k	26.9k	2.0k
E	30k	2.5k	twice a year	17	475.0k	44.0k	253.0k	35.6k
S	–	–	twice a year	0	0	0	0	0
SCCMS				36	253.0k	23.5k	253.0k	23.5k
Total				345	2255.6k	163.2k	1200.9k	128.8k

- Class A is for trial use by new users; proposals for Class A projects are accepted throughout the year.
- Proposals for projects in Classes B (small), C (mid-size), E (large-scale), and S (exceptional) can be submitted twice a year. Approved projects in Classes A, B, C, and E continue to the end of the school year.
- In Class D, projects can be proposed on rapidly-developing studies that need to perform urgent and relatively large calculations. An approved project continues for 6 months from its approval.
- Class S is for projects that are considered extremely important for the field of condensed matter physics and requires extremely large-scale computation. The project may be carried out either by one research group or cooperatively by several investigators at different institutions. A project of this class should be applied with at least 10,000 points; there is no maximum. We require group leaders applying for Class S to give a presentation on the proposal to the Steering Committee of the SCC-ISSP. Class S projects are carried out within one year from its approval.
- Project leaders can apply for points so that the points for each system do not exceed the maximum point shown in this table.

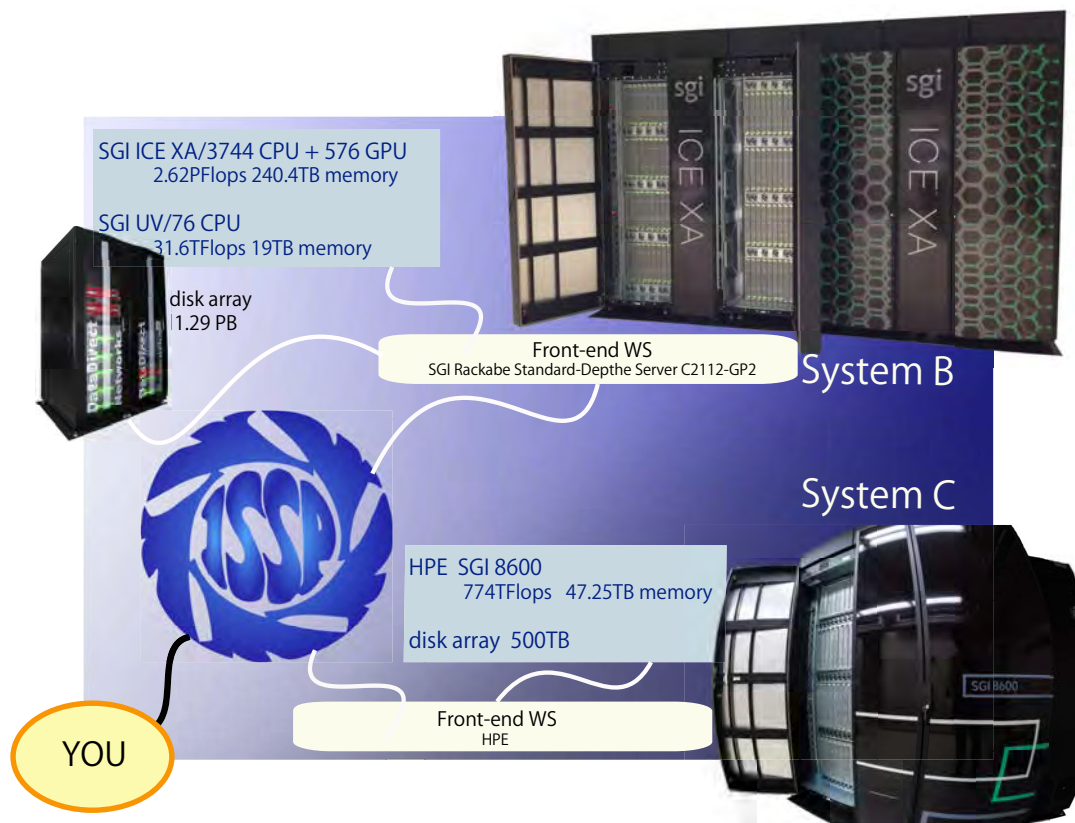


Figure 1: Supercomputer System at the SCC-ISSP

In addition, from SY 2016, ISSP Supercomputer is providing 20% of its computational resources for Supercomputing Consortium for Computational Materials Science (SCCMS), which aims at advancing parallel computations in condensed matter, molecular, and materials sciences on the 10-PFlops K Computer and the exascale post-K project. Computational resources have also been allotted to Computational Materials Design (CMD) workshops, as well as for Science Camps held in ISSP for undergraduate students.

1.3 Committees

In order to fairly manage the projects and to smoothly determine the system operation policies, the Materials Design and Characterization Laboratory (MDCL) of the ISSP has organized the Steering Committee of the MDCL and the Steering Committee of the SCC-ISSP, under which the Supercomputer Project Advisory Committee (SPAC) is formed to review proposals. The members of the committees in SY 2019 were as follows:

Steering Committee of the MDCL

HIROI, Zenji

ISSP (Chair person)

KAWASHIMA, Naoki	ISSP
OZAKI, Taisuke	ISSP
NOGUCHI, Hiroshi	ISSP
UWATOKO, Yoshiya	ISSP
SUGINO, Osamu	ISSP
TOHYAMA, Takami	Tokyo Univ. of Sci.
ONO, Tomoya	Kobe Univ.
YAMAURA, Jun-ichi	Tokyo Tech.
TAKAHASHI, Hiroki	Nihon Univ.
MOTOME, Yukitoshi	Univ. of Tokyo
HOSHI, Takeo	Tottori Univ.
KIMURA, Kaoru	Univ. of Tokyo
HASEGAWA, Masashi	Nagoya Univ.
NAKATSUJI, Satoru	ISSP

Steering Committee of the SCC-ISSP

KAWASHIMA, Naoki	ISSP (Chair person)
NOGUCHI, Hiroshi	ISSP
OZAKI, Taisuke	ISSP
SUGINO, Osamu	ISSP
TSUNETSUGU, Hirokazu	ISSP
KATO, Takeo	ISSP
KONDO, Takeshi	ISSP
MORITA, Satoshi	ISSP
HIGUCHI, Yuji	ISSP
FUKUDA, Masahiro	ISSP
KAWAMURA, Mitsuaki	ISSP
NAKAJIMA, Kengo	Univ. of Tokyo
TSUNEYUKI, Shinji	Univ. of Tokyo
HATANO, Naomichi	Univ. of Tokyo
MOTOME, Yukitoshi	Univ. of Tokyo
ONO, Tomoya	Kobe Univ.
TOHYAMA, Takami	Tokyo Univ. of Sci.
YOSHINO, Hajime	Osaka Univ.
SUZUKI, Takafumi	Univ. of Hyogo
YOSHIMOTO, Yoshihide	Univ. of Tokyo
OKUMURA, Hisashi	NINS-RSCS
HOSHI, Takeo	Tottori Univ.
YATA, Hiroyuki	ISSP
FUKUDA, Takaki	ISSP

Supercomputer Project Advisory Committee

KAWASHIMA, Naoki	ISSP (Chair person)
------------------	---------------------

NOGUCHI, Hiroshi	ISSP
SUGINO, Osamu	ISSP
OZAKI, Taisuke	ISSP
TSUNETSUGU, Hirokazu	ISSP
KATO, Takeo	ISSP
KONDO, Takeshi	ISSP
HIGUCHI, Yujih	ISSP
MORITA, Satoshi	ISSP
FUKUDA, Masahiro	ISSP
KAWAMURA, Mitsuaki	ISSP
NAKAJIMA, Kengo	Univ. of Tokyo
TSUNEYUKI, Shinji	Univ. of Tokyo
IMADA, Masatoshi	Toyota Riken/Waseda Univ.
HATANO, Naomichi	Univ. of Tokyo
SUZUKI, Takafumi	Univ. of Hyogo
YOSHIMOTO, Yoshihide	Univ. of Tokyo
OKUMURA, Hisashi	NINS-RSCS
HOSHI, Takeo	Tottori Univ.
ONO, Tomoya	Univ. of Tsukuba
YOSHINO, Hajime	Osaka Univ.
MOTOME, Yukitoshi	Univ. of Tokyo
TOHYAMA, Takami	Tokyo Univ. of Sci.
KITAO, Akio	Tokyo Tech.
ARITA, Ryotaro	Univ. of Tokyo
IKUHARA, Yuichi	Univ. of Tokyo
SHIBATA, Naokazu	Tohoku Univ.
AKAGI, Kazuto	Tohoku Univ.
YANASE, Yoichi	Kyoto Univ.
HATSUGAI, Yasuhiro	Univ. of Tsukuba
OKADA, Susumu	Univ. of Tsukuba
KOBAYASHI, Nobuhiko	Univ. of Tsukuba
NAKAYAMA, Takashi	Chiba Univ.
HOTTA, Takashi	Tokyo Metropolitan Univ.
MATSUKAWA, Hiroshi	Aoyama Gakuin Univ.
YAMAUCHI, Jun	Keio Univ.
HAGITA, Katsumi	National Defense Academy
KONTANI, Hiroshi	Nagoya Univ.
SAITO, Mineo	Kanazawa Univ.
KAWAKAMI, Norio	Kyoto Univ.
YUKAWA, Satoshi	Osaka Univ.
SUGA, Seiichiro	Univ. of Hyogo
TATENNO, Masaru	Univ. of Hyogo
YASUDA, Chitoshi	Univ. of the Ryukyus
OGATA, Masao	Univ. of Tokyo
WATANABE, Satoshi	Univ. of Tokyo

OKAMOTO, Yuko	Nagoya Univ.
HUKUSHIMA, Koji	Univ. of Tokyo
NEMOTO, Koji	Hokkaido Univ.
YABANA, Kazuhiro	Univ. of Tsukuba
HIDA, Kazuo	Saitama Univ.
WATANABE, Kazuyuki	Tokyo Univ. of Sci.
FURUKAWA, Nobuo	Aoyama Gakuin Univ.
KUROKI, Kazuhiko	Osaka Univ.
TAKANO, Hiroshi	Keio Univ.
YASUOKA, Kenji	Keio Univ.
TANAKA, Yukio	Nagoya Univ.
MASUBUCHI, Yuichi	Nagoya Univ.
KAWAMURA, Hikaru	Osaka Univ.
KUSAKABE, Koichi	Osaka Univ.
SHIRAI, Koun	Osaka Univ.
SAKAI, Toru	Univ. of Hyogo
ISHIBASHI, Shoji	AIST
OTANI, Minoru	AIST
TOMITA, Yusuke	Shibaura Inst. Tech.
MIYASHITA, Seiji	JPS
SHIRAISHI, Kenji	Nagoya Univ.
OGUCHI, Tamio	Osaka Univ.
KAWAKATSU, Toshihiro	Tohoku Univ.
KOBAYASHI, Kazuaki	NIMS
TATEYAMA, Yoshitaka	NIMS
KIM, Kang	Osaka Univ.
OTSUKI, Tomi	Sophia Univ.
MORIKAWA, Yoshitada	Osaka Univ.
ODA, Tatsuki	Kanazawa Univ.
OTSUKI, Junya	Okayama Univ.
KOGA, Akihisa	Tokyo Tech.
SHIMOJO, Fuyuki	Kumamoto Univ.
TAKETSUGU, Tetsuya	Hokkaido Univ.
TSURUTA, Kenji	Okayama Univ.
HAMAGUCHI, Satoshi	Osaka Univ.
NISHIDATE, Kazume	Iwate Univ.
KAGESHIMA, Hiroyuki	Shimane Univ.
SATO, Tetsuya	Keio Univ.
ISHII, Fumiyuki	Kanazawa Univ.
TATETSU, Yasutomi	Meio Univ.
YANAGISAWA, Susumu	Univ. of the Ryukyus
SHUDO, Ken-ichi	Yokohama Natl. Univ.
OHMURA, Satoshi	Hiroshima Inst. Tech.
NOGUCHI, Yoshifumi	Shizuoka Univ.
NAKAMURA, Kazuma	Kyushu Inst. Tech.

GOHDA, Yoshihiro	Tokyo Tech.
HAMADA, Ikutaro	Osaka Univ.
RAEBIGER, Hannes	Yokohama Natl. Univ.
WATANABE, Hiroshi	Keio Univ.
TADA, Tomofumi	Tokyo Tech.
TODO, Syngé	Univ. of Tokyo

1.4 Staff

The following staff members of the SCC-ISSP usually administrate the ISSP Supercomputer.

KAWASHIMA, Naoki	Professor (Chair person)
NOGUCHI, Hiroshi	Associate Professor
OZAKI, Taisuke	Professor
SUGINO, Osamu	Professor
IDO, Kota	Research Associate
FUKUDA, Masahiro	Research Associate
HIGUCHI, Yuji	Research Associate
KAWAMURA, Mitsuaki	Research Associate
MORITA, Satoshi	Research Associate
YOSHIMI, Kazuyoshi	Project Researcher
MOTOYAMA, Yuichi	Project Researcher
YATA, Hiroyuki	Technical Associate
FUKUDA, Takaki	Technical Associate
ARAKI, Shigeyuki	Technical Associate

2 STATISTICS (SCHOOL YEAR 2019)

2.1 System and User Statistics

In the following, we present statistics for operation time taken in the period from April 2019 to March 2020 (SY 2019). In Table 2, we show general statistics of the supercomputer system in SY 2019. The total numbers of compute nodes in System B and System C are 1891 and 252, respectively. Consumed disk points amount to about 3% and 2% of the total consumed points in System B and System C, respectively.

In the left column of Fig. 2, availabilities, utilization rates, and consumed points in Systems B and C are plotted for each month. Throughout the school year, the utilization rates were very high, exceeding 80% throughout most of the year.

The user statistics are shown in the right column of Fig. 2. The horizontal axis shows the rank of the user/group arranged in the descending order of the execution time (hour \times nodes). The execution time of the user/group of the first rank is the longest. The vertical axis shows the sum of the execution time up to

Table 2: Overall statistics of SY 2019

	System B	System C
total service time ($\times 10^3$ node-hours)	16242	2165
number of executed jobs	756817	51444
total consumed points ($\times 10^3$ point)	656	59
CPU points ($\times 10^3$ point)	635	58
disk points ($\times 10^3$ point)	21	1
total exec. time ($\times 10^3$ node-hours)	14529	1843
availability	98.04%	98.06%
utilization rate	89.39%	85.13%

the rank. From the saturation points of the graphs, the numbers of “active” users of Systems B and C are around 400 and 100, respectively. The maximum ranks in the graphs correspond to the number of the users/groups that submitted at least one job.

2.2 Queue and Job Statistics

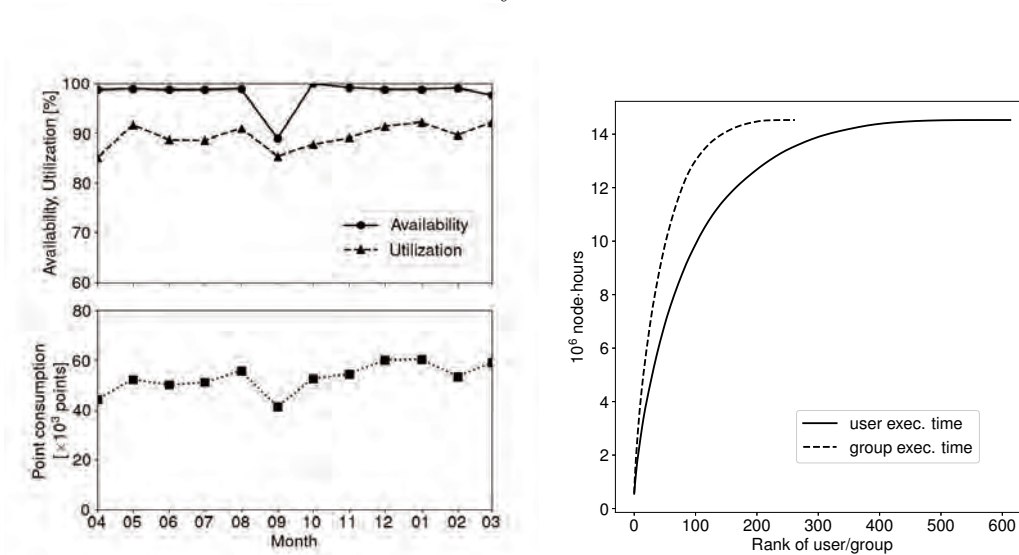
Queue structures of Systems B and C in SY2019 are shown in Table 3. In System B, users can choose from three types of compute nodes; jobs submitted to queues with “cpu”, “acc”, and “fat” at the end of their queue names are submitted to CPU, ACC, and Fat nodes, respectively, while only CPU nodes are available in System C. See Sec. 1.1 for a description of each type of compute node. The user then has to choose the queue according to the number of nodes to use and the duration of their calculation jobs. Queue names starting with “F” are for jobs taking 24 hours or less, while those starting with “L” can run much longer up to 120 hours. More nodes are allotted to “F” queues in order to maximize the turnaround time of user jobs. The queue names starting with “i” are used for interactive debugging of user programs and the elapsed time limit is 30 minutes. The number following “F”, “L”, or “i” correspond to the number of nodes that can be used by one user job. Note that F/B72acc queue were abolished in November 2018.

To prevent overuse of the storage, points are charged also for usage of disk quota in the three systems, as shown in Table 4. Disk points are revised often for optimal usage of the resources by examining usage tendencies each year.

Although we do not mention here in detail, to promote utilization of the massively parallel supercomputer, background queues for system B (“B4cpu”, “B36cpu”, “B144cpu”, “B18acc”, and “B2fat”) and background queues for system C (“B4cpu”, “B9cpu”, “B36cpu”) which charge no points for the jobs have also been open.

The number of jobs, average waiting time, and total execution time in each

System B



System C

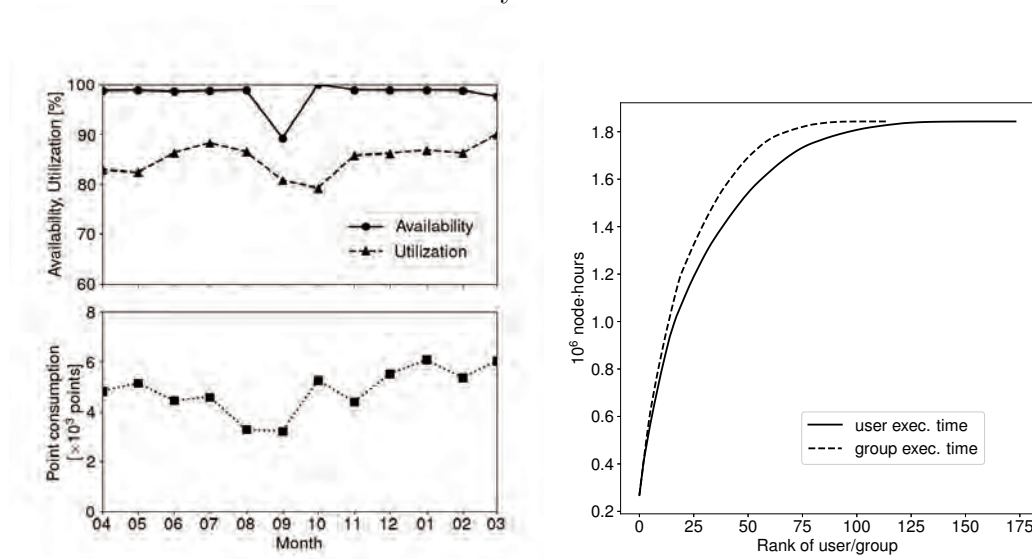


Figure 2: Left: Availabilities, utilization rates and point consumptions of each month during SY 2019. Right: User statistics. The horizontal axis shows the rank of the user/group arranged in the descending order of the execution time (hour \times nodes). The vertical axis shows the sum of the execution time up to the rank.

queue are shown in Table 5. In System B, a large portion of jobs have been executed in “F” queues. The largest amount of the execution time has been consumed in the large-scale “F144cpu” queue, but substantial number of jobs were run in every queue, suggesting that a wide variety of user needs are met by this queuing scheme. In most of these queues, the queue settings meet the user’s tendencies in that the waiting times are on the order of the elapsed-time limit.

2.3 Project for Advancement of Software Usability in Materials Science

From School Year 2015, the supercomputer center (SCC) has started “Project for advancement of software usability in materials science”. In this project, for enhancing the usability of the supercomputer system in ISSP, we perform some software-advancement activity such as implementing a new function to an existing code, releasing a private code on Web, writing manuals. Target programs are publicly offered in December and selected in the review by the Steering Committee of SCC. The projects are carried out by the software development team composed of three members in ISSP. In SY 2019, two projects were selected as listed in Table 6.

2.4 GPGPU Support Service

As noted in Sec. 1.1, ACC nodes with graphics processing units (GPU) were introduced in System B in School Year 2015. Since GPUs were introduced in the ISSP Supercomputer center for the first time, many programs developed or utilized by users of this center have not been programmed for GPU computing. To help users take advantage of GPUs, the supercomputer center has started a service for porting users’ materials science software to General Purpose GPUs (GPGPU). After a call for proposals (which will usually be in December), target programs for the next school year are selected by the Steering Committee of SCC. The porting service is carried out on each program for about two months; the coding is performed by engineers from the computer vendor supplying the ISSP supercomputer system, and ISSP staff oversee the progress of the project and manage necessary communications with the proposer. Copyrights of the resulting software basically belong to the proposers, but the supported contents might be published under agreement with the proposer. In SY 2019, one project was selected as listed in Table 7.

Acknowledgments

The staffs would like to thank Prof. Takafumi Suzuki (now at University of Hyogo) for developing WWW-based system (SCM: SuperComputer Management System) for management of project proposals, peer-review reports by the SPAC committee, and user accounts. We also thank Ms. Reiko Iwafune for creating and maintaining a new WWW page of the ISSP Supercomputer Center.

Table 3: Queue structures in SY 2019

System B					
queue name	Elapsed time limit (hr)	# of nodes /job	# of nodes /queue	Memory limit (GB)	job points / (node·day)
F4cpu	24	1–4	216	120/node	1
L4cpu	120	1–4	108	120/node	1
F36cpu	24	5–36	288	120/node	1
L36cpu	120	5–36	144	120/node	1
F144cpu	24	37–144	1008	120/node	$72(144)/(\# \text{ of nodes})^*$
L144cpu	120	37–144	144	120/node	$72(144)/(\# \text{ of nodes})^*$
i18cpu	0.5	1–18	72	120/node	1
F18acc	24	1–18	180	120/node	2
L18acc	120	1–18	90	120/node	2
i9acc	0.5	1–9	36	120/node	2
F2fat	24	1–2	17	1000/node	4
L2fat	120	1–2	6	1000/node	4
i1fat	0.5	1	2	1000/node	4

* For F/L144cpu queue, the number of occupied node increases in increments of 72 nodes.

System C					
queue name	Elapsed time limit (hr)	# of nodes /job	# of nodes /queue	Memory limit (GB)	job points / (node·day)
F4cpu	24	1–4	54	170/node	1
L4cpu	120	1–4	18	170/node	1
i4cpu	0.5	1–4	18	170/node	1
F9cpu	24	5–9	36	170/node	1
L9cpu	120	5–9	18	170/node	1
F36cpu	24	10–36	144	170/node	$18(36)/(\# \text{ of nodes})^*$
L36cpu	120	10–36	36	170/node	$18(36)/(\# \text{ of nodes})^*$

* For F/L36cpu queue, the number of occupied node increases in increments of 18 nodes.

Table 4: Disk points of Systems B and C

		point/day
System B	/home	$0.001 \times \theta(q - 300)$
	/work	$0.0001 \times \theta(q - 3000)$
System C	/home	$0.001 \times \theta(q - 150)$
	/work	$0.0001 \times \theta(q - 1500)$

* q is denoted in unit of GB.

* $\theta(x)$ is equal to the Heaviside step function $H(x)$ multiplied by x , i.e., $xH(x)$.

Table 5: Number of jobs, average waiting time, total execution time, and average number of used nodes per job in each queue.

System B				
queue	# of Jobs	Waiting Time (hour)	Exec. Time ($\times 10^3$ node·hour)	# of nodes
F4cpu	169958	12.85	1223.79	1.38
L4cpu	9051	26.04	570.60	1.71
F36cpu	26234	30.71	1342.06	8.54
L36cpu	2295	64.56	812.25	9.57
F144cpu	9950	33.30	7208.66	90.65
L144cpu	194	83.32	829.66	109.86
i18cpu	76809	0.52	106.56	8.74
F18acc	201751	3.93	831.48	3.07
L18acc	6661	11.86	536.87	3.28
i9acc	6519	0.15	2.31	3.94
F2fat	7310	24.27	75.56	1.28
L2fat	753	30.50	26.75	1.37
i1fat	3504	0.22	0.54	1.00

System C				
queue	# of Jobs	Waiting Time (hour)	Exec. Time ($\times 10^3$ node·hour)	# of nodes
F4cpu	25640	12.06	268.51	1.54
L4cpu	1718	79.26	110.23	1.61
i4cpu	10297	0.06	2.86	2.63
F9cpu	2863	40.39	159.26	7.43
L9cpu	203	31.61	46.64	6.36
F36cpu	2588	19.52	652.58	24.94
L36cpu	130	70.88	160.24	24.37

Table 6: List of Project for advancement of software usability in materials science for SY 2019.

Project Proposer	Project Name
Shusuke Kasamatsu Yamagata University	Coupling of extended ensemble sampling and first-principles solvers
Naoki Kawashima The University of Tokyo	Tensor Network Solver for Quantum Lattice Problems

Table 7: List of supported software and project proposers for the GPGPU support service for SY 2019.

Project Proposer	Project Name
Junya Otsuki Okayama University	GPU acceleration of matrix calculations in the solver of Bethe-Salpeter equation

3 RESEARCH REPORTS

3.1 Invited Articles

First-Principles Calculation of Thermophysical Properties
of Solids with Strong Phonon Anharmonicity 15

Terumasa TADANO

Development of Open-Source Parallelized Tensor Network
Softwares: mptensor and TeNeS 25

Satoshi MORITA and Naoki KAWASHIMA

Disorder-Free Glass Transitions of Spins and Orbitals
in a Frustrated Pyrochlore Magnet 35

Kota MITSUMOTO, Chisa HOTTA, and Hajime YOSHINO

First-principles calculation of thermophysical properties of solids with strong phonon anharmonicity

Terumasa TADANO

*Research Center for Magnetic and Spintronic Materials,
National Institute for Materials Science (NIMS),
Sengen, Tsukuba, Ibaraki 305-0047*

Abstract

Optimizing thermophysical properties of solids, including thermal expansion, thermal conductivity, and thermodynamic stability is crucial for developing energy- or light-harvesting material that shows a high device performance at operating temperatures. To achieve a simulation-guided design of such materials, lattice vibration (phonon excitation) needs to be modeled accurately beyond the quasi-harmonic level. In recent years, several important theoretical and technical improvements have been made in the field of *ab initio* phonon calculation. These methods have overcome the limitation of the conventional phonon calculation method and further strengthened the predictive power of first-principles calculations based on density functional theory. In this report, we review some of the new computational approaches and demonstrate their validity through applications to a hydrogen-rich superconductor and thermoelectric materials in which phonons are strongly anharmonic.

1 Introduction

Predicting and understanding thermophysical properties of solids only from the crystal structure is crucial for achieving a simulation-guided design of high-performance energy- and light-harvesting materials including but not limited to thermoelectric, photovoltaic, and superconducting materials. For example, lattice thermal conductivity, κ_L , needs to be reduced to achieve a high thermoelectric figure-

of-merit ZT . Also, the critical temperature (T_c) of ferroelectric phase transition plays a crucial role in realizing a giant dielectric constant of polar semiconductors at ambient temperature, as exemplified by the commercially used BaTiO₃-based ceramics. Since these finite-temperature thermophysical properties are characterized by the thermal and quantum fluctuation of nuclei, it is necessary to consider the excitation of phonons for achieving a meaningful prediction.

First-principles phonon calculation is performed actively and routinely based on density functional theory (DFT). In most cases, the harmonic approximation (HA) is adapted, assuming that the atomic displacements are much smaller than interatomic distances. While the HA gives reasonable phonon dispersion curves and thermodynamic quantities for many semiconductors and metals, it often becomes inaccurate and sometimes breaks down completely for high-performance thermoelectric and dielectric materials where the atomic displacements can be as large as 10% of an interatomic distance. Moreover, the HA obviously fails to describe physical properties related to the anharmonicity of the potential, including phonon-phonon scattering and structural phase transition. To solve these limitations of the HA, a more advanced phonon calculation method that can include phonon anharmonicity is required.

In the last few decades, several new *ab initio* phonon calculation methods have been proposed as an efficient way to include anharmonic effects [1–7]. Among them, the self-consistent

phonon (SCP) based approaches [3–7] are particularly important because they enable us to access finite-temperature phonon frequencies and polarization vectors as well as T_c values of structural phase transition [8, 9]. Also, the recent advances in thermal transport theory are noteworthy [10, 11]. The advent of these new methods, as well as their efficient implementations in open-source software, have opened up a way to study complicated lattice dynamics in emergent materials and to predict finite-temperature thermophysical properties that cannot be reached by the conventional method.

In this short report, we introduce the basics of the new phonon calculation methods and demonstrate their validity through applications to a hydrogen-rich superconductor, thermoelectric clathrate, and thermoelectric tetrahedrite.

2 Recent progress of *ab initio* phonon calculation

Self-consistent phonon theory

The self-consistent phonon (SCP) theory, which was originally developed by Hooton [12], aims to calculate phonon frequencies and polarization vectors that are renormalized by anharmonicity of the potential. In this theory, an existence of a well-defined *effective* one-body Hamiltonian

$$\mathcal{H}_0 = \sum_{\mathbf{q}\nu} \hbar \Omega_{\mathbf{q}\nu} \left(b_{\mathbf{q}\nu}^\dagger b_{\mathbf{q}\nu} + \frac{1}{2} \right) \quad (1)$$

is assumed. Here, \mathbf{q} and ν are the momentum and branch index of phonons, respectively, and $b_{\mathbf{q}\nu}^\dagger$ ($b_{\mathbf{q}\nu}$) is creation (annihilation) operator of the phonon $\mathbf{q}\nu$. The frequency $\Omega_{\mathbf{q}\nu}$ is the *effective* frequency that is renormalized by anharmonic effects; therefore, its value differs from the harmonic frequency $\omega_{\mathbf{q}\nu}$. In addition, since the *effective* polarization vectors $\{\epsilon_{\mathbf{q}\nu}\}$ are also different from the harmonic ones $\{e_{\mathbf{q}\nu}\}$, b^\dagger and b in Eq. (1) differ from the creation and annihilation operators of the harmonic Hamiltonian H_0 .

Now, let us consider how to determine $\Omega_{\mathbf{q}\nu}$ and $\{\epsilon_{\mathbf{q}\nu}\}$. To this end, we introduce the exact Hamiltonian H and associated density operator $\rho_H =$

$e^{-\beta H} / \text{Tr}(e^{-\beta H})$, with $\beta = 1/kT$. The Hamiltonian H includes all anharmonic terms; therefore, it may be written as $H = H_0 + U_3 + U_4 + \dots$ where U_n is the potential energy of the n th-order anharmonicity. By using H and ρ_H , the exact Helmholtz free-energy is given as

$$F_H = \text{Tr}(\rho_H H) + \frac{1}{\beta} \text{Tr}(\rho_H \ln \rho_H). \quad (2)$$

Next, let us substitute a trial density matrix defined as $\rho_{\mathcal{H}_0} = e^{-\beta \mathcal{H}_0} / \text{Tr}(e^{-\beta \mathcal{H}_0})$ for ρ_H in Eq. (2). We then obtain $F_H(\mathcal{H}_0) = \text{Tr}(\rho_{\mathcal{H}_0} H) + \frac{1}{\beta} \text{Tr}(\rho_{\mathcal{H}_0} \ln \rho_{\mathcal{H}_0})$. By using the Jensen's inequality $e^{\langle X \rangle} \leq \langle e^X \rangle$, it is straightforward to show the following Feynman–Gibbs–Bogoliubov inequality holds:

$$F_H \leq F_H(\mathcal{H}_0). \quad (3)$$

In the SCP theory, $\Omega_{\mathbf{q}\nu}$ and $\{\epsilon_{\mathbf{q}\nu}\}$ are determined so that the right-hand side of Eq. (3) is minimized. This is nothing but a mean-field approximation. Indeed, the SCP theory is a phonon version of the Hartree–Fock theory.

The minimization of $F_H(\mathcal{H}_0)$ can be performed by repeatedly calculating atomic forces in supercells with stochastically sampled atomic configurations and updating the variational parameters in \mathcal{H}_0 [5]. An alternative approach we have developed is to derive the SCP equation via the condition of $\partial F_H(\mathcal{H}_0) / \partial X_i = 0$, where X_i comprises all variational parameters including $\Omega_{\mathbf{q}\nu}$ and $\{\epsilon_{\mathbf{q}\nu}\}$. For the brevity of the explanation, let us assume that the polarization vectors do not change by anharmonic effects. Also, we consider the anharmonic terms up to the fourth-order because fifth- and higher-order terms are less significant. We then obtain the following SCP equation [6, 13]:

$$\Omega_{\mathbf{q}\nu}^2 = \omega_{\mathbf{q}\nu}^2 + \frac{1}{2} \sum_{\mathbf{q}_1\nu_1} \Phi(\mathbf{q}\nu; -\mathbf{q}\nu; \mathbf{q}_1\nu_1; -\mathbf{q}_1\nu_1) \times \frac{\hbar[1 + 2n(\Omega_{\mathbf{q}_1\nu_1})]}{2\Omega_{\mathbf{q}_1\nu_1}}. \quad (4)$$

The second term on the right-hand side is the renormalization term associated with the quartic anharmonicity, whose magnitude is proportional to the mean-square displacement of normal coordinate

$\langle Q_{q\nu}^* Q_{q\nu} \rangle = \hbar[1 + 2n(\Omega_{q\nu})]/2\Omega_{q\nu}$ with $n(\omega)$ being the Bose–Einstein distribution function. Since $n(\omega)$ is temperature dependent, the *effective* frequency $\Omega_{q\nu}$ also changes as a function of temperature.

We have shown that Eq. (4) gives phonon dispersion curves of cubic SrTiO₃ that agree well with the results of inelastic neutron scattering measurements. Once we compute all quartic coefficients $\Phi(\mathbf{q}\nu; -\mathbf{q}\nu; \mathbf{q}_1\nu_1; -\mathbf{q}_1\nu_1)$ in Eq. (4), the *effective* frequencies at various temperatures can be obtained quickly. To compute the quartic coefficients, we first calculate the real-space fourth-order interatomic force constants (IFCs) in a supercell. Then, the real-space IFCs are transformed into the normal coordinate representation $\Phi(\mathbf{q}\nu; -\mathbf{q}\nu; \mathbf{q}_1\nu_1; -\mathbf{q}_1\nu_1)$. The computational complexity of this transformation is $\mathcal{O}(N_q^{\text{irred.}} N_{q_1} N_\nu^2)$, where $N_q^{\text{irred.}}$ is the number of irreducible sets of \mathbf{q} points, N_{q_1} is the number of \mathbf{q}_1 points, and N_ν is the number of phonon branches. When we consider the anharmonic mixing of polarization vectors, we also need to compute the off-diagonal elements of the quartic coefficients. In that case, the computational complexity becomes $\mathcal{O}(N_q^{\text{irred.}} N_{q_1} N_\nu^4)$. In our implementation of Eq. (4) in ALAMODE [14], we use a hybrid parallelization of MPI and OpenMP. With this implementation, the SCP calculation has been successfully performed even for complex structures. For example, a SCP calculation of thermoelectric clathrate Ba₈Ga₁₆Ge₃₀ ($N_\nu = 162$, $N_q^{\text{irred.}} N_{q_1} = 1$) with the polarization mixing finishes within 10 hours when we use 432 CPU cores of ISSP system B (sekirei).

Phonon scattering

While the SCP method can compute anharmonic phonon frequencies and polarization vectors efficiently, it is still based on a non-interacting picture [Eq. (1)]. Therefore, the phonon linewidth is zero, which leads to the unphysical result that the phonon lifetime and lattice thermal conductivity are infinite. To solve this problem, phonon scattering processes must be considered. In bulk semi-

conductors, the most dominant source of phonon scatterings is the phonon-phonon scattering associated with the lattice anharmonicity. In the low-temperature region, other scattering processes, including phonon-impurity scattering and phonon-boundary scattering, also become relevant. However, *ab initio* treatment of these extrinsic phonon scatterings is still challenging. Therefore, we will focus on the intrinsic phonons scattering below.

The intrinsic scattering rate of phonons can be obtained by applying many-body perturbation theory to the anharmonic Hamiltonian. Here, the lowest-order perturbation term is the cubic anharmonicity U_3 . The unperturbed Hamiltonian may be the true harmonic Hamiltonian H_0 , only if all phonons are dynamically stable ($\omega_{q\nu}^2 > 0$), or the *effective* one-body Hamiltonian \mathcal{H}_0 obtained by an SCP calculation. When we use H_0 as the unperturbed Hamiltonian, the phonon self-energy of the bubble, which gives a first-order correction, is given as [15]

$$\Sigma_{q\nu}^{(B)}(i\omega_m) = \frac{1}{16} \sum_{\mathbf{q}_1 \mathbf{q}_2} \sum_{\nu_1 \nu_2} \frac{\hbar |\Phi(-\mathbf{q}\nu; \mathbf{q}_1\nu_1; \mathbf{q}_2\nu_2)|^2}{\omega_{q\nu} \omega_{\nu_1} \omega_{\nu_2}} \times \Delta(-\mathbf{q} + \mathbf{q}_1 + \mathbf{q}_2) f(1, 2, i\omega_m), \quad (5)$$

$$f(1, 2, i\omega_m) = \sum_{\sigma=\pm 1} \sigma \left[\frac{1 + n_1 + n_2}{i\omega_m + \sigma(\omega_1 + \omega_2)} - \frac{n_1 - n_2}{i\omega_m + \sigma(\omega_1 - \omega_2)} \right], \quad (6)$$

where $\omega_m = 2\pi m/\beta\hbar$. Here, for the brevity of the notation, we represent $\omega_{\mathbf{q}_1\nu_1}$ as ω_1 and $n(\omega_1)$ as n_1 . The function $\Delta(\mathbf{q})$ in Eq. (5) becomes 1 when \mathbf{q} is an integral multiple of the reciprocal lattice vector \mathbf{G} and 0 otherwise. Therefore, the double loop over \mathbf{q} points in Eq. (5) can be reduced to a single loop. After performing an analytic continuation to the real axis, we obtain the phonon linewidth as $\Gamma_{q\nu}^{(B)} = \text{Im}\Sigma_{q\nu}^{(B)}(\omega_{q\nu})$ and the phonon frequency shift as $\Delta_{q\nu}^{(B)} = -\text{Re}\Sigma_{q\nu}^{(B)}(\omega_{q\nu})$.

In many semiconductors, the linewidth calculated from $\Gamma_{q\nu}^{(B)}$ shows reasonable agreement with experimental data, including its linear temperature-dependence in the high-temperature range. However, in some cases, the theoretical value may un-

derestimate the experimental linewidth most likely due to the presence of additional scattering channels of phonons, including phonon-impurity scattering and higher-order phonon-phonon scatterings. Recently, the self-energies of these additional scattering processes have been evaluated based on DFT for relatively simple systems and reported to be important in correctly understanding the thermal transport behavior [16, 17], which is the main topic of the next subsection.

Thermal transport

First-principles calculation of κ_L has been an active research topic in recent years because its active control would lead to efficient energy conversion and thermal management devices. In particular, significant effort has been placed on elucidating the atomistic-level origin of ultralow thermal conductivity of efficient thermoelectric materials such as intermetallic clathrates and SnSe. To compute κ_L from first principles, the semi-classical Peierls–Boltzmann theory (PBT) is usually adopted. In the PBT, we first assume that the heat flux is carried by phonon quasiparticle; therefore, the heat flux operator is approximated as

$$\hat{j}_{\text{ph}} = \sum_{q\nu} \hbar\omega_{q\nu} \mathbf{v}_{q\nu} b_{q\nu}^\dagger b_{q\nu}. \quad (7)$$

Here, $\mathbf{v}_{q\nu} = \partial\omega_{q\nu}/\partial\mathbf{q}$ is the group velocity of phonon, which is readily obtained from the phonon dispersion curves. Then, after introducing the single-mode relaxation-time approximation, we obtain the thermal conductivity tensor

$$\kappa_{\text{P}} = \sum_{q\nu} c_{q\nu} \mathbf{v}_{q\nu} \otimes \mathbf{v}_{q\nu} \tau_{q\nu}, \quad (8)$$

with $c_{q\nu}$ being the mode specific heat. The phonon lifetime $\tau_{q\nu}$ can be obtained from the phonon linewidth as $\tau_{q\nu} = \hbar/(2\Gamma_{q\nu})$. When we consider the dominant bubble self-energy for $\Gamma_{q\nu}$, the thermal conductivity shows the temperature dependence of $\kappa_L \propto T^{-1}$ in the high-temperature range, in accord with many experimental observation. So far, the PBT-based calculations have been performed for many thermoelectric materials and

explained their thermal transport behavior successfully.

While the PBT has been successful for many crystalline solids, it fails to describe the temperature profile of κ_L observed in amorphous solids and other disordered solids. In these systems, the thermal conductivity shows little temperature dependence and does not decrease even in the high-temperature region. To understand thermal transport physics in disordered solids, a beyond PBT treatment would be necessary. One of the most problematic assumptions made within the PBT formalism is the approximation of Eq. (7). More specifically, when we express the harmonic heat flux operator $\hat{j}^{(2)}$ with the creation and annihilation operators of phonons, we obtain the band diagonal and off-diagonal terms as follows:

$$\begin{aligned} \hat{j}^{(2)} &= \sum_{q\nu\nu'} \frac{\hbar(\omega_{q\nu} + \omega_{q\nu'})}{2} \mathbf{v}_{q\nu\nu'} b_{q\nu}^\dagger b_{q\nu'} \\ &= \hat{j}_{\text{ph}} + \sum_{q\nu \neq \nu'} \frac{\hbar(\omega_{q\nu} + \omega_{q\nu'})}{2} \mathbf{v}_{q\nu\nu'} b_{q\nu}^\dagger b_{q\nu'}. \end{aligned} \quad (9)$$

Here, $\mathbf{v}_{q\nu\nu'}$ is the band off-diagonal extension of the group velocity. In the PBT, the band off-diagonal terms of the heat flux operator is omitted. In the pioneering work by Allen and Feldman [18, 19], however, they showed that the off-diagonal contribution is dominant in the disordered solids and successfully explained the temperature-dependence of κ_L observed in amorphous silicon. In the Allen–Feldman (AF) theory, however, the effect of phonon scattering is not considered. Therefore, their theory is still not suited for studying thermal transport in disordered solids that also show strong anharmonicity.

Recently, a new thermal transport theory that unifies the PBT and the AF theory has been developed [10]. According to their result, the thermal conductivity is given as

$$\kappa_L = \kappa_{\text{P}} + \kappa_{\text{C}}, \quad (10)$$

where κ_{P} is the Peierls term defined by Eq. (8), and κ_{C} is the coherent term associated with the inter-band components of the heat flux operator, which

is given as

$$\kappa_C = \sum_{\mathbf{q}} \sum_{\nu \neq \nu'} \frac{c_{q\nu}\omega_{q\nu'} + c_{q\nu'}\omega_{q\nu}}{\omega_{q\nu} + \omega_{q\nu'}} \mathbf{v}_{q\nu\nu'} \otimes \mathbf{v}_{q\nu'\nu} \times \frac{\Gamma_{q\nu} + \Gamma_{q\nu'}}{(\omega_{q\nu} - \omega_{q\nu'})^2 + (\Gamma_{q\nu} + \Gamma_{q\nu'})^2}. \quad (11)$$

While this new theory has been tested only for a few systems so far, it is expected to improve the prediction accuracy of κ_L and help us deepen our understanding of anomalous thermal transport in strongly anharmonic and/or disordered materials.

Efficient calculation of force constants

So far, we have introduced the state-of-the-art *ab initio* phonon calculation methods. To study phonon-related properties by using these methods, the harmonic, cubic, and quartic IFCs are necessary as inputs. These IFCs can be estimated by repeatedly calculating atomic forces in a supercell with suitably chosen atomic configurations. In the conventional supercell approach, only a few atoms in a supercell are displaced. For instance, the harmonic IFC between atom i and j , Φ_{ij} , is estimated as $\Phi_{ij} = -[F_j(u_i = +h) - F_j(u_i = -h)]/2h$, where $F_j(u_i = \pm h)$ represents the atomic force acting on the atom j when the atom i is displaced slightly ($h \approx 0.01 \text{ \AA}$) from its equilibrium position. This procedure needs to be repeated for all irreducible ij pairs. To estimate the cubic IFC, Φ_{ijk} , in the same fashion, we need to consider, at most, four displacement patterns for each element. Therefore, the number of displacement patterns necessary to obtain all relevant IFCs increases rapidly for the higher-order terms, and the calculation of quartic IFCs would be infeasible or extremely expensive if possible.

To mitigate this issue, we employ the compressive sensing approach [20, 21]. First, to increase the information density obtained from a single DFT calculation, we displace all atoms in a supercell in random directions. For these sampled atomic configurations, we compute the atomic forces; these displacement-force data sets will be served as training data sets of a linear model. Second, instead of

calculating the IFC one by one by the central difference, we estimate all IFCs simultaneously by performing linear regression. Since the atomic forces \mathbf{F} can be expressed as a linear function of IFCs Φ as $\mathbf{F} = A\Phi$ with A being a sensing matrix comprising atomic displacements, we can estimate the parameter vector Φ by using ordinary least-squares or other regression methods. In particular, the L_1 penalized regression models such as LASSO are useful because they select and compute physically important IFCs somewhat automatically and set the other irrelevant parameters exactly zero.

We have applied LASSO to various systems and tested its performance. As shown in Fig. 1, the number of static DFT calculations could be reduced dramatically from what would be required if the conventional approach were used. In these LASSO calculations, we gradually increased the training data sets and the cutoff radii of interaction until we obtained an accurate model that reproduces the DFT forces within $\sim 5\%$ error. The numbers shown for the conventional method are estimated by symmetry argument, where anharmonic IFCs up to the fourth-order are considered within the cutoff radii as the LASSO calculation. The efficient approach, which can be 100 times as efficient as the conventional one, enables us to perform the SCP and PBT calculations of complex systems.

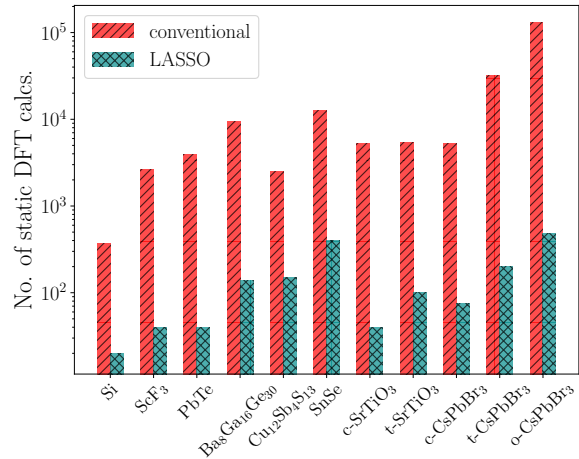


Figure 1: Number of displacement patterns that was used to extract IFCs by LASSO (cyan) compared with the estimated number of patterns required by the conventional approach (red).

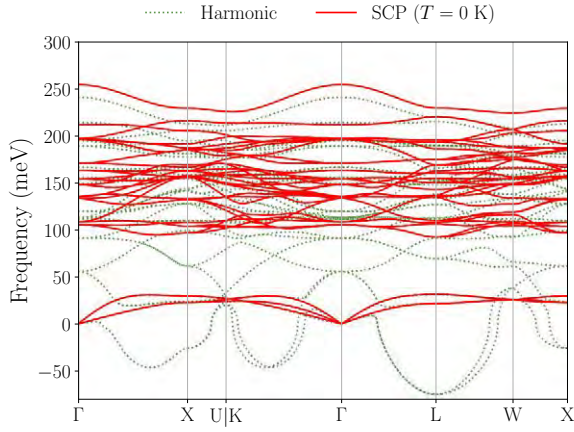


Figure 2: Phonon dispersion curves of $Fm\bar{3}m$ - LaH_{10} at 150 GPa calculated within the HA and the SCP theory at $T = 0$ K.

3 Applications

Quantum fluctuation in record superconductor LaH_{10}

Recently, record superconductivity at ~ 250 K has been reported for LaH_{10} under the high pressure of 137–218 GPa [22, 23]. The possibility of the high- T_c superconductivity in LaH_{10} was first predicted by DFT calculations [24, 25] and subsequently confirmed experimentally. In the previous DFT predictions, a sodalite-like structure of LaH_{10} with space group $Fm\bar{3}m$ has been suggested as a crystal structure that realizes a high- T_c . However, if the phase stability is evaluated based on enthalpy, LaH_{10} is predicted to be thermodynamically unstable against decomposition below 200 GPa. Moreover, $Fm\bar{3}m$ - LaH_{10} is predicted to be dynamically unstable over the whole pressure range where a ~ 250 K T_c has been observed experimentally. These contradictions likely indicate the limitation of the conventional computational approaches.

To solve this puzzle, we have performed phonon calculations of LaH_{10} with including anharmonic effects [26]. Figure 2 shows the phonon dispersion of $Fm\bar{3}m$ - LaH_{10} calculated within the HA and the SCP theory at 150 GPa. The $Fm\bar{3}m$ structure is dynamically unstable when the HA is employed, indicating the $Fm\bar{3}m$ structure distorts into a low-symmetry structure. Indeed, we have

confirmed that the enthalpies of $R\bar{3}m$ - and $C2$ - LaH_{10} are lower than that of $Fm\bar{3}m$ - LaH_{10} by ~ 50 meV per formula unit (f.u.) at 150 GPa. However, this conclusion changes when we consider the zero-point motion of hydrogen atoms. As shown in Fig. 2, the quartic anharmonicity renormalizes phonon frequencies significantly and stabilizes the phonons in the entire Brillouin zone even at $T = 0$ K, which is possible due to the large zero-point motion of hydrogen atoms. After obtaining the stable phonons, we have also estimated the zero-point energy (ZPE) and evaluated the relative stability of the $Fm\bar{3}m$ structure over the distorted phases based on enthalpy+ZPE. As a result, the $Fm\bar{3}m$ phase is found to be stable than the $R\bar{3}m$ structure by ~ 110 meV / f.u., which agrees better with the experimental observation. The inclusion of the ZPE also changes the thermodynamic stability of $Fm\bar{3}m$ - LaH_{10} . For example, the formation enthalpy defined as

$$\Delta H[\text{LaH}_{10}] = H[\text{LaH}_{10}] - \frac{7}{8}H[\text{LaH}_{11}] - \frac{1}{8}H[\text{LaH}_3] \quad (12)$$

is about 140 meV/f.u. at 200 GPa, indicating that LaH_{10} decomposes into LaH_3 ($Cmcm$) and LaH_{11} ($P4/nmm$). However, this conclusion changes when we consider the ZPE additionally; the formation enthalpy becomes negative as $\Delta H + \Delta \text{ZPE} = -280$ meV/f.u.

To summarize, our calculations have clearly shown that the large quantum fluctuation of hydrogen nuclei plays a crucial role in stabilizing the highly-symmetric $Fm\bar{3}m$ - LaH_{10} over the wide pressure range of 137–218 GPa. We have also calculated the superconducting T_c based on the Migdal–Eliashberg theory and obtained an excellent agreement with the experimental values obtained for LaH_{10} and LaD_{10} [26]. This agreement further confirms that the $Fm\bar{3}m$ phase of LaH_{10} is indeed responsible for the record superconductivity at ~ 250 K.

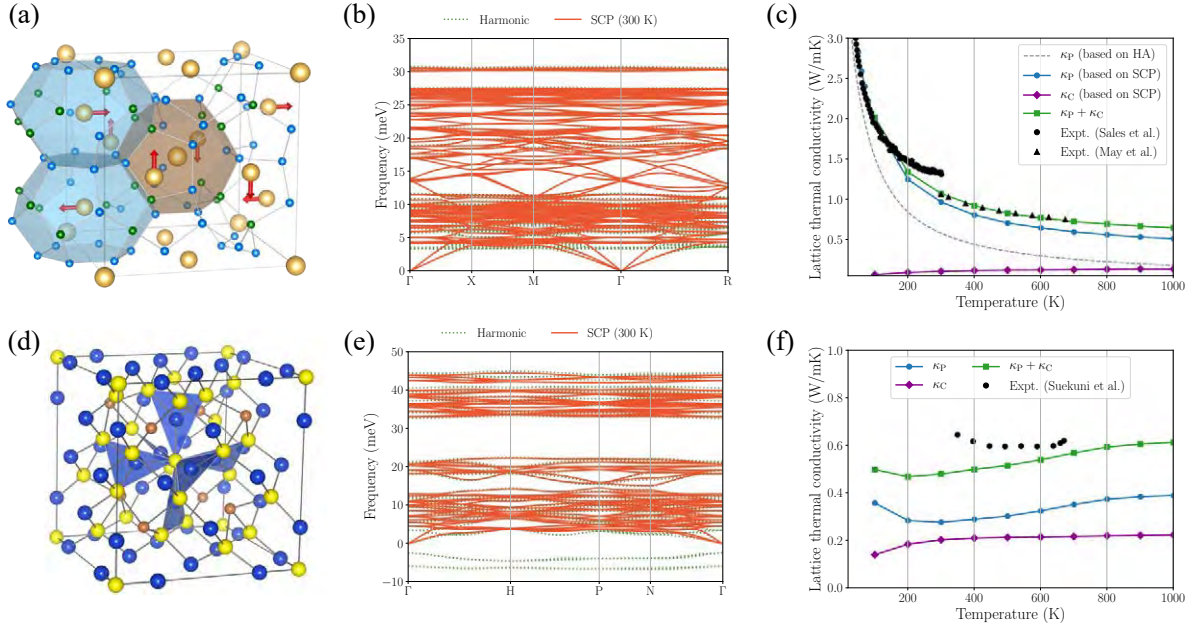


Figure 3: Crystal structures and phonon properties of thermoelectric clathrate $\text{Ba}_8\text{Ga}_{16}\text{Ge}_{30}$ (BGG) and tetrahedrite $\text{Cu}_{12}\text{Sb}_4\text{S}_{13}$. (a) Crystal structures of (a) BGG, adopted from Ref. [27], and (d) tetrahedrite. (b,e) Phonon dispersion curves of BGG and tetrahedrite, respectively, calculated within the HA (dotted lines) and the SCP method at 300 K (solid lines). (c,f) Thermal conductivities of BGG and tetrahedrite, respectively, calculated by different methods. For comparison, the experimental values of Refs. [28–30] are also shown.

Thermal conductivity in complex thermoelectric materials

The thermal transport in complex thermoelectric materials has attracted special attention not only because their thermal conductivity is unusually low but because they sometimes show a *glasslike* temperature dependence even though they possess periodic crystal structures. In this report, we will focus on the origin of the unusual temperature dependence of κ_L observed in type-I clathrate $\text{Ba}_8\text{Ga}_{16}\text{Ge}_{30}$ (BGG) and tetrahedrite $\text{Cu}_{12}\text{Sb}_4\text{S}_{13}$, whose crystal structures are shown in Figs. 3 (a) and (d). In our previous study [31], we have shown that the low- κ_L value of BGG can be attributed to the strong phonon-phonon scattering induced by the presence of low-frequency optical phonons. We could successfully reproduce the experimental κ_L values up to ~ 100 K by using Eq. (8). However, the temperature dependence weaker than $\kappa_L \propto T^{-1}$ could not be explained by the conventional PBT. In $\text{Cu}_{12}\text{Sb}_4\text{S}_{13}$, κ_L is almost tempera-

ture independent, which cannot be explained by the conventional PBT. Actually, the HA yields imaginary phonons for $\text{Cu}_{12}\text{Sb}_4\text{S}_{13}$, which hinders a direct application of Eq. (8).

To understand the origin of the unusual temperature dependence in BGG and tetrahedrite, we have recently performed SCP calculations of these complex materials. Also, the thermal conductivity is evaluated based on Eq. (10) for which the SCP eigenvalues and eigenvectors are used as inputs.

Figures 3 (b) and (e) show the calculated phonon dispersion curves of BGG and tetrahedrite, respectively. The phonon dispersion curves calculated within the HA and SCP theory are somewhat similar, particularly for the high-frequency phonon modes. In the low-frequency range, however, we can see notable differences. In BGG, the frequency of low-lying optical phonon modes around 4.5 meV increases with heating. These phonon modes correspond to the collective vibration of Ba guest atoms inside the large cavities made by the host frame-

work, as indicated by the red arrows of Fig. 3 (a). These phonon modes are often called “rattling” motion. In tetrahedrite, the unstable phonon modes exist within the HA. These phonon modes correspond to the collective vibrations of Cu(2) atoms, which are located on the triangle planes made by sulfur atoms (see Fig. 3(d)). Since the displacement of the Cu(2) atoms occur in the direction perpendicular to the triangle planes, these characteristic phonon modes were named “planar rattling” [30]. In our SCP calculations, the planar rattling modes were stabilized by anharmonic renormalization above ~ 80 K.

Next, we have calculated κ_P and κ_C of Eq. (10) separately; the results are compared with available experimental data in Figs. 3 (c) and (f). When we employed the harmonic phonon dispersion in calculating the phonon lifetimes and κ_P , the thermal conductivity was significantly underestimated, as shown by the dashed line of Fig. 3 (c). When the SCP dispersion was used instead, we could reach a nice agreement with the experimental data, including the temperature dependence weaker than $\kappa_L \propto T^{-1}$. Since the low-lying optical phonons strongly hybridize with the heat-carrying acoustic phonons, a little temperature-dependence of the rattling-mode frequency gives rise to the unusual temperature profile of κ_L [27]. The coherent contribution κ_C calculated from Eq. (11) accounts for about 10% of total κ_L of BGG at 300 K. For tetrahedrite, the temperature dependence of κ_L is more exceptional as shown in Fig. 3 (f). Interestingly, the little temperature dependence can be explained qualitatively by the Peierls term based on the temperature-dependent SCP wave functions. Still, the calculated κ_P value significantly underestimates the experimental thermal conductivity for the entire temperature range. This discrepancy can be cured by including the coherent term κ_C ; the sum of two contributions, $\kappa_P + \kappa_C$, reproduces the experimental values even quantitatively. Such a large coherent contribution has already been reported for orthorhombic halide perovskite CsPbBr₃ [10], where the particle-like thermal transport is hindered by the strong phonon-

phonon interaction. We believe the coherent term κ_C should be significant not only in disordered solids but also in strongly anharmonic (ordered) solids where the phonon linewidths become broad, and the phonon spectral weights overlap with each other.

4 Summary

In this short report, we reviewed the recent development of new phonon calculation methods that can treat the intrinsic effects of lattice anharmonicity beyond the quasiharmonic level. We showed that the self-consistent phonon scheme solves the limitations of the harmonic phonon theory by incorporating the quartic anharmonicity at the mean-field level. Also, the unified theory of thermal transport, which can account for the coherent thermal transport in addition to the particle-like contribution, was shown to better explain the anomalous thermal transport observed in complex thermoelectric materials.

All of the methods focused in this report are already available in the `ALAMODE` software [32]. We kindly invite interested readers to visit the homepage and try the software.

This work was partially supported by Grant-in-Aid for Scientific Research (number 16H06345) from the Ministry of Education, Culture, Sports, Science and Technology, Japan. A part of the computation in this work was performed using the facilities of the Supercomputer Center, Institute for Solid State Physics, The University of Tokyo. This report is based on the recent studies done in collaboration with K. Suekuni, S. Tsuneyuki, J. A. Flores-Livas, I. Errea, R. Arita, and T. Koretsune.

References

- [1] O. Hellman and I. A. Abrikosov: *Phys. Rev. B* **88** (2013) 144301.
- [2] T. Sun, D.-B. Zhang, and R. M. Wentzcovitch: *Phys. Rev. B* **89** (2014) 094109.

- [3] P. Souvatzis, O. Eriksson, M. I. Katsnelson, and S. P. Rudin: *Comp. Mater. Sci.* **44** (2009) 888.
- [4] B. Monserrat, N. D. Drummond, and R. J. Needs: *Phys. Rev. B* **87** (2013) 144302.
- [5] I. Errea, M. Calandra, and F. Mauri: *Phys. Rev. B* **89** (2014) 064302.
- [6] T. Tadano and S. Tsuneyuki: *Phys. Rev. B* **92** (2015) 054301.
- [7] A. van Roekeghem, J. Carrete, and N. Mingo: *Phys. Rev. B* **94** (2016) 020303.
- [8] R. Bianco, I. Errea, L. Paulatto, M. Calandra, and F. Mauri: *Physical Review B* **96** (2017) 014111.
- [9] T. Tadano and S. Tsuneyuki: *Journal of the Ceramic Society of Japan* **127** (2019) 404 .
- [10] M. Simoncelli, N. Marzari, and F. Mauri: *Nature Physics* **15** (2019) 809.
- [11] L. Isaeva, G. Barbalinardo, D. Donadio, and S. Baroni: *Nature Communications* **10** (2019) 3853.
- [12] D. J. Hooton: *Philos. Mag.* **3** (1958) 49.
- [13] Y. Oba, T. Tadano, R. Akashi, and S. Tsuneyuki: *Physical Review Materials* **3** (2019) 033601.
- [14] T. Tadano, Y. Gohda, and S. Tsuneyuki: *J. Phys: Condens. Matter* **26** (2014) 225402.
- [15] A. A. Maradudin and A. E. Fein: *Phys. Rev.* **128** (1962) 2589.
- [16] T. Feng, L. Lindsay, and X. Ruan: *Physical Review B* **96** (2017) 72 .
- [17] N. K. Ravichandran and D. Broido: *Physical Review B* **98** (2018) 1 .
- [18] P. B. Allen and J. L. Feldman: *Physical Review Letters* **62** (1989) 645.
- [19] P. B. Allen and J. L. Feldman: *Physical Review B* **48** (1993) 12581 .
- [20] F. Zhou, W. Nielson, Y. Xia, and V. Ozoliņš: *Phys. Rev. Lett.* **113** (2014) 185501.
- [21] T. Tadano and S. Tsuneyuki: *Journal of the Physical Society of Japan* **87** (2018) 041015 .
- [22] M. Somayazulu, M. Ahart, A. K. Mishra, Z. M. Geballe, M. Baldini, Y. Meng, V. V. Struzhkin, and R. J. Hemley: *Physical Review Letters* **122** (2019) 027001.
- [23] A. P. Drozdov, P. P. Kong, V. S. Minkov, S. P. Besedin, M. A. Kuzovnikov, S. Mozaffari, L. Balicas, F. F. Balakirev, D. E. Graf, V. B. Prakapenka, E. Greenberg, D. A. Knyazev, M. Tkacz, and M. I. Eremets: *Nature* **569** (2019) 528 .
- [24] H. Liu, I. I. Naumov, R. Hoffmann, N. Ashcroft, and R. J. Hemley: *Proceedings of the National Academy of Sciences* **114** (2017) 6990.
- [25] F. Peng, Y. Sun, C. J. Pickard, R. J. Needs, Q. Wu, and Y. Ma: *Physical review letters* **119** (2017) 107001.
- [26] I. Errea, F. Belli, L. Monacelli, A. Sanna, T. Koretsune, T. Tadano, R. Bianco, M. Calandra, R. Arita, F. Mauri, and J. A. Flores-Livas: *Nature* **578** (2020) 66.
- [27] T. Tadano and S. Tsuneyuki: *Physical review letters* **120** (2018) 105901.
- [28] B. C. Sales, B. C. Chakoumakos, R. Jin, J. R. Thompson, and D. Mandrus: *Phys. Rev. B* **63** (2001) 245113.
- [29] A. F. May, E. S. Toberer, A. Saramat, and G. J. Snyder: *Phys. Rev. B* **80** (2009) 125205.
- [30] K. Suekuni, C.-H. Lee, H. I. Tanaka, E. Nishibori, A. Nakamura, H. Kasai, H. Mori, H. Usui, M. Ochi, T. Hasegawa, M. Nakamura, S. Ohira-Kawamura, T. Kikuchi, K. Kaneko, H. Nishiate, K. Hashikuni, Y. Kosaka, K. Kuroki, and T. Takabatake: *Advanced Materials* **285** (2018) 1706230 .

- [31] T. Tadano, Y. Gohda, and S. Tsuneyuki: Phys. Rev. Lett. **114** (2015) 095501.
- [32] T. Tadano. ALAMODE.
<https://github.com/ttadano/alamode>.

Development of Open-Source Parallelized Tensor Network Softwares: mptensor and TeNeS

Satoshi MORITA and Naoki KAWASHIMA

Institute for Solid State Physics, University of Tokyo, Kashiwa, Chiba 277-8581

Abstract

In this activity report, we overview two open-source softwares, mptensor [1] and TeNeS [2], for tensor network methods. The former is a library for massively parallel computing of tensor networks. It provides useful functions for tensor operations which are commonly appeared in tensor network methods. TeNeS, named for “Tensor Network Solver”, is a solver for two-dimensional quantum lattice systems based on an infinite tensor network state. TeNeS is originally developed as pTNS by Tsuyosi Okubo [3] and released under the support of Project for Advancement of Software Usability in Materials Science (PASUMS) of the Institute for Solid State Physics, the University of Tokyo [4]. TeNeS can calculate the ground state wave function for user-defined Hamiltonian and evaluate physical quantities including the magnetization and the correlation functions.

1 Introduction

In strongly correlated quantum many-body physics, numerical simulation of low-energy states is quite important for understanding of interesting phenomena including high-temperature superconductivity, quantum spin liquid, topological nature, etc. To attack these problems, many computational approaches are proposed. The exact diagonalization method (ED) provides the exact ground state for small systems [5]. However, exponentially divergence of its computational cost and memory usage tightly limits the size of systems. The quantum Monte Carlo method

(QMC) also can calculate the exact results within statistical errors, but the negative sign problem occurs in the frustrated systems [6]. The variational Monte Carlo method (VMC) is another Monte Carlo method based on the variational principle [7]. Variational parameters are optimized to minimize the energy and the resulted wave function is expected to approximate the ground state well. The expectation value of physical quantities is estimated by using the Monte Carlo sampling. Results of VMC are biased by choice of the variational wave function ansatz. The density matrix renormalization group method (DMRG) is a quite accurate method for one-dimensional systems [8, 9].

Recently, tensor network methods are proposed as a powerful tool [10–16]. DMRG can be viewed as a variational method based on a one-dimensional tensor network, i.e., the matrix product state (MPS) [17]. Its higher-dimensional generalization including the projected entangled pair state (PEPS) is quite successful [18–20]. In classical systems, the partition function can be expressed as tensor networks [21, 22]. The physical properties of the systems can be obtained by the contraction of tensor networks.

Information compression based on the singular value decomposition is a key idea of tensor network methods in order to avoid exponentially divergence of computational cost. Accuracy of tensor network simulations is determined by the size of tensors. However, computational cost and memory usage still increase very rapidly as a function of tensor size. Thus parallel computation of tensor network methods is unavoidable to approach inter-

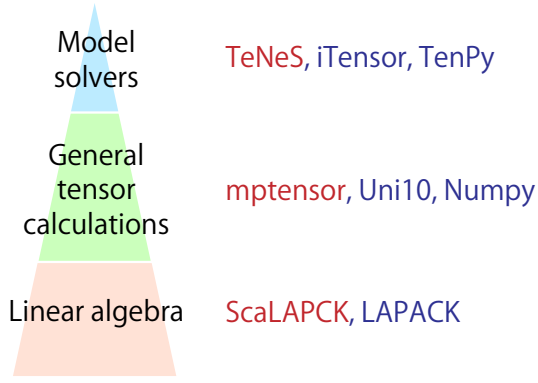


Figure 1: Hierarchical structure of tensor network calculations. Our softwares, TeNeS and mptensor, belongs to the top and middle levels. The softwares written in red support parallel computation on a distributed memory system.

esting phenomena.

Tensor network calculations are classified in hierarchical structure as shown in Fig. 1. The top level is lattice model solvers of tensor network methods. iTensor [23] and TenPy [24] are a famous software for MPS in this level. The former is written in C++ language but the latter is a Python package. The middle level provides a framework for tensor calculations including tensor contraction and tensor decomposition A C++ library, Uni10 [25] and a famous Python package NumPy [26] are in this level. Recently, a team of Google released a Python library "TensorNetwork" for physics and machine learning [27]. Since almost tensor calculations are written as matrix operations, this level is a kind of wrapper to a library for linear algebra, which is the bottom level. The well-known libraries, LAPACK [28] is located in this level.

As we mentioned before, parallel computation of tensor network methods is necessary to investigate interesting physical phenomena within sufficient accuracy. However, the softwares listed in the previous paragraph are not parallelized. To resolve this situation, we are developing two softwares, mptensor [1] and TeNeS [2] (Fig. 2). mptensor is an open-source C++ library for parallel computation of tensor networks on a distributed memory

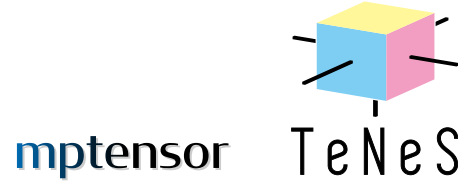


Figure 2: Logo images of mptensor and TeNeS. The latter represents a shape of a local tensor in the tensor network state.

system. It provides many tensor operations commonly used in tensor network methods. mptensor uses ScaLAPACK [29] which is a parallel version of LAPACK, and supports MPI/OpenMP hybrid parallel computing. On the other hand, TeNeS is a lattice solve built on mptensor. It can solve quantum many-body problems on a two-dimensional infinite lattice based on a infinite tensor network wavefunction. TeNeS originates from pTNS developed by Tsuyoshi Okubo [3]. The official version of TeNeS (v1.0) is released on April 2020 under the support of the support of Project for Advancement of Software Usability in Materials Science (PASUMS) of the Institute for Solid State Physics, the University of Tokyo [4].

In the next section, we briefly review tensor network methods and introduce graphical representations of tensor networks. In the third and fourth sections, we introduce our softwares and show its performance. The last section is devoted to summary.

2 Basics of tensor networks

In many-body problems, a huge tensor often appears naturally. One typical example is a coefficient in a wave function of a quantum N -body system

$$|\psi\rangle = \sum C_{i_1 i_2 \dots i_N} |i_1\rangle |i_2\rangle \dots |i_N\rangle, \quad (1)$$

where $|i_x\rangle$ denotes a basis states on a site x and $C_{i_1 i_2 \dots i_N}$ can be regarded as a N -rank tensor. The number of elements in such a tensor is $O(d^N)$ if each index takes a value from 1 to d . Here d corresponds the degrees of freedom on each site. Since computational cost grows exponentially with the

system size N , it is difficult to treat such a huge tensor directly.

A tensor network effectively represents a many-index tensor by decomposing it into small tensors only with a few indices, like as,

$$C_{i_1 i_2 \dots i_N} = \sum_{\{k_j\}} T_{i_1 k_1 k_2} T'_{i_2 i_3 k_2 k_3} T''_{i_4 k_3 k_4 k_5} \dots \quad (2)$$

We introduce new indices k_1, k_2, \dots , which connect between small tensors. Summation over these indices is nothing but tensor contraction. Since k_j does not represent any physical degrees of freedom, it is called a virtual index. On the other hand, the original indices in $C_{i_1 i_2 \dots i_N}$ are named the physical indices. If the dimension of each virtual index is D and each tensor has z indices, the number of elements in each tensor is $O(D^z)$. When the number of tensors in a tensor network is polynomial in N , tensor network methods reduce exponentially large computational cost to polynomial order.

In a tensor network, many small tensors connect each other by virtual indices. Its mathematical expression becomes messy for large networks. A graphical representation of tensor networks is useful and intuitive. A tensor is represented by an object (circle, square, etc.) and its indices is shown by lines from a tensor. In other words, a tensor locates on a node of a graph and its indices correspond to edges. Several examples are shown in Fig. 3(a). Clearly, a scalar has no index, a vector has only one leg, and a matrix has two legs. By using terminology of the graph theory, an index of a tensor is also called as a bond, and the dimension of index is a bond dimension. A bond connecting between two tensors indicates tensor contraction of two tensors. For example, a graphical representation of matrix multiplication $C_{ij} = \sum_k A_{ik} B_{kj}$ is shown in Fig. 3(b).

Of course, decomposition of a huge tensor into a tensor network is approximation. Its accuracy depends on the virtual bond dimension D and a shape of network. As a variational state for the ground state of the quantum many-body problems, several kinds of structures are proposed. One of the simplest network is the matrix product state (MPS), whose wave function is written as a product of ma-

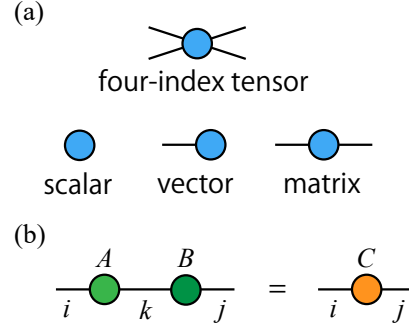


Figure 3: Graphical representation of tensor networks. (a) A tensor is represented by a node of graph and indices of a tensor corresponds to edges. (b) A graphical representation of matrix multiplication, $C_{ij} = \sum_k A_{ik} B_{kj}$.

trices,

$$C_{i_1 i_2 \dots i_N} = \sum_{\{k_j\}} M_{i_1 k_1}^{(1)} M_{i_2 k_1 k_2}^{(2)} M_{i_3 k_2 k_3}^{(3)} \dots M_{i_N k_{N-1}}^{(N)}. \quad (3)$$

Note that the three-index matrix $M_{i_n k_{n-1} k_n}^{(n)}$ can be regarded as a matrix when the physical index i_n fixed. Its graphical representation is shown in Fig. 4(a). This form can be easily derived by iteration of the singular value decomposition. The MPS is appeared in DMRG and achieves great success in simulations of the one-dimensional gapped systems [17]. The projected entanglement pair state (PEPS) [19] is two-dimensional generalization of MPS (Fig. 4(b)).

Important feature of PEPS is the fact that it satisfies the area law for the entanglement entropy [30]. The area law states that the entanglement entropy in the ground state of a region A is proportional to $|\partial A|$, the boundary area of the region. The entanglement entropy of a tensor network state is bounded by the number of bonds which connects a region A and its complement. If we consider an $L \times L$ region, the entanglement entropy of PEPS clearly scales as $O(L)$, which satisfies the area law in two-dimensional systems. In critical (gapless) one-dimensional systems, entanglement entropy logarithmically increases with the system size. Since entanglement entropy of MPS is bounded from above by $\log D$, MPS can not represent entanglement structure of such a system.

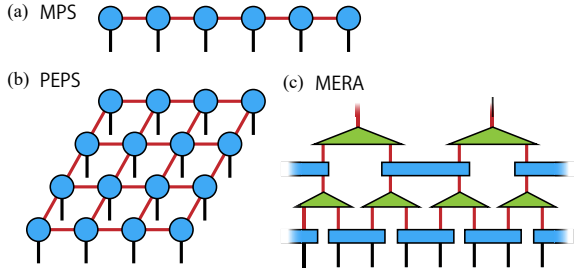


Figure 4: Some structures of tensor network states. The black (red) line indicates physical (virtual) bonds. (a) The matrix product state. (b) The projected entanglement pair state. (c) The multi-scale entanglement renormalization ansatz.

The multi-scale entanglement renormalization ansatz (MERA) shown in Fig. 4(c) resolves this problem by introducing additional dimension [31]. When we split the system into two parts, we need to cut $O(\log L)$ bonds in the MERA wavefunction, which indicates that upper bound of entanglement entropy is $O(\log L)$ instead of $O(1)$.

Important problems in a tensor network wavefunction for the ground state are how to calculate expectation values and how to optimize tensor elements based on the variational principle. These problems are touched in the fourth section.

Another important application is tensor network representation of the partition function in the statistical physics. The simplest example is the transfer matrix method for one-dimensional classical systems, in which the partition function is written as a product of transfer matrices. In the classical Ising chain with the Hamiltonian $H = -J \sum_i S_i S_{i+1}$, the transfer matrix is given as a 2×2 matrix,

$$M = \begin{pmatrix} e^{\beta J} & e^{-\beta J} \\ e^{-\beta J} & e^{\beta J} \end{pmatrix}, \quad M_{ij} = e^{\beta J S_i S_j} \quad (4)$$

where β denotes the inverse temperature and S_i takes ± 1 .

A generalization of the transfer matrix to higher dimensional systems is possible. Let us consider the square lattice tilted by 45 degrees and put a local tensor on half of plaquettes as shown in Fig.5. Obviously an index of a tensor corresponds to the

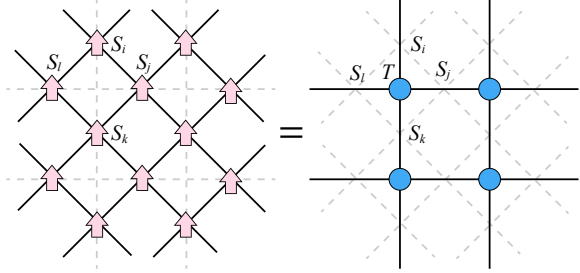


Figure 5: A tensor network representation of a classical spin model on the square lattice.

direction of spins. Tensor elements for the Ising model are written as

$$T_{ijkl} = e^{\beta J (S_i S_j + S_j S_k + S_k S_l + S_l S_i)}. \quad (5)$$

Another sophisticated way to obtain a tensor network representation is based on the singular value decomposition of the bond Boltzmann factor W . In the Ising model, W is 2×2 matrix with $W_{ss'} = e^{\beta J s s'}$. From the singular value decomposition, $W = U \Sigma V^\dagger$, we obtain a local tensor as

$$\tilde{T}_{ijkl} = \sum_s \sqrt{\sigma_i \sigma_j \sigma_k \sigma_l} U_{si} U_{sj} V_{sk}^* V_{sl}^*, \quad (6)$$

where σ_i denotes the singular value of W . In contrast to the previous example, a network of \tilde{T} is the same as the original lattice of the model.

Contraction of the tensor network is a quite important task of tensor network methods. For quantum systems, it appears in the inner product of two tensor network states and the expectation value of physical quantities. In the classical systems, it directly relates to the partition function. However, exact contraction is usually impossible because of exponentially large computational cost. The tensor renormalization group method (TRG) [32] provides an efficient contraction scheme, which is based on the real-space renormalization group (Fig. 6). Let us consider a tensor network on the square lattice. A local tensor with four indices is approximated by the product of two three-index tensors, which are calculated by the truncated singular value decomposition. Then the coarse-grained tensor is obtained by contraction of four tensors. This step is regarded as a real-space renormalization with scaling factor $b = \sqrt{2}$. After

t times iteration of TRG steps, the trace of tensor, $Z = \sum_{i,j} T_{ijij}$, corresponds to the partition function with $N = 2^t$ under the periodic boundary condition. The animation of TRG method is available in Ref. [33]. Although the computational cost of the original TRG method is $O(D^6)$, we showed that it can be reduced to $O(D^5)$ by using a randomized algorithm for the singular value decomposition [34].

Many derivatives of TRG are proposed as a more efficient and accurate method [35–38]. Since the higher-order tensor renormalization group (HOTRG) [35] can be used in a higher-dimensional system, it attracts attention also from computational elementary particle physics. Recently we proposed a calculation method for higher-order moments of physical quantities based on HOTRG [39]. We showed that the finite-size scaling analysis provides critical exponents and distinguishes the weakly first-order and the continuous transitions. The TRG method can also be applicable to systems with open boundaries. The fixed-point boundary tensor at criticality has the information of the conformal tower described by the boundary conformal field theory [40,41].

3 mptensor

mptensor is a C++ library for parallel computation of tensor networks and provides tensor operations used commonly in tensor network methods [1]. Its target users are researchers who want to parallelize their codes of tensor network methods. To make it easy to translate a serial code written with Python to a parallelized C++ code, interface of mptensor is as much like as NumPy [26], which is a famous

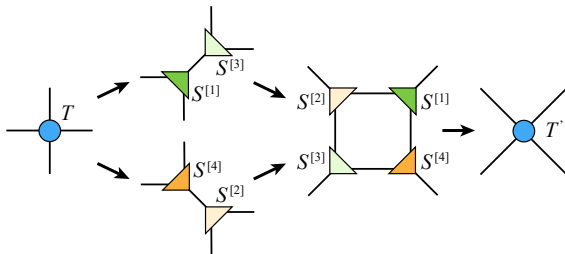


Figure 6: Diagrams of the TRG method.

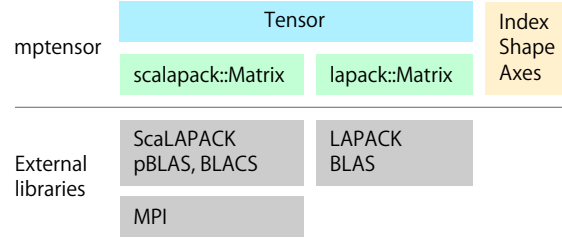


Figure 7: The class structure of mptensor.

Python module of a multi-dimensional array and is a de-facto standard in the field of machine learning.

For high-performance computing, mptensor supports hybrid parallel computing using MPI and openMP. With MPI, mptensor distributes tensor elements based on a block-cyclic matrix uses ScaLAPACK, which is a library for linear algebra on distributed-memory machines [29]. A tensor is matricized and distributed by the block-cyclic way. mptensor also supports LAPACK for a system without MPI.

3.1 Class structure

mptensor is composed of three classes as shown in Fig. 7. The Tensor class is a main object of mptensor, which represents a tensor and corresponds to ndarray in NumPy. In the Tensor class, a tensor is automatically matricized and its elements are stored in a Matrix object. mptensor has two kinds of Matrix classes, a wrapper class of a linear-algebra library. One uses ScaLAPACK and the other LAPACK, which are separated by C++ namespace.

The Index class is a short array of non-negative integers to represent an index of a tensor. The Shape and Axes classes are just an alias of the Index class. These classes have a simple constructor to mimic a list of Python. The index class can create the same list by `Index(1, 2, 3)` as well as Python can easily create a list of integer by `[1, 2, 3]`. For C++11, an initializer list `{1, 2, 3}` is also available instead of the index class.

The Tensor class is implemented as a template class. Its template parameters specify a Matrix

class and a value type of elements (`double` or `complex`). For examples, a real-valued distributed tensor is `Tensor<scalapack::Matrix, double>` and a complex-valued non-distributed tensor is `Tensor<lapack::Matrix, complex>`. Since all functions for the tensor class accepts any patterns of template parameters, users can easily change a type of tensors. In addition, `mptensor` is designed to make it easy to support another library for linear algebra in the future. It is because the tensor class can accept any matrix class if it satisfies necessary interfaces.

3.2 Access to tensor elements

To access an element of a tensor, `mptensor` provides two ways. One is to access an element with an index of a tensor, which we call a global index. For example, we can get and set an element of a four-index tensor T by specifying (i, j, k, l) . The other way is to specify a local index of a one-dimensional array where distributed elements are stored. In `mptensor`, a tensor is matrixized like as $T_{ijkl} = M_{(ij),(kl)}$. The huge matrix M is decomposed into small matrices by using the two-dimensional block-cyclic distribution in ScaLAPACK. A small distributed matrix on each MPI process is flattened and stored as a one-dimensional array. The local index specifies a position in this one-dimensional array. In `mptensor`, matrixization of a tensor is done in the tensor class, while translation between a index of the global matrix M and a local index is calculated in the matrix class.

Since tensor elements are distributed on MPI processors, access by the global index needs to check which process has an element T_{ijkl} . On the other hands, such a check is not necessary for the local index. Thus access by the local index has simpler interface like as usual array access, `T[i]`. We recommend a for-loop with the local index to access all the elements of a tensor. Member functions of the tensor class, `global_index` and `local_position` perform translation between the global and local indices. We note that `local_position` also calcu-

lates which process has the element with the given global index.

3.3 Tensor operations

In `mptensor`, many tensor operations are already implemented. Some typical operations are listed as follows.

- Tensor contraction (`tensor_dot`)
- Tensor decomposition
 - Singular value decomposition (`svd`)
 - QR decomposition (`qr`)
 - Diagonalization (`eigh`)
- Linear-equation solver (`solve`)
- Arithmetic operators ($T + T'$, $a \times T$, etc.)
- Element-wise vector multiplication
- Find minimum and maximum elements

These are sufficient to implement various tensor network methods including PEPS and TRG.

Tensor contraction is one of the main operation in tensor network methods. The `tensor_dot` function takes the almost same arguments of that in Numpy. For example, let us consider the following tensor contraction,

$$C_{abc} = \sum_{i,j} A_{aibj} B_{jci}. \quad (7)$$

In `mptensor`, it is written as

```
C = tensor_dot(A, B,
               Axes(1, 3),
               Axes(2, 0));
```

The third argument indicates that the second and fourth indices of the first tensor A will be contracted. (Note that array index starts from zero in C++.) The fourth argument is for the second tensor B . The third index i in B (specified by the first element in the fourth argument) will be contracted with the second index of A and the first index j in B will connects with the fourth index of A . The resulted tensor C has three indices abc which consists of the non-contracted indices of the first tensor, followed by the non-contracted indices of the second.

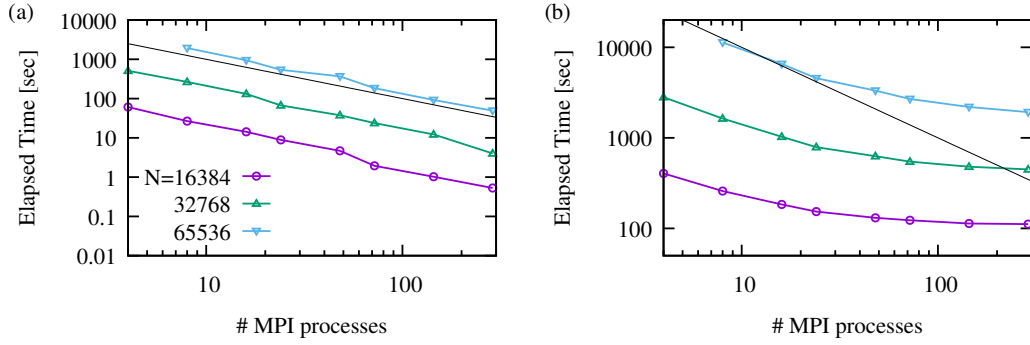


Figure 8: Elapsed time of ScaLAPACK routines, (a) a matrix-matrix multiplication (`pdgemm`) and (b) the singular value decomposition (`pdgesvd`). N is the linear size of a square matrix. The number of OpenMP threads per MPI process is 12. The solid lines indicate the perfect strong scaling.

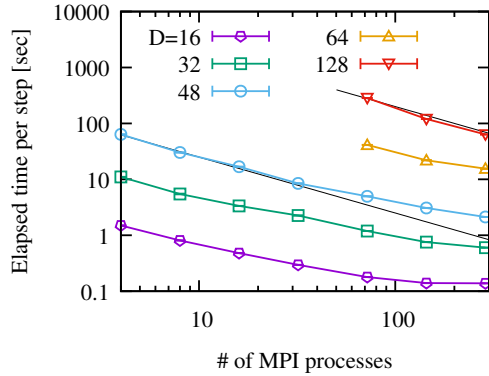


Figure 9: Elapsed time per step of the HOTRG method on the two-dimensional Ising model. The number of OpenMP threads per MPI process is 12. The solid lines indicate the perfect strong scaling.

Another important operation in tensor network methods is the singular value decomposition (SVD). For SVD of a tensor, we need to specify the way of matricization. For example, let us consider the following decomposition,

$$T_{ijkl} = \sum_a U_{ika} S_a (V^\dagger)_{alj}. \quad (8)$$

To perform this operation in NumPy, a tensor T is matricized as $T_{(ik),(lj)}$ before SVD. The resulted singular value vectors are returned as a matrix, $U_{(ik),a}$ and $(V^\dagger)_{a,(lj)}$. Thus we need to reshape from a matrix to a tensor. `mptensor` provides a useful function for SVD of a tensor and the above decomposition is written in single line as

$$\text{svd}(T, \text{Axes}(0, 2), \text{Axes}(3, 1),$$

$$U, S, VT);$$

The second and third arguments specify the way of matricization. The first and third indices of T become the row index and the others do the column index. The order of indices specified in the second and third arguments also determines that of U and VT . The result of SVD is stored in the last three arguments. U and VT are an isometric tensor corresponding to the singular value vectors, while S is a one-dimensional array and has the singular values.

The performance of `mptensor` strongly depends on that of ScaLAPACK. The tensor contraction is performed by using the matrix-matrix multiplication routines (`pdgemm` and `pzgemm`). Thus it shows very high execution efficiency and parallel efficiency. On the other hand, parallel performance of SVD becomes worse in many processes as shown in Fig. 8.

We show the parallel efficiency of the HOTRG method implemented by using `mptensor` (Fig. 9). Clearly the strong scaling is satisfied for larger bond dimension D . It is because the heaviest part of HOTRG is contraction of a tensor network, which is scaled as $O(D^7)$. We note that deviation from the strong scaling in small bond dimensions is due to the singular value decomposition which has $O(D^6)$ scaling.

4 TeNeS

TeNeS is a tensor-network solver for quantum many-body problems on an infinite two-dimensional lattice [2]. TeNeS can calculate the ground-state wavefunction for user-defined Hamiltonian and evaluate user-defined physical quantities, including the magnetization and the correlation functions. TeNeS uses TOML [42] as the format of input files. This is a very simple configuration file format, easy to parse into data structures and also human-readable. The input file of the main program, `tenes`, defines simulation parameters, unit cell information for TNS, observables, and time-evolution operators. Since it is rather complicated for beginners, we provide two helper programs, `tenes_simple` and `tenes_std`, to generate an input file as similar to HΦ [5] and mVMC [7]. By using `tenes_simple`, users easily create an input file of the predefined models and lattices. TeNeS (v1.0) supports generation of the input file for the spin- S Hamiltonian

$$H = \sum_{\langle ij \rangle} \left[\sum_{\alpha=x,y,z} J_{ij}^{\alpha} S_i^{\alpha} S_j^{\alpha} + B (\vec{S}_i \cdot \vec{S}_j)^2 \right] - \sum_i \left[HS_i^z + \Gamma S_i^x - D(S_i^z)^2 \right] \quad (9)$$

on the square, triangular or honeycomb lattice. A more complicated model is also possible by editing an input file directly.

The variational wave function of TeNeS is represented by infinite tensor network called an infinite projected entangled paired state (iPEPS) or an infinite tensor network state (iTNS). Each tensor has five indices. One corresponds to the physical degrees of freedom. The others, called virtual bonds, connect with tensors on the nearest neighbor sites. The bond dimensions of the physical and virtual bonds are denoted by d and D , respectively. In iTNS, we need to assume a lattice translational symmetry with a certain period. Figure 10(a) shows a diagram of iTNS with 2×2 sublattice structure. We note that TeNeS always uses a tensor network on the square lattice. Other two-dimensional lattices including the honeycomb and

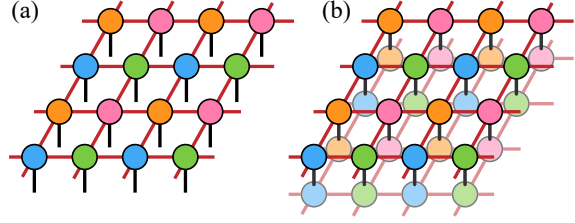


Figure 10: (a) Graphical representation of the iTNS wavefunction with 2×2 sublattice structure. (b) Diagram of the inner product $\langle \Psi | \Psi \rangle$, which is called the double layered tensor network.

triangular lattices is properly mapped to the square one.

To obtain the expectation value of a physical quantity in iTNS, we need to calculate tensor networks corresponding to $\langle \Psi | O | \Psi \rangle$ and $\langle \Psi | \Psi \rangle$. The diagram of $\langle \Psi | \Psi \rangle$ is called the double layered tensor network (Fig. 10(b)). To calculate contraction of this infinite network, TeNeS uses the corner transfer matrix method (CTMRG) [19,20]. We focus on a part of the network and the other part is approximated by the corner transfer matrices and the edge tensors [43,44]. These environment tensors are optimized by absorbing the local tensor until convergence. The accuracy of the environment tensors is determined by its bond dimension χ . Since the bond dimension after contraction of the physical bond in the double layered tensor network is D^2 , we usually take that χ is proportional to D^2 . The computational cost of CTMRG is $O(D^{10})$ or $O(D^{12})$ depending on the way of the partial (truncated) SVD in CTMRG.

In order to approximate the ground state by iTNS, we need to optimize elements of tensors. TeNeS supports the imaginary-time evolution method based on

$$|\Psi_{\text{iTNS}}\rangle \simeq e^{-\tau H} |\Psi_0\rangle, \quad (10)$$

where $|\Psi_0\rangle$ is the initial iTNS. If τ is sufficiently large, the right hand side converges to the ground state and then the left hand side is expected to be a good approximation of the ground state with iTNS ansatz. TeNeS assumes that the Hamiltonian can be written as a sum of short range two-body interactions and uses the Suzuki-Trotter decompo-

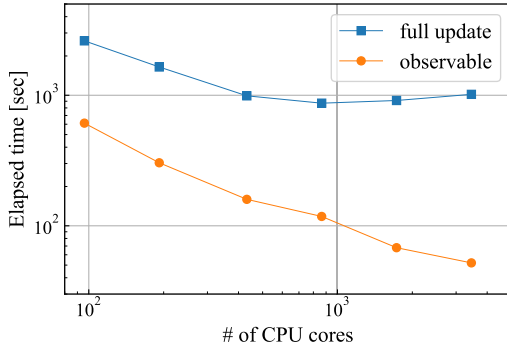


Figure 11: Elapsed time of TeNeS simulations with the virtual bond dimension $D = 10$. The blue square denotes elapsed time per step of the full update. The orange circle is tensor contraction for calculation of the expectation value.

sition. To avoid divergence of the dimension of virtual bonds, TeNeS supports two kinds of truncation approaches, so-called the full update [46] and the simple update [47]. The former solves the optimization problems of the whole network by using the CTM environment and has higher accuracy than the latter. Its computational cost is the same as CTMRG, that is, $O(D^{10})$ or $O(D^{12})$. On the other hand, the simple update considers only a part of network. Its computational cost is $O(D^5)$, which is much cheaper than the full update. It is known that the simple update has strong dependence on the initial value and usually overestimates the magnetization. Thus we need to take care of results obtained by the simple update.

The accuracy of iTNS calculation depends on the bond dimension D . However, the computational cost is rapidly increases. Thus parallel computation is necessary to obtain accurate results. TeNeS supports parallel computation since tensor operations are done by using mptensor. We show elapsed time of TeNeS in Fig. 11, where we simulate the transverse field Ising model on the square lattice. We use a real-valued iTNS with the virtual bond dimension $D = 10$ and set $\chi = D^2$ for CTM. Since calculation of the expectation value is tensor contraction, its parallel efficiency is quite good. On the other hand, the full update includes the singular value decomposition. Its performance

is similar to that of SVD in ScaLAPACK (Fig. 8). We note that elapsed time of the simple update per step is 0.01% of the full update.

5 Summary

In this paper, we have reported recent activities of developing tensor network softwares, mptensor and TeNeS. The former is an MPI/OpenMP hybrid parallelized tensor operation library. It provides many tensor operations commonly used in the tensor network methods and is already used in the published papers [48, 49]. One of future issues for mptensor is implementation of quantum number conserving tensors. If the system has a certain symmetry, its tensor network representation has a corresponding non-trivial structure [52]. This technique not only improves accuracy but also reduces computational cost and memory usage because such a tensor is block-diagonal. Another future issue is automatic differentiation, which becomes a common tool in a field of machine learning. Recently, application of automatic differentiation to tensor network methods was proposed and succeeded to obtain accurate results [53]. Since it requires huge memory, its parallelization should become important for large-scale calculation.

TeNeS is an open-source program package for calculation of two-dimensional quantum states based on iTNS. An advantage of TeNeS over other numerical approaches is that it can treat infinite systems. In this article, we only show the parallel performance of TeNeS because of space limitations. Accuracy of TeNeS simulations will be appeared elsewhere [50]. We hope that TeNeS becomes a useful standard tool for a wide range of researchers who are interested in the strongly-correlated many-body problems.

Acknowledgements

TeNeS is developed by Tsuyoshi Okubo, Yuichi Motoyama, Kazuyoshi Yoshimi, Takeo Kato and the authors. The original version of TeNeS is developed as pTNS by Tsuyoshi Okubo [3]. Development and

release of TeNeS are supported by “Project for advancement of software usability in materials science” of the Institute for Solid State Physics, the University of Tokyo. We would like to thank Kenji Harada, Hiroshi Watanabe and Synge Todo for collaborations in developing mptensor. The numerical calculations of this work were performed with the supercomputer System B (sekirei) in the Institute for Solid State Physics, the University of Tokyo. This work was supported by MEXT as “Exploratory Challenge on Post-K computer” (Frontiers of Basic Science: Challenging the Limits) and Priority Issue on Post-K Computer (Creation of New Functional Devices and High-Performance Materials to Support Next-Generation Industries), and by JSPS KAKENHI Grant Number 19H01809.

References

- [1] <https://github.com/smorita/mptensor>
- [2] <https://www.pasums.issp.u-tokyo.ac.jp/tenes>
- [3] <https://github.com/TsuyoshiOkubo/pTNS>
- [4] <https://www.pasums.issp.u-tokyo.ac.jp/>
- [5] M. Kawamura, et al., *Comput. Phys. Commun.* **217**, 180 (2017).
- [6] <https://www.pasums.issp.u-tokyo.ac.jp/dsqss>
- [7] T. Misawa, et al., *Comput. Phys. Commun.* **235**, 447 (2019).
- [8] S. R. White, *Phys. Rev. Lett.* **69**, 2863 (1992).
- [9] U. Schollwöck, *Rev. Mod. Phys.* **77**, 259 (2005).
- [10] R. Orús, *Ann. Phys.* **349**, 117 (2014).
- [11] R. Orús, *Nature Rev. Phys.* **1**, 538 (2019).
- [12] J. C. Bridgeman and C. T. Chubb, *J. Phys. A: Math. Theor.* **50** 223001 (2017).
- [13] J. Biamonte and V. Bergholm, arXiv:1708.00006 (2017)
- [14] S.-J. Ran, et al., “*Tensor Network Contractions: Methods and Applications to Quantum Many-Body Systems*”, *Lecture Notes in Physics*, vol. 964, Springer (2020).
- [15] G. Evenbly, <https://www.tensors.net/>
- [16] <http://tensornetwork.org/>
- [17] U. Schollwöck, *Ann. Phys.* **326**, 96 (2011).
- [18] F. Verstraete, J. I. Cirac, arXiv:cond-mat/0407066 (2004).
- [19] R. Orús and G. Vidal, *Phys. Rev. B* **80**, 094403 (2009).
- [20] P. Corboz, T. M. Rice, and M. Troyer, *Phys. Rev. Lett.* **113**, 046402 (2014)
- [21] R. J. Baxter, *Exactly Solved Models in Statistical Mechanics*, Academic Press, London (1982).
- [22] H. H. Zhao, et al., *Phys. Rev. B* **81**, 174411 (2010).
- [23] <https://itensor.org>
- [24] <https://github.com/tenpy/tenpy>
- [25] <https://uni10.gitlab.io>
- [26] <https://numpy.org>
- [27] <https://github.com/google/tensornetwork>
- [28] <http://www.netlib.org/lapack>
- [29] <http://www.netlib.org/scalapack>
- [30] J. Eisert, M. Cramer, and M. B. Plenio, *Rev. Mod. Phys.* **82**, 277 (2010).
- [31] G. Vidal, *Phys. Rev. Lett.* **99**, 220405 (2007).
- [32] M. Levin and C. P. Nave, *Phys. Rev. Lett.* **99**, 120601 (2007).
- [33] https://smorita.github.io/TN_animation
- [34] S. Morita, R. Igarashi, H.-H. Zhao, and N. Kawashima, *Phys. Rev. E* **97**, 033310 (2018).
- [35] Z. Y. Xie, et al., *Phys. Rev. B* **86**, 045139 (2012).
- [36] G. Evenbly and G. Vidal, *Phys. Rev. Lett.* **115**, 180405 (2015).
- [37] S. Yang, Z.-C. Gu, and X.-G. Wen, *Phys. Rev. Lett.* **118**, 110504 (2017).
- [38] G. Evenbly, *Phys. Rev. B* **98**, 085155 (2018)
- [39] S. Morita and N. Kawashima, *Comput. Phys. Commun.* **236**, 65 (2019).
- [40] S. Iino, S. Morita, and N. Kawashima, *Phys. Rev. B* **100**, 035449 (2019).
- [41] S. Iino, S. Morita, and N. Kawashima, *Phys. Rev. B* **101**, 155418 (2020).
- [42] <https://github.com/toml-lang/toml>
- [43] T. Noshino and K. Okunishi, *J. Phys. Soc. Jpn.* **65**, 891 (1996).
- [44] T. Noshino and K. Okunishi, *J. Phys. Soc. Jpn.* **66**, 3040 (1997).
- [45] N. Halko, P. G. Martinsson, and J. A. Tropp, *SIAM Rev.* **53**, 217 (2011).
- [46] J. Jordan, et al., *Phys. Rev. Lett.* **101**, 250602 (2008).
- [47] H. G. Jiang, et al., *Phys. Rev. Lett.* **101**, 090603 (2008).
- [48] H.-Y. Lee and N. Kawashima, *Phys. Rev. B* **97**, 205123 (2018).
- [49] H.-Y. Lee, R. Kaneko, T. Okubo, and N. Kawashima, *Phys. Rev. Lett.* **123**, 087203 (2019).
- [50] Y. Motoyama, T. Okubo, K. Yoshimi, S. Morita, T. Kato, and N. Kawashima, in preparation.
- [51] P. Corboz, *Phys. Rev. B* **94**, 035133 (2016)
- [52] S. Singh, R. N. C. Pfeifer, and G. Vidal, *Phys. Rev. A* **82**, 050301, *Phys. Rev. B* **83**, 115125
- [53] H.-J. Liao, J.-G. Liu, L. Wang, and T. Xiang, *Phys. Rev. X* **9**, 031041 (2019)

Disorder-Free Glass Transitions of Spins and Orbitals in a Frustrated Pyrochlore Magnet

Kota Mitsumoto¹, Chisa Hotta² and Hajime Yoshino^{1,3}

¹*Graduate School of Science, Osaka University, Toyonaka, Osaka 560-0043, Japan*
Osaka University, Toyonaka 560-0043, Japan.

²*Department of Basic Science, University of Tokyo, Tokyo 153-8902, Japan*

³*Cybermedia Center, Osaka University, Toyonaka, Osaka 560-0043, Japan*

Abstract:

In this activity report, we present an overview of our recent extensive Monte Carlo simulations performed on the ISSP supercomputer (SYSTEM B) [1][2][3] to study our effective theoretical model for the disorder-free spin-glass transition observed experimentally in the pyrochlore oxide $Y_2Mo_2O_7$. By taking into account not only the spin but also the orbital degrees of freedom of the Mo ions, we found a new type of glass transition - spin-orbital glass transition.

1 Introduction

Glass is a generic state of matters which can be found in a diverse range of systems ranging from soft to hard condensed matters. Yet, unlike crystalline states with long-ranged ordering of periodic structures, the very mechanism(s) of the emergence of glasses remain quite elusive. The exceptional case is the family of disordered magnets with quenched disorder, i. e. spin-glasses. In spin-glasses, the existence of thermodynamic glass transitions is established by experiments, theories and simulations (see for reviews [4, 5, 6, 7]). But apparently, glasses without quenched disorder is more ubiquitous in nature and in industrial materials. Understanding the mechanism of the emergence of glasses *without* quenched disorder remains as one of the most important unsolved problems in physics [8].

Majority of glassy systems without quenched disorder emerge from *supercooled liquids*. Typical examples are the structural

glasses obtained by supercooling molecular liquids or making densely packed soft-matters like colloids. The most important basic question there is to clarify whether the so-called Kauzmann transition[9], which is a putative, idealized thermodynamic glass transition, can take place in the supercooled liquid state. Recently important progress was made on the theoretical side: a mean-field theory which combines the density functional theory of liquids [10] and the replica method used in statistical mechanics of disordered systems [11] established that the ideal glass transition exists (at least) in the large dimensional limit (see for a review [12]). However, the fate of ideal thermodynamic transition in *finite* dimensions is largely unknown [13]. The problem is difficult to solve precisely because of the glassiness: the extremely sharp increase of the relaxation time (viscosity) going deeper into the supercooled liquid state makes it very difficult to measure quantities in equilibrium. Another reason is that the super-cooled liquid state is a meta-stable state which should be replaced by the crystalline state in true equilibrium. A possible way out of these difficulties is to seek simple lattice models, which mimic the basic phenomenology of structural glasses, carefully designed to avoid crystalline transitions, and allow various simulation techniques developed for lattice models [14].

In principle, glass transitions similar to those found in the supercooled liquids can also take place in spin systems. Indeed one can show exactly that the ideal glass tran-

sitions can take place in spin systems without quenched disorder, by examining *supercooled paramagnetic states* in the large dimensional limit [15]. However, in reality, the metastability limit of the paramagnetic state toward long-ranged ordering of periodic structures (corresponding to the Kirkwood instability of liquids [16]) may preempt the ideal glass transition (see for instance [17]).

A very promising playground to explore glass physics is geometrically frustrated magnets on corner-shared lattices such as the Kagome lattice and pyrochlore lattice (see Fig. 1 (a)). In general, glassy states appear when periodic long-range ordering is avoided down to very low temperatures or high densities where strong interactions become important. Therefore frustration is a key ingredient for glass physics [18]. The most spectacular example is the pyrochlore oxide $\text{Y}_2\text{Mo}_2\text{O}_7$, which is known experimentally to exhibit clear-cut spinglass transitions *without appreciable quenched disorder* [19, 20, 21, 22, 23, 24, 25]. Moreover, in sharp contrast to the structural glass transition mentioned above, the spin-glass transition emerges directly out of the paramagnetic state as a 2nd order transition much like the conventional spin-glass transitions [4, 5, 6, 7], without the need to go through the metastable 'supercooled' paramagnetic state. Actually, quite remarkably, the phenomenology of the spin-glass transition and even the critical exponents associated with the spin-glass transition [19, 20, 25] are nearly indistinguishable from that of the conventional, canonical spinglasses with quenched disorder.

On the theoretical side, microscopic explanation of the disorder-free spin-glass transition remained a big challenge for more than 30 years. The principal magnetic interaction in the pyrochlore oxide $\text{Y}_2\text{Mo}_2\text{O}_7$ is the antiferromagnetic interaction between the magnetic moments of the Mo ions sitting on vertices of the pyrochlore lattice. It has been established that the purely antiferromagnetic Heisenberg spin model on the pyrochlore lattice exhibits no transitions down to $T = 0$ because of the very strong geometrical frustration [26, 27]. This is remarkable given that the system is three dimensional. Coming back to the exper-

imental system, this observation means that the model is too crude to capture the real system which exhibits a spin-glass transition. In order to explain the spin-glass transition of the $\text{Y}_2\text{Mo}_2\text{O}_7$ system, previous theoretical studies assumed the presence of some amount of quenched disorder [28, 29]. However, from the mean-field theoretical point of view, disorder-free spin-glass transitions are possible [15]. Albeit in a somewhat artificial case with a highly non-linear interaction, where the model is built to describe an optimization problem like the graph coloring with continuous colors, a 2nd order disorder-free spin-glass transition involving full replica symmetry breaking emerges without passing through the superparamagnetic phase has been found (See sec. 10 of [15]).

The purpose of the present work is to uncover the microscopic mechanism of the disorder-free spin-glass transition observed in the pyrochlore magnet. Our key observation in the present work [1], which is motivated by a recent experiment [23], is that in the pyrochlore oxides, not only the spins but also the orbitals (lattice displacements) exhibit glass transitions simultaneously - spin-orbital glass transition. In the following, we first explain our theoretical model and then present our results obtained by extensive Monte Carlo simulations at ISSP.

2 Model

We consider two kinds of dynamical variables associated with the $\text{Mo}^{4+}(4d^2, S = 1)$ ions which sit on the vertices $i = 1, 2, \dots, N$ of the pyrochlore lattice. The first is the classical Heisenberg spin $\mathbf{S}_i = (S_i^x, S_i^y, S_i^z)$ normalized as $|\mathbf{S}| = 1$ which represents the magnetic moments of the Mo ion.

The second is the 'displacement' of the Mo ions $\boldsymbol{\sigma}_i = (\sigma_{i,x}, \sigma_{i,y}, \sigma_{i,z})$. The recent experiment [23] suggests that the pyrochlore lattice is distorted by displacements of the Mo ions. The displacement of a vertex (the Mo ions) take place along the lines connecting the two tetrahedra that share the vertex. Thus the displacements of the vertices of a given tetrahedron are either pointing toward or away

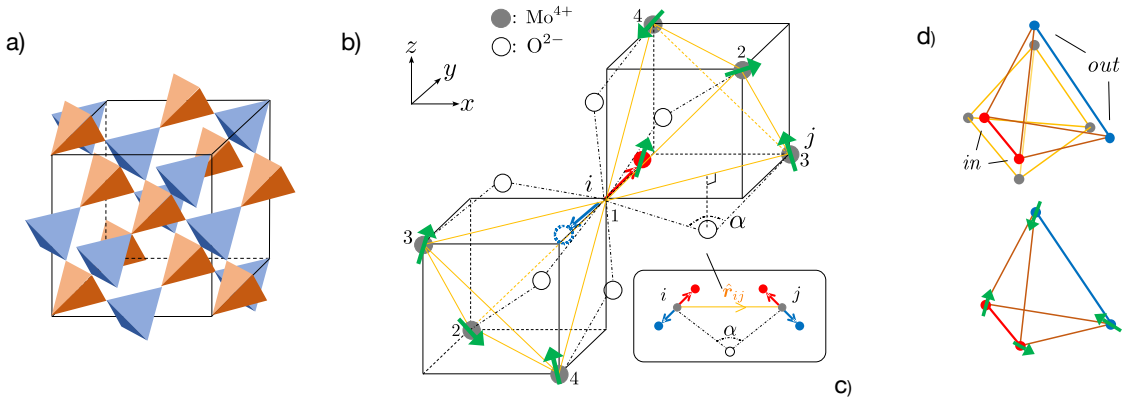


Figure 1: Spins on deforming pyrhoclore lattice. (a): Pyrhoclore lattice. (b): O² ions and magnetic Mo⁴⁺ ions around the *i* site, where the numbers 1 – 4 are the sublattice indices of Mo⁴⁺ ions. Red and blue dashed circles represent the positions of the Jahn-Teller distorted *i* ion. Spins on a pair of Mo⁴⁺ ions (*i*, *j*) interact through the O² ion as shown in the inset panel, where alpha is the Mo-O-Mo angle and \hat{r}_{ij} is the unit vector in the *i* → *j* direction. (c): Ice-type displacements of the Mo tetrahedron. The different color bonds represent different exchange interactions. (taken from [1, 2])

from the center of the tetrahedron. Furthermore, the experiment suggests that the displacements follow the 'ice-rule' [30]: the '2-in-2-out' structure (see Fig. 1 (d)). As suggested by the experiment, we parametrized the displacements as $\sigma_i = \sigma_i \hat{e}_\nu$. Here we introduced an Ising variable $\sigma_i = \pm 1$ to represent 'in' and 'out' displacements depending on \hat{e}_ν which is a unit vector in the $[111]$, $[\bar{1}\bar{1}\bar{1}]$, $[\bar{1}1\bar{1}]$ and $[\bar{1}\bar{1}1]$ directions respectively for the sub-lattices $\nu = 1, 2, 3, 4$ which the *i*-th spin belongs to (See Fig. 1.(b)). The microscopic mechanism of the peculiar displacements is presumably a Jahn-Teller effect: the displacements break the 3-fold rotational symmetry of the trigonal crystal field for the Mo ions resulting in the splitting of its e'_g orbital [3]. Thus we regard σ_i as the variable which represents the configuration of the orbital of the Mo ion.

Our effective model for the pyrhoclore magnet Y₂Mo₂O₇ is given by the following effective Hamiltonian,

$$H = \sum_{\langle ij \rangle} J_{\sigma_i, \sigma_j} \mathbf{S}_i \cdot \mathbf{S}_j - \epsilon \sum_{\langle ij \rangle} \sigma_i \cdot \sigma_j \quad (\epsilon > 0) \quad (1)$$

with

$$J_{\sigma_i, \sigma_j} = J[1 + \delta(\hat{r}_{ij} \cdot \sigma_i + (-\hat{r}_{ij}) \cdot \sigma_j)] \quad (\delta > 0), \quad (2)$$

The 1st term of Eq. (1) describes the exchange interaction between the spins on the nearest-neighbour sites $\langle i, j \rangle$ on the pyrhoclore lattice. The exchange interaction Eq. (2) between the spins on the *i*-th and *j*-th Mo ions, with the energy scale $J (> 0)$, is mediated by the O ion and depends on the angle α of the Mo-O-Mo bond. (see Fig. 1 (b)(c)) Thus the exchange interaction depends on the displacements σ_i and σ_j of the Mo ions. This form is constructed in a way to reproduce the values of the effective interactions derived microscopically from the perturbation process on a Kanamori-type of Hamiltonian [1, 2]. More precisely we parametrize it as $J_{\sigma_i, \sigma_j} = (1 + 2\tilde{\delta})J(\text{in}, \text{in}), J(\text{in}, \text{out}), (1 - 2\tilde{\delta})J(\text{out}, \text{out})$, where $\tilde{\delta} = \sqrt{6}\delta/3$.

The 2nd term of Eq. (1) represents the elastic energy of the Mo⁴⁺ displacements. The elastic energy is minimized if the ice-rule is satisfied.

There are three parameters in this system; $\tilde{T} = k_B T / J$ is the dimensionless temperature, $\tilde{\epsilon} = \epsilon / 3J$ the ratio of the energy scales between the exchange interaction and the elastic energy

of the displacement, and $\tilde{\delta} = \sqrt{6}\delta/3$ is the amplitude of the displacement (hereafter we call them simply as T , ϵ , δ). At $\epsilon \rightarrow \infty$, the lattice distortion becomes static.

Finally let us note what happens if we switch off the coupling between the spins and orbitals (lattice displacements) $\delta = 0$. Then our system is decoupled into (1) the spin part with purely antiferromagnetic interactions [26, 27] and (2) the orbital (lattice) part with pure 'spin-ice' type interaction [30, 31]. Both of them have essentially flat energy landscape so that the two degrees of freedom remain disordered down to $T = 0$.

3 Simulation Methods

In order to perform simulations in equilibrium, we combined the following methods in our Monte Carlo simulations.

Single spin update: The usual single spin updates by the conventional Metropolis algorithm is employed for the Ising variables $\sigma_i = \pm 1$ ($i = 1, 2, \dots, N$).

Loop update method: We also adopted a nonlocal update method called the loop update algorithm, used to simulate spin-ice systems [32], to for the Ising variables σ_i .

Monte Carlo reflection method: For the Heisenberg spins \mathbf{S}_i ($i = 1, 2, \dots, N$), we used the single spin updates by the Metropolis reflection method [33].

Over-relaxation method: We also used the over-relaxation method to update the Heisenberg spins. [34]

Replica exchange method: On top of the above methods we used the replica-exchange method [35] to accelerate the equilibration of the whole system.

We consider the periodic systems of cubic geometry consisting of L^3 unit cells with totally $N = 16L^3$ spins, and perform 120 statistically independent runs for the system size $L = 4, 5, 6, 8$, evaluating the averages and mean-squared errors of observable. In the following analysis, we mainly focus on a representative system at $\delta = 1.5, \epsilon = 0.6$.

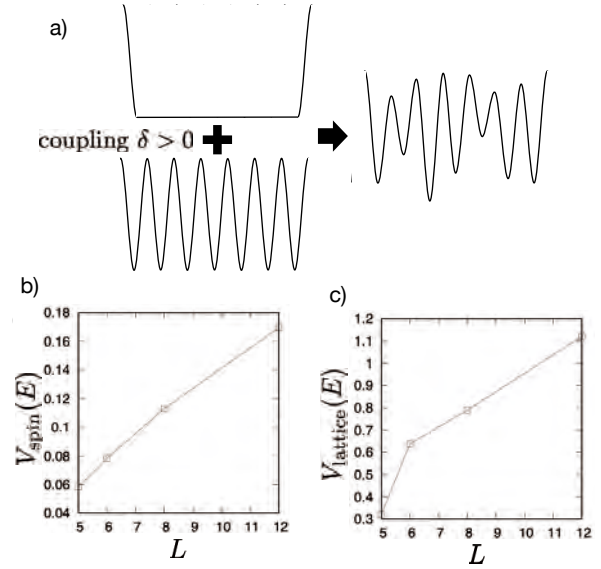


Figure 2: Energy landscape. (a): Schematic picture of energy landscape. The essentially flat energy landscapes (with many energetically degenerate minima) of the spins (left/top) and orbitals (left/bottom) in the absence of the coupling $\delta = 0$ change into a complex one in the presence of the coupling $\delta > 0$ (right). (b),(c) variance of the energy between different energy minima obtained by quench experiments (taken from [2])

4 Results

4.1 A simple analysis of the energy landscape

As we mentioned at the end of sec. 2, the energy landscape of our system becomes essentially flat (with many energetically degenerate minima) if we switch off the coupling between the spins and orbitals (lattice displacements), i. e. $\delta = 0$. Here let us show the result of a simple quench experiment which provides some insights on how the energy landscape changes in the presence of the coupling $\delta > 0$. First we generated 'spin-ice' configurations of σ_i 's randomly. Note that any of them minimizes the 2nd term of the Hamiltonian Eq. (1). Second, we performed a simple energy descent simulation with respect to the 1st term of the Hamiltonian Eq. (1) by zero

temperature, greedy Monte Carlo updates of the spins with orbitals σ_i being fixed. Repeating this procedure we obtained a large number of energy minima of various energies E . In Fig. 2 (b) we display the variance of the energy $V_{\text{spin}}(E) = \overline{\langle E^2 \rangle} - \langle E \rangle^2$ between different realizations of the spins with a common orbital (lattice) configuration (averaged over different realizations of such orbitals). Here $\langle \dots \rangle$ represents the average over different realizations of the spins with a common orbital (lattice) configuration and $\overline{\dots}$ the average over different realizations of the orbitals. In Fig. 2 (c) we show the corresponding one to measure the fluctuation between different realizations of the orbitals (lattice) $V_{\text{lattice}}(E) = \overline{\langle E^2 \rangle} - \langle E \rangle^2$. Both (b) and (c) show that the variance grows with the system size L suggesting rugged, complex energy landscape.

4.2 Critical slowing down without long-ranged ordering

By lowering the temperature we observed that the dynamics of both the spins and orbitals (lattice displacements) slow down significantly. In Fig. 3 (a)-(b) we display the time autocorrelation functions of the spins $C_s(t)$ and orbitals $C_\sigma(t)$ plotted against time t . Here we used 'single spin updates' for the spins and orbitals to measure the dynamical observables, starting from the initial configurations equilibrated using all protocols listed in sec 3. As shown in (c)-(d), the relaxation times grow in lowering the temperature following a power law. The independent power-law fits on the two observables suggest a common critical temperature $T_c \sim 0.07$ with different exponents $z\nu \sim 4.2$ (orbital) and $z\nu \sim 3.5$ (spin). As shown in (e)-(f) the auto-correlation functions follow scaling laws in terms of scaled times. We have checked that finite-size effects of the auto-correlation function is negligible within the temperature and time scales shown in the Figure. We have found that the same type of scaling holds for $\epsilon = 0.65$, with $T_c \sim 0.086$ and almost the same exponents as obtained above [2, 3].

As shown in Fig. 4, the structure factor of the spins S_s and orbitals (lattice displacements) S_σ show no hints of long-range order-

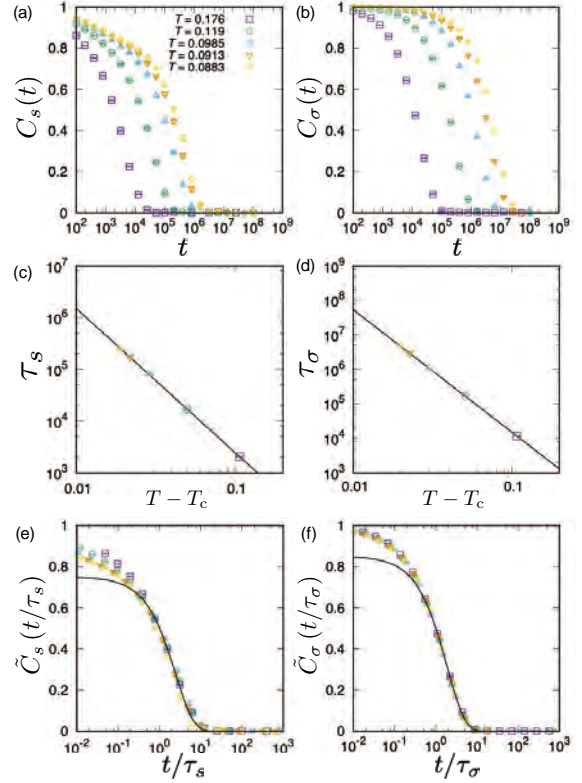


Figure 3: Autocorrelation functions and relaxation times of the spins and orbitals. $L = 6$, $\epsilon = 0.6$. (taken from [1])

ing. Some pinch points can be seen in S_σ , for example at $(1/2, 1/2, 1/2)$, at low temperatures as well known in spin-ice systems [31].

To summarize the above observations suggests a simultaneous, 2nd order glass transitions of the spins and orbitals (lattice displacements) at a common temperature, into a new glass phase - spin-orbital glass phase, which emerges directly from the high temperature paramagnetic (liquid) phase.

4.3 Non-linear susceptibilities

The signatures of the spin-orbital glass can be detected by observing non-linear susceptibilities of the two degrees of freedom. As shown in Fig. 5, the non-linear susceptibilities computed using fluctuation formulae (see [1] for the details) at lower temperatures grow *negatively* rapidly when increasing the system size L . This observation provides an interesting suggestion for experiments: by observing not

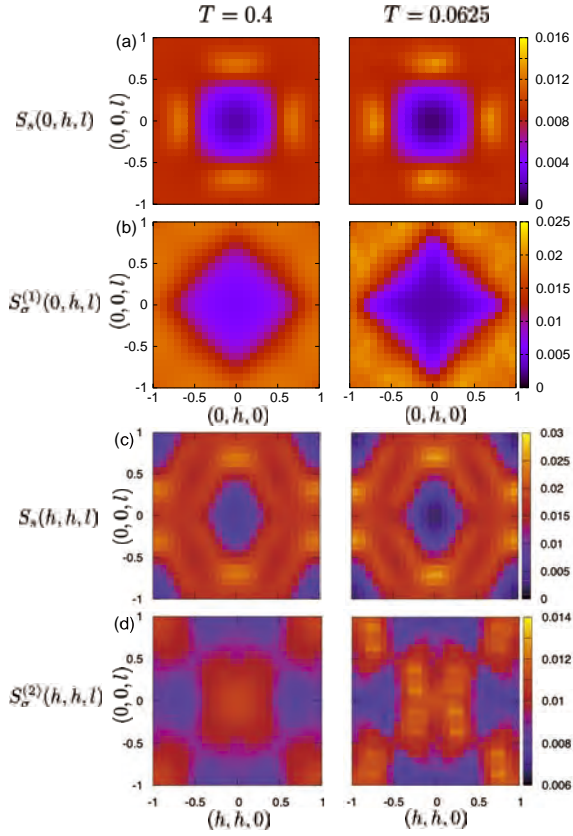


Figure 4: Heat maps of the structure factors of the spins and lattice displacements. $L = 6$, $\epsilon = 0.6$ above T_c ($T = 0.4$) in the left side and below T_c ($T = 0.0625$) in the right side. (taken from [1])

only the usual magnetic non-linear susceptibility, which is used often to study conventional spin-glasses [4, 6, 7], but also dielectric non-linear susceptibility, the simultaneous spin-orbital glass transitions suggested by the present work may be detected experimentally.

4.4 Static or dynamic distortions?

In our study we regard the lattice distortions (orbitals) as *dynamical* degrees of freedom rather than as frozen-in, static quenched disorder. But by increasing the energy scale of the lattice displacements given by the parameter ϵ in Eq. (1), one would wonder whether the lattice displacements can freeze independently from the spins at higher temperatures. If this happens, the spin-glass transitions of a con-

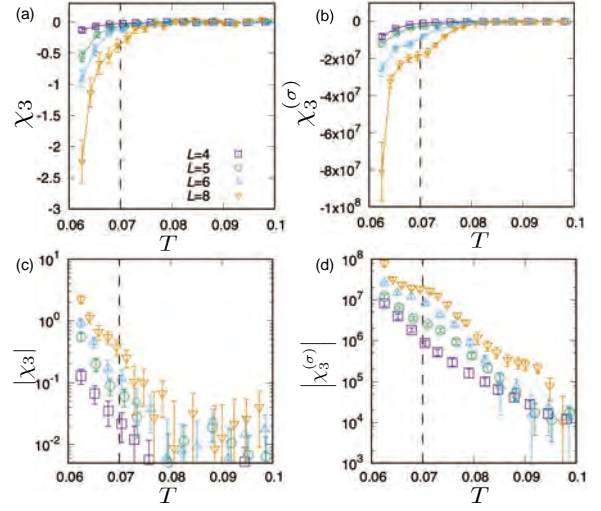


Figure 5: Non-linear susceptibilities of the spins and orbitals (lattice displacements). $\epsilon = 0.6$. Panels (a),(c) display the non-linear susceptibilities of the spin while (b),(d) display the non-linear susceptibilities of the lattice displacements (orbitals). (taken from [1])

ventional type, i. e. the one due to *quenched* disorder, may take place at a lower temperature.

To get some insight into this issue within the available computational resources, we analyzed the heat capacity C and the fraction P of the tetrahedra which satisfies the ice rule at various values of ϵ . At $\epsilon = 0.6, 0.65$, for which we have determined the critical temperature of the spin-orbital glass transition, we found that the heat-capacity exhibit a peak at slightly higher temperatures, similarly to the case of the conventional spin-glasses [4] and the experimental result in the $Y_2Mo_2O_7$ system [36]. We have checked that the finite-size effects of the heat capacity are very weak [1]).

As shown in Fig. 6, the heat-capacity exhibit an additional peak at a higher temperature at larger values of $\epsilon > 1.0$. The peak at the higher temperatures appears to follow the peak of dP/dT . This observation suggests that at larger values of ϵ , the liquid state of the lattice distortions exhibits a smooth crossover from purely random one to more spin-ice like one at higher temperatures. On the other hand, the other peak of the heat capacity located at

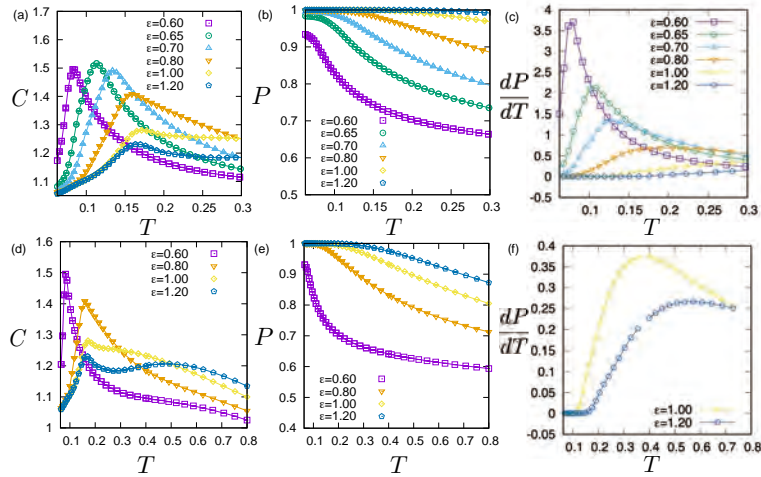


Figure 6: Heat capacity C and fraction P of tetrahedra which satisfy the ice-rule. $L = 5$. (a)-(c) for $0 < T < 0.3$ (d)-(f) for a wider temperature range $0 < T < 0.8$. (taken from [1])

the lower temperatures tend to saturate to a finite temperature $T \sim 0.16$ by increasing ϵ . Very importantly we confirmed that the orbital degrees of freedom remain dynamically fluctuating between the intermediate temperatures between the higher and lower peak temperatures of the heat-capacity [2, 3]. This means that the orbitals do *not* produce the putative static quenched disorder for spins but remain dynamical. We consider that the spin and orbital degrees of freedom interact cooperatively at the energy scale corresponding to the lower peak temperature and exhibit the simultaneous glass transition at that energy scale.

5 Summary and Outlook

To summarize we constructed a theoretical model to describe the spontaneous glass transition observed in the pyrochlore oxide $\text{Y}_2\text{Mo}_2\text{O}_7$ and performed extensive Monte Carlo simulations of the model. Our results strongly suggest a new type of glass transition - spin-orbital glass transition.

There are numerous possibilities for further works. Exploration of the parameter space, especially along the ϵ -axis, should be done to clarify to what extent our present scenario holds. Construction of a mean-field theory [37] would provide a useful guideline in this respect.

The criticality of the spin-orbital glass transition and its universality, consistency with the experimental results [19, 20, 25], should be examined by approaching more closer to the critical temperatures.

Acknowledgments This work was supported by KAKENHI (No. 19H01812, 17K05533, 17K05497, 18H01173, 17H02916) from MEXT, Japan. The computation in this work has been done using system B of the Supercomputer Center, the Institute for Solid State Physics, the University of Tokyo.

References

- [1] Kota Mitsumoto, Chisa Hotta, and Hajime Yoshino. *Physical Review Letters*, 124(8):087201, 2020.
- [2] Kota Mitsumoto, doctoral thesis, Osaka Univ., 2020.
- [3] Kota Mitsumoto, Chisa Hotta, and Hajime Yoshino. *in preparation*.
- [4] John A Mydosh. *Spin glasses: an experimental introduction*. CRC Press, 2014.
- [5] M Mézard, G Parisi, and M Virasoro. volume 9. World Scientific Publishing Company, 1987.

- [6] K Binder and AP Young. *Reviews of Modern physics*, 58(4):801, 1986.
- [7] H Kawamura and T Taniguchi. volume 24. Elsevier, 2015.
- [8] PW Anderson. *Science*, 267:1615, 1995.
- [9] W. Kauzmann. *Chem Rev*, 43:219–256, 1948.
- [10] Jean-Pierre Hansen and Ian R McDonald. *Theory of simple liquids*. Elsevier, 1990.
- [11] M. Mézard, G. Parisi, and M. A. Virasoro. *Spin glass theory and beyond*. World Scientific, Singapore, 1987.
- [12] Giorgio Parisi, Pierfrancesco Urbani, and Francesco Zamponi. *Theory of Simple Glasses: Exact Solutions in Infinite Dimensions*. Cambridge University Press, 2020.
- [13] Ludovic Berthier and Giulio Biroli. *Reviews of Modern Physics*, 83(2):587, 2011.
- [14] Yoshihiko Nishikawa and Koji Hukushima. *arXiv preprint arXiv:2003.02872*, 2020.
- [15] Hajime Yoshino. *SciPost Phys*, 4:040, 2018.
- [16] J. G. Kirkwood. *in in Phase Transitions in Solids, edited by R. Smoluchowski, J. E. Mayer, and A. Weyl (Wiley, New York, 1951)*.
- [17] Leticia F Cugliandolo, Laura Foini, and Marco Tarzia. *Physical Review B*, 101(14):144413, 2020.
- [18] Gilles Tarjus, Steven A Kivelson, Z Nussinov, and Pascal Viot. *Journal of Physics: Condensed Matter*, 17(50):R1143, 2005.
- [19] MJP Gingras, CV Stager, BD Gaulin, NP Raju, and JE Greedan. *Journal of applied physics*, 79(8):6170–6172, 1996.
- [20] MJP Gingras, CV Stager, NP Raju, BD Gaulin, and JE Greedan. *Physical review letters*, 78(5):947, 1997.
- [21] JS Gardner and et al. *Physical review letters*, 83(1):211, 1999.
- [22] HD Zhou, CR Wiebe, A Harter, NS Dalal, and JS Gardner. *Journal of Physics: Condensed Matter*, 20(32):325201, 2008.
- [23] PMM Thygesen and et al. *Physical review letters*, 118(6):067201, 2017.
- [24] CH Booth and et al. *Physical Review B*, 62(2):R755, 2000.
- [25] N Hanasaki and et al. *Physical review letters*, 99(8):086401, 2007.
- [26] JN Reimers, AJ Berlinsky, and AC Shi. *Physical Review B*, 43(1):865, 1991.
- [27] R Moessner and JT Chalker. *Physical review letters*, 80(13):2929, 1998.
- [28] TE Saunders and JT Chalker. *Physical review letters*, 98(15):157201, 2007.
- [29] H Shinaoka, Y Tomita, and Y Motome. *Physical review letters*, 107(4):047204, 2011.
- [30] L Pauling. volume 260. Cornell university press Ithaca, NY, 1960.
- [31] ST Bramwell and MJP Gingras. *Science*, 294(5546):1495–1501, 2001.
- [32] Roger G Melko, Byron C den Hertog, and Michel JP Gingras. *Physical review letters*, 87(6):067203, 2001.
- [33] S Große Pawig and K Pinn. *International Journal of Modern Physics C*, 9(05):727–736, 1998.
- [34] JL Alonso and et al. *Physical Review B*, 53:2537–2545, 1996.
- [35] K Hukushima and K Nemoto. *Journal of the Physical Society of Japan*, 65(6):1604–1608, 1996.
- [36] NP Raju, E Gmelin, and RK Kremer. *Physical Review B*, 46(9):5405, 1992.
- [37] Kota Mitsumoto and Hajime Yoshino. *in preparation*.

3.2 First-Principles Calculation of Material Properties

Mechanisms of Semiconductor Interface Formation and its Electronic Properties based on Quantum Theory

Atsushi Oshiyama

Institute of Materials and Systems for Sustainability, Nagoya University

Furo-cho, Chikusa-ku, Nagoya 464-8601

In the fiscal year of 2019, on the basis of the total-energy electronic-structure calculations and molecular dynamics simulations within the density-functional theory, we have studied atom-scale behavior during the epitaxial growth of power semiconductors, silicon carbide (SiC) and gallium nitride (GaN). The main computational tools are our RSDFT (Real Space Density Functional Theory) code and RS-CPMD (Car-Parrinello Molecular Dynamics) code. We have clarified 1) the structures and energetics, and then the morphology of SiC surface steps [1,2], 2) the liquid-like behavior of the topmost Ga atoms [3] and 3) the mechanism of oxygen incorporation during the epitaxial growth of GaN [4,5]. The group identification codes for the achievements above are k0042 and m0001. Below, I explain the issues 1) and 2).

1. Step structures and morphology of Si-face SiC Polar Surface

SiC is now emerging as a promising material for power electronics. This is due to its physical properties superior to Si, a current premier material, such as the wider band gap and the higher electric break-down voltage. The thin-film growth of SiC in the step-flow mode is essential

in the fabrication of electronic devices. Understanding of bond configurations near the step on the atomistic level is necessary in order to identify the reactivity at the step edges. Furthermore, epitaxial graphene can be prepared on SiC surfaces, and the surface steps of SiC also play an important role. Hence, it is certainly important and inevitable from both science and technology viewpoints to identify the atomic steps on SiC and clarify their energetics, that has not been achieved yet. Our previous calculations [6] show that the single-bilayer height steps are

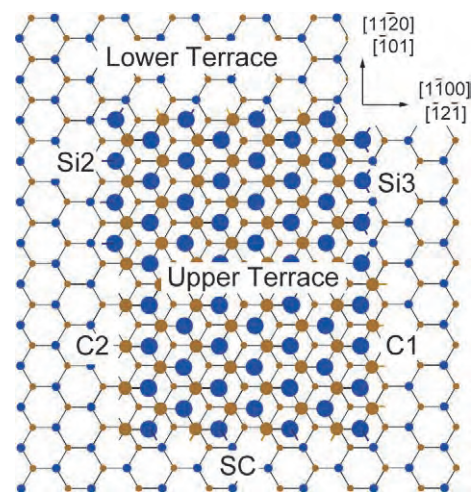


Fig.1: Schematic view of the five distinct mono-bilayer steps on SiC (0001) surface. Si and C atoms are represented by the larger (blue) and smaller (brown) balls, respectively. The Si2, Si3, C1 and C2 steps along the $\langle 11-20 \rangle$ direction and the SC step along the $\langle 1-100 \rangle$ direction are shown all together.

energetically favorable compared with higher steps on SiC(0001) or (111) surface.

Figure 1 shows schematic view of 5 distinct single-bilayer height steps. There are two different classes of steps: One is [11-20] oriented and the other is the [1-100] oriented; further in the latter, four different step edges exist which are labelled by the atomic species at the edge and the number of the dangling bonds before the structural relaxation as Si2, Si3, C1 and C2.

We have performed detailed structural optimization for all the possible atomic steps and determined their structures. Near step edges we have found prominent rebonding between the upper-terrace and the lower terrace Si atoms in Si2 and SC steps and also a peculiar resonant-like rebonds for Si3 steps, as well as the C dimerization for the C2 step.

Figure 2 shows calculated formation energies

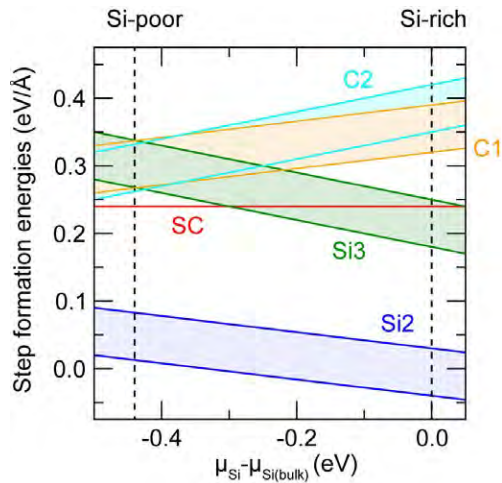


Fig. 2: Calculated formation energies of the mono-bilayer atomic steps on SiC(0001) surface as a function of the Si chemical potential μ_{Si} , measured from that in crystalline Si, $\mu_{\text{Si}(\text{bulk})}$. Shaded areas surrounded by each pair of solid lines represent the uncertainty in the calculated formation energy.

for 5 distinct steps as a function of Si chemical potential (Near step edges, the numbers of Si and C atoms are different so that we need the chemical potential). We have found that Si2 step toward [1-100] is the most stable and Si3 step follows. The SC step toward [11-20] is comparable with the Si3 step.

The energetics obtained above predicts some interesting morphology of atomic steps on SiC(0001). Experimentally, the (0001) surface is slightly inclined along either [1-100] or [11-20] direction. When it is inclined along the [1-100], the surface consists of the [0001] terrace and several steps among Si2, Si3, C1 and C2, whereas it consists of the terrace and SC steps when inclined along [11-20]. In the former, the Si2 or Si3 steps are energetically favorable (Fig. 2). However, in the latter, the SC step is energetically unfavorable compared with Si2 and also Si3 in some range of the Si chemical potential. Hence we expect that the steps toward [11-20] show zig-zag shape consisting of, for instance, Si2 and Si3. We have indeed found that such zigzag-shaped step-edge pairs of Si2 + Si3 is lower in the formation energy than the straight-shape SC step on the [0001] surface inclined along [11-20] direction.

2. Two-Dimensional Ga liquid on growing GaN surface

GaN, a fundamental material worldwide used for high performing opto-electronic devices, is rapidly becoming another candidate to unseat Si in power electronics. Yet, their practical

realization asks for the realization of thin epitaxial films of higher quality with respect to what is done nowadays for optoelectronic applications. It is thus highly demanded to clarify the nature of the growing GaN surface at atomistic level.

It is known that under typical conditions of the epitaxial growth of GaN, the surface is Ga-rich. Hence we prepare Ga-rich surface and raise the temperature by CPMD simulations from room temperature. We have found that, when the temperature reaches the typical growth temperature, i.e., 1300 K, the topmost Ga atom suddenly moves from their original position. The calculated Ga-Ga pair correlation function is shown in Fig. 3. At room temperature, the top-layer Ga atoms vibrate around their original positions. The pair correlation function shows a peak determined by the Ga coverage. Then with increasing temperature, the pair correlation function shows the peak at the same position with increasing peak width, showing the enhanced thermal vibration. However, at the growth

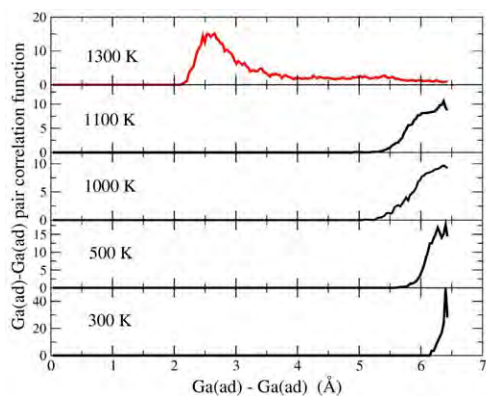


Fig. 3: Evolution of the Ga-Ga pair correlation function in the top-layer of GaN during the heating process. The initial distance of 6.4 Å corresponds to the relaxed system from which dynamical simulations were started.

temperature, the top-layer Ga atoms get together and exhibit the peak at much shorter distance, indicating some condensed phase of Ga.

By using Kubo-formula (velocity-velocity correlation function), we have computed the diffusion coefficient of the top-layer Ga atom. We have found that the diffusion coefficient jumps at 1300 K from its value of $0.382 \times 10^{-5} \text{ cm}^2/\text{s}$ at 1100 K to the value of $0.492 \times 10^{-4} \text{ cm}^2/\text{s}$. We thus conclude that this condensed phase is not a solid phase but a two-dimensional liquid phase. This is corroborated by the absence of the peaks except for the first peak at 1300 K in Fig. 3. The notion that the GaN surface during the epitaxial growth is 2-dimensional liquid is unrecognized in the past and important to consider mechanism of the epitaxial growth.

Related Publications

- [1] K. Seino and A. Oshiyama, *Appl. Phys. Exp.* **13**, 015506 (2020).
- [2] K. Seino and A. Oshiyama, *Phys. Rev. B* (2020) to be published.
- [3] K. M. Bui, M. Boero, K. Shiraishi and A. Oshiyama, *Jpn. J. Appl. Phys.* **59**, SGK04 (2020).
- [4] F. Shintaku *et al.*, *Appl. Phys. Exp.*, **13**, 055507 (2020)
- [5] D. Yosho *et al.*, *Phys. Sta. Solidi - Rapid Res. Lett.* 2000142 (2020).
- [6] K. Sawada, J.-I. Iwata, a. Oshiyama, *Appl. Phys. Lett.* **104**, 051605 (2014).

Analyses on electronic structure and magnetic property in high-performance spintronics and magnetic materials

Tatsuki ODA^{1,2}, Indra PARDEDE^{1,2}, Afrioni Roma RIO², Achmad Maulana GANI², Daiki YOSHIKAWA², Tomosato KANAGAWA², Hasan Al RASYID², Masao OBATA^{1,2}

¹*Institute of Science and Engineering, Kanazawa University, Kanazawa, Ishikawa 920-1192*

²*Graduate School of Natural Science and Technology, Kanazawa University, Kanazawa, Ishikawa, 920-1192*

Magnetic anisotropy calculation.

We have developed a computational method of magnetic anisotropy energy (MAE) using the noncollinear spin density functional theory (NC-SDFT). This method enables us to estimate the MAE including both contributions to the MAE from magnetocrystalline anisotropy energy (MCAE) originating from spin-orbit coupling and the shape magnetic anisotropy energy (SMAE) originating from spin dipole-dipole interaction [1]. In the calculation of SMAE, the contribution was estimated from the spin density distribution that is obtained in the NC-SDFT. One can expect an accurate SMAE. Indeed, we have found some corrections on SMAE coming from the quadrupole component of atomic spin density [2,3].

We applied the method to the free-standing Co/Ni(111) multilayer that indicates a perpendicular anisotropy [1]. The results indicated a good agreement

with an available experimental measurement, as shown in Fig.1. This agreement implies that our method is promising on the estimation of MAE.

We have established a calculation method of MCAE in the same time. The MCAE part was evaluated from both methods of total energy (TE) and grand-canonical force theorem (GCFT) [1]. All MCAE values from the TE were well reproduced by those from the GCFT method. The advantage of GCFT method over the TE method makes analysis of the atom-resolved and k-resolved contributions of MCAE. In Fig.2, one can easily recognize the portions of large contribution to MCAE. Such figure can be compared with the orbital-resolved component of band dispersion curves. As a result, the MCAE is deeply understood, combined with its anisotropy of orbital components. The atom-resolved MCAE is also very useful to understand the atom/layer alignment giving rise to large

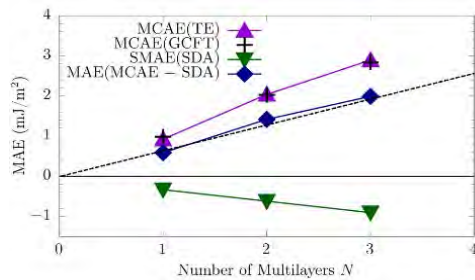


Fig. 1. MAE in Co/Ni multilayer structure as num. of multilayer.

MCAEs. In the application of Co/Ni(111), we recognized that the Co/Ni interface makes a large perpendicular magnetic anisotropy.

NC-SDFT under magnetic field.

We implemented a density functional scheme which enables application of a uniform external magnetic field. In the implementation, the rotation of the magnetic moment on an atom was described using the NC-SDFT calculation. The new scheme was successfully applied to a ferromagnetic slab with a perpendicular magnetic anisotropy and an antiferromagnetic material [4]. These results were discussed along with the simple model. This approach may provide a useful tool in analyzing magnetic properties of materials. In the scheme, the Kohn–Sham equation was solved self-consistently with the noncollinear spin density in the system.

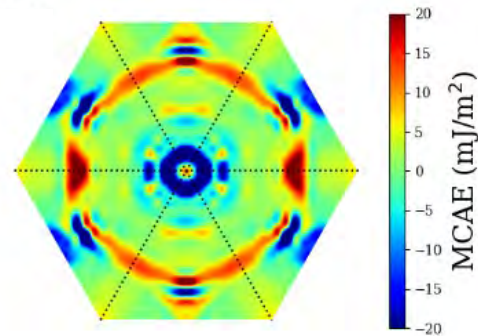


Fig. 2 k-resolved MCAE in Co/Ni(111) multilayer structure.

Other contributions.

We have developed a noncollinear spin version of van der Waals density functional scheme [5]. We have also contributed a theoretical part of the spintronics application in the system of interfacial magnetic anisotropy of PtCoO/ZnO [6].

References.

- [1] I. Pardede *et al.*: J. Magn. Magn. Mater. **500** (2020) 166357.
- [2] T. Oda and M. Obata: J. Phys. Soc. Jpn. **87** (2018) 064803.
- [3] T. Oda *et al.*: IEEE Trans. Magn. **55** (2018) 1300104.
- [4] A. R. Rio *et al.*: J. Phys. Soc. Jpn. **89** (2020) 035002.
- [5] M. Christivana *et al.*: J. Phys. Soc. Jpn. **55** (2019) 104601.
- [6] M. Al-Mahdawi *et al.*: Phys. Rev. B **100** (2019) 054423.

Ab initio optimization of $4f$ - $3d$ intermetallic ferromagnets for permanent magnets

Munehisa Matsumoto

Institute for Solid State Physics, University of Tokyo

Kashiwa-no-ha, Kashiwa, Chiba 277-8581

and

Institute of Materials Structure Science, High Energy Accelerator Research Organization

Oho 1-1, Tsukuba, Ibaraki 305-0801

April 30, 2020

Today's main-stream commercial permanent magnets are made of sintered Nd-Fe-B alloys [1], or rapidly quenched alloys with analogous ingredients [2] that is fabricated into hot-deformed magnets. Their main-phase compound is a $4f$ - $3d$ intermetallic ferromagnet, $\text{Nd}_2\text{Fe}_{14}\text{B}$ [3]. Its magnetization of 1.6 Tesla at room temperature and relatively good temperature dependence of anisotropy field [4] makes $\text{Nd}_2\text{Fe}_{14}\text{B}$ a champion magnet compound for practical applications in the temperature range from 300 K to 500 K, while its relatively low Curie temperature at 585 K, almost half of the Curie temperature of elemental Fe, leaves only a small temperature margin as compared to Sm-Co magnets whose Curie temperature reaches the range of 1000 K. The high-temperature properties that are not very excellent pose a drawback for the Nd-Fe-B alloy, leading to various proposals for alternative materials including NdFe_{12}N [5, 6] and SmFe_{12} [7], which cannot escape other problem concerning structure instability. In parallel with such quest for the possible next-generation champion magnets, it is important to better understand today's champion magnets and verify if there is any marginal space left for a possible improvement of $\text{R}_2\text{Fe}_{14}\text{B}$ -based permanent magnets (R=rare earth). Thus we have been investigating optimally degined materi-

als with a pool of candidate chemical compositions, made of preferably light rare earth elements and iron-group elements, where a good compromise involving all of the desired properties, such as structure stability, magnetization, magnetic anisotropy and Curie temperature, can be reached within a restricted lattice structure of $\text{R}_2\text{T}_{14}\text{B}$ (T=Fe or Co).

In order to explore the chemical composition space in a combinatorial way, we run massively parallel computer simulations for $\text{R}_2\text{T}_{14}\text{B}$ covering a virtual space spanned by R's and T's utilizing *AkaiKKR* [8], the open-source package for *ab initio* electronic structure calculations based on Korringa-Kohn-Rostoker (KKR) Green's function method implementing coherent potential approximation. Once a self-consistent electronic structure is reached, an estimate of the Curie temperature can be done as a post-processing to the converged result, based on an approximation to consider the low-most excitations on the Fermi level dominantly contributed from the ferromagnetic spin waves. Atomic-pair wise exchange couplings can be estimated based on a magnetic force theorem following Liechtenstein *et al.* [9] and a realistic Heisenberg model defined from them can be solved by the mean-field approximation. The working lattice constants are basically taken from past experiments [3].

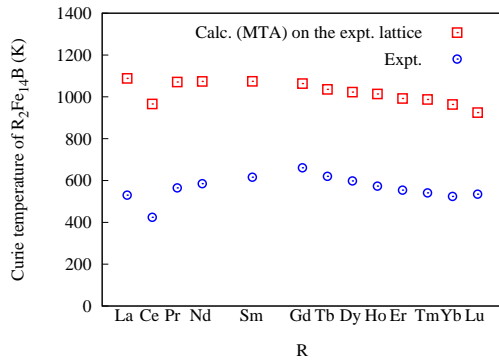


Figure 1: Calculated Curie temperature of $R_2Fe_{14}B$ (red square) based on muffin-tin approximation (MTA). For a comparison, the experimental data (blue circle) taken from Ref. [3] are also shown.

Calculated Curie temperature in a representative cross section of the overall chemical composition space, (R,T) , are shown in Fig. 1. Here we show the computational data set based on local density approximation [10] and within muffin-tin approximation. An analogous and more comprehensive data set within atomic-sphere approximation is published elsewhere [11]. It is seen that the overall trend with respect to the species of rare-earth elements is described satisfactorily, while the quantitative accuracy is not as excellent. The systematic deviation is reasonable, considering one of the biggest approximations we have made in modeling a metallic system only with spin degrees of freedom, as if our target systems were insulators. On top of that, temperature dependence of lattice constants would not entirely be negligible under the strong influence of the magnetovolume effect in such a strong ferromagnet [12]. Since the Curie temperature is mostly contributed from $3d$ -electrons, the relative trend within a materials family where the $3d$ -electron part is common seems to be well described. As long as we are aware of the particular way the systematic deviation between theory and experiment comes in, it is expected that we can care-

fully utilize the data obtained within the prohibitively crude approximation based on spin models even for intermetallics.

More extensive data collections to elucidate the overall trends have been in progress and will be published elsewhere.

References

- [1] M. Sagawa, S. Fujimura, N. Togawa, H. Yamamoto, and Y. Matsuura, *J. Appl. Phys.* **55** (1984) 2083.
- [2] J. J. Croat, J. F. Herbst, R. W. Lee, and F. E. Pinkerton, *J. Appl. Phys.* **55** (1984) 2078.
- [3] For a review, see e.g. J. F. Herbst, *Rev. Mod. Phys.* **63** (1991) 819.
- [4] S. Hirosawa, Y. Matsuura, H. Yamamoto, S. Fujimura, M. Sagawa, H. Yamauchi, *J. Appl. Phys.* **59** (1986) 873.
- [5] T. Miyake, K. Terakura, Y. Harashima, H. Kino, S. Ishibashi, *J. Phys. Soc. Jpn.* **83** (2014) 043702.
- [6] Y. Hirayama, Y. K. Takahashi, S. Hirosawa, K. Hono, *Scr. Mater.* **95** (2015) 70.
- [7] Y. Hirayama, Y. K. Takahashi, S. Hirosawa, K. Hono, *Scr. Mater.* **138** (2017) 62.
- [8] <http://kkr.issp.u-tokyo.ac.jp>
- [9] A. I. Lichtenstein, M. I. Katsnelson, V. P. Antropov, V. A. Gubanov, *J. Mag. Mag. Mater.* **67** (1987) 65.
- [10] S. H. Vosko, L. Wilk, and M. Nusair, *Can. J. Phys.* **58** (1980) 1200.
- [11] MM, H. Akai, *Phys. Rev. B* **101** (2020) 144402.
- [12] for a review, see A. V. Andreev, *Handbook of Magnetic Materials*, Ed. K. H. J. Buschow, Vol. 8, Chapter 2 (1995).

Data integration between theory and experiment for rare-earth permanent magnets

Munehisa Matsumoto

*Institute of Materials Structure Science, High Energy Accelerator Research Organization
Oho 1-1, Tsukuba, Ibaraki 305-0801*

June 15, 2020

Materials in practical use are characterized with macroscopic properties in a space-time scale comparable to the human scale, as rare-earth permanent magnets are with remanent magnetization and coercivity that works in operation environments that are typically out of thermal equilibrium. It is desirable to have a working methodology to understand and control those macroscopic properties of materials from the fundamental laws for atoms and molecules.

We have been in quest for such materials design scheme spanning over the microscopic and macroscopic physics. We have recently constructed an iterative approach between experimental data and theoretical data, taking as our playground a material of recent interest, namely, SmFe_{12} with substitution elements such as Ti, Co, and Zr, a candidate material for a new permanent magnet. Effects of Ti, Co, and Zr for multiple prerequisite properties for permanent magnet utilities, put in multiple sublattices, are investigated utilizing both of *ab initio* theoretical data and experimental data from neutron diffraction. Going back and forth between the Rietveld analysis for the latter and *ab initio* calculations based on local density approximation (LDA) until a fixed point is reached, dual site preference of Zr in SmFe_{12} has been newly elucidated, in contrast to the prevailing assumption in the literature that Zr replaces Sm only. This way of data-integration analysis has been tenta-

tively called “LDA+Rietveld” method [1], as has been constructed in an analogous spirit to LDA+DMFT (DMFT =dynamical mean field theory) [2].

For LDA+Rietveld, we have utilized *AkaiKKR* [3] for incorporating the substitute elements with a continuous variables of the concentration. *OpenMX* [4] is needed as well in order to address the structure stability with calculated formation energy. In LDA+DMFT, *LmtART* [5] has been utilized combined with a continuous-time quantum Monte Carlo impurity solver adapted for our realistic simulations.

Taking LDA+DMFT as a prototype, we have made one step forward in constructing a working simulation framework to bridge over the microscopic scale and the macroscopic scale.

References

- [1] MM, T. Hawaii, K. Ono, *Phys. Rev. Applied* **13** (2020) 064028.
- [2] MM, *Phys. Rev. Materials* **4** (2020) 054401.
- [3] <http://kkr.issp.u-tokyo.ac.jp>
- [4] <http://www.openmx-square.org>
- [5] http://savrasov.physics.ucdavis.edu/mindlab/MaterialResearch/Scientific/index_lmtart.htm

Physics of Electrochemical Interfaces

Osamu SUGINO

Institute for Solid State Physics,

The University of Tokyo, Kashiwa-no-ha, Kashiwa, Chiba 277-8581

The metal-solution interface exhibits various properties under the influence of the electrical double layer formed around the interface. Our group has been elucidating the reaction dynamics and adsorption processes from a microscopic perspective using interface-adapted first-principles computational methods. This year, our lab focuses on the following two different themes: (A) the quantum nuclear effect of hydrogen adsorption at the Pt(111)-solution interface [1] and (B) the role of defects in the activation of oxygen reduction reactions at the TiO₂-solution interface [2].

(A) Hydrogen atoms are known to exhibit large quantum effects, but these effects have been investigated only at the full mono-layer coverage ($\theta = 1$) or the low coverage limit ($\theta \ll 1$). In the former, hydrogen is recognized as a classical particle modified by the zero-point energy, and in the latter, hydrogen is

recognized as a quantum mechanically extended particle; our first-principles path-integral simulations for $\theta = 2/3$ and 1 capture the crossover, which can be explained by a lattice gas model with a quantum hopping term, or the Boson-Hubbard model. The results provide new insights into the mechanism of the hydrogen evolution reaction.

(B) Defective TiO₂ has been recognized as a future material for hydrogen fuel cell catalysts because of coexistence of the stability and activity, but the mechanism of the oxygen reduction reaction (ORR) is unknown. To search for the active site of this material, we took a high-throughput approach based on thermodynamics. Since important key to the activity is in the relative stability of the reaction intermediates, O and OH, we investigated how one can control the stability by doping. Contrary to

many materials like platinum, TiO_2 surfaces were found to bond O and OH differently when doped differently, suggesting it possible to sufficiently flatten the potential energy profile for ORR. This discovery has stimulated experimental collaborators to design

a novel fuel cell.

References

- [1] L. Yan et al. Phys.Rev.B101, 165414 (2020).
- [2] Y. Yamamoto et al. J.Phys.Chem.C123 19486 (2019).

DFT sampling analysis on interfaces and electrolytes in novel batteries

Yoshitaka TATEYAMA

Institute for Solid State Physics,

Center for Green Research on Energy and Environmental Materials (GREEN), National

Institute for Materials Science (NIMS), 1-1 Namiki, Tsukuba, Ibaraki 305-0044

We are working on (1) developments of theoretical, computational and data-driven techniques [1,2] as well as (2) understanding of surface and interface reactions, essential in the energy and environmental technologies such as battery and catalyst [3-8]. Recently, we have made a progress for DFT-based efficient calculations of solid-solid interfaces, mainly for all-solid-state batteries [1].

We have been exploring the atomistic understanding of this interfacial resistance mechanism with DFT-based calculations [4]. We first devised some systematic ways for the solid-solid interfaces and discussed possible origins such as the space-charge layer and the reaction layer. Recently, we incorporated the CALYPSO structure prediction technique with our method for the interface structure search, including mismatch treatment and lateral shift etc [1]. In this way, we have found several microscopic electrochemistry of the interfacial Li-ion states.

As a representative model, we investigated the system with LiCoO_2 (LCO), $\beta\text{-Li}_3\text{PS}_4$ (LPS), and LiNbO_3 (LNO) acting as a cathode, a

sulfide electrolyte, and a buffer layer, respectively. For the LCO/LPS interfaces, we sampled over 20000 configurations and found several stable disordered structures involving mixing cations and anions, leading to the formation of a reaction layer. On the other hand, Li-ion sites that can be preferentially depleted upon charging always exist around the cathode-SE interfaces irrespective of the interfacial order/disorder (See Li Chemical potential in Figure). Therefore, we conclude that the dynamic Li-ion depletion is likely to be a major cause that prevents successive Li-ion transport, leading to resistance.

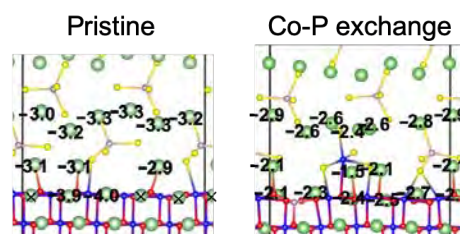


Fig. 1 Li chemical potentials around an interface between LiCoO_2 cathode and $\beta\text{-Li}_3\text{PS}_4$ solid electrolyte; Pristine interface (left) and Co-P exchange interface (right).

Through investigating the buffer layer effects and the interfacial electronic states, we also deduced a probable origin for the interfacial Li depletion and a mean to suppress this problematic behavior.

References

- [1] B. Gao, R. Jalem, Y. Ma, Y. Tateyama, *Chem. Mater.* **32** (2020) 85.
- [2] A. Ishikawa, Y. Tateyama, *J. Comp. Chem.* **40** (2019) 1866.
- [3] C. Yamaguchi, K. Natsui, S. Iizuka, Y. Tateyama, Y. Einaga, *Phys. Chem. Chem. Phys.* **21** (2019) 13788.
- [4] Y. Tateyama, B. Gao, R. Jalem, J. Haruyama, *Curr. Opin. Electrochem.* **17** (2019) 149.
- [5] B. Gao, R. Jalem, Y. Tateyama, *ACS Appl. Mater. Interfaces*, **12** (2020) 16350.
- [6] M. H. N. Assadi, M. Okubo, A. Yamada, Y. Tateyama, *Phys. Rev. Mater.* **4** (2020) 015401.
- [7] A. Ishikawa, K. Sodeyama, Y. Igarashi, T. Nakayama, Y. Tateyama, M. Okada, *Phys. Chem. Chem. Phys.* **21** (2019) 26339.
- [8] A. Ishikawa, Y. Tateyama, *J. Phys. Chem. C* **124** (2020) 6054.

Theoretical study on defects in wide-gap semiconductors: SiC and α -Ga₂O₃

Yu-ichiro MATSUSHITA

Institute for Innovative Research,

Tokyo Institute of Technology, Ookayama, Meguro-ku, Tokyo 152-8550

We have studied the stabilities of defects in wide-gap semiconductors on the basis of the density-functional theory (DFT). In this study, we focus on SiC and α -Ga₂O₃ as next-generation of power semiconducting materials. To clarify the stable defect structures and its electronic properties is necessary to move the power device applications forwards.

First, we have discussed the energetics of carbon-related defects in the SiC, SiO₂, and just at their interface for the systematic comparison of the stabilities of them in the three regions. As a result, we have found that the stable forms of the carbon defects depend on the oxidation environment. In the oxygen-rich condition at 1600K, nano carbon clusters likely to stay just at the SiC/SiO₂ interfaces [1]. According to the calculations, a high temperature oxygen-poor condition is preferable for reducing the remained carbon defects near the interface.

Very recently, an EDMR experiment detected carbon-dangling bonds along the direction perpendicular to the interface. We

succeeded in identifying the atomic structure of the defect as an ad-atom with a dangling bond (P_b center) based on the DFT calculations [2].

We have also calculated the formation energies of point defects in α -Ga₂O₃ [3]. We have used the extended FNV method to remove the artifacts derived from the background charge. We have found that Ga interstitials and Ga vacancies are the major defects when the Fermi energy approaches to valence and conduction bands, respectively.

References

- [1] T. Kobayashi and Y. Matsushita: J. Appl. Phys. **126** (2019) 145302. T. Kobayashi, K. Harada, Y. Kumagai, F. Oba, and Y. Matsushita: J. Appl. Phys. **125** (2019) 125701.
- [2] T. Umeda, T. Kobayashi, M. Sometani, H. Yano, Y. Matsushita, and S. Harada: Appl. Phys. Lett. **116** (2020) 071604.
- [3] T. Kobayashi, T. Gake, Y. Kumagai, F. Oba, and Y. Matsushita: Appl. Phys. Expr. **12** (2019) 091001.

First-principles configurational sampling of highly-doped ionic conductors

Shusuke KASAMATSU

Faculty of Science, Academic Assembly, Yamagata University

1-4-12 Kojirakawa, Yamagata-shi, Yamagata 990-8560

Ceramic-based electrolytes are under intense research for application in battery, fuel cell, and electrolyzer applications. These materials are usually prepared by doping insulating materials. When the charge-compensating defect is the hole or electron, you have a semiconductor. When the compensating defect is a mobile ion (or ion vacancy), you obtain an ionic conductor. Often, these materials are used at rather high dopant percentages of up to ~30% where the conductivity is maximized. There is still much controversy as to what determines this maximum, and computer simulations are expected to help in this regard.

At such high dopant concentrations, the short to middle-range order of the dopant arrangements should have a profound effect on the conductivity. To simulate this, i.e., dopant arrangements as functions of temperature and dopant content, we combined the replica exchange Monte Carlo method directly with DFT calculations [1] (the software for achieving this was selected as this year's Software Advancement Project, so details can

be found in that section). For example, Figure 1 shows the percolation of dopants in Y-doped BaZrO₃ vs. temperature calculated for several dopant concentrations. A profound temperature dependence is seen at 15%, which is close to the percolation threshold. Further discussion including successful reproduction of the dopant concentration for maximum conductivity can be found in Ref. [2].

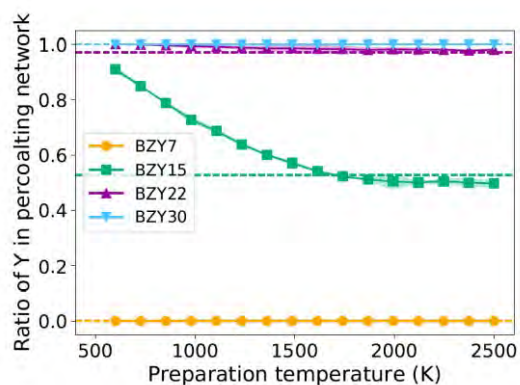


Figure 1 Percolation as functions of temperature for dopant ratios of 7, 15, 22, and 30 mol% in Y-doped BaZrO₃.

References

- [1] S. Kasamatsu and O. Sugino: *J. Phys.: Condens. Matter* **31** (2019) 085901.
- [2] S. Kasamatsu et al., *Chemrxiv*. Preprint. <https://doi.org/10.26434/chemrxiv.11786286.v1>

Analyses of Atomic Structures and Atom Dynamics at Surfaces, Interfaces and Defects

Satoshi WATANABE

*Department of Materials Engineering, the University of Tokyo
7-3-1 Hongo, Bunkyo-ku, Tokyo, 113-8656*

1 Introduction

The understanding on atomic structures and atom dynamics at surfaces, interfaces and defects is crucial to facilitate innovation of novel nanoscale information and energy devices. First-principles calculation is a powerful tool to obtain such understanding, but still insufficient to tackle with complex models corresponding to real devices.

Keeping the above in minds, we have been investigating atomic structures and atom dynamics in various systems via first-principles calculations combined with multi-scale or machine-learning approaches. In the followings, some of our results in the fiscal year 2018 are described.

2 Structure of interfaces between metal and solid electrolyte

The distribution and dynamics of Li ions near the interfaces between metal electrode and solid electrolyte play important roles in the operation mechanisms of novel memory device named VOLRAM [1] and all-solid-state Li-ion batteries. We examined Li ion distribution at the interfaces between γ -Li₃PO₄ and metal electrodes by the method [2] combining first-principles data of defect formation energies with a one-dimensional continuum model.

Our results [3] show that within the allowed range of the chemical potential of Li in γ -Li₃PO₄, upward band bending occurs near Au(111) and Ni(111) interfaces. This upward

bending is caused by the accumulation of interstitial Li-ions at the metal-Li₃PO₄ interfaces, and the thickness of the Li-ion accumulation layer is the order of a few Å. For the Li(100) interface, the band bending behavior depends on the chemical potential of Li, μ_{Li} : Slight upward bending occurs for $\mu_{\text{Li}} = -2.59$ eV, while downward bending occurs for $\mu_{\text{Li}} = -6.11$ eV owing to the accumulation of Li vacancies.

Since Au and Li are known to form alloys, we also performed simulations taking account of the alloy formation in the form of work function change. Figure 1 shows the calculated electrostatic potentials and interstitial Li distribution profiles in γ -Li₃PO₄ with Au(111), LiAu₃ and Li₃Au(100). In all cases, the potential profiles show upward bending and the accumulation of interstitial Li ions near the interfaces. However, the amount of interstitial Li-ions decreases for the alloy cases. From this result, we can explain the switching of VOLRAM.

3 Phonon-related properties of GaN

Considering the facts that GaN is promising for power semiconductor device and thermal management is important in power semiconductor device, we have been examining phonon band structures and thermal transport properties of GaN. In the fiscal year 2018, we had constructed the high-dimensional neural network potential (HDNNP) [4] for crystalline GaN, and calculated the phonon band structures and thermal conductivities using the

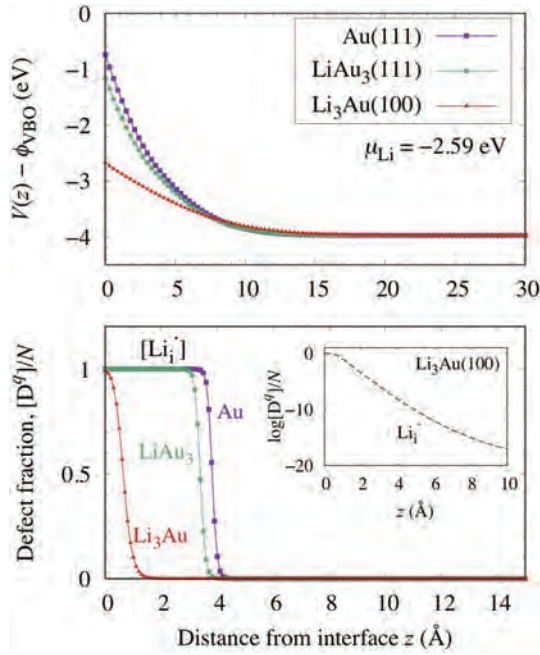


Figure 1: Calculated electrostatic potential and the interstitial Li fraction profiles of γ - Li_3PO_4 as a function of the distance from the interface z , with Au(111), LiAu_3 (111), and Li_3Au (100) (reproduced from Ref. [3]). The reference of the electrostatic potential corresponds to the Fermi level of metal surfaces. The chemical potential of Li is set to -2.59 eV.

constructed HDNNP. Our preliminary results were described in the Activity Report 2018.

In the fiscal year 2019, we improved the HDNNP and examined the phonon band structures and thermal conductivities more closely [5]. To obtain data of atomic structures, energies and forces, we performed classical molecular dynamics (MD) simulations with a well-established interatomic potential and then evaluated the energies and forces by the density functional theory (DFT) for structures sampled from the trajectories of classical MD. The final root mean square errors of force and total energy prediction in the validation data were $37.8 \text{ meV } \text{\AA}^{-1}$ and $66.5 \text{ meV atom}^{-1}$, respectively. The lattice thermal conductivity were calculated based on anharmonic lattice

dynamics using the phono3py package. The calculation results from HDNNP and DFT under the same simulation conditions are in good agreement, indicating the strong potential of HDNNP for application in thermal conductivity simulations: The deviation from the DFT calculation results is within 5.4% from 200 to 1000 K.

Then we constructed HDNNP for GaN crystal with N vacancies, and calculated the phonon band structures and thermal conductivities of GaN with N vacancies. In our preliminary calculations, we obtained reasonable phonon energy bands and thermal conductivities. We will check the reliability of the HDNNP and examine the effects of N vacancy on the phonon band and thermal conductivity in more detail in the fiscal year 2020.

References

- [1] I. Sugiyama, R. Shimizu, T. Suzuki, K. Yamamoto, H. Kawasoko, S. Shiraki, and T. Hitosugi: *APL Mater.* **5** (2017) 046105.
- [2] S. Kasamatsu, T. Tada, and S. Watanabe: *Solid State Ionics* **183** (2011) 20.
- [3] K. Shimizu, W. Liu, W. Li, S. Kasamatsu, Y. Ando, E. Minamitani, and S. Watanabe: *Phys. Rev. Mater.* **4** (2020) 015402.
- [4] J. Behler and M. Parrinello: *Phys. Rev. Lett.* **98** (2007) 146401.
- [5] E. Minamitani, M. Ogura, and S. Watanabe: *Appl. Phys. Express* **12** (2019) 095001.

First-principles molecular dynamics simulation of the water/air interface using hybrid functionals

Tatsuhiko OHTO

Graduate School of Engineering Science,

Osaka University, 1-3 Machikaneyama, Toyonaka, Osaka 560-8531

Density functional theory-based molecular dynamics simulations are increasingly being used for simulating aqueous interfaces. Nonetheless, the choice of the appropriate density functional, critically affecting the outcome of the simulation, has remained arbitrary. Here, we assess the performance of various exchange-correlation (XC) functionals, based on the metrics relevant to sum-frequency generation spectroscopy. The structure and dynamics of water at the water-air interface are governed by heterogeneous intermolecular interactions, therefore providing a critical benchmark for XC functionals. We find that the revPBE and revPBE0 with the dispersion correction show excellent performance. The poor performance of the empirically optimized density-functional (M06-L) manifests the importance of satisfying exact functional condition. Understanding the performance of different XC functionals can aid resolving the controversial interpretation of the interfacial water structure and direct the design of novel, improved XC functionals better suited to describe the heterogeneous interactions in

condensed phases. [1]

We employed the CP2K code [2], which is based on the mixed Gaussian and plane wave basis sets.

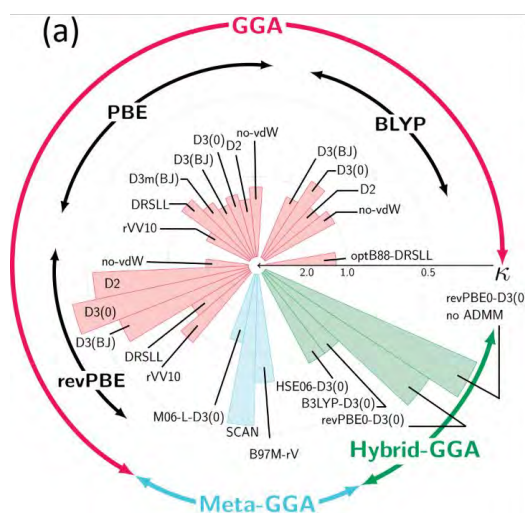


Fig. 1: The ability of different functionals to accurately predict water properties is directly compared. The smaller (larger) score κ corresponds to better (worse) predictive power of the functional [1].

References

- [1] T. Ohto et al. *J. Phys. Chem. Lett.* **10**, 4914 (2019).
- [2] The CP2K developers group, <http://cp2k.berlios.de/>

First-principles molecular dynamics simulation of electron-doped graphene/water interfaces

Tatsuhiko OHTO

Graduate School of Engineering Science,

Osaka University, 1-3 Machikaneyama, Toyonaka, Osaka 560-8531

Ab initio molecular dynamics (AIMD) simulation is a powerful tool to describe heterogeneous systems such as the water/solid interface. Although AIMD is computationally expensive, it describes electronic states beyond classical force fields,[1] which is important for interfaces.

We have simulated sum-frequency generation (SFG) spectra of isotopically diluted water at the water-graphene and water-hexagonal boron-nitride (hBN) sheet interfaces, using ab initio molecular dynamics simulations. The simulations themselves were performed using ISSP several years ago and recently the paper was published.[2] A sharp ‘dangling’ O-D peak around $\sim 2640\text{ cm}^{-1}$ appearing in both simulated SFG spectra evidences that both graphene and hBN are hydrophobic. The dangling O-D peak is 10 cm^{-1} red-shifted at the water-hBN interface relative to the peak at the water-graphene interfaces. This frequency difference manifests a stronger O-D...N intermolecular interaction between water and hBN than a O-D...C interaction between water and graphene.

To modify the hydrophobic interaction, we calculated electron-doped-graphene water interfaces using the CP2K code [3]. Although I got preliminary results, it seems that the integer number of electrons is too strong electron doping. It will be required to think about using plane wave codes (though they are computationally demanding).

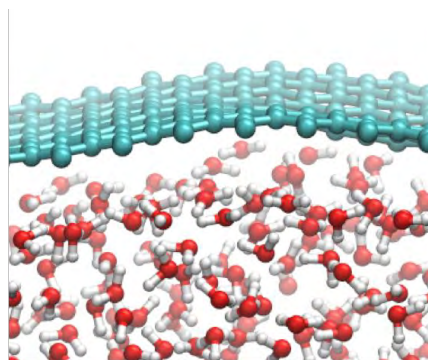


Fig. 1: Structures of the graphene-water interface.

References

- [1] T. Ohto et al. *Phys. Chem. Chem. Phys.* **19**, 6909 (2017).
- [2] T. Ohto et al. *Phys. Chem. Chem. Phys.* **20**, 12979 (2018)
- [3] The CP2K developers group, <http://cp2k.berlios.de/>

Development of first-principles electronic-structure and transport calculation code RSPACE and simulations for device

Tomoya ONO

*Graduate School of Engineering, Kobe University
Rokkodai-cho, Nada, Kobe 657-8501*

Silicon carbide (SiC) has attracted considerable attention owing to its excellent physical properties, such as its high thermal conductivity, high breakdown strength, and large band gap. It is also advantageous that the oxidation of SiC leads to SiO₂, since it is well known that SiO₂ exhibits good dielectric properties in Si device technology. However, unlike Si MOSFETs, SiC MOSFETs have unacceptably low carrier mobility. One of the origins of the low carrier mobility is the generation of a large number of interface defects at the SiC/SiO₂ interface during the thermal oxidation. In this study, we carried out density functional theory calculations to examine the oxidation process of SiC(0001)/SiO₂ interfaces shown in Fig. 1.[2]

It is not straightforward to characterize the atomic structure of the SiC(0001)/SiO₂ interface because SiO₂ at the SiC/SiO₂ interface is mainly amorphous. Here, I assume that crystalline structures exist locally at the SiC/SiO₂ interface and employ the most possible candidate for the interface atomic structures reported in Ref. 2. RSPACE code[4] is used for the first-principles calculations. The energy barriers in the oxidation process are computed by the nudged elastic band method. The lateral lengths of the supercell are chosen to be $\sqrt{3}a$ and $3a$ along the $[1\bar{1}00]$ and $[11\bar{2}0]$ directions of the 4H-SiC(0001) surface, where a is the lattice constant of SiC, and integration over the Brillouin zone is carried out using a 2

$\times 3 \vec{k}$ -point mesh.

The oxidation of 4H-SiC is assumed to proceed by the process which we proposed in the previous study:[3] (a) an O₂ molecule arrives at the interface, splits, and cuts into the Si-C bonds ($2O_{if}$). (b) One of the O atoms among the Si-C bonds migrates to a site between the Si and C atoms connecting the first and second SiC bilayers ($O_{sub}+O_{if}$). (c) the third O atom comes by migration between the SiC bonds ($O_{sub}+2O_{if}$) (d) Due to the interface lattice mismatch, CO molecule detachment occurs at the interface ($2O_{if}V_C+CO$). I found that the largest energy barrier is 3.21 eV for process (a). Gavrikov *et al.* [5] employed the interface model, where two- and three-fold structures are mixed, and reported that the activation barrier is larger than 3.5 eV, which is required for the penetration of an O₂ molecule through the interfacial layer of SiO₂. It is reported by Shen *et al.* [6] that the barrier for an O₂ molecule penetration is ~ 4.0 eV. Akiyama *et al.* [7] reported the activation barrier of 3.2 eV using the computational model similar to the 4H-SiC(0001)/ β -tridymite SiO₂. Their reaction path resembles the atomic oxygen mechanism, in which O atoms diffuse by hopping from one bond to another, rather than an O₂ molecule penetration. Shen *et al.* also reported that the barrier for the atomic oxygen mechanism is ~ 3.1 eV. Although my reaction process (a) is similar to that proposed by Akiyama *et al.*, in which the O₂ molecule

is not a molecule after passing the interfacial SiO₂ layer, my process is different from their situation, in which the interfacial O atom hops to the SiC bond and Si₂-CO structure is generated. When I assume that the O₂ molecule behaves like two O atoms at the oxidation front, the activation barriers obtained by these theoretical calculations are comparable. Thus, O₂ molecules dissociate when they pass the interfacial SiO₂ layer with the barrier of ~ 3.2 eV.

Next, let me discuss the barrier after the O atoms cut into the SiC bonds. Gavrikov *et al.* reported that the CO molecule is emitted from the Si₂-CO structure with the activation barrier of 2.8 eV. Since the Si₂-CO structure is less stable than the O_{sub}+O_{if} structure by 0.6 eV, the total activation barrier from the O_{sub}+O_{if} structure is 3.4 eV. Köhler *et al.* reported the barrier for the CO molecule detachment of 3.1 eV. If the energy difference reported by Gavrikov *et al.* is added, the total barrier from the O_{sub}+O_{if} structure is 3.7 eV. It is also reported by Akiyama *et al.* that the activation barrier for the CO molecule detachment from the Si₂-CO structure is 1.7 eV, which is much smaller than the results calculated by Gavrikov *et al.* and Köhler *et al.* If I believe the larger barrier calculated by Gavrikov *et al.* and Köhler *et al.*, these results imply that the CO detachment also limits the reaction. However, in our previous study [3], we reported that the CO desorption preferentially occurs when the interfacial C atom is surrounded by three O atoms. The activation barriers for the migration of O atoms at the SiC/SiO₂ interface are 2.72 eV for process (b) and 2.08 eV for process (c). It is noteworthy that these barriers vary between 2.0 eV and 2.8 eV depending on the configuration of the O atoms at the interface. When the third O atom is considered, the barrier for the O₂ molecule penetration is still higher than that for the CO detachment. Thus, it can be concluded that the CO detachment does not limit the reaction and the O₂ molecule penetration

is the reaction-limiting process.

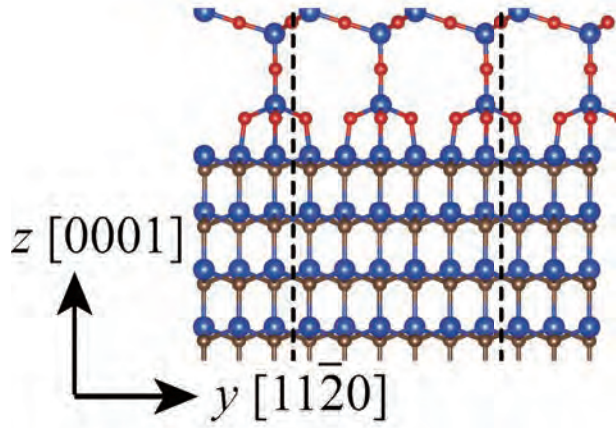


Figure 1: Interface atomic structure of β -tridymite SiO₂ on SiC. Blue, brown, and red balls are Si, C, and O atoms, respectively. The supercell contains 30 Si, 24 C, 14 O, and 8 H atoms. H atoms are used for termination of dangling bonds at the surfaces.

References

- [1] T. Ono *et al.*, Phys. Rev. B **96** (2017) 115311.
- [2] T. Ono, Mater. Sci. Forum **963** (2019) 208.
- [3] T. Ono and S. Saito, Appl. Phys. Exp. **4** (2011) 021303.
- [4] K. Hirose, T. Ono, Y. Fujimoto, and S. Tsukamoto: First Principles Calculations in Real-Space Formalism (Imperial College, London, 2005).
- [5] A. Gavrikov *et al.*, J. Appl. Phys. **104** (2008) 093508.
- [6] X. Shen *et al.*, J. Appl. Phys. **114** (2013) 033522.
- [7] T. Akiyama *et al.*, Surf. Sci. **641** (2015) 174.
- [8] C. Köhler *et al.*, Phys. Rev. B **64** (2001) 085333.

First-Principles Study of Excited Electron, Positron and Atom Dynamics and Optical and Thermoelectric Properties of Nanostructures

Kazuyuki WATANABE, Yasumitsu SUZUKI,
Kazuki UCHIDA, Tomokazu YAMAGUCHI and Masashi YOSHISATO
Department of Physics, Tokyo University of Science
1-3 Kagurazaka, Shinjuku-ku, Tokyo 162-8601

In this project we investigated the following four topics on the basis of time-dependent density functional theory (TDDFT). 1) Angle-resolved photoemission spectroscopy (ARPES) in low-dimensional periodic structures, 2) Stationary-state electron scattering using a complex injecting potential (CIP), 3) Optical and thermoelectric properties of low dimensional materials, and 4) Development of the exchange-correlation term in TDDFT.

1) *Angle-resolved photoemission spectroscopy in low-dimensional periodic structures* [1]:

We proposed a new approach based on TDDFT for the calculation of ARPES of low-dimensional periodic structures, such as graphene, silicene, and polyacetylene. The calculated ARPES spectra reproduced the occupied energy band structures fairly well. We further investigate the electron doping effect on ARPES by considering Li-intercalated bilayer graphene and found a shift in the Fermi energy. These show that the present method can provide reliable ARPES spectra for materials for which ARPES experiments are difficult to perform under some conditions. We note that the present method is simpler and uses a more direct one-shot TDDFT calculation for ARPES than previous theories. Further applications to time-resolved and spin-resolved ARPES simulations will be presented elsewhere. The simulations have been conducted by our homemade TDDFT code,

KENS. Parallelized calculations have been performed using System B.

2) *Stationary-state electron scattering using a complex injecting potential* [2]:

We simulated stationary electron scattering by solving the time-dependent Schrödinger equation with a CIP. The calculated electron transmission probabilities through one-dimensional potentials and the electron interference patterns caused by double slits show good agreement with analytical results. The Aharonov–Bohm effect is also clearly demonstrated by the presence of a vector potential at one side of the double-slit configuration. Also, from the simulation of the arranged-CIP method, we predict that this new method can be applied to BEC interference simulations. Since the present method can be straightforwardly extended to TDDFT, we can simulate field electron emission, photo-induced electron emission, secondary electron emission, thermionic emission, and so on. The simulations have been conducted by our homemade code, SCIP, using System B.

3) *Optical and thermoelectric properties of low dimensional materials* [3]:

We studied the optical and thermoelectric properties of various low dimensional materials by means of the first-principles method.

First, we applied TDDFT to the calculation of absorption spectra for two-dimensional atomic-layer materials: mono-layer and bi-

layer hexagonal boron nitride (h-BN) and mono-layer transition metal dichalcogenides, MoS₂ and MoSe₂. We demonstrated that the TDDFT approach with the meta GGA exchange-correlation potential and the bootstrap kernel can capture the characteristics of the first bright excitonic peak of bi-layer h-BN that is dependent on the layer stacking type. We also revealed that the TDDFT method can capture the qualitative features of the absorption spectra for mono-layer transition metal dichalcogenides, although the exciton binding energies are underestimated compared to those obtained by the many-body perturbation theory (MBPT) calculation. This study elucidates the usefulness of the TDDFT approach for the qualitative investigation of the optical properties of two-dimensional atomic layer materials. MBPT calculations and TDDFT calculations have been conducted using EXCITING (<http://exciting-code.org/>) and ELK (<http://elk.sourceforge.net/>) code, respectively. Parallelized calculations have been performed using System B.

Next, we calculated the thermoelectric power factor of pnictogen (P, As, Sb, Bi) nanoribbon structures using the density functional theory (DFT) and non-equilibrium Green's function (NEGF) method. We found that the power factor properties strongly depend on the structure of nanoribbons, i.e., the buckled nanoribbon generally exhibit higher power factor than the puckered one. It was also found that the light pnictogens (P, As, Sb) have an advantage over the heavy one (Bi) in giving a high power factor. This study reveals a part of the relationship between the electronic structure and the thermoelectric property of pnictogen nanoribbons, and provides the useful information to develop the thermoelectric devices based on pnictogen nanoribbons. All DFT calculations and NEGF calculations have been conducted using Quantum Espresso (<https://www.quantum-espresso.org/>) and

WanT (<http://www.wannier-transport.org/>) code, respectively. Parallelized calculations have been performed using System B.

4) *Development of the exchange-correlation term in TDDFT:*

We developed a machine learning based approach to improve the approximation to the exchange-correlation potential of TDDFT. We trained the neural-network projection from the time-varying electron densities to the corresponding correlation potentials in the time dependent Kohn-Sham equation using a few exact datasets for a model system of electron-hydrogen scattering. We demonstrated that this neural-network potential can capture the complex structures in the time-dependent correlation potential during the scattering process and provide correct scattering probabilities, which are not obtained by the standard adiabatic functionals. This study offers a novel way to improve the exchange-correlation potential of TDDFT. The simulations have been conducted by our homemade code. Parallelized calculations have been performed using System B.

References

- [1] K. Uchida, Y. Akimoto, K. Einaga, and K. Watanabe, *Jpn. J. Appl. Phys.* **58**, 128001 (2019).
- [2] T. Yamaguchi, K. Uchida, K. Varga, and K. Watanabe, *J. Phys. Soc. Jpn.* **89**, 044002 (2020).
- [3] Y. Suzuki and K. Watanabe, *Phys. Chem. Chem. Phys.* **22**, 2908 (2020).

Ab initio phonon calculation for $\text{Ca}_5\text{Ir}_3\text{O}_{12}$

Kazuma NAKAMURA

*Quantum Physics Section, Kyushu Institute of Technology
1-1 Sensui-cho, Tobata, Kitakyushu, Fukuoka, 804-8550*

The title compound has recently attracted attention as a thermoelectric material because it has a relatively high Seebeck coefficient. In this study, we report an ab initio study about electronic and phononic properties for $\text{Ca}_5\text{Ir}_3\text{O}_{12}$. In particular, we investigated the effect of spin-orbit interaction (SOI) on the low-energy properties [1].

Density functional calculations with plane-wave basis sets were performed using the xTAPP code [2], where the ultrasoft pseudopotential and the generalized gradient approximation (GGA) of the exchange correlation potential were employed. The cutoff energies in the wavefunction and charge densities were 64 and 900 Ry, respectively, and the SOI was explicitly considered. To study the effects of SOI, we performed the usual GGA calculation and compared it with the result including the SOI. Below, we refer to the former as GGA and to the latter as SO-GGA. The atomic and lattice parameters were optimized with an $8 \times 8 \times 8$ k-point sampling, and we found that SO-GGA reproduces the experimental crystal structure quite well. The Fermi-surface calculations were performed with the dense $21 \times 21 \times 63$ k-point sampling to obtain the detailed surface structure [3]. Phonon calculations with a frozen phonon approximation were performed using the PHONOPY for $1 \times 1 \times 3$ and $2 \times 2 \times 1$ supercells [5, 6]. For the k -point sampling, $11 \times 11 \times 11$ was used for $1 \times 1 \times 3$ supercell calculation, and somewhat coarse $9 \times 9 \times 5$ was used for the $2 \times 2 \times 1$ supercell calculation.

Figure 1(a) shows our calculated band structure. To see the SOI effect, the SO-GGA band

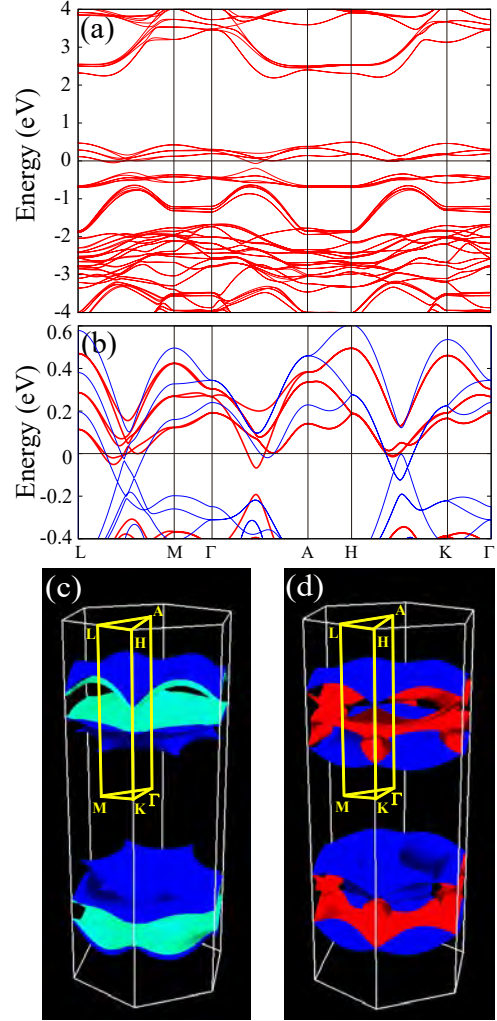


Figure 1: (Color online) (a) Ab initio electronic band structure considering the SOI in $\text{Ca}_5\text{Ir}_3\text{O}_{12}$. The energy zero is the Fermi level. (b) A zoom of the low-energy band structure, where the SO-GGA result (thick red curves) is compared with the usual GGA result (thin blue curve). (c) Calculated Fermi surface for SO-GGA and (d) GGA.

(thick red curves) is compared with the GGA band (thin blue curves) in Fig. 1(b). An appreciable difference can be observed in the low-energy bands; the GGA result exhibits metallic bands, particularly along the L-M or H-K lines. When the SOI is switched on, the metallic bands are split and a pocket-like band structure appears. The gap size due to the SOI is about 0.3 eV, which is comparable to the valence bandwidth 0.5 eV.

Figures 1(c) and 1(d) show the Fermi surfaces based on the SO-GGA and GGA, respectively. We see that the GGA Fermi surface is contributed from the two bands (indicated in dark-blue and bright-red colors), while the SO-GGA Fermi surface is basically formed by the one band; the SOI makes the bright-red colored GGA Fermi surface disappear. In the SO-GGA Fermi surface, since the SOI resolves the band degeneracy, the Fermi surfaces are seemingly two (dark-blue and bright-blue colored surfaces); however, these two are originated from the same band. Also, in the SO-GGA Fermi surface, we see a sheet structure along the c^* -axis (the Γ -A line), which indicates a nesting trend along this direction. We note that the SOI is relevant to the narrowing of the sheet separation between the blue colored Fermi surfaces.

Figures 2(a) and 2(b) are our calculated phonon dispersions with SOI for $1\times 1\times 3$ and $2\times 2\times 1$ supercells, respectively. It was found that the experimental results at the room temperature are better reproduced by the $1\times 1\times 3$ supercell calculation. The panel (b) is a preliminary phonon calculation on a $2\times 2\times 1$ supercell. This supercell includes the displacement degree of freedom in an in-plane 2×2 superlattice, and we can investigate the phonon instability within this superlattice. On the other hand, the $1\times 1\times 3$ supercell can clarify the triple-period phonon instability along the c -axis. Within these two supercells, we observe phonon softening in the $2\times 2\times 1$ supercell calculation; there is a sign of softening at the K and

M points. However, since the calculation conditions for the $2\times 2\times 1$ calculation are rough, it is necessary to perform the calculation under more severe conditions.

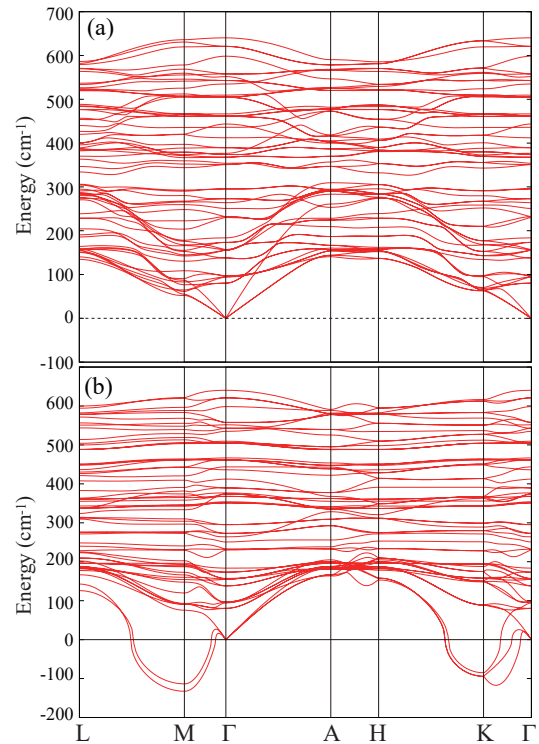


Figure 2: (Color online) Ab initio phonon dispersion with the SOI in $\text{Ca}_5\text{Ir}_3\text{O}_{12}$. Panels (a) and (b) show results based on $1\times 1\times 3$ and $2\times 2\times 1$ superlattice, respectively.

References

- [1] K. Matsuhira, K. Nakamura, Y. Yasukuni, Y. Yoshimoto, D. Hirai, Z. Hiroi: *J. Phys. Soc. Jpn.* **87** (2018) 013703/1-5.
- [2] <http://xtapp.cp.is.s.u-tokyo.ac.jp>
- [3] <http://fermisurfer.osdn.jp>
- [4] <https://atztogo.github.io/phonopy>
- [5] T. Hasegawa, W. Yoshida, K. Nakamura, N. Ogita, and K. Matsuhira: *J. Phys. Soc. Jpn* **89** (2020) 054602/1-11.
- [6] H. Hanate, T. Hasegawa, S. Tsutsui, K. Nakamura, Y. Yoshimoto, N. Kishigami, S. Haneta, and K. Matsuhira: *J. Phys. Soc. Jpn* **89** (2020) 053601/1-5.

Ab initio derivation of effective low-energy model of $\text{Ca}_5\text{Ir}_3\text{O}_{12}$

Kazuma NAKAMURA

*Quantum Physics Section, Kyushu Institute of Technology
1-1 Sensui-cho, Tobata, Kitakyushu, Fukuoka, 804-8550*

In this report, we report a first-principles derivation of an effective low-energy model for $\text{Ca}_5\text{Ir}_3\text{O}_{12}$. In order to perform the effective-model derivation of materials with strong spin-orbit interaction (SOI) such as iridium system, we extended the first principle effective-model derivation software RESPACK [1] to the spinor type.

The density-functional band-structure calculations for $\text{Ca}_5\text{Ir}_3\text{O}_{12}$ are performed using xTAPP [2] with the experimental lattice parameters [3]: $a = 9.3490 \text{ \AA}$ and $c = 3.1713 \text{ \AA}$. We use the norm-conserving pseudopotential and the generalized gradient approximation (GGA) of the exchange correlation potential. We use $8 \times 8 \times 8$ k -points for sampling in the first Brillouin zone. The energy cutoff is set to be 144 Ry for the wave functions, and 576 Ry for the charge density. The interaction parameters are calculated using the constrained random-phase approximation method, in which we employ the scheme for the band disentanglement. The energy cutoff for the dielectric function is set to be 20 Ry. The total number of bands used in the calculation of the polarization is 300, which includes the unoccupied states up to $\sim 26 \text{ eV}$ with respect to the Fermi level. To study the effects of SOI, we performed the usual GGA calculation and compared it with the result including the SOI. Below, we refer to the former as GGA and to the latter as SO-GGA.

From the fat band analysis, it was found that the band structure near the Fermi energy is

d_{xy} and d_{yz} orbitals. Here, the notation of the orbital follows a local coordinate system fixed to the IrO_6 octahedron. Based on this observation, we perform parameter derivation of the d_{xy}/d_{yz} model. Figure 1 is a comparison of the Wannier-interpolation band (green-dashed curves) and the original band (red-solid curves). We see that the original band has been completely reproduced. Note that the initial guess setting is very important for obtaining such reproducibility. We set the d_{xy} and d_{yz} orbitals as initial guesses, where the initial guess orbitals are represented in the local coordinate system fixed to IrO_6 octahedrons, and additionally rotated the spin quantization axis. This treatment is very important to satisfy the symmetry of the calculated Wannier orbitals, that is, all 12 Wannier orbitals have the same spread.

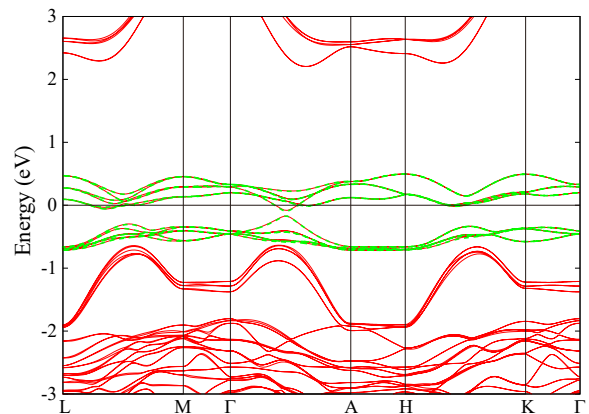


Figure 1: (a) *Ab initio* density functional band structure considering the spin-orbit interaction in $\text{Ca}_5\text{Ir}_3\text{O}_{12}$.

We next show in Fig. 2 the resulting maximally localized Wannier functions for d_{xy}/d_{yz} model. The panels (a) and (b) indicate the d_{xy} and d_{yz} Wannier functions, respectively. Note that in this plot, three independent Wannier functions are shown in one panel.

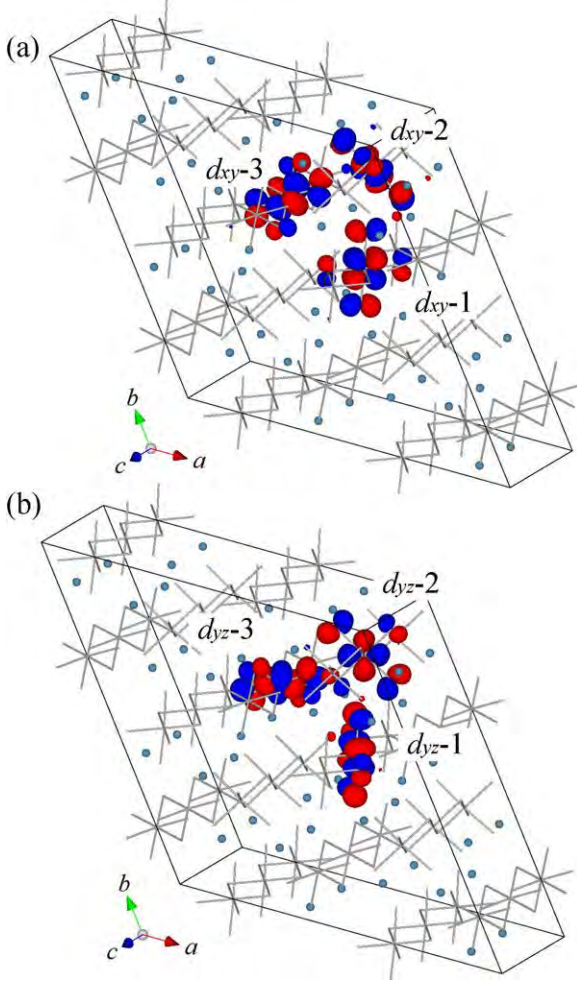


Figure 2: Maximally localized Wannier functions of $\text{Ca}_5\text{Ir}_3\text{O}_{12}$: (a) d_{xy} and (b) d_{yz} Wannier functions.

Our derived model parameters for $\text{Ca}_5\text{Ir}_3\text{O}_{12}$ are summarized in the Table 1. The spin-orbit coupling is estimated as 0.213 eV. The nearest neighbor parameter t_{NN} is 0.167 eV, the onsite interaction U based on constrained RPA is 2.43 eV, and the nearest-neighbor interaction V is estimated as 0.99 eV. Then, the correlation degree of freedom $(U - V)/t$ is 8.62.

Table 1: Main parameters of d_{xy}/d_{yz} model of $\text{Ca}_5\text{Ir}_3\text{O}_{12}$, where we show 3 nearest-neighbor (NN) transfers, onsite transfers, and largest interchain electron transfer. $t_{xy\uparrow,yz\uparrow}^{NN}$ and $t_{yz\uparrow,xy\uparrow}^{NN}$ are nearest neighbor transfers. Also, $t_{xy\uparrow,yz\downarrow}^{onsite}$ is the spin-orbital couplings in the same site. The interaction parameters with the bare (unscreened) and constrained RPA (cRPA) are listed. V_{NN} is the orbital-averaged value of the nearest-neighbor interactions. Also, V_{IC} is the orbital-averaged value of the interchain interaction. The unit of the parameters is eV.

	SO-GGA		GGA	
$t_{xy\uparrow,yz\uparrow}^{NN}$	0.167		0.167	
$t_{yz\uparrow,xy\uparrow}^{NN}$	0.210		0.208	
$t_{interchain}^{largest}$	0.032		0.039	
$t_{xy\uparrow,yz\downarrow}^{onsite}$	0.213		-	
	bare	cRPA	bare	cRPA
U	9.87	2.43	10.03	2.23
U'	9.19	1.95	9.28	1.68
V_{NN}	4.43	0.99	4.39	0.77
$V_{interchain}$	2.86	0.52	2.86	0.44
J	0.27	0.21	0.29	0.23

As another achievement, we calculated the Raman frequency [4] and the phonon dispersion curves [5].

References

- [1] <https://sites.google.com/view/kazuma7k6r>
- [2] <http://xtapp.cp.is.s.u-tokyo.ac.jp>
- [3] M. Wakeshima, N. Taira, Y. Hinatsu, and Y. Ishii, Solid State Commun. **125**, 311 (2003).
- [4] T. Hasegawa, W. Yoshida, K. Nakamura, N. Ogita, and K. Matsuhira: J. Phys. Soc. Jpn **89** (2020) 054602/1-11.
- [5] H. Hanate, T. Hasegawa, S. Tsutsui, K. Nakamura, Y. Yoshimoto, N. Kishigami, S. Haneta, and K. Matsuhira: J. Phys. Soc. Jpn **89** (2020) 053601/1-5.

First-principles calculations of thermoelectric properties in magnetic materials

Fumiyuki ISHII, Susumu MINAMI, Rifky SYARIATI, Akihiro HORI,
Hikaru SAWAHATA, Naoya YAMAGUCHI, Monika NUR

Nanomaterials Research Institute, Kanazawa University

Kanazawa, 920-1192, Japan

1. *Development of Methods and Codes*

The thermoelectric conversion based on the anomalous Nernst effect (ANE) has attracted much attention because the ANE realizes the high-density integration more easily compared to that based on the Seebeck effect[1]. The ANE is the phenomenon that the electric power is created along the direction perpendicular to both the temperature gradient and the magnetization in magnetic materials. This effect is induced by the anomalous Hall conductivity (AHC), and if the AHC changes drastically as a function of the Fermi level, we expect the large ANE[2]. In our previous first-principles study, we predicted that an electron doped EuO skyrmion crystal shows the large ANE induced by the finite Chern number at the Fermi level[3]. For discovery and design of new materials which have the large ANE via computational high throughput screening, we need an efficient computational method to investigate the Fermi level dependence of the AHC. We have implemented the code of computing the AHC applicable to metallic systems in OpenMX package[4] by improving Fukui-Hatsugai-Suzuki method[5]. Using this code, we computed AHCs $\sigma_{xy}(\varepsilon)$ and transverse thermoelectric conductivities $\alpha_{xy}(\varepsilon)$ in two-dimensional ferromagnetic materials.

2. *Applications to 2D Materials*

The discovery of magnetism in the two-dimensional materials[6] open a way for realizing thermoelectric devices based on anoma-

lous Nernst effect. The surface phonon scattering advantage in the two-dimensional materials can decrease the thermal conductivity which can increase the thermoelectric figure of merit ZT [7]. The magnitude of anomalous Nernst effect itself depend on Seebeck effect or anomalous Hall effect[2, 3]. In our previous study, we reported that the half-metallic materials possess large anomalous Nernst effect[8]. Here, we performed first-principles calculations to explore the anomalous Nernst effect of half-metallic transition-metal dihalides monolayer using OpenMX package[4]. We analyzed its magnitude based on the semiclassical transport theory and found that there is large anomalous Nernst effect at 100 K. The large Berry curvature which contributed by bands near Fermi level is the main reason of its large magnitude. These results suggest that transition-metal dihalides monolayer can potentially be used in thermoelectric devices.

3. *Thermal Conductivity and ZT*

To evaluate efficiency of thermoelectric materials, it is important to examine the contribution of thermal conductivity to the thermoelectric figure of merit ZT that represents the performance of the material. Since the thermal conductivity can be described for each electron and lattice, in this research, we theoretically computed both electronic and lattice thermal conductivity, and then evaluated ZT . Theoretical analysis of lattice thermal conductivity is conducted by Boltzmann transport the-

ory with relaxation time approximation. In order to do this, it is necessary to determine the inharmonic atomic force constant exactly, and an accurate analysis is carried out by first-principles calculations based on density functional theory. As computational codes, OpenMX package[4] is used as a density functional calculation, and ALAMODE[9, 10] is used as a lattice thermal conductivity calculation. The half-Heusler compounds are ternary compounds, have composition formula of XYZ, and are expected as thermoelectric materials that exhibit high power factor in a medium temperature range of about 600 to 1000 K. We analyzed thermoelectricity and thermal conductivity of ferromagnetic half-metallic half-Heusler MnCoSb[8]. We evaluated the ZT for the Seebeck and anomalous Nernst effect. We discussed carrier and temperature dependence of ZT .

4. Surface Structures and Atomic Radii

To design new functional materials, surface alloying is an effective way to obtain desired materials. Surface alloys are synthesized by inserting atoms into the surface. This topic has attracted a lot of research attention lately because of some of its applications, such as spintronics[11], where there is a giant spin splitting in Bi/Ag(111) surface alloys[12, 13]. Many types of surface alloys have been studied: for example, Ge/Ag(111), Pb/Ag(111), Bi/Ag(111), and Sn/Ag(111). One structure that has been observed in experiments with surfaces is $\sqrt{3} \times \sqrt{3}$ R 30°. Structural studies for surfaces alloys can provide important information for forming metal-semiconductors interface and metal interfaces. The metal-semiconductor interface is very important to industry, for example, the Si/Ag interface is a promising candidate for solar cells. We systematically explored the structural stability of $M/\text{Ag}(111)$ surface alloys by first-principles calculation using the OpenMX package[4], where M is group III (B, Al, Ga, In and Tl), IV (C, Si, Ge, Sn and Pb) and V

atom (N, P, As, Sb and Bi). We focused on the corrugation parameter d which is determined by the height of the M atom from the Ag atom in the plane of the top-most atom. We introduced concept of atomic radii to understand the tendencies of corrugation in $M/\text{Ag}(111)$. The formation energy for each M atom is also calculated to determine the stability of the surface alloys. We discussed the dependence of M atoms on corrugation parameters.

References

- [1] Y. Sakuraba, *Scr. Mater.* **111**, 29 (2016).
- [2] Y. P. Mizuta and F. Ishii, *Sci. Rep.* **6**, 28076 (2016).
- [3] Y. P. Mizuta, H. Sawahata, and F. Ishii, *Phys. Rev. B* **98**, 205125 (2018).
- [4] T. Ozaki *et al.*, <http://www.openmx-square.org/>
- [5] T. Fukui, Y. Hatsugai, and H. Suzuki, *J. Phys. Soc. Jpn.* **74**, 1674 (2005).
- [6] B. Huang *et al.*, *Nature* **546**, 270 (2017).
- [7] R. Anufriev, J. Maire, and M. Nomura, *Phys. Rev. B* **93**, 045411 (2016).
- [8] S. Minami, F. Ishii, Y. P. Mizuta, and M. Saito, *Appl. Phys. Lett.* **113**, 032403 (2018)
- [9] T. Tadano, <https://alamode.readthedocs.io>
- [10] T. Tadano, Y. Gohda, and S. Tsuneyuki, *J. Phys.: Condens. Matter* **26**, 225402 (2014)
- [11] C. R. Ast *et al.*, *Phys. Rev. Lett.* **98**, 186807 (2007).
- [12] I. M. Mcleod *et al.*, *Surf. Sci.* **604**, 1395 (2010).
- [13] N. Yamaguchi, H. Kotaka, and F. Ishii, *J. Cryst. Growth* **468**, 688 (2017).

Reduction of Rare Metals in Formic Acid Decomposition Catalysts and Oxygen Storage Materials

Yuji KUNISADA

*Center for Advanced Research of Energy and Materials, Faculty of Engineering,
Hokkaido University, Sapporo, Hokkaido 060-8628*

We investigated the catalyst adsorption and diffusion properties on non-metal element doped graphene with the aid of the first-principles calculation based on the density functional theory (DFT). We also investigated the corresponding catalytic activity. Besides, we investigated the oxygen absorption properties of substituted brownmillerite oxides.

At first, we investigated adsorption and diffusion properties of Cu clusters on non-metal element doped graphene. We also considered Cu oxide clusters and Cu atoms embedded in the graphene basal plane. We performed the total energy and electronic structure calculations using The Vienna Ab initio simulation package (VASP). We installed a parallelized VASP with Intel® MPI Library and Intel® Math Kernel Library. We found that the adsorption energies and diffusion activation barriers of Cu clusters increase by non-metal element doping into graphene lattice. We note that Cu oxide clusters also show the same trend, and the embedded Cu atoms in graphene have quite high stability. We also investigated the

catalytic activity using a theoretical volcano plot reported in the previous study.[1] From the adsorption energy of intermediates, we estimated the reaction activities. We found that the embedded Cu atoms in graphene show higher activity than Cu clusters on graphene.

We also investigated the oxygen absorption properties of partially substituted $\text{Ca}_2\text{AlMnO}_5$. We revealed that Mn-site substitution is favorable for the oxygen absorption-desorption process than Al-site substitution.

We also studied the isotope effect on the alkene hydrogenation process on Rh-based Intermetallic catalyst [2] and the structure and magnetism of Ca_2RuO_4 nanofilm.[3]

References

- [1] J. S. Yoo, F. A.-Pedersen, J. K. Nørskov, F. Studt: ACS Catal. 4 (2014) 1226.
- [2] S. Furukawa, P. Yi, Y. Kunisada, K. Shimizu, Sci. Technol. Adv. Mater. 20 (2019) 805.
- [3] H. Nobukane, K. Yanagihara, Y. Kunisada, Y. Ogasawara, K. Nomura, Y. Asano, S. Tanda, Sci. Rep. 10 (2020) 3462.

Material exploration by advanced first-principles simulation

Shinji TSUNEYUKI

Department of Physics, School of Science,

The University of Tokyo, 7-3-1 Hongo, Bunkyo-Ku, Tokyo 113-0033

Institute for Solid State Physics,

The University of Tokyo, Kashiwa-no-ha, Kashiwa, Chiba 277-8581

The density functional theory (DFT)-based first-principles electronic structure calculation method has played an important role as a powerful research tool in material properties and as a predictor of new materials and structures. We have been developing fundamental simulation methods, such as the accurate calculation of the lattice thermal conductivity using DFT calculations and the prediction of the superconducting transition temperature using superconducting density functional theory (SCDFT), in collaboration with experimentalists.

In this fiscal year, we focused on determining the crystal structure of unknown materials, and predicting the physical properties of these new materials in collaboration with the experimental groups of the Grant-in-Aid for Scientific Research on Innovative Areas "Hydrogenomics: Creation of Innovative Materials, Devices, and Reactive Processes using Higher-Order Hydrogen Functions" (FY 2018-2022) and the Tokodai Institute for Element Strategy. In particular, by developing data-assimilated structure simulation methods based on incomplete experimental data (e.g., incomplete

X-ray diffraction data from high-pressure experiments), we aimed to establish simulation methods that strongly support experimental research on materials under extreme conditions, new materials with only poor quality crystals, and materials containing hydrogen that are difficult to observe experimentally.

In this method, instead of finding the global minimum of the multi-dimensional potential energy surface $E(\mathbf{R})$ as a function of the atomic positions \mathbf{R} , we define the effective potential $F(\mathbf{R})$ by the sum of $E(\mathbf{R})$ and a so-called penalty function $D[I_{\text{obs}}, I_{\text{calc}}(\mathbf{R})]$, which increases when the simulated diffraction intensity $I_{\text{calc}}(\mathbf{R})$ deviates from the experimental one I_{obs} :

$$F(\mathbf{R}) = E(\mathbf{R}) + \alpha ND[I_{\text{obs}}, I_{\text{calc}}(\mathbf{R})].$$

Here, N is the number of atoms in the simulation cell and α is a control parameter. Note that, in case of the powder diffraction, I_{obs} and $I_{\text{calc}}(\mathbf{R})$ are functions of diffraction angle.

Previously, as a first trial, we adopted "crystallinity" for the penalty function, in which we used diffraction angles but not the diffraction intensity [1]. The method is useful when the

relative intensity of diffraction peaks is not reliable. It is, however, not necessarily robust when the crystal symmetry is extremely low, or the noise in the experimental data is very large.

Therefore, in FY 2019, we introduced the correlation between $I_{\text{calc}}(\mathbf{R})$ and I_{obs} for the penalty function. With this penalty function, we can treat all the diffraction data, including even the noise, on the same footing and utilize as much information as possible. We found the new penalty function improves the predictability of crystal structures.

We also developed a method to search for structures by treating the potential energy $E(\mathbf{R})$ and the penalty function $D[I_{\text{obs}}, I_{\text{calc}}(\mathbf{R})]$ independently of each other, using their gradients to avoid local stable solutions [2].

Using these methods, it is possible to search for complex structures containing more than 100 atoms in the simulation cell. However, the search becomes difficult when a specific element in a material is disordered, *i.e.*, a specific element partially occupies multiple sites or arrangements in a unit cell, or two components occupy the same site with a certain

probability. Therefore, we also investigated the efficient sampling of the average diffraction pattern of the system (Fig. 1). We are currently working on a test calculation combining this method with the neural network potential.

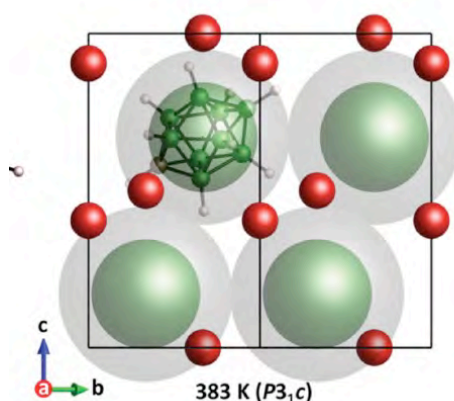


Fig. 1 An average structure of the high-temperature phase of $\text{LiCB}_9\text{H}_{10}$ determined by the data assimilation method.

References

- [1] N. Tsujimoto, D. Adachi, R. Akashi, S. Todo and S. Tsuneyuki, *Phys. Rev. Materials* 2, 053801 (2018).
- [2] D. Adachi, N. Tsujimoto, R. Akashi, S. Todo, and S. Tsuneyuki, *Comput. Phys. Commun.* 241, 92 (2019).

First-principles study for widening the potential of spin-polarized positron experiments

Mineo SAITO

Institute of Science and Technology, Kanazawa University

Kakuma, Kanazawa, 920-1192 Japan

Spin polarized positron annihilation technique detected some spin polarized vacancies in semiconductors. We study spin-polarized cation vacancies in wurtzite structure semiconductors (BeO, ZnO, ZnS, CdS, BN, AlN, GaN and GaP) by using first-principles calculations based on the density functional theory. We find that C3v geometries are the most stable and are spin-polarized. Two majority spin electrons occupying the defect E level lead to the magnetic moment of $2 \mu_B$ in the case of II-VI semiconductors. On the contrary, in the case of III-V semiconductors, three majority spin electrons occupying the defect E and A1 levels induce the magnetic moment of $3 \mu_B$.

The spin polarization energies are large in the semiconductors consisting of first-row anions, i.e., oxides and nitrides. The stabilities in the cases of the

oxides and nitrides are due to the fact that the atomic radii of the first row atoms are small and thus the spin densities are substantially localized at the four nearest anions in the cation vacancies.

Finally, we study the symmetry lowering effect from C3v to Cs which reduces the magnetic moments; we study the possibilities of both pairing and departing distortions. The magnetic moment becomes 0 in the case of II-VI semiconductors and the magnetic moments become $1 \mu_B$ in the case of III-V semiconductors. We find that these low spin states have higher energies than the C3v high spin states due to the fact that the symmetry lowering effect do not significantly stabilize the system.

Unification of massively parallel quantum material simulation and data-driven science

Takeo Hoshi

*Department of Applied Mathematics and Physics, Tottori University,
4-101 Koyama-Minami, Tottori 680-8550, Japan.*

The present project was carried out for the joint research between quantum material simulation and data driven science. Related mathematical studies and software development were also carried out. The main collaborators are K. Tanaka (Tottori U, D. student), H. Imachi (Tottori U, now in Preferred Networks), K. Yoshimi (ISSP), I. Mochizuki, T. Hyodo (KEK-IMSS), T. Fujita (IMS), T. Fukaya (Hokkaido U), Y. Yamamoto (UEC), H. Matsui (Yamagata U) and T. Ogita (TWCU).

The main achievements are explained hereafter. (i) The data analysis software was developed for total-reflection high-energy positron diffraction (TRHEPD), a novel experimental technique for surface structure determination [1,2]. Experiments using TRHEPD are being conducted intensively at the Slow Positron Facility, Institute of Materials Structure Science, High Energy Accelerator Research Organization, revealing surface structure of interest. Figure 1 demonstrates the structure determination of the Ge(001)-c(4x2) surface [2]. At April of 2020, the software development activity was promoted to Project for Advancement of Software Usability in Materials Science in ISSP

(<https://www.pasums.issp.u-tokyo.ac.jp>). Since the analysis method has a general mathematical foundation, it is also applicable to other experiments, such as X-ray or electron diffraction experiments. (ii) Large-scale electronic structure calculations were carried out for a 10-nm-scale pentacene thin film as a foundation of flexible transistor [3]. Semi-localized wavefunctions that expand over several tens of molecules were obtained, which is consistent to electron spin resonance experiment. The study was carried out by our original code ELSESES (<http://www.elses.jp/>), an order- N electronic state calculation code with a *ab initio* based tight-binding method. In addition, several fundamental methodologies were developed for large-scale calculation of organic flexible device materials [4,5]. (iii) Several fundamental numerical algorithms were investigated [6-8]. (iv) Two books were published for reviews of our recent research activities in large-scale electronic structure calculations with supercomputers [9,10].

References

[1] Development of data-analysis software for total-reflection high-energy positron diffraction

(TRHEPD), K. Tanaka, T. Hoshi, I. Mochizuki, T. Hanada, A. Ichimiya, T. Hyodo, *Acta. Phys. Pol. A* 137, 188-192 (2020).

[2] Two-stage data-analysis method for total-reflection high-energy positron diffraction (TRHEPD), K. Tanaka, I. Mochizuki, T. Hanada, A. Ichimiya, T. Hyodo, and T. Hoshi: Submitted; Preprint: <https://arxiv.org/abs/2002.12165>

[3] Numerical aspect of large-scale electronic state calculation for flexible device material, T. Hoshi, H. Imachi, A. Kuwata, K. Kakuda, T. Fujita, H. Matsui, *Japan J. Indust. Appl. Math* 36, 685-698 (2019).

[4] Charge-transfer excited states in the donor/acceptor interface from large-scale GW calculations, T. Fujita, Y. Noguchi, T. Hoshi, *J. Chem. Phys.* 151, 114109/1-8 (2019)

[5] Computational study for electrical conductivity properties of organic semiconducting polymers and metal complex-host systems, M. Ishida, M. Arita, S. Nishino, T. Hoshi, submitted.

[6] EigenKernel - A middleware for parallel generalized eigenvalue solvers to attain high scalability and usability, K. Tanaka, H. Imachi, T. Fukumoto, A. Kuwata, Y. Harada, T. Fukaya, Y. Yamamoto, T. Hoshi, *Japan J. Indust. Appl. Math* 36, 719-742 (2019)

[7] An a posteriori verification method for generalized Hermitian eigenvalue problems in large-scale electronic state calculations, T. Hoshi, T. Ogita, K. Ozaki, T. Terao, *J. Comp.*

Appl. Math. 376, 112830/1-13 (2020)

[8] $K\omega$ -- Open-source library for the shifted Krylov subspace method, T. Hoshi, M. Kawamura, K. Yoshimi, Y. Motoyama, T. Misawa, Y. Yamaji, S. Todo, N. Kawashima, T. Sogabe, Submitted; Preprint: <http://arxiv.org/abs/2001.08707>

[9] Recent progress in large-scale electronic state calculations and data-driven sciences, T. Hoshi and S. Ito, Chap. 14 of *Handbook of Silicon Based MEMS Materials and Technologies* 3rd Ed., Elsevier (2020).

[10] Numerical methods for large scale electronic state calculation on supercomputer, T. Hoshi, Y. Yamamoto, T. Sogabe, K. Shimamura, F. Shimojo, A. Nakano, R. Kalia, P. Vashishta, Chap. 15 of *21st Century Nanoscience - A Handbook: Nanophysics Sourcebook (Volume One)*, CRC Press (2019).

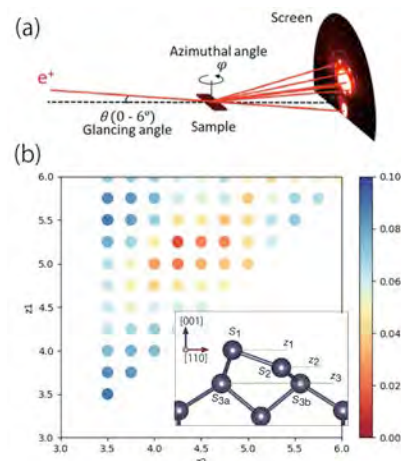


Fig.1 (a) Schematic figure of total-reflection high-energy positron diffraction (TRHEPD) experiment. (b) The data analysis of experimental TRHEPD data for Ge(001)-c(4x2) surface [2].

Reduction of Rare Metals in Fuel Cell Catalysts and Hydrogen Permeable Membrane

Norihito Sakaguchi

*Center for Advanced Research of Energy and Materials, Faculty of Engineering,
Hokkaido University, Sapporo, Hokkaido 060-8628*

We investigated the catalyst adsorption and diffusion properties on non-metal element doped graphene and hydrogen dissolution and diffusion properties in the interfaces of ceramic materials, with the aid of the first-principles calculation based on the density functional theory (DFT).

At first, we investigated adsorption and diffusion properties of Pt clusters on non-metal element doped graphene. This year, we also considered Pt atoms embedded in the graphene basal plane. We performed the total energy and electronic structure calculations using The Vienna Ab initio simulation package (VASP). We installed a parallelized VASP with Intel® MPI Library and Intel® Math Kernel Library. We found that the adsorption energies and diffusion activation barriers of Pt clusters on graphene increase by substitutional non-metal element doping. This is because of the strong covalent bonds between the Pt atom and substitutional dopants. Therefore, we concluded that these dopants in graphene can prevent the detachment and surface diffusion of Pt clusters. We also investigated the catalytic

activity of Pt clusters on non-metal element doped graphene based on the energy diagram.[1] We revealed that the Pt clusters show less support effect than Pt single atoms.

We also investigated the hydrogen dissolution and diffusion properties in the interfaces of TiN containing O impurities. We found that H atoms do not prefer the O sites.

We also studied the tunneling effect on the alkene hydrogenation process on Rh-based Intermetallic catalyst using quantum dynamics simulation of atomic nuclei [2] and thickness dependence of the structure and magnetism of Ca₂RuO₄ nanofilm.[3]

References

- [1] J. K. Nørskov, J. Rossmeisl, A. Logadottir, L. Lindqvist, J. R. Kitchin, T. Bligaard, H. Jónsson, *J. Phys. Chem. B*, 108 (2004) 17886.
- [2] S. Furukawa, P. Yi, Y. Kunisada, K. Shimizu, *Sci. Technol. Adv. Mater.* 20 (2019) 805.
- [3] H. Nobukane, K. Yanagihara, Y. Kunisada, Y. Ogasawara, K. Nomura, Y. Asano, S. Tanda, *Sci. Rep.* 10 (2020) 3462.

Ab-initio analysis of phonon and electron-phonon interaction

Emi Minamitani

Institute for Molecular Science,

Okazaki, Aichi 444-8585

Heat generation in semiconducting materials has become a critical problem in modern nanoscale electronics. As the size of electric devices decreases, the power density and device temperature increase, which is one of the major factors contributing to the degradation of device performance and reliability.

The main carrier of heat in semiconductors is the phonon, which is a quantum of lattice vibration. Current theoretical frameworks require accurate prediction of the interatomic force in the solid. Density functional theory (DFT) calculation is one of the most well-established techniques for accurate force prediction, including the effect of changes in the electronic state with atomic displacement. However, the high computational cost limits the application of DFT calculation in thermal conductivity simulations.

We apply the high-dimensional neural network potential (HDNNP). We generated the random but reasonable structures were first generated from the trajectories of classical molecular dynamics simulations, and then the energy and forces in each structure were evaluated by DFT. These

DFT calculation results are used as dataset to train HDNNP. We found that the training procedure based on force makes the root mean square error between the forces predicted by HDNNP and DFT less than 40 meV/Å. As typical examples, we present the results of Si and GaN bulk crystals. The deviation from the thermal conductivity calculated using DFT is within 1% at 200 to 500 K for Si and within 5.4% at 200 to 1000 K for GaN.

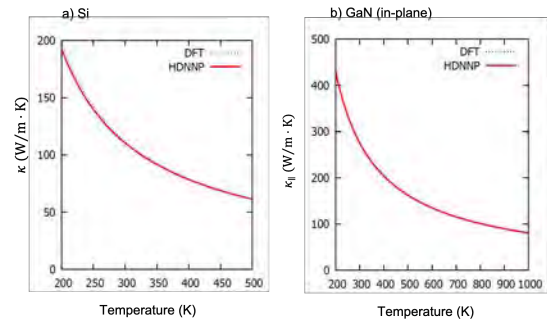


Fig. 1 Comparison of thermal conductivity obtained from DFT calculation and HDNNP for bulk Si (a) and GaN (b).

References

- [1] E. Minamitani, M. Ogura, and S. Watanabe, *Appl. Phys. Express*, (2019) **12**, 095001

Electrochemical Reaction Analysis Using Density Functional Calculation + Implicit Solvation Model

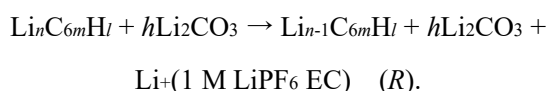
Jun HARUYAMA

Institute for Solid State Physics,

The University of Tokyo, Kashiwa-no-ha, Kashiwa, Chiba 277-8581

We have studied charge transfer reaction at electrode/electrolyte solution interfaces in Li-ion batteries (LIB) using density functional theory (DFT) calculation combined with implicit solvation model. This simulation is called ESM-RISM,¹ i.e., the effective screening medium (ESM)² + the reference interaction site model (RISM)³, and implemented in Quantum Espresso package.⁴

This year, we focused on Li-ion transfer reaction (R) at the interface of graphite electrode/solid electrolyte interphase (SEI)/solution (1 M LiPF₆ EC) as follows:



ESM-RISM calculations were performed on the configuration of a vacuum/slab/solution system as shown in Fig. 1 (a), where the DFT slab domain represents Li-inserted graphite (Li_nC_{6m}H_l)/SEI (inorganic lithium carbonic acid, hLi₂CO₃), and the RISM solvent and ions, (EC, Li⁺, and PF₆⁻). Since the electrolyte concentration of typically 1.0 M gives a small Debye screening length of several angstroms, the RISM region (> 40 Å) used in this calculation was sufficiently long.

Figure 1 (b) shows the grand potential Ω of pristine, Li_nC_{6m}H_l/hLi₂CO₃, and V_{Li} + Li⁺, Li_{n-1}C_{6m}H_l/hLi₂CO₃ + Li⁺(1 M LiPF₆ EC), as a function of the chemical potential of an electron μ_e . In the ESM-RISM calculations, μ_e is measured from the potential at inner solution region Φ_s . It is possible to compare μ_e at different electrodes contacting the same solution directly.⁵ The difference between two equilibrium potentials on different electrodes provides the electromotive force, E_{emf} , between the two electrodes as:

$$E_{\text{emf}} = -(\mu_{\text{eq}} - \mu_{\text{Li/Li}^+})/e \quad (1),$$

where μ_{eq} represent the equilibrium potential of reaction (R) and e is the elementary charge. Once an equilibrium potential $\mu_{\text{Li/Li}^+}$ of Li transfer reaction at Li metal electrode is determined in the ESM-RISM calculation, the electromotive force (or electrode potential relative to the Li/Li⁺ reference) can be immediately derived. Because it was obtained $\mu_{\text{Li/Li}^+} = -3.06$ eV vs Φ_s in a previous study,⁶ the result of $\mu_{\text{eq}} = -3.17$ eV vs Φ_s gave $E_{\text{emf}} = 0.11$ V vs Li/Li⁺, which is in good agreement with experiment (0.1 – 0.2 V vs Li/Li⁺).

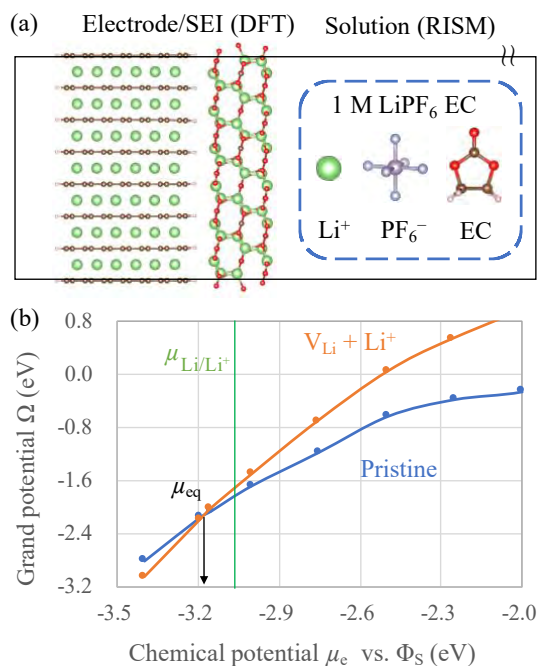


Fig. 1: (a) ESM-RISM configurations of the vacuum/slab/solvent system: the simulation cells of $\text{Li}_n\text{C}_{6m}\text{H}/h\text{Li}_2\text{CO}_3|1\text{M LiPF}_6\text{ EC}$ interfaces. (b) Profiles of Ω as a function of μ_e . The blue and orange lines show Ω of $\text{Li}_n\text{C}_{6m}\text{H}/h\text{Li}_2\text{CO}_3$ and $\text{Li}_{n-1}\text{C}_{6m}\text{H}/h\text{Li}_2\text{CO}_3 + \text{Li}+(1\text{ M LiPF}_6\text{ EC})$, respectively.

Additionally, it was confirmed that the equilibrium potential of reaction (R) cannot depend on such as the thickness and component of SEI. In the next physical year, the activation energy of reaction (R) will be revealed under operated LIB working conditions.

References

- [1] S. Nishihara and M. Otani: Phys. Rev. B **96** (2017) 115429.
- [2] M. Otani and O. Sugino: Phys. Rev. B **73** (2006) 115407.
- [3] A. Kovalenko and F. Hirata: J. Chem. Phys. **110** (1999) 10095 (1999).
- [4] P. Giannozzi et al.: J. Phys.: Condens. Matter **21** (2009) 395502; **29**, (2017) 465901.
- [5] J. Haruyama, T. Ikeshoji, and M. Otani, Phys. Rev. Mater. **2** (2018) 095801.
- [6] J. Haruyama, T. Ikeshoji, and M. Otani: J. Phys. Chem. C **122** (2018) 9804.

Van der Waals density functional study of molecules adsorbed on metal surfaces

Ikutaro Hamada

*Department of Precision Science and Technology, Graduate School of Engineering,
Osaka University, 2-1 Yamada-Oka, Suita, Osaka 565-0871*

Accurate description of the molecule-surface interaction is prerequisite for precise understanding of chemical processes at surfaces and interfaces in diverse systems including electrochemical energy conversion devices such as fuel cell, photoelectrochemical cell, and rechargeable battery, as well as heterogeneous catalyst for emission control, name only a few. For this purpose, the van der Waals density functional (vdW-DF) [1] and its variants have been used to study a variety of systems and proven accurate in describing molecule/surface interfaces, as well as bulk systems.

In this project, we have studied quasi one dimensional chain composed exclusively of pentagonal water on Cu(110). In particular, we have studied the small water clusters on Cu(110) to investigate the origin of the pentagonal water chain.

All the calculations were performed using STATE, our in-house plane-wave pseudopotential code. We used an efficient implementation [2,3] of the self-consistent vdW-DF. The rev-vdW-DF2 functional was used [5].

Previously we constructed and optimized

water clusters from monomer to hexamer, and found that the pentagonal water cluster is more stable than the hexagonal one on Cu(110). We further constructed larger water clusters such as octamers composed of pentamers, nonamers composed of pentagon and hexagon, those with two pentagons plus water monomer, and dimer composed of pentamers. We found that the clusters composed of pentagons are consistently more stable and that the calculated water clusters can explain the high-resolution noncontact atomic force microscopy images [6]. Furthermore, we found that the 2D ice rule applies to explaining and predicting the structure of water clusters on Cu(110).

References

- [1] M. Dion et al.: Phys. Rev Lett. **92** (2014) 246401.
- [2] J. Wu and F. Gygi: J. Chem. Phys **136** (2012) 224107.
- [3] Y. Hamamoto, I. Hamada, K. Inagaki, and Y. Morikawa: Phys. Rev. B **93** (2016) 245440.
- [4] I. Hamada: Phys. Rev. B **89** (2014) 121103(R).
- [5] A. Shiotari and Y. Sugimoto: Nat. Commun. **8** (2017) 14313.

Energy Transport in Hybrid Organic-Inorganic Thermoelectric Materials

Shenghong JU

Department of Mechanical Engineering, The University of Tokyo

7-3-1 Hongo, Bunkyo, 113-8656

Thermoelectric materials can directly convert waste heat energy to useful electricity. During the last decade, the organic polymers have shown unique features such as low density, low thermal conductivity, easy synthesis and versatile process ability. Using organic polymers in thermoelectric materials appears to have great potential for producing relatively low cost and high performance thermoelectric devices. However, little work on modeling and simulation is reported at present.

The first main part of last year work is about the thermoelectric property investigation of metastable phases of silicon. In this work, the phonon and electron transport properties of metastable Si-III and Si-XII are investigated by density functional theory, as shown in Fig 1 and 2. The metastable Si-III and Si-XII show one magnitude lower thermal conductivity than the stable Si-I phase. The effect of different three-phonon scattering processes on the thermal conductivity of different phases were evaluated by removing specific scattering processes from the Brillouin zone. Further electron transport property calculation suggests that the metastable Si-III and Si-XII phases have higher thermoelectric figure-of-merit than the Si-I phase in

which the low lattice thermal conductivity and the high electrical conductivity at low chemical potential region contributes the most. The results suggest an effective way to improve the thermoelectric performance of Si-based materials.

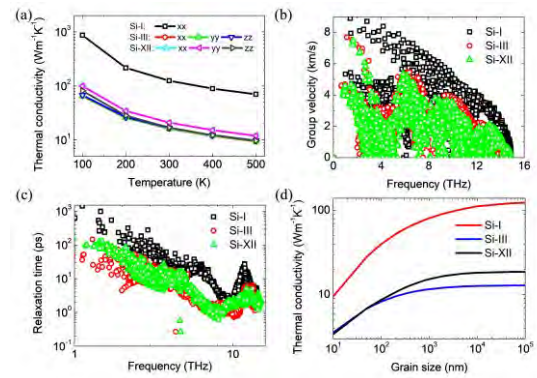


Figure 1: Comparison of phonon transport property in Si-I, Si-III and Si-XII.

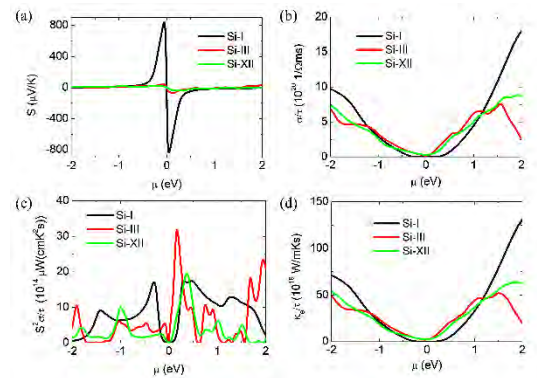


Figure 2: Comparison of electron transport property in Si-I, Si-III and Si-XII.

The second main part of last year work is about the design of magnetic tunnel junctions (MTJs) using disordered MgAl_2O_4 . Through Bayesian optimization and the least absolute shrinkage and selection operator technique combined with first-principles calculations, we investigated the tunnel magnetoresistance (TMR) effect of Fe/disordered- MgAl_2O_4 (MAO)/Fe(001) magnetic tunnel junctions to determine structures of disordered-MAO that give large TMR ratios. The optimal structure with the largest TMR ratio was obtained by Bayesian optimization with 1728 structural candidates, where the convergence was reached within 300 structure calculations. Characterization of the obtained structures suggested that the in-plane distance between two Al atoms plays an important role in determining the TMR ratio. Since the Al-Al distance of disordered MAO significantly affects the imaginary part of complex band structures, the majority-spin conductance of the Δ_1 state in Fe/disordered-MAO/Fe MTJs increases with increasing in-plane Al-Al distance, leading to larger TMR ratios. Furthermore, we found that the TMR ratio tended to be large when the ratio of the number of Al, Mg, and vacancies in the [001] plane was 2:1:1, indicating that the control of Al atomic positions is essential to enhancing the TMR ratio in MTJs with disordered MAO. The present work reveals the effectiveness and advantage of material informatics combined with first-principles transport calculations in designing high-performance spintronic devices based on MTJs.

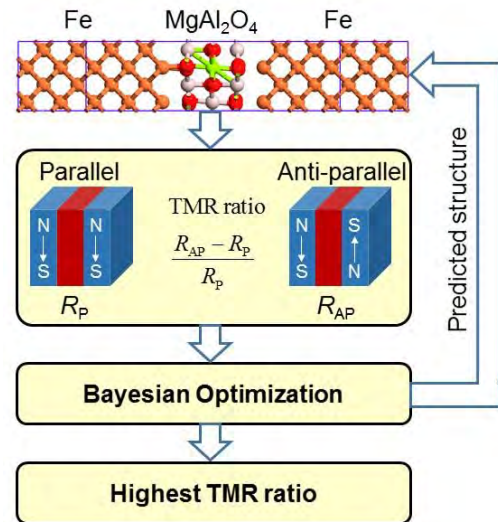


Figure 3: Schematics of designing magnetic tunnel junction for high tunnel magneto-resistance ratio by combining Bayesian optimization and first-principles calculation.

In summary: (1) We have shown that metastable Si-III and Si-XII phases have higher thermoelectric figure-of-merit than the Si-I phase. (2) We have successfully designed the optimal disordered Fe/ MgAl_2O_4 /Fe (001) structure with the highest tunnel magnetoresistance ratio optimal by combining the first-principles transport calculations and Bayesian optimization.

References

- [1] S. Ju, H. Chen, M. Kohno, J. Shiomi: High thermoelectric performance in metastable phases of silicon: a density functional theory study, under preparation.
- [2] S. Ju, Y. Miura, K. Yamamoto, K. Masuda, K. Uchida, J. Shiomi: Physical Review Research, accepted, 2020.

Quantum Chemical Analysis for High-Performance Polymer Electret

Yucheng ZHANG, Zetian MAO, and Yuji SUZUKI

Department of Mechanical Engineering

The University of Tokyo, Hongo, Bunkyo-ku, Tokyo 113-8656

Electret is dielectric material with quasi-permanent charges. Vibration Electret Energy harvesting (VEEH) is a clean way to convert environmental energy into electricity by electrostatic induction more efficiently than electromagnetic or piezoelectric counterparts [1]. VEEH can be applied to low power electronics such as wireless sensors, implantable medical equipment and wearable device. Since the power output of the VEEH is proportional to the square of surface potential of the electret, it is necessary to discover electret material with high surface charge density. Furthermore, if we could find electret suitable for both negative and positive charging, the power output of VEEH will boom by 4 times theoretically.

CYTOP (AGC Co. Ltd.) is a fluorinated amorphous polymer, with its chemical structures shown in Figure 1. There are three kinds of commercialized CYTOP, S, A and M. CTX-A has carboxyl end groups and CTX-M has alkoxysilane/amide end groups. According to quantum chemical analysis of CYTOP series with different end groups, the amino bond formed after

reaction can act as a strong charge trapping site [2]. Therefore, we investigate charge stability of candidates with free amine functional group which can react with -COOH end group of CTX-A. Electron affinity and ionization potential obtained from quantum chemical calculation are used to evaluate the electron trap energy and hole trap energy of possible candidates after dehydration condensation respectively.

Electron affinity is calculated by comparing molecular energy at neutral and negatively-charged state while ionization potential is computed by comparing molecular energy at neutral and positively-charged state. The calculated ionization potential of CYTOP based electret is as follows: 13.12 eV (CTX-S), 12.03 eV (CTX-A), 9.81 eV (CTX-M) and 7.81 eV (CTX-A/TAEA). Figure 2 visualizes the

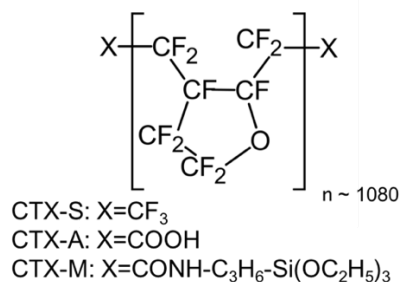


Fig. 1. Chemical structure of CYTOP series.

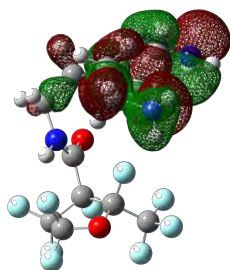


Fig. 2. Visualization of hole trapped orbitals for positive state of CTX-A/TAEA.

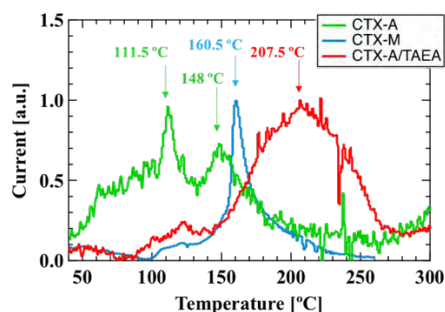


Fig. 3. Normalized TSD spectra of CYTOP electrets charged to +2 kV.

hole trapped orbitals of positively charged CTX-A/TAEA monomer. It is shown that the hole is located near the amide bond, which is formed by the reaction between the carboxy end group and TAEA.

Thermally stimulated discharge (TSD) measurement is also done for comparison between calculation and experiment. Figure 3 shows the TSD spectra of CYTOP polymers for positive charging. It is found that CTX-A/TAEA has the highest charge thermal stability with smallest computed ionization potential value. In addition, the TSD spectra for positive charging exhibit multiple peaks, indicating the difference in the charge trapping mechanisms between negative and positive charges [3], which will be analyzed in the future.

This work was partially supported by JST CREST Grant Number JPMJCR15Q3 and JPMJCR19Q1, Japan. The calculation is performed with SGI ICE XA ISSP system B and every calculation is held with 1 node (24 CPUs). The energy of the molecule is computed by DFT to CAM-B3LYP/6-31+G(d,p) level by using quantum chemical simulation software GAUSSIAN [4]. Molecular dynamic simulation package GROMACS [5] and solid-state analysis package VOTCA-CTP are also used [6] for more accurate estimation. In case of CYTOP hexamers, the calculation cost is approximately 150 CPU hours for quantum chemical calculation, 100 CPU hours for MD simulation and 5 CPU hours for multipole analysis and solid-state analysis.

References

- [1] Suzuki Y. IEEJ Trans. Electr. Electr. Eng., Vol. 6, 101-111 (2011).
- [2] Kim S., et al. Sci. Technol. Adv. Mater., Vol. 19, 486-494 (2018).
- [3] Kim S., et al., IEEE Conf. Electr. Insul. Dielectr. Phenom., Richland, 8-1, (2019).
- [4] M. Frisch et al., "Gaussian 09, Rev. A. 1," Gaussian, Inc. Wellingford, CT, 2009.
- [5] S. Pronk et al., Bioinformatics, 29, (2013) 845-854.
- [6] V. Rulhe et al., J. Chem. Theory Comput., 7, (2011), 3335-3345.

Theoretical modeling of carrier localization/delocalization and related phase transitions

Hannes RAEBIGER

*Department of Physics, Yokohama National University
79-5 Tokiwadai, Hodogaya-ku, Yokohama 250-8501*

1 Introduction

We investigate trends in carrier localization in defective semiconductor/insulator systems focusing on phase transitions. We have previously illustrated the mechanistic origin of the Mott transition and related excitonic insulator phases [1], as well as strain induced piezomagnetic transitions in magnetic semiconductors [2]. This year, we have clarified carrier-induced magnetic transitions in transition-metal doped Ga_2O_3 systems [3, 4], as well as charge trapping in resistive memory (ReRAM) devices [5]. Also, an introductory review of first principles methods for defects in semiconductors/insulators was published as a book chapter [6].

2 Ga_2O_3 systems

We carry out density-functional calculations using the VASP code with in-house developed corrections for band-gap [7] and self-interaction [2]. Band-gap correction of Ga_2O_3 is achieved applying non-local external potential parameters as follows. $V_{O,s}^{NLEP} = -6.4$ eV, $V_{O,p}^{NLEP} = -2.0$ eV for oxygen [7], and for Ga, we use $V_{Ga,s}^{NLEP} = 10.0$ eV, $V_{Ga,p}^{NLEP} = 2.5$ eV, and $U_{Ga,d} = 9.0$ eV to achieve best fit of several physical parameters (see Table 1). For Cr 3d, we set $U = 2.6$ and $J = 1.0$ eV. [7] We further cross-validate these parameters against self-interaction corrected VP-SIC in the KKR-CPA

framework (see [3] for details).

Table 1: Physical properties of $\beta\text{-Ga}_2\text{O}_3$. E_g is band gap energy (eV) and m_e^* is effective electron mass.[3]

	pure GGA	GGA+NLEP	Exp.
$a(\text{\AA})$	12.40	11.90	12.214
b/a	0.250	0.251	0.249
c/a	0.475	0.471	0.475
$V(\text{\AA}^3)$	219.43	197.26	208.85
$\Delta V(\%)$	+5.1	-5.5	
$\beta(\text{deg})$	103.8	104.1	103.82
E_g	2.0	4.7	4.9
m_e^*/m_e	0.19	0.37	0.28

Carrier-mediated ferromagnetism in Cr-doped $\beta\text{-Ga}_2\text{O}_3$.[3] First of all, we find that Cr prefers the octahedral lattice site in $\beta\text{-Ga}_2\text{O}_3$ by ~ 1 eV against the tetrahedral site. We then show that Cr in the octahedral site has a negative charge transition close to conduction band minimum, so the system may become charged. Magnetic interaction among Cr impurities is investigated as a function of Cr–Cr distance up to $\sim 8.5\text{\AA}$. For nonconductive systems, we find a weak antiferromagnetic coupling for nearest neighbor Cr–Cr pairs, and zero interaction for all other pairs investigated. We then include carrier-electrons, which cause negative charging of Cr impurities. We further find that such carrier-doping switches on a strong ferromag-

netic interaction, which persists up to $\sim 6\text{\AA}$ Cr–Cr separation.

Optical properties ϵ and κ phases of Ga_2O_3 doped with cobalt.[4] In collaboration with experimental work, we investigate the modulation of optical absorption edge in ϵ and κ phases of Ga_2O_3 by Co doping. Co impurity levels, as well as those of some typical native impurities, are calculated from first principles. We then calculate the optical absorbance for several Co doped systems at several defect concentrations. This is used to re-interpret experimental observations, which previously asserted band-gap modulation based on changes in optical gap upon Co doping. However, our calculation shows that the optical gap changes instead are due to Co impurity levels. We further present a new band diagram to clarify changes in work function due to Co doping in these systems.

3 Charge trapping in ReRAM systems

We describe resistive memory ReRAM devices by a metal/insulator/metal sandwich structure, and investigate charge trapping by numerically solving Poisson’s equation. We develop a self-consistent Poisson solver, where charge stored in device is solved self-consistently together with potential over device under different bias voltages. We discover new band-bending solutions characterized by different amount of charged stored in the system, and reversible switching between these differently charged states, illustrated in Figure 1. This electrostatic switching mechanism provides a novel interpretation for ReRAM operation, and resolves the mystery of extremely fast sub-nanosecond switching.

References

- [1] S. Bae and H. Raebiger: Phys. Rev. B (Rapid Communications) **94** (2016)

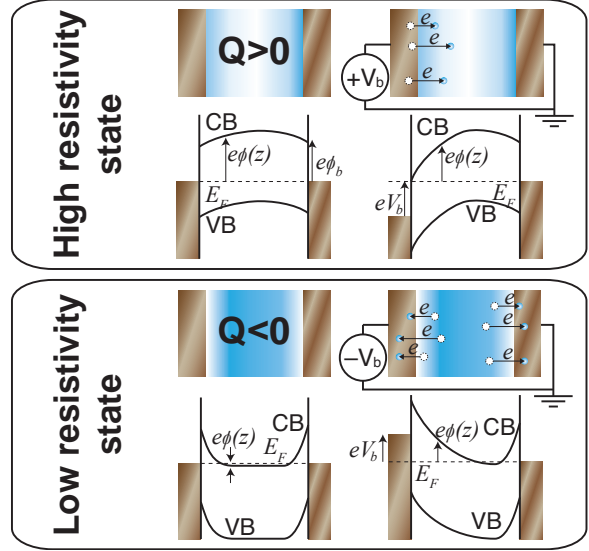


Figure 1: Band bending solutions of ReRAM device, and switching by external bias.

241115(R).

- [2] H. Raebiger, S. Bae, C. Echeverría-Arrondo, and A. Ayuela: Phys. Rev. Mater. **2** (2018) 024402.
- [3] K. Ichihashi, H. Shinya, and H. Raebiger: Appl. Phys. Express **13** (2020), 021002.
- [4] K. Yamanaka, H. Raebiger, K. Mukai, and K. Shudo: J. Appl. Phys. **127** (2020) 065701.
- [5] H. Raebiger, A. C. M. Padilha, A. R. Rocha, and G. M. Dalpian: J. Phys. D (accepted, 2020, DOI: 10.1088/1361-6463/ab7a58).
- [6] E. Ertekin and H. Raebiger: Ch. 7 in Characterisation and Control of Defects in Semiconductors, ed. F. Tuomisto (IET, United Kingdom 2019) pp. 289–343.
- [7] H. Raebiger, S. Lany, and A. Zunger: Phys. Rev. Lett. **101** (2008) 027203.

Ab initio study on the metallization and superconductivity in metallic superhydrides

Ryosuke Akashi

Department of Physics, University of Tokyo

Hongo, Bunkyo-ku, Tokyo 113-0033

In this project, we studied the mechanism of the metallic and superconducting properties of the superhydrides—the compounds containing anomalously large formula ratio of hydrogen—recently synthesized under megabar pressures. The discovery of the 200-kelvin superconductivity in the compressed H₂S (Ref. [1]) has triggered extensive study on the pressure induced superconductivity of hydrogen compounds. Later studies revealed that the novel phase containing excess hydrogen atoms, H₃S, emerges under extreme pressures, which is responsible for the experimentally observed high- T_c superconductivity. This has motivated the exploration of pressure induced hydrogen-excess compounds.

First, we numerically examined the superconducting properties of some crystalline lanthanum and yttrium superhydrides, LaH_{*x*} and YH_{*x*}, for possible explanation of the experimentally observed superconducting transition temperature (T_c) (260 K and 240 K, respectively) in these systems. We calculated T_c for theoretically predicted crystal structures of LaH₁₀ and LaH₁₆ from first principles. Specifically, we solved the gap equation of the density functional theory for superconductors (SCDFT) (Ref. [2, 3, 4])

$$\Delta_{n\mathbf{k}} = -\mathcal{Z}_{n\mathbf{k}}\Delta_{n\mathbf{k}} - \frac{1}{2} \sum_{n\mathbf{k}'} \mathcal{K}_{n\mathbf{k}n'\mathbf{k}'} \frac{\tanh \frac{\beta E_{n'\mathbf{k}'}}{2}}{E_{n'\mathbf{k}'}} \Delta_{n'\mathbf{k}'}. \quad (1)$$

Here, the phonon-mediated Cooper pairing effect is included within the Eliashberg theory

with the Migdal approximation. Also, the electron-electron Coulomb repulsion that suppresses the pairing is also incorporated. Δ is the order parameter and $n\mathbf{k}$ labels the Kohn-Sham band index and crystal wavenumber, respectively. $E_{n\mathbf{k}} = \sqrt{\xi_{n\mathbf{k}}^2 + \Delta_{n\mathbf{k}}^2}$ and β is the inverse temperature. The non-diagonal part of the kernel of Eq. (1) \mathcal{K} is composed of the phononic and electronic contributions: $\mathcal{K} = \mathcal{K}^{\text{ph}} + \mathcal{K}^{\text{el}}$. On the other hand, the diagonal part \mathcal{Z} includes only the phononic one: $\mathcal{Z} = \mathcal{Z}^{\text{ph}}$. To evaluate the phononic parts we need to calculate the Eliashberg function $\alpha^2F(\omega)$, which is roughly the phonon density of states weighted by the coupling strength to the electrons. The electronic part is calculated as the two-particle matrix element of the screened Coulomb interaction, where the one-particle states and dielectric function are calculated by the first-principles Kohn-Sham equation. All the components were calculated with the plane-wave basis code package QUANTUM ESPRESSO (Ref. [5]). The phononic properties of the yttrium compound was supplemented with the anharmonic correction using the stochastic self consistent harmonic approximation [6].

We show in Table I the values of T_c calculated with the SCDFT gap equation [Eq.(1)], as well as characteristic parameters of $\alpha^2F(\omega)$

$$\lambda = 2 \int d\omega \frac{\alpha^2F(\omega)}{\omega}, \quad (2)$$

$$\omega_{\text{ln}} = \exp \left[\frac{2}{\lambda} \int d\omega \frac{\alpha^2F(\omega)}{\omega} \log \omega \right]. \quad (3)$$

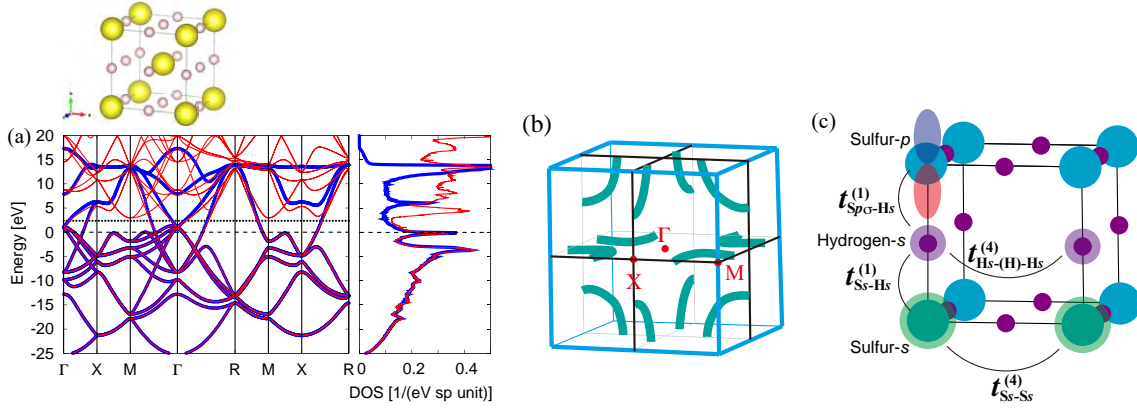


Figure 1: (a) Crystal structure of the high- T_c phase of cubic H₃S and its band structure and DOS. The thin and bold lines represent the first-principle and Wannier band structures, respectively. (b) The simple cubic Brillouin zone and positions of the loop-like continuous saddle points in the band structures. (c) The minimal Wannier model that reproduces the saddle loop around the M point. See Ref. [12] for more details.

Table 1: Coupling constant λ (Eq. (2)), typical frequency ω_{ln} (Eq. (3)), and the superconducting transition temperature T_c calculated with the SCDFt gap equation Eq. (1).

	LaH _x [9]		YH _x
	LaH ₁₀	LaH ₁₆	YH ₆
Pressure (GPa)	200	200	165
λ	3.75	1.82	1.71
ω_{ln}	905	1366	1332
T_c (K)	271	156	156

Experimentally observed T_c for the lanthanum systems strongly depends on the trials [7, 8]. The synthesis with excess hydrogen yielded T_c varying from 250 K to 210 K. Our calculation indicates that the high- T_c phase corresponds to LaH₁₀ (left column), whereas the low- T_c phase could be a mixture of LaH₁₀ and LaH₁₆ (middle column). We have published this result in Ref. [9]. For the yttrium hydride, on the other hand, our calculated T_c (right column) was substantially lower than the experimental value (~ 240 K). At this point we have not reached to a plausible understanding of the origin of the discrepancy [10].

We also addressed the metallic electronic

state in the sulfur superhydride H₃S. According to preceding studies, it hosts a sharp peak at the Fermi level in the electronic density of states (DOS) $N(E)$ (Fig. 1 (a)), which has a role of boosting the T_c via the relation $\lambda \propto N(E_F)$ with E_F being the Fermi level. Its origin has, however, yet been clarified. To elucidate the mechanism of its formation, we first performed a close analysis of the band structure and found that the DOS peak structure mainly originates from the loop-like continuous saddle points around the M point in the primitive cubic Brillouin zone (Fig. 1 (b)). Next, we constructed the Wannier model using QUANTUM ESPRESSO and WANNIER90 (Ref. [11]) program packages. Our model consists of sulfur- s , p and hydrogen- s like orbitals and almost perfectly reproduces the first-principles band structure especially around the Fermi level (Fig. 1 (a)). We then calculated the effective band structures with this Wannier model with omitting the interorbital hopping parameters. Finally, we found that a simple model reproduces the key feature in the band structure; the saddle-point loops around the M point. In this model (Fig. 1 (c)), the simple cubic ScF₃ sites and the nearest-neighbor and selected far-

ther neighbor hopping parameters have been extracted from the original Wannier model. The nearest-neighbor hoppings for the s -like and p -like orbitals on the simple cubic ScF_3 lattice geometry yields a saddle point at the M point, and in addition, the selected farther neighbor hopping “pushes down” the state at the M point to form the continuous loop of the saddle point. This understanding on the origin of the DOS peak in the celebrated high- T_c superconductor H_3S has been published [12].

Computational detail. The generalized gradient approximation for the exchange-correlation potential was employed [13] for the calculations of LaH_x , YH_x and H_3S . MPI parallelized calculations were performed with respect to k points (-npool option) as implemented in *pw.x* code. The screened electron-electron Coulomb matrix elements [4] were calculated with an in-house code with the OPENMP parallelization. The calculations were mainly done in System B.

References

- [1] A. P. Drozdov, M. I. Erements, and I. A. Troyan, V. Ksenofontov, and S. I. Shylin, *Nature (London)* **525**, 73 (2015).
- [2] M. Lüders, M. A. L. Marques, N. N. Lathiotakis, A. Floris, G. Profeta, L. Fast, A. Continenza, S. Massidda, and E. K. U. Gross, *Phys. Rev. B* **72**, 024545 (2005).
- [3] M. A. L. Marques, M. Lüders, N. N. Lathiotakis, G. Profeta, A. Floris, L. Fast, A. Continenza, E. K. U. Gross, and S. Massidda, *Phys. Rev. B* **72**, 024546 (2005).
- [4] R. Akashi, M. Kawamura, S. Tsuneyuki, Y. Nomura, and R. Arita, *Phys. Rev. B* **91**, 224513 (2015).
- [5] P. Giannozzi *et al.*, *J. Phys.: Condens. Matter* **21**, 395502 (2009); <http://www.quantum-espresso.org/>.
- [6] I. Errea, M. Calandra, and F. Mauri, *Phys. Rev. B* **89**, 064302 (2014).
- [7] M. Somayazulu, M. Ahart, A. K. Mishra, Z. M. Geballe, M. Baldini, Y. Meng, V. V. Struzhkin, and R. J. Hemley, *Phys. Rev. Lett.* **122**, 027001 (2019).
- [8] A. P. Drozdov, P. P. Kong, V. S. Minkov, S. P. Besedin, M. A. Kuzovnikov, S. Mozaffari, L. Balicas, F. F. Balakirev, D. E. Graf, V. B. Prakapenka, E. Greenberg, D. A. Knyazev, M. Tkacz, and M. I. Erements, *Nature (London)* **569**, 528 (2019).
- [9] I. A. Kruglov, D. V. Semenok, H. Song, R. Szczeńiak, I. A. Wrona, R. Akashi, M. M. D. Esfahani, D. Duan, T. Cui, A. G. Kvashnin, and A. R. Oganov: *Phys. Rev. B* **101**, 024508 (2020).
- [10] D. V. Semenok, R. Akashi *et al.*, in preparation.
- [11] A. A. Mostofi, J. R. Yates, G. Pizzi, Y.-S. Lee, I. Souza, D. Vanderbilt, and N. Marzari, *Comput. Phys. Commun.* **185**, 2309 (2014).
- [12] R. Akashi: *Phys. Rev. B* **101**, 075126 (2020).
- [13] J. P. Perdew, K. Burke, and M. Ernzerhof, *Phys. Rev. Lett.* **77**, 3865 (1996).

First-principles study on physics of gap-state control at metal/semiconductor interfaces

Takashi NAKAYAMA

Department of Physics, Chiba University

1-33 Yayoi, Inage, Chiba 263-8522

Due to the break of atomic bonds and the lack of translational symmetry, gap states appear in semiconductor layers around metal/semiconductor interfaces, which have the energy position in the band gap and are localized around the interface. These states induce the electron transfer between metal and semiconductor layers and determine a variety of physical phenomena at the interface, such as Schottky barrier (SB), defect density, and metal-atom ionization. However, it is still unclear how to control the gap states. In this work, we studied the SB and tunneling current at various interfaces and clarify the origins of gap-state generation/annihilation and deformation using the first-principles calculations.

We first consider metal/Ge interfaces, where Fermi energies of most of metals are located around the valence-band top of Ge irrespective of the kinds of metals. This is called the Fermi-level (FL) pinning and interrupts desirable low-resistive metal/n-Ge contacts. Although the breakdown of FL pinning was recently observed at TiN/Ge(001) interfaces, its origin has not been clarified. To simulate the interfaces, we adopt (1×1) – (3×3) TiN/Ge(01) repeated-slab models with various interface structures and calculate their SBs using local potential profiles.

Figure 1 shows calculated SBs for hole carriers at various interfaces. The SBs at Ti-rich interfaces like abrupt (a-2) are around 0.0eV corresponding to the FL pinning, while the SBs at N-rich interfaces such as (b-2) and (c) have large values above 0.3eV, which is in good agreement with experiments. The origin of such SB variation is understood by observing the projected densities of states (PDOS) of interface atoms, which are shown in Fig.2.

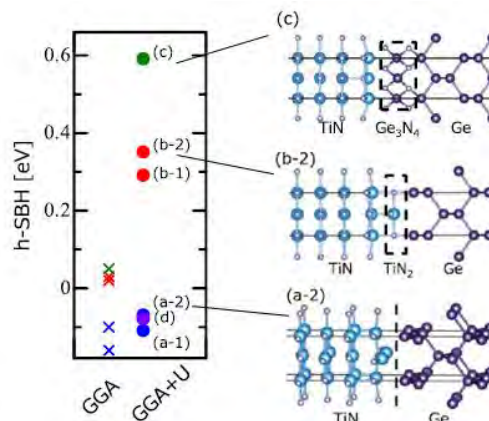


Fig.1. Left: calculated Schottky barriers for hole carriers at various TiN/Ge interfaces. Right: schematic pictures of interface structures. (a-2): abrupt Ti-rich interface, (b-2) and (c): N-rich interfaces with TiN₂ and Ge₃N₄ interface layers.

For (a-2) interface, the continuous PDOS, thus the gap states, appear around 0.0eV for interface Ge atoms due to the orbital hybridization between Ti and Ge, which induces electron transfer from TiN to Ge and realizes the FL pinning. On the other hand, we can see the suppression of gap states in the PDOS of interface Ge for (b-2) interface, which is caused by the production of interface N-Ge bonds. In this way, the interface covalent bonds eliminate the gap states in interface Ge layers.

Next, we consider how the interface bonds affect the SBs. We artificially produce metal/X/Ge(001) interfaces with various segregation atoms, X, that terminate interface Ge, and calculate the SBs, the results being shown in Fig.3 for Al/X/Ge cases. We found the chemical trend that the segregation of II- and III-family atoms lowers the SBs, while that of V- and VI-family atoms raises the SBs. By analyzing electronic structures in details, it was shown that such trend reflects the valency of X

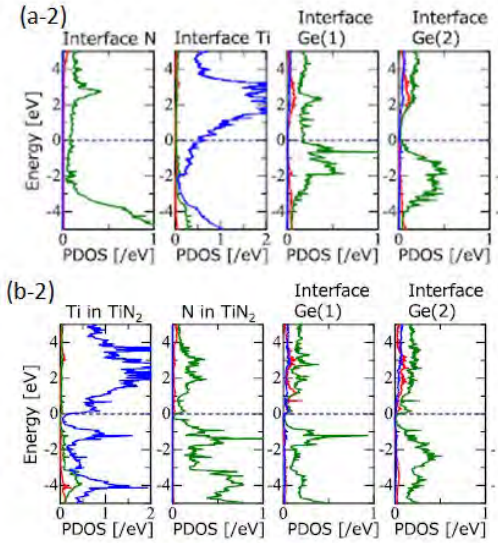


Fig.2. Calculated projected densities of states of interface atoms around TiN/Ge interfaces with (a-2) and (b-2) structures shown in Fig.1. Ge(1) and Ge(2) correspond to the first and second layer germanium atoms, respectively.

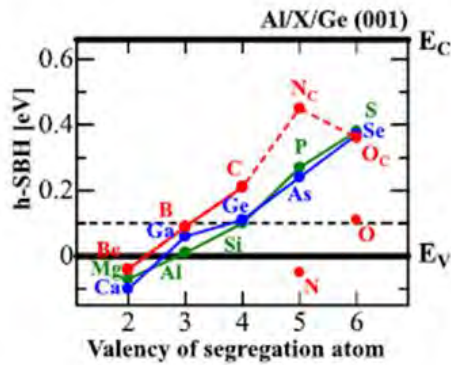


Fig.3. Calculated Schottky barriers for hole carriers at Al/X/Ge interfaces with various segregation atoms, X. E_c and E_v denote the conduction-band-bottom and valence-band-top positions of bulk Ge, respectively.

atoms; when X-Ge bonds are produced at the interface, the electron transfer occurs from X to Ge for X atoms with less than 4 valence electrons, while the additional transfer occurs from X to Al for X atoms having more than 4 electrons. In this way, not only the termination of interface Ge bonds but also the kinds of termination atom is important to deform the gap state and depin the FL.

Finally, we study how the gap states change in electric field. We consider the tunneling current at

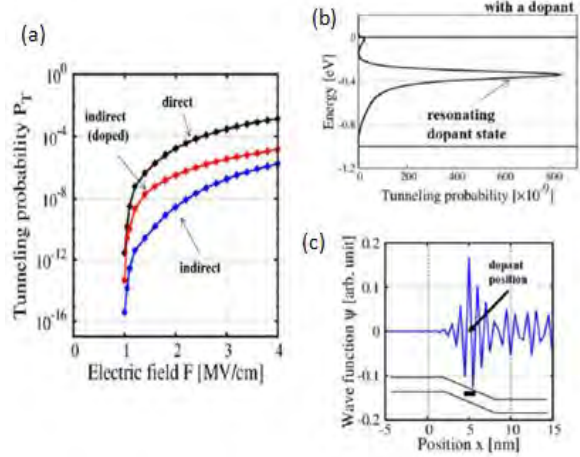


Fig.4. (a): calculated tunneling probability of electrons at Si-p/n junction as a function of electric field, for the cases with (red line) and without (blue) dopants. (b) and (c): energy distribution of tunneling electrons and resonance state at doped p/n junction.

Si-p/n junction. Figure 4(a) shows calculated current as a function of applied electric field. When the dopant is embedded in p/n junction (red line), the current is markedly enhanced, which is caused by the tunneling through the dopant state as seen in the energy spectra in Fig. 2(b). Figure 2(c) shows a wavefunction of such dopant state. This state is a resonance state between isolated dopant state and gap state produced by the penetration of conduction-band state of right-handed bulk Si layers into the band gap. By changing not only the spacial and energy positions of dopant state but also the electric field, we can control such resonance. In this way, the gap-state characteristics are controlled by the electric field.

All these calculations were performed using the xTAPP, VASP, and pspwf codes. In order to realize the calculations for the present interface systems, because the system is made of a large number of atoms (300-1000 atoms), the advanced computing facility having multi-task and higher-speed CPU (more than 64 cores \times 2.5GHz), larger-size memory (around 128GB), and larger-size storage (more than 1 TB) is indispensable. These conditions are realized only by the ISSP supercomputing systems.

Theoretical analysis of ion conduction mechanism of highly concentrated electrolytes for secondary batteries

Atsuo YAMADA

*Department of Chemical System Engineering,
The University of Tokyo, Bunkyo-ku, Hongo, Tokyo 113-8656*

Highly concentrated electrolytes have recently attracted much attention owing to their unique electrochemical properties derived from an unusual coordination structure, where the ligand (solvent/anion) exchange reactions are responsible for the ion transport, while the vehicular-type mechanism is dominant in the diluted electrolyte [1]. Herein, we theoretically investigated the salt concentration dependence of ionic conduction mechanism in AFSA/DME electrolyte ($A = \text{Li, Na, K}$) using quantum molecular dynamics (MD) simulations.

All the calculations were performed using divide-and-conquer density functional tight-binding (DC-DFTB) method [2]. A modified 3OB parameter set based on first-principles calculations was adopted, and a constant temperature condition of 298.15 K was

imposed under NVT ensemble. The equilibration of 10 ps at 1 fs time interval was followed by the sampling of 200 ps.

With increasing the salt concentration, the ligand exchange reactions become active mainly via FSA anions (Fig. 1). The increased ion radius (decreased Lewis acidity) of cations also activates the ligand exchange reactions by weakening the interaction with the ligands. Therefore, both the higher concentration and increased cation size should promote the ligand exchange-type ion transport.

References

- [1] M. Okoshi, C.-P. Chou and H. Nakai, *J. Phys. Chem. B* **122**, 2600 (2018).
[2] Y. Nishimura, H. Nakai, *J. Comput. Chem.*, **40**, 1538 (2019).

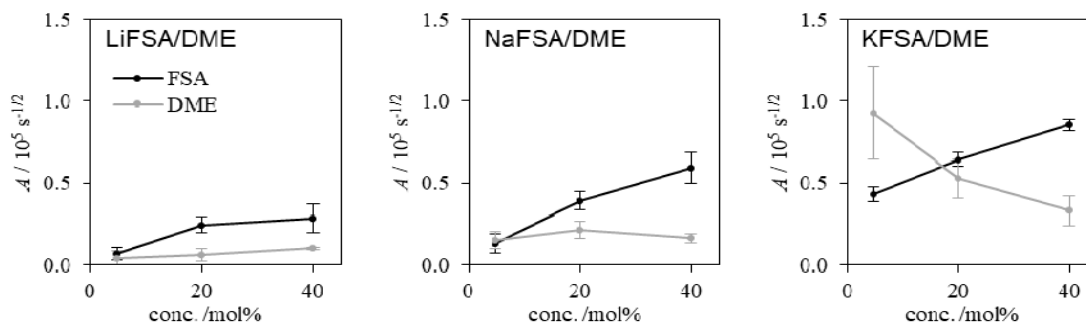


Fig. 1 Relationships between frequencies of ligand exchange, A , and salt concentration.

First-principles Theoretical Study of Chemical Reactions in Heterogeneous Catalysts

S. E. M. PUTRA, T. N. PHAM, S. A. Wella, F. MUTTAQIEN, Y. J. WONG, H. KIZAKI, K. INAGAKI, Y. HAMAMOTO, I. HAMADA, and Y. MORIKAWA
Department of Precision Engineering, Graduate School of Engineering, Osaka University, 2-1 Yamadaoka Suita, Osaka 565-0871

In 2019-2020, we carried out theoretical analysis of chemical processes at surfaces and interfaces, formic acid adsorption and decomposition on Cu(111) [1], enhancement of CO₂ hydrogenation by O-C-O bending vibration mode [2], trimer formation of NO Cu(111) [3], and CO oxidation and oxygen reduction reaction at Pt single atom catalyst supported by graphene edges [4]. We also investigated dopant in semiconductors, namely, transition metal doped ZnSnAs₂ [5], and As and B codoping in Si [6]. In this report, we report the enhancement of CO₂ hydrogenation by vibration excitation [2].

Recently, formic acid (HCOOH) has been considered as a potential material for hydrogen storage. Storage of HCOOH is easier and safer compared with other hydrogen storage material because HCOOH is a non flammable liquid at STP. HCOOH can be decomposed on metal surfaces through dehydrogenation process into CO₂ and H₂, or dehydration process into CO and H₂O. Cu catalysts have been reported to selectively decompose HCOOH through dehydrogenation process. The decomposition of HCOOH does not occur on Cu(111) when exposed to the gas phase HCOOH at room temperature. On the Cu(111) surface, HCOOH was reported to form polymeric structures when exposed to the gas phase HCOOH at low temperatures, then the decomposition occurs by heating those polymeric HCOOH.

In the present study, we have investigated

the adsorption and decomposition mechanisms of monomeric HCOOH on Cu(111) by using density functionals that account for the vdW forces and compared with room temperature experimental results.

Our calculations were performed using the STATE (Simulation Tool for Atom TEchnology) code[7]. Here, we compared results obtained using the PBE functional with those using the van der Waals density functionals (vdW-DFs), i.e., optB86b-vdW and rev-vdW-DF2 [8] functionals. We also included the dispersion correction proposed by Grimme with PBE (PBE-D2). The implementation of the self-consistent vdW-DF in the STATE code is described in Ref. [9].

The reaction path for the decomposition (E_{dec}) of the OH-perpendicular configuration on the Cu(111) surface is shown in Fig. 1. The calculated activation energies of decomposition (E_{dec} 's) with ZPE correction are 0.37 eV, 0.31 eV, 0.32 eV, and 0.30 eV for PBE, PBE-D2, rev-vdW-DF2, and optB86b-vdW functionals, respectively, indicating that the E_{dec} are almost independent among the considered functionals in this work. PBE-D2 and vdW-DFs produce lower E_{dec} than E_{des} by (0.16–0.27 eV).

Figure 2 shows the calculated desorption and decomposition rates per surface adsorbate. In this analysis, we used the calculated results by rev-vdW-DF2 energy functional. At low temperatures, the decomposition process

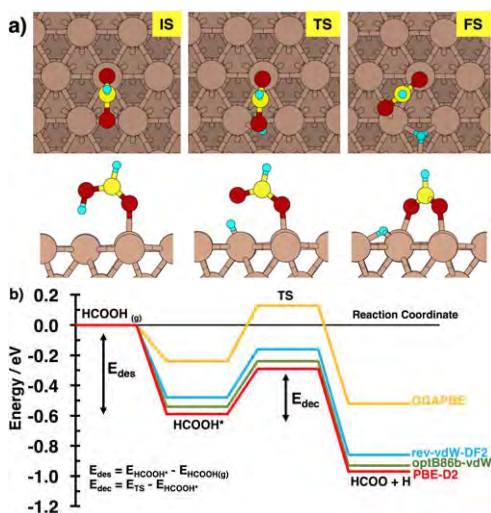


Figure 1: (a) Decomposition process of the OH-perpendicular configuration. IS, TS, and FS represent initial state, transition state, and final state, respectively. (b) Energy profile for the OH-perpendicular configuration decomposition on Cu(111).

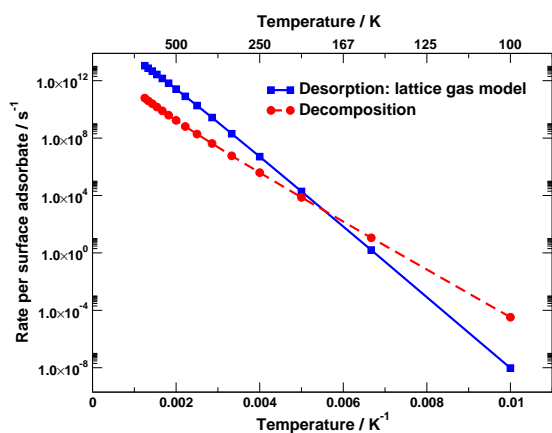


Figure 2: Calculated reaction rates per surface adsorbate for the desorption and decomposition of OH-perpendicular configuration. Red dashed line with circle and blue solid line with square dots line represent the decomposition and desorption rates obtained by using the 2D lattice gas, respectively.

becomes faster than the desorption process, while at higher temperatures, the desorption process becomes dominant due to large pre-exponential factor for the desorption process and the transition temperature between the two processes is ~ 187 K. These results are in very good agreement with the experimental situation that there is no HCOOH decomposition on Cu(111) by exposing the surface to the gas phase HCOOH at room temperature.

References

- [1] S. E. M. Putra, F. Muttaqien, Y. Hamamoto, K. Inagaki, I. Hamada, and Y. Morikawa: *J. Chem. Phys.* **150** (2019) 154707.
- [2] J. Quan, F. Muttaqien, T. Kondo, T. Kozarashi, T. Mogi, T. Imabayashi, Y. Hamamoto, K. Inagaki, I. Hamada, Y. Morikawa, and J. Nakamura: *Nature Chem.* **11** (2019) 722.
- [3] T. N. Pham, Y. Hamamoto, K. Inagaki, D. N. Son, I. Hamada, and Y. Morikawa: *J. Phys. Chem. C* **124** (2020) 2543.
- [4] S. A. Wella, Y. Hamamoto, F. Iskandar, Suprijadi, Y. Morikawa, and I. Hamada: *J. Chem. Phys.* **152** (2020) 104707.
- [5] H. Kizaki and Y. Morikawa: *Jpn. J. Appl. Phys.* **58** (2019) 110601.
- [6] K. Tsutsui and Y. Morikawa: *Jpn. J. Appl. Phys.* **59** (2020) 010503.
- [7] Y. Morikawa: *Phys. Rev. B* **51** (1995) 14802.
- [8] I. Hamada: *Phys. Rev. B* **89** (2014) 121103.
- [9] Y. Hamamoto, I. Hamada, K. Inagaki, Y. Morikawa: *Phys. Rev. B* **93** (2016) 245440.

Theoretical Design of Gate Dielectrics of Future GaN Power Devices

Kenji SHIRAISHI

*Institute for Materials and Systems for Sustainability,
Nagoya University, Furo-cho, Chikusa-ku, Nagoya, Aichi 464-8601*

We performed the density-functional calculations that clarify atomic and electronic structures of the oxygen vacancy V_O in amorphous $(Al_2O_3)_{1-x}(SiO_2)_x$ mixed oxides, a promising candidate for the gate insulator in future GaN power devices [1]. We constructed microscopic models for the amorphous structure by the melt-quench scheme and then examine all the possible oxygen vacancies and determine the total-energy minimized V_O structures. We found a clear tendency that the V_O formed at the oxygen site surrounded by less Al atoms has lower formation energy. More importantly, we find that V_O surrounded by Si atoms alone induces no deep levels in the energy gap of GaN, whereas V_O surrounded by more Al atoms induces a deep level. This theoretical finding strongly infers that the majority of V_O in amorphous $(Al_2O_3)_{1-x}(SiO_2)_x$ is electrically inactive and not very harmful in device operations. We further explore the possibilities of the structural transformation from the electrically active V_O to the electrically inactive V_O . We identified reaction pathways for such transformation and obtain the corresponding

energy barriers. The calculated occurrence rate for the transformation is high enough to assure that the thermal annealing at typical temperature and time causes the conversion of the electrically active V_O to the inactive V_O , providing a further advantage of $(Al_2O_3)_{1-x}(SiO_2)_x$ as the gate insulator over other oxides such as SiO_2 and Al_2O_3 .

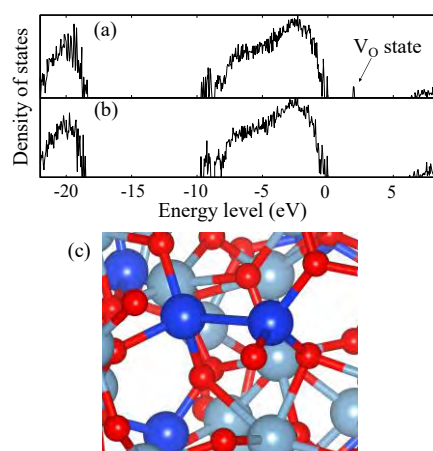


Fig.1: Density of states of the $(Al_2O_3)_{0.70}(SiO_2)_{0.30}$ mixed oxide containing a single oxygen vacancy V_O obtained by HSE, (a) surrounded by Al atoms and (b) surrounded by Si atoms. The origin of the energy is set at the valence band maximum. (c) Atomic structure of a V_O surrounded by Si atoms. A Si-Si bond is formed after removal of the oxygen atom. Silver, blue, and red spheres represent the Al, Si, and O atoms, respectively.

References

- [1] D. Kikuta, K. Itoh, T. Narita, and T. Mori, Al_2O_3/SiO_2 nanolaminate for a gate oxide in a GaN-based MOS device, *J. Vac. Sci. Technol. A* 35, 01B122 (2017).

Analysis of Thermoelectric Properties of Clathrate Compounds with *Ab Initio* Calculations

Masato OHNISHI

7-3-1, Hongo, Bunkyo-ku, The University of Tokyo, Tokyo 113-8656

Clathrate compounds are promising candidates for thermoelectric materials in terms of the “electron-crystal phonon-glass” concept. Clathrate compounds are composed of guest atoms encapsulated in cagelike structures. It is expected that electrons can smoothly transport in the frame work while phonons are scattered by guest atoms. Particularly, in type-I clathrate compounds, guest atoms vibrate in a strong anharmonic potential because they are composed of a Weaire-Phelan structure, which divides a space with the maximum volume with the same cross-sectional area. While off-center clathrates such as type-I $\text{Ba}_8\text{Ga}_{16}\text{Sn}_{30}$, in which guest atoms vibrate in a double-well anharmonic potential, have low thermal conductivity, silicon-based clathrates are preferable for actual use in terms of the material cost.

In this study, we show that aluminum substitutions can enhance thermoelectric performance of silicon-based clathrates, type-I $\text{Ba}_8\text{Ga}_{16}\text{Si}_{30}$. Comparing calculated thermoelectric figure of merits (ZT) with those obtained in experiment, we concluded that (a) aluminum additive enhances ZT with lowering doping level and (b) further suppression of

doping level can enhance ZT significantly (see Figure). To investigate thermoelectric properties, we obtained possible structures at finite temperature with using a cluster expansion and Monte Carlo method [1] and thermoelectric properties were averaged for different possible structures. Phonon properties of the clathrates were calculated with using a self-consistent phonon (SCP) theory based on first-principles calculations [2]. Our state-of-the-art analysis method shows a good agreement with experimental data.

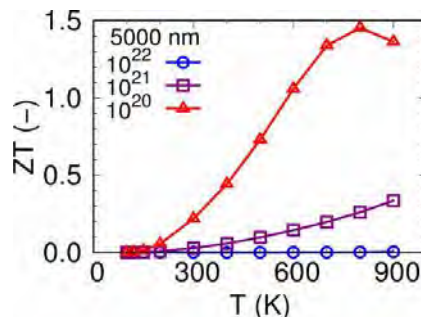


Fig. Temperature-dependent dimensionless thermoelectric figure of merit (ZT) of type-I Si-based clathrate with different carrier concentrations.

References

- [1] R. Kubo: J. Phys. Soc. Jpn. **12** (1957) 570. M. Ångqvist, P. Erhart et al., Chem. Mater. **29**, 7554 (2017) and **28**, 6877 (2016).
- [2] Tadano et al. Phys. Rev. Lett **120**, 105901 (2018).

First-principles calculations of multiferroic interfaces

Yoshihiro GOHDA

*Department of Materials Science and Engineering, Tokyo Institute of Technology
J1-3, Nagatsuta-cho 4259, Midori-ku, Yokohama 226-8502, Japan*

To obtain large magnetoelectric coupling in multiferroic materials, multiferroic interfaces are promising, because single-phase multiferroic materials exhibit typically antiferromagnetism preventing from having net magnetization [1, 2]. In addition to multiferroic interfaces, many types of magnetic interfaces are of fundamental importance to enhance the performance of magnetic materials. Nevertheless, our understanding from electron theory is far from being satisfactory. Since first-principles calculations of magnetic interfaces are computationally challenging, such study is also of importance in the sense of large scale computations.

In this project, we performed first-principles calculations of magnetic interfaces related with multiferroic materials [3–5] and permanent magnets [6–8]. We demonstrated enhancement of magnetoelectric coupling by insertion of Co atomic layer into $\text{Fe}_3\text{Si}/\text{BaTiO}_3(001)$ interfaces from first principles [3]. As is shown in Fig. 1, the interface Co monolayer helps the interface ferroelectric polarization exhibit enough, whereas the interface electric polarization is killed by Si without the Co monolayer at the interface. Other transition-metal monolayers are also investigated [4]. In addition, crystal-growth mechanism was also clarified for Co_2FeSi and Co_2MnSi films on single-crystalline oxides by identifying the initial disorder at the deposition and the formation energy of random alloys relative to ordered alloy [5] by using both of OpenMX [9] and Akai-KKR [10]. Substantial progresses were obtained also for microstructure interfaces in per-

manent magnets [6–8].

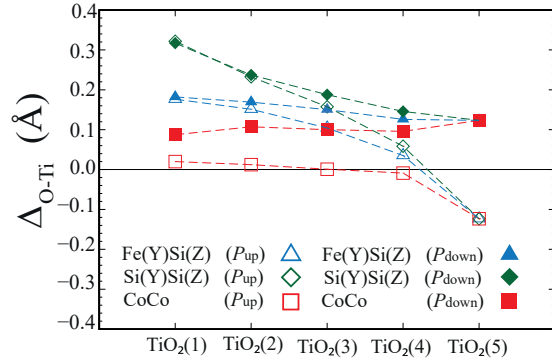


Figure 1: Relative displacements $\Delta_{\text{O-Ti}} = z_{\text{O}} - z_{\text{Ti}}$ in the tetragonal $\text{BaTiO}_3(001)$ film for each interface. For the $\text{Fe}(\text{Y})\text{Si}(\text{Z})$ case, average values for $\Delta_{\text{O-Ti}}$ are shown. The first layer $\text{TiO}_2(1)$ is the interface layer, whereas the fifth layer $\text{TiO}_2(5)$ has the bulk atomic positions of BaTiO_3 .

- [1] T. Taniyama, *J. Phys.: Condens. Matter* **27**, 504001 (2015).
- [2] K. Fujita and Y. Gohda, *Phys. Rev. Appl.* **11**, 024006 (2019).
- [3] Y. Hamazaki and Y. Gohda, *J. Appl. Phys.* **126**, 233902 (2019).
- [4] R. Costa-Amaral and Y. Gohda, in preparation.
- [5] K. Kudo, Y. Hamazaki, S. Yamada, S. Abo, Y. Gohda, and K. Hamaya, *ACS Appl. Electron. Mater.* **1**, 2371 (2019).
- [6] A. Terasawa, M. Matsumoto, T. Ozaki, and Y. Gohda, *J. Phys. Soc. Jpn.* **88**, 114706 (2019).
- [7] Y. Ainai, Y. Tatetsu, A. Terasawa, and Y. Gohda, *Appl. Phys. Express* **13**, 017006 (2020).
- [8] Y. Ainai, T. Shiozawa, Y. Tatetsu, and Y. Gohda, *Appl. Phys. Express* **13**, 045502 (2020).
- [9] T. Ozaki, *Phys. Rev. B.* **67**, 155108 (2003).
- [10] H. Akai, *J. Phys. Condens. Matter* **1**, 8045 (1989).

Determination of the ionization energy and the electron affinity of organic molecular crystals from first-principles

Susumu Yanagisawa

*Faculty of Science, Department of Physics and Earth Sciences, University of the Ryukyus
Nishihara, Okinawa, 903-0213*

Ionization energy (IE) and electron affinity (EA) are fundamental quantities of organic semiconductors, and understanding the factors that determine the energy levels is of primary importance to the research and development of the organic electronics materials such as those of organic light-emitting diodes, organic field-effect transistors, and organic photovoltaics, dominating energy barrier for injection of a charge carrier (hole and electron).

IE and EA are measured with direct photoemission and inverse photoemission techniques, respectively. Notice here that the energy of the hole or electron injected into the sample is measured, i.e., IE (EA) is the magnitude of the energy difference between the neutral N -electron and the positively-(negatively-)charged $N-1$ ($N+1$)-electron systems. Thus, the measured IE and EA implies many-body interaction between the injected charge and the surrounding polarization clouds inside the organic solids which screen the injected charge. A complex of the injected charge and the surrounding dynamically induced polarization clouds are referred to as quasiparticles, which are theoretically well-described with the self-energy determined by the many-body perturbation theory within the GW approximation.

Given an experimental measurement of a few organic monolayers on a substrate such as silica and graphite, it is of importance to investigate the electronic structure of an organic film of a few monolayer thickness with a reliable

theoretical method. For such purposes, a periodic slab model approach is useful. To avoid the computationally demanding periodic slab calculation with GW , the electrostatic potential in a periodic slab was described within DFT-GGA, which was aligned to that in a bulk system. In the bulk system, the electronic polarization upon the injected charge was described within the GW approximation.

In this study, with a combination of the GW approximation suitable in general to solid or bulk systems and a periodic slab approach at the DFT-GGA level, I investigated polymorphs of pentacene (PEN) and perfluoropentacene (PFP). I theoretically demonstrated that the IE and EA at the surface are dominated by the electronic polarization (E_p) upon the injected charge induced by the surrounding polarization clouds, and the electrostatic energy (S) crucially affected by the orientation of the molecule at the surface of the organic semiconductor[1].

The geometrical configurations of the organic semiconductor bulk was determined with the STATE program code, with the lattice constants fixed to the experimental values. For the crystal structure and the lattice constants, two typical polymorphs were considered: single crystal and thin film phases of PEN, fabricated on SiO_2 and graphene substrates, respectively, and, herringbone and π -stacking motifs for PFP, that were reported to grow on the SiO_2 and graphene, respectively.

For the optimized crystal geometries, I estimated the E_p upon the excess hole and electron, based on the quasiparticle self-energy within the GW approximation. I used the modified version of the GW space-time code, which enables highly parallelized calculations.

The resulting ionization energy (I_s) and electron affinity (A_s) are displayed by horizontal dotted dashed lines in Fig. 1. Here, the electronic polarization E_p was obtained as half the difference between the crystalline fundamental gap and that in a gas phase, assuming that $E_p^+ = E_p^-$. The I_s and A_s change drastically when the molecular orientation at the surface is taken into account, and thus, the non-zero S^+ and S^- contribute. The calculated I_s and A_s are in agreement with experiments.

Overall, while E_p , which is approximated by the charge-induced dipole interaction, is quantitatively described within the GW approximation, the present methodology of estimating the electrostatic contribution S seems to describe well the electrostatic nature of the molecular orientation dependence of I_s and A_s at the surface, i.e., the charge-quadrupole interaction[2]. The method lacks description of the decreasing polarization at the surface which amounts to the change of the quantities by ≈ 0.2 eV[3]. Nevertheless, considering the huge computational cost involved in treatment of the slab within GW , the method is suitable for quantitative treatment of an organic semiconductor nano-scale thin film, which is required for nano-scale or sub-nanoscale control of the materials properties.

References

- [1] S. Yanagisawa: Jpn. J. Appl. Phys. **59** (2020) 031002.
- [2] B. J. Topham and Z. G. Soos: Phys. Rev. B **84** (2011) 165405.
- [3] J. Li et al.: J. Phys. Chem. Lett. **7** (2016) 2814.

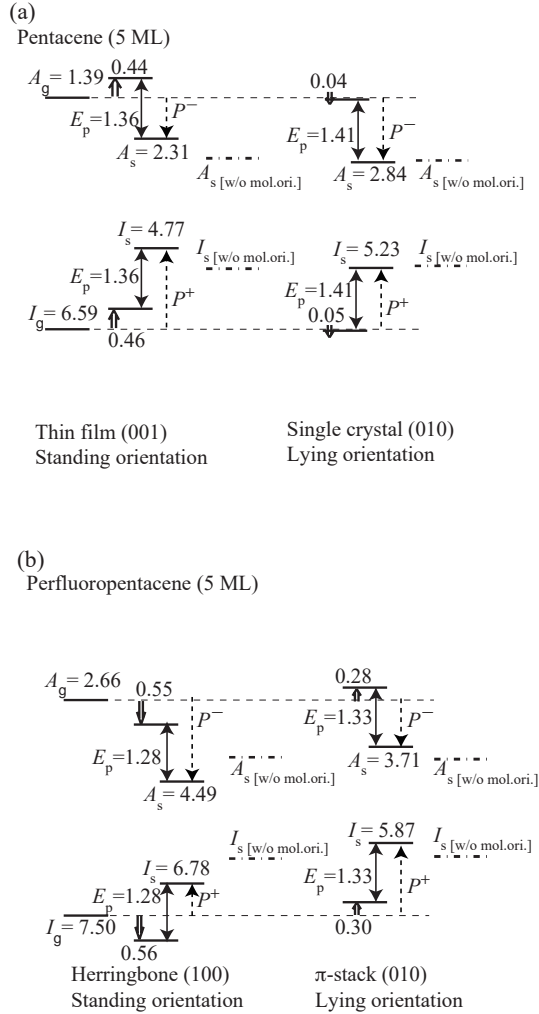


Figure 1: Determination of ionization energy (I_s) and electron affinity (A_s) for the pentacene and perfluoropentacene polymorphs. The experimental gas phase ionization energy (I_g) and electron affinity (A_g) are indicated by the horizontal dashed lines, and the thick horizontal solid lines indicate I_s and A_s at the crystalline surfaces. The vertical dashed lines display the polarization energies P^+ or P^- , which are comprised of the electronic polarization E_p displayed by the double-headed arrows and the electrostatic energies S^+ or S^- indicated by the thick one-headed arrows. For comparison, the ionization energy and the electron affinity without taking into account the molecular orientation at the surface, i.e. $S^+=S^-=0$, are shown by horizontal dotted dashed lines.

DFT Prediction of Bulk Rashba Effect in Multiferroic Oxide

Kunihiko Yamauchi

ISIR-SANKEN, Osaka University, Ibaraki, Osaka 567-0047

Based on *ab-initio* approach using massive parallel computer simulations, we studied Rashba effect, which causes spin splitting of bands through the spin-orbit interaction. This year, we focused on multiferroics — the materials which show both ferroelectric and antiferromagnetic orders — in order to investigate the particular Rashba effect emerging with the magnetic symmetry that contains spin-flipping symmetry operations.

Density-functional theory (DFT) calculations were performed using the VASP code with GGA+ U method. BiCoO_3 crystalizes in the polar $P4mm$ crystal structure in which the Co^{3+} (d^6) ion located at the center of the O_6 octahedron is significantly displaced toward the apical O ion, leading to a pyramidal coordination rather than an octahedral coordination. The magnetic symmetry with the C-type antiferromagnetic order (defined by magnetic space group $P4'mm'$) keeps the spin-degeneracy of bands at the high-symmetric \mathbf{k} points. As shown in Fig.1, we found that the characteristic “vortex-like” in-plane components of the spin texture of the Rashba effect developing around the Z point while the out-of-plane spin component is negligible [1].

The magnetic symmetry can be reduced when the Co spins are canted with respect to the C-AFM configuration in the real space. We assumed the application of external magnetic field along the $[100]$ direction, by canting two Co spins simultaneously. As a result, we observed a distortion of the energy isocontour along the k_y axis and a downward shift of the

center of spin vortex.

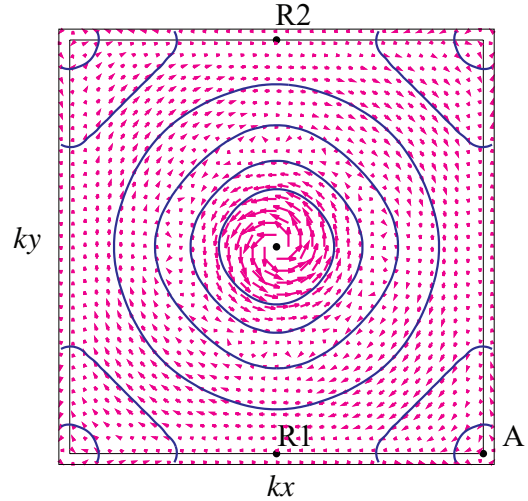


Figure 1: Spin texture (shown by magenta arrows) and energy contour plot of the conduction-bottom band in the $k_z = 1/2$ plane (centered at the Z point) in BiCoO_3 .

While the theoretical predictions in the present study call for future experimental confirmation, we speculate that this phenomenon can be rather common among the antiferromagnetic polar systems; in future works, one can explore the possibility of Rashba effects in various multiferroic systems, such as BiFeO_3 and PbVO_3 .

References

- [1] Kunihiko Yamauchi, Paolo Barone, and Silvia Picozzi, *Phys. Rev. B* **100** (2019) 245115.

First-Principles Molecular-Dynamics Study of Structural and Electronic Properties of Covalent Liquids and Glasses under Pressure

Fuyuki SHIMOJO, Shogo FUKUSHIMA, and Akihide KOURA

Department of Physics, Kumamoto University, Kumamoto 860-8555

The investigation of the dynamic properties of covalent liquids and glasses under pressure is important from perspectives of geophysics as well as fundamental liquid-state science. For this purpose, it would be important to consider the stability of materials states under various conditions from the viewpoint of free energy. To accurately evaluate which state is most stable, the thermodynamic integration (TI) method has been used by calculating the free energy [1]. While the TI method based on first-principles molecular dynamics (FPMD) simulations can obtain the free energy with sufficient precision [2], the system size is severely limited by its high computational cost.

In order to handle adequate system sizes while retaining first-principles accuracy, we adopt an interatomic potential constructed by artificial neural-network (ANN) models trained by FPMD simulations. This study aims to establish a method for the precise evaluation of the free energy using the TI based on the ANN-MD simulations. To that end, we have calculated the size dependence of the melting temperature of rubidium as shown in Fig. 1 [3].

We successfully reduced the computational

cost of numerical integration in the TI method by using an ANN potential compared with FPMD-based TI calculations, while keeping first-principles accuracy. By comparing with the results by FPMD, we confirmed that the ANN-based TI method gives the free energy within the accuracy of less than 0.1 meV/atom with more than 100 atoms.

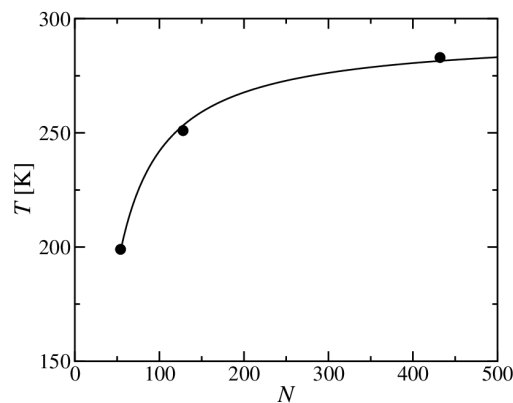


Fig. 1: Melting temperature T as a function of the number of atoms N .

References

- [1] D. Frenkel and A. J. C. Ladd, *J. Chem. Phys.* **81**, 3188 (1984).
- [2] O. Sugino and R. Car, *Phys. Rev. Lett.* **74**, 1823 (1995).
- [3] Fukushima *et al.*, *Phys. Rev. B* **100**, 214108 (2019)

Elucidation of diffusion process of ionic species in organic solvent

Kazuto AKAGI

WPI-AIMR, Tohoku University, Katahira, Aoba-ku, Sendai, Miyagi 980-8577

Further improvement of Li-ion batteries (LIB) is strongly expected still now. The performance of LIB depends on various factors, and optimizing transport properties of Li-ion is one of the most important items. The microscopic transport mechanism in organic electrolytes, however, remains unclear. To elucidate it, we have developed a genetic algorithm based optimized force field (FF) which achieves large-scale and long-time classical MD simulation.

Polarizable FFs such as AMOEBA and APPLE&P are potentially applicable to large scale simulation for LIB systems, but their reliability is not sufficient as they are. In order to optimize AMOEBA FF and mimic the thermodynamic properties obtained by rev-vdW-DF2 density functional for target systems, we made a framework of multi-objective genetic algorithm, in which not only relative potential energy but atomic forces on each atom from VASP are reproduced by TINKER.

Pure ethylene carbonate (EC) and EC with Li-ion systems were assessed. The dimension of parameter space to be optimized is 132, and more than 150 MD snapshots sampled from “9

EC” and “43 EC + 3 Li⁺” systems were used as training set. “360 EC + n Li⁺” systems (from 0.1M to 3.0M) were used for production run. The initial generation was prepared from the original parameters of AMOEBA FF with 20% random noise. The parameter sets formed four groups with the evolution, and only one group survived at 60th generation. Some of them successfully reproduced the diffusion coefficient and density calculated by VASP. Not only the solvation structure of Li-ions but also potential of mean force (PMF) for detachment and attachment of EC were also reasonably described. The diffusion of Li-ion becomes slower at high concentration and it statistically turned out that the lack of free EC molecules decreases attachment/detachment events. The detailed results are prepared for publication.

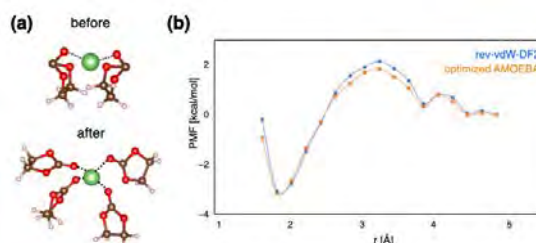


Fig. 1: (a) Improvement of solvated structure. (b) PMF along detachment of EC (DFT and FF).

First-principles study on the stability of magnetic alloys

Yasutomi TATETSU

Meio University, Biimata, Nago, Okinawa 905-8585

Transforming crystal structures of materials by adding pressure, heat, or other elements is one of the fundamental approaches to discover novel physical properties. Recently, a new $Z3$ -type $\text{Fe}(\text{Pd},\text{In})_3$ crystal structure, was discovered by Teranishi's group in Kyoto University [1]. The new structure was obtained by introducing a third element of In into $L1_2$ - FePd_3 , which is the thermodynamically stable phase of binary Fe–Pd systems. Although the addition of In might be the key behind this new finding, the physical aspects of In in stabilizing the new structure is unclear and cannot be understood deeply only through experiments.

In this study, we performed theoretical analyses for the stability of an In-doped novel Fe–Pd phase to check the systems' formation energies using OpenMX. The model structures for the calculations were based on the chemical composition ratio of $Z3$ - FePd_3 obtained from experiments. The In sites were chosen by replacing Fe or Pd sites with a special-quasirandom-structure method implemented in the Alloy Theoretic Automate Toolkit [3]. We investigated stable sites for In in the $Z3$ - FePd_3 structure by comparing formation energies which is illustrated in the figure. We found that an In stably occupies the Pd site rather than the

Fe site. There are two different Wyckoff positions of Pd labelled by 2e and 2g in $Z3$ - FePd_3 . From detailed analyses, we concluded that the new $Z3$ -type $\text{Fe}(\text{Pd},\text{In})_3$ structure, in which a Pd atom at a 2e site is replaced with an In atom, is more stable than In-doped $L1_2$ - FePd_3 structures. These results are consistent with the experimental results from XRD, EXAFS, and STEM-EDS analyses.

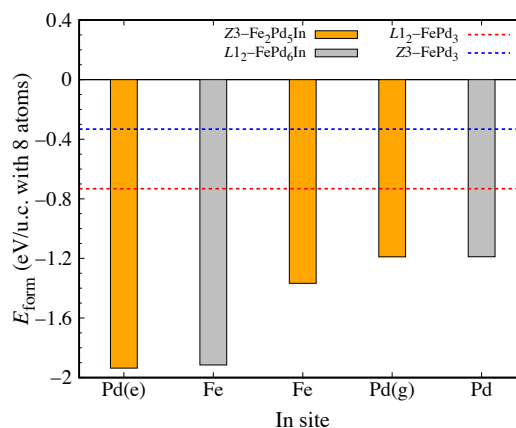


Figure : The comparison of the formation energies of In-doped $Z3$ - and $L1_2$ -type FePd_3 .

References

- [1] K. Matsumoto *et al.*, in preparation.
- [2] <http://www.openmx-square.org>
- [3] A. van de Walle *et al.*, *Calphad Journal* **42**, 13 (2013).

Electrode Properties of Novel Lithium-Ion Secondary Battery Materials: First-Principles Calculations

Hiro Yoshi MOMIDA, Motoyuki HAMAGUCHI, Hiroshi KATSUMOTO, Tatsuya TAKAHASHI

Institute of Scientific and Industrial Research, Osaka University

8-1 Mihogaoka, Ibaraki, Osaka 567-0047

We have studied electrode properties of Li- and Na-ion secondary battery materials by first-principles calculations. The computations are done by using HiLAPW and Quantum Espresso codes.

X-ray absorption spectra in NaFeSO₄F for exploring Na-ion battery reactions

We study electronic and spectroscopic properties of NaFeSO₄F, which has been a candidate cathode material for Na-ion batteries [1, 2]. NaFeSO₄F have been often synthesized experimentally from NaF and FeSO₄, and the calculated result shows that NaFeSO₄F is slightly stable in energy than the two-phase mixture of NaF and FeSO₄. The average voltage of NaFeSO₄F cathode is calculated to be 3.08 V with respect to the Na anode, and that comes dominantly from valence changes as Fe²⁺/Fe³⁺ in NaFeSO₄F/FeSO₄F. X-ray absorption spectra (XAS) near *K*-edges at Fe, Na, and F are calculated for NaFeSO₄F and FeSO₄F as the cathodes in fully-discharged and fully-charged states, respectively, and also for NaF and FeSO₄ as possible residual materials in real cathodes (Fig. 1). The results show that XAS near *K*-edges, especially at F as well as Fe, provides us useful information to clarify battery reactions and structures in the cathodes.

O-redox and O₂-release reactions in Li-excess cation-disordered rock-salt oxides Li_{2+2x}Mn_{1-x}Ti_{1-x}O₄

The cation-disordered rock-salt oxides Li_{2+2x}Mn_{1-x}Ti_{1-x}O₄ with the Li-excess

amount x are one of promising Li-ion battery cathodes. We study the cathode properties of the Li_{2+2x}Mn_{1-x}Ti_{1-x}O₄ models (Fig. 2) with x ranging from 0 to 0.3 by the first-principles calculations, considering cation and anion redox reactions with O₂-releases [3]. Effects of x on voltage-capacity curves and electronic structures are studied, and the results show that Mn-redox reactions predominate in early charging processes. As charging reactions further proceed, O-redox reactions contribute to the cathode reactions more significantly for higher x . From the formation energy analyses, it is found that O atoms tend to be released from the cathodes especially in late charging processes with a trend of easier O₂-release for higher x , possibly accounting for lower experimental capacities than the theoretical values.

Na-ion battery performance and reaction mechanism of SnS anode

We study the Na-ion battery performance of SnS as an anode material by the first-principles calculations [4, 5]. From formation energy analyses, the discharge reaction processes of the Na/SnS half-cell system are clarified. We calculate the phase diagram of Na–Sn–S ternary systems by constructing convex-hull curves of Na–Sn–S, and show a possible reaction path considering intermediate products in discharge reactions. Voltage-capacity curves are calculated based on the Na–SnS reaction path that is obtained from the ternary phase diagram. It is found that the conver-

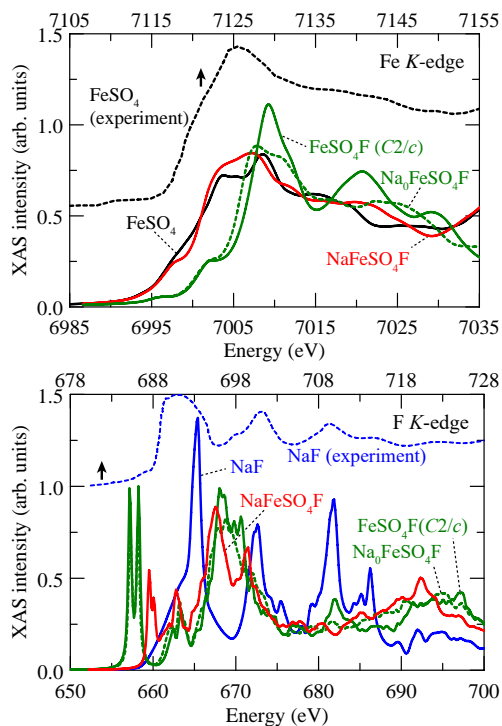


Figure 1: Calculated x-ray absorption spectra (XAS) near Fe and F *K*-edges of NaFeSO₄F materials [1]. Experimental XAS is also plotted with the upper energy scale.

sion reactions and subsequently the alloying reactions proceed in the SnS electrode, contributing to its high capacity compared with the metallic Sn electrode, in which only the alloying reactions progresses stepwise. To confirm the calculated reaction process, x-ray absorption spectra (XAS) are calculated for Na₂S and SnS in discharged and charged states, respectively.

Conversion-type reaction mechanism of FeF₃ cathodes for Li-ion batteries

The perovskite-type FeF₃ is one of promising cathodes for Li-ion batteries because of its high capacity, but reaction mechanism has not been clarified yet. In this work, we study discharge reaction processes by calculating formation energies of Li–Fe–F materials. We theoretically find that the discharge reaction proceeds as $\text{FeF}_3 + 3\text{Li} \rightarrow \text{Li}_{0.5}\text{FeF}_3 + 2.5\text{Li} \rightarrow \text{FeF}_2 + \text{LiF} + 2\text{Li} \rightarrow \text{Fe} + 3\text{LiF}$, showing

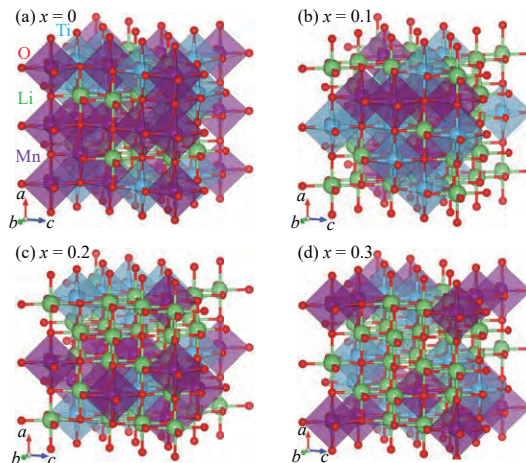


Figure 2: Calculated model structures of Li_{2+2x}Mn_{1-x}Ti_{1-x}O₄ [$x =$ (a) 0, (b) 0.1, (c) 0.2, and (d) 0.3] with the cation-disordered rock-salt structures [3].

the insertion and the conversion reactions at early and late discharging processes, respectively. Based on the estimated reaction formula, voltage-capacity curve is calculated, and the result well accounts for the experimentally observed two-plateau behavior.

References

- [1] H. Momida, A. Kitajou, S. Okada and T. Oguchi: J. Phys. Soc. Jpn. **88** (2019) 124709/1-6.
- [2] A. Kitajou, H. Momida, T. Yamashita, T. Oguchi and S. Okada: ACS Appl. Energy Mater. **2** (2019) 5968-5974.
- [3] M. Hamaguchi, H. Momida and T. Oguchi: Electrochim. Acta **330** (2020) 135286/1-8.
- [4] H. Kotaka, H. Momida, A. Kitajou, S. Okada and T. Oguchi: Chem. Rec. **19** (2019) 811-816.
- [5] H. Kotaka, H. Momida, A. Kitajou, S. Okada and T. Oguchi: J. Comput. Chem. Jpn. **18** (2019) 78-83.

First-principles study of quantum transport in nanostructures

NOBUHIKO KOBAYASHI

*Department of Applied Physics, University of Tsukuba
1-1-1 Tennodai Tsukuba Ibaraki 305-8573*

1 Introduction

An understanding of the electron transport properties of materials has resulted in the emergence of an important and versatile problem, not only for the fundamental research of science but also for the applications of electronics. Quantum nature is essential in nanoscale systems, and atomistic analysis based on detailed electronic states calculations are indispensable to discuss the transport property. In order to investigate transport properties, we have developed the nonequilibrium Green's function (NEGF) method, and the $O(N)$ time dependent wave-packet diffusion (TD-WPD) method on the basis of the density functional theory (DFT). Using these methods, we have investigated charge, head and spin transport properties of materials. [1, 2]

2 $O(N)$ method for transport calculations

Organic semiconductors have attracted much attention for their applications to flexible, printable, lightweight, and low-cost electronic devices. They are crystals that are assemblies of π -conjugated molecules weakly bonded by van der Waals interactions, and single crystallization has been achieved, enhancing the mobility. It is expected that the mechanism of carrier transport in organic semiconductors can be elucidated and that materials exhibiting high mobility can be developed by novel molecular synthesis.[3]

We developed the $O(N)$ TD-WPD method for the quantum transport calculation of huge systems of up to 100 million atoms a decade ago. We calculated the conductance and the

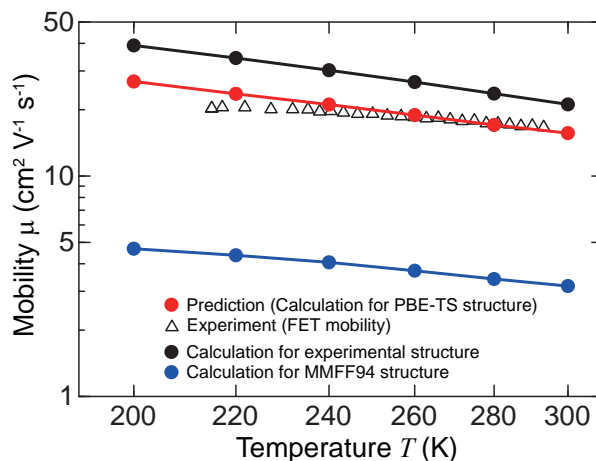


Figure 1: Temperature dependence of mobility along the column direction in a C10-DNBDT single crystal. For comparison, the experimental values of FET mobilities are also shown as triangles.

mobility of the system with micron-order lengths at room temperature at the atomistic levels. Using this method we can study the transport properties from diffusive to ballistic regimes including the effect of realistic electron-phonon scattering, and determine the mean free path and relaxation time from an atomistic viewpoint. We performed DFT calculations of electronic structures and interactions between molecules of single-crystal organic semiconductors including the effect of the van der Waals interaction, and applied the TD-WPD method to the analysis of transport properties of the organic semiconductors.

Using TD-WPD method, we have proposed a prediction methodology to obtain charge transport properties of organic single crystals from their structural formula. Pre-

diction of material properties of newly designed molecules is a long-term goal in organic electronics. As a demonstration, we employ the promising molecule C10-DNBDT. We succeeded in quantitative evaluation of charge mobility of the single crystal using our quantum wave-packet dynamical simulation method. Here, the single-crystal data is computationally obtained by searching possible packing structures from structural formula of the molecule. The proposed methodology can be a theoretical design technique for efficiently developing new high-performance organic semiconductors, since it can estimate the charge transport properties at early stage in the process of material development.[4]

3 NEGF-DFT method

We have developed a Simulation code for Atomistic Kohn-sham Equation (SAKE) for the ab-initio electron transport calculation based on the DFT and NEGF formalism.[5] We have applied the method to analyses of thermoelectricity of magnetic semiconductors.

Thermoelectric materials have attracted considerable attention from viewpoints not only of materials science but also of applications for energy harvesting by waste heat, and intensive works have been devoted to enhance conversion efficiency from thermal energy into electricity. The efficiency is expressed as a function of the figure of merit $ZT = \sigma S^2 T / \kappa$, where σ, S, κ and T are the electrical conductivity, the Seebeck coefficient, the thermal conductivity and the temperature, respectively, and the thermoelectric power factor is written as σS^2 . Enhancement of thermoelectric efficiency is not an easy task since the Seebeck coefficient, the electrical conductivity, and the thermal conductivity are not independent of each other. There is the trade-off between σ and S , and materials with high electric conductivity tend to have high thermal conductivity.

We analyze the thermoelectric properties of a magnetic semiconductor using SAKE program. The electronic transport properties, Seebeck coefficient, and the figures of merit are estimated for doped systems and thin films. We theoretically demonstrate the en-

hancement in the figure of merit by doping, which is in agreement with experimental work, and show further enhancement by the optimized doping. Furthermore, electronic structures of thin films are examined. It is shown that calculated electrical conductances reach to twice larger than that in the bulk, and the calculated Seebeck coefficients in thin films are suppressed by the metallicity, remain maximally to about a half of the results in the bulk.[6]

References

- [1] N. Kobayashi, H. Ishii, K. Hirose, *Jpn. J. Appl. Phys.* 57, 08NA01 (2018).
- [2] N. Kobayashi, H. Ishii, K. Hirose, in *3D Local Structure and Functionality Design of Materials* eds H. Daimon, Y. C. Sasaki (World Scientific, 2018) p133.
- [3] A. Yamamura, H. Fujii, H. Ogasawara, D. Nordlund, O. Takahashi, Y. Kishi, H. Ishii, N. Kobayashi, N. Niitsu, B. Blulle, T. Okamoto, Y. Wakabayashi, S. Watanabe, and J. Takeya, *Commun. Phys.* 3 20 (2020)
- [4] H. Ishii, S. Obata, N. Niitsu, S. Watanabe, H. Goto, K. Hirose, N. Kobayashi, T. Okamoto, and J. Takeya, *Sci. Rep.* 10, 2524 (2020)
- [5] H. Takaki, N. Kobayashi, K. Hirose, *J. Phys. Cond. Matter.* (2020) in press.
- [6] H. Takaki, K. Kobayashi, M. Shimono, N. Kobayashi, K. Hirose, N. Tsujii, T. Mori, *Jpn. J. Appl. Phys.* 58 SIIB01 (2019).

Prediction of properties of organic ferroelectrics and piezoelectrics by first-principles calculation

Shoji ISHIBASHI

*Research Center for Computational Design of Advanced Functional Materials (CD-FMat),
National Institute of Advanced Industrial Science and Technology (AIST)
Tsukuba, Ibaraki 305-8565*

Organic charge transfer complexes show a variety of crystal structures and electronic properties. Among them, there is a class of compounds called “mixed-stack compounds”, in which electron-donor and electron-acceptor molecules stack alternatively along a certain direction. Some of them show ferroelectricity. Tetrathiafulvalene-p-chloranil (TTF-CA) is a typical example. Kobayashi et al. successfully measured spontaneous polarization in TTF-CA and obtained a value of $6.3 \mu\text{C cm}^{-2}$ [1]. Furthermore, they found that the polarization value is more than 20 times larger than that of the point charge model, and their directions are opposite. To clarify the origin of this exotic ferroelectricity in TTF-CA, we made theoretical analyses in terms of Born effective charges as well as maximally-localized Wannier orbitals [2, 3]. We have shown that only 2 bands below the band gap are responsible for the emergence of polarization and also that the electron flow from cell to cell on these electronic states is the origin of the exotic polarization in TTF-CA.

Recently, Mezzadri et al. reported the structure of the low-temperature phase of 3,3',5,5'-tetramethylbenzidine-tetracyanoquinodimethane (TMB-TCNQ) and pointed out that this phase is potentially ferroelectric [4]. Similarly to the TTF-CA case, TMB and TCNQ molecules stack alternately and form one-dimensional columns. We have applied the above-mentioned computational methods to investigate the

ferroelectricity in TMB-TCNQ and found similarities and dissimilarities with TTF-CA [5].

In addition, theoretical calculations to obtain spontaneous-polarization vectors for organic ferroelectrics D22bpy-Dia and D55dmbp-Dia have been performed. The obtained results explain the experimentally-observed values well [6].

References

- [1] K. Kobayashi, S. Horiuchi, R. Kumai, F. Kagawa, Y. Murakami, and Y. Tokura: *Phys. Rev. Lett.* **108** (2012) 237601.
- [2] S. Ishibashi and K. Terakura: *J. Phys. Soc. Jpn.* **83** (2014) 073702.
- [3] K. Terakura and S. Ishibashi: *Phys. Rev. B* **91** (2015) 195120.
- [4] F. Mezzadri, N. Castagnetti, M. Masino, and A. Girlando: *Cryst. Growth Des.* **18** (2018) 5592.
- [5] S. Ishibashi, S. Horiuchi, and K. Terakura: unpublished.
- [6] S. Horiuchi, S. Ishibashi, K. Kobayashi, and R. Kumai: *RSC Adv.* **9** (2019) 39662.

Analysis of metal/oxide interfaces with large mismatches

Hongping LI¹, Mitsuhiro SAITO², Chunlin CHEN¹, Kazutoshi INOUE¹, Kazuto AKAGI¹,
and Yuichi IKUHARA^{1,2,*}

¹ *Advanced Institute for Materials Research, Tohoku University, Sendai, Miyagi, 980-8577*

² *Institute of Engineering Innovation, The University of Tokyo, Yayoi, Tokyo, 113-8656*

Metal/oxide heterointerfaces are widely used in engineering, and their microstructures govern the macroscopic properties. We investigated the interaction and bonding reconstruction at Pd/ZnO {0001} interfaces with large mismatches by density functional theory calculations combined with atomic-resolution scanning transmission electron microscopy. It has been believed that the interfacial interactions are very weak at incoherent interfaces with large mismatches, and metal-oxide interfaces can be more favorable than metal-metal interfaces.

To gain insight into the local atomic structures of each interface, first-principles calculations were performed using the Vienna ab initio Simulation Package (VASP). The electronic wave functions were expanded by plane waves up to a kinetic energy cutoff of 400eV. The generalized gradient approximation in the form of the Perdew-Burke-Ernzerhof exchange-correlation functional was implemented in our calculations. A supercell containing seven Pd lattices matching six ZnO lattices along the interfaces was constructed to compensate the mismatch which agree with the experimental result. The surface atoms of the ZnO slabs were passivated by H atoms to eliminate the effects of dangling bonds, and a 15Å vacuum area was embedded into the outer Pd surfaces to avoid unwanted interactions. For k -point sampling, a $1 \times 1 \times 1$ Monkhorst-Pack grid was applied in the irreducible Brillouin zone for the supercell calculations. Convergence with a $2 \times 2 \times 1$ Monkhorst-Pack mesh was also tested for both interfaces, and the differences in the total energy and atomic configura-

tions could be neglected. The convergence threshold for self-consistent iteration was set at 1.0×10^{-4} eV/atom, and the atomic positions were fully relaxed until the maximal force on each atom was less than 0.05eV/Å. To analyze the interfacial stability of the epitaxial systems, the adhesive energy was calculated by $E_{ad} = [E_{Pd-slab} + E_{ZnO-slab} - E_{total}]/A$, where E_{total} , $E_{Pd-slab}$, and $E_{ZnO-slab}$ are the interfacial total energy and the energies of individual Pd and ZnO slabs, respectively, and A is the interfacial area. Then, we get $E_{ad} = 2.66\text{J/m}^2$ and 3.52J/m^2 for the Zn-terminated Pd (111)/ZnO (0001) and (000 $\bar{1}$) interface, respectively, implying that the nonstoichiometric Zn-terminated Pd (111)/ZnO (000 $\bar{1}$) interface is energetically favorable. The interfacial atoms were located almost at bulk lattice points for the stoichiometric Zn-terminated Pd(111)/ZnO(0001) interface while the interfacial Pd and Zn atoms underwent relatively large relaxations at the nonstoichiometric Zn-terminated Pd(111)/ZnO(000 $\bar{1}$) interface, making the interface relaxed to release the large interfacial mismatch. The Pd-Zn bonds exhibited site-dependent characteristics and gradually transitioned from covalent to ionic at the Pd(111)/ZnO(0001) interface, whereas most of Pd-Zn bonds exhibited strong covalent behavior at the Pd/ZnO(000 $\bar{1}$) interface [1].

References

- [1] H. Li, M. Saito, C. Chen, K. Inoue, K. Akagi, Y. Ikuhara: *Acta Mater.* **179** (2019) 237-246.

Firefly Oxyluciferin Anions in Aqueous Solutions

Yoshifumi NOGUCHI

Department of Applied Chemistry and Biochemical Engineering, Graduate School of Engineering, Shizuoka University, Johoku 3-5-1, Hamamatsu, Shizuoka 432-8561, Japan

Oxyluciferin anion, known as a light emitter in the firefly bioluminescence process, is a key molecule in understanding the mechanism of the firefly bioluminescence process. Although significant effort has been taken in various studies targeting the oxyluciferin anion, most of its properties still remain unclear. This is because, from the perspective of simulations, the environmental conditions surrounding the oxyluciferin anion are too complicated. In addition, the oxyluciferin anion is too sensitive for the environments.

In this study, we applied the first-principles Born-Oppenheimer molecular dynamics simulations (BOMD) to three possible isomers of the oxyluciferin anion (see Fig. 1) surrounded by 64 water molecules, and simulated the photoabsorption spectra for 1000 randomly selected molecular geometries from the trajectory [1].

The simulated spectra are in a good agreement with the experiments. The remaining error is less than 0.1 eV in comparison with the peak top positions. Our full QM simulations

indicated a charge leakage from the oxyluciferin anion to the surrounding water molecules. In addition, we discussed the validity of a modeled aqueous solution, such as QM/MM or PCM methods, in which the charge transfer between solute and solvent is restricted. In order to describe the charge leakage from the oxyluciferin anion and reproduce our full QM results, at least 10 water molecules should be included into QM region.

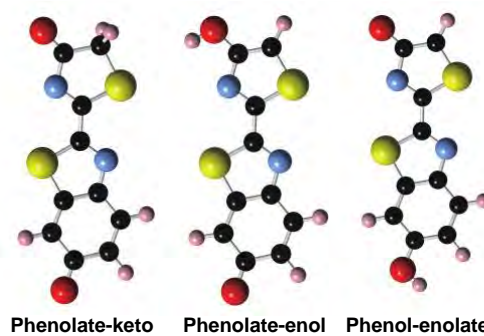


Fig. 1. Three possible isomers of the oxyluciferin anion.

References

- [1] Y. Noguchi, M. Hiyama, M. Shiga, H. Akiyama, and O. Sugino: *J. Chem. Theory Compt.*, **15** (2019) 5474.

First-principles investigation on electronic structure modulation via coherent phonon excitation

Yasushi SHINOHARA^{1,2}

¹*Photon Science Center,*

The University of Tokyo, Hongo, Bunkyo-ku, Tokyo 113-8656

²*Department of Nuclear Engineering and Management,*

The University of Tokyo, Hongo, Bunkyo-ku, Tokyo 113-8656

Recent progress of coherent light source technology allows us to observe quantum dynamics in time-domain (TD) driven by intense and short laser pulses [1,2], rather than frequency-domain (FD) observation such as the standard spectroscopies. The TD information usually contains more than complementary information of FD data because of phase information, namely time-origin is clearly introduced by the pulse. Very recently, more extreme and flexible pulse shaping is available such that two-color mixing pulse composing infrared (IR) and ultraviolet (UV) photon energies. We have investigated coherent phonon excitation encoded in temporal modulation in angle-resolved photoemission spectra (ARPES) by using IR pump and UV probe pulses.

We observe TD-ARPES of Ta₂NiSe₅, a candidate of the excitonic insulators, pumped by 1.55 eV pulse. In the time-dependent E-k spectral distribution $S(E, k; t)$, oscillatory behaviors appear. The frequencies of the oscillation well coincide with the optical phonon frequencies belonging to Ag irreducible

representation, all-symmetric, modes. These results invoke that electronic structure modulation due to the optical phonon, excited as coherent phonon via the IR pump pulse. Each part of the energy-dispersion has a different coupling with the phonon modes. By extracting a frequency structure $|S(E, k; \omega = \omega_{\text{phonon}})|$, much finer information of electron-phonon interaction than Raman spectra is expected to be extracted. To prove this scenario, we perform an *ab-initio* simulation that band structure modulation due to the optical phonon modes within the density-functional theory (DFT) framework within the abinit code.

Firstly, we optimize the atomic position of the Ta₂NiSe₅ crystal with two functionals, Perdew-Wang local density approximation (PW-LDA), and Perdew-Burke-Ernzerhof generalized gradient approximation (PBE-GGA). Secondly, we obtain normal modes of the lattice vibration at Γ -point via density-functional perturbation theory (DFPT) with each functional. By performing symmetry operations of the crystal, we assign irreducible representation to

the modes. We only pick up Ag irreducible representation because this mode is only excited as the coherent phonon based on displacive excitation of coherent phonon mechanism. The DFPT computation demands the heaviest computational resource. Our crystal is a semimetal with PW-LDA and PBE-GGA functional. To capture small Fermi surface, we need fine Brillouin zone sampling that has 864 k -points. The existence of Ta requires rather high energy cutoff, 50 eV, for the plane wave. The calculation takes 11 hours with 64 nodes, 1536 cores in the system B. Finally, we evaluate band dispersion with distorted atomic positions along with the normal modes obtained by DFPT. To compare with the experimental spectra, we construct similar spectral information as differences of k -resolved density-of-state (k -DoS) between the optimized atomic position and the distorted ones. The comparison between experimental and theoretical data shows an agreement that a symmetry breaking mode, having 2 THz frequency, shows the most

prominent change around Fermi-level of the spectra [3]. This mode has been argued as the driving mode of insulator-metal (IM) transition via photoexcitation. Our investigation posts an additional clue to understand the mechanism of the IM transition.

References

- [1] F. Krausz and M. Ivanov, *Rev. Mod. Phys.* **81** (2009) 163.
- [2] Stanislav Yu. Kruchinin, Ferenc Krausz, and Vladislav S. Yakovlev, *Rev. Mod. Phys.* **90** (2018) 021002.
- [3] Takeshi Suzuki, Yasushi Shinohara, Yangfan Lu, Mari Watanabe, Jiadi Xu, Kenichi L. Ishikawa, Hide Takagi, Minoru Nohara, Naoyuki Katayama, Hiroshi Sawa, Masami Fujisawa, Teruto Kanai, Jiro Itatani, Takashi Mizokawa, Shik Shin, Kozo Okazaki, submitted, arXiv: 2002.10037.

first-principles calculation of exchange coupling constants and investigation of interface magnetism for various phases and their interfaces of permanent magnets

Asako TERASAWA

*Department of Materials Science and Engineering, Tokyo Institute of Technology
J1-3, Nagatsuta-cho 4259, Midori-ku, Yokohama 226-8502, Japan*

Improvement of Nd-Fe-B magnets without heavy rare earth elements is one of the topics of increasing importance in the applied physics and materials science. The key for high-coercivity Nd-Fe-B magnets lies in the Nd-rich grain boundary (GB) phases [1]. However, the details of structural and magnetic properties of those GB phases are not clarified yet. Some experiments revealed the relationship between the crystallinity of GB phases and the relative angles between the interfaces and the c-plane of neighboring grains [2], which indicates the complexity of the physics in grain boundary phases in Nd-Fe-B magnets. Particularly, we targeted the exchange couplings inside and between the various phases for a computational study of magnetism in Nd-based permanent magnets.

For this purpose, we developed “jx”, a post-process program for OpenMX [3] to calculate exchange coupling constants between atoms based on the Liechtenstein formula [4]. The details of the implementation is explained in the published paper of [5]. During the development of jx, we found a remarkable problem about the combination of the Liechtenstein method and the linear combination of atomic orbitals (LCAO) approximation. When adopting diagonal elements of non-orthogonal (NO) Hamiltonian as effective single-site potentials, the calculated exchange coupling constants do

not converge as increasing the number of basis. Figure 1(a) shows the exchange coupling constants J_{ij} as functions of atomic distance r_{ij} for different choice of basis sets. Here, the notation *sxpydzfw* means that the basis set is constructed from x types of s orbitals, y types of p orbitals, z types of d orbitals, and w types of f orbitals. It is possible to see in Fig. 1 that the J_{ij} profiles are similar for s2p2d1, s2p2d2, and s3p2d2 with fluctuations of about a few meV, whereas the J_{ij} profiles deviate strongly to negative values for the larger basis sets.

To solve this problem, we introduced a new scheme to orthogonalize the atomic orbitals, namely the single-site orthogonalization (SO) scheme. In the SO scheme, we derive a basis set $\{|i\rangle_i\}$ to orthogonalize only i -th element from the original non-orthogonal orbitals $\{|i\rangle\}$. The single-site orthogonalized basis set is defined by the following equations:

$$|i\rangle_i \equiv |i\rangle - \sum_{j \in \bar{i}} |j\rangle [\mathbf{S}_{i,\bar{i}}^{-1} \mathbf{S}_{i,i}]_{ji} \quad (1)$$

$$|j\rangle_i \equiv |j\rangle, \quad j \neq i \quad (2)$$

with the definitions of the neighbor set \bar{i} for site i as

$$\bar{i} \equiv \{j | j \neq i, \langle i|j\rangle \neq 0\}. \quad (3)$$

We found that the J_{ij} profiles calculated with the SO scheme exhibit a convergent behavior as increasing the number of bases, while they

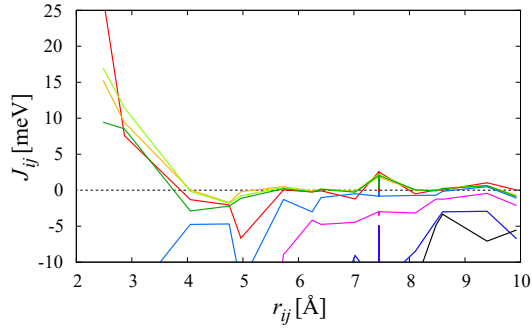
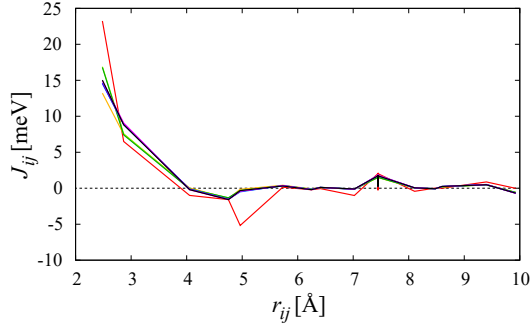
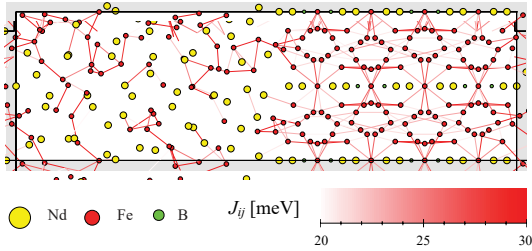
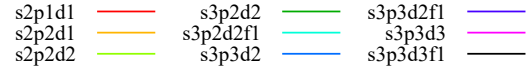
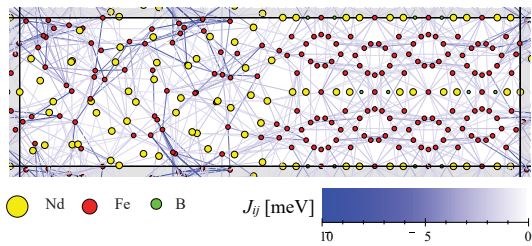
(a) J_{ij} of bcc Fe by SO scheme(b) J_{ij} of bcc Fe by SOS scheme(c) large positive J_{ij} in the ab interface model(d) negative J_{ij} in the ab interface model

Figure 1: Calculated exchange coupling constants J_{ij} of various systems. (a) J_{ij} of bcc Fe as functions of atomic distance r_{ij} for different choices of basis sets when adopting diagonal elements of NO Hamiltonian as effective single-site potentials and (b) when adopting diagonal elements of SO Hamiltonian as effective single-site potentials and applying the spin population scaling to the SO results. (c) and (d) J_{ij} in the ab interface model of Nd-Fe-B permanent magnet.

decreases slightly depending on the basis size. The slight decreases in SO results are well collected by introducing spin population scaling, namely single-site orthogonalization with spin population scaling (SOS) scheme:

$$J_{ij}^{(\text{SOS})} \equiv \frac{\Delta n_i}{\Delta n_j^{(\text{SO})}} \frac{\Delta n_j}{\Delta n_i^{(\text{SO})}} J_{ij}^{(\text{SO})}. \quad (4)$$

where $J_{ij}^{(\text{SO})}$ is the exchange coupling constant derived by the SO scheme, $\Delta n_i^{(\text{SO})}$ and $\Delta n_j^{(\text{SO})}$ are the spin population at site i calculated using the NO basis and SO basis, respectively. Figure 1 (b) shows the exchange coupling constants as functions of atomic distances calculated with the SOS scheme. We can see a remarkable convergence as increasing the number of bases in Fig. 1(b).

We also applied the newly developed scheme to larger scale systems. Figures 1(c) and 1(d) show the calculated exchange coupling constants of the model of ab interface, where the amorphous Nd-Fe phase of a few nm are attached to the main phase in ab axis direction. It can be seen in Figs. 1(c) and (d) that the exchange coupling constants behave differently in the main phase and in the amorphous Nd-Fe phase.

We are now preparing the submission of the above results to refereed papers, and modified patch of jx including the SOS scheme for future release of OpenMX.

References

- [1] K. Hono *et al.*, *Scripta Mater.* **67**, 530 – 535 (2012).
- [2] T. T. Sasaki *et al.*, *Acta Mater.* **115**, 269 (2016).
- [3] T. Ozaki, *Phys. Rev. B* **67**, 155108 (2003).
- [4] A. I. Liechtenstein *et al.*, *J. Magn. Magn. Mater.* **67**, 65–74 (1987).
- [5] A. Terasawa, M. Matsumoto, T. Ozaki, and Y. Gohda, *J. Phys. Soc. Jpn.* **88** 114706 (2019).

Machine-learning-driven molecular simulations for grain-boundary atomic dynamics

Tatsuya YOKOI

Department of Materials Physics,

Nagoya University, Furo-cho, Chikusa-ku, Nagoya, Aichi, 464-8603

Grain boundaries (GBs), crystalline interfaces between misoriented grains, often govern material properties in polycrystals, in spite the fact that changes in atomic arrangement and chemical composition occur within few nanometers from GBs. Experiments with bicrystals and theoretical calculations have reported that not only atomic arrangements but also local properties arising from atomic dynamics significantly vary with each GB. Such properties includes thermodynamic stability, diffusivity and thermal conductivity. A better understanding of the connection between GB structures and their atomic dynamics is thus essential for designing polycrystals with desired properties and functionalities.

In order to reveal their connection, density-functional-theory (DFT) calculations have been often employed. However, DFF calculations are computational demanding as the number of atoms in a computational cell increases, since their computational time typically grows with $O(N^3)$ or $O(M \ln N)$. Due to this drawback, most DFT studies have investigated only GBs with simple atomic arrangements, such as symmetric tilt GBs with low Σ values. Still less is known

about general or random GBs, which generally require a large number of atoms for their computational cells, in the atomic level.

In order to predict atomic structure and energetics of GBs while maintaining high accuracy and low computational cost, we constructed artificial-neural-network (ANN) interatomic potentials trained with DFT-calculation data, Furthermore, we integrated the ANN potentials into molecular simulation algorithms, with the goal of predicting local diffusional and lattice vibrational properties at GBs. Here, oxide systems and semiconductor compounds were chosen.

The architecture of ANN potentials was based on the previous studies by Behler [1]; the feed-forward network was employed. Atomic environments were encoded using two- and three-body symmetry functions [1]. Their cutoff radii were set to 5 and 7 Å for oxides and compound semiconductors, respectively.

Training datasets were generated by accounting for various atomic environments to increase the generalizability of ANN potentials. Here the training datasets contained not only single-crystal structures but also lattice defects:

point defects, surfaces and grain boundaries. DFT total energies and atomic forces were used to train ANN potentials. DFT calculations were performed using the VASP code [2].

Figure 1 and 2 show the error of total energies and atomic forces with respect to the reference DFT data in the training dataset for Al_2O_3 and PbTe, respectively. A data point distributed near the black dashed line indicates that the ANN potential accurately learns the training data without large error. These figures show that all the data points are distributed near the diagonal line, without large deviation, for both total energies and atomic forces. Thus the ANN potentials accurately learn the reference DFT results even for GBs.

The trained ANN potentials were then integrated into a structural optimization algorithm and molecular dynamics (MD) simulations to predict energetically favorable atomic arrangements at GBs not included in the training dataset. Figure 3 shows an example of Al_2O_3 GBs. The obtained structure was in agreement with an experimental observation and a theoretical calculation in the literature [3], demonstrating excellent predictive ability of our ANN potential even for GBs.

Finally we examined computational time of ANN-MD simulations. The computational time was found to linearly increase with the number of atoms. Ultimately, MD simulations with 10^4 steps was finished in an hour even for GB structures with several thousands of atoms.

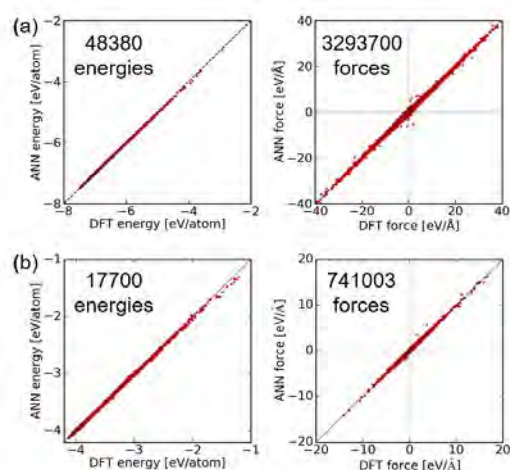


Fig. 1 Error of total energies and atomic forces with respect to the reference DFT data for (a) Al_2O_3 and (b) PbTe.

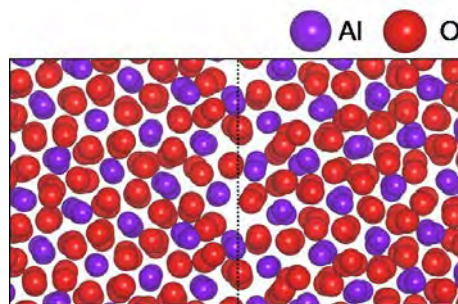


Fig. 2 GB structure obtained from molecular simulations with the trained ANN potential for Al_2O_3 .

References

- [1] J. Behler, *Int. J. Quantum Chem.* **115** (2015) 1032.
- [2] G. Kresse and J. Hafner, *Phys. Rev. B* **47** (1993) 558.
- [3] H. Nishimura, K. Matsunaga, T. Saito, T. Yamamoto, and Y. Ikuhara, *J. Am. Ceram. Soc.* **86** (2003) 574.
- [4] H. Guhl, H.-S. Lee, P. Tangney, W.M.C. Foulkes, A.H. Heuer, T. Nakagawa, Y. Ikuhara, M.W. Finnis, *Acta Mater.* **99** (2015) 16.

First-principles study on controlling of electronic structures and electron-transport properties of low-dimensional materials

Yoshiyuki EGAMI

*Division of Applied Physics, Faculty of Engineering, Hokkaido University
Kita 13, Nishi 8, Kita-ku, Sapporo, Hokkaido 060-8628*

Recently, there has been a lot of energetic research and development of devices using low-dimensional materials. In the first-principles investigations, to estimate electron-transport properties of the nanoscale materials suspended between semi-infinite electrodes, self-energy matrices of the electrodes are required. The computational cost for obtaining the self-energy matrix is proportional to the cube of the lateral length of the electrode which is a direction perpendicular to the transport direction. Therefore, the computational cost increases dramatically as the system size increases.

In this subject, the method to calculate the self-energy matrices without any approximations and accuracy deteriorating is proposed. [1] In most cases, the electrode has a supercell structure in which a primitive unit cell is repeated in the lateral direction. Exploiting the repetition, the proposed method calculates the self-energy matrices of a large electrode by extending the self-energy matrices of the primitive unit cell using the singular-value decomposition. This makes it possible to greatly reduce the computational costs because calculating the inverse of a large matrix (for the supercell structure), which is the most computationally expensive, can be replaced by that of the small matrix (for the primitive unit cell). Furthermore, by comparing the self-energy matrix directly obtained from the large-sized electrode structure with that obtained using the

proposed method, it was confirmed that the self-energy matrices can be reproduced without deterioration in the accuracy.

For demonstration of the proposed method, the computational time in generating the self-energy terms for several supercell models is examined. For generating the self-energy terms, the computational time increases proportional to N^3 where N means the number of the total grid points in the supercell. In some cases, the computational efficiency exceeds the theoretical value (the square of the supercell size) because the order of the computational time for the recursive iteration to generate the self-energy terms is slightly larger than N^3 . On the other hand, the computational time for reproducing the self-energy terms is notably reduced by the proposed method, and this benefit becomes more remarkable as the supercell size increases. These works have been performed on System B and System C.

References

- [1] Y. Egami, S. Tsukamoto and T. Ono: Phys. Rev. B **100**, 075413 (2019).

Elucidation of Reaction Mechanism of d-sorbitol Dehydration in High Temperature Water with Metadynamics

Tomomi Kondo^{1,2}, Chang Yong Lik¹, Takehiko Sasaki¹, Motoyuki Shiga²

¹ Department of Complexity Science and Engineering, Graduate School of Frontier Sciences,
The University of Tokyo, Kashiwa-no-ha, Kashiwa, Chiba 277-8561

² Center for Computational Science and E-Systems, Japan Atomic Energy Agency
148-4 Kashiwanoha Campus, 178-4 Wakashiba, Kashiwa, Chiba, 277-0871

1 Introduction

Chemical reactions in high temperature pressurized water without organic solvent or poisonous materials such as metals are worthy of attention with respect to environmentally friendly chemistry, i.e., Green Chemistry. In this study metadynamics calculation was achieved to elucidate the reaction mechanism for the cyclodehydration of sorbitol (SBT) [1] (Fig. 1) in high temperature water (HTW). Reaction pathways were searched on the free energy surface (FES) and the activation barriers were compared with the experimental values.

2 Method

In Metadynamics (MTD) simulations chemical reactions that do not happen in a regular time scale of molecular dynamics simulations are induced by adding a bias potential proportional to the appearance frequency on the FES defined with collective variables (CV). Bias potential at time t is expressed by a Gaussian function (equation (1)) with height h and width w_i , where $\mathbf{w}^{-1} = \{1/w_i\}$. Bias potential is the history-dependent term given by the sum of Gaussian functions (hills) deposited along the path followed by the fictitious particle (s_k) on the FES until time t . Sampling is effectively achieved by summing over N fictitious particles (walkers) which are allowed to move simultaneously on the FES. The point corresponding to the maximum accumulated potential and the point at the onset of the reaction correspond to the minimum point and the saddle point on the FES, respectively.

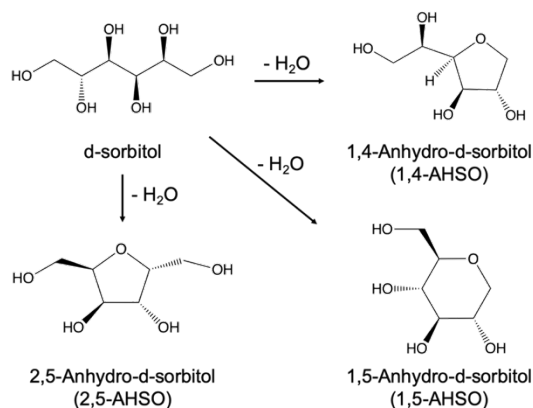


Fig. 1. The dehydration reaction of d-sorbitol (SBT).

$$V_{\text{hills}}(t, \mathbf{s}) = \sum_{\tau < t} \sum_{k=1}^N h \exp \left[-\frac{(s_k(t) - s_k(\tau)) \cdot \mathbf{w}^{-1}}{2} \right] \quad (1)$$

We used PIMD [2] to achieve MTD simulations associated with the Density Functional based Tight Binding (DFTB) method

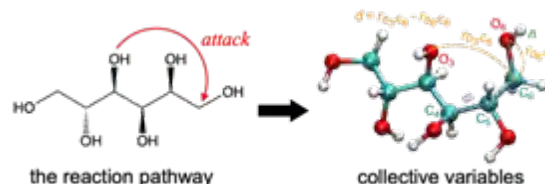


Fig. 2. The reaction pathway and the collective variables (1,4-AHSO6).

using DFTB⁺ [3]. The present system contains one molecule of SBT, 30 molecules of H₂O, one proton and one Cl⁻ anion. The other system containing H₂CO₃ instead of H⁺ and Cl⁻ was also examined. The thermodynamic condition at 573 K and 20 MPa was the same as the experimental results [1]. Fig. 1 shows structures of SBT molecule and three products (1,4-AHSO, 2,5-AHSO and 1,5-AHSO) for the cyclodehydration of

SBT. Considering the reaction pathway of cyclodehydration, there are two pathways for each product. CV is chosen for each pathway [4]. For example, there are two reaction pathways (1,4-AHSO3 and 1,4-AHSO6) for 1,4-AHSO depending on the position of OH group and the carbon atom involved in the reaction. Fig. 2 illustrates the pathway 1,4-AHSO6 and the associated CV. Here, the oxygen atom O3 in OH group on the carbon atom C3 attacks the carbon atom C6. In order to describe this reaction pathway the dihedral angle ϕ ($O_6-C_6-C_5-C_4$) defined by the O_6-C_6 bond and the bond C_5-C_4 , the difference in the O-C bonds d ($= r_{O_3-C_6} - r_{O_6-C_6}$) between the O_3-C_6 bond and the O_6-C_6 bond, and the coordination number n of hydrogen atoms toward O_6 are selected as CV. The height of the Gaussian function was set as $h = 500$ K, and the step width of the variables are set as follows: $w_\phi = 10.0^\circ$, $w_d = 0.10$ Bohr, $w_n = 0.10$ and time step = 0.25 fs.

3 Results and Discussion

Over 3.6 ns of MTD simulations with DFTB along the pathway 1,4-AHSO6 the dehydration reaction was observed with the CV at $\phi = 155^\circ$, $d = 0.0$ and $n = 2.1$. Fig. 3 shows the calculated FES, where the shallow path was observed, leading to the transition state marked as the red arrow. With the Molecular Dynamics calculation started from this transition state as the initial state it was found that after the addition of proton to the oxygen atom (Fig. 4 ①) the dehydration (Fig. 4 ②) and the formation of a five-membered ring (C-O bond formation Fig. 4 ③) happened almost simultaneously. Hence, it is concluded that the hydroxyl group of SBT is protonated, the five-membered ring is formed via S_N2 mechanism, and finally the excess proton is released (Fig. 4 ④). This mechanism is the same as that for our previous study for the cyclodehydration of polyalcohol [4].

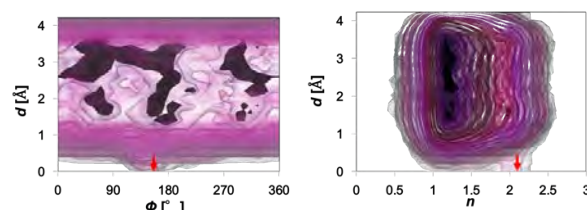


Fig. 3. The dehydration reaction of SBT to 1,4-AHSO6.

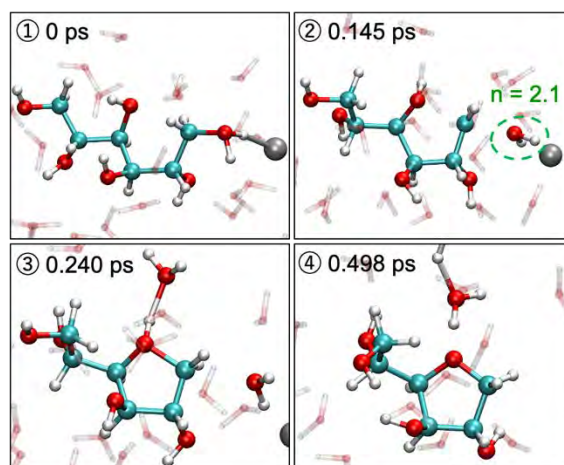


Fig. 4. The dehydration reaction of SBT to 1,4-AHSO6.

The activation energy with H^+ and Cl^- was lower than that with H_2CO_3 , indicating the activation energy has a negative correlation with acidity. However, relative relationship of calculated activation energies of products was not in agreement with the experimental results [1]. In order to overcome this problem, a method for smoothing FES was developed to decrease the sampling error and the calculation with this method is under way.

References

- [1] A. Yamaguchi *et al.* *Green Chem.*, **13**, 873 (2011).
- [2] <http://ccse.jaea.go.jp/ja/download/pimd/index.jp.html>.
- [3] <https://www.dftbplus.org>.
- [4] Y. L. Chang, *et al.*, *J. Phys Chem. B*, **23**, 1662 (2019).

Ab initio molecular dynamics study of stability of artificial retina molecule

Satoshi Ohmura

Research Center for Condensed Matter Physics / Department of Environmental and Civil Engineering

Hiroshima Institute of Technology, Hiroshima, Hiroshima 738-5193

By means of ab initio molecular-dynamics simulations, we have investigated the light absorption properties in a photoelectric dye (2-[2-[4-(dibutylamino)phenyl] ethenyl]-3-carboxymethylbenzothiazolium bromide) (retina molecule) coupled to polyethylene. We adopted the Time-Dependent Density-Functional Linear-Response Theory (TDDFRT), proposed and formulated by Casida, for calculating light-absorption spectrum. The absorption spectrum of retina molecule obtained by the simulation have a main peak at approximately 550, which is in agreement with the experimental result. Counterion substitution is considered one of the effective methods to improve the performance of retinal molecule. Figure 1 shows absorption spectra of the non-substituted retina molecule (counter ion = Br⁻) and substituted retina molecules (counter ion = F⁻, Cl⁻, I⁻). The absorption spectra of the substituted system also have the main and small peak, and the profile of spectrum of I-substituted system is almost the same as non-substituted system. On the other hand, for F⁻ and Cl⁻ substituted system, the profiles of the absorption

spectra are different from that of non-substituted system in a sense that there are small peaks at longer wavelength region. In addition to halogen atoms, we also substitute Br with [(CF₃SO₂)₂N]⁻ (TFSI) molecule, and investigated the stability and light-absorption properties. Our simulation found that substitution for TFSI molecule has the potential for increasing stability of the artificial retina. For absorption spectrum, the main peak is maintained, and no additional peak appears at longer wavelength region. Moreover, we have investigated effects of the water. Our simulation indicated that water stabilize the energy around the counter ion.

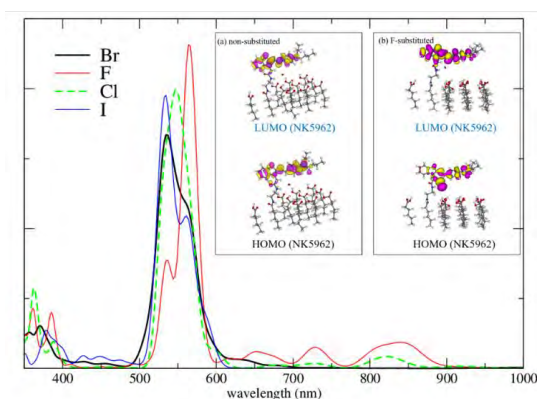


Fig1. Light-absorption spectra, inset shows spatial distribution of wavefunctions for HOMO and LUMO of non- and F-substituted system

Ab initio molecular dynamics study of structural properties and immiscibility of liquid Fe-Si-O mixtures under high pressure

Satoshi Ohmura

Research Center for Condensed Matter Physics / Department of Environmental and Civil Engineering

Hiroshima Institute of Technology, Hiroshima, Hiroshima 738-5193

Liquid iron is a major constituent of Earth's outer core, but the core density is approximately 10 % lower than that of pure iron. Therefore, light elements (LE) such as hydrogen, carbon, oxygen, silicon, and sulfur are expected to exist in the core. Under this circumstance, we have studied the effects of light element on the structural and transport properties of liquid iron mixtures by means of ab initio molecular-dynamics simulations. For Fe-LE binary systems, we clarified the structural properties and interactions between LE atoms at core-mantle boundary condition [1]. The C-C interactions are stronger than those of other light elements. The S-S interactions depend on the S concentration, in the sense that the shape of pair distribution functions for the S-S correlation change with increasing S concentration. In addition to the binary systems, we have investigated the structural properties of liquid Fe-Si-O ternary systems. From the radial distribution function obtained from our simulations, it is found that Si and O atoms shows "substitutional" and "interstitial" behavior even in liquid Fe-Si-O ternary system. The interaction between Si and O

atoms is stronger than those between other atoms, which means that a covalent like interactions exists between Si and O under outer core conditions. Moreover, our simulation found that liquid Fe-Si-O ternary systems shows immiscible tendency under outer core conditions. Figure 1 shows atomic configuration of liquid Fe-Si-O at about 140 GPa obtained from our simulation. As shown in figure 1, oxygen atoms confined to the narrow area (red area in Fig. 1).

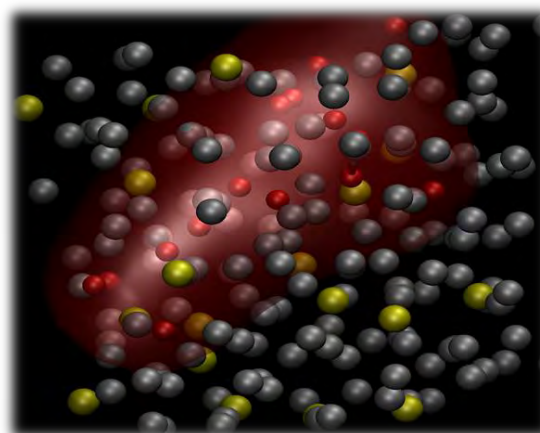


Fig1. Snapshot of the atomic configuration. Gray, yellow and red ball show Fe, Si and O atoms. Red area shows the area in which oxygen atoms exist.

References

- [1] S. Ohmura, T. Tsucniya and F. Shimojo: *Physica Status Solidi B*, accepted for publication

Construction of Neural Network Force Field for Molecular Dynamics Simulation in Multicomponent System

Kohei Shimamura

Department of Physics,

Kumamoto University, 2-39-1 Kurokami, Chuo-ku, Kumamoto 860-8555

In this study, we aimed to development of an interatomic potential using an artificial neural network (ANN) applicable to multicomponent systems such as life systems. This is one of the data-driven interatomic potential that takes advantage of ANN's universal function approximation, and automatically constructs a functional form that represents the input data through training. Since first-principles (FP) calculation data is mainly used for the training, molecular dynamics (MD) simulations with ANN potentials (ANN-MD) are expected to be accessible to large-scale systems or long-term calculations while maintaining FP accuracy. However, the current construction method may yield less robust ANN potentials, making long-term MD calculation difficult. Therefore, we first have investigated the factors affecting the robustness of ANN potential [1], where the ion-conducting phase of α -Ag₂Se is employed as an example system.

The most important factor was found in training data. Generally, it is difficult to prepare highly diverse FP data due to its large calculation cost. However, minority data can be physically very important. That is the FP data with the interatomic distance approaching.

Even if the interatomic distance approaches during ANN-MD simulation, the ANN potential does not learn such a state, thereby failing continuing the calculation. For long-term MD simulations, it was thus necessary to oversample such rare FP data and let ANN learn. (Actually, FP data for the relaxation process from the state where the atoms are close to each other is also needed.)

Next, we tried whether the key findings obtained through the ANN potential construction for α -Ag₂Se can be applied to the multicomponent systems. The amorphous glycine taken as an example is a system in which glycine molecules composed of four elements H, C, N, and O are irregularly aggregated, and proton transport occurs between the molecules. In the case of ANN potential without training rare FP data, the MD simulation cannot be continued for a few fs. When it is learned, at least ns order is possible. Although the glycine amorphous system is not a living system, we consider that this result is a great step forward.

Reference

[1] K. Shimamura, *et al.*: J. Chem. Phys. **151**, 124303 (2019).

Manipulation the cross-plane thermal conductivity of the 2D hetero-junction materials

Hu Shiqian

Department of Mechanical Engineering,

The University of Tokyo, Hongo, Bunkyo City, Tokyo 113-8654

We have studied the two-path phonon-interference resonance which induces a stop band in silicon crystal matrix by embedded nanoparticles array [1] and the coherent phonon transport in van der Waals graphene-MoS₂ hetero-structure, using the massive parallel computer simulations.

Massive efforts have been devoted to control phonon transport in the phononic crystals utilizing phonon interference and in the phononic metamaterials (local nanostructures) utilizing local phonon resonance. However, since the phononic crystals require strict global periodicity and the local resonances in the metamaterials only affect phonons with specific discrete frequencies, further development of phonon engineering has been a pressing and baffling challenge. A new mechanism that can mitigate the strict requirement of the globally periodic nanostructure and can influence a broader and continuum range of frequencies (the stop band) is urgently needed.

We have studied a new stop-band formation mechanism that is the two-path phonon-interference resonance by using the atomistic Green's function calculation and the wave-

packet molecular-dynamics simulation. Compared with the traditional stop-band formation mechanism (single-path Bragg scattering), the two-path resonance mechanism has a significant advantage in not requiring the strict periodicity in nanostructures, due to the local origin of the phonon resonance.

Moreover, there are growing efforts to control thermal transport via coherent phonons in the one-dimensional superlattice. However, in general, the difference in the intrinsic lattice structures of the constituent materials inevitably generate interface disorder during the fabrication process, greatly limiting direct experimental observation of the coherent phonon transport. The flexible integration and atomistic interlayer smoothness of van der Waals hetero-structure provide an ideal platform for the coherent phonon transport manipulation. Thus, in the second work, using the non-equilibrium molecular dynamics simulations, we investigate the coherent phonon transport in van der Waals graphene-MoS₂ hetero-structure with different stacking order at room temperature. The histogram of the phonon transmissions in different

disordered structure exhibits a log-normal distribution, which reveals a localization of the coherent phonons. Furthermore, the optimal stacking order of the graphene and MoS₂ is efficiently identified from tens of thousands of candidates by machine learning. The significantly suppressed of the phonon transmission in the low frequency (<5THz) phonons of the optimized structure lead to a significant reduction (~95%) of the thermal conductance compared with the pristine graphite. Finally, the effects of the temperature and strain effect on the thermal conductivity of graphite and optimized structures are also discussed. Our work provides a deep insight into the coherent phonons transport behavior in the atomistically smooth van der Waals structure, which is beneficial for further development of phononics.

References

- [1] Hu, Shiqian, et al. arXiv preprint arXiv:2001.10321 (2020)

Development of algorithms in crystal structure prediction

Tomoki YAMASHITA

*Top Runner Incubation Center for Academia-Industry Fusion,
Nagaoka University of Technology
1603-1 Kamitomioka-machi, Nagaoka, Niigata, 940-2188*

We have developed a crystal structure prediction tool, CrySPY as an open source software [1]. CrySPY is interfaced with VASP[2], Quantum ESPRESSO[3], soiap[4], and LAMMPS code for structure optimization. Several searching algorithms are available in CrySPY, such as random search (RS), evolutionary algorithm (EA), Bayesian optimization (BO), and LAQA. RS is a basic algorithm and widely used. EA[5, 6, 7] is currently very popular. We have implemented EA into our CrySPY code. Previously we have developed selection-type algorithms with machine learning. BO can efficiently select potential candidates from a large number of candidate structures by machine learning[8]. LAQA is one of the reinforcement learning, which can reduce the computation time[9]. The key point here is that the selection-type algorithms are not exclusive with EA. In this study, we develop a hybrid algorithm of BO and EA. This hybrid algorithm could be the most promising way to find the global minimum structure in large and complicated systems. Moreover, we compare searching efficiency among the RS, EA, BO, and hybrid algorithm.

Searching efficiencies of RS, EA, BO, and the hybrid algorithm have been investigated in two systems of Si₁₆ and Si₃₂. The former is a relatively easy system to find the most stable structure, and the latter is slightly difficult. For the system of Si₁₆, we optimized a hundred structures using interatomic potential calcula-

tions with the soiap code in each algorithm. Here, a hundred structures were selected from three hundred structures particularly in BO and the hybrid algorithm. A hundred structures were obtained by random structure generation and the remaining two hundred structures were generated by EA in the hybrid algorithm. To statistically investigate searching efficiencies, we carried out simulations of crystal structure prediction 50 times. The success rates to find the most stable structure were 64%, 58%, 70%, and 82% for RS, EA, BO, and the hybrid algorithm, respectively. The success rates of RS and BO were slightly better than that of EA. Random structure generation is sufficiently effective to find the most stable structure in this small system. The number of searching trials (100 structures) might be too small for EA. The success rate of the hybrid algorithm was the highest in which we generated 200 structures by EA. This is because EA was able to generate good candidates and BO efficiently selected the good ones. For the system of Si₃₂, three hundred structures were optimized in each algorithm. In BO and the hybrid algorithm, three hundred structures were selected from six hundred structures. Three hundred structures were obtained by random structure generation and the remaining half of the structures were generated by EA in the hybrid algorithm. The success rates were 46%, 60%, 54%, and 74% for RS, EA, BO, and the hybrid algorithm, respectively. The success

rate of RS was lower than others since the system became complex. Although the success rate of BO was better than that of RS, BO was not as good as EA. Random structure generation is no longer effective in this system. However, the success rate of the hybrid algorithm was still the highest. These results show the hybrid algorithm is superior to EA and BO and could be the most promising method for the crystal structure prediction.

References

- [1] <https://github.com/Tomoki-YAMASHITA/CrySPY>.
- [2] G. Kresse and J. Furthmüller, *Phys. Rev. B* **54**, 11169 (1996).
- [3] P. Giannozzi et al., *J.Phys.:Condens.Matter* **21**, 395502 (2009).
- [4] <https://github.com/nbsato/soiap>.
- [5] A. R. Oganov and C. W. Glass, *J. Chem. Phys.* **124**, art. 244704 (2006).
- [6] A. R. Oganov, A. O. Lyakhov and M. Valle, *Acc. Chem. Res.* **44**, 227 (2011).
- [7] A. O. Lyakhov, A. R. Oganov, H. T. Stokes, and Q. Zhu, *Comp. Phys. Comm.* **184**, 1172 (2013).
- [8] T. Yamashita, N. Sato, H. Kino, T. Miyake, K. Tsuda, and T. Oguchi, *Phys. Rev. Materials* **2**, 013803 (2018).
- [9] K. Terayama, T. Yamashita, T. Oguchi, and K. Tsuda, *Npj Comput. Mater.* **4**, 32 (2018).

Large scale ab initio calculations on the fundamental processes of solar energy convergence devices and on designing principles for new materials

Koichi YAMASHITA

Elements Strategy Initiative for Catalysts and Batteries (ESICB),

Kyoto University, Nishikyo-ku, Kyoto 615-8510, Japan

1. Electron-phonon interactions in tungsten oxide photocatalysts

Water-splitting photocatalysts, which decompose water into hydrogen and oxygen by sunlight, are promising for a clean and renewable energy source for the next generation of hydrogen production. A considerable amount of literature has been published on the photoexcited state of tungsten oxide, and long-lived trapped photocarriers have been found to play a key role in photocatalytic reactions. Using XAFS techniques, Uemura *et al.* found that the photoexcited electrons stay on the tungsten atom and the local structure is changed [1,2]. However, there has been no detailed investigation of the structural changes caused by photoexcited electrons and the changes in electronic states associated with these structural changes. In this work, electronic states, phonon, and electron-phonon interaction calculations for tungsten oxide were performed by using first-principles calculations based on density functional theory in order to discuss the lattice distortions caused by photoexcited electrons. These calculations were performed by using Quantum ESPRESSO 6.3 and Yambo 4.2.4. GGA-PBE and “on the mass shell” approximation were used for these

calculations. An integral approach utilizing 500 random Q points was used for the electron-phonon interaction calculations. The results showed that the bandgap of the direct transition at the Γ point is larger than the bandgap of the indirect transition. It is suggested that the bandgap of the indirect transition is more preferred and reduce carrier recombination. Next, the Eliashberg function was calculated to find the phonons that contribute significantly to the electron-phonon coupling. The transition dipole moment on the Γ point of the structure, which is displaced in the direction of the strain caused by the phonon, was calculated. It is suggested that the strain caused by the phonon, which is strongly coupling with the electrons on the CBM, reduces the transition dipole moment, and also reduces the recombination of the photocarriers.

2. Device-Scale Simulations of Organic Photovoltaics for Performance Improvement

Organic photovoltaics, OPVs, are promising energy harvesting devices, but their power conversion efficiencies are lower than traditional silicon ones. For performance enhancement, it is important to control properties of donor and

acceptor materials, such as HOMO and LUMO levels, by molecular design. Fullerene derivatives, *e.g.*, phenyl-C₆₁ butyric acid methyl ester, PCBM, have been used for acceptors, but recently non-fullerene acceptors are attracting attentions because of easiness of LUMO level tuning and light harvest. A non-fullerene acceptor is composed of three units: π -conjugated core; alkyl side chains, which control solubility; and electron-withdrawing end groups, which control LUMO level. It is however challenging to synthesize and evaluate device performances for combinations of donors and acceptors.

In this work, density functional theory, DFT, code as implemented in NTChem was employed to evaluate material properties of donors and non-fullerene acceptor candidates. We implemented programs to generate NTChem inputs—Cartesian products of cores, side chains

and end groups—from SMILES. HOMO and LUMO levels of indacenodithiophene, IDT, derivatives were evaluated at ω B97X-D/def2-SVP level of theory, which reproduces dependence of LUMO levels on electronegativities of end groups. In future work, it is planned to evaluate other properties such as electron mobilities, absorptions spectra, and exciton lifetimes.

References

- [1] Y. Uemura, H. Uehara, Y. Niwa, S. Nozawa, T. Sato, S. Adachi, B. Ohtani, S. Takakusagi, K. Asakura, *Chem. Lett.* **43** (2014) 977.
- [2] Y. Uemura, D. Kido, Y. Wakisaka, H. Uehara, T. Ohba, Y. Niwa, S. Nozawa, T. Sato, K. Ichianagi, R. Fukaya, S. Adachi, T. Katayama, T. Togashi, S. Owada, K. Ogawa, M. Yabashi, K. Hatada, S. Takakusa, Y. Yokoyama, B. Ohtani, K. Asakura, *Angew. Chem. Int. Ed.* **55** (2016) 1364.

Computational physics and chemistry approach to develop the artificial photosynthesis and fuel cell catalysts

Kazume NISHIDATE

Faculty of Science and Engineering, Iwate University

Ueda 4-3-5, Morioka, Iwate 020-8551

TiO₂ is well known as an efficient photo catalytic material and has a wide range of application area from air-purifier to antimicrobial coating. However, TiO₂ uses only the ultraviolet ray which is less than 3 % of the whole sunlight pouring on the earth surface. Therefore extensive studies have been devoted to develop photo-catalytic materials sensitive to visible light that makes up 50 % of the sunlight.

A large number of double-perovskite oxides, A₂B'^{III}B''^VO₆, have been studied due to their intriguing physical and chemical properties originating in their mixed valence nature. Above all, Ba₂PrBiO₆ was found to show an efficient photo catalytic activity to dissolve water molecules into oxygen and hydrogen gases under the visible light. However, detailed theoretical analysis on the electronic structures and the crystal geometries of the double-perovskites has not been performed. In this work, we study the structural and electronic properties of Ba₂Bi^{III}Bi^VO₆, Ba₂PrBiO₆, and Ba₂PrSbO₆ double-perovskites using the first-principles density functional theory [1]. The Heyd-Scuseria-Ernzerhof hybrid functional was applied to the calculations to handle the strong electron-correlation.

First of all, we evaluate the structural and electronic properties of Ba₂Bi^{III}Bi^VO₆ as it gives the basis in analyzing the double perovskite crystals. Unit cell contains four BaBiO₃ chemical units where the Bi^{III} octahe-

dra and the Bi^V octahedra are arranged alternately forming the *B*-site ordering. Where the distortions of octahedra caused by the mixed valencies are characterized by breathing distortion and tilting angle as depicted in Figure 1. We find that the Bi^{III} 6s states at the top of

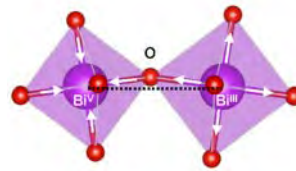


Figure 1: Distorted octahedra of Ba₂Bi^{III}Bi^VO₆.

valence band of Ba₂Bi^{III}Bi^VO₆ vanish on the Pr substitution for Bi at B'^{III}-site. When Sb is substituted for Bi at B''^V-site, the Bi^V 6s states at the bottom of the conduction band vanish causing additional widening of the band gap. Further, our calculation suggests that the Ba₂PrPrBiO₆ is a possible candidate as a source of the Pr^{IV} signal observed in the experiment. We find that the anti-*B*-site atomic configurations, Ba₂B''^VB'^{III}O₆, are easily restored to those of the original structures. This demonstrates the stability of the *B*-site ordering in the double-perovskite framework.

References

- [1] K. Nishidate: *submitted*.

Reveal the mechanism of thermal transport in PbS quantum dot system

Cheng SHAO

*Department of Mechanical Engineer, University of Tokyo
Hongo 7-3-1, Bunkyo-ku, Tokyo 113-8656 JAPAN*

Colloidal quantum system has attracted a lot attention recently due to their controllable electronic and optoelectronic properties.[1] Therefore, the colloidal quantum dot systems are promising for a wide range of applications from solar cells, thermoelectric devices, photodetectors, and many others. [2] Understanding the thermal properties of such quantum dots system is crucial for the thermo-stability and the performance of the above-mention application. However, due to the large unit cell size and complex inter-atomic interaction, the thermo properties for such system is still less understood. In this project, we applied the molecular dynamics simulations to systematically investigate the thermal transport in PbS quantum dot system. The large-scale molecule dynamics simulations is carried out by the open source software LAMMPS with the computational resource from The Institute for Solid State Physics (ISSP) of the University of Tokyo.

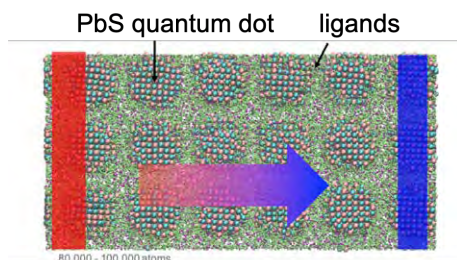


Figure 1: Illustration of the non-equilibrium molecular dynamics simulation for thermal conductivity calculation in PbS ligand system

The simulation model used for thermal properties calculations is shown in Fig.1. The size of the PbS dots is about 3 nm, which contains about 600 atoms. $C_5H_{10}S_2$ ligands are used to bridging the connection between the quantum dots. The length of the system range from 20-100 nm, while are cross-section of 10 nm \times 10 nm with periodic boundary is used in the direction perpendicular to the heat flux. The simulated thermal conductivity from the non-equilibrium molecular dynamics simulations is as lower as ~ 0.1 W/mK at temperature of 300 K. As a reference, the thermal conductivity of bulk PbS is about ~ 5.0 W/mK based on the same interatomic potential.

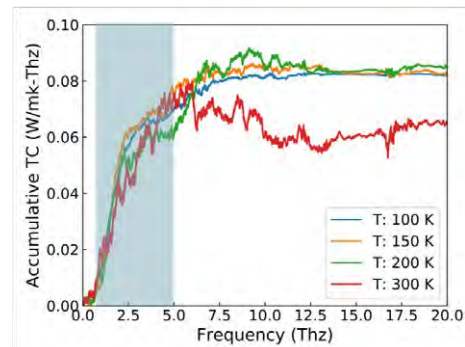


Figure 2: Illustration of the non-equilibrium molecular dynamics simulation for thermal conductivity calculation in PbS ligand system

To understand the origin of the lower thermal conductivity in such system, we calculated the spectral-resolved thermal conductivity at different temperature and the results are shown in Fig. 2. From this figure, we

can clearly see that thermal transport in PbS quantum dots system is dominated by low frequency phonon in the frequency range of 0.2~5 THz, while the high frequency vibrational modes are mainly scattered at the PbS-ligand interface. This explained the ultra-low thermal conductivity in such quantum dot system.

References

- [1] Ellingson, Randy J., et al. Nano letters 5.5 (2005): 865-871.
- [2] Cao, Yiming, et al. Nature Energy 1.4 (2016): 1-6..

Exploration of surface reactions on model real catalyst II

Wataru Mizukami

*Center for Quantum Information and Quantum Biology, Institute for Open and Transdisciplinary Research Initiatives,
Osaka University, Toyonaka, Osaka 560-8531, Japan*

This year, as in the previous year, we studied two chemical reactions on inorganic surfaces using density functional theory (DFT) utilizing parallel computational resources of ISSP's supercomputer system and the Vienna Ab initio Simulation Package (VASP) version 5.4.4. On top of that, we worked on the development of an electronic structure theory for quantum computing.

The first reaction was the industrially relevant Ziegler–Natta catalysis for olefin polymerization, which is based on titanium chlorides supported by MgCl_2 . In the previous year, we had revealed that two alkyl aluminum molecules are involved during the active-site formation process. This year, we examined three possible reaction paths of the active-site formation in detail, and found a new possible transition state.

The second reaction was a diffusion of 3,4,9,10-perylene-tetracarboxylic-dianhydride (PTCDA), which is an organic semiconductor molecule, on the $\text{Ge}(001)$ surface. In the previous year, we had located the transition state of this reaction using the climbing-image nudged elastic band method. This year, we

performed a detailed analysis of the reaction. It was found that the adsorption character transforms from the chemisorption with the physisorption at the reactant and product into the physisorption at the transition state during the diffusion.

In addition to the above two studies, we developed a new quantum chemical method for quantum computing based on the variational quantum eigensolver (VQE). The VQE is a quantum-classical hybrid algorithm to optimized wave-function, where quantum-circuit parameters are determined variationally. Our method, called orbital-optimized unitary coupled cluster doubles, optimizes both quantum circuit parameters and molecular orbitals simultaneously, which allows computing first-order molecular properties easily in the framework of the VQE. Taking advantage of this property, we realized the first geometry optimizations of polyatomic molecules using the analytical energy derivatives of the VQE.[1]

References

[1] W. Mizukami, et al., arXiv:1910:11526

DFT calculation of atomic displacements captured by energy dissipation of noncontact atomic force microscope

Toyoko ARAI¹, Taichi Shikichi¹, Jun-Ichi Iwata², Atsushi Oshiyama³

¹*Graduate school of Natural Science and Technology, Kanazawa University, Kanazawa, Ishikawa, 920-1192*

²*AdvanceSoft Corporation, Tokyo 101-0062*

³*IMaSS, Nagoya University, Nagoya, Aichi 464-8601*

In the last two decades the conservative and non-conservative (dissipative) force interactions between a tip and a sample in proximity have been examined by non-contact atomic force microscopy (nc-AFM). In particular, the channel of nc-AFM to measure the energy dissipation through the non-conservative force interactions has been regarded to have great potential to explore nano-mechanical phenomena; the dissipation channel gives the change in the amount of mechanical energy to maintain the constant oscillation amplitude of an AFM cantilever. We had experimentally found that, when the nc-AFM image showed the high resolution for the individual adatoms on a

Si(111)-(7×7) surface, the simultaneously obtained energy dissipation signal increased in close proximity over the hollow sites surrounded by a Si adatom and a Si rest atom with a dangling bond per each (Fig. 1) [1]. Based on the experimental results, the dynamic atomic processes responsible for the dissipation had been discussed in regard to breaking of the backbonds of the Si adatom and subsequent bond formation in an alternative atomic configuration of the Si surface atoms, including the Si atom at the apex of AFM tip. In this study, to elucidate the phenomena, the surface diffusion potentials of a Si adatom were calculated using real-space density functional theory (RSDFT) [2] when the Si tip was brought closer to the Si(111)-(7×7) surface. RSDFT is a first-principles program developed by Oshiyama and Iwata, which uses a real-space difference method and a pseudopotential method.

First, we optimized the structure of Si(111)-(7×7) reconstructed surface consisting of 298 Si atoms and 49 H atoms by RSDFT, as shown in Fig. 2. Then, the surface diffusion potential for a

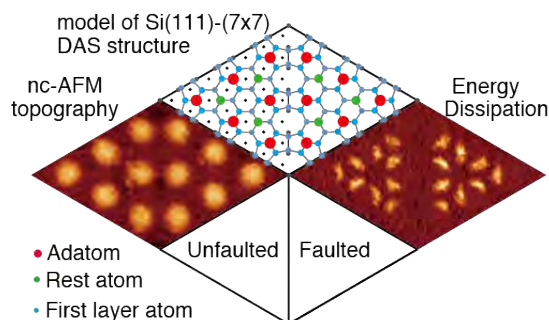


Fig. 1: Simultaneously obtained nc-AFM image and the energy dissipation image, with the structure model of Si(111)-(7×7).

corner Si adatom was calculated from its original position to the neighboring hollow site (Fig. 3). The hollow site seems metastable because of a diffusion barrier from the hollow site to the adatom site, the barrier height of which was several tenth of 1 eV. Our preliminary calculations anticipated that the diffusion barrier is lowered and the adatom can move to the hollow site, when the tip is in close proximity to the surface [3]. It is deduced that the oscillating nc-AFM cantilever can provide the Si adatom with the kinetic energy to overcome the barrier

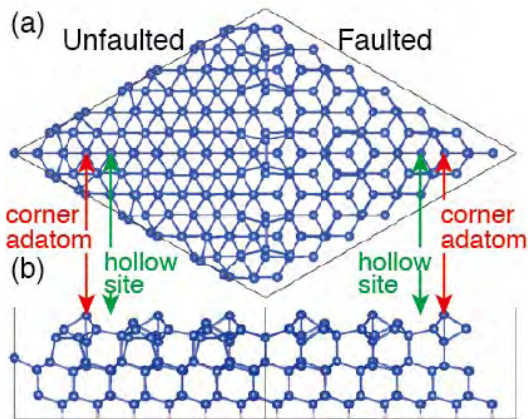


Fig. 2: Optimized atomic structure of Si(111)-(7 \times 7). (a) top view. (b) side view.

from the adatom site to the hollow site. This energy of less than 1 eV could be captured as a dissipation energy in the nc-AFM experiment.

References

- [1] T. Arai, R. Inamura, D. Kura, and M. Tomitori, Phys. Rev. B **97**, 115428 (2018).
- [2] J.-I. Iwata, D. Takahashi, A. Oshiyama et al., J. Comput. Phys. **229**, 2339 (2010).
- [3] B. Enkhtaivan, Y. Sugimoto, and A. Oshiyama, Phys. Rev. B **96**, 155417 (2017).

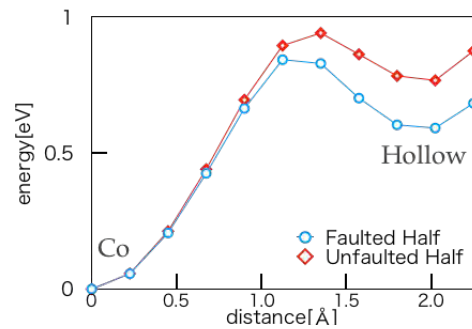


Fig. 3: Surface diffusion potential of the Si adatom from the original position ($x = 0$, denoted by Co (corner adatom site)) to the neighboring hollow site ($x = 2.25$ Å) without the Si tip.

Hybrid *Ab-Initio*/Machine-Learning Computation for Designing Nano/Molecular Structure

Kenji TSURUTA, Kyosuke SATO, Md. Abdullah Al ASAD, Tadahiro MIMURA, and

Satoshi OHMURA^a

Graduate School of Natural Science and Technology, Okayama University, Okayama 700-8530

^a Department of Civil and Environmental Engineering, Hiroshima Institute of Technology, Hiroshima 731-5193

Designing and developing functional materials/molecules often require vast searching of target properties from extra-large data set, which is far out of the capability of conventional computing algorithms. In recent years, the Deep-Learning (DL)-based molecular design methods have been extensively studied. One of the recent studies has reported [1] a machine learning method for predicting molecular properties by mapping a graph representation of a molecule to a latent variable space and by linking the variable to physical property of the molecule. Representing molecules in the latent space enables an efficient property search within existing data, because the DL model transforms the discrete representation of a molecular graph into a continuous variable space suitable for various numerical algorithms.

In the present study, we have developed a hybrid algorithm that combines the continuous representation of molecules with an optimization algorithm to predict physical properties of organic molecule [2]. Here the Grammar Variational Autoencoder (GVAE) [3] algorithm was adopted for transforming discrete representation of a molecular graph into continuous representation. The optimum value of the HOMO-LUMO gap obtained by an *ab-initio* quantum-chemical calculation was predicted by searching a molecular structure within the latent space.

The input of GVAE is a Simplified Molecular Input Line Entry System (SMILES) string, which represents a molecular graph. The GVAE consists of two neural networks: An encoder and a decoder. The encoder converts SMILES into latent variables z , whereas the decoder converts z back to the original SMILES string. These neural networks are trained so that an input SMILES coincides with the output SMILES. The distance between molecules with

closer SMILES is mapped to a closer point in the latent variable space. By using this method, molecular design with desired characteristics can be treated as an optimization problem in a continuous variable space. We have examined the algorithm for predicting molecules using the Quantum Machine 9 (QM9) as a training dataset.


Target gap	Maximum
HOMO-LUMO gap	0.62151 hartree
SMILES	FC(F)(F)F
Optimized structure	

Fig. 1 The molecule and its properties predicted by the present method

Figure 1 shows the molecule possessing a targeted HOMO-LUMO gap among possible molecular structures with atomic species of C, O, N, F, and H, predicted by the present algorithm. In this case, CF_4 was predicted to have the widest gap of 0.62151 hartree among the possible molecular formula in the QM9 [2]. Parallely, we have performed an *ab-initio* molecular dynamics study on water-molecule dissociation in a nanostructured perovskite material ($MAPbI_3$) [4]. These computations have been done in part by using the Super-computing System at SCC-ISSP

References

- [1] R. Gómez-Bombarelli *et al*, ACS Cent. Sci. **4** (2018) 268–276.
- [2] K. Sato and K. Tsuruta, Mater. Sci. Forum, in press.
- [3] M. J. Kusner, B. Paige, J. M. Hernández-Lobato, <http://arxiv.org/abs/1703.01925>.
- [4] M.A.A. Asad, K. Sato, and K. Tsuruta, MRS Adv. **4**, 1965 (2019).

Analysis of ion conduction in materials of proton-conducting solid electrolyte and application to catalytic surface reaction with proton conductors

Fumiya Murase, Hiroki Matsuo, Junichiro Otomo

Graduate School of Frontier Sciences,

The University of Tokyo, Kashiwa-no-ha, Kashiwa, Chiba 277-8561

1. Introduction

Ammonia has been regarded as one of the attractive energy carrier for storage and transport of hydrogen because of its high hydrogen content and high energy density. Electrosynthesis of ammonia from nitrogen and water has been studied as a novel process replacing the conventional Haber-Bosch process which consumes a lot of energy.

We reported electrosynthesis of ammonia using an electrolyzer cell with a proton-conducting electrolyte and cathode catalyst of Fe and Ru. We found the ammonia formation rate is remarkably enhanced with increasing cathode polarization (electrochemical promotion effect)¹. Since dissociation of nitrogen triple bond is a rate-determining step in the ammonia formation reaction, we consider that the application of the cathodic polarization promoted the dissociation reaction of nitrogen triple bond.

As for the dissociation reaction of nitrogen molecule on the metal catalyst, previous studies based on theoretical calculations suggested majorly two different mechanisms for the N₂ dissociation reaction on a surface of the cathode catalyst metals^{2,3}. One is the direct dissociation mechanism in which nitrogen molecule adsorbed on the surface of the catalyst directly dissociate into two adsorbed nitrogen atoms. The other is associative mechanism in which hydrogen atom initially reacts with the adsorbed nitrogen molecule to form N₂H species and successive reaction with

hydrogen atom dissociate the nitrogen bond step by step. However, the roles of the cathodic polarization of the catalyst and protons supplied from the electrolyte on the nitrogen dissociation reaction in the ammonia electrosynthesis process are still unclear.

In this study, the roles of the cathode polarization of the catalyst and protons from the electrolyte are investigated by theoretical calculations based on density functional theory (DFT) to reveal the mechanism of the electrochemical promotion effect of ammonia formation reaction.

2. Computational methods

For the calculation of the surface reaction, a slab-and-vacuum model was employed. We chose BaCeO₃ (BCO) with a BaO₂-terminated (001) plane as a proton-conducting oxide slab and a Ru cluster on the surface of the BCO surface as a catalyst. DFT calculations were performed with VASP5.5.4 code. The generalized gradient approximation proposed by Perdew, Burke, and Ernzerhof (GGA-PBE) represented the exchange-correlation energy functional⁴. Plane-wave cut-off energy of 400 eV was adopted. Monkhorst-Pack *k*-mesh of 2 × 2 × 1 centered at the Γ point for the geometry optimized supercells.

To reveal the effect of the cathodic polarization on the nitrogen dissociation, density of states (DOS) of the systems with one nitrogen molecule apart from the catalyst and that with nitrogen molecule adsorbed on the catalyst were calculated. Moreover, one electron was added to the system with adsorbed nitrogen molecule to reproduce the cathodic polarization in the ammonia electrosynthesis.

3. Results

In the calculation for the model without adsorbed nitrogen, electron-occupied Ru 4d state was emerged at around Fermi level after the addition of an electron, which suggested that the cathodic polarization activates an electron-donating property of the Ru catalyst. Moreover, the calculation for the model with adsorbed nitrogen showed that an anti-bonding orbital of the adsorbed nitrogen located around the Fermi level after the electron addition. Then, charges of constituent atoms of the Ru cluster and the adsorbed nitrogen molecule (Fig. 1) were calculated for the system before and after the electron addition. As summarized in table 1, the N2 atom and the Ru atoms were negatively charged after the electron addition. These results suggested that back donation of electron from the Ru catalyst to the adsorbed nitrogen molecule can be promoted by the application of the cathodic polarization.

To clarify the possible nitrogen dissociation mechanism, the reaction activation energies for the two mechanisms were calculated with the nudged elastic band (NEB) method. Though the apparent difference in the activation energy was not observed, side-on

configuration of the adsorbed nitrogen molecule was stabilized in the dissociative model by the addition of an electron. This result allows us to expect that the dissociation mechanism can be promoted by the cathodic polarization.

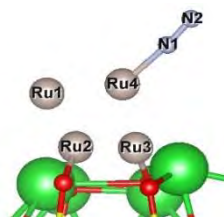


Fig. 1. The Ru cluster and the adsorbed N₂ molecule on the BCO (001) surface with BaO₂-termination.

Table 1. Calculated charges normalized by elementary charge for constituent atoms of the Ru cluster and the adsorbed nitrogen molecule before and after the addition of an electron normalized by elementary charge.

Atom	Before	After	Variation
N1	-0.36	-0.35	0.01
N2	-0.05	-0.15	-0.10
Ru1	-0.42	-0.51	-0.09
Ru2	0.16	0.07	-0.09
Ru3	-0.03	-0.09	-0.06
Ru4	0.09	0.04	-0.05

References

- [1] F. Kosaka *et al.*, *Sustainable Chem. Eng.*, **5**, 10439–10446 (2017).
- [2] S. Back and Y. Jung, *Phys. Chem. Chem. Phys.* **18**, 9161–9166 (2016).
- [3] D. Bao *et al.*, *Adv. Mater.*, **29**, 1604799 (2017)
- [4] Perdew, J. P. *et al.*, *Phys. Rev. Lett.* **77**, 3865 (1996).

Transport and reaction properties of nanographene

Koichi KUSAKABE

Graduate School of Engineering Science, Osaka University
1-3 Machikaneyama, Toyonaka, Osaka 560-8531

1. A cross-correlation transport effect of a magnetic Ni/h-BN/Ni junction

We found that a thin magnetic Ni/h-BN/Ni junction allows a novel magnetoresistance effect controllable by the external electric-field, *i.e.* a cross-correlation effect. The effect comes from realization of local pyramidal B-N₃ structures of the h-BN monolayer. When the anti-parallel spin configuration of two ferromagnetic Ni layers is fixed, the spin-polarized tunnel current is reversed in its spin-moment direction by the electric field whose field strength is within a realizable range. Switching upright pyramids to inverted pyramids, the electronic polarization direction in the h-BN layer and the spin-moment direction are reversed.[1]

2. The strong-correlation effect in an elastic property of defect-free graphite

We developed new DFT-based simulation methods, *i.e.* LDA+U+RPA and ACFDT-RPA+U, for the explanation of unexpectedly large elastic constant C_{33} of the defect-free monocrystalline graphite by KANEKA, which is measured by the microscopic picosecond ultrasound method.[2] The short-range correlation effect described by the U term causes unharmonic potential profile raising C_{33} from the value by ACFDT-RPA by more than 20%.

3. Hydrogen production catalyzed by graphene with vacancies

We found that hydrogenated graphene vacancies promote dehydrogenation processes of several alkane molecules in simulations. Based on these results, we can propose that creation of atomic vacancy becomes the activa-

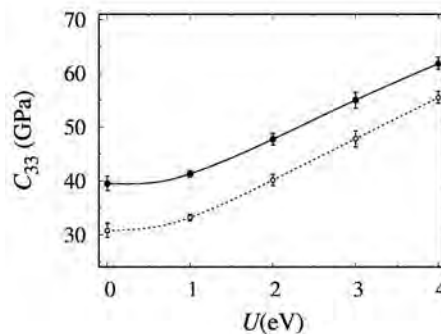


Figure 1: Calculated C_{33} by LDA+U+RPA (solid line) and LDA+U.[2]

tion of the dehydrogenation catalytic property of graphene, which is shown to be realized in experiments.[3]

4. Zero modes in PTM molecules

The counting rule of zero modes by Morishita holds generally in a set of phenalenyl tessellation molecules (PTM).[4] Based on the ruled creation of zero modes, we can construct a certified ferrimagnetic Hubbard model in two dimensions. An effective low-energy model becomes a Kondo-lattice model, where extending orbitals causes the Kondo screening in localized spins of arrayed zero modes.

Acknowledgement

This work was partly supported by KAKENHI (Nos. JP18K03456 and JP19H00862).

References

- [1] H. Harfar, *et al.*, ACS Appl. Elec. Materials, in press.
- [2] K. Kusakabe, *et al.*, Phys. Rev. Materials, **4**, 043603 (2020).
- [3] K. Kusakabe, *et al.*, Japan patent appl. JP2019-135780
- [4] N. Morishita and K. Kusakabe, J. Phys. Soc. Jpn. **88**, 124707 (2019).

van der Waals density functional study of image-potential states at organic-metal interfaces

Yuji HAMAMOTO

*Department of Precision Science and Technology, Graduate School of Engineering,
Osaka University, Yamada-oka, Suita, Osaka 565-0871*

Recent progresses in observation techniques enable us to elucidate the transport properties of unoccupied states on solid surfaces. Among them, image-potential states (IPs) are of particular importance, since they appear ubiquitously on metal surfaces, exhibiting a Rydberg series with parabolic dispersions. From an applicational point of view, IPs could influence the properties of molecular-based electronic devices such as organic light-emitting diodes, interacting with unoccupied molecular orbitals of adsorbates. Recently, we have applied van der Waals density functional (vdW-DF) method [1] to naphthalene physisorbed on graphene and revealed that IPs are induced on a close-packed naphthalene monolayer, hybridizing with graphene IPs [2]. The resultant hybrid IPs show an anisotropic effective mass that reflects the molecular structure of naphthalene, demonstrating that the transport properties of IPs of metal surfaces can be fine-tuned by molecular adsorption.

As an extension of our previous study on hybrid IPs at molecular-metal interfaces, we here theoretically investigate lead phthalocyanine (PbPc) physisorbed on graphene

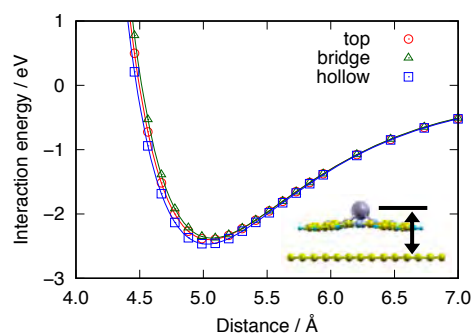


Fig. 1: Determination of the equilibrium distance between PbPc and graphene

as shown in Fig. 1. Experimentally, IPs of PbPc adsorbed on HOPG has been investigated intensively using two-electron photoemission spectroscopy [3-5]. Unlike naphthalene, PbPc has a non-planar shuttlecock structure due to the central lead atom, which results in a dipole moment. To understand the influence of the dipole moment on hybrid IPs, we investigate the band structure of PbPc on graphene and analyze the effective mass of the IPs. Our results reveal that the dipole moment reduces the overlap of wave functions between neighboring molecules, which enhances the effective mass of the hybrid IPs. Moreover, unlike the IPs of graphene, the hybrid IPs in PbPc on graphene displays an anisotropic effective mass with

nearly C_4 symmetry, which prominently reflects the molecular structure of PbPc [6].

References

- [1] M. Dion, H. Rydberg, E. Schröder, D. C. Langreth, and B. I. Lundqvist, *Phys. Rev. Lett.* **92**, 246401 (2004).
- [2] S. A. Wella, H. Sawada, N. Kawaguchi, F. Muttaqien, K. Inagaki, I. Hamada, Y. Morikawa, and Y. Hamamoto, *Phys. Rev. Materials* **1**, 061001(R) (2017).
- [3] M. Shibuta, K. Miyakubo, T. Yamada, and T. Munakata, *J. Phys. Chem. C* **115**, 19269 (2011).
- [4] N. Kawakita, T. Yamada, M. Meissner, R. Forker, T. Fritz, and T. Munakata, *Phys. Rev. B* **95**, 045419 (2017).
- [5] T. Yamada, N. Kawakita, C. Okui and T. Munakata, *J. Phys.: Condens. Matter* **31**, 044004 (2019).
- [6] Y. Hamamoto, H. Sawada, S. A. Wella, K. Inagaki, I. Hamada, and Y. Morikawa, in preparation.

STM simulations for Fe-adsorbed Si(111) surfaces

Kei TANIMOTO and Ken HATTORI

Graduate School of Science and Technology, Nara Institute of Science and Technology
Takayama, Ikoma, Nara 630-0192

Using scanning tunneling microscopy (STM), author's group has been studied iron-silicides formation on Si(111) [1] prepared in ultra-high vacuum. In the initial stage of Si(111)7×7 with isolated Fe atoms, we observed 5 different adsorption types in experimental STM images [2]. In order to understand (meta) stable actual structures of Fe/Si(111)7×7, we carried out first principles calculations using the super computing system in the institute for solid state physics.

We utilized the calculation package of Simulation Tool for Atom TEchnology (STATE)-Senri [3] for 17 models of Fe single-atom adsorption including *atop*, *ins*, T_4 , and H_3 sites, based on a Si(111)4×4 surface-substrate model [4]. The 4×4 model (i.e., 4 Si adatoms on 2×2 T_4 sites, and 2 of 4 restatoms terminated with H atom, in a unit) has an advantage of fast calculation, because of smaller number of atoms compared to that in the 7×7 model, maintaining the specific Si surface property of the 7×7 model of the dimer-adatom-stacking-fault, though the 4×4 model is not equal to the 7×7 model.

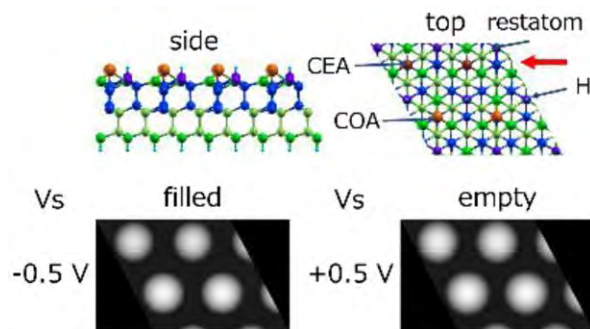


Figure 1: A model of Si(111)4×4 clean surface and STM simulation results.

The clean Si(111)4×4 model consisting of a Si adatom-layer, six Si-layers, and a bottom H-terminated layer has 118 atoms, while 7×7 has 347 atoms. The top-view and side-view schematics in Fig. 1 show the atomic structure of the clean 4×4 model; upper adatom (brown ball) corresponds to center adatom (CEA) with two neighbored restatoms (purple ball, note another restatom is terminated by H atom), and lower adatom corresponds to corner adatom (COA). The bottom panel represents STM simulation images of filled (empty) states at -0.5 (+0.5) V in bias voltage, displaying clear adatom images.

In the simulation, the atoms in the top six layers were relaxed with the spin polarization, from the converged configurations without the spin polarization.

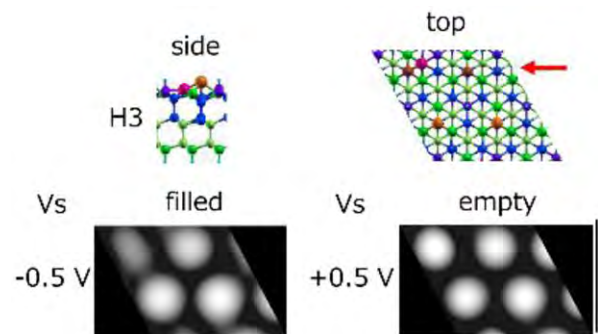


Figure 2: A model of Si(111)4×4 surface with Fe atom near a H_3 site and STM simulation results.

During the 17 models, the stable configuration was Fe atom close to H_3 site as shown in Fig. 2; Fe atom (pink ball) locates between CEA and restatom, with the formation energy of -7.59 eV. The STM images showed darkened adatom at filled states at -0.5 V while no drastic change at empty states at +0.5 V. The sec-

ond (meta) stable configuration was also near H_3 site COA and restatom with the formation energy of -7.55 eV. The third meta-stable configuration group was near T_4 sites with -6.87 eV to -6.35 eV in formation energy. The fourth group was *ins* sites with -6.34 eV to -6.28 eV, and the last (much unstable) group was *atop* sites with -5.32 eV to -5.28 eV.

The authors thank Profs. Morikawa, Hamada, and Inagaki in Osaka University, and Prof. Yanagisawa in Ryukyu University for their great support in STATE-Senri calculations.

References

- [1] K. Kataoka, K. Hattori, Y. Miyatake, and H. Daimon, Phys. Rev. B **74** (2006) 155406.
- [2] K. Kataoka, Dr.. Thesis, Nara Institute of Science and Technology, Nara (2006).
- [3] Y. Morikawa, Phys. Rev. B **63** (2001) 033405, and references therein.
- [4] Guo-Xin Qian and D. J.Chadi, Phys. Rev. B **35** (1987) 1288.

Analysis on atomic and magnetic structure in magnetic molecular complex, crystal and interface and investigation of external field effect

Masao OBATA^{1,2}

¹*Institute of Science and Engineering, Kanazawa University, Kanazawa, Ishikawa 920-1192*

²*Graduate School of Natural Science and Technology, Kanazawa University, Kanazawa, Ishikawa, 920-1192*

We have investigated the weak-bound magnetic material systems such as magnetic molecular crystal and magnetic-layered material. They have received a lot of attention due to their unique physical properties, such as external field-controllable its magnetization and crystal structure. Since prediction of structural and energetic properties with high accuracy is essential for weak-bond magnetic materials, we have enhanced the computational accuracy of density functional theory (DFT) by including physical interactions, e.g. van der Waals (vdW) interaction and magnetic dipole-dipole (MDI) energy, which were neglected in standard DFT calculation. While MDI energy is often considered as weak, it plays important role for magnetic anisotropy (MA) and diamagnetic field. Moreover, we also attempt to build a framework to investigate the external magnetic field effect.

We developed the method for each material dimensionality (chain, film, bulk) to estimate their MDI energy, since MDI interaction is basically long-range interaction

proportional to minus cube of distance. It can be estimated using spatial spin density obtained from DFT calculation. We applied this approach to antiferromagnetic molecular crystal [1] (monoclinic crystal solid oxygen α phase: α -O₂) and ferromagnetic thin film and chain (Fe, Co, Ni). We found that its contribution to MA is comparable to those of Spin-Orbit Interaction. Moreover, the spatial distribution of intra-atomic spin density occasionally contributes to MDI energy. For solid oxygen α -phase case, noncolinear spin-dependent vdW-DF method, which developed in our previous work [2], was employed. External magnetic field effect due to Zeeman interaction can be considered for oxygen α -phase case, in order to investigate the effect towards its magnetization [3].

References

- [1] M. Obata et al., *AIP Adv.* **8**, 10149 (2018).
- [2] M. Christivana et al., *JPSJ* **88**, 104601 (2019).
- [3] A. R. Rio et al., *JPSJ* **89**, 035002 (2020)

Effects of electron-phonon scattering on electronic structure of half-metallic Heusler alloys

H. Akai

*Institute for Solid State Physics, University of Tokyo
Kashiwa-no-ha, Kashiwa, Chiba 277-8581*

In some Heusler alloys, despite the fact that there exists a band gap in one of spin channels expected, established through first-principles calculations, the half-metallicity of the materials often turns out fragile under realistic situations such as in device structures. It has been pointed out that chemical disorders and defects might easily degrade the half-metallic nature of such materials. These degradations are structure oriented, and therefore, static. This means, once a perfect structure is attained, there exists no reason of this kind of degradation for the half-metallicity. However, there still exist another source of degradation, i.e., dynamical effects. The main sources of such effects are phonons and magnons at finite temperature. In the present research, we discuss the effects of electron-phonon scattering on the half-metallicity of Co_2MnSi , as a typical example, on the basis of first-principles calculations. The phonons are treated as giving local and static (adiabatic) effects [1], where correlations of the displacements between neighboring sites as well as dynamical effects are neglected, i.e. we take a quasi-dynamical treatment. The phonons are expressed as random displacements of atoms from their equilibrium positions. Using the distribution of the atomic displacements, the electronic structures of the system at finite temperature are calculated by regarding the system as a disordered system with randomly distributed atomic positions. This kind of randomness can be treated using KKR-CPA code [2]. The results show

that even at 300 K, the perfect half-metallicity is lost (Fig.1), showing that the effects of phonons are important at usual operating temperatures of devices. The effects on the GMR is also discussed. It turns out that, though the half-metallicity is lost at finite temperature, the conductivity of the spin-down state is much lower than that of the spin-up state by virtue of the strong electron-phonon scattering. Thus, the system can still be used in GMR devices at finite temperatures.

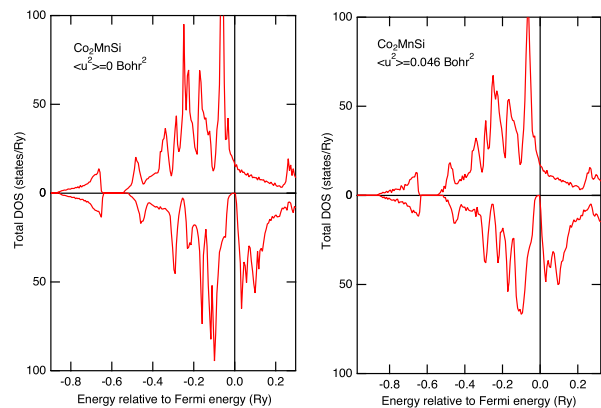


Figure 1: DOS of Co_2MnSi with an average displacement $\langle u^2 \rangle = 0$ (left) and 0.046 (right) in units of Bohr².

References

- [1] S. Kou and H. Akai, Solid State Commun. **276**, 1 (2018).
- [2] H. Akai, AkaiKKR, <http://kkri.sissp.u-tokyo.ac.jp/> (2002).

Systematics of Curie temperature in rare earth permanent magnet materials

H. Akai

*Institute for Solid State Physics, University of Tokyo
Kashiwa-no-ha, Kashiwa, Chiba 277-8581*

Curie temperatures T_C 's of permanent-magnet materials $R_2(\text{Fe,Co})_{14}\text{B}$, $R_2(\text{Fe,Co})_{17}$, and $R\text{Fe}_{11.5}\text{Ti}_{0.5}$ ($R = \text{La, Ce, \dots, Lu, Y}$), are calculated within the mean field approximation using the exchange coupling constants J_{ij} 's that are obtained by first-principles KKR–Green's function method[1]. While the agreement between the calculations and experiments is rather well for the Co-based systems, there arise some discrepancies in the case of Fe-bases systems. Despite these discrepancies, however, the systematic changes seen in T_C as the rare earth element R changes across the lanthanoid are fairly well reproduced by the calculation. In the case of $R_2\text{Fe}_{14}\text{B}$, the discrepancies can be largely diminished by using J_{ij} 's that are calculated for local-moment disordered states (LMD), which is considered to correspond to the paramagnetic state above T_C , as is shown in Fig.1 and 2. However, this is not the case in general: the discrepancies seen in $R_2\text{Fe}_{17}$ (Fig. 3), cannot be remedied. From the analyses of calculated and experimental data, it is concluded that data assimilations are possible and necessary to make reasonable predictions of T_C for rare earth permanent-magnet materials, in particular, the Fe-based ones.

References

- [1] H. Akai, AkaiKKR, <http://kkk.issp.u-tokyo.ac.jp/> (2002).

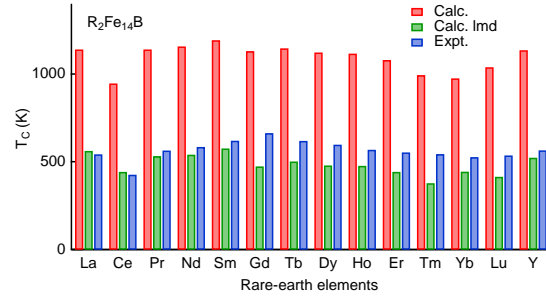


Figure 1: Calculated T_C of $R_2\text{Fe}_{14}\text{B}$ compared with experiments.

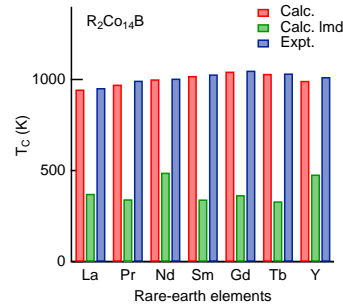


Figure 2: Calculated T_C of $R_2\text{Co}_{14}\text{B}$ compared with experiments.

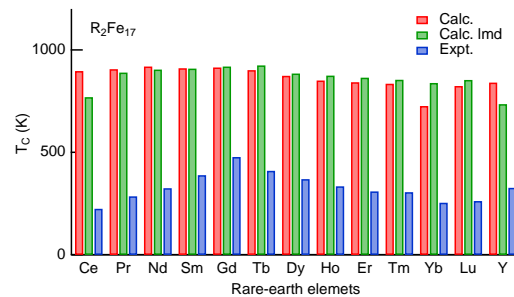


Figure 3: Calculated T_C of $R_2\text{Fe}_{17}$ compared with experiments.

Electronic state of water under various environments

Ryosuke YAMAMURA, Kento AKIHIRO, Nozomu FUTAMATA, and Osamu TAKAHASHI

Graduate School of Science, Hiroshima University, Kagamiyama, Higashihiroshima, Hiroshima 739-8526

We have studied aqueous solution using massive parallel computer simulations. This year, we focus on aqueous oxalic and malonic acid observed by X-ray absorption and emission spectroscopy [1]. To obtain the theoretical spectra of an aqueous solution, a molecular dynamics (MD) simulation based density functional theory (DFT) was adopted to simulate the structure of the solution. The MD simulations were performed using the Vienna ab initio simulation package (VASP). The MD simulations were performed for 5 ps, with 0.2-fs time steps. Cluster sampling was performed using python and fortran code for the results of the MD simulations. From the cluster obtained by structure sampling, a carboxylic acid molecule at the center of the cluster was used to model the OC=O,1s and OC-O-,1s core-hole and core excited state dynamics. The time steps used for these simulations were 0.25 and 20 fs, respectively. During the core excited state dynamics, each snapshot was used to calculate the relative line intensities of the X-ray

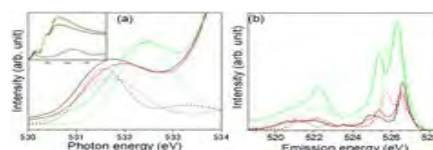


Fig. 1: (a) XAS and (b) XES spectra of aqueous oxalic acid (solid line: experiment, dash: theoretical, black: pH 1.1, red: pH 2.7, green: pH12.9).

emission spectra. The core excited dynamics and relative peak intensities of the spectra were calculated within the framework of DFT using deMon2k code.

We found that the theoretical XAS and XES spectra of cluster models reproduced the trends of the experimental spectra with respect to emission energy compared with single molecular models. We found that the dependence of XAS and XES spectra on pH is different from monocarboxylic acid.

References

- [1] R. Yamamura, T. Suenaga, M. Oura, T. Tokushima, and O. Takahashi: Chem. Phys. Lett. **738** (2020)13689

Temperature-Dependent Optical Properties in Rare-earth Sesquioxides and Related Phonon Calculations

Takayuki MAKINO

Department of Electric and Electronics Engineering,

University of Fukui, Fukui 910-8557, Japan

The natural oxide of Si, amorphous SiO_2 , is important for the CMOS technology. Due to the problem related to its fundamental size limits, reduction of the gate-oxide thickness in devices is strongly demanded. As one of the expected candidates satisfying these properties, attention is paid on rare-earth metal sesquioxides. Their optical properties are almost far from the full understanding. It is expected that such a temperature-dependent optical study can yield in several insights not only on electronic or excitonic properties, but also on phononic properties. In this activity report, we report the optical properties and related phonon calculations of ytterbia (Yb_2O_3) and lutetia (Lu_2O_3) thin films.

The phonon properties of the structure are obtained by a frozen phonon method: The forces acting on the ions are calculated upon a small displacement of each ion by using Quantum ESPRESSO package. The set of forces can be converted into the force constants, which are required to construct the dynamical matrix. We used the PHONOPY package to generate a set of $2 \times 2 \times 2$ supercells with displaced atoms, to compute the phonon dispersion and density-of-states (DOS) spectra.

Figure 1 shows temperature dependences of the band-gap energies. Alloted symbols are open circles for ytterbia and open squares in lutetia, respectively. We here use Pässler model to fit to the experimental data. the detailed values of deduced parameters have been given elsewhere [1]. We could reduce of the number of running parameters in the regression analysis which are an advantage and significance of the abovementioned phonon-property-related discussion.

References

- [1] T. Makino *et al.*: Jpn. J. Appl. Phys. **59** (2020) SCCB13.
- [2] R. Pässler, Phys. Rev. B **66**, (2002) 085201.

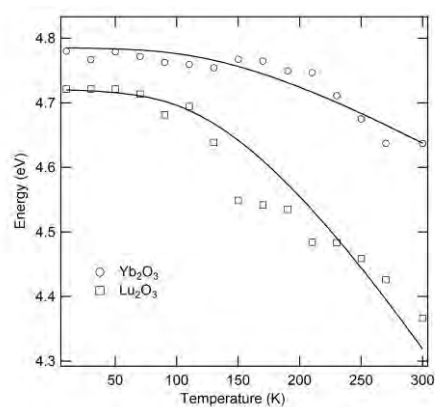


Fig. 1: Temperature dependences of band-gap E_g in Yb_2O_3 (circles) and Lu_2O_3 (squares).

First-principles calculation of organic modified metal oxide nanoparticles

Akira YOKO

*WPI-Advanced Institute for Materials Research,
Tohoku University, Katahira 2-1-1, Sendai, Miyagi 980-8577*

We have studied an interface system of organic molecules on metal oxide surface. From the experiments, it is known that surface stability of metal oxide greatly changes depending on the environment, resulting in the difference in the properties. For example, CeO_2 is ordinary stable with (111) surface, but it turns to be stable with (100) facet when hydrothermally treated with carboxylic acid. As a result, catalytic activity is greatly enhanced with (100) facet exposure of CeO_2 [1]. In this year, we studied the interaction between octanoic acid and CeO_2 surface using first-principles simulation.

Plane-wave basis density functional theory simulations were conducted with VASP code. Simulations were The generalized gradient approximation proposed by Perdew, Burke, and Ernzerhof (PBE) represented the exchange-correlation energy functional. The DFT+ U method introduced by Dudarev was used to treat electron localization. The parameter U - J was set to 5.0 eV for $\text{Ce}4f$ state. The valence configurations of the pseudopotentials were $5s^25p^64f^15d^16s^2$ for Ce, $2s^22p^4$ for O, and $2s^22p^2$ for C. The energy cutoff for the plane-wave

basis was set at 500 eV for all the calculations. Monkhorst-Pack k-point set of $4 \times 4 \times 1$ was used for the a slab model. Convergence criteria was set at less than 0.01 eV/Å for the force.

Figure 1 shows the adsorption, deprotonation, and dehydration of octanoic acid on CeO_2 (100) surface considered in this study. From the results, energy stabilization was calculated as -26.63 kJ/mol for adsorption and -26.57 kJ/mol for deprotonation. Deprotonation does not contribute stabilization. Dehydration of octanoic acid and hydroxide on CeO_2 surface, much larger stabilization as -43.20 kJ/mol was observed.

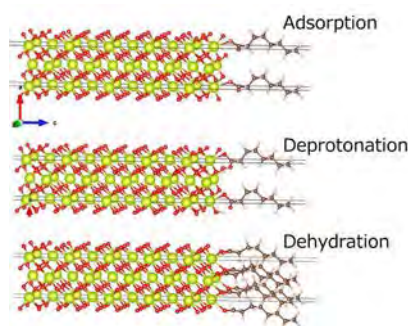


Figure 1 Adsorption, deprotonation, and dehydration of octanoic acid on CeO_2 (100)

References

- [1] X. Hao, A. Yoko, C. Chen, K. Inoue, M. Saito, G. Seong, S. Takami, T. Adschiri, Y. Ikuhara: *Small* **14** (42), (2018) 1802915

First principles study on leaking current at a dislocation in doped semiconductors

Yosuke HARASHIMA

*Institute of Materials and Systems for Sustainability, Nagoya University
Furo-cho, Chikusa-ku, Nagoya, Aichi 464-8601*

In the second half fiscal year of 2019, we have revealed the following results related with the performance of gallium nitride (GaN) power devices [1].

- The threading screw dislocations attract Mg impurities, and the electronic levels in the energy gap induced by the threading dislocations elevate towards the conduction band as the Mg approaches the dislocation line.

This results suggest that the leakage current which degrade the performance of the devices is induced by the presence of the Mg and the screw dislocation complexes.

GaN is one of the most promising compounds for the power devices since it has a large band gap. For the realization of the device, suppressing the leakage current is an important issue. The leakage current has been observed at the position of the threading dislocation. Recent experimental study suggests that the Mg impurities are condensed around the dislocation. The electronic structure of the Mg-dislocation complexes should be related with the origin of the leakage current, and it is important to guarantee the device reliability.

In this study, we systematically perform first-principles total-energy calculations for possible 16 core structures of the screw dislocations as shown in Fig. 1. The core structures are expressed as $D(n | m)$ or $S(n | m)$. The first capital letter denotes the position of the dislocation line. One is called single core,

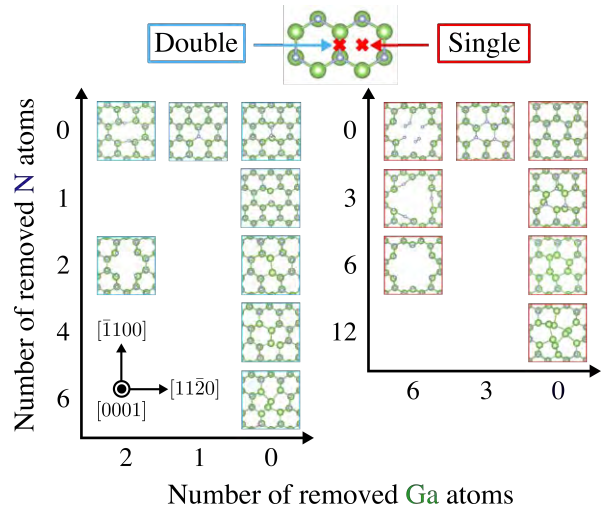


Figure 1: The 16 core types of the screw dislocations. A red cross in the top panel denotes the position of the dislocation line. The left is for $D(n | m)$ and the right is for $S(n | m)$, where n is the number of removed Ga and m is that of N.

in which the dislocation line is at the center of the single hexagon; Another is called double core, in which the dislocation line is at the middle of the bond of hexagon. n and m represent the numbers of Ga and N atoms removed from the fully filled structures. An example of $D(0 | 0)$ is shown in Fig. 2

Those first-principles calculations are done by using the Vienna Ab initio Simulation Package (VASP) [2] which is based on the projector augmented-wave (PAW) method. The exchange-correlation energy is treated within the generalized gradient approxima-

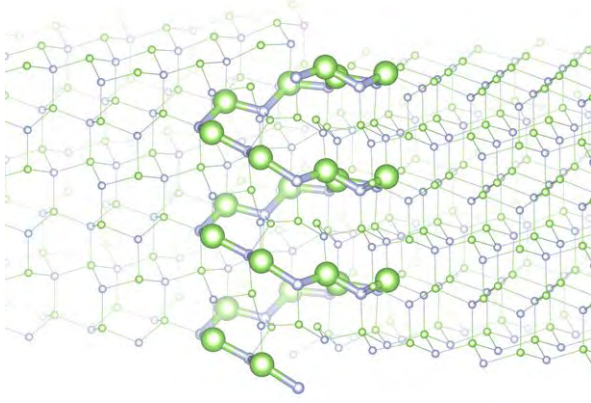


Figure 2: The core structure $D(0 | 0)$. Green and blue spheres denote Ga and N, respectively. The atoms surrounding the dislocation line are enlarged to emphasize the position.

tion (GGA) with the Perdew-Burke-Ernzerhof functional. We also use the Heyd-Scuseria-Ernzerhof (HSE) hybrid functional to evaluate more accurate electronic levels in the band gap. The unit cell contains about 800 Ga and N atoms in total. The GaN pillar is surrounded by the vacuum on the lateral directions perpendicular to the $[0001]$. We expect that this vacuum relaxes artificial strain caused by rounding the lateral surfaces. The dangling bonds on the lateral surface of the GaN pillar are terminated by ≈ 100 fictitious hydrogens. The schematic picture of the unit cell on the $[0001]$ plane is shown in Fig. 3. The integration over Brillouin zone is taken with 4 sampling points along the $[0001]$ direction. The structural optimization is performed for each core structures.

We found that $D(0 | 2)$, $S(0 | 3)$, and $S(0 | 6)$ are stable. Then we replace one Ga atom in these three core structures with an Mg atom. The relative position of the Mg from the dislocation line is sampled. The resultant binding energy of the Mg shows that Mg is attracted by the screw dislocation and the electronic levels in the gap elevate towards the conduction band, as mentioned above.

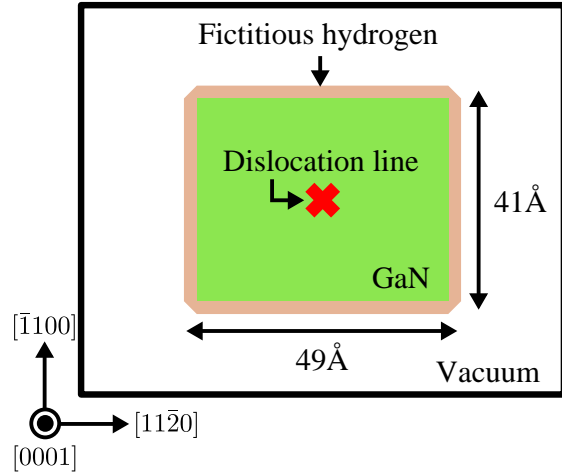


Figure 3: A schematic picture of the $[0001]$ plane of the unit cell. The green region denotes GaN and it is terminated by the fictitious hydrogen atoms. The outermost region is the vacuum. A red cross denotes the position of the dislocation line.

References

- [1] T. Nakano, Y. Harashima, K. Chokawa, K. Shiraishi, A. Oshiyama, Y. Kangawa, S. Usami, N. Mayama, K. Toda, A. Tanaka, Y. Honda, and H. Amano: arXiv, 2004.06876 (2020).
- [2] G. Kresse and J. Furthmuller: Phys. Rev. B **54**, 11169 (1996).

Ab Initio Band Structure Calculation of InSb Using VASP Based on Hybrid Density Functional Theory

Hiroki I. FUJISHIRO, Yoshitaka MATSUMOTO, Takahiro SUZUKI, and Akira ENDOH

Department of Applied Electronics,

Tokyo University of Science, Niijuku, Katsushika, Tokyo 125-8585

Terahertz-wave frequency range (0.1 to 10 THz) will be the major resources in future communication and sensing systems. InSb channel high electron mobility transistors (HEMTs) are one of the most promising devices that can operate in the terahertz band. Although InSb has the lightest electron effective mass in III-V semiconductors, the lattice constant of InSb is the largest. Therefore, compressive strain is always applied to the InSb channel.

In our previous work [1], we carried out Monte Carlo (MC) simulations of InSb channel HEMTs to predict device performance. We used the band parameters calculated by the empirical pseudopotential method [2]. However, the band structure obtained from the first-principles calculation seems to be preferable. In 2018, we carried out ab initio band structure calculations

of unstrained and compressively strained InSb using Vienna Ab initio Simulation Package (VASP) based on the method in the local density approximation to obtain band parameters [3]. We obtained nonzero bandgap energy E_g values by using PBE0 (Perdew-Burke-Ernzerhof 0) as a functional. In this work, we investigated functionals used for band structure calculation in order to obtain the E_g values close to the literature ones.

We studied the hybrid coefficient of the density functional [4]. The hybrid functional used in this work was a modification of PBE0. The functional is constructed by the mixing of a fraction α of the Fock exchange with a fraction $1 - \alpha$ of the PBE exchange. The exchange-correlation energy E_{xc} can be expressed by the following equation:

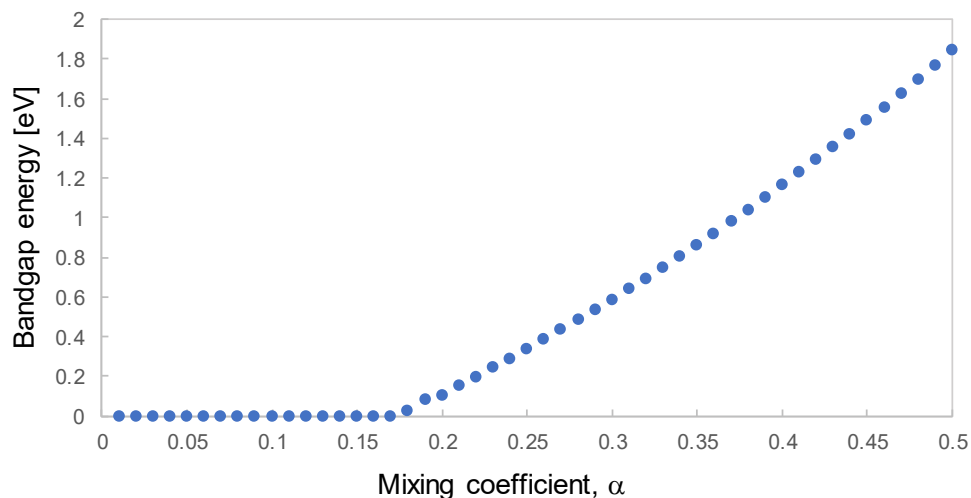


Fig. 1 Calculated bandgap energy as a function of mixing coefficient, α .

$$E_{xc} = \alpha E_x + (1 - \alpha) E_x^{PBE} + E_c^{PBE} \quad (1)$$

where E_x is the Fock exchange, E_x^{PBE} is the PBE exchange, and E_c^{PBE} is the PBE correlation [4]. In PBE0, the mixing coefficient $\alpha = 0.25$. In our previous work [3], we obtained the bandgap energy E_g values of unstrained and compressively strained InSb. However, the E_g values are too large when using $\alpha = 0.25$ (PBE0). We calculated the bandgap energy values as a function of α . Figure 1 shows the calculation results of bandgap energy. We obtained the closest bandgap energy E_g to the previous work [5, 6] with $\alpha = 0.21$.

Table 1 summarizes the band parameters of InSb in Refs. [3, 5, 6] and in this work. In our previous work [3], we obtained the bandgap energy E_g of 0.34 and 0.48 eV for unstrained (0%) and compressively strained (-1.32%) InSb, respectively. The E_g value for unstrained InSb in [3] is much larger than that in [5, 6]. In the present work, the E_g value was relatively reasonable because the mixing coefficient α was set to match the “general” bandgap value of InSb [5, 6]. On the other hand, the increase in E_g when compressive strain is applied seems to be small for $\alpha = 0.21$. The electron effective mass in the Γ valley m_{Γ}^* of unstrained InSb is almost same as the values in the previous results [3, 5, 6].

However, the increase in the value of m_{Γ}^* for the -1.32% compressively strained InSb also appears to be small. Furthermore, there is room for reconsideration of the energy difference between Γ and L valleys, $E_{\Gamma-L}$ and Γ and X valleys, $E_{\Gamma-X}$.

Regarding the mixing coefficient of the density functional, further work is necessary considering the correspondence with various literature and experimental values.

References

- [1] T. Takahashi, S. Hatsushiba, S. Fujikawa, and H. I. Fujishiro: Phys. Status Solidi A **214** (2017) 1600599.
- [2] H. Nishino, I. Kawahira, F. Machida, S. Hara, and H. I. Fujishiro: Proc. 22nd Int. Conf. on IPRM (2010) p. 156.
- [3] H. I. Fujishiro, Activity Report 2018, Supercomputer Center, Institute for Solid State Physics, The University of Tokyo, p. 137.
- [4] T. Garwood, N. A. Modine, and S. Krishna: Infrared Physics & Technology, 2017.
- [5] M. Levinshtein, S. Rumyantsey, and M. Shur: Handbook Series on Semiconductor Parameters in 2 Volumes, World Scientific, 1996.
- [6] H. Rodilla, T. González, D. Pardo, and J. Mateos: J. Appl. Phys. **105** (2009) 113705.

Table 1 Main band parameters of InSb.

	0% [5, 6]	0% (VASP) [3]	-1.32% (VASP) [3]	0% (VASP) [This work]	-1.32% (VASP) [This work]
E_g (eV)	0.18	0.34	0.48	0.151	0.154
m_{Γ}^*	0.014	0.015	0.022	0.012	0.013
$E_{\Gamma-L}$ (eV)	0.76	1.04	1.06	1.05	1.05
$E_{\Gamma-X}$ (eV)	0.46	2.64	2.69	2.64	2.64

First-principles investigation of electronic properties of carbon nanotubes and graphene

Yoshitaka FUJIMOTO

*Department of Physics, Tokyo Institute of Technology
Ohokayama, Meguro, Tokyo 152-8551*

Graphene and carbon nanotubes (CNTs) show high charge mobility at room temperature, and therefore they are expected to be a promising device material to be used in nano-electronics such as field-effect transistors. Substitutional doping is one of the effective ways to tune the electronic properties of graphene and CNTs, and is also shown to improve the chemical reactivity to adsorbates. Therefore doped graphene and doped CNTs are a good candidate for future sensor device materials.

We here present the adsorption properties of toxic NO and NO₂ molecules on the boron-doped graphene and (8,0) CNT using a first-principles density-functional calculation [1, 2, 3]. It is found that the NO and NO₂ molecules can be adsorbed strongly with short distances and large adsorption energies on the B-doped monolayer graphene [2]. For the AB-stacked bilayer graphene, NO and NO₂ molecules can be also strongly adsorbed [1, 3]. It is also found that the adsorption energies of NO and NO₂ molecules on the B-doped (8,0) CNTs are much larger than those of monolayer and bilayer graphenes.

Table 1 lists the adsorption energies and the

Table 1: Adsorption energy E_a (eV) and distance d (Å) between adsorbed molecule and B atom for molecules adsorbed on B-doped monolayer and AB-stacked bilayer graphenes.

	Monolayer		Bilayer	
	E_a	d	E_a	d
NO	-1.23	2.15	-1.19	2.14
NO ₂	-1.16	1.59	-1.13	1.60

distances between the B atom in the doped graphene layer and the adsorbed molecules for NO and NO₂ molecules on the B-doped monolayer and AB-stacked bilayer graphenes. The NO and NO₂ molecules are found to be adsorbed strongly with short distances and large adsorption energies on the B-doped monolayer graphene. For the case of the AB-stacked bilayer graphene, it is interesting that the adsorption energies as well as the binding distances for the adsorptions of the NO and NO₂ molecules are comparable to those of the B-doped monolayer graphene.

We also study the adsorption energies and the binding distances of NO and NO₂ molecules on the B-doped (8,0) carbon nanotubes (CNTs). Like monolayer and bilayer graphenes, the NO and NO₂ molecules are found to strongly bind on the B-doped (8,0) CNTs with the large adsorption energies and the short binding distances. Furthermore, the adsorption energies for NO and NO₂ molecules on the B-doped (8,0) CNTs are considerably larger than those on the B-doped monolayer as well as the B-doped bilayer graphenes due to the curvature effects.

In summary, we have studied the adsorption properties of the toxic NO and NO₂ molecules on the B-doped graphene and B-doped (8,0) CNT, based on first-principles density-functional calculations. The NO and NO₂ molecules strongly bind on the B-doped monolayer and bilayer graphenes. The adsorption energies of NO and NO₂ molecules on the B-doped (8,0) CNTs are larger than those on the B-doped graphene layers.

References

- [1] Y. Fujimoto and S. Saito, Chem. Phys. **478**, 55 (2016).
- [2] Y. Fujimoto and S. Saito, Jpn. J. Appl. Phys. **58**, 015005 (2019).
- [3] Y. Fujimoto and S. Saito, to be published.

Study of appearance of ferromagnetism by electric field application to Pt thin film

Tatsuru Yamada¹, Hiroyuki Kageshima², and Tetsuya Sato¹

1Department of Applied Physics and Physico-Informatics, Keio University, 3-14-1 Hiyoshi, Kohoku-ku, Yokohama 223-0061, Japan

2Graduate School of Natural Science and Technology, Shimane University, 1060 Nishikawatsu-cho, Matsue 690-8504, Japan

Recently, It was reported that ferromagnetism appears in an oscillatory manner in the Pt(100) thin films depending on the film thickness[1][2]. This property suggests that magnetism in Pt(100) thin film can be controlled by electric field. In order to clarify the magnetism change with application of electric field, we performed first-principles calculation using the PHASE/0 program.

The first-principles calculation based on the DFT within the GGA was performed, where Vanderbilt type pseudopotential and a plane-wave basis set were used to evaluate electric structure and magnetization of Pt(100) thin film. We used $88 \times 88 \times 1$ k points (based on Monkhorst-Pack) and a cutoff energy of 36 Rydberg.

We calculated lattice constant that minimizes the energy. Using the obtained lattice constant, we calculated the Pt layer thickness dependence of the magnetic moment of Pt slab. Calculations of electronic structure for the free-standing Pt(100) thin films from 2 monolayers(ML) up to 17 ML were performed and it was clarified

that the ferromagnetism appeared in oscillatory manner with a period of 6 ML only when spin-orbit interaction (SOI) was not included (Fig.1). This oscillatory behavior agrees with the experiment[2]. These results suggest that magnetism in Pt(100) thin film is intrinsically unrelated to SOI. For the next step, we calculate magnetism in Pt(100) thin film under application of electric field.

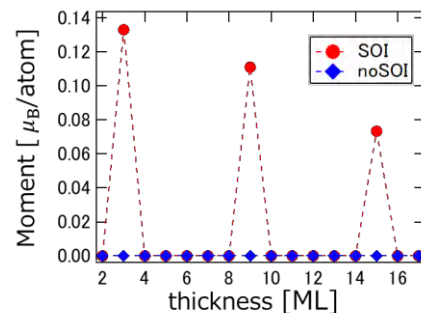


Fig. 1: Thickness-dependent magnetic moment per Pt atom.

References

- [1] A. M. N. Niklasson *et al.*: Phys. Rev. **B** 75, 172402 (2007).
- [2] K. Ochiai *et al.*: JPS2019, Gifu, 10aPS27 (2019).

Ab Initio Calculation of High-Rate Deposition of Copper Film by Low-Pressure Chemical Vapor Deposition with CuI on Ru Substrate

Tatsuya JOUTSUKA

Institute of Quantum Beam Science,

Graduate School of Science and Engineering, Ibaraki University, Hitachi, 316-8511 Ibaraki, Japan

We have studied low-pressure chemical vapor deposition of Cu on Ru substrate using CuI [1] using VASP program package (MPI parallelization with multiple threads). This year, we focused on the molecular mechanism of adsorption, migration and desorption. This is a collaborative work with the experimentalist [2] (Prof. Satoshi Yamauchi at Ibaraki University), who conducted the LPCVD experiment.

In this study, we elucidated the molecular mechanism of Cu deposition using copper(I) iodide (CuI) on Ru substrate by low-pressure chemical vapor deposition through electronic structure calculations. Using density functional theory calculations, we show that CuI molecules adsorb and decompose exothermically due to a strong adsorption of iodine atoms onto the Ru(001) surface. The rate-limiting step of the Cu deposition is found to be the desorption of iodine molecules from the Cu(111) surface, suggesting that the removal of iodine species is necessary to achieve the high-rate deposition of highly-conductive copper films for ultra large scale

integration metallization.

Based on this study, we are now extending our calculations to analyze the dynamical properties in more detail. In addition, new sets of precursor and substrate are explored for ultra large scale integration metallization together with experiment.

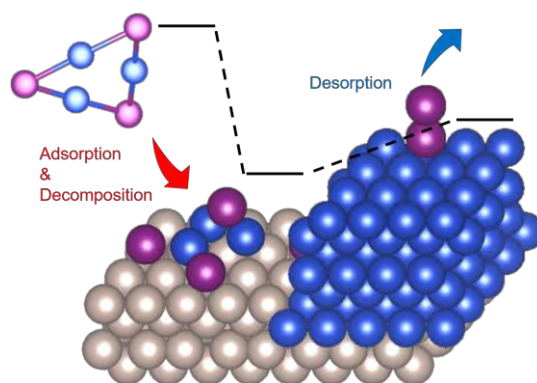


Fig. 1: Molecular mechanism of LPCVD of Cu.

References

- [1] T. Joutsuka, S. Yamauchi: Chem. Phys. Lett. **741** (2020) 137108.
- [2] T. Nishikawa, K. Horiuchi, T. Joutsuka and S. Yamauchi: submitted.

Theoretical Analysis of Photocatalytic Reaction Mechanism at Titanium Dioxide Interfaces

Tatsuya JOUTSUKA

Institute of Quantum Beam Science,

Graduate School of Science and Engineering, Ibaraki University, Hitachi, 316-8511 Ibaraki,

Japan

We have studied photocatalytic reaction mechanism at anatase TiO_2 surfaces [1] using cp2k program package (MPI parallelization with multiple threads). This year, we focused on the energetics and structure during the hole migration. This is a collaborative work with the experimentalist [2] (Prof. Satoshi Yamauchi at Ibaraki University), who conducted the LPCVD experiment.

Anatase TiO_2 shows a high photocatalytic activity to decompose organic compounds and plays a crucial role in chemistry and physics. To enhance the photocatalytic activity, proper control of surface properties is crucial and the molecular-level mechanism can offer valuable insight. We herein clarify the facet dependence of hole trapping at the anatase TiO_2 surface by density functional theory (DFT) calculations using the constrained DFT method with the hybrid functionals. The photocatalytic activity by UV irradiation around 365 nm in methylene blue aqueous solution is significantly high, which is two-order larger than that on the multi-oriented TiO_2 . The DFT calculations show the (112) surface can stabilize water

adsorption and the photogenerated hole can be trapped not on the neat surface but on the hydroxylated surface better at the (112) and (001) surfaces. The experimental and theoretical findings elucidate that the (112) facet shows the larger stabilization of absorbed water and trapped holes than other facets by larger structural relaxation at the surface.

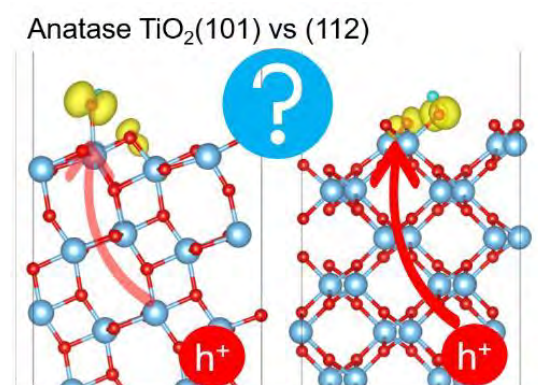


Fig. 1: Molecular mechanism of hole migration.

References

- [1] T. Joutsuka, H. Yoshinari, K. Yamamoto and S. Yamauchi: in preparation for submission.
- [2] S. Yamauchi, K. Yamamoto, and S. Hatakeyama: *J. Chem. Eng.*, **3** (2015) 28–38.

Search and realization of novel electronic properties of solid surfaces and interfaces and of small particles

Takeshi INAOKA

*Department of Physics and Earth Sciences, Faculty of Science,
University of the Ryukyus, 1 Senbaru, Nishihara, Okinawa 903-0213*

We mention two subjects which we addressed this year.

Graphene is a very popular single-layer structure of carbon (C) atoms arranged in a hexagonal lattice. However, we explore different monolayer structures of C atoms. Previously, we showed that the monolayer structure in Fig. 1 is stable, and that the electron system is a semi-metal which is characterized by the electron pocket around the \bar{M} point and the hole pocket around the $\bar{\Gamma}$ point. We applied the tight-binding method to this system and clarified its utility and limitation for this system.

In scanning tunneling microscopy (STM) light emission spectra of Ni(110)-(2x1)-O surface emerge stepwise structures due to oxygen (O) atom vibration parallel to the surface [1]. These structures are considered to arise from the change in the local density of states (LDOS) below the STM tip owing to the vibration [1]. Using first-principles calculations, we examined the variation in LDOS due to adiabatic in-plane displacement of an adsorbed O atom.

We employed the program package 'Vienna Ab initio Simulation Package' (VASP) [2,3] on systems B and C.

(1) Application of the tight-binding method to a novel single-layer structure of carbon atoms [4]

The above-stated electron pocket and the hole pocket are formed by π -orbital-derived bands around the Fermi level E_F . Therefore, we can expect that the tight-binding method in terms of p_z orbitals of C atoms is effective for this system. Figure 2 exhibits the band dispersion on the $\bar{\Gamma} - \bar{M}$ line for the hybrid density-functional method (Hyb) and the tight-binding method (TB). The transfer integral for a diagonal nearest-neighbor p_z pair and

that for a lateral nearest-neighbor p_z pair were chosen to be -2.9 eV and -3.2 eV, respectively. In view of band dispersions on other symmetric dispersion lines as well, we found that the tight-binding method can reproduce adequately the band dispersions around E_F , and consequently the electron and hole pockets. The tight-binding method provides a useful tool for evaluating electronic properties of this system arising from π -orbital-derived bands.

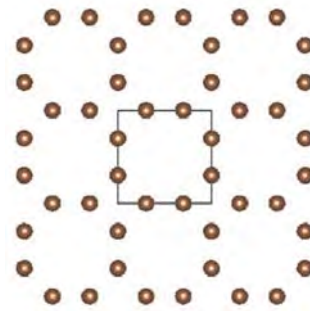


Fig. 1 Carbon monolayer structure considered here

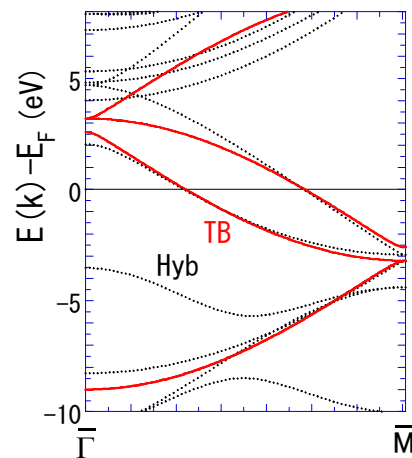


Fig. 2 Band dispersions on the $\bar{\Gamma} - \bar{M}$ line for the hybrid density-functional method (Hyb) and the tight-binding method (TB).

(2) Electronic structure of Ni(110)-(2x1) O surface [5]

Last year, by means of the generalized gradient approximation, we investigated the ground state of a proposed promising structure, namely, the missing-row reconstructed O p(2x1)/Ni(110) surface. We optimized a slab composed of 11 Ni atom layers and an O atom adsorbed at each surface. This year, for a 21 Ni atom-layer slab, we treated phonon vibration adiabatically, and examined the change in the orbital-projected DOS (op-DOS) at each atom when O atoms are displaced in the surface-parallel direction. We optimized the structure when the distance between the O atom and the Ni atom numbered 40 (see Fig. 3) in the y direction is reduced by a certain length and fixed. The height of the O atom measured from the No.40 Ni atom is 0.29 Å in the ground state. As the O atom gets closer to the No.40 Ni atom by 0.3 Å, this height rises to 0.71 Å. We pay attention to p orbitals of the O atom and d orbitals of Ni atoms. We analyzed the variation in the op-DOS at each atom due to O-atom displacement. Here, we present a part of our results for majority spin originating from ferromagnetic Ni. Figure 4 exhibits the p_y -projected DOS at the O atom which is quite important in the STM experiment with the tip placed right above the O atom. The broken curve marked 'GS' and the full curve labelled as '0.3 Å disp' display the results for the ground state and for 0.3 Å displacement in the y direction, respectively. The peak around the Fermi level E_F shifts to the higher energy side, and the peak intensity increases with O-atom displacement. The peak position reaches E_F at 0.3 Å displacement. The peak in the p_y -projected DOS for minority spin also shows a similar shift to the higher energy side. Our analysis including d -orbital-projected DOS at Ni atoms indicated that approach of the O atom to the No.40 Ni atom leads to stronger hybridization between the p_y orbital of the O atom and the d_{yz} orbital of the Ni atom. The above peak shift implies that the phonon vibration affects the STM light emission through the change in opDOS.

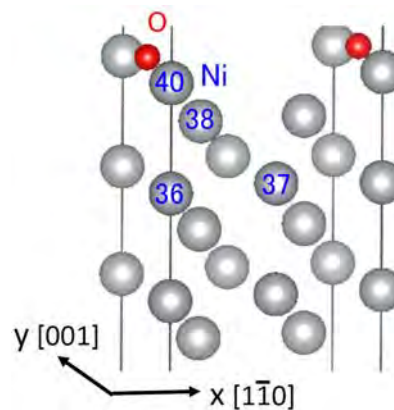


Fig. 3 Optimized slab structure of O p(2x1) Ni(110) surface. The slab is composed of 21 Ni atom layers and an adsorbed O atom at each surface.

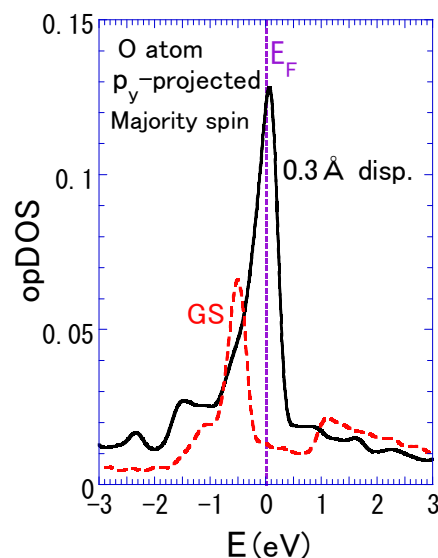


Fig. 4 p_y -orbital-projected density of states at the adsorbed O atom for the ground state and for O-atom displacement by 0.3 Å.

References

- [1] Y. Uehara, T. Inaoka, T. Nishio, and S. Katano: J. Appl. Phys. **123** (2018) 224302 (8 pages).
- [2] G. Kresse and J. Hafner: Phys. Rev. B **47** (1993) 558–561.
- [3] G. Kresse and J. Furthmüller: Comput. Mat. Sci. **6** (1996) 15–50.
- [4] T. Inaoka and M. Furugen: unpublished.
- [5] T. Inaoka and Y. Uehara: to be prepared.

Atomic and electronic structures of intermetallic compound catalysts

Kazuki NOZAWA

Department of Physics and Astronomy, Kagoshima University
1-21-35, Korimoto, Kagoshima 890-0065

In this fiscal year we have studied the initial stage of oxidation of Ni₃Al(210) and PdZn(111) surfaces. All calculations are carried out using VASP with the PAW method and the PBE exchange-correlation functional.

It was reported that Ni₃Al is highly active for hydrogen production from methanol and methane, and its catalytic performance is considered to be attributed to the selective oxidation and hydroxylation of Al and the formation of metallic Ni particles at low oxygen partial pressures[1]. An X-ray photoelectron spectroscopy study shows Al oxide is formed preferentially in the beginning of the oxidation process, and Ni oxides start to form at 1.6 ML oxygen coverage[2]. We first searched for the stable adsorption sites at 0.25 and 0.5 ML. In both cases, it turned out that the most stable adsorption site is a pseud-threefold site surrounded by two Al atom at the top layer and one Ni atom at the second layer. The adsorption geometry is similar to the result reported for NiAl(110)[3], but this structure is not consistent with the XPS experiment showing no sign of Ni oxides formation at this coverage. Inspired by the previous study[3], we introduced some antisite defects in the oxidized surface, and it is found that antisite defect stabilizes the surface when they form a specific structure. According to the simulated STM images using the Tersoff-Hamann approximation, this structure shows a unique image easily distinguished from other structures with different antisite arrangement or without the defect.

Although pure Pd is not active for methanol steam reforming (MSR), PdZn exhibits comparable catalytic activity and selectivity to the conventional Cu catalyst in MSR. Recently, some groups reported that ZnO formed during the reaction is essential for the catalytic performance of PdZn. However, this is not straightforward because Zn has no d-state around the Fermi level implying the chemical inactivity of ZnO. We first determined the stable adsorption structure of oxygen on PdZn(111), and investigated the electronic structure of this system. We previously reported that bulk PdZn has a similar electronic structure to Cu[5], but the Pd 4d-band of PdZn is broadened when oxygen is adsorbed. It was also found that Zn-d states appear below the Fermi level when oxygen adsorbs on the most stable site.

References

- [1] D. H. Chun *et al.*, J. Catal. **243** (2006)99, Y. Xu *et al.*, J. Phys. Chem. C **114** (2010)6047.
- [2] Y. Xu *et al.*, Appl. Surf. Sci., **39** (2017)18.
- [3] A. Y. Lozovoi *et al.*, Phys. Rev. Lett., **85** (2000)610.
- [4] K. Yamaguchi, Master Thesis (Kagoshima University, 2020).
- [5] A. P. Tsai *et al.*, Acc. Chem. Res. **50** (2017)2879.

Switching of magnetism via modifying phase shift of quantum-well states by tailoring the interface electronic structure

Shunsuke SAKURAGI

Institute for Solid State Physics, University of Tokyo

Kashiwa-no-ha, Kashiwa, Chiba 277-8581

In this project, we expanded Phase model for the Quantum-well states (QWs), and suggested the method to control the QW induced ferromagnetism in Pd(100) by changing scattering phase shift. Then, we verified this theory using density functional theoretical (DFT) calculation [1].

The following Phase model, describing the QWs, indicates the conditions under which a standing wave can exist:

$$2k_z d + \Phi = 2\pi n, \quad (1)$$

where k_z is the confined wave number, d is the film thickness, Φ is the scattering phase shift at surface and interface, and n is an integer quantum number. Previous experiments and DFT calculations showed that the period of oscillation by modification of magnetic properties via QWs is expressed as $p = 1/k_{Fz}$, where p is the period of oscillation (where thickness of the film is d) and k_{Fz} is the vertical Fermi wave number i.e. the Fermi wave number of the confined band. This and eq. (1) indicate that the confined wave number k_z reaches Fermi energy periodically depending on the film thickness d and the phase shift Φ is unrelated to the period of oscillation.

Previous DFT calculations and experiments predicted that $d_{xz,yz}$ electrons are confined at the QWs of Pd(100) films, and this induces ferromagnetism in Pd(100) ultrathin films. These orbital characters express one dimensional dispersion in the in-plane direction. For these

electrons, phase shift Φ of the QWs might depend on k_x, k_y , and ϵ . Thus, it is necessary to expand the phase model to include k_x and k_y (i.e. the wave number of the in-plane direction \mathbf{k}_{\parallel}) dependencies.

First, $k_z(n) = (2\pi n - \Phi) / 2d$ is defined from eq. (1). Then, the n -th energy level of Pd(100) film quantum well $\epsilon_{\text{QW}}(n, \mathbf{k}_{\parallel})$ can be obtained from the Pd bulk energy band structure $\epsilon(k_z, \mathbf{k}_{\parallel})$ as

$$\epsilon_{\text{QW}}(n, \mathbf{k}_{\parallel}) = \epsilon(k_z(n), \mathbf{k}_{\parallel}), \quad (2)$$

where $\mathbf{k}_{\parallel} = (k_x, k_y)$ is the in-plane wave vector because the band dispersion of the QWs is a projection of the specific bulk band. Then, the binding energy of the quantum-well state ϵ_{QW} in Pd(100) can be described by expanding ϵ_{QW} around the Fermi energy as

$$\begin{aligned} \epsilon_{\text{QW}}(n, \mathbf{k}_{\parallel}) &\sim \epsilon_{\text{F}} + [k_z(n) - k_{Fz}] \frac{\partial \epsilon}{\partial k_z}(k_{Fz}, \mathbf{k}_{\text{F}\parallel}) \\ &\quad + \Delta \mathbf{k}_{\parallel} \cdot \frac{\partial \epsilon}{\partial \mathbf{k}_{\parallel}}(k_{Fz}, \mathbf{k}_{\text{F}\parallel}), \end{aligned} \quad (3)$$

where $\mathbf{k}_{\text{F}\parallel}$ is the in-plane Fermi wave vector, $\Delta \mathbf{k}_{\parallel} = \mathbf{k}_{\parallel} - \mathbf{k}_{\text{F}\parallel}$, and $\epsilon_{\text{F}} = \epsilon(k_{Fz}, \mathbf{k}_{\text{F}\parallel})$.

Considering Pd bulk band dispersion, dispersion of $d_{xz,yz}$ has a flat shape around Γ point and zone edges. Therefore, in Pd(100) film, the following relation is satisfied:

$$\frac{\partial \epsilon}{\partial \mathbf{k}_{\parallel}}(k_{Fz}, \mathbf{k}_{\text{F}\parallel}) \sim 0. \quad (4)$$

According to eq. (5), this means that $\epsilon_{\text{QW}}(n, \mathbf{k}_{\parallel})$ almost coincides with the Fermi energy ϵ_{F} being independent of \mathbf{k}_{\parallel} , if $k_z(n)$ matches $k_{\text{F}z}$. Then the density of states at the Fermi energy $D(\epsilon_{\text{F}})$ diverges and induces ferromagnetism from the standpoint of the Stoner criterion. The condition $k_z(n) = k_{\text{F}z}$ leads to oscillatory appearance of ferromagnetism with the periodicity p depending on the film thickness d .

Now we extend the theory above as shall be discussed later, the phase shift Φ generally depends on \mathbf{k}_{\parallel} . If we permit such \mathbf{k}_{\parallel} -dependence for Φ , $k_z(n)$ also depends on \mathbf{k}_{\parallel} . Since $k_z(n, \mathbf{k}_{\parallel}) = (2\pi n - \Phi(\mathbf{k}_{\parallel})) / 2d$ eq. (5) must be modified into

$$\begin{aligned} \epsilon_{\text{QW}}(n, \mathbf{k}_{\parallel}) &\sim \epsilon_{\text{F}} \\ &+ [k_z(n, \mathbf{k}_{\text{F}\parallel}) - k_{\text{F}z}] \frac{\partial \epsilon}{\partial k_z}(k_{\text{F}z}, \mathbf{k}_{\text{F}\parallel}) \\ &+ \Delta \mathbf{k}_{\parallel} \cdot \frac{\partial \epsilon}{\partial \mathbf{k}_{\parallel}}(k_{\text{F}z}, \mathbf{k}_{\text{F}\parallel}) \\ &+ \Delta \mathbf{k}_{\parallel} \cdot \frac{\partial k_z}{\partial \mathbf{k}_{\parallel}}(n, \mathbf{k}_{\text{F}\parallel}) \frac{\partial \epsilon}{\partial k_z}(k_{\text{F}z}, \mathbf{k}_{\text{F}\parallel}), \end{aligned} \quad (5)$$

Because of the fourth term on the right hand side of eq. (7), $\epsilon_{\text{QW}}(n, \mathbf{k}_{\parallel})$ is no longer the constant for \mathbf{k}_{\parallel} and the divergence of $D(\epsilon_{\text{F}})$ does not occur often, even when $k_z(n, \mathbf{k}_{\text{F}\parallel})$ matches $k_{\text{F}z}$ and eq. (6) is satisfied. Furthermore, the divergence of $D(\epsilon_{\text{F}})$ can be promoted if we appropriately modify the \mathbf{k}_{\parallel} -dependence of Φ even when $k_z(n, \mathbf{k}_{\text{F}\parallel})$ does not match $k_{\text{F}z}$ or eq. (6) is not satisfied. Thus, we can expect that a fine control of the \mathbf{k}_{\parallel} -dependence of phase shift Φ can reduce the magnetism in a similar way to induce the magnetism for non-magnetic materials.

In the case of quantum confinement of Pd $d_{xz,yz}$ electrons, which we discussed in this paper, the hybridization between the d -electron wave function of the stacking layer and Pd at the zone edge (S-point) is intrinsically important for producing a flat band. Because typical 3, 4, 5d transition metals forming fcc structure have d -electron bands around the S-point, this effect generally occurs by stacking of these

transition metals on Pd(100) films. In addition, if the d -electron band of a stacking layer appears near the Fermi energy at S-point, magnetic change via modifying phase shift might be clearly observed, as indicated in eq. (5).

The present DFT calculation using Phase/0 code [2] well verified the above theory [1]. The electronic states of Au stacked Pd film were modified by changing the Au-Pd layer distance, and the QW induced ferromagnetism was controlled. Contrastingly, we observed that stacking of Al, which contains only s -electrons around Fermi energy, cannot modify the shape of the band dispersion of d -electron QWs because there is no hybridization between the s - and d -electrons. We see above behaviour from the calculated band dispersion and the shape of wave function. Our findings suggest a mechanism for controlling magnetism using modification of interface electronic states in metal-nano structures.

References

- [1] Shunsuke Sakuragi, Hiroyuki Kageshima, and Tetsuya Sato : Phys. Rev. B. **101** (2020) 014410.
- [2] <https://azuma.nims.go.jp/software/phase>

Stability of vacancy cluster and interaction with impurities in tungsten lattice

Kazuhito Ohsawa

Institute for Applied Mechanics,

Kyushu University, Kasuga-koen, Kasuga, Fukuoka 816-8580

Introduction

The study of lattice defects in tungsten (W) are important issue in the field of fusion reactor because W is one of the plausible plasma facing materials (PFMs). Usually, hydrogen (H) and H isotopes seldom dissolve in W. However, H atoms are trapped in the vacancy-type lattice defects (vacancy clusters etc.) created in the irradiation circumstance. In particular, tritium (T) retention in the PFM is one of the serious problem associated with fusion reactor because T is radioisotope whose half-life is 12 years. So, the stability and binding energy of the vacancy clusters in the bulk W were investigated by simulations and experiments.

Small vacancy clusters in the W lattice has been reported to be unstable by the first-principle calculations. On the other hand, such small clusters and their growth to larger clusters were observed in positron annihilation lifetime measurements. In the present work, we investigate the reason why the small vacancy clusters exist in the W lattice. The vacancy clusters are stabilized by impurities. In particular, they are greatly stabilized by the presence of oxygen.

Simulation method

The binding energies of the vacancy clusters were calculated in terms of first-principle calculations based on density functional theory. We used the Vienna ab-initio simulation package (VASP). A large simulation cell, composed of 6x6x6 bcc lattice (432 atoms), were used in order to reduce the effects of periodic boundary condition imposed on the simulation cell. The cut-off energy of plane wave was 520eV.

The binding energy of vacancy cluster composed of n mono-vacancies V_n was defined

$$E_b(V_n) = nE[V] - \{E[V_n] + (n-1)E[P]\},$$

where E is cohesive energy of the supercell and P indicates perfect lattice of W. Positive binding energy corresponds to attractive interaction. Similarly, the binding energy of vacancy cluster containing an oxygen V_nO is

$$E_b(V_nO) = E[VO] + (n-1)E[V] - \{E[V_nO] + (n-1)E[P]\}.$$

Results

We investigated the most stable structure of vacancy clusters composed of n mono-vacancies without and with an oxygen ($n \leq 6$). We examined di-vacancy V_2 in the first (1nn),

second (2nn), and third (3nn) nearest neighbor configurations. The di-vacancy in the 1nn configuration is the most stable among them. However, small vacancy clusters, V_2 and V_3 , are energetically unstable compared with isolated mono-vacancies, as shown in Fig. 1. On the other hand, larger vacancy clusters, V_n ($n \geq 4$), are stable. Therefore, if V_4 were nucleated in the bulk W, the vacancy cluster growth would spontaneously occur.

The presence of impurities in W lattice contributes to the stabilization of vacancy clusters. Fig. 2 shows the most stable structure of vacancy clusters with an oxygen V_nO . The most stable structure of V_2O is the 2nn configuration, which is different from that without an oxygen V_2 . According to Fig. 1, all vacancy clusters trapping an oxygen are stable and the binding energy increases as a function of the number of vacancies composed of the vacancy clusters.

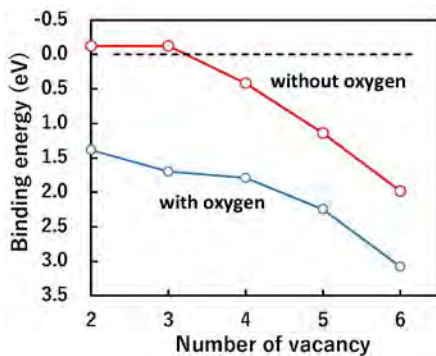


Fig. 1: Binding energies of vacancy clusters without and with an oxygen, (V_n and V_nO).

Discussion

Growth of vacancy cluster in W lattice was observed in the positron annihilation lifetime measurements but the vacancy clusters were expected to be energetically unstable in the first-principle calculations. We examined the stabilization effects by impurities contained in the W specimen. Even if high purity metal specimen were prepared, some kinds of impurities would be inevitably contained. Carbon, nitrogen, and oxygen are the typical inevitable impurities in the actual metals. Actually, vacancy clusters are greatly stabilized by the presence of such impurities. Besides, the diffusivity and binding energy to a mono-vacancy of oxygen in the W lattice are remarkably larger, compared with other impurities. The presence of oxygen is the most plausible candidate to explain the vacancy cluster growth observed in the positron annihilation lifetime measurements.

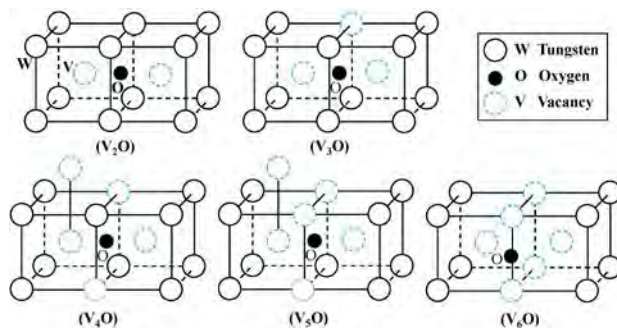


Fig. 2: Schematic view of the most stable structure of vacancy clusters trapping an oxygen (V_nO). The dotted circles indicate positions of mono-vacancies in bcc W lattice.

First principles study on static structure of glass materials

Akihide KOURA

Student Affairs Department,

Kumamoto University, Kurokami, Kumamoto, Kumamoto 860-8555

Cu_2GeTe_3 (CGT) is one of fast phase transition materials. This material changes between crystalline and amorphous phases quickly like $\text{Ge}_2\text{Sb}_2\text{Te}_5$. In order to clarify the phase transition mechanism, many experimental and theoretical studies were carried out so far. From results of anomalous x-ray scattering and extended x-ray absorption fine structure experiments, the local and intermediate range structures of glass were preserved structural motifs of the crystal [1]. However, the ring structure from theoretical study [2] was different from the experimental result [1]. In order to clarify the structure of amorphous CGT, we have performed *ab initio* molecular dynamics simulations.

In this study, we made two amorphous states, which were called a1 and a2 amorphous states. Figure 1 shows the distribution of number of M -membered ring $P(M)$ [3]. In the crystalline state, there are only six-membered rings. In the amorphous state, some six-membered rings are distorted from 6 to 3+5 rings, and distorted six-membered rings also remain in the amorphous state [1]. Using ring analysis method for our *ab initio* molecular dynamics simulations, the similar distribution

of number of ring to that from the experiment [1] was obtained [3]. This result shows that the distribution of six-membered ring is higher than that by Chen *et al.* [2]. The coexistence of 3+5 and distorted 6 membered rings would enhance the fast phase transition between crystal and amorphous phases.

References

- [1] J. R. Stellhorn, B. Paulus, S. Hosokawa, W.-C. Pilgrim, N. Boudet, N. Blanc, and Y. Sutou: arxiv:1908.07297v1 [cond-mat.mtrl-sci] (2019).
- [2] N.-K. Chen, X.-B. Li, X.-P. Wang, M.-J. Xia, S.-Y. Xie, H.-Y. Wang, Z. Song, S. Zhanga, H.-B. Suna: *Acta Matter.* **90** (2015) 88.
- [3] A. Koura and F. Shimojo: *J. Phys.: Condens. Matter* **32** (2020) 244001.

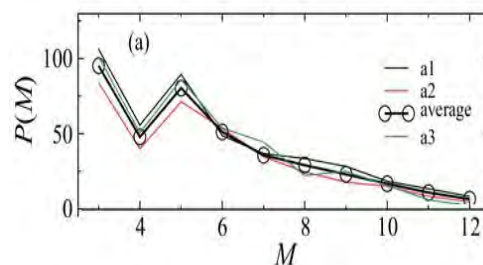


Fig. 1 The distribution of number of M -membered ring $P(M)$ [3].

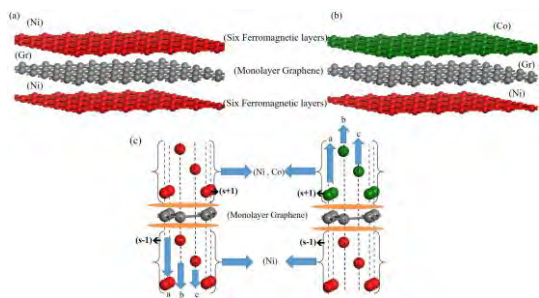
Graphene-based Symmetric and Non-Symmetric Magnetoresistive Junctions

Arqum Hashmi

Center for Computational Sciences,

University of Tsukuba, Tsukuba, Ibaraki 305–8577, Japan

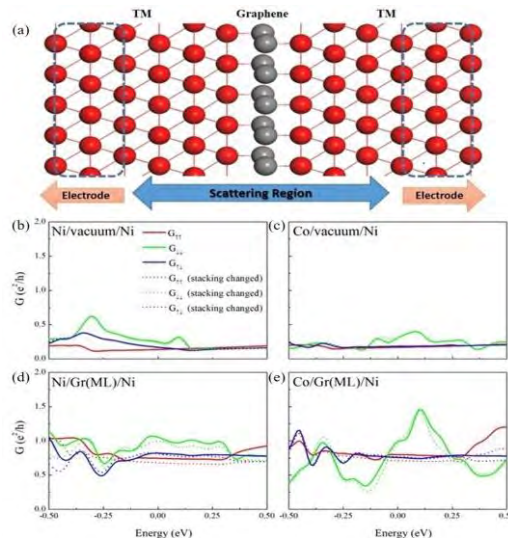
We have studied the structural, magnetic, and spin-dependent transport properties of Graphene based MTJs using massive parallel computer simulations. Gr layer is sandwiched between ferromagnetic electrodes.



Typical Dirac cone feature of Gr is not preserved upon the formation of MTJ and Gr derived π states near the Fermi level was strongly hybridized with the dz^2 orbital of the Ni and Co surfaces. APC was found to be stable in the Gr-based ML junctions and distinct hybridization of the Gr π states are observed with symmetric and non-symmetric junctions. Spin filtering is quite sensitive to the electrode materials. The symmetric junction has higher TMR ratio compared to non-symmetric junction.

The highest TMR ratio observed in symmetric junction is 13.60%, while it is 8.26% in non-symmetric Gr based junction. Gr based junctions displayed the higher transmission

spectra indicating low contact resistance irrespective of the electrode material.



Furthermore, the influence of different stacking of electrode layers on transport properties is also checked although not much difference is observed in conductance spectra. Both symmetric and non-symmetric junctions exhibit distinctive selection rules due to the incompatibility of wave functions of electrodes. Our comparative study reveals the effect of various electrode materials on spin transport property that can help to develop Gr-based high TMR ratio devices.

References

- [1] A. Hashmi, K. Nakanishi, T. Ono: J. Phys. Soc. Jpn. 89, 034708 (2020).

Local physical quantities analysis based on the quantum field theory in material surface

Masahiro FUKUDA

Institute for Solid State Physics, University of Tokyo

Kashiwa-no-ha, Kashiwa, Chiba 277-8581

The local physical quantities, which is defined in the framework of quantum field theory (energy-momentum tensor density, current density, chiral current density, and so on), are significant to understand the fundamental aspect of nature of materials. In particular, since surface materials and two dimensional materials may have physical or chemical properties which cannot be explained by bulk feature in solids, it is important not only to evaluate the energy of the whole system and band structures but also to investigate the local physical properties.

In the previous work, the local physical quantities in molecular systems have been investigated by using a post-process calculation from wave packets obtained by molecular orbital method [1].

In this project, we developed a program code which enables us to calculate local physical quantities as a post-process calculation from OpenMX [2] (DFT calculation program code) in order to evaluate the local physical quantities in large periodic systems. It supports OpenMP/MPI parallelization to handle large system calculations.

The physical and chemical nature around the interaction region between a $\sqrt{7} \times \sqrt{7}$ Si(111) surface and a Si cluster (a model of atomic force microscopy tip), were investigated as a demonstration. The system is a periodic system including 402 atoms in a unit cell. The Fig. 1 shows that the maximum eigenvalues of the electronic stress tensor density around the

region between the surface and the Si tip are positive (tensile stress) and the eigenvectors form the spindle structure [1], which visualizes a covalent bonding. In the future work, more detail analysis will give a deep understanding of chemical bond formation between a material surface and a molecular cluster.

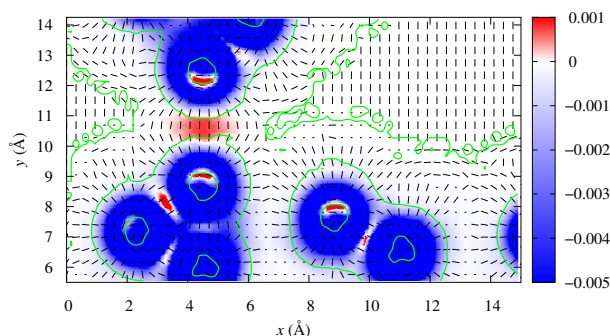


Figure 1: Distribution of maximum eigenvalues and eigenvectors of the electronic stress tensor density and zero surface of the electronic kinetic energy density in the region between Si tip and $\sqrt{7} \times \sqrt{7}$ Si(111) surface.

References

- [1] A. Tachibana, *Journal of Chemical Physics*, **115**, 3497 (2001); A. Tachibana, “New Aspects of Quantum Electrodynamics”, Springer (2017); M. Fukuda, K. Soga, M. Senami, and A. Tachibana, *Int. J. Quant. Chem.*, **116**, 920 (2016).
- [2] OpenMX, <http://www.openmx-square.org/>.

First principle simulation on reactions and electronic structures of new material synthesized from organic molecules

Toshihiro SHIMADA, Wei LIU, Ichiro YAMANE, Taro NAGAHAMA, Takashi YANASE

Division of Applied Chemistry, Faculty of Engineering

Hokkaido University, Kita-ku, Sapporo, Hokkaido 060-8628

We have experimentally synthesized new carbon materials by applying high temperature and / or high pressure to organic molecules. Using this ISSP supercomputer time, we have studied the reactions and electronic structures of these materials[1-3]. We present some of the examples.

Figure 1 shows optimized structure of graphitic carbon nitride ($g\text{-C}_3\text{N}_4$) and a nitrogen molecule. We developed a liquid nitrogen based quenching process to prepare photocatalyst materials with atomic layer separated. This process greatly improved the photocatalytic activity of the material. This calculation supports N_2 molecule can be intercalated to $g\text{-C}_3\text{N}_4$, which assists exfoliation of the layers.

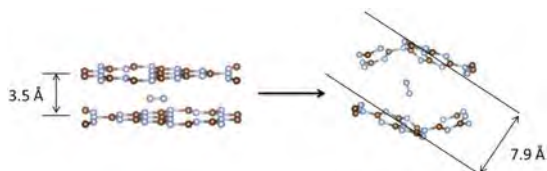


Fig. 1: Optimized crystal structure of two-layered $g\text{-C}_3\text{N}_4$ and N_2 -inserted interlayer of $g\text{-C}_3\text{N}_4$.

Figure 2 shows optimized structure of dibenzo[a,c]dibenzo[5,6:7,8]quinoxalino[2,3-

i]phenazine (DDQP) under pressure[4]. It shows Diels-Alder type intermolecular reaction. The electronic band structures showed three-dimensional dispersion (Fig.3).

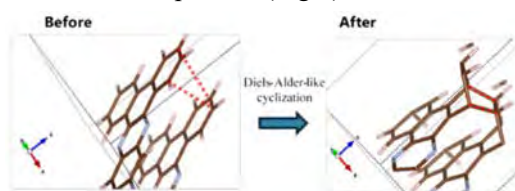


Fig. 2: Pressure-induced bond formation reaction of DDQP revealed by calculation.

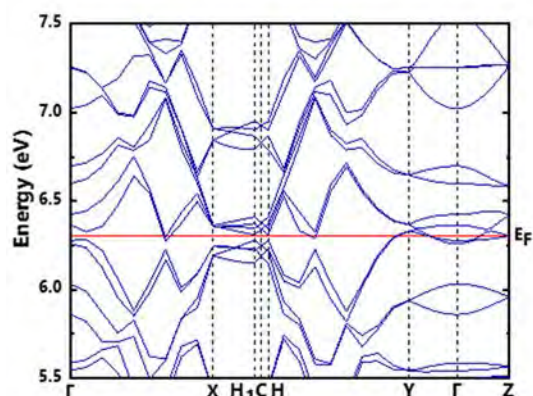


Fig.3 Band dispersion of pressure-polymerized DDQP.

References

- [1] W. Liu, T. Shimada et al.: *Journal of Colloid & Interface Science* **567** (2020) 369.
- [2] W. Liu, T. Shimada et al.: *International J. of Hydrogen Energy* **44** (2020) 8444.
- [3] W. Liu, T. Shimada et al.: *Applied Surface Science* **499** (2020) 143901.

Developments of a derivation method of a low-energy models in first-principles

Hirofumi Sakakibara

Department of Applied Mathematics and Physics, Tottori university, Tottori 680-8552, Japan

First principles calculation is useful method to determine the electronic structure. Most of the first-principles assumes local density approximation(LDA) in density functional theory, however, LDA usually underestimates band gaps of semiconductor. This underestimation is overcome by the consideration of the effect of particle excitation. The quasiparticle self-consistent *GW* method (QSGW) is a first-principles method to determine the one-body Hamiltonian H_0 taking into such excitation effects account.

However, even QSGW improves the size of band gaps compared to LDA, there still have some errors. For example, QSGW systematically overestimates the size of band gaps [1]. This overestimation is investigated from the viewpoint of vertex correction on the proper polarization P by Shishkin *et al.*. Their work has shown that such vertex corrections improve the dielectric constant very well. However, their method is somewhat ambiguous and consuming for computing resource.

To solve this problem, we introduced a method to numerically estimate the vertex correction[3]. Our method is to determine the vertex correction by a self-consistent calculation applying static electric fields to obtain the linear response of electronic density. On this purpose, we implemented the combination of QSGW and effective screening medium method (ESM, Ref. [4]). Namely, we calculate a slab model applying an external electrostatic potential varying along z axis. Fig. 1 is a schematic picture of ESM method applied to

MgO slab. Then, it is better that slabs are as thick as possible because we intend to estimate the vertex correction of bulk materials.

To access the effectiveness of our method, we calculate optical dielectric constant ϵ_∞ , where ϵ_∞ is measured by the slope of the electrostatic potential. In Tab.1, we compare ϵ_∞ of bulk calculation in the random phase approximation (RPA) and the QSGW+ESM method. Here we applied generalized gradient approximation(GGA) instead of LDA. We have chosen five simple ionic materials LF, KF, NaCl, MgO, and CaO for the examination system. We can find that QSGW+ESM is in an extremely good agreement with experiments. It is interesting that LDA(GGA)+ESM method does not necessarily improve the value of ϵ_∞ . This may because that the exchange effect taken in the exchange correlation functional of GGA is not accurate.

In Tab.1, the underestimation of ϵ_∞ of bulk system corresponds to the overestimation of band gaps. It is also found that the material dependence of the vertex corrections is not so large. From this result, some hybrid methods between QSGW and GGA may be applicable instead of present QSGW+ESM method as a compromise. In the previous work by Deguchi *et al.*, a hybrid method named QSGW80 (hybridization between QSGW and GGA at the ratio 8:2) has shown good agreements with experiments. Therefore, the systematic overestimation of QSGW may be improved by considering vertex corrections, which are effectively taken into account in QSGW80.

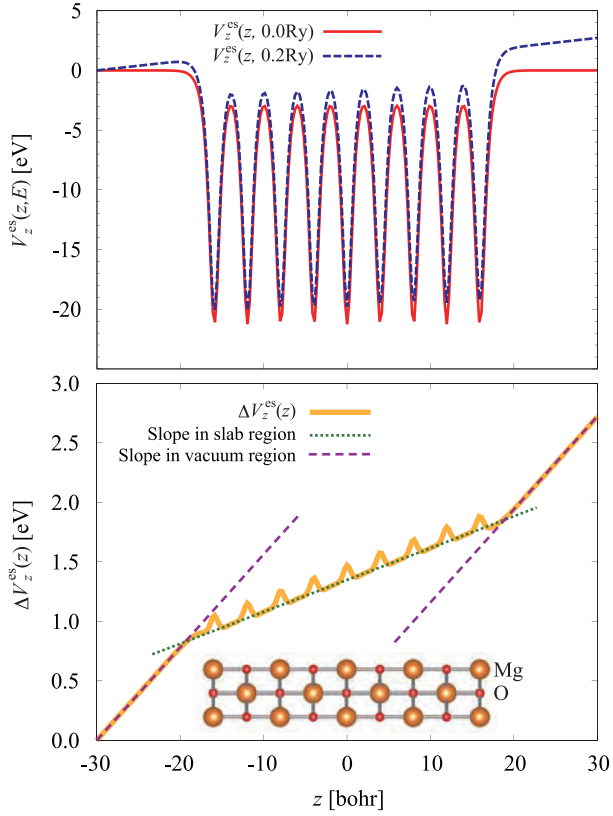


Figure 1: Schematic picture of ESM method. The upper panel shows the electrostatic potential when the difference bias voltages at $z = 30, -30$ are 0.0 Ry and 0.2, respectively. The lower panel shows the difference between the potentials among these two cases. The optical dielectric constant ϵ_∞ is measured from the ratio of the slope between vacuum and slab region, as indicated in the lower panel.

To summarize, we have developed QSGW+ESM method to determine the vertex correction in QSGW. Our method can calculate dielectric function in a good agreement with experimental observation. The future problem is to derive a low-energy model Hamiltonian based on the one-body Hamiltonian H_0 derived from QSGW or QSGW80.

Table 1: Calculated optical dielectric constant ϵ_∞ . ‘RPA’ are in bulk calculations. ‘Slab’ are calculated from the slab models in the setting of Fig.1.

		RPA	Slab	Experiments
LiF	GGA	1.95	2.01	1.96
	QSGW	1.67	1.94	
KF	GGA	1.96	1.94	1.85
	QSGW	1.68	1.86	
NaCl	GGA	2.33	2.42	2.34
	QSGW	1.92	2.31	
MgO	GGA	2.96	3.09	2.96 2.91
	QSGW	2.50	2.37	
CaO	GGA	3.59	3.68	3.33 3.31
	QSGW	2.88	2.68	

References

- [1] D. Deguchi, K. Sato, H. Kino, and T. Kotani, Jpn. J. Appl. Phys. **55**, 051201 (2016).
- [2] M. Shishkin, M. Marsman, and G. Kresse, Phys. Rev. Lett. **99**, 246403 (2007).
- [3] H. Sakakibara, T. Kotani, M. Obata, and T. Oda, Phys. Rev. B (2020)(in press).
- [4] M. Otani and O. Sugino, Phys. Rev. B **73**, 115407 (2006).

First-principles calculation of the higher-order phonon-phonon scattering strength

Haruhiko DEKURA

Geodynamics Research Center

Ehime University, 2-5 Bunkyo-cho, Matsuyama 790-8577, Japan

Phonon-phonon interaction is a key parameter that describes thermal transport properties in solids [e.g., 1]. First-principles calculation of lifetimes of phonon quasiparticles owing to the interaction is computationally demanding for precise determination of phonon thermal conductivity. From the theoretical point of view for the many-body interacting systems, the phonon-phonon scattering rate is approximately inversely proportional to the imaginary part of the phonon self-energy [1]. Most density-functional theoretic calculations for determining phonon thermal conductivity is limited to the lowest order phonon-phonon interaction. The higher-order anharmonicity is likely to contribute to the conductivity particularly at temperatures higher than the Debye temperature as would be seen in the deep Earth's interior [2]. The primary purpose of this project in this period is to try to establish a roadmap as a first step for the accurate determination of phonon thermal conductivity at high temperature considering the effect of higher-order phonon-phonon scattering. Silicon was selected for this purpose for its simplicity.

We have performed the density-functional theoretic calculations based on the plane-wave basis pseudopotential method within the local density approximation. In order to extract harmonic and anharmonic force constants (AFC), the higher-order derivatives of the adiabatic potential surface were determined by the self-consistent field calculations for the structures in which some atoms are slightly shifted from the equilibrium positions. The $3\times 3\times 3$ cubic supercell containing 216 atoms in total was primarily adopted in this study to capture the anharmonic interaction.

During this period, by the use of supercomputer (system B) in ISSP, we have launched test calculations to check the computational conditions regarding the size dependency in the AFC, convergency in the with respect to the simulation cell size of the mesh to sample the phonon wave number vectors. Also, the self-consistent field calculations to extract AFC using the optimum condition have been almost finished. In parallel, post-processors to calculate the total phonon-phonon scattering rate including up to the fourth-order anharmonicity and thermal conductivity based on the Boltzmann transport equation have been almost developed. Using the complete data set

obtained in this study, we will make a thorough examination of the effect of the higher-order scattering on the lattice thermal conductivity at high temperatures. After the establishment of the procedure to compute the thermal conductivity, we plan the application of the developed technique to Earth's minerals under very high-temperature conditions [2].

References

- [1] G. K. Horton, A.A. Maradudin, eds., *Dynamical Properties of Solids: Crystalline solids, fundamentals* (North-Holland, Amsterdam), (1974).
- [2] 出倉春彦, *高圧力の科学と技術*, (2020), *in press*.

Theoretical Study on the Aggregation-Induced Emission

Norifumi YAMAMOTO

Department of Applied Chemistry,

Chiba Institute of Technology, 2-17-1 Tsudanuma, Narashino, Chiba 275-0016

In this study, the mechanism of aggregation-induced emission (AIE) of diphenyldibenzofulvene (DPDBF) was studied theoretically.

The DPDBF has been known to exhibit the AIE, which is non-emissive in dilute solutions but becomes highly emissive in solid or aggregates [1]. In this study, the AIE of DPDBF was investigated by using *ab initio* electronic structure calculations, together with molecular dynamics (MD) simulations.

In order to elucidate the characteristics of the potential energy profiles for the photochemical processes of DPDBF, the minimum energy paths for the photo relaxation process of DPDBF in an isolated phase were investigated using *ab initio* electronic structure calculations. The spin-flip approach within the time-dependent density functional theory (SF-TDDFT) method was used to compute the potential energies and analytical gradients for the electronic ground (S_0) and first excited (S_1) states of the molecule. All electronic structure calculations of DPDBF presented herein were performed using the GAMESS program.

The results of SF-TDDFT calculations showed that the potential energies of DPDBF for electronic ground (S_0) and first excited (S_1)

states are degenerated at a conformation with the twist angle of 90° around its ethylenic C=C bond, which can lead the fluorescence quenching of DPDBF molecule in dilute solutions.

The free-energy profile of the photo isomerization of DPDBF in condensed phase was computed using MD simulations based on an empirical force field representation. All MD simulations of DPDBF presented herein were carried out using the GROMACS program.

The results of MD simulations revealed that DPDBF tends to assemble in close contact, where the ethylenic C=C bond rotation is markedly restricted in aggregates, preventing the fluorescence quenching via the S_0/S_1 conical intersection; DPDBF in acetonitrile solution, however, proceeds a barrierless non-radiative transition. These results gave a clear picture of the AIE of DPDBF, which is agree with that of a cyanostilbene derivative [2].

References

- [1] Tong, H, et al., *J. Phys. Chem. C*, Vol. 111, pp. 2287–2294 (2007).
- [2] Yamamoto, N., *J. Phys. Chem. C*, Vol. 122, pp. 12434–12440 (2018).

Benchmark of density functional theory for superconductors in elemental materials

Mitsuaki Kawamura

Institute for Solid State Physics, University of Tokyo

Kashiwa-no-ha, Kashiwa, Chiba 277-8581

1 introduction

The first-principles calculation of the superconducting properties, such as the transition temperature (T_c) and the gap function, is of great interest to explore new materials as well as to understand the physical mechanism of known superconductors. Density functional theory for superconductors (SCDFT) is one of the frameworks for such calculations; this method enables us to perform fully non-empirical simulations in the superconducting phases at a reasonable computational cost. In SCDFT, we can treat the electron-phonon interaction, the electron-electron repulsion, the spin-orbit interaction (SOI) [1], and the spin-fluctuation (SF)-mediated interaction in a first-principles manner.

However, the accuracy of the current approximated functional of SCDFT and the effects of SOI and SF have not been verified systematically, although such verification is highly desirable before applying this method to a wide range of materials. Such a high-throughput calculation was performed, for example, in the exploration of low-thermal-conductivity compounds using first-principles calculations together with the materials informatics. A benchmark is also a useful tool used to find a guideline for improving the theory and approximations of the superconducting density functional. For this purpose, in this project, we are presenting the benchmark calculations of SCDFT [2]. As benchmark targets, we have chosen the simplest superconducting, and non-

superconducting materials, i.e., elemental materials; each material in this group comprises a single element. The particular computational cost is relatively low because most materials in this group contain only one or two atoms in the unit cell. Moreover, we can see the effects of the chemical difference and the strength of the SOI of each element.

2 method

Within SCDFT, T_c is obtained as a temperature where the following Kohn-Sham superconducting gap $\Delta_{n\mathbf{k}}$ becomes zero at all the band n and wavenumber \mathbf{k} :

$$\Delta_{n\mathbf{k}} = -\frac{1}{2} \sum_{n'\mathbf{k}'} \frac{K_{n\mathbf{k}n'\mathbf{k}'}(\xi_{n\mathbf{k}}, \xi_{n'\mathbf{k}'})}{1 + Z_{n\mathbf{k}}(\xi_{n\mathbf{k}})} \times \frac{\Delta_{n'\mathbf{k}'}}{\sqrt{\xi_{n'\mathbf{k}'}^2 + \Delta_{n'\mathbf{k}'}^2}} \tanh\left(\frac{\sqrt{\xi_{n'\mathbf{k}'}^2 + \Delta_{n'\mathbf{k}'}^2}}{2T}\right), \quad (1)$$

where $\xi_{n\mathbf{k}}$ is the Kohn-Sham eigenvalue measured from the Fermi level (ε_F) at the band index n and wave-number \mathbf{k} . $\xi_{n\mathbf{k}}$ is obtained by solving the spinor Kohn-Sham equation. The integration kernel $K_{n\mathbf{k}n'\mathbf{k}'}(\xi, \xi')$ indicates the superconducting-pair breaking and creating interaction and comprises the following three terms:

$$K_{n\mathbf{k}n'\mathbf{k}'}(\xi, \xi') \equiv K_{n\mathbf{k}n'\mathbf{k}'}^{ep}(\xi, \xi') + K_{n\mathbf{k}n'\mathbf{k}'}^{ee}(\xi, \xi') + K_{n\mathbf{k}n'\mathbf{k}'}^{sf}(\xi, \xi'), \quad (2)$$

namely, the electron-phonon, Coulomb repulsion, and spin-fluctuation kernel, respectively. However, the renormalization factor $Z_{nk}(\xi_{nk})$ comprises only the electron-phonon and spin-fluctuation terms as follows.

$$Z_{nk}(\xi) \equiv Z_{nk}^{ep}(\xi) + Z_{nk}^{sf}(\xi), \quad (3)$$

because the Coulomb-repulsion contribution to this factor is already included in the Kohn-Sham eigenvalue ξ_{nk} .

3 Result and Discussion

We have plotted the computed- and experimental- T_c in Fig. 1 to visualize the effect by SOI and SF; we can detect the following trends by inspecting this graph: SF always reduces T_c s for the elemental systems. This reduction becomes significant for the transition metals and is crucial to reproduce the experimental T_c quantitatively. In the transition metals, the effect of SF weakens with the increasing of the period number in the periodic table. The effect of SOI is small in most cases, excepting Tc, Sn, Re, Tl, Pb. In these elements, the Fröhlich's parameter λ changes drastically by turning on the SOI. We can reproduce the absence of the superconductivity in alkaline, alkaline earth, and noble metals, excepting Pt and Au with SOI and SF; we have observed small finite T_c for these two elements; we can reproduce the non-superconductivity also in Sc by including SF while we observe $T_c = 2.711$ K by ignoring SF. Since Sc has highly localized 3d electrons, the SF largely reduces T_c . For the group 12 elements (Zn and Cd), T_c s are overestimated even if we include SF. For these materials, the SF effect is small because the d orbitals are fully occupied.

References

- [1] T. Nomoto, M. Kawamura, T. Koretsune, R. Arita, T. Machida, T. Hanaguri,

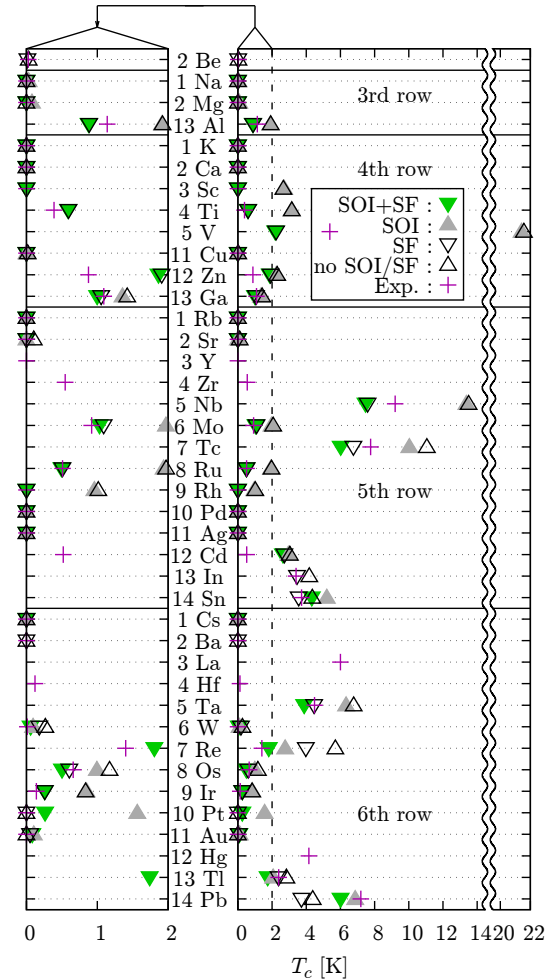


Figure 1: Theoretical and experimental T_c s [2]. The vertical axis is the atomic symbol together with the group of the periodic table. Downward (upward) triangles indicate the T_c s computed with (without) SF. Filled (empty) triangles indicate the T_c s computed with (without) SOI. “+” indicates the experimental value of T_c . The plot which ranges from zero to two Kelvin in the upper panel is magnified into the bottom panel.

M. Kriener, Y. Taguchi, and Y. Tokura,
Phys. Rev. B **101**, (2020) 014505.

- [2] M. Kawamura, Y. Hizume, and T. Ozaki,
Phys. Rev. B **101**, (2020) 134511.

Simulation of scanning tunneling microscopy images of graphene ribbons with edges

Junhuan LI, Kenta ARIMA

Graduate School of Engineering, Osaka University, Yamadaoka, Suita, Osaka 565-0871

We are aiming at elucidating local electronic structures of finite-size graphene sheets and their impact on scanning tunneling microscopy (STM) images. For this purpose, we have started first-principles calculations of single-layer graphene ribbons possessing either zigzag or armchair edges by the use of a simulation package named STATE (Simulation Tool for Atom TEchnology).

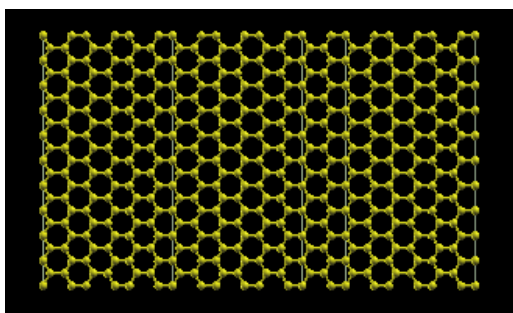


Fig. 1(a) Structure of single-layer graphene

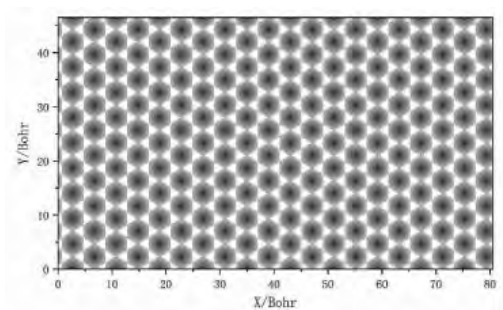


Fig. 1(b) Simulated STM image of single-layer graphene

STATE is based on the density functional theory. The exchange and correlation potential is described by the generalized gradient approximation by Perdew-Burke-Ernzerhof (GGA-PBE). We also used both a plane-wave basis set and pseudopotentials. When running STATE, we first defined the atomic structure of a finite-size graphene. This model as well as other parameters were placed as an input file on a supercomputer. The self-consistent field method was employed, which is an iterative method that involves selecting a Hamiltonian, solving the Kohn-Sham equation to obtain a more accurate set of orbitals, constructing the potential for each wave function, and solving the Kohn-Sham equation again with these until the results converge. In order to draw a map of local density of states, an electron density was integrated over an energy window of 0.05 eV below the HOMO (Highest Occupied Molecular Orbital). At each (x, y) coordinate, a z -height possessing the same electron density (1×10^{-4} /Bohr³) was investigated and its contour map was depicted, which is regarded as a simulated STM image at the sample bias of -0.05 V. We

used the module (intel/18.0.5.274) for the compilers and mpt/2.16 for MPI library. The set of calculation was usually executed on F4cpu or F36cpu with suitable nodes in ISSP.

To check both the validity of our parameters in the input file for STATE calculations and the performance of STATE itself, we first modeled an infinite, single-layer graphene. The created model is shown in Fig.1(a). The cutoff energies were 36 Ry (GMAX=6) and 400 Ry (GMAXP=20) for the wave functions and the augmentation charge, respectively. Then we conducted first-principles calculations within STATE to get the electronic structure of the model. Figure 1(b) shows a simulated STM

image of the surface in Fig. 1(a) at the sample bias of -0.05V. A brighter area in Fig.1(b) indicates a higher corrugation, which is caused by a higher density of the occupied states. It is apparent that a hexagonal pattern is formed in which the position of a bright dot coincides with that of a carbon atom comprising the graphene network. Figure 1 insists that the combination of our modeling and parameters with the STATE software works well. In the next fiscal year, we are going to characterize the distribution of local charge densities near the edges of a graphene ribbon and to unveil its relationship with an STM image around the Fermi level.

An open source code for QUANTUM ESPRESSO to compute irreducible representations of Bloch wave functions

Seishiro ONO

Institute for Solid State Physics,

The University of Tokyo, Kashiwa-no-ha, Kashiwa, Chiba 277-8581

Since the remarkable discovery of \mathbb{Z}_2 topological insulators, topological materials have attracted researchers around the world. Topological materials host robust surface states and exhibit unique bulk responses, which could be leveraged for new low-power devices. Therefore, discovering various topological materials is one of the important tasks for engineering.

Given a symmetry setting, establishing topological invariants that characterize all possible topological phases is a pending problem. Furthermore, it is sometimes difficult to compute topological invariants even when we know the mathematical definition of topological invariants. However, when spatial symmetries exist, it is effortless to diagnose topological phases by using information of spatial symmetries. A prototypical example of this relation is the Fu-Kane formula, which can evaluate the topological invariant of insulators from eigenvalues of the inversion symmetry. In recent years, this idea has been generalized to all combinations of crystalline symmetries by using irreducible representations of wave functions instead of eigenvalues, and the generalized theory is called symmetry indicators [1]. While it does not bring the complete classification, this theory is suitable to discover realistic topological materials. In fact, this method is a basis of recent comprehensive surveys of topological materials among existing databases of inorganic substances. As a result, thousands of candidates of topological (crystalline) insulators and semimetals have been discovered. In addition to these developments, the theory of symmetry

indicators has been extended to magnetic space groups and superconductors [2].

As seen in the preceding paragraphs, it is helpful to compute irreducible representations by using DFT. Although the authors of Refs. [3,4] implemented programs for WIEN2k and VASP to calculate irreducible representations, these packages need paid licenses. In contrast, QUANTUM ESPRESSO, a free package for ab initio calculations, can obtain irreducible representations only for symmorphic space groups.

In this work, we developed an open-source code for QUANTUM ESPRESSO to get irreducible representations for all space groups. In addition to this function, we implemented a function to automatically compute the \mathbb{Z}_4 index that can diagnose various topological phases such as higher-order topological insulators. Furthermore, we also apply our program to about 40 magnetic materials. Then, we used the facilities of the Supercomputer Center to get wave functions for these materials. We are still searching for new topological materials by using our program and DFT calculations.

References

- [1] H. C. Po, A. Vishwanath, and H. Watanabe, *Nat. Commun.* **8**, 50 (2017).
- [2] S. Ono, H. C. Po, and H. Watanabe, *Sci. Adv.* **6**, eaaz8367 (2020).
- [3] F. Tang, *et al.*, *Nature*, **566**, 486-489 (2019).
- [4] M. G. Vergoniry, *et al.*, *Nature*, **566**, 480-485 (2019).

First Principles Calculation of 2-Dimensional Silicides Formed on Nickel Surfaces

Tsuneo FUKUDA¹ and Ippei KISHIDA^{2*}

¹*Department of Physical Electronics and Informatics, Graduate School of Engineering, Osaka City University, 3-3-138 Sugimoto, Sumiyoshi-Ku, Osaka 558-8585*

²*Department of Mechanical and Physical Engineering, Graduate School of Engineering, Osaka City University, 3-3-138 Sugimoto, Sumiyoshi-Ku, Osaka 558-8585*

Metal silicides are indispensable materials for advanced microelectronics. We have recently proposed a new route to form a robust two-dimensional (2-D) silicide [1,2]. Unlike conventional thin film silicide formed by depositing metal on the silicon surface, Si was deposited on a clean metal surface to form silicide. Our recent studies show that robust 2-D silicides are formed on Ni(110) and Ni(100) surfaces due to the large diffusion asymmetry between Si in bulk metal and metals in bulk Si [1,2]. However, the lack of theoretical support clearly undermines the significance of our research findings.

First-principles calculation code VASP was adopted to compare the experimentally obtained 2-D atomic structure with theoretical simulations. A typical scanning tunneling microscope (STM) image of a Si-deposited Ni(100) surface is shown in Fig. 1 [2]. The initial clean surface was essentially a 1×1 structure, but many dark sites were formed after Si deposition. These dark sites are not due to structural defects, but Si replaced by Ni in the

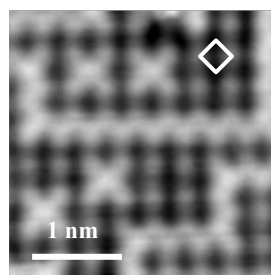


Fig. 1 Typical STM image for a 0.39 ML Si deposited surface. White square corresponds to the 1×1 unit cell.

top layer. Since the STM image is reflected by the surface local density of states (LDOS) near E_F , the embedded Si reduces the tunneling current without the large LDOS due to Ni $3d$ bands, making it a dark site. Therefore, the discrimination between individual Si and Ni is fairly straightforward, but the relationship between Si and Ni is unsolved.

Therefore, the first principle calculation was performed in this system. The calculation parameters are shown in Table 1. Before performing surface slab calculations, we evaluated the ground state energies of Ni and Si atoms, and bulk Ni and Si, respectively. Because of the slow convergence of self-consistent electronic states in the surface structure, we adjusted the mixing parameters as

shown in Table 1 (so-called linear mixing, see VASP manual). First, all atoms except for the middle layer has been completely relaxed. Then 0-8 surface Ni atoms in the top layer were replaced by Si, and the top 5 layers were fully optimized. A total of 36 different surface configurations were evaluated for 0-1 ML Si coverage.

In order to compare the formation energy for different numbers of surface species, we evaluated chemical potential as,

$$E_{total} = E_{slab} - n_{Ni}E_b^{Ni} - n_{Si}E_b^{Si},$$

where E_{slab} is a total energy of a particular slab structure, n_{Ni} and n_{Si} are respectively numbers of Ni and Si atoms in the slab, and E_b^{Ni} and E_b^{Si} are respectively bulk cohesive energies for Ni and Si.

As shown in Fig. 2, the relative energies of various configurations referenced from that for the Ni(100) surface are plotted as a function of Si coverage. Negative formation energy means that energies of Si embedded structures are lower than that of the Ni(100). There is a negative slope for Si coverage from 0 to 0.5 ML, indicating that Si substitution with Ni is energetically favorable. On the other hand, a positive slope above 0.5 ML means that Si will be ejected from the structure, which is in good agreement with experimental observations.

In conclusion, the first-principles study of two-dimensional Ni silicide formed on Ni (100) is in good agreement with the experimental

Table 1 Parameters for present calculation

VASP Version	5.3.5
slab geometry	Ni(100) 2×4 unit 11 layers
vacuum region	2.12 nm
k-points	16×8×1
potential	PBE [3]
cut off energy	350.39 eV
Fermi level smearing	Methfessel & Paxton $\sigma = 0.12$ eV
convergent condition	
ion cordination	0.01 eV/Ang.
electronic states	10^{-5} eV
mixing parameters	spin-resolved AMI = 0.02 BMIX = 0.0001 AMIX_MAG = 0.08 BMIX_MAG = 0.0001

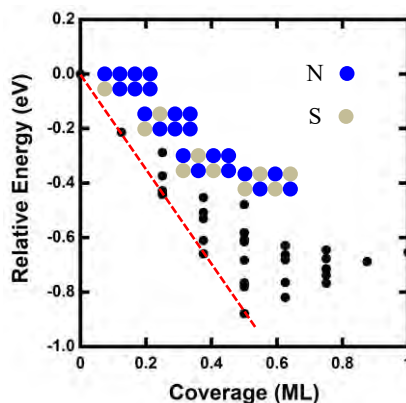


Fig. 2 Relative formation energies of Si-embedded Ni(100) surfaces with various configurations of Si coverage between 0-1 ML. Inset: The most stable configurations with Si coverage of 0.125, 0.25, 0.375, and 0.5 ML.

results. As a future study, the displacement process, so-called depressive adsorption, should be revealed by molecular dynamics simulations.

*present address: Nagamori Institute of Actuators, Kyoto University of Advanced Science, 18 Yamanouchi, Gotanda-Cho, Ukyo-Ku, Kyoto 615-8577, Japan

References

- [1] T. Fukuda, I. Kishida, and K. Umezawa, *Surf. Sci.* **659** (2017) 1.
- [2] T. Fukuda, I. Kishida, and K. Umezawa, *Jpn. J. Appl. Phys.* *in press*.
- [3] J. P. Perdew, K. Burke, and M. Ernzerhof, *Phys. Rev. Lett.* **77**, (1996) 3865.

First-principles Study of Defects of Magnesium Alloys

Daisuke Matsunaka

Department of Mechanical Systems Engineering,

Shinshu University, 4-17-1 Wakasato, Nagano 380-8553

Magnesium (Mg) has been of increasingly interest from the engineering viewpoint, because of its low density and relatively high specific strength. Despite intensive research efforts, there remain various problems to be overcome; low ductility and low toughness at room temperature. To understand active deformation mode under an applied load, the Schmid factor and the critical resolved shear stress (CRSS) for each deformation mode are helpful. However, several studies showed that the activated deformation mode under various uniaxial loadings deviated the Schmid's law and their CRSSs were not uniquely determined. In order to investigate influences of non-glide stress on deformation modes, we carried out molecular dynamics (MD) simulations for slips with $\langle a \rangle$ Burgers vector under several normal stress conditions. For basal slip, extended dislocations were generated and glided on the basal planes, irrespective of the applied normal stress conditions. In MD simulations of shear deformation for first-pyramidal slip, distinct dislocation gliding was not observed and alternatively (10-11) twin was generated. For prismatic slip, deformation behavior depended on the applied normal stress as well as

interatomic potentials.

One way for improving the limited ductility of Mg at room temperature is to activate non-basal slips. In particular, Mg-Y alloy has shown a significantly enhanced ductility. It has been suggested that the improvement of ductility was attributed to the reduction of the intrinsic I_1 stacking fault (SF) energy by Y addition. We investigated defect nucleation in the vicinity of a pre-existing intrinsic I_1 SF by MD simulations. While formation of (11-21) twin was observed under shear stress on (0001) along [11-20], $\langle c+a \rangle$ partial dislocations were generated with SFs for higher resolved shear stress for pyramidal slips. The dissociation reactions of the dislocations at the side ends of the I_1 SF were energetically evaluated, and it was implied that nucleation of the $\langle c+a \rangle$ dislocations on the first-pyramidal planes is more favorable than on the second-pyramidal planes.

References

- [1] S. Yoshikawa and D. Matsunaka: Mater. Trans. **61** (2020) 127.
- [2] S. Yoshikawa and D. Matsunaka: Comp. Mater. Sci. **179** (2020) 109

First-principles study of magnetoresistance ratios and magnetic anisotropy in magnetic tunnel junctions

Keisuke MASUDA, Tsuyoshi SUZUKI, and Kenji NAWA

Research Center for Magnetic and Spintronic Materials,

National Institute for Materials Science, Sengen, Tsukuba, Ibaraki 305-0047

Magnetic tunnel junctions (MTJs), where an insulating tunnel barrier is sandwiched between two ferromagnetic electrodes, are the most practical spintronic devices. The MTJs have various applications such as nonvolatile magnetic random access memories (MRAMs) and many types of magnetic sensors including read heads of hard-disk drives. For these applications, we have several requirements in the physical properties of MTJs. In the present work, we studied such properties using the first-principles calculations.

The spinel oxides AB_2O_4 can be hopeful insulating tunnel barriers in MTJs. Among them, $MgGa_2O_4$ (MGO) has recently attracted attention because the MGO-based MTJs have low resistance-area products (RA) and high magnetoresistance (MR) ratios [1], both of which are necessary for MRAM and read-head applications. To understand the mechanism of such properties, we calculated RA and MR ratios in the Fe/MGO/Fe(001) MTJ by combining the density-functional theory (DFT) and the Landauer formula. As a result, a low RA ($\sim 0.5 \Omega\mu m^2$) and a high MR ratio ($\sim 200\%$) were obtained when the thickness of the MGO

barrier is around 10 \AA , which is consistent with experiments. We found that the low RA is attributed to a small band gap in the MGO barrier. In addition, our detailed analysis of the electronic structure clarified that the obtained high MR ratio can be understood from the interfacial resonance effect [2].

As a second topic, we tried the calculation of MR ratios in unconventional (111)-oriented MTJs, which have not been examined well so far owing to the successful history in the (001)-oriented MTJs. By using the first-principles approach mentioned above, we calculated a MR ratio of Co/MgO/Co(111) and obtained a quite high value ($>2000\%$). We found that such a high MR ratio also comes from the interfacial resonance effect [3].

References

- [1] H. Sukegawa *et al.*, Appl. Phys. Lett. **110**, (2017) 122404.
- [2] K. Nawa, K. Masuda, and Y. Miura, 第24回半導体スピン工学の基礎と応用, 東北大学, 2019年12月.
- [3] K. Masuda, H. Itoh, and Y. Miura, Phys. Rev. B **101**, (2020) 144404.

Study on Carrier Dynamics in Nano Scale Semiconductor Devices with Machine Learning

Masakazu Muraguchi

Faculty of Engineering, Hokkaido University of Science,

Maeda, Teine, Sapporo 006-8585

We have studied a Machine Learning (ML) approach to make a model of electron transport process in nanostructures. The transmission coefficients and time-development of electron density in the nanostructures are computed by time-dependent schrödinger equation to provide training and test datasets to the machine learning [1,2]. Calculations are performed on the motion of electron wave packets of different energies in a two-dimensional nanostructure under random impurity distribution.

We work on the creation of two types of predictive models; the transmission probability of electron wave packet from the impurity distribution; the impurity distribution from the image sequence of electron density distribution in the transmission process. By combining these predictive models, we expect to achieve a more efficient device design method with time-dependent calculation than ever before.

As the ML methods, a Random Forest (RF) and a Neural Network (NN) are employed for modeling the relationship between the impurity distributions and the transmission coefficients of electron. The mean absolute error is compared to each model. In both methods, it is found

that the approach of capturing the impurity distribution as an image could build a better model than using simple impurity coordinates as input.

In addition, we investigate the predictive model for the impurity distribution from the image sequence of the time evolution of electron density as shown in Fig.1. Modeling by convolutional NN is performed, and the accuracy is compared when the image sequence is individually inputted, when the mean of the image sequence is inputted, and when the image sequence is inputted with a recurrent network.

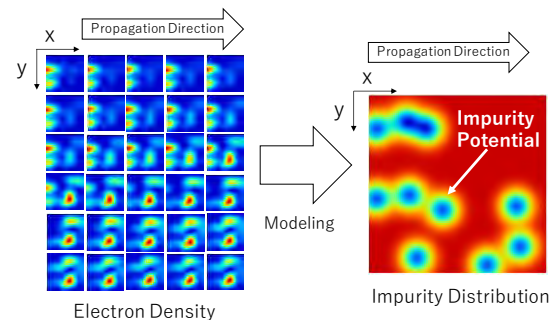


Fig.1 Modeling the impurity distribution from the image sequence of the time evolution of electron density.

References

- [1] N. Watanabe and M. Tsukada: Phys. Rev. B 62 (2000) 2914.
- [2]. T. Okunishi, Y. Ohtsuka, M. Muraguchi, K. Takeda, Phys. Rev. B, 75, 24 (2007), 245314-1~245314-15.

Analysis of absorption spectra for caged compounds in aqueous solution

Miyabi HIYAMA

*Graduate School of Science and Technology, Gunma University,
Tenjin-cho, Kiryu, Gunma 376-8515*

Coumarin caged-luciferins, which can generate firefly luciferin ('luciferin' in this article) by UV photolytic reaction, would be useful to understand the firefly bioluminescence. We synthesized the new caged-luciferin (coumarin caged-luciferin) and obtained the absorption spectra for this caged-luciferin itself and irradiated caged-luciferin[1]. When we use this caged-luciferin for spectroscopic studies, we need the detail of electronic states of this molecule in aqueous solutions. In this year, we performed the density functional theory (DFT) calculations for coumarin caged-luciferin .

The polarized continuum model was used for the description of water solute molecules. All calculations were performed using the GAUSSIAN09 [2] program on system B and C of Super Computer Center in ISSP. The ground states for 40 equilibrium structures for coumarin caged-luciferin in aqueous solution were obtained. The time dependent DFT (TDDFT) calculations for these structures were performed to obtain the theoretical absorption spectra.

Figure 1 shows the experimental and theoretical absorption spectra of coumarin caged-luciferin. The experimental absorption spectrum of luciferin is also shown in Figure 1. The shape of the theoretical absorption spectrum of coumarin caged-luciferin is quite similar to that of experimental spectrum.

We found that the peak near 384 nm of theoretical absorption spectrum corresponds to the absorption from the ground electronic state (S_0) to the first excited state (S_1) and that the peak near 339 nm corresponds to the absorptions from S_0 to the second (S_2) and third (S_3) excited state[3]. We also found that the characteristics of 339 nm peak in the theoretical absorption spectrum of coumarin caged luciferin is similar to that of the peak in the absorption spectrum of luciferin.

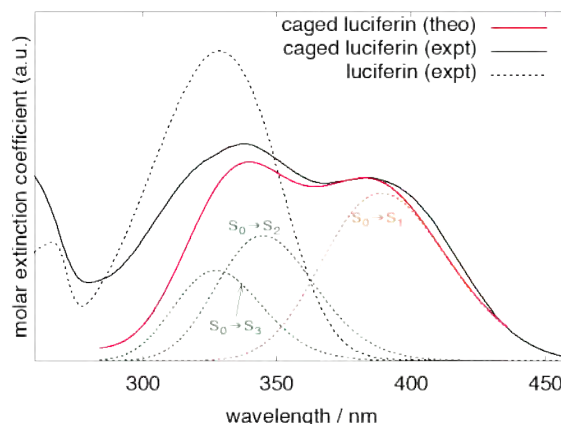


Figure 1: Absorption spectra for coumarin caged luciferin and luciferin[3]. Black solid line : Experimental absorption spectrum of coumarin caged luciferin, Red solid line: Theoretical absorption spectrum of coumarin caged luciferin, Black dashed line: Experimental absorption spectrum of luciferin, Orange dashed line: the component of absorption from S_0 to S_1 , Green dashed line: the components of absorptions from S_0 to S_2 and S_3 .

References

- [1] Kurata et al. , J. Photochem. Photobiol. B, **189** (2018) 81.
- [2] Gaussian 09, Revision D.01, M. J. Frisch et al.
- [3] Usukura et al. Photochem. Photobiol. (2020) in press

Calculation of multication oxide surface properties for catalyst informatics

Yoyo HINUMA

Center for Frontier Science

Chiba University, 1-33 Yayoicho, Inage, Chiba, Chiba 263-8522

Surface point defects of metal oxides, for instance O vacancies, have a dominant effect on heterogeneous catalysis. The Mars-Van Krevelen mechanism is one of the most frequently encountered catalytic process. In one example, O vacancies on a metal oxide catalyst surface act as reaction sites. The energy minimum required to remove O from a surface, which is denoted as the surface O vacancy formation energy (E_{Ovac}), can be used to rationalize and predict catalytic performance in such a catalytic process. Calculation of E_{Ovac} requires a slab-and-vacuum model with sufficient spacing between O vacancies, hence some estimation of E_{Ovac} from less costly calculations, such as slab-and-vacuum model calculations with minimum cell size and even bulk calculations, will be effective in screening materials for a given purpose.

The E_{Ovac} of ZnM_2O_4 , where M is one of Al, Ga, In, V, Cr, Mn, Fe, or Co, was calculated. These compounds take the normal spinel structure, and the (100), (110), and (111) surfaces were evaluated. The automated nonstoichiometric and nonpolar slab-and-model generation algorithm already by Hinuma et al.

[1,2] was expanded to allow automatic derivation of models where the topmost and bottommost surfaces need to be reconstructed, which is the case in the normal spinel surfaces in this study [3]. The surface energy was smallest in the (100) surface in all systems, and E_{Ovac} was largest in the (100) surface in all systems except ZnCo_2O_4 . The reactivity of a site is expected to be high if the site is unstable. In other words, a site with low E_{Ovac} is expected to have a higher reactivity and therefore can open up new capabilities in, for example, catalysis. The importance of finding unstable sites, which roughly translates to having a lower E_{Ovac} for surface O sites, that are expected to have lower surface energy was identified in this study. Needless to say, the surface must be proven to be experimentally accessible, which is a very important issue that need to be worked on.

References

- [1] Y. Hinuma et al.: *Comp. Mater. Sci.* 113 (2016) 221.
- [2] Y. Hinuma et al.: *Phys. Rev. Mater.* 2 (2018) 124603.
- [3] Y. Hinuma et al.: *Mater. Trans.* 61 (2020) 78.

Study on physical properties of structural elementary excitations of semiconductor surfaces and interfaces

Hiroyuki KAGESHIMA

*Graduate School of Natural Science and Technology, Shimane University
1060 Nishi-Kawatsucho, Matsue, Shimane 690-8504*

Our project has been focused on physical properties of structural elementary excitations of semiconductor surface and interfaces. We have performed three topics in this year. One is the physical properties of SiO interstitials in SiO₂ at interface with Si [1, 2]. The second is the physical properties of oxygen vacancies (V_O) in SiO₂ at interface with Si. And the third is the physical properties of vacancies in a two-dimensional material MoSe₂. The calculations were performed based on the first-principles calculation. Program package VASP was employed for the first and the third topics, while program package PHASE0 was employed for the second topic.

In the first topic, we focus on the role of SiO interstitials for the selfdiffusions in SiO₂ under compressive pressure. It is known that SiO interstitials are injected into the oxide when Si is thermally oxidized. In addition, for Si pillar oxidation, it is known that a large compressive pressure as high as 5 GPa is induced in the oxide. We have calculated the pressure effect for temperatures 3000, 4000, 5000, and 6000 K, and derived activation volumes as well as activation energies. We found that the SiO really acts as a unit for the diffusion mechanism. As the result, the pressure dependence of Si diffusion is largely affected by the SiO incorporation, while that of O diffusion is not much affected. [1, 2]

In the second topic, we focus on the strain effect on V_O diffusion in SiO₂. As described before, for the Si pillar oxidation, a large com-

pressive pressure is accumulated in SiO₂. We have calculated activation barriers as the function of modulated lattice constants. We have also checked crystal polymorph dependence for Quartz, Cristobalite, or Tridymite. As the results, we found that the barrier height increases with the Si density almost being independent of the polymorph type. The reason comes from the fact that the initial Si-Si distance at V_O controls the barrier height.

In the third topic, we focus on the supporting effect on vacancy formation in monolayer MoSe₂. The results are similar to our previous study on MoS₂. We found that the supporting effect makes the charging more difficult because the reduced quantum confinement shrinks the band gap. The hetero-stacking also makes the charging more difficult because the type II band alignment also shrinks the band gap. These lead to the reduction of charging effect on the vacancy formation.

References

- [1] H. Kageshima, Y. Yajima, K. Shiraishi, and T. Endoh, *Jpn. J. Appl. Phys.* **58** (2019) 111004 (11pages).
- [2] Y. Yajima, H. Kageshima, K. Shiraishi, and T. Endoh, 2019 International Workshop on Dielectric Thin Films for Future Electron Devices – Science and Technology – (2019 IWDTF), Tokyo, Japan, p-7 (Nov. 18, 2019).

Theoretical Study on Electronic Properties in New Nanoscale Surfaces and Interfaces

Katsuyoshi KOBAYASHI, Yoko TANAKA
Department of Physics, Ochanomizu University
2-1-1 Otsuka, Bunkyo-ku, Tokyo 112-8610

In 2019 we theoretically studied electron transport properties through higher-order topological insulators. Higher-order topological insulators were recently proposed theoretically [1]. Higher-order topological insulators are materials that have topologically protected states in two or more lower spatial dimensions. There are several reports that higher-order topological insulators are experimentally observed [2, 3]. We calculated electrical conduction properties through topological edge states in a three dimensional crystal.

We used a tight-binding model of higher-order topological insulators given by Langbehn *et al.* [4]. This model is a three dimensional insulator and has one dimensional edge states protected by mirror symmetry. Transmission properties through the edge states are investigated. We consider a cubic structure of higher-order topological insulator. Two electrodes are attached to two corners of the cube. The electrodes are normal conductors. We solve scattering states of the Hamiltonian of the open system. Electrical conductance is calculated using the Landauer formalism.

We consider several different conditions of contact between the high-order topological insulator and electrodes. Calculated conductance depends strongly on contact conditions. Conductance increases with increasing the strength of the contact for weak strength of contact. But, it turns to decrease with further increase of the contact strength. There is a peak in conductance as a function of the contact strength. This result is due to a following reason.

The incident electrons are transmitted to another electrode or reflected to the incident elec-

trode with conserved or inverted spin. The reflection with conserved spin is dominant in the region of weak contact strength. The spin-conserved reflection decreases with increasing the contact strength. The transmission to the other electrode increases in place of the decrease of conserved reflection. However, with further increase of the contact strength, the reflection with inverted spin increases and it becomes dominant. Accordingly, the transmission turns to decrease. This result means that there is moderate contact strength for high transmission.

In addition to the study of electron transmission properties through the high-order topological insulators, we also developed the calculation method of spin and angle resolved photoelectron spectroscopy. We extended the method for obtaining time-reversed LEED states from the results of repeated-slab calculations. It became possible to treat general cases containing any number of bulk Bloch states by using the singular value decomposition.

References

- [1] F. Schindler *et al.*: *Sci. Adv.* **4** (2018) eaat0346.
- [2] F. Schindler *et al.*: *Nat. Phys.* **14** (2018) 918.
- [3] S. N. Kempkes *et al.*: *Nat. Mater.* **18** (2019) 1292.
- [4] J. Langbehn *et al.*: *Phys. Rev. Lett.* **119** (2017) 246401.

Development of First-principles calculations method of Seebeck coefficient in the framework of linear response theory

Sonju KOU

Department of Materials Science and Engineering, Tokyo Institute of Technology J1-3, KNagatsuta-cho 4259, Midori-ku, Yokohama 226-8502, Japan

The simulation of the Seebeck coefficient is mainly calculated by using the relaxation time approximation to the Boltzmann equation, but this approximation is correct only if the relaxation time is constant, and it is not a good approximation method for transition metal systems where the band structure on the Fermi surface is very complex. As a method to solve this problem and calculate the Seebeck coefficient in a non-semi-classical quantum mechanical way, a method to calculate the Seebeck coefficient from the energy dependence of electrical conductivity near the Fermi energy using linear response theory has been proposed. In this study, we deal with the temperature dependence of the phonon density of states and anharmonic oscillations, which are not considered in the method for obtaining Seebeck coefficients from electrical conductivities using linear response theory in previous studies.

The study combines three approaches: phonon density of state calculations, the CPA method for static phonons, and linear response theory in the framework of the KKR method. The electrical conductivity and Seebeck coefficients at finite temperature were calculated by using this method. Concretely, we first calculate the phonon density of states assuming harmonic oscillations by the direct method using the first-principles packages VASP[1] or Quantum-ESPRESSO[2] and ALAMODE[3]. Next, the average displacement of the atoms at each temperature is obtained from the phonon

density of states, and the effect is incorporated into the Green function in AkaiKKR, which extends the CPA method to handle the effect of displacement. Finally, the Green function is substituted into the Kubo-Greenwood equation[4] of the KKR-CPA method by Butlar to calculate the temperature-dependent electrical conductivity, and the Seebeck coefficient is obtained from Mahan's equation[5]. In the transition metal system, which is considered to be difficult to calculate using the Boltzmann equation and the relaxation time approximation, we calculate the Seebeck coefficients for the simplest single transition metals using the above method, and confirm that the coefficients reproduce the experimental values well[6].

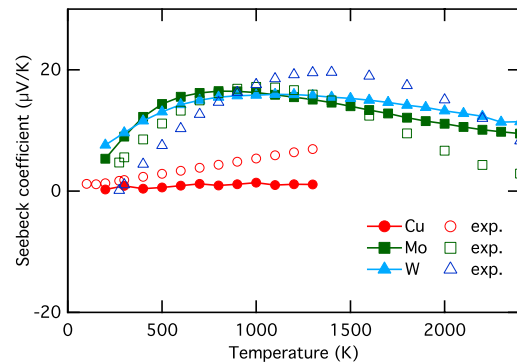


Figure 1: (Color online) Calculated (closed symbol) and experimental[7] (open symbol) Seebeck coefficients S of pure Cu, Mo, and W as functions of temperature.

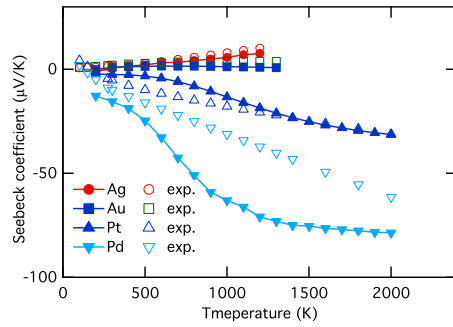


Figure 2: (Color online) Calculated (closed symbol) and experimental[7] (open symbol) Seebeck coefficients S of pure Ag, Au, Pt, and Pd as functions of temperature.

References

- [1] G. Kresse and D. Joubert, *Phys. Rev. B* 59, 1758 (1999)
- [2] Paolo Giannozzi et al., *Phys. Condens. Matter* 21 395502 (2009)
- [3] T Tadano et al., *Phys. Condens. Matter* 26, 225402 (2014)
- [4] W. H. Butler, *Phys. Rev. B* 31 3260 (1985)
- [5] M. Jonson and G. D. Mahan, *Phys. Rev. B* 21, 4223 (1980)
- [6] S. Kou and H. Akai *Solid State Communications* 276 1-4 (2018)
- [7] N. Cusack and P. Kendall, *Proc. Phys. Soc.* 72, 898 (1958)

First-principles calculation of spin-density wave state in chromium metals

Yohei KOTA

*National Institute of Technology, Fukushima College
Iwaki, Fukushima 970-8034*

Chromium metal films are one of practical materials for strain gauge sensor due to showing the high-sensitive response of the electrical resistivity by strain effect. [1] Though the mechanism of the high sensitivity is still unclear, we consider a possibility that the electrical resistivity of chromium metal is greatly influenced by lattice strain, through the modulation of the spin-density wave state. To verify this possibility in the theoretical view point, we analyze the strain effect on the electronic structure in the spin-density wave state of chromium metals by first-principles calculations. For the calculation of the incommensurate spin-density wave state in chromium metals, large unit cells including more than 40 atoms were adopted, with reference to the previous works by Hirai and Hafner *et al.* [2, 3] The Vienna ab-initio simulation package [4] was used for the calculations, where the exchange correlation functional was described within the general gradient approximation.

Figure 1 shows the calculation result of the total energy in the nonmagnetic (NM) state, the commensurate spin-density wave (CSDW) state, and the incommensurate spin-density wave (ISDW) state as a function of the lattice constant a . Note that the wave-number in the ISDW state was set to $q = 0.95 \cdot 2\pi/a$ [\AA^{-1}]. The equilibrium lattice constant in the ISDW state is $a_{\text{eq}} = 2.845$ [\AA], which is approximately 1% smaller than the experimental value $a_{\text{exp}} = 2.884$ [\AA]. We should mention here that the ground state is not the ISDW state but

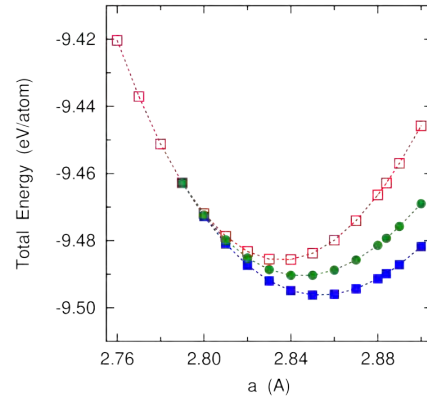


Figure 1: Total energy per atom in NM (red), CSDW (blue), and ISDW (green) states as a function of the lattice constant a .

the CSDW state in the calculation, however, the similar result was obtained in the previous works [2, 3]. On the other hand, it is remarkable that the magnetism of chromium metal disappears for $a \leq 2.78$ [\AA]; this feature is qualitatively consistent with an experiment that the Néel temperature of metallic chromium becomes zero for applying 15 GPa of hydrostatic pressure. [5] This result implies that the magnetism of chromium metal is sensitively variable by lattice strain, corresponding to the fact that the magnetovolume effect is observed significantly in chromium metal.

References

- [1] E. Niwa and Y. Sasaki, IEEJ Trans. SM **134**, 385 (2014).

- [2] K. Hirai, J. Phys. Soc. Jpn. **66**, 560 (1997).
- [3] R. Hafner *et al.*, Phys. Rev. B **65**, 184432 (2002).
- [4] G. Kresse *et al.*, Phys. Rev. B **47**, 558 (1993); Phys. Rev. B **54**, 11169 (1996).
- [5] K. Shimizu *et al.*, Physica B **378-380**, 632 (2006)

Development and application of the first-principles approach

Hiroaki IKEDA

Department of Physics,

Ritsumeikan University, Kusatsu, Shiga 525-8577

We have investigated unconventional superconductors in the strongly correlated electron systems (SCES). The main theme is to develop the first-principles calculations and well describe the electronic structure of SCES. This year, using a Class B, we have studied two topics; superconducting gap anisotropy of the layered Bismuth chalcogenide superconductors (BiCh_2) and the electron correlation effect of the gap structure in iron-based superconductors.

The layered BiCh_2 superconductors possess non-symmorphic structure. Locally inversion symmetry breaking and the strong spin-orbit coupling (SOC) on a Bismuth site can lead to the parity mixing between spin singlet and triplet pairing. In addition, the observed charge / orbital fluctuations potentially yield the gap anisotropy even without strong repulsive interactions. First, we performed the DFT band structure calculations using Quantum espresso [1] in Sekirei system, and made an effective four-orbital models with the SOC using the maximum localized Wannier functions. We have solved the superconducting gap equation in multi-orbital attractive Hubbard model. In the obtained phase diagram, we have found a possibility of topological superconductivity. This study was reported in the JPS autumn meeting 2019 [2].

Next, in the iron-based superconductors, we have applied the quasi-particle self-consistent GW (QSGW) method to KFe_2As_2 and studied the gap structure in the effective Hubbard

model. In general, the conventional LDA / GGA calculations describe the overall feature of the band structure. However, the size and curvature of the Fermi surface and the composed orbital characters are significantly deviated from the experimental observations. This has a sizable effect on the gap structure. In Fig. 1, we indicate the Fermi surface and the gap structure. Emergence of propeller-type Fermi pockets is well consistent with the experimental data. Furthermore, the change of orbital characters turns the gap structure from horizontal nodes to octet node structure. This study was reported in MRM2019 [3].

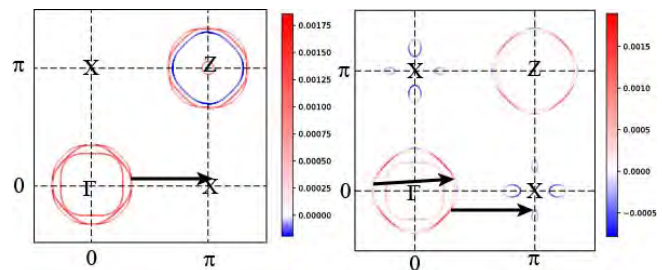


Fig. 1 Gap structure on the Fermi surface in KFe_2As_2 obtained by GGA (left) and QSGW (right).

References

- [1] P. Giannozzi *et al.*, *J.Phys.:Condens.Matter* **21**, 395502 (2009)
- [2] K. Suzuki, JPS Autumn meeting 10pB17-4
- [3] K. Suzuki, MRM2019 D3-13(1)-113

3.3 Strongly Correlated Quantum Systems

Mechanism of quantum spin liquid and high- T_c superconductivity studied by excitation spectra and nonequilibrium dynamics calculation by variational Monte Carlo methods

Masatoshi IMADA

Toyota Physical and Chemical Research Institute

41-1 Yokomichi, Nagakute, Aichi, 480-1192

and

Research Institute for Science and Engineering, Waseda University

3-4-1 Okubo, Shinjuku-ku, Tokyo, 169-8555

Understanding physics of high- T_c cuprate superconductors remains one of the important problems in materials science. In this project, we have reproduced the experimental phase diagram of $\text{HgBa}_2\text{CuO}_{4+y}$ [1] by solving its *ab initio* low-energy effective Hamiltonian without adjustable parameters [2]. It shows a superconducting phase in a wide range of hole density δ , and its competition with charge period-4 plus spin period-8 stripe order near $\delta \sim 0.1$, in agreement with experimental results.

A crucial role of off-site interactions in stabilizing the superconductivity is elucidated with emphasis on charge fluctuations. It also clarifies the condensation energy mainly contributed from the on-site Coulomb interaction. The present achievement will enable deeper, predictable understanding on open issues of the high- T_c superconducting mechanism and promote *ab initio* studies on strongly correlated electrons beyond parametrized model studies.

In former studies on a simplified effective

model, namely Hubbard model on the square lattice had clarified that the *d*-wave superconducting state is severely competing with the stripe ordered state, while most of the phase diagram in the parameter space of the carrier doping concentration is dominated by the stripe order and the superconducting state remains an excited state [3,4]. Therefore, the Hubbard model does not properly account for the experimental phase diagram of the cuprate superconductors. However, it has also been shown that the superconducting phase in the *ab initio* Hamiltonian is adiabatically connected with that found in the superconducting excited state of the Hubbard model. Therefore, it is intriguing to understand the distinction of the superconducting state in between the *ab initio* and Hubbard cases. The method for dynamical properties newly developed offer useful insights into this issue as we describe in the next section.

Calculations of dynamical quantities are a challenging subject for strongly correlated electron systems even in the linear response

regime. Recently we have developed a method to calculate the dynamical correlation functions based on the variational Monte Carlo method [3,4]. We first developed a method to calculate the charge dynamical structure factors for the ground states of correlated electron systems. Our benchmarks for the one- and two-dimensional Hubbard models show that inclusion of composite-fermion excitations in the basis set greatly improves the accuracy, in reference to the exact charge dynamical structure factors for clusters. Together with examination for larger systems beyond tractable sizes by the exact diagonalization, our results indicate that the variational Monte Carlo method is a promising way for studies on the nature of charge dynamics in correlated materials such as the copper oxide superconductors if the composite-fermion excitations are properly included in the restricted Hilbert space of intermediate states in the linear response theory. Our results on the charge dynamical structure factor are consistent with the particle-hole excitations inferred from the single-particle spectral function $A(k,\omega)$ in the literature. The importance of incorporating nonlocal composite fermion for a more accurate description is also pointed out [3].

This method can be extended to calculate the one-body Green's function by improving the variational Monte Carlo method. We benchmark against the exact diagonalization for the one- and two-dimensional Hubbard models of 16 site lattices, which proves high accuracy of the

method. The application of the method to larger-sized Hubbard model on the square lattice correctly reproduces the Mott insulating behavior at half filling and gap structures of d -wave superconducting state of the hole doped Hubbard model in the ground state optimized by enforcing the charge uniformity, evidencing a wide applicability to strongly correlated electron systems.

From the obtained d -wave superconducting gap of the charge uniform state, we find that the gap amplitude at the antinodal point is several times larger than the experimental value, when we employ a realistic parameter as a model of the cuprate superconductors. The effective attractive interaction of carriers in the d -wave superconducting state inferred for an optimized state of the Hubbard model is as large as the order of the nearest-neighbor transfer, which is far beyond the former expectation in the cuprates. The nature of the superconducting state of the Hubbard model in terms of the overestimate of the gap and the attractive interaction in comparison to the cuprates are clarified [4].

Finding quantum spin liquids is another important subject of the present research project. Topological properties of the strongly correlated systems with strong spin-orbit interaction are one of such subjects. We have studied Heisenberg model with spin-orbit interaction (Dzyaloshinskii-Moriya interaction) on the pyrochlore lattice by using the variational Monte

Carlo method. This system has been proposed to be a candidate of the quantum spin liquid in earlier studies. We will report the result on this subject in the future.

Another candidate of the quantum spin liquid is found in a quantum Heisenberg model with the geometrically frustrated square lattice, called J_1 - J_2 model. By utilizing the machine learning method, we have found a firm evidence for the quantum spin liquid and clarified its excitation spectra, which indicate the fractionalization of spins into spinons. The subject has a close connection to the experimentally observed spin liquid state in molecular conductors. Studies on the *ab initio* low-energy effective Hamiltonian for a dmit compound are underway and will be reported elsewhere.

This is a combined report for E project “Mechanism of quantum spin liquid and high- T_c superconductivity studied by excitation spectra and nonequilibrium dynamics calculation by variational Monte Carlo methods”, “Development of methodology for analysis of nonequilibrium superconductivity in strongly correlated systems via integration of electronic state theory and time-resolved experimental data”, and shared project for post-K project “Studies on quantum spin liquids in molecular

conductors based on first-principles Hamiltonian”.

and “Studies on Quantum Spin Liquids in Materials with Strong Spin-Orbit Interaction”

This series of work has been done in collaboration with T. Ohgoe, T. Misawa, M. Hirayama, K. Ido, Y. Nomura, Y. Yamaji, R. Pohle and M. Charlebois. The calculations were performed on computers at the Supercomputer Center, ISSP, Univ. of Tokyo. The work is also supported by JSPS Kakenhi 16H06345, the RIKEN Center for Computational Science under the HPCI project (hp190145) and the MEXT HPCI Strategic Programs, CDMSI. This project has used the software HPhi and mVMC.

References

- [1] Motoaki Hirayama, Takahiro Misawa, Takahiro Ohgoe, Youhei Yamaji, Masatoshi Imada, Phys. Rev. B **99** (2019) 245155.
- [2] Takahiro Ohgoe, Motoaki Hirayama, Takahiro Misawa, Kota Ido, Youhei Yamaji, Masatoshi Imada, Phys. Rev. B **101** (2020) 045124.
- [3] Kota Ido, Masatoshi Imada, Takahiro Misawa, Phys. Rev. B **101** (2020) 075124.
- [4] Maxime Charlebois, and Masatoshi Imada, arXiv:1912.09960.

Numerical studies on energy current correlations in frustrated quantum spin systems

Youhei YAMAJI

*Department of Applied Physics, The University of Tokyo
Hongo 7-3-1, Bunkyo-ku, Tokyo 113-8656*

Topological states of matters are often characterized by quantized transport properties. As a prototypical example, two dimensional Chern insulators are characterized by the quantized charge Hall effect. In the Mott insulators, however, the quantization of thermal Hall transports characterizes the topological states, instead of the charge transports [1, 2]. The quantum spin liquid state of the Kitaev model is a typical example of the topological state that shows half-integer quantized thermal Hall transports [1]. The observation of the half-integer quantized thermal Hall coefficient in a spin-orbit coupled Mott insulator α -RuCl₃ has attracted broad attention [3].

We studied numerical methods to characterize the topological spin liquids. The thermal transport is calculated by correlations of thermal currents and energy magnetization [4]. These quantities are formulated by energy current operators, which are given by the continuity equation of the energy density.

For the lattice hamiltonian, the energy density is represented by the bond energy as follows. Here, we show the continuity equation of the energy density of the Kitaev-type magnets on the honeycomb lattice as an example. The nearest-neighbor bonds on the honeycomb lattice have three different directions. When the three bonds are labeled as x , y , and z , an effective hamiltonian of α -RuCl₃, the Kitaev- Γ

hamiltonian,

$$\hat{H} = \sum_{\gamma=x,y,z} \sum_{\langle \ell,m \rangle \in \gamma} \hat{H}_{\ell m}^{(\gamma)}, \quad (1)$$

is defined by the exchange coupling for the γ ($= x, y, z$) bond,

$$\hat{H}_{\ell m}^{(\gamma)} = K \hat{S}_{\ell}^{\gamma} \hat{S}_{m}^{\gamma} + \Gamma \left(\hat{S}_{\ell}^{\alpha} \hat{S}_{m}^{\beta} + \hat{S}_{\ell}^{\beta} \hat{S}_{m}^{\alpha} \right) \quad (2)$$

where (α, β, γ) is a permutation of (x, y, z) and K (Γ) is the Kitaev (off-diagonal symmetric) exchange coupling. The bond energy of the hamiltonian is, then, introduced as the Fourier components,

$$\begin{aligned} \hat{H}_{\mathbf{q}} &= \sum_{\gamma} \sum_{\langle \ell,m \rangle_{\gamma}} e^{+i(\mathbf{q}/2) \cdot (\mathbf{R}_{\ell} + \mathbf{R}_m)} \\ &\times \left[K \hat{S}_{\ell}^{\gamma} \hat{S}_{m}^{\gamma} + \Gamma \left(\hat{S}_{\ell}^{\alpha} \hat{S}_{m}^{\beta} + \hat{S}_{\ell}^{\beta} \hat{S}_{m}^{\alpha} \right) \right], \quad (3) \end{aligned}$$

where $\epsilon_{\alpha\beta\gamma}$ ($\alpha, \beta, \gamma = x, y, z$). By using the small \mathbf{q} limit of the continuity equation of the bond energy,

$$\frac{d\hat{H}_{\mathbf{q}}}{dt} \sim -i\mathbf{q} \cdot \mathbf{j}_E, \quad (4)$$

we determine the energy current operator \mathbf{j}_E . When, for simplicity, $K = 0$ is chosen, the Heisenberg equation of motion,

$$\frac{d\hat{H}_{\mathbf{q}}}{dt} = \frac{i}{\hbar} \left[\hat{H}, \hat{H}_{\mathbf{q}} \right], \quad (5)$$

defines \mathbf{j}_E with the commutator,

$$\begin{aligned}
\frac{i}{\hbar} [\hat{H}, \hat{H}\mathbf{q}] &= \frac{i}{\hbar} \Gamma^2 \sum_{\ell} \left[\mathbf{q} \cdot \boldsymbol{\delta}_{xz,\ell} \left(\hat{S}_{m_x}^y \hat{S}_{\ell}^x \hat{S}_{m_z}^x + \hat{S}_{m_x}^z \hat{S}_{\ell}^z \hat{S}_{m_z}^y - \hat{S}_{m_x}^y \hat{S}_{\ell}^y \hat{S}_{m_z}^y \right) \right. \\
&+ \mathbf{q} \cdot \boldsymbol{\delta}_{zy,\ell} \left(\hat{S}_{m_z}^x \hat{S}_{\ell}^z \hat{S}_{m_y}^z + \hat{S}_{m_z}^y \hat{S}_{\ell}^y \hat{S}_{m_y}^x - \hat{S}_{m_z}^x \hat{S}_{\ell}^x \hat{S}_{m_y}^y \right) \\
&+ \left. \mathbf{q} \cdot \boldsymbol{\delta}_{yx,\ell} \left(\hat{S}_{m_y}^z \hat{S}_{\ell}^y \hat{S}_{m_x}^y + \hat{S}_{m_y}^x \hat{S}_{\ell}^x \hat{S}_{m_x}^z - \hat{S}_{m_y}^z \hat{S}_{\ell}^z \hat{S}_{m_x}^x \right) \right] \\
&+ \frac{i}{\hbar} \Gamma^2 \sum_m \left[\mathbf{q} \cdot \boldsymbol{\delta}_{xz,m} \left(\hat{S}_{\ell_x}^y \hat{S}_m^x \hat{S}_{\ell_z}^z + \hat{S}_{\ell_x}^z \hat{S}_m^z \hat{S}_{\ell_z}^y - \hat{S}_{\ell_x}^y \hat{S}_m^y \hat{S}_{\ell_z}^z \right) \right. \\
&+ \mathbf{q} \cdot \boldsymbol{\delta}_{zy,m} \left(\hat{S}_{\ell_z}^x \hat{S}_m^z \hat{S}_{\ell_y}^z + \hat{S}_{\ell_z}^y \hat{S}_m^y \hat{S}_{\ell_y}^x - \hat{S}_{\ell_z}^x \hat{S}_m^x \hat{S}_{\ell_y}^y \right) \\
&+ \left. \mathbf{q} \cdot \boldsymbol{\delta}_{yx,m} \left(\hat{S}_{\ell_y}^z \hat{S}_m^y \hat{S}_{\ell_x}^y + \hat{S}_{\ell_y}^x \hat{S}_m^x \hat{S}_{\ell_x}^z - \hat{S}_{\ell_y}^z \hat{S}_m^z \hat{S}_{\ell_x}^z \right) \right], \tag{6}
\end{aligned}$$

where $\boldsymbol{\delta}_{\alpha\beta,\ell}$ is the vector from the center of the α -bond terminated by ℓ th site and to the center of the β -bond terminated also by ℓ th site.

The energy-current–energy-current correlations and energy magnetization for the Kitaev- Γ hamiltonian at finite temperatures are calculated by combining the Krylov subspace methods and typicality approaches [5] and will be reported elsewhere [6].

The topological nature of the Mott insulating states will be destroyed by spontaneous symmetry breakings. Therefore, to clarify the topology, we need to examine whether the spin liquid candidates show spontaneous symmetry breakings or not. We have modified mVMC [7] to calculate higher-order spin correlations and calculated the singlet-singlet correlators of a typical frustrated quantum spin systems, the Heisenberg model on pyrochlore lattices. So far, the inversion symmetry is spontaneously broken in the lowest variational state.

References

- [1] A. Kitaev: Ann. Phys. **321** (2006) 2.
- [2] C. Wang, A. C. Potter, and T. Senthil: Science **343** (2014) 6171.
- [3] Y. Kasahara, *et al.*: Nature **559** (2018) 227.
- [4] T. Qin, Q. Niu, and J. Shi: Phys. Rev. Lett. **107** (2011) 236601.
- [5] Y. Yamaji, T. Suzuki, and M. Kawamura: arXiv:1802.02854.
- [6] Y. Yamaji, *et al.*: in preparation.
- [7] T. Misawa, *et al.*: Compt. Phys. Commun. **235** (2019) 447.

Theoretical study of spin-orbit coupled phenomena in correlated electron systems

Yukitoshi MOTOME

Department of Applied Physics,

The University of Tokyo, Bunkyo, Tokyo 113-8656

We have theoretically studied a variety of intriguing phenomena in correlated electron systems with spin-orbit coupling, ranging from Mott insulators to metals. During this fiscal year, we have achieved substantial progress on the following topics (project numbers: H31-Ca-0052 and H31-Cb-0032). We summarize the main results below.

(i) *Kitaev quantum spin liquids*: By using *ab initio* based calculations, we theoretically proposed new candidates for the Kitaev magnets with unconventional antiferromagnetic Kitaev interactions: Pr-based *f*-electron compounds [1,2] and polar asymmetric systems [3]. We also clarified real-time dynamics of fractional excitations in the Kitaev quantum spin liquids [4], Majorana-magnon crossover in an applied magnetic field [5], and exotic phase transitions in three-dimensional extensions of the Kitaev models [6,7]. In addition, we have collaborated with several experimental groups for identifying the signatures of Majorana excitations in the Kitaev magnets: nuclear quadrupole and magnetic resonances [8], Raman scattering [9], and thermal Hall effect [10]. We have summarized the recent results on

this topic in review articles [11,12,13].

(ii) *Chiral magnets*: We theoretically unveiled that a nonreciprocal spin transport, which is switchable by a magnetic field, can occur in monoaxial magnets [14]. We also clarified that interplay between spin, charge, and orbital degrees of freedom plays a crucial role in stabilizing the magnetic hedgehog lattices recently found in *B20* chiral magnets [15]. We also showed that the magnetic monopoles and antimonopoles associated with the magnetic hedgehogs annihilate in pair by magnetic fields and cause topological phase transitions [15,16].

(iii) *Multipole physics*: We theoretically proposed that the successive phase transitions in a spin-orbit coupled metal $\text{Cd}_2\text{Re}_2\text{O}_7$ are driven by electric toroidal quadrupoles [17]. We also clarified that nonmagnetic impurities can induce magnetic and toroidal multipoles in ferromagnets [18].

(iv) *Spin current generation*: We discovered a new mechanism of spin current generation, which can work even in the absence of the spin-orbit coupling [19]. We also developed the understanding of this phenomenon based on the cluster multipole picture [20].

References

- [1] S.-H. Jang, R. Sano, Y. Kato, and Y. Motome, Phys. Rev. B **99**, 241106(R) (2019).
- [2] S.-H. Jang, R. Sano, Y. Kato, and Y. Motome, preprint (arXiv:1912.03422).
- [3] Y. Sugita, Y. Kato, and Y. Motome, Phys. Rev. B **101**, 100410(R) (2020).
- [4] J. Nasu and Y. Motome, Phys. Rev. Research **1**, 033007 (2019).
- [5] J. Yoshitake, J. Nasu, Y. Kato, and Y. Motome, Phys. Rev. B **101**, 100408(R) (2020).
- [6] T. Eschmann, P. A. Mishchenko, T. A. Bojesen, Y. Kato, M. Hermanns, Y. Motome, and S. Trebst, Phys. Rev. Research **1**, 032011(R) (2019).
- [7] P. A. Mishchenko, Y. Kato, K. O'Brien, T. A. Bojesen, T. Eschmann, M. Hermanns, S. Trebst, and Y. Motome, Phys. Rev. B **101**, 045118 (2020), *Editors' Suggestion*.
- [8] Y. Nagai, T. Jinno, Y. Yoshitake, J. Nasu, Y. Motome, M. Itoh, and Y. Shimizu, Phys. Rev. B **101**, 020414(R) (2020).
- [9] Y. Wang, G. B. Osterhoudt, Y. Tian, P. Lampen-Kelley, A. Banerjee, T. Goldstein, J. Yan, J. Knolle, H. Ji, J. Cava, J. Nasu, Y. Motome, S. Nagler, D. Mandrus, and K. S. Burch, npj Quant. Mat. **5**, 14 (2020).
- [10] T. Yokoi, S. Ma, Y. Kasahara, S. Kasahara, T. Shibauchi, N. Kurita, H. Tanaka, J. Nasu, Y. Motome, C. Hickey, S. Trebst, and Y. Matsuda, preprint (arXiv:2001.01899).
- [11] Y. Motome and J. Nasu, J. Phys. Soc. Jpn. **89**, 012002 (2020), *INVITED REVIEW PAPER*.
- [12] 求 幸年, 那須 讓治, 固体物理 **54**, 217 (2019).
- [13] Y. Motome, R. Sano, S.-H. Jang, Y. Sugita, and Y. Kato, preprint (arXiv:2001.03731), in press in J. Phys.: Condens. Matter, *Special Issue Article*.
- [14] S. Okumura, H. Ishizuka, Y. Kato, J. Ohe, and Y. Motome, Appl. Phys. Lett. **115**, 012401 (2019).
- [15] S. Okumura, S. Hayami, Y. Kato, and Y. Motome, preprint (arXiv:1908.05044), in press in Phys. Rev. B.
- [16] S. Okumura, S. Hayami, Y. Kato, and Y. Motome, JPS Conf. Proc. **30**, 011010 (2020).
- [17] S. Hayami, Y. Yanagi, H. Kusunose, and Y. Motome, Phys. Rev. Lett. **122**, 147602 (2019), *selected as a Cover Image*.
- [18] S. Hayami, H. Kusunose, and Y. Motome, J. Phys. Soc. Jpn. **88**, 063702 (2019).
- [19] M. Naka, S. Hayami, H. Kusunose, Y. Yanagi, Y. Motome, and H. Seo, Nat. Commun. **10**, 4305 (2019).
- [20] S. Hayami, Y. Yanagi, M. Naka, H. Seo, Y. Motome, and H. Kusunose, JPS Conf. Proc. **30**, 011149 (2020).

Numerical Studies on the Role of the Incipient Band Played in Two-band Unconventional Superconductivity

KAZUHIKO KUROKI

Department of Physics, Osaka University

1-1 Machikaneyama, Toyonaka, Osaka, 560-0043, Japan

We have been studying spin-fluctuation-mediated superconductivity in two-band systems with one of the bands intersecting the Fermi level while the other band (“incipient band”) sits in the vicinity of the Fermi level. In ref.[1, 2], we studied the Hubbard model on a two-leg ladder lattice, which is characterized by the nearest neighbor hoppings in the leg (t) and the rung (t_r) directions, and also the diagonal next nearest neighbor hoppings t' (Fig.1).

In 2019 fiscal year, we have extended the study to two dimensional (2D) systems. A simplest extension of the two-leg ladder Hubbard model to two dimensions is the bilayer square lattice Hubbard model, where two Hubbard models on a square lattice are coupled by vertical hoppings t_\perp along with diagonal hoppings t' (Fig.1). Here, t_\perp controls the relative energy between the two bands like t_r in the two-leg ladder. We adopted the fluctuation exchange (FLEX) approximation, and solved the linearized Eliashberg equation to obtain the eigenvalue at a fixed temperature ($T = 0.05t$), which gives a measure for the superconducting transition temperature. We investigated a large parameter space of (t_\perp, t', n, U) , where n is the band filling and U is the on-site Hubbard interaction.[3] Simultaneously, we also performed similar calculation for

the two-leg ladder Hubbard model, and made a comparison between the two models.

In Fig.2, we show for $t' = 0$ the eigenvalue λ plotted against t_\perp for the bilayer and t_r for the two-leg ladder. For each t_\perp or t_r , the maximum eigenvalue is searched by varying the band filling n . We perform the calculation for $U = 6t$ and $U = 3t$. For $U = 6t$ in the bilayer and for both values of U in the ladder, λ is maximized when the bonding band touches the Fermi level, i.e., when the band is incipient. This is not the case for $U = 3t$ in the

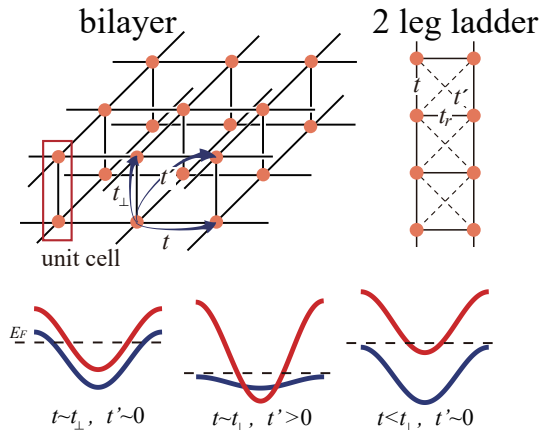


FIG. 1. Upper panel : the bilayer lattice (left) and the two-leg ladder lattice (right). Lower panels : schematic images of the bonding and antibonding bands of the bilayer lattice. Left : $t \sim t_\perp, t' \sim 0$, middle : $t \sim t_\perp, t' > 0$, right : $t < t_\perp, t' \sim 0$. In the middle and right panels, the bonding band is incipient.

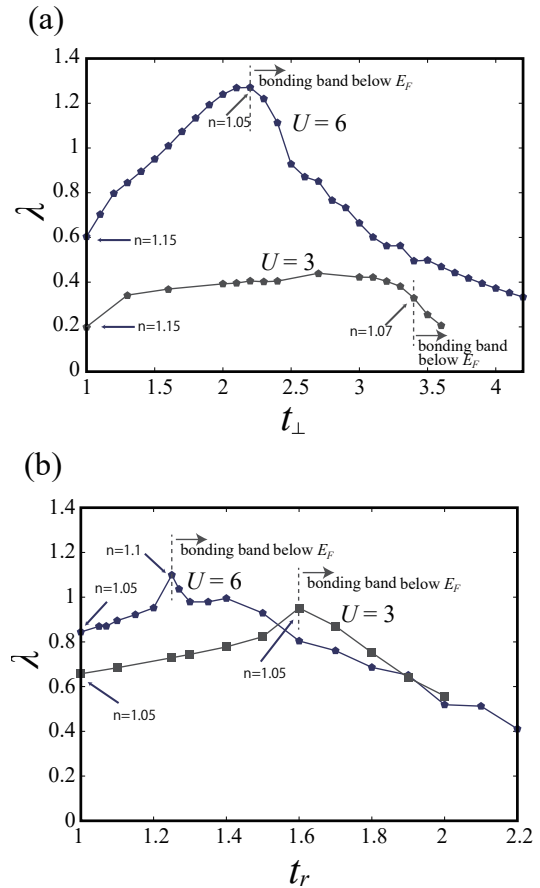


FIG. 2. (a) Maximized λ at $T = 0.05$ of the bilayer Hubbard model with $U = 6t$ or $3t$ and $t' = 0$ plotted against t_\perp . λ is maximized at each t_\perp by varying the band filling n . At some points, n that maximizes λ is denoted by arrows. (b) Similar plot for the two-leg Hubbard ladder model, where t_\perp is replaced by t_r . From Ref.[3].

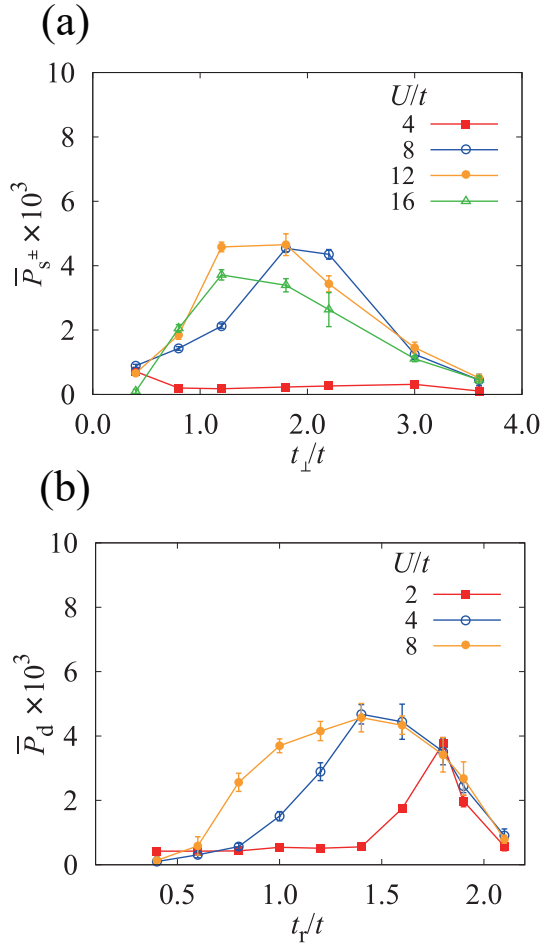


FIG. 3. mVMC calculation results of the pairing correlation for the two models with $t' = 0$. (a) t_{\perp}/t dependence of the pairing correlation $\bar{P}_{s\pm}$ (interlayer nearest neighbor pairing) for the bilayer model with various values of U/t . The band filling is $n = 1.06$. (b) t_r dependence of the pairing correlation \bar{P}_d (interchain nearest neighbor pairing) for the two-leg ladder model with various values of U/t . The band filling is $n = 1.03$. From Ref.[6].

bilayer, where λ is significantly reduced.

We also performed multivariable variational Monte Carlo calculation (mVMC) [4, 5] study for the two models, and calculated the pairing correlation function against t_{\perp} (bilayer) or t_r (two-leg ladder)[6]. The results shown in Fig.3 resemble the FLEX results of the eigenvalue of the Eliashberg equation shown in Fig.2 (note that FLEX is performed only in the $t_{\perp} \geq t$ or $t_r \geq t$ regime).

The above FLEX and mVMC results suggest that, when U is sufficiently large, superconductivity is strongly enhanced in both the bilayer and two-leg ladder models when the bonding band is incipient. As t_{\perp} or t_r becomes small and the bonding band intersects the Fermi level, superconductivity is significantly degraded for the bilayer model, but not so strongly in the ladder. When U be-

comes small, the overall tendency does not change much in the ladder (except that larger t_r is needed for the bonding band to be incipient because the band width renormalization is weak), but for the bilayer model, superconductivity is strongly suppressed and it is no longer optimized in the incipient band situation.

It is known that the spin fluctuations within a certain moderate energy range work effectively as pairing glue, while those in the very low energy range are pair breaking[7]. This, combined with the difference in the density of states (DOS) for the two models due to the difference in the dimensionality, enables us to understand the obtained results[3, 6]. Namely, when the bonding band is incipient, the low-energy spin fluctuations is suppressed because only the states around the bonding band edge can contribute to their development, while there is significant contribution from the bonding band to the moderate-energy spin-fluctuations. This is the reason why superconductivity is strongly enhanced in the incipient band situation. As t_{\perp} or t_r is reduced and the bonding band intersects the Fermi level, the low energy spin fluctuation rapidly develops in the bilayer lattice because the DOS of the bonding band at the Fermi level increases, while the development of the low energy spin fluctuation in the ladder is moderate because the DOS of the bonding band decreases as the Fermi level moves toward the middle of the band. This explains the difference between the two models. As for the effect of U , the band width is reduced by the renormalization, so that the bonding band becomes incipient for a smaller t_{\perp} or t_r for larger U . This effect is essential for superconductivity to be strongly enhanced in the bilayer model because in this way the portion of the DOS that contributes to superconductivity is squeezed into a narrower energy range. This effect is not so important in the ladder, where the DOS at the band edge is diverging.

-
- [1] K. Kuroki, T. Higashida, and R. Arita, Phys. Rev. B **72**, 212509 (2005).
 - [2] K. Matsumoto, D. Ogura, and K. Kuroki, Phys. Rev. B **97**, 014516 (2018).
 - [3] K. Matsumoto, D. Ogura, and K. Kuroki, J. Phys. Soc. Jpn. **89**, 044709 (2020).
 - [4] D. Tahara and M. Imada, J. Phys. Soc. Jpn. **77**, 114701 (2008).
 - [5] T. Misawa *et al.*, Comp. Phys. Comm. **235**, 447 (2019).
 - [6] D. Kato and K. Kuroki, Phys. Rev. Research, to appear (2020) (arXiv:1912.11983).
 - [7] A.J. Millis, S. Sachdev and C.M. Varma, Phys. Rev. B **37**, 4975 (1988).

Study of magnetism and transport phenomena in strongly correlated quantum systems using computational approaches including non-equilibrium methods

Norio KAWAKAMI

Department of Physics,

Kyoto University, Kitashirakawa, Sakyo-ku, Kyoto 606-8502

We have studied strongly correlated quantum systems with a focus on magnetism and transport phenomena, using computational approaches, including non-equilibrium methods.

We have analyzed the effect of correlations on the emergence of quantum oscillation in narrow-gap topological Kondo insulators by performing dynamical mean-field theory (DMFT) calculations. We have demonstrated that the interplay between correlations and nonlocal hybridizations can lead to observable quantum oscillations even without a Fermi surface and that quantum oscillations in a three-dimensional system can be understood from the physics of the two-dimensional planes in the momentum space for which the hybridization in the direction of the magnetic field vanishes. This scenario should be relevant for understanding the observations in SmB₆ and YbB₁₂. [1]

We have studied the impact of non-Hermiticity due to strong correlations in f -electron materials, by analyzing the periodic-Anderson model with local and nonlocal hybridization in the insulating and metallic regimes by DMFT combined with numerical renormalization group (NRG). We have shown that exceptional points, momenta in the

Brillouin zone at which the effective non-Hermitian Hamiltonian cannot be diagonalized, occur at the Kondo temperature, at which the magnetic moments are screened, and the well-known crossover between localized and itinerant f electrons takes place. [2]

Furthermore, we have studied the one-band Hubbard model on the honeycomb lattice by DMFT as well as by numerically exact quantum Monte Carlo simulations. We have shown that the DMFT approximation is very accurate in the Dirac semi-metallic phase, where local moment formation is present, and the spin correlation length small. Moreover, we have shown that although the quantum critical point can only be understood by lattice Quantum Monte Carlo techniques, DMFT gives a reasonable estimate of the critical interaction strength. [3]

References

- [1] R. Peters, T. Yoshida, and N. Kawakami, *Phys. Rev. B* **100**, 085124 (2019).
- [2] Y. Michishita, T. Yoshida, and R. Peters, *Phys. Rev. B* **101**, 085122 (2020).
- [3] M. Raczkowski, R. Peters, T. T. Phung, N. Takemori, F. F. Assaad, A. Honecker, and J. Vahedi, *Phys. Rev. B* **101**, 125103 (2020).

Study on metal-insulator transition in nickel oxides

Yusuke NOMURA

RIKEN Center for Emergent Matter Science, 2-1 Hirosawa, Wako, 351-0198

Rare-earth nickelates LuNiO_3 shows an interesting phase diagram. Starting from the room temperature, by cooling, it exhibits two-step transitions. The first one is the metal-insulator transition, and the second one is the magnetic transition. At the first transition, interestingly, bond disproportionation occurs, where one set of octahedra is compressed, and the other is expanded. It means that the displacement of breathing phonon mode is induced, and the Jahn-teller mode becomes inactive despite the $(e_g)^1$ configuration.

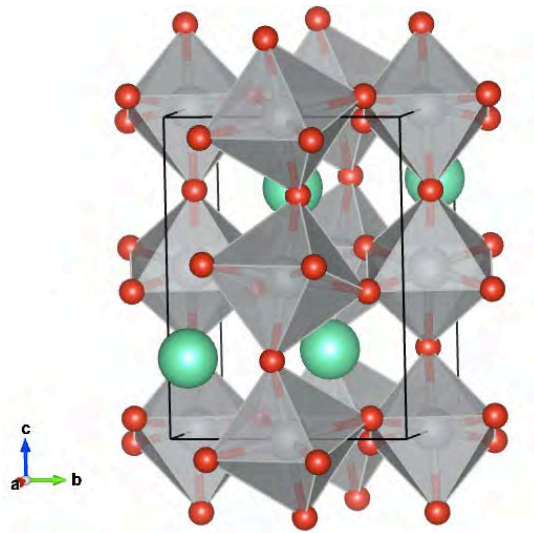


Fig. 1: Crystal structure of LuNiO_3 at high temperature.

In this study, we derive the effective low-

energy Hamiltonians for LuNiO_3 e_g manifold. We explicitly include the phonon degrees of freedom using newly-developed constrained density functional perturbation theory (cDFPT) [1]. We calculate the magnitude of phonon-mediated electron-electron interaction as well as the effective Coulomb interactions.

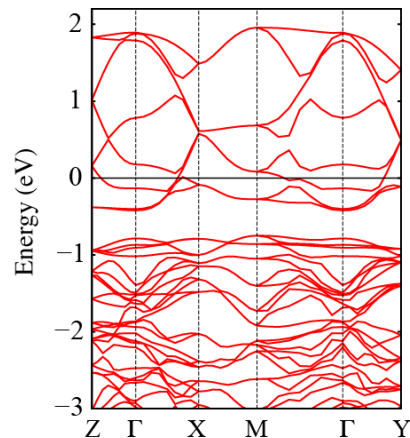


Fig. 2: Band structure of LuNiO_3 .

As a result, we find that coupling to the Jahn-Teller phonon mode indeed exists, which favors Jahn-Teller distortion. However, at the same time, non-local Coulomb interaction, which favors bond disproportionation, is substantial. Therefore, the coupling to Jahn-Teller mode and the non-local Coulomb interaction compete with each other. In the real material, the latter wins, and the bond disproportionation takes

place at the metal-insulator transition.

References

- [1] YN et al., Phys. Rev. Lett. **112**, 027002 (2014); YN and R. Arita, Phys. Rev. B **92**, 245108 (2015)

Study on frustrated magnetism using machine learning

Yusuke NOMURA

RIKEN Center for Emergent Matter Science, 2-1 Hirosawa, Wako, 351-0198

Quantum spin liquid (QSL) is an exotic state of the matter, in which long-range magnetic order is suppressed even at zero temperature. The QSL has attracted much attention not only because of its unique property such as the fractionalization of the excitation but also because of possible applications to quantum computing and memory devices. However, to show the existence of the QSL in the realistic quantum-spin Hamiltonians, except for rare cases such as the Kitaev model where the exact ground state can be constructed by hand, we need highly accurate numerical methods.

To achieve high accuracy, we focus on machine learning. Machine learning is good at extracting essential patterns in the data. By applying it to the quantum-many body problems, we can obtain an accurate representation of the quantum many-body wave functions (vector with exponentially large dimensions) with a finite number of parameters (data compression). Starting from the seminal work by Carleo and Troyer [1], now, there is growing evidence for the powerfulness of the machine learning method to study many-body problems. However, studies so far are limited to

the benchmark to check the usefulness of machine learning, and interesting applications to explore many-body physics have not yet performed.

In the study, by using a newly-developed machine learning method (RBM+PP), which combines the restricted Boltzmann machine (RBM) and pair-product (PP) state [2], we obtain strong support for the existence of the QSL phase in the thermodynamic limit of the spin-1/2 Heisenberg spin system on the square lattice with the nearest-neighbor and next-nearest-neighbor exchanges, J_1 and J_2 , respectively, called the J_1 - J_2 Heisenberg model. The QSL phase shows unconventional excitation spectrum, in which both the singlet and triplet excitations become gapless at high-symmetry momenta $(0,0)$, $(\pi,0)$, $(0,\pi)$, (π,π) , in support of the nodal Dirac dispersion of the fractionalized spinon at $(\pm\pi/2, \pm\pi/2)$.

References

- [1] G. Carleo and M. Troyer, *Science* **355**, 602 (2017).
- [2] Y. Nomura, A. S. Darmawan, Y. Yamaji, and M. Imada, *Phys. Rev. B* **96**, 205152 (2017).

Variational Monte Carlo calculation of two-dimensional Wigner crystal under lattice commensurability

Takeo KATO

*Institute for Solid State Physics, University of Tokyo
Kashiwa-no-ha, Kashiwa, Chiba 277-8581*

Wigner crystallization, which breaks the translational symmetry due to the long-range Coulomb interactions, is a fundamental problem in strongly correlated electron systems. By the diffusive quantum Monte Carlo method (DQMC), the critical electron density for crystallization is obtained as $r_s = r_0/a_B^* \simeq 150$ for a three-dimensional electron gas ($r_0 = (\pi n_e)^{-1/2}$, a_B^* : the effective Bohr radius) [1]. The critical value of r_s is lowered down to $r_s \simeq 31$ for a two-dimensional electron gas [2, 3]. In addition to the Coulomb interaction, the lattice commensurability reduces the critical Coulomb interaction for crystallization [4].

In this work, we studied the Wigner crystallization in spinless Fermion systems on a square lattice at finite fillings by highly accurate simulation based on the many-variable variational Monte Carlo (mVMC) method [5]. By performing the calculations up to the order of 10^3 sites, we determine the transition points for $n = 2, 4, 8, 12, 16$ and draw the phase diagram as functions of r_s and $1/n$ as shown in Fig. 1.

In contrast to the previous works by path-integral renormalization group (PIRG) [4], we found that the transition points at finite fillings becomes significantly small. Nevertheless, the transition points seem to continuously connect to its continuum limits, which is consistent with the previous works. We also examined the nature of the associated metal-insulator transition by calculation the momentum distribution

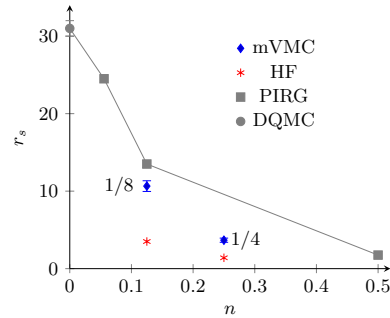


Figure 1: Phase diagram in the plane of the electron-density and r_s . We also show the result of the Hartree-Fock (HF) approximation.

and the charge gap [6].

References

- [1] D. M. Ceperley and B. J. Alder, Phys. Rev. Lett. **45**, 566 (1980).
- [2] M. Imada and M. Takahashi, J. Phys. Soc. Jpn. **53**, 3770 (1984).
- [3] N. D. Drummond and R. J. Needs, Phys. Rev. Lett. **102**, 126402 (2009).
- [4] Y. Noda and M. Imada, Phys. Rev. Lett. **89**, 176803 (2002).
- [5] T. Misawa, et al., Comput. Phys. Commun. **235**, 447 (2019).
- [6] M. K. Ritter, K. Ido, T. Misawa, and T. Kato, in preparation.

Magnetic and transport properties in double-exchange systems with quasiperiodicity

Akihisa Koga

Department of Physics, Tokyo Institute of Technology, Meguro, Tokyo 152-8551

Quasicrystals (QCs) have no translational symmetry but possess long-range order and special rotational symmetry. Since its first discovery in 80's, intensive efforts have been made to search various type of QC materials and to reveal characteristic features. In this decade, there have been several important experimental findings in QC materials, which include quantum critical behaviors in Au-Al-Yb alloy and the emergence of superconductivity in Al-Zn-Mg QC alloy. These experiments suggest important roles of electronic correlations in these materials, and stimulate theoretical studies of the correlation and induced ordered phases in QC systems.

Motivated by this situation, we have studied possibility of the excitonic insulating (EI) state in the two-band Hubbard model [1] and the magnetism of the double exchange model [2] on the Penrose lattice. In the former study [1], we considered the vertex model and the center model on the Penrose lattice to determine their ground state phase diagram in terms of the real-space mean-field theory. We have revealed the existence of the stable EI phase induced by small interband interactions [Fig. 1(a)]. We pointed out that this originates from the electron-hole pairing for the completely or nearly degenerated states, which is characteristic of the QC systems. In addition, we also discussed the spatial structure of the order in terms of the so-called perpendicular space [Fig. 1(b)]. In the second study [2], we investigated the double exchange model on the Penrose lattice in terms of a Monte Carlo method. We showed the existence of the ferromagnetism and revealed that its general fea-

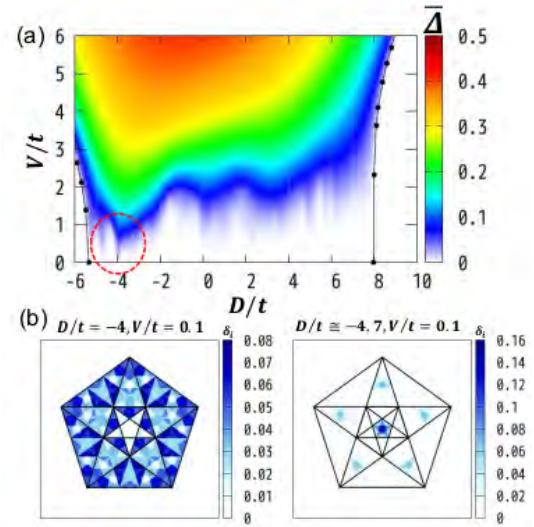


Figure 1: (a) EI order parameter of the two-band Hubbard model of the center model on the Penrose lattice. Red dotted circles indicates the stable EI states with small interactions. (b) Analysis in the perpendicular space for the stable EI phases.

tures such as temperature dependence resemble those of the system on the normal square lattice. By means of the analysis in the perpendicular space, we discussed the characteristic real-space structure of the magnetism in this QC system.

References

- [1] K. Inayoshi, Y. Murakami, and A. Koga: arXiv:2002.05870 (2020).
- [2] Y. Takeuchi, Master thesis, Tokyo Institute of Technology (2020. Mar).

Numerical analysis for nonequilibrium dynamics in correlated electron systems with orbital degrees of freedom

Akihisa Koga

Department of Physics, Tokyo Institute of Technology, Meguro, Tokyo 152-8551

Strongly correlated systems with orbital degrees of freedom can lead to intriguing spin systems. One of the important examples is the Kitaev quantum spin model, which consists of anisotropic exchange couplings on the honeycomb lattice and shows the quantum spin liquid (QSL) state at low temperatures. Although the Kitaev model was originally proposed theoretically, it is considered to be realized in α - RuCl_3 , and other strongly correlated systems such as A_2IrO_3 ($\text{A} = \text{Na}, \text{Li}$) are also candidates of the Kitaev QSL. So far, the static properties in the Kitaev QSL have been the main focus of this field and many characteristic features such as the fractionalization of specific heats and the thermal Hall effects have been reported. Thus, a simple question naturally arises what is the characteristic dynamical properties of the Kitaev QSL.

Motivated by this, we studied the spin transport through the QSL by investigating the real-space dynamics of the $S = 1/2$ Kitaev system with a zigzag edge structure [2] [Fig.1(a)]. We followed the dynamics after the magnetic field pulse applied to one of the edges with the time-dependent Majorana mean-field theory and the exact diagonalization. We showed that, although no spin moments are induced in the Kitaev QSL region, the spin moments are excited in the opposite edge region [Fig.1(b)]. We revealed that this anomalous spin transport originates from the fractionalization of the spins in the Kitaev QSL into the itinerant and localized Majorana fermions. Namely, after the excitation, only the itinerant Majorana fermions can propagate through the QSL, hence the magnetization is absent there. When the itinerant Majorana reaches

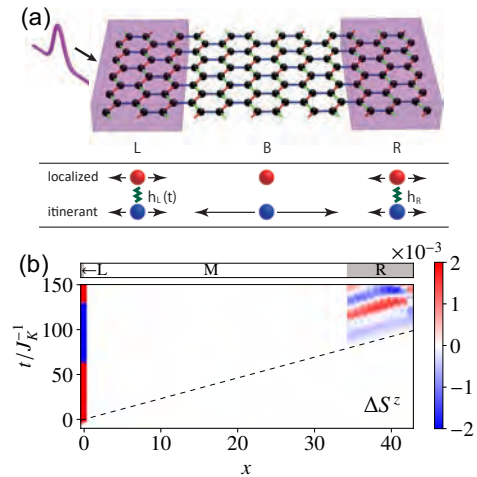


Figure 1: (a) Schematic pictures of our setup and the process involved in the anomalous spin transport. (b) the mean-field result of the spin dynamics of the Kitaev model.

the other edge under the static magnetic field, the hybridization between the local Majorana fermions yields the finite spin momentum. We also studied the $S = 1$ Kitaev model to show the existence of the similar anomalous spin transport [3].

References

- [1] A. Kitaev: *Ann. Phys.* **321** (2006) 2.
- [2] T. Minakawa, Y. Murakami, A. Koga and J. Nasu: arXiv:1912.10599 (2019).
- [3] A. Koga, T. Minakawa, Y. Murakami and J. Nasu: *J. Phys. Soc. Jpn.* **89** (2020) 033701.

Novel topological phenomena induced by strongly correlated dynamics

Tsuneya YOSHIDA

*Department of Physics, University of Tsukuba
Tsukuba, Ibaraki 305-8571*

Focusing on non-Hermitian topological phenomena, we have analyzed correlated systems. Specifically, we have analyzed exceptional band touching for quasi-particle spectrum of correlated systems in equilibrium [1, 2, 3]. Our works [1, 3] have discovered novel exceptional band touching which we dub symmetry-protected exceptional rings (surfaces) in two (three) dimensions, respectively. In addition, we have also elucidated that for Kondo insulators, such non-Hermitian band touching emerges around Kondo temperatures. Furthermore, focusing on dynamics of open quantum systems with two-body loss, we have discovered a non-Hermitian fractional quantum Hall state (see Fig. 1), which extends the non-Hermitian physics to long range entangled states. The above set up is relevant to the cold atoms with two-body loss.

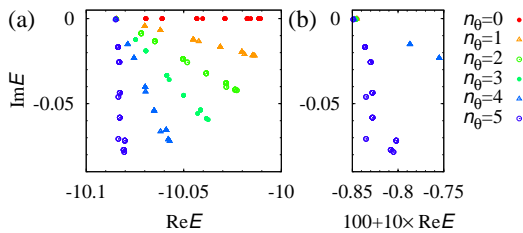


Figure 1: (Color Online). Energy spectrum of non-Hermitian Hamiltonian. Panel (b) is the magnified version of the range in $-10.085 < \text{Re}E < -10.075$.

In addition to the above works on non-Hermitian systems, we have addressed topology with crystalline effects [5, 6]. In par-

ticular, we have found that mirror symmetry and non-Hermitian topology induces novel skin effect protected by mirror symmetry which may be realized for an electric circuit composed of negative impedance converters. Besides that we have elucidated the other topological phases protected by crystalline symmetry [7, 8, 9]. For instance, we have extended the notion of higher order topology to correlated systems, which discovered a new topological state, a higher-order topological Mott insulating state [9]. We also have proposed an efficient method to compute Z_4 topological invariant for glide symmetric systems [7].

References

- [1] Kazuhiro Kimura, Tsuneya Yoshida, and Norio Kawakami: Phys. Rev. B **100**, 115124 (2019).
- [2] Yoshihiro Michishita, Tsuneya Yoshida, and Robert Peters: Phys. Rev. B **101**, 085122.
- [3] Tsuneya Yoshida, Robert Peters, Norio Kawakami, Yasuhiro Hatsugai: arXiv:2002.11265.
- [4] Tsuneya Yoshida, Koji Kudo, and Yasuhiro Hatsugai: Sci. Rep. **9**, 16895 (2019).
- [5] Tsuneya Yoshida and Yasuhiro Hatsugai: Phys. Rev. B **100**, 054109 (2019).

- [6] Tsuneya Yoshida, Tomonari Mizoguchi, and Yasuhiro Hatsugai: arXiv:1912.12022.
- [7] Tsuneya Yoshida, Akito Daido, Norio Kawakami, and Youichi Yanase: Phys. Rev. B **99**, 235105 (2019).
- [8] Kazuhiro Kimura, Tsuneya Yoshida, and Norio Kawakami: JPS Conf. Proc. **30**, 011012 (2020).
- [9] Koji Kudo, Tsuneya Yoshida, and Yasuhiro Hatsugai: Phys. Rev. Lett. **123**, 196402 (2019).

Two-Channel Kondo Effect Emerging in a Multiorbital Anderson Model Hybridized with Γ_7 and Γ_8 Conduction Bands

Takashi HOTTA

*Department of Physics, Tokyo Metropolitan University
1-1 Minami-Osawa, Hachioji, Tokyo 192-0397*

To explore the emergence of a quantum critical point (QCP) between non-Fermi-liquid and Fermi-liquid phases, we investigate the states in the vicinity of two-channel Kondo phase. For the purpose, we analyze a seven-orbital impurity Anderson model hybridized with three conduction bands (one Γ_7 and two Γ_8) by employing a numerical renormalization group (NRG) method.

First we consider one f -electron state, which is the eigenstate of spin-orbit and crystalline electric field (CEF) potential terms. Under the cubic CEF potential, we obtain Γ_7 doublet and Γ_8 quartet from $j = 5/2$ sextet, whereas we find Γ_6 doublet, Γ_7 doublet, and Γ_8 quartet from $j = 7/2$ octet. By using those one-electron state as bases, we describe the local f -electron Hamiltonian as

$$\begin{aligned}
 H_{\text{loc}} = & \sum_{j,\mu,\tau} (\lambda_j + B_{j,\mu} + E_f) f_{j\mu\tau}^\dagger f_{j\mu\tau} \\
 & + \sum_{j_1 \sim j_4} \sum_{\mu_1 \sim \mu_4} \sum_{\tau_1 \sim \tau_4} I_{\mu_1 \tau_1 \mu_2 \tau_2, \mu_3 \tau_3 \mu_4 \tau_4}^{j_1 j_2, j_3 j_4} \quad (1) \\
 & \times f_{j_1 \mu_1 \tau_1}^\dagger f_{j_2 \mu_2 \tau_2}^\dagger f_{j_3 \mu_3 \tau_3} f_{j_4 \mu_4 \tau_4},
 \end{aligned}$$

where $f_{j\mu\tau}$ denotes the annihilation operator of a localized f electron in the bases of (j, μ, τ) , j is the total angular momentum, $j = 5/2$ and $7/2$ are denoted by “ a ” and “ b ”, respectively, μ distinguishes the cubic irreducible representation, Γ_8 states are distinguished by $\mu = \alpha$ and β , while Γ_7 and Γ_6 states are labeled by $\mu = \gamma$ and δ , respectively, τ is the pseudo-spin which distinguishes the degeneracy concerning

the time-reversal symmetry, and E_f is the f -electron level to control the local f -electron number at an impurity site.

As for the spin-orbit coupling term, we obtain $\lambda_a = -2\lambda$ and $\lambda_b = (3/2)\lambda$, where λ is the spin-orbit coupling of f electron. For Pr ion, we set $\lambda = 0.1\text{eV}$ in this research. Concerning the CEF potential term for $j = 5/2$, we obtain $B_{a,\alpha} = B_{a,\beta} = 1320B_4^0/7$ and $B_{a,\gamma} = -2640B_4^0/7$, where B_4^0 denotes the fourth-order CEF parameter for the angular momentum $\ell = 3$. Note that the sixth-order CEF potential term B_6^0 does not appear for $j = 5/2$, since the maximum size of the change of the total angular momentum is less than six. On the other hand, for $j = 7/2$, we obtain $B_{b,\alpha} = B_{b,\beta} = 360B_4^0/7 + 2880B_6^0$, $B_{b,\gamma} = -3240B_4^0/7 - 2160B_6^0$, and $B_{b,\delta} = 360B_4^0 - 3600B_6^0/7$. Note also that B_6^0 term appears in this case. In the present calculations, we treat B_4^0 and B_6^0 as parameters.

The matrix element of the Coulomb interaction is expressed by I . Here we do not show the list for the explicit forms of I , but they are expressed with the use of four Slater-Condon parameters, F^0 , F^2 , F^4 , and F^6 . Although the Slater-Condon parameters of a material should be determined from experimental results, here we simply set the ratio as $F^0/10 = F^2/5 = F^4/3 = F^6 = U$, where U is the Hund’s rule interaction among f orbitals. It is reasonable to set U as 1 eV in this research.

In Fig. 1, we show the local CEF ground-

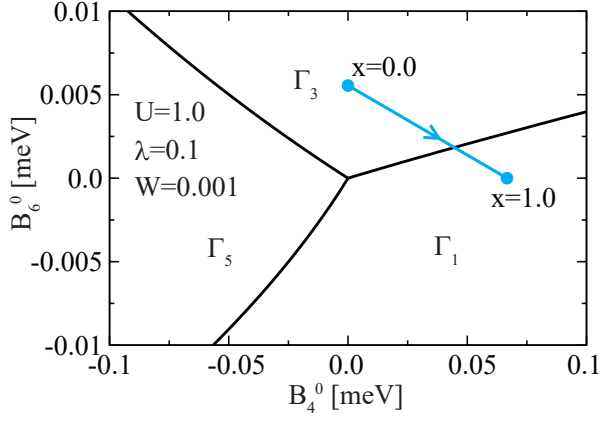


Figure 1: Local CEF ground-state phase diagram on the plane of (B_4^0, B_6^0) for $n = 2$. The line is given by $B_4^0 = Wx/15$ and $B_6^0 = W(1 - |x|)/180$ with $W = 10^{-3}$.

state phase diagram for $n = 2$, obtained from the diagonalization of H_{loc} . For $n = 2$, the ground-state multiplet for $B_4^0 = B_6^0 = 0$ is characterized by total angular momentum $J = 4$. Under the cubic CEF potentials, the nonet of $J = 4$ is split into four groups as Γ_1 singlet, Γ_3 doublet, Γ_4 triplet, and Γ_5 triplet. Among them, Γ_4 triplet does not appear as a solo ground state under the cubic CEF potential with O_h symmetry.

Now we include the Γ_7 and Γ_8 conduction electron bands. Here we consider only the hybridization between conduction and $j = 5/2$ electrons. The Hamiltonian is given by

$$H = \sum_{\mathbf{k}, \mu, \tau} \varepsilon_{\mathbf{k}} c_{\mathbf{k}\mu\tau}^\dagger c_{\mathbf{k}\mu\tau} + \sum_{\mathbf{k}, \mu, \tau} V_\mu (c_{\mathbf{k}\mu\tau}^\dagger f_{a\gamma\tau} + \text{h.c.}) + H_{\text{loc}}, \quad (2)$$

where $\varepsilon_{\mathbf{k}}$ is the dispersion of conduction electron with wave vector \mathbf{k} , $c_{\mathbf{k}\gamma\tau}$ is an annihilation operator of conduction electrons, and V_μ denotes the hybridization between f electron in the μ orbital and conduction electron of the μ band. Here we set $V_\alpha = V_\beta = V_\gamma = V$.

In this research, we analyze this model by employing the NRG method [1]. We introduce a cut-off Λ for the logarithmic discretization of the conduction band. Due to the limitation of computer resources, we keep M low-energy

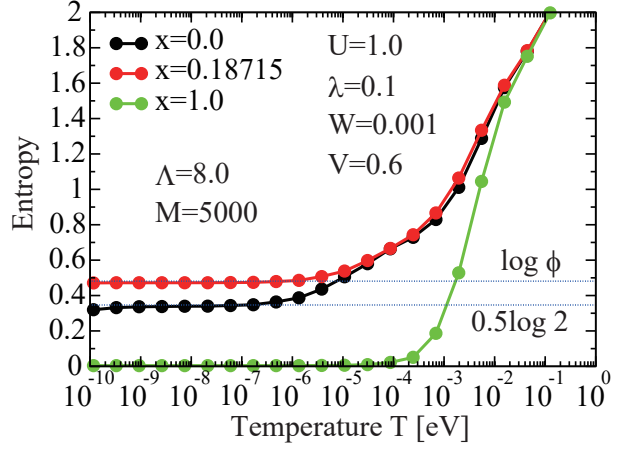


Figure 2: Entropies vs. temperature for $x = 0$, 0.18715 , and 1 with $W = 10^{-3}$.

states. Here we use $\Lambda = 8$ and $M = 5,000$. Note that the temperature T is defined as $T = D\Lambda^{-(N-1)/2}$ in the NRG calculation, where N is the number of the renormalization step and D is a half of conduction band width. Here we set $D = 1$ eV.

In Fig. 2, we show the calculation results for entropies, when we change the local CEF states from Γ_3 doublet ($x = 0$) to Γ_1 singlet ($x = 1$) on the line in Fig. 1. For $x = 0$, we find an entropy of $0.5 \log 2$ at low temperatures, indicating the two-channel Kondo state (non-Fermi-liquid phase), while for $x = 1$, we obtain the CEF singlet state (Fermi-liquid phase). After repeating the NRG calculations, at $x = 0.18715$, we find an entropy plateau of $\log \phi$ with $\phi = (\sqrt{5} + 1)/2$. This is the same as the residual entropy for the three-channel Kondo effect. We consider that the entropy $\log \phi$ suggests the emergence of QCP between non-Fermi-liquid and Fermi-liquid phases. Details will be discussed elsewhere in future [2].

References

- [1] H. R. Krishna-murthy, J. W. Wilkins, and K. G. Wilson, Phys. Rev. B **21**, 1003 (1980).
- [2] T. Hotta, in preparation.

Research of Two-Channel Kondo Effect in Transuranium Systems

Dai MATSUI and Takashi HOTTA

*Department of Physics, Tokyo Metropolitan University
1-1 Minami-Osawa, Hachioji, Tokyo 192-0397*

On the basis of the electron-hole relation between f^2 and f^4 states in a j - j coupling scheme, we hit upon an idea that two-channel Kondo phenomena can be observed even in cubic transuranium compounds including Np and Pu ions with local Γ_3 non-Kramers doublet ground state. To clarify this point, we analyze a seven-orbital impurity Anderson model hybridized with degenerate Γ_8 conduction electron bands by employing a numerical renormalization group (NRG) method [1].

The model Hamiltonian is given by

$$\begin{aligned}
 H = & \sum_{\mathbf{k}, \mu, \tau} \varepsilon_{\mathbf{k}} c_{\mathbf{k}\mu\tau}^\dagger c_{\mathbf{k}\mu\tau} + \sum_{\mathbf{k}, \mu, \tau} V (c_{\mathbf{k}\mu\tau}^\dagger f_{a\mu\tau} + \text{h.c.}) \\
 & + \sum_{j, \mu, \tau} (\lambda_j + B_{j, \mu} + E_f) f_{j\mu\tau}^\dagger f_{j\mu\tau} \\
 & + \sum_{j_1 \sim j_4} \sum_{\mu_1 \sim \mu_4} \sum_{\tau_1 \sim \tau_4} I_{\mu_1 \tau_1 \mu_2 \tau_2, \mu_3 \tau_3 \mu_4 \tau_4}^{j_1 j_2, j_3 j_4} \\
 & \times f_{j_1 \mu_1 \tau_1}^\dagger f_{j_2 \mu_2 \tau_2}^\dagger f_{j_3 \mu_3 \tau_3} f_{j_4 \mu_4 \tau_4},
 \end{aligned} \tag{1}$$

where $\varepsilon_{\mathbf{k}}$ denotes the energy of Γ_8 conduction electron with wave vector \mathbf{k} , $c_{\mathbf{k}\mu\tau}$ indicates the annihilation operator of Γ_8 conduction electron, μ distinguishes the cubic irreducible representation, Γ_8 states are distinguished by $\mu = \alpha$ and β , while Γ_7 and Γ_6 states are labeled by $\mu = \gamma$ and δ , respectively, τ is the pseudo-spin which distinguishes the degeneracy concerning the time-reversal symmetry, V is the hybridization between conduction and localized electrons, $f_{j\mu\tau}$ indicates the annihilation operator of a localized f electron in the bases of (j, μ, τ) , j is the total angular momentum, $j = 5/2$ and $7/2$ are denoted by “a” and “b”, respectively, and E_f is the f -electron

level to control the local f -electron number at an impurity site. In the present case, we consider the hybridization between Γ_8 conduction electrons and the Γ_8 quartet of $j = 5/2$.

As for the spin-orbit coupling term, we obtain $\lambda_a = -2\lambda$ and $\lambda_b = (3/2)\lambda$, where λ is the spin-orbit coupling of f electron. The magnitude of λ depends on the kind of actinide atoms, but in this research, we set $\lambda = 0.3$ eV, since we consider Np and Pu ions. Concerning the CEF potential term for $j = 5/2$, we obtain $B_{a, \alpha} = B_{a, \beta} = 1320B_4^0/7$ and $B_{a, \gamma} = -2640B_4^0/7$, where B_4^0 denotes the fourth-order CEF parameter for the angular momentum $\ell = 3$. Note that the sixth-order CEF potential term B_6^0 does not appear for $j = 5/2$, since the maximum size of the change of the total angular momentum is less than six. On the other hand, for $j = 7/2$, we obtain $B_{b, \alpha} = B_{b, \beta} = 360B_4^0/7 + 2880B_6^0$, $B_{b, \gamma} = -3240B_4^0/7 - 2160B_6^0$, and $B_{b, \delta} = 360B_4^0 - 3600B_6^0/7$. Note also that B_6^0 terms appear in this case. In the present calculations, we treat B_4^0 and B_6^0 as parameters.

The matrix element of the Coulomb interaction is expressed by I . To save space, we do not show the explicit forms of I here, but they are expressed by four Slater-Condon parameters (F^0, F^2, F^4, F^6) and Gaunt coefficients. As for the magnitudes of Slater-Condon parameters, first we set $F^0 = 10$ eV by hand. Others are determined so as to reproduce excitation spectra of U^{4+} ion with two $5f$ electrons. The results are $F^2 = 6.4$ eV, $F^4 = 5.6$

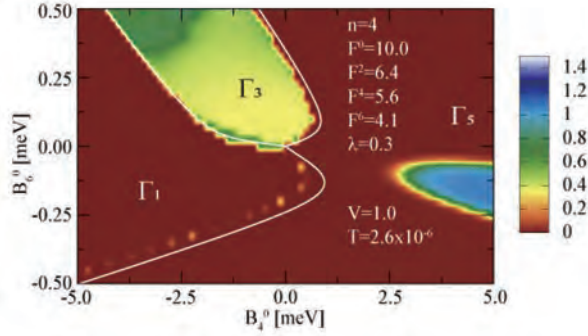


Figure 1: Color contour map of the entropy for $n = 4$ on the plane of (B_4^0, B_6^0) for $V=1.0$ and $T = 2.6 \times 10^{-6}$. White curves denote the boundaries among local CEF ground states.

eV, and $F^6 = 4.1$ eV [2].

In this research, we analyze the model by employing the NRG method [3]. We introduce a cut-off Λ for the logarithmic discretization of the conduction band. Due to the limitation of computer resources, we keep M low-energy states. Here we use $\Lambda = 5$ and $M = 2,500$. Note that the temperature T is defined as $T = D\Lambda^{-(N-1)/2}$ in the NRG calculation, where N is the number of the renormalization step and D is a half of conduction band width. We set $D = 1$ eV in this research.

In Fig. 1, we show the contour color map of the entropy on the plane of (B_4^0, B_6^0) for $V = 1.0$ and $T = 2.6 \times 10^{-6}$. To visualize precisely the behavior of entropy, we define the color of the entropy between 0 and 1.5, as shown in the right color bar. Note that the green and yellow regions indicate the entropy of $\log 2$ and $0.5 \log 2$, respectively. We immediately notice that a region with an entropy of $0.5 \log 2$ (yellow region) almost corresponds to that of the Γ_3 CEF ground state. Note that for large B_6^0 , the color becomes green, but when we decrease the temperature, we find the entropy of $0.5 \log 2$ even for large B_6^0 . The results strongly suggest the emergence of quadrupole two-channel Kondo effect for the case of $n = 4$. Note that in the present model, we have observed the discontinuous change in entropy behavior between yellow (Γ_3) and red

(Γ_1 or Γ_5) regions. Quantum critical behavior which may occur between non-Fermi-liquid and Fermi-liquid phases will be discussed elsewhere in future.

Here we remark that there exists a blue region corresponding to $\log 3$ in the local Γ_5 state. This is quite natural, since the local Γ_5 state is triply degenerate. The Γ_5 moment is screened by Γ_8 conduction electrons and thus, it is expected that the conventional Kondo effect occurs in the Γ_5 region, although the magnitude of the Kondo temperature significantly depends on the hybridization and excitation energy.

Note also that in the region of $B_6^0 < 0$, we observe some blurry yellow spots along the boundary curve between Γ_1 singlet and Γ_5 triplet local ground states. The QCP is known to appear between the CEF and Kondo singlet states for $n = 2$ [4]. Thus, we deduce that those spots form a QCP curve, although we could not obtain enough amounts of numerical results to depict the smooth curve here.

Finally, we provide a brief comment on actual materials to observe the two-channel Kondo effect for the case of $n = 4$. In rare-earth ions, the case of $n = 4$ corresponds to Pm^{3+} , but unfortunately, there exist no stable isotopes for Pm. Thus, we turn our attention to actinide ions such as Np^{3+} and Pu^{4+} with $5f^4$ configurations. It may be difficult to synthesize new Np and Pu compounds, but we expect that Np 1-2-20 compound will be synthesized in future.

References

- [1] D. Matsui and T. Hotta, JPS Conf. Proc. **30**, 011125 (2020).
- [2] T. Hotta, Phys. Rev. B **80**, 024408 (2009).
- [3] H. R. Krishna-murthy, J. W. Wilkins, and K. G. Wilson, Phys. Rev. B **21**, 1003 (1980).
- [4] T. Hotta, Physica B **536**, 203 (2018).

First-principles and quantum many-body calculations for electronic states and superconductivity in the multi-band systems

Yoshiaki ŌNO

*Department of Physics, Niigata University
Ikarashi, Nishi-ku, Niigata, 950-2181*

Tungsten bronzes $A_x\text{WO}_3$ ($A=\text{Na, K, Rb, Cs}$) are known to show the superconductivity for $0.15 < x < 0.35$, where the superconducting transition temperature T_c is found to increase rapidly with decreasing x up to 7K. In addition, at further low doping $x \sim 0.05$, remarkable high- T_c superconductivities are reported at $T_c=91\text{K}$ for $A=\text{Na}$ and $T_c=120\text{K}$ for $A=\text{H}$. The systems also show rich structural phases such as cubic for $x > 0.4$, tetragonal for $0.1 < x < 0.4$, orthorhombic for $0.03 < x < 0.1$ and monoclinic for $x < 0.03$, which are well accounted for by the first-principles calculations. However, the superconductivity in which the structural phases and those transitions are considered to play important roles for determining T_c was not discussed there. The purpose of this work is to study the superconductivity in $A_x\text{WO}_3$ on the basis of the first-principles calculation and to discuss the effect of the ferro-orbital fluctuation which is found to be largely enhanced around the structural phase transition and is expected to induce the pairing interaction as previously discussed in the iron-based superconductivity.

We calculate T_c on the basis of the first-principles calculation by using Quantum ESPRESSO and find that the x dependence of T_c is qualitatively consistent with the experiments. The significant x dependence of T_c is mainly due to that of the electron-phonon coupling constant λ which decreases with increasing x because of the screening effect as

discussed by several authors. However, the calculated value of T_c is considerably smaller than the experimental values, and hence the pairing interaction mediated by the electronic fluctuation such as the orbital fluctuation is expected to be responsible for the pairing mechanism in addition to the BCS phonon mechanism which is exclusively taken into account in the present first-principles calculation. Then, we also calculate the pairing interaction on the basis of the effective three band model consists of $W-t_{2g}$ orbitals by taking into account of the Jahn-Teller electron-phonon coupling within the random phase approximation and find that the pairing interaction is largely enhanced due to the ferro-orbital fluctuation which becomes large around the structural phase transition[1].

Recently, the Pr 1-2-20 systems $\text{PrT}_2\text{X}_{20}$ have been intensively investigated concerning their specific features including quadrupole orders, superconductivity and non-Fermi liquid behaviors. The crystalline electric field ground states of the Pr ions are the non-Kramers doublets Γ_{23} which have the electric quadrupole moments with no magnetic moment. In fact, $\text{PrTi}_2\text{Al}_{20}$ and $\text{PrV}_2\text{Al}_{20}$ exhibit the ferro-quadrupole (FQ) and the antiferro-quadrupole (AFQ) orders, respectively. They also show remarkable superconductivities coexisting with the quadrupole orders. To discuss the quadrupole order and the superconductivity, the details of the energy bands and the Fermi surfaces are important. In the Pr

1-2-20 systems, the de Haas-van Alphen experiments revealed that the Fermi surfaces are well accounted for by the first-principles band calculations for the corresponding La 1-2-20 systems, indicating that the Pr 4f electrons are sufficiently localized. Therefore, the quadrupole orders are considered due to the Ruderman-Kittel-Kasuya-Yosida (RKKY) interaction between the quadrupole moments of the localized Pr 4f electrons. The purpose of this study is to evaluate the RKKY interaction on the basis of the realistic energy band structure extracted from the first-principles calculation and to discuss the quadrupole orders in $\text{PrTi}_2\text{Al}_{20}$ and $\text{PrV}_2\text{Al}_{20}$.

We perform the first-principles calculations for $\text{LaT}_2\text{Al}_{20}$ ($T=\text{Ti, V}$) by using WIEN2k code where we also employ the GGA+ U method with $U = 60\text{eV}$ to exclude the La-4f components near the Fermi level. The obtained Fermi surfaces of $\text{LaTi}_2\text{Al}_{20}$ are in good agreement with those in the previous study. Then, we construct the tight-binding model for the conduction electrons so as to reproduce the electronic structure near the Fermi level by using the maximally localized Wannier functions which consist of 196 orbitals: La- d (5 orbitals \times 2 sites), La- s (1 orbital \times 2 sites), T- d (5 orbitals \times 4 sites), T- s (1 orbital \times 4 sites), Al- p (3 orbitals \times 40 sites) and Al- s (1 orbital \times 40 sites) in the conventional unit cell. Based on the effective model, we calculate the quadrupole susceptibility of the conduction electrons and then evaluate the RKKY interaction mediated by the conduction electrons. The obtained results indicate that the wave vectors of the expected quadrupole orders are $Q = (0, 0, 0)$ (FQ) for $\text{PrTi}_2\text{Al}_{20}$ and $Q = (\pi/a, \pi/a, 0)$ (AFQ) for $\text{PrV}_2\text{Al}_{20}$, respectively, as consistent with the experiments[2].

Quasicrystals first discovered by Shechtman *et al.* in Al-Mg alloy have been extensively investigated as they show various anomalous properties due to their specific structures which are not periodic but have kinds of trans-

lational orders with the 5-fold (8-, 10- and 12-fold) rotational symmetry. Recently, the bulk superconductivity at a transition temperature $T_c \sim 0.05\text{K}$ has been discovered by Kamiya *et al.* in the Al-Mg-Zn quasicrystal and its approximant, where the basic cluster is considered to be the Bergman-type cluster, and has attracted much attention for its symmetry and pairing mechanism. As for the theoretical study, the $\text{Al}_{30}\text{Mg}_{40}\text{Zn}_{30}$ 1/1 approximant was previously studied on the basis of the first-principles calculation and the origin of the pseudo gap near the Fermi level was discussed. However, the electronic state with the composition ratio corresponding to the superconducting compound was not discussed there. Then, we perform the first-principles calculations (OpenMX code) for the Al-Mg-Zn 1/1 approximants with various composition ratios including the superconducting one and find that the over-all structure of the density of states seems to be almost independent of the composition ratio but the energy band dispersions near the Fermi level and the Fermi surfaces are largely dependent on the composition ratio. On the basis of the obtained electronic states, we also discuss the possible superconductivity[3].

References

- [1] Takuya Sekikawa, Rai Watabe, Jun Ishizuka, Yoshihiro Nitta, Kazuhiro Sano and Yoshiaki Ōno, JPS Conf. Proc. **30**, 011043 (2020).
- [2] Yuto Iizuka, Takemi Yamada, Katsurou Hanzawa and Yoshiaki Ōno, JPS Conf. Proc. **30**, 011152 (2020).
- [3] Masaki Saito, Takuya Sekikawa and Yoshiaki Ōno, *14th International Conference on the Structure of Non-Crystalline Materials* (NCM14).

Search for new types of skyrmion crystals based on point group symmetry

Satoru Hayami

Department of Applied Physics, The University of Tokyo, Tokyo 113-8656

Multiple- Q magnetic states, which are characterized as a superposition of different wave vectors, open a new path toward applications to next-generation electronics and spintronics device in condensed matter physics. Amongst them, the superposition of spiral states gives rise to unconventional noncollinear and non-coplanar magnetic textures, such as the magnetic vortex crystal and magnetic skyrmion crystal, which become a source of unconventional topological excitations and transport properties [1]. Especially, since the discovery of the magnetic skyrmions in noncentrosymmetric magnets, their studies have been extensively done in both theory and experiments.

Meanwhile, recent theoretical studies point out the emergence of the skyrmion crystals in centrosymmetric Mott insulators. They are stabilized by taking into account various factors, such as frustrated exchange interactions and thermal fluctuations [2, 3, 4, 5]. Moreover, another interesting situation is brought by considering the interplay between itinerant electrons and localized spins. There, effective long-ranged interactions mediated through itinerant electrons play an important role in stabilizing the skyrmion and vortex crystals [6, 7, 8], which might provide a deep understanding of the microscopic mechanism of the multiple- Q skyrmion, vortex, and hedgehog crystals found in d - and f -electron materials.

In this project, we investigate the skyrmion physic in itinerant magnets by considering an anisotropic magnetic interaction [9]. We start from the Kondo lattice model with

the anisotropic xxz -type spin-charge coupling. The Hamiltonian is represented by

$$\begin{aligned} \mathcal{H} = & - \sum_{i,j,\sigma} t_{ij} c_{i\sigma}^\dagger c_{j\sigma} + J_z \sum_{i,\sigma,\sigma'} \sigma_{\sigma\sigma'}^z S_i^z c_{i\sigma}^\dagger c_{i\sigma'} \\ & + J_{xy} \sum_{i,\sigma,\sigma'} (\sigma_{\sigma\sigma'}^x S_i^x + \sigma_{\sigma\sigma'}^y S_i^y) c_{i\sigma}^\dagger c_{i\sigma'}, \quad (1) \end{aligned}$$

where $c_{i\sigma}^\dagger$ and $c_{i\sigma}$ are creation and annihilation operators of an itinerant electron at site i and spin σ , respectively. The first term represents the hopping of itinerant electrons and the second and third terms denote the spin-charge coupling where $|\mathbf{S}_i| = 1$ and $\boldsymbol{\sigma}$ is the Pauli matrix. J_{xy} and J_z are the anisotropic coupling constants for xy and z spin components, respectively.

We derive an effective spin model in Eq. (1) by assuming (i) the weak-coupling regime for $J_{xy}, J_z \ll W$ (W is the bandwidth) and (ii) the multiple peak structures of the bare magnetic susceptibility. Then, the spin model is obtained as

$$\mathcal{H} = -2 \sum_{\nu=1-3} (\tilde{J}\Gamma_{\mathbf{Q}_\nu} + \tilde{K}\Gamma_{\mathbf{Q}_\nu}^2), \quad (2)$$

where $\Gamma_{\mathbf{Q}_\nu} = \sqrt{1-A^2}(S_{\mathbf{Q}_\nu}^x S_{-\mathbf{Q}_\nu}^x + S_{\mathbf{Q}_\nu}^y S_{-\mathbf{Q}_\nu}^y) + AS_{\mathbf{Q}_\nu}^z S_{-\mathbf{Q}_\nu}^z$. We adopt a triangular lattice with six peaks in the bare susceptibility: $\pm\mathbf{Q}_1 = \pm(\pi/3, 0)$, $\pm\mathbf{Q}_2 = \pm(-\pi/6, \sqrt{3}\pi/6)$, and $\pm\mathbf{Q}_3 = \pm(-\pi/6, -\sqrt{3}\pi/6)$. The first term represents the bilinear interaction with $\tilde{J} = 1$ and the second term represents the biquadratic interaction with the positive coupling constant $\tilde{K} = K/N > 0$ (N is the number of spins). The former originates from the

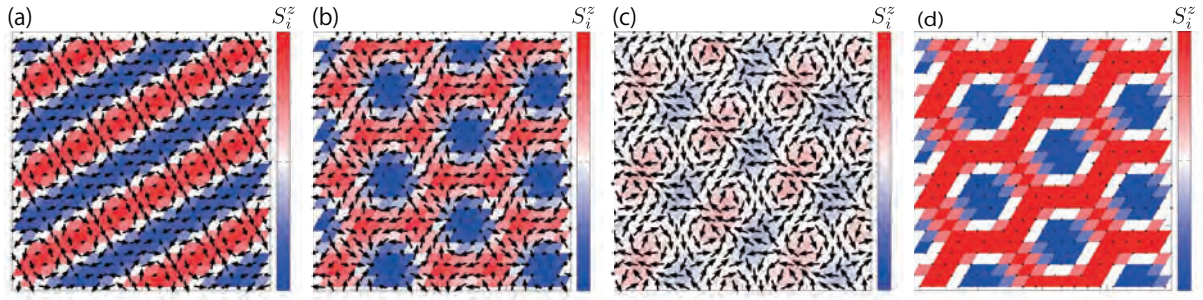


Figure 1: Snapshots of the spin configurations (see the text). The arrows represent the xy component and the contour shows the z component of the spin moment.

second-order perturbation, while the latter arises from the fourth-order perturbation. The magnetic anisotropy is represented by A ; $0 \leq A < 1/\sqrt{2}$ for the easy-axis interaction and $1/\sqrt{2} < A \leq 1$ for the easy-plane interaction.

The magnetic phase diagram of the effective spin model in Eq. (2) is investigated by performing simulated annealing from high temperature. We apply the Metropolis local updates under periodic boundary conditions in both directions for the 96^2 spins. To find the optimal spin configurations, we gradually reduce the temperature with the rate $T_{n+1} = \alpha T_n$, where T_n is the temperature in the n th step. We start from the initial temperature $T_0 = 10^{-1}$ - 10^0 . We typically set $\alpha \sim 0.99999$ and the final temperature $T = 10^{-4}$ - 10^{-3} .

As a result, we find several magnetic ordered states with a net scalar chirality including the skyrmion and vortex crystals by constructing the ground-state phase diagram in a wide range of model parameters. We show that two types of the skyrmion crystal phases with the topological number of two are realized for large K : one is identified as the superposition of the magnetic vortex structures in the xy spin component and the sinusoidal wave in the z spin component [Fig. 1(a)] and the other is denoted as the bubble-type magnetic configurations satisfying the sixfold rotational symmetry in both xy and z spin components [Fig. 1(b)]. We also find a triple- Q

state with a finite net scalar chirality, which is different from the skyrmion crystal by increasing the easy-plane anisotropic interaction [Fig. 1(c)]. Moreover, we find that the strong easy-axis anisotropic interaction gives rise to the triple- Q magnetic bubble crystal with the collinear z spin component [Fig. 1(d)].

References

- [1] N. Nagaosa, Y. Tokura, *Nat. Nanotech.* **8** (12) (2013) 899–911.
- [2] T. Okubo, S. Chung, H. Kawamura, *Phys. Rev. Lett.* **108** (2012) 017206.
- [3] A. O. Leonov, M. Mostovoy, *Nat. Commun.* **6** (2015) 8275.
- [4] S.-Z. Lin, S. Hayami, *Phys. Rev. B* **93** (2016) 064430.
- [5] S. Hayami, S.-Z. Lin, C. D. Batista, *Phys. Rev. B* **93** (2016) 184413.
- [6] Y. Akagi, M. Udagawa, Y. Motome, *Phys. Rev. Lett.* **108** (2012) 096401.
- [7] R. Ozawa, S. Hayami, K. Barros, G.-W. Chern, Y. Motome, C. D. Batista, *J. Phys. Soc. Jpn.* **85** (10) (2016) 103703.
- [8] S. Hayami, R. Ozawa, Y. Motome, *Phys. Rev. B* **95** (2017) 224424.
- [9] S. Hayami, submitted.

Multipole and anisotropic superconductivity from first-principles

Jun Ishizuka

*Department of Physics, Graduate School of Science, Kyoto University,
Kyoto 606-8502, Japan*

Recently discovered heavy fermion superconductor UTe_2 [1], as a member of the ferromagnetic superconductors [2, 3], provides a new platform to study the spin-triplet superconductivity. The spin-triplet state in UTe_2 is supported by various experimental results: large upper critical field H_{c2} along the three principal axes [1, 4], reentrant superconductivity under magnetic field along b axis [5], and the temperature dependence of the Knight shift in superconducting state [6].

In this project, we theoretically study anisotropic superconductivity in UTe_2 [7]. Theoretically, a band structure has been investigated for UTe_2 from first-principles [4]. However, previously obtained result shows insulating state with an extremely small gap, incompatible with superconducting instability. To overcome this program, we perform a $\text{GGA}+U$ calculation using WIEN2k package [8] and find the insulator-metal transition by Coulomb interaction. The insulator-metal transition is characterized by multi-orbital effect in Kondo lattice system. The insulator-metal transition is a peculiar property of UTe_2 , which was not observed in other uranium-based superconductors nor in Kondo insulators. We can identify the three-dimensional winding number ω

and three two-dimensional \mathbb{Z}_2 numbers by Fermi surface formulas [9, 10, 11]:

$$\omega = \frac{1}{2} \sum_{K_i} n(K_i) \pmod{2}. \quad (1)$$

The $\text{GGA}+U$ Fermi surfaces indicate topological superconductivity for the reasonable values of U , and accompanied surface states are provided. We also predict the superconducting gap node at zero magnetic field and under magnetic field along b axis. Based on these results, we proposed multiple superconducting phases under the magnetic field.

Our another aim of this project is to study the exotic phenomena due to the spatial inversion symmetry breaking. Recently, it was found that the noncentrosymmetric Nb/V/Ta superlattice shows superconducting transition at 4.4 K [12] and exhibits nonreciprocal charge transport in superconducting state. To identify the Rashba spin-orbit interaction in the artificial superlattice $[\text{Nb/V/Ta}]_n$ without a center of inversion, we carried out density functional theory calculations using WIEN2k package [8]. We created a slab $[\text{Nb/V/Ta}]_5$ containing 30 atoms, which corresponds to the five times stacking of two layers Nb, V, and Ta of a bcc structure. We obtained the Rashba splitting at the Fermi level, and the magnitude of the Rashba

splitting is around 10 meV, which originate from V atoms and is the origin of the nonreciprocity.

References

- [1] S. Ran, C. Eckberg, Q.-P. Ding, Y. Furukawa, T. Metz, S. R. Saha, I.-L. Liu, M. Zic, H. Kim, J. Paglione, and N. P. Butch, *Science* **365**, 684 (2019).
- [2] D. Aoki and J. Flouquet, *J. Phys. Soc. Jpn.* **83**, 061011 (2014).
- [3] D. Aoki, K. Ishida, and J. Flouquet, *J. Phys. Soc. Jpn.* **88**, 022001 (2019).
- [4] D. Aoki, A. Nakamura, F. Honda, D. Li, Y. Homma, Y. Shimizu, Y. J. Sato, G. Knebel, J.-P. Brison, A. Pourret, D. Braithwaite, G. Lapertot, Q. Niu, M. Vališka, H. Harima, and J. Flouquet, *J. Phys. Soc. Jpn.* **88**, 043702 (2019).
- [5] G. Knebel, W. Knafo, A. Pourret, Q. Niu, M. Vališka, D. Braithwaite, G. Lapertot, M. Nardone, A. Zitouni, S. Mishra, I. Sheikin, G. Seyfarth, J.-P. Brison, D. Aoki, and J. Flouquet, *J. Phys. Soc. Jpn.* **88**, 063707 (2019).
- [6] G. Nakamine, S. Kitagawa, K. Ishida, Y. Tokunaga, H. Sakai, S. Kambe, A. Nakamura, Y. Shimizu, Y. Homma, D. Li, F. Honda, and D. Aoki, *J. Phys. Soc. Jpn.* **88**, 113703 (2019).
- [7] J. Ishizuka, S. Sumita, A. Daido, and Y. Yanase: *Phys. Rev. Lett.* **123**, 217001 (2019).
- [8] P. Blaha, K. Schwarz, G. K. H. Madsen, D. Kvasnicka, J. Luitz, R. Laskowski, F. Tran, and L. D. Marks, *WIEN2k, An Augmented Plane Wave+Local Orbitals Program for Calculating Crystal Properties* (Karlheinz Schwarz, Techn. Universität, Wien, Austria, 2018).
- [9] M. Sato, *Phys. Rev. B* **79**, 214526 (2009).
- [10] M. Sato, *Phys. Rev. B* **81**, 220504(R) (2010).
- [11] L. Fu and E. Berg, *Phys. Rev. Lett.* **105**, 097001 (2010).
- [12] F. Ando, D. Kan, Y. Shiota, T. Moriyama, Y. Shimakawa, T. Ono *J. Magn. Soc. Japan* **43**, 17-20 (2019).

Development and applications of continuous-time quantum Monte Carlo method in the thermodynamic limit

Takahiro OHGOE

*Research Institute for Science and Engineering,
Waseda University, Okubo, Shinjuku-ku, Tokyo 169-8555*

Quantum Monte Carlo methods are powerful tools for investigating quantum many-body systems. However, they often suffer from the notorious negative-sign problem for fermionic systems and frustrated spin systems when the system-size is increased. Recently, a novel determinant quantum Monte Carlo method was proposed, which is formulated in the thermodynamic limit [1]. The method is called *connected determinant Monte Carlo method* (CDet), and its applications to the Hubbard model revealed non-trivial analytic structure of the self-energy in strongly-correlated regime [2]. Therefore, it is a promising method for tackling challenging problems of quantum many-body systems.

Here, we developed the original CDet code which is applicable to the two-component unitary Fermi gas. To show its advantage, the method was compared with the diagrammatic Monte Carlo method in the case of balanced population [3,4]. In the diagrammatic Monte Carlo method, the maximum expansion order which we could reach was 9, whereas we could

reach the 11th order in shorter CPU time by using the CDet code. Furthermore, we also obtained some results of density and Tan's contact for *imbalanced* cases where the conventional quantum Monte Carlo method suffers from the negative-sign problem. The developed code will be useful for revealing fascinating physics such as FFLO or *p*-wave superconducting instability which are expected in imbalanced populations. This work was done in collaboration with Riccardo Rossi (Flatiron institute), Felix Werner and Kris Van Houcke (ENS, Paris).

References

- [1] R. Rossi: Phys. Rev. Lett. **119** (2017) 045701
- [2] F. Simkovic IV. and E. Kozik, Phys. Rev. B **100** (2019) 121102
- [3] R. Rossi, T. Ohgoe, K. Van Houcke, and F. Werner: Phys. Rev. Lett. **121** (2018) 130405
- [4] R. Rossi, T. Ohgoe, E. Kozik, N. Prokof'ev and B. Svistunov, K. Van Houcke, and F. Werner: Phys. Rev. Lett. **121** (2018) 130406

Kitaev spin liquid under time-dependent magnetic field

Joji NASU

*Department of Physics, Yokohama National University
Hodogaya, Yokohama 240-8501*

Nonequilibrium phenomena in insulating magnets such as real-time dynamics of magnetization and transport of spin excitations have attracted considerable attention in condensed matter physics. In the insulating magnets, spin excitations are carried by magnons in the presence of a magnetic order. On the other hand, it was suggested that the spin transport can be also governed by spinons, which are elementary excitations fractionalized from spins in one-dimensional Heisenberg systems. This was confirmed in the cuprate Sr_2CuO_3 by the spin Seebeck experiments under the magnetic field.

The Kitaev quantum spin model is another candidate of the magnetic systems associated with fractional quasiparticles. In this model, the ground state is exactly shown to be a quantum spin liquid and the elementary excitations are described by two kinds of quasiparticles: itinerant and localized Majorana fermions. In this work, we study spin dynamics under the time dependent magnetic field to clarify the role of the fractional quasiparticles for the nonequilibrium phenomena.

Here, we examine the the real-time dynamics of the spin moments in the Kitaev model under the time-dependent magnetic field. In particular, we investigate the following two cases by using the Majorana mean-field theory. First, 1) we study the effect of the field quench of the uniform magnetic field to understand fundamental properties of nonequilibrium dynamics of the fractional quasiparticles in the

Kitaev model. Next, 2) we consider the effect of the time-dependent magnetic field pulse at the edge of the cluster to mimic the spin injection into the Kitaev magnet.

With respect to 1), we find that two kinds of Majorana fermions are observed separately in distinct time-scales in the time evolution of the magnetization; the low-energy localized Majorana fermions survive as long-lived excitations whereas the high-energy itinerant ones are damped in the early stage [3].

With respect to 2), we find that the propagation of the spin excitations occurs even in the absence of the magnetic field in the bulk without spin polarization. We clarified that this is attributed to the itinerant Majorana fermions [2]. We also discuss the effect of the Heisenberg interaction and extension to the $S = 1$ Kitaev model [3] on this phenomenon.

References

- [1] J. Nasu, and Y. Motome: Phys. Rev. Research **1**, 033007-1-16 (2019).
- [2] T. Minakawa, Y. Murakami, A. Koga, and J. Nasu: arXiv:1912.10599.
- [3] A. Koga, T. Minakawa, Y. Murakami, and J. Nasu: J. Phys. Soc. Jpn. **89**, 033701-1-4 (2020).

Magnetocaloric effect on the Shastry–Sutherland lattice antiferromagnet $\text{SrCu}_2(\text{BO}_3)_2$

Subaru AKIMOTO and Yasuhiro H. MATSUDA
Institute for Solid State Physics, University of Tokyo
Kashiwa-no-ha, Kashiwa, Chiba 277-8581

We have studied the magnetocaloric effect (MCE) of the Shastry–Sutherland (SS) lattice antiferromagnet $\text{SrCu}_2(\text{BO}_3)_2$ [1] with numerical simulations using the thermal pure quantum (TPQ) state. We used the $\text{H}\Phi$ as a numerical solver. The magnetic field dependence of the entropy (S_M) and specific heat (C_M) have been computed and compared with those experimentally obtained from the magnetic field variation of the MCE at different initial temperatures. Figures 1 (a) and (b) show the calculated S_M and C_M . The five trial curves and the averaged result are shown for the S_M and C_M , respectively.

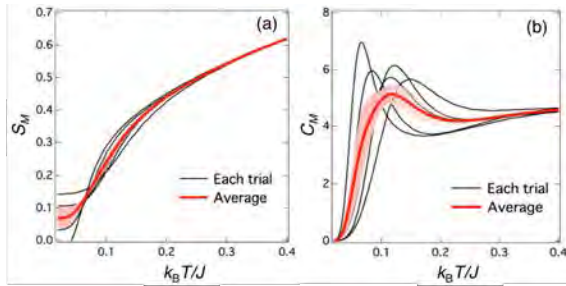


Figure 1: The five trial curves and the averaged result of the calculation with TPQ state are shown. The magnetic field is set to be 57 T corresponding to the 1/3 plateau. (a) Calculated S_M . (b) Calculated C_M .

The distinct peak is shown in the temperature dependence of the C_M at a magnetic field and the peak positions at different temperatures and magnetic fields would give the phase boundaries of the quantum spin states of the

SS lattice such as 1/4 and 1/3 plateaux [2]. The computed B – T (magnetic field – temperature) phase diagram shown in Fig. 2 is found to semiquantitatively reproduce the experimental results.

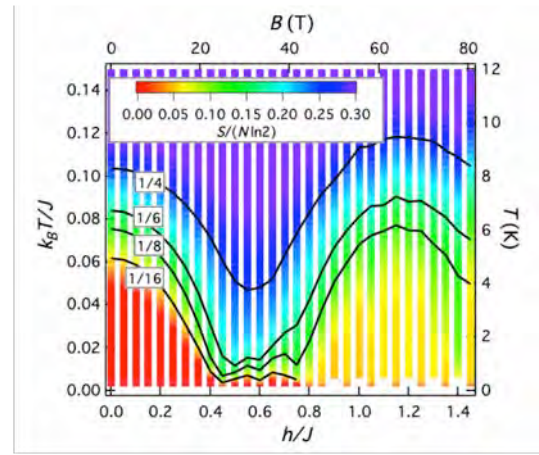


Figure 2: The calculated S_M are plotted in a B – T plane with color gradation. Several isentropic curves are also plotted.

References

- [1] H. Kageyama, K. Yoshimura, R. Stern, N. V. Mushnikov, K. Onizuka, M. Kato, K. Kosuge, C. P. Slichter, T. Goto, and Y. Ueda: *Phys. Rev. Lett.* **82** (1999) 3168.
- [2] Y. H. Matsuda, N. Abe, S. Takeyama, H. Kageyama, P. Corboz, A. Honecker, S. R. Manmana, G. R. Foltin, K. P. Schmidt, and F. Mila: *Phys. Rev. Lett.* **111** (2013) 137204.

Spin-Charge Separation in Charge Order Phase of Organic Dirac Electron System α -(BEDT-TTF)₂I₃

Akito KOBAYASHI

*Department of Physics, Nagoya University**Nagoya 464-8602*

The organic Dirac electron system α -(BEDT-TTF)₂I₃ exhibits a phase transition between a massless Dirac electron phase and a charge-ordered phase under pressure as shown in Fig. 1. In the charge-ordered phase, the spin gap measured by NMR, the optical gap in the optical conductivity, and the resistance gap determined by the DC resistance show completely different values and pressure dependences. The mechanism of this novel spin-charge separation has not been elucidated yet. We have theoretically studied the mechanism of the spin-charge separation in α -(BEDT-TTF)₂I₃.

First, we have investigated the Dirac electron system with charge order in α -(BEDT-TTF)₂I₃ using the real-space-dependent mean-field approximation, and have shown that there is a domain wall of the charge order that spontaneously appears due to ferroelectricity. We have shown that the wall-bound Dirac electrons form a one-dimensional conduction channel. Furthermore, we have shown that the linear response theory can explain the large difference between the optical gap and the resistivity gap[1].

Next, we have performed the first principles calculation for α -(BEDT-TTF)₂I₃ under hydrostatic pressure using Quantum ESPRESSO in the Supercomputer Center, the ISSP. However, the result exhibits a type-II Dirac semimetal, which is different from the experimental results. Similar results have been independently shown by the first-principles calcula-

tions by H. Kino and T. Tsumuraya. This fact strongly suggests that the type-I Dirac electronic state observed under hydrostatic pressure cannot be explained without the strong correlation effect. We will study the type-I Dirac electronic state under hydrostatic pressure using the variational Monte Carlo method in cooperation with Dr. Yoshimi of ISSP, and then elucidate the mechanism of spin charge separation of charge-ordered phase.

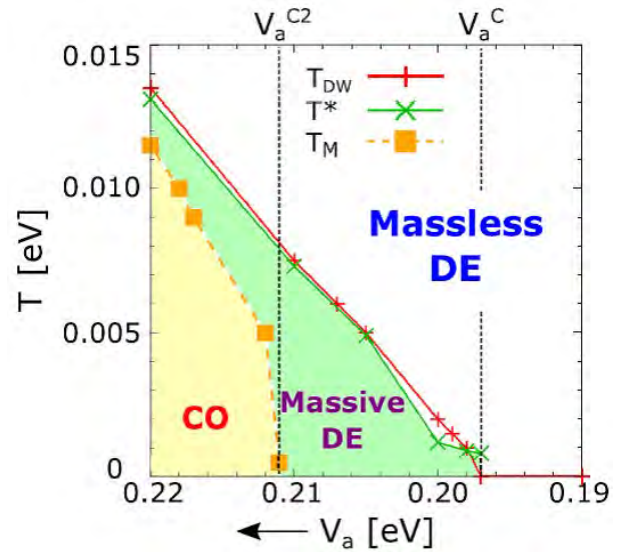


Figure 1: Phase diagram of α -(BEDT-TTF)₂I₃.

References

- [1] D. Ohki, Y. Omori, and A. Kobayashi, *Phys. Rev. B* **100**, 075206 (2019).

Quantum Monte Carlo simulation and electronic state calculations in correlated electron systems

Takashi YANAGISAWA

Electronics and Photonics Research Institute

National Institute of Advanced Industrial Science and Technology (AIST)

AIST Central 2, 1-1-1 Umezono, Tsukuba 305-8568

Our calculations are based on the optimized variational Monte Carlo method[1, 2, 3, 4]. We have investigated the ground-state phase diagram of the two-dimensional Hubbard model and the two-dimensional d-p model. We performed parallel computation in Monte Carlo calculations. In order to reduce statistical errors, we carried out 100 ~ 200 parallel calculations. Parallel computing is very important to reduce Monte Carlo statistical errors.

We used the wave function of an $\exp(-\lambda K) - P_G$ -type wave function. This wave function is a very good many-body wave function because the ground-state energy is lowered greatly and the ground-state energy is lower than that evaluated by any other wave functions[2]. We can improve the wave function systematically by multiplying by operators P_G and $e^{-\lambda K}$ many times.

We show the phase diagram as a function of the hole doping rate x in Fig. 1. The calculations were performed on a 10×10 lattice with $U/t = 18$ and $t' = 0$. There are three phases: the antiferromagnetic insulator state (AFI), the coexistent state of antiferromagnetism and superconductivity (AF+SC) and the d -wave superconducting state (SC). Near half-filling for approximately $0 \leq x < 0.06$, the ground state is an AF insulator. The coexistent state exists for $0.06 < x < 0.09$. When the doping rate is as large as $x > 0.09$, the ground state is d -wave superconducting state. High-temperature superconductivity will occur in the SC phase in this figure.

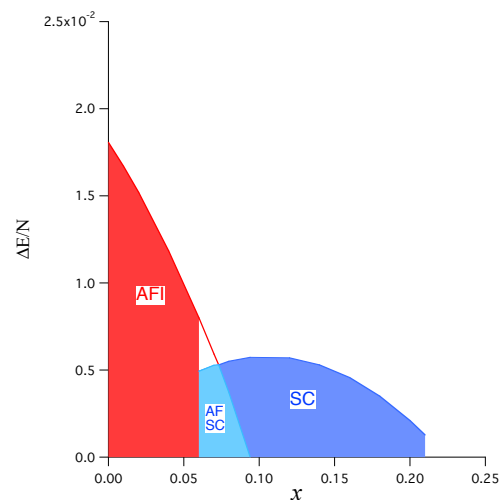


Figure 1: Phase diagram for the two-dimensional Hubbard model. The condensation energy per site as a function of the hole doping rate $x = 1 - n_e$ on a 10×10 lattice. We set $t' = 0$ and $U/t = 18$. AFI indicates the antiferromagnetic insulating state and SC denotes the d -wave SC phase. There is the coexistent state indicated as AF-S between these states.

References

- [1] T. Yanagisawa et al., J. Phys. Soc. Jpn. 67, 3867 (1998).
- [2] T. Yanagisawa, J. Phys. Soc. Jpn. 85, 114707 (2016).
- [3] T. Yanagisawa, J. Phys. Soc. Jpn. 88, 054702 (2019).
- [4] T. Yanagisawa, Condensed Matter 4, 57 (2019).

Dynamical mean-field theory + quantum Monte Carlo approach to strongly correlated electron systems with multi-orbitals

Shintaro HOSHINO

Department of Physics, Saitama University, Saitama 338-8570, Japan

The electrons with multiple orbital degrees of freedom show a variety of intriguing phenomena as realized in heavy-electron materials and also in d -electron systems such as ruthenate and iron-based superconductors. In addition, the fulleride superconductors are another example of the multiorbital electron systems [1], where the three-degenerate t_{1u} molecular orbitals are occupied by electrons originating from alkaline doping. Due to the effectively sign-inverted Hund coupling by Jahn-Teller phonons, the electrons favor the low-spin state and show superconductivity at low temperatures. Recently the experimental study has revealed the existence of anomalous metallic state near the Mott insulator [2], and the possibility of active orbital degrees of freedom is pointed out theoretically [3]. The characteristic dynamical structure in the self-energy is identified and can be a source of the anisotropic response function [4].

We have also mapped out the phase diagram of the doped fulleride, which is also experimentally realized [1]. To do this, we have analyzed the three-orbital Hubbard model with antiferromagnetic Hund's coupling by using the dynamical mean-field theory. In this theory, the many-body problem in the lattice is mapped onto the effective impurity problem without spatial periodicity, for which the continuous-time quantum Monte Carlo solver [5] has been used. Using the facilities of ISSP supercomputer, we have calculated the susceptibilities which signal the instability of the normal state toward ordering state with spontaneously broken symmetries. The exemplary

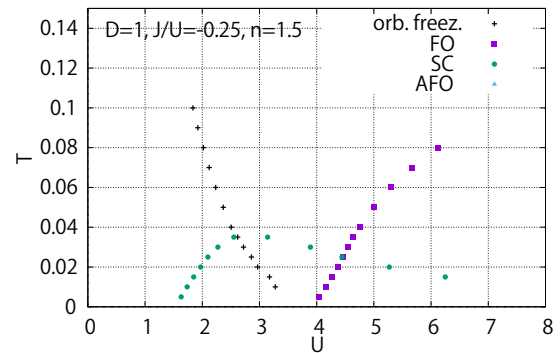


Figure 1: Temperature-interaction phase diagram. The phase boundaries for orbital ordering (FO) and superconductivity (SC) are shown, together with orbital freezing line.

results at the electron number $n = 1.5$ per molecule are shown in the figure. Here the phase diagram in the plane of temperature and Coulomb interaction is mapped out, where the horizontal axis indicates the pressure or lattice constant dependence when one compares the results with the experiments. We have demonstrated that the superconductivity appears with dome-shaped transition temperatures, while the orbital ordering dominates at large Coulomb repulsive interaction.

References

- [1] For a review, see O. Gunnarsson, *Rev. Mod. Phys.* **69**, 575 (1997). [2] R.H. Zadik *et al.*, *Sci. Adv.* **1**, e1500059 (2015). [3] S. Hoshino and P. Werner, *Phys. Rev. Lett.* **118**, 177002 (2017). [4] S. Hoshino, P. Werner, and R. Arita, *Phys. Rev. B* **99**, 235133 (2019). [5] E. Gull *et al.*, *Rev. Mod. Phys.* **83**, 349 (2011).

Superconductivity and magnetic properties of the Hubbard model

Atsushi Yamada

*Department of Physics, Chiba University
Chiba 263-8522, Japan, Chiba 277-8581*

Frustrated magnetic systems yield a rich variety of phenomena. For example, a spin liquid state, which is a purely non-magnetic Mott insulator without spontaneously broken spatial or spin symmetry, has attracted a lot of interest. This state is realized in geometrically frustrated systems like the charge organic transfer salts κ -(BEDT-TTF)₂X[1] and Cs₂CuCl₄. [2] A simple theoretical model of these compounds is the Hubbard model on the an-isotropic triangular lattice, and spin liquid state is in fact found in this model.[3] A spin liquid could arise also in the intermediate coupling region of strongly correlated systems between a semi-metal and ordered state, because in this case a correlation-driven insulating gap might open before the system becomes ordered. This possibility might be realized in the half-filled Hubbard model on the honeycomb lattice.

We have studied the magnetic and metal-to-insulator transitions in the half-filled Hubbard model on the honeycomb lattice by variational cluster approximation using 10-site and 16-site clusters as a reference system.[5] This approach uses an exact diagonalization of the Hubbard model defined on these clusters and parts of numerical calculations were done using the computer facilities of the ISSP. Our results agree with recent large scale Quantum Monte Carlo simulations.[4] We are currently studying the effect of the frustration on various physically measurable quantities in the Hubbard model on the $\frac{1}{5}$ -depleted square lattice.

References

- [1] Y. Shimizu, K. Miyagawa, K. Kanoda, M. Maesato, and G. Saito, Phys. Rev. Lett. **91**, 107001 (2003); Y. Kurosaki, Y. Shimizu, K. Miyagawa, K. Kanoda, and G. Saito, Phys. Rev. Lett. **95**, 177001 (2005).
- [2] R. Coldea, D.A. Tennant, A.M. Tsvelik, and Z. Tylczynski, Phys. Rev. Lett. **86**, 1335 (2001); R. Coldea, D.A. Tennant, and Z. Tylczynski, Phys. Rev. Lett. **68**, 134424 (2003).
- [3] T. Yoshioka, A. Koga, and N. Kawakami, Phys. Rev. Lett. **103**, 036401 (2009); P. Sahebsara and D. Sénéchal, Phys. Rev. Lett. **100**, 136402 (2008); L.F. Tocchio, H. Feldner, F. Becca, R. Valentí, and C. Gros, Phys. Rev. B **87**, 035143 (2013); A. Yamada, Phys. Rev. B **89**, 195108 (2014); L.F. Tocchio, C. Gros, R. Valentí, F. Becca, Phys. Rev. B **89**, 235107 (2014); A. Yamada, Phys. Rev. B **90**, 235138 (2014).
- [4] S. Sorella, Y. Otsuka, and S. Yunoki, Sci. Rep. **2**, 992 (2012); F. F. Assaad and I. F. Herbut, Phys. Rev. X **3**, 031010 (2013); F. Parisen Toldin, M. Hohenadler, F. F. Assaad, and I. F. Herbut, Phys. Rev. B **91**, 165108 (2015).
- [5] A. Yamada, Int. J. Mod. Phys. B **30**, 1650158 (2016).

Exploring low-rank tensor representation of Matsubara Green's functions

Hiroshi SHINAOKA

*Department of Physics, Saitama University,
Saitama 338-8570*

We have studied a low-rank representation of two-particle Green's functions [1]. Two-particle Green's functions and the vertex functions play a critical role in theoretical frameworks for describing strongly correlated electron systems. However, numerical calculations at the two-particle level often suffer from large computation time and massive memory consumption. Example includes parquet approximation and diagrammatic non-local extensions of dynamical mean-field theory. For example, a simulation for the single-band two-dimensional Hubbard model based on the parquet approximation requires more than **a TB of memory** even at a high temperature. Thus, a compact representation of two-particle Green's functions is highly desired.

In Ref. [1], we introduced a sparse sampling scheme in the Matsubara frequency domain as well as a tensor network representation for two-particle Green's functions. The sparse sampling is based on the intermediate representation basis [2, 3, 4] and allows an accurate extraction of the generalized susceptibility from a reduced set of Matsubara frequencies. The tensor network representation provides a system independent way to compress the information carried by two-particle Green's functions.

We used System B at the ISSP supercomputer center to demonstrate efficiency of the present scheme for calculations of static and dynamic susceptibilities in single- and two-band Hubbard models in the framework of dynamical mean-field theory.

Figure 1 shows the dynamical lattice susceptibility computed by Bethe-Salpeter equation (BSE) based on dynamical mean-field theory for a two-band Hubbard model. In solving BSE, we compressed the local two-particle Green's function using the tensor-network representation. The uncompressed data takes up **700 MB** even on the sparse grid, while the tensor network representation takes up only **330 kB** for $D = 60$. Here, D is a bond dimension in the tensor network.

In future studies, we will use the new techniques to study real compounds by means of the non-local extension of the dynamical mean-field theory and the parquet approximation.

This report is based on the collaboration with D. Geffroy, M. Wallerberger, J. Otsuki, K. Yoshimi, E. Gull, J. Kuneš.

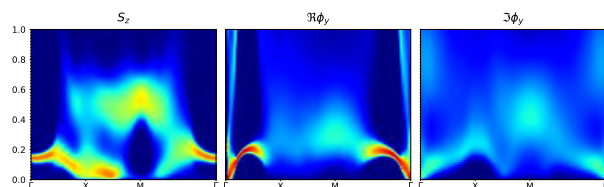


Figure 1: Dynamical lattice susceptibility computed for a two-band Hubbard model. Reproduced from Ref. [1] under the CC BY 4.0 license.

References

- [1] H. Shinaoka, D. Geffroy, M. Wallerberger, J. Otsuki, K. Yoshimi, E. Gull, J. Kuneš,

SciPost Phys. **8**, 012 (2020)

- [2] H. Shinaoka, J. Otsuki, M. Ohzeki and K. Yoshimi, Phys. Rev. B **96**, 035147 (2017)
- [3] H. Shinaoka, J. Otsuki, K. Haule, M. Wallerberger, E. Gull, K. Yoshimi and M. Ohzeki, Phys. Rev. B **97**, 205111 (2018)
- [4] J. Otsuki, M. Ohzeki, H. Shinaoka and K. Yoshimi, Sparse modeling in quantum many- body problems, J. Phys. Soc. Jpn. **89**, 012001 (2020)

Photoinduced dynamics and high harmonic generation in magnetism

Sumio Ishihara

Department of Physics, Tohoku University

Sendai 980-8578

Nonequilibrium susceptibility in Floquet states

Recent great progress in laser light technology significantly promotes scientific research in strongly coupled light-matter systems. One of the fascinating phenomena induced by the strong light-matter coupling is the appearance of the Floquet states, in which a time-periodic electromagnetic field behaves as photons and hybridizes with electrons. We examine the spin/charge susceptibility in photoinduced Floquet states [1]. We consider a free-electron system coupled to a fermionic heat bath. We adopt the Hamiltonian given by

$$H = \sum_{ks} \varepsilon_k c_{ks}^\dagger c_{ks} + \sum_{\nu} b_{\nu}^\dagger b_{\nu} + \sum_{ks\nu} V_n u \left(c_{ks}^\dagger b_{\nu} + b_{\nu}^\dagger c_{ks} \right), \quad (1)$$

where c_{ks}^\dagger is a creation operator of an electron with momentum k and spin $s(=\uparrow, \downarrow)$, and b_{ν}^\dagger is that of a fermion in a bath with a quantum number ν .

The susceptibility is formulated on the basis of the Floquet Green's function method, and its perturbative expression is derived from a series expansion. Through the numerical calculations, we have the following results.

1) In the case of the large electric-field frequency Ω in comparison with the electron bandwidth, we demonstrate that the bandwidth reduction due to the dynamical localization effect enhances the susceptibility and a deformation of the Fermi surface which depends on light polarization shifts the peak positions of the susceptibility (Fig. 1).

2) On the other hand, in the case of small Ω comparable to the bandwidth, the multiple Floquet bands cross the Fermi level of the bath and the additional peaks emerge at momenta corresponding to “nesting vectors” between the Floquet-band Fermi surfaces (Fig. 2).

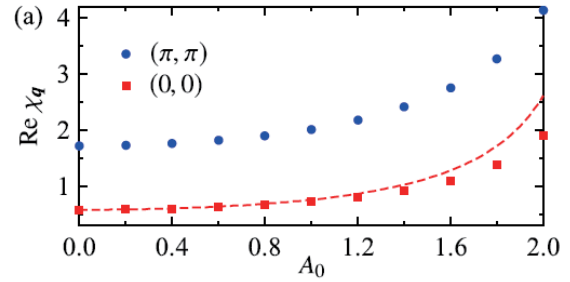


Figure 1: The susceptibility at $q = (0, 0)$ and (π, π) as a function of the light amplitude A_0 [1].

Optical response in the excitonic insulating state

The excitonic insulating (EI) state was proposed more than a half century ago in semiconductors and semimetals and has been studied intensively on both the experimental and theoretical sides. We study the optical responses in EI states [2]. We adopt the two-orbital Hubbard model with finite energy difference between the orbitals defined by

$$H = \Delta \sum_{i\sigma} (n_{i\alpha\sigma} - n_{i\beta\sigma}) + \sum_{\langle ij \rangle \alpha\sigma} t_{\alpha} c_{i\alpha\sigma}^\dagger c_{j\alpha\sigma} + \sum_i (U \sum_{\alpha} n_{i\alpha\uparrow} n_{i\alpha\downarrow} + U' n_{i\alpha} n_{i\beta})$$

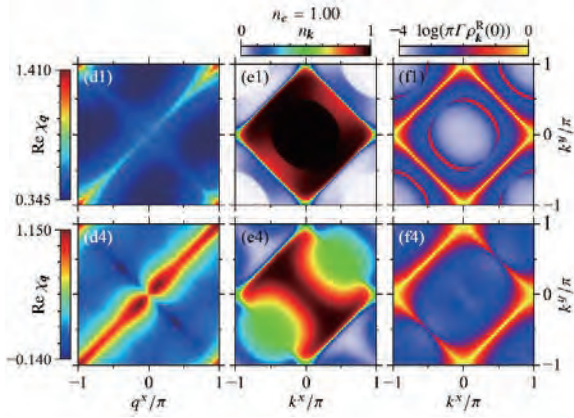


Figure 2: The susceptibility, the momentum distribution function; and the spectral function at $\omega = 0$, under the linearly polarized light of $A_0 = 0.4$ and 1.6 [1].

$$\begin{aligned}
 & + J \sum_{i\sigma\sigma'} c_{i\alpha\sigma}^\dagger c_{i\beta\sigma'}^\dagger c_{i\alpha\sigma'} c_{i\beta\sigma} \\
 & + I \sum_{i\alpha} c_{i\alpha\uparrow}^\dagger c_{i\alpha\downarrow}^\dagger c_{i\bar{\alpha}\downarrow} c_{i\bar{\alpha}\uparrow}, \quad (2)
 \end{aligned}$$

where $c_{i\alpha\sigma}$ is an annihilation operator of an electron with spin $\sigma (= \uparrow, \downarrow)$ and the orbital $\alpha (= a, b)$ at site i , and $n_{i\alpha\sigma} = c_{i\alpha\sigma}^\dagger c_{i\alpha\sigma}$ is the particle number operator.

The variational cluster approach method was applied to the two-orbital Hubbard model with a finite energy difference between the orbitals. In the analyses of the ground state, we considered possibilities of the low-spin state, the high-spin antiferromagnetic state, the EI state. The optical conductivity spectra were formulated by the Green's function method, where the vertex correction is taken into account. Figure 3 shows the optical conductivity spectra. In the EI phase, a new peak around $\omega/t \sim 10$ and a continuum around $3 < \omega/t < 8$ appear. The intensity of the EI component increases with increasing J/t in the EI phase. It is shown that the intensity of this structure at low temperatures almost follows the EI order parameter.

These researches have been performed with collaboration with A. Ono, H. Li, M. Naka and J. Ohtsuki. The numerical calculations in

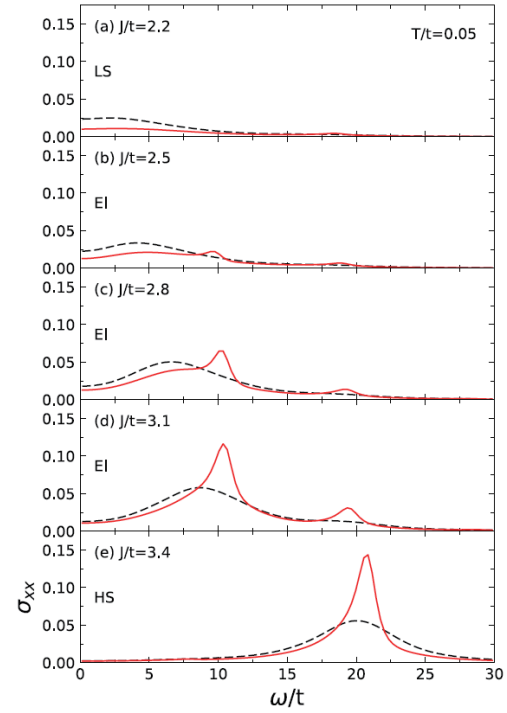


Figure 3: Optical conductivity spectra for several values of the Hund coupling J . The red solid lines show results including the vertex corrections, while the black dashed results show results without the vertex corrections. [2].

these works have been done using the facilities of the Supercomputer Center, the Institute for Solid State Physics, the University of Tokyo.

References

- [1] A. Ono and S. Ishihara: Phys. Rev. B **100**, 075127 (2019).
- [2] H. Li, J. Otsuki, M. Naka and S. Ishihara Phys. Rev. B **101** 125117 (2020).

Mechanism of superconductivity and electron-hole asymmetry in molecular conductors

κ -(BEDT-TTF)₂X

Hiroshi WATANABE

Cluster for Pioneering Research (CPR), RIKEN

2-1 Hirosawa, Wako-shi, Saitama 351-0198

The family of quasi two-dimensional molecular conductors κ -(BEDT-TTF)₂X has been extensively studied as a typical example of strongly correlated electron system. Depending on the monovalent anion X, they show various quantum phases such as antiferromagnetic (AF) and spin-liquid dimer-Mott insulators, and superconductivity (SC) [1]. Owing to the similarities in the experimental phase diagrams, κ -(BEDT-TTF)₂X system is often compared with high- T_c cuprates, which exhibit Mott metal-insulator transition and SC [2]. Recently, carrier doping in κ -(BEDT-TTF)₂X has been realized using electric-double-layer transistor [3], and the direct comparison with cuprates becomes possible. The experimental result shows the electron-hole doping asymmetry, reminiscent of the high- T_c cuprates.

Here, we theoretically study the doping effect in κ -(BEDT-TTF)₂X. We consider a four-band extended Hubbard model including on-site (U) and intersite Coulomb interactions (V_{ij}) with κ -type geometry with the largest hopping integral t_{b1} as an energy unit. The ground state properties are studied with the variational Monte Carlo (VMC) method. The Gutzwiller-Jastrow type wave function is used for the VMC trial wave function. The system sizes for calculation are from 288 ($2 \times 12 \times 12$) to 1152 ($2 \times 24 \times 24$).

Figure 1 shows the ground-state phase diagram of the extended Hubbard model for κ -(BEDT-TTF)₂X [4]. We find significant

electron-hole doping asymmetry in the phase diagram where AF spin order, different patterns of charge order, and SC compete with each other. Hole-doping stabilizes the dimer-type AF phase and promotes SC with d_{xy} -wave symmetry, which has similarities with high- T_c cuprates. In contrast, in the electron-doped side, geometrical frustration destabilizes the AF phase and the enhanced charge correlation induces another SC with extended- $s+d_{x^2-y^2}$ -wave symmetry. Our results disclose the mechanism of each phase appearing in filling-control molecular Mott systems, and elucidate how physics of different strongly-correlated electrons are connected, namely, molecular conductors and high- T_c cuprates.

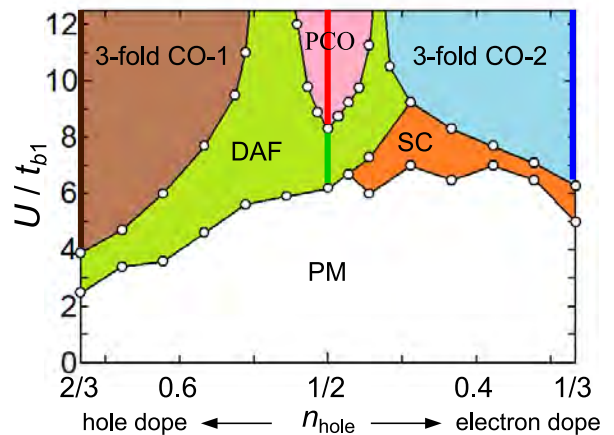


Figure 1: Ground-state phase diagram of the extended Hubbard model for κ -(BEDT-TTF)₂X [4].

References

- [1] K. Kanoda: J. Phys. Soc. Jpn. **75** (2006) 051007.
- [2] R. H. McKenzie: Science **278** (1997) 820.
- [3] Y. Kawasugi et al., Sci. Adv. **5** (2019) eaav7282.
- [4] H. Watanabe, H. Seo, and S. Yunoki: Nat. Commun. **10** (2019) 3167.

3.4 Cooperative Phenomena in Complex Macroscopic Systems

Tensor-network-based methods and their application to discrete lattice models

Naoki KAWASHIMA

Institute for Solid State Physics,

The University of Tokyo, Kashiwa-no-ha, Kashiwa, Chiba 277-8581

Tensor network (TN) is a useful concept in various fields, not only in the condensed matter theory, but also in data science and machine learning. Even in the condensed matter theory alone, the application of the TN concept is multi-fold. In variational principles calculation, the TN is used as a new type of variational wave function. In the real-space renormalization group (RG) theory, it serves as a natural representation of a renormalized system. In the pure mathematical physics, it is used as a new language for discussing the topological nature of the quantum states. In SY2019, we developed new algorithms for general TN-based computation [1], the boundary conformal-field theory [2,3], the classical dynamics [4], and variational optimization of topological quantum states. [5,6]

In [1], we proposed a new method for obtaining an efficient representation of a many-ranked tensor in terms of a ring network of smaller-ranked tensors. This kind of operations is vital both in TN application to the real space renormalization group and in data science. The central technical problem here is, how to avoid

the local-minima-trapping due to the formation of redundant entanglement loops. Our benchmark showed that the new method efficiently removes such loops when the target tensor has, at least approximately, the structure of the corner double line tensor, which is typical in TN-based RG calculations.

In [2,3], we developed the tensor renormalization group (TRG) algorithm for statistical systems with open boundaries. This allows us to investigate properties of boundary operators. We applied the method to several two-dimensional classical spin models with open boundaries. The boundary conformal spectrum was obtained and turned out consistent with the underlying boundary conformal field theories (BCFTs) for the Ising, tricritical Ising, and three-state Potts models.

In [4], we developed a method for tracing the time-evolution of the probability distribution function of a given dynamical systems, which is otherwise difficult. We studied (1+1)-dimensional directed percolation, a canonical model of a nonequilibrium continuous transition. We find a universal relaxation of Rényi entropy at the absorbing

transition point. We also detected a singularity in the "entanglement entropy" in the active (i.e., non-absorbing) phase. Although the absorbing states is exponentially rare in this phase, its rare appearance causes this singularity.

In [5], we studied the Kitaev model by the TN representation. We proposed a new wave function that is extremely simple in the TN representation but still shares many essential properties with the ground state of the Kitaev model, such as the quasi-long-range correlation, the short-range magnetic correlation, the flux-free property, the Z_2 gauge structure, and the 2D Ising universality. We call this state the "loop gas state" because of its mathematical equivalence to the loop gas model, one of the standard and solvable statistical physical models. We showed that the loop gas state is adiabatically connected to the ground state of the Kitaev model, indicating a similar role to the AKLT state for the $S=1$ AFH chain.

Later we extended our method to several other models: $S=1$ Kitaev model [6], and Kitaev-Gamma model [7,8]. In particular, in [8], we studied field-induced quantum phases in theoretical models of the Kitaev magnets, such as α - RuCl_3 for which the half quantized thermal Hall conductivity was discovered. Our TN calculation suggested that a field-induced

phase appears between the low field zig-zag magnetic order and the high field polarized state. We found that the chiral Kitaev spin liquid occupies an area in the phase diagram, smaller than predicted by other groups.

References

- [1] Hyun-Yong Lee and Naoki Kawashima: J. Phys. Soc. Jpn. **89**, 054003 (2020)
- [2] Shumpei Iino, Satoshi Morita, and Naoki Kawashima: Phys. Rev. B **101**, 155418 (2020)
- [3] Shumpei Iino, Satoshi Morita, and Naoki Kawashima: Phys. Rev. B **100**, 035449 (2019)
- [4] Kenji Harada and Naoki Kawashima: Phys. Rev. Lett. **123**, 090601 (2019)
- [5] Hyun-Yong Lee, Ryui Kaneko, Tsuyoshi Okubo, and Naoki Kawashima: Phys. Rev. Lett. **123**, 087203 (2019)
- [6] Hyun-Yong Lee, Naoki Kawashima, and Yong Baek Kim: arXiv:1911.07714
- [7] Hyun-Yong Lee, Ryui Kaneko, Tsuyoshi Okubo, Naoki Kawashima: Phys. Rev. B **101**, 035140 (2020)
- [8] Hyun-Yong Lee, Ryui Kaneko, Li Ern Chern, Tsuyoshi Okubo, Youhei Yamaji, Naoki Kawashima and Yong Baek Kim: Nature Communications **11**, 1639 (2020)

Kármán-Vortex Cavitation Around Circular-Cylinder Arrays

Yuta ASANO¹, Hiroshi WATANABE^{1,2}, and Hiroshi NOGUCHI¹

¹ *Institute for Solid State Physics, University of Tokyo,
Kashiwa-no-ha, Kashiwa, Chiba 277-8581, Japan*

² *Department of Applied Physics and Physico-Informatics, Keio University,
Yokohama, Kanagawa 223-8522, Japan*

Cavitation is a flow phenomenon accompanied by the formation, growth, and collapse of bubbles caused by local pressure changes in a liquid with the high flow velocity. Since cavitation has adverse effects on fluid machinery such as performance degradation, vibration and noise, and erosion, the elucidation of its mechanism is of great engineering importance. The cavitation inception is thought to be caused by the growth of small bubble nuclei in a low-pressure region for enough time to grow [1]. However, since it is extremely difficult to discuss the dynamics of microscopic bubble nuclei in a macroscopic flow field, the mechanism of cavitation generation is not well understood. In addition, because the phase transition has to be directly discussed in the flow field, it is extremely difficult to analyze the cavitation inception of the liquid in which no bubble nuclei are contained as in the case of flow in hydraulic machines.

In the present study, molecular dynamics (MD) calculations are performed to analyze cavitation around periodically aligned cylinders, and the formation and growth processes of

bubbles and their effects on the surrounding flow are investigated by MD calculations [2].

3-dimensional MD simulation is carried out to analyze the flow around the periodically aligned cylinders. The Lennard-Jones (LJ) interaction is used for the interaction between the fluid particles. The cylinder is modeled by fixing LJ particles on its surface. Periodic boundary conditions are used for all directions in the system, and two cylinders are arranged perpendicular to the flow to represent an infinite row of cylinders. In this way, interference of the vortices behind the upper and lower cylinders can be taken into account. The temperature and velocity are controlled by the Langevin heat bath at the downstream side of the cylinder. Fluids in the supercritical region are inflow. Cavitation is generated by a decrease in the local temperature of the inflow fluid.

Figure 1 shows a snapshot of the density (left panels) and vorticity (right panels) fields. At high temperature (temperature $T=2$), there are no bubbles and therefore non-cavitating flow is obtained. An anti-phase synchronized Kármán

vortex is generated behind the cylinder. It is also found that this synchronization amplifies the vibrations acting on the cylinder. At the lower temperature, $T=1.3$, bubbles are generated in conjunction with the shedding cycle of the Kármán vortex. The Kármán vortex remains synchronized in the anti-phase as in the non-cavitating flow. At $T=1.25$, a gas-phase region is formed behind the cylinder and the distance to the formation of the Kármán vortices increases. The phase of the Kármán vortices is slightly disturbed. As the temperature is further reduced to $T=1.2$, the gas-phase region behind the cylinder is further expanded and the upper and lower Kármán vortices become asymmetric. It is also found that this asymmetric structure is switched by a long period of time. In Newtonian fluids in which no phase transitions occur, no such

changes occur due to temperature changes.

The change in the vortex structure should change the characteristics of the vibrations excited by the vortex. It is found that the bubbles generated near the cylinder inhibit the propagation of the vibration associated with the ejection of the vortex, and the vibration amplitude decreases and eventually disappears.

In summary, the analysis from the molecular scale reveals that bubbles generated near the cylinder significantly change the properties of the lift and flow fields.

References

- [1] C. E. Brennen, *Cavitation and Bubble Dynamics* (Oxford University Press, 1995).
- [2] Y. Asano, H. Watanabe, and H. Noguchi: *J. Chem. Phys.* 152 (2020) 034501.

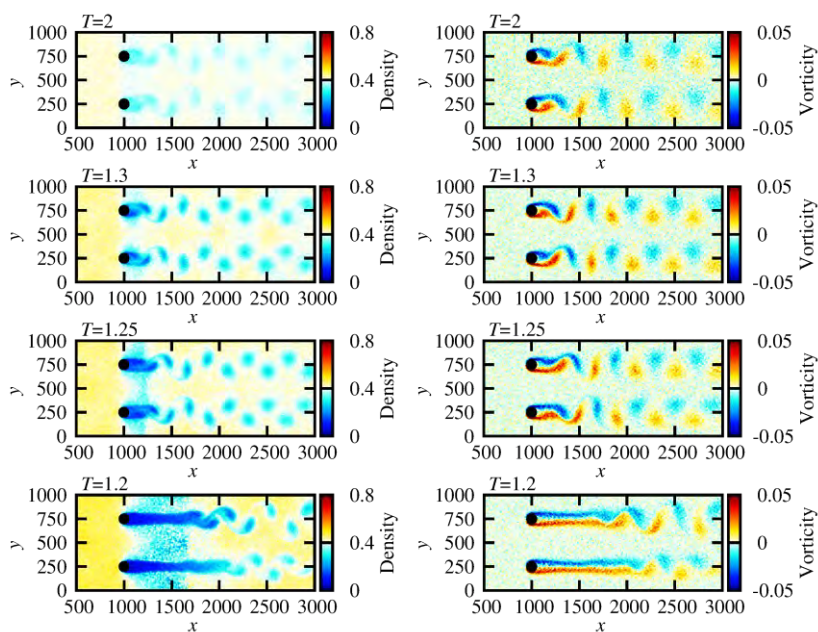


Figure 1: Snapshots of density (left panels) and vorticity (right panels) fields of LJ fluid. The black circles in the figure represent cylinders.

Detachment of fluid membrane from substrate by protein adhesion

Hiroshi NOGUCHI

Institute for Solid State Physics, University of Tokyo, Kashiwa, Chiba 277-8581

Lipid membranes supported on a solid substrate are considered as a model system for biological membranes and are extensively used to study protein functions and membrane properties. Recently, the membrane detachment from the substrate was reported by the adhesion of Ca^{2+} -dependent membrane-binding proteins annexin. The membrane rolling and blebbing have been observed. To understand the mechanism to form these membrane structures, we have performed meshless membrane simulations with the isotropic spontaneous curvatures. We focus on the generation of the spontaneous curvature by the protein adhesion here.

Before considering the detachment from the substrate, we investigated the closing transition from a membrane patch to a vesicle at a finite spontaneous curvature [1]. We have determined the theoretical condition of the closure and proposed the estimation method of the membrane Gaussian modulus from the curvature of the membrane patch.

Next, we added the attraction to a solid substrate by the Lennard-Jones potential. When a high curvature C_0 is imposed, a membrane disk is detached from the substrate, and vesicles are formed [see Fig. 1] [2]. The membrane edge is rolled up, and the edge undulation expands leading to the vesicle formation. The average vesicle size is several times larger than the minimum vesicle size formed by the membrane closure of a cup-shaped membrane patch.

With strong adhesion, the competition between the bending and adhesion energies determines the minimum value of the spontaneous curvature for the detachment. In contrast, with weak adhesion, a detachment occurs at smaller spontaneous curvatures due

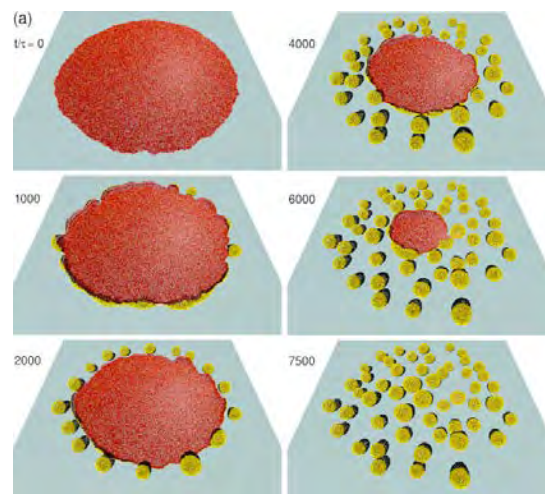


Figure 1: Sequential snapshots of the detachment and vesiculation of the disk-shaped membrane from a solid substrate.

to the membrane thermal undulation. When parts of the membrane are pinned on the substrate, the detachment becomes slower, and a remained membrane patch forms straight or concave membrane edges. The edge undulation induces vesiculation of long strips and disk-shaped patches. Therefore, membrane rolling is obtained only for membrane strips shorter than the wavelength for deformation into unduloid. This suggests that the rolling observed for the annexins A3, A4, A5, and A13, results from by the anisotropic spontaneous curvature induced by the proteins.

References

- [1] H. Noguchi: *J. Chem. Phys.* **51**, 094903 (2019).
- [2] H. Noguchi: *Soft Matter* **15**, 8741 (2019).

Brittle structure of semicrystalline polymers by large-scale coarse-grained molecular dynamics simulation

Yuji HIGUCHI

*Institute for Solid State Physics, University of Tokyo
Kashiwa-no-ha, Kashiwa, Chiba 277-8581*

We have studied mechanical properties of semicrystalline polymers [1, 2, 3] and double-network gels [4] via coarse-grained molecular dynamics simulations. Understanding the fracture process of the semicrystalline polymers at the molecular level is essential to increase its toughness against the stretching. This year, void formation and growth processes in the fracture process of semicrystalline polymers were studied on System B.

Figure 1 shows the fracture process of the lamellar structure consisting of 1.5×10^7 monomers. The lamellar structure consists of amorphous and crystalline layers. Voids are generated in amorphous layers, and then they grow parallel to the stretching direction cylindrically. This process is different from those in elastomers and glassy polymers. The void structures during their growth process at the molecular level are still debatable in experiments. The maximum length of voids along x , y , and z -directions are monitored during the stretching. At first, the maximum length of voids in x and y -directions, which are perpendicular to the stretching direction, is larger than that in z -direction, which is parallel to the stretching direction. Then, the length in z -direction becomes larger than those in x and y -directions. This result is consistent with that observed in the experiment [5]. Thus, the void generation and growth processes in the lamellar structure of crystalline polymers at the molecular level are successfully revealed.

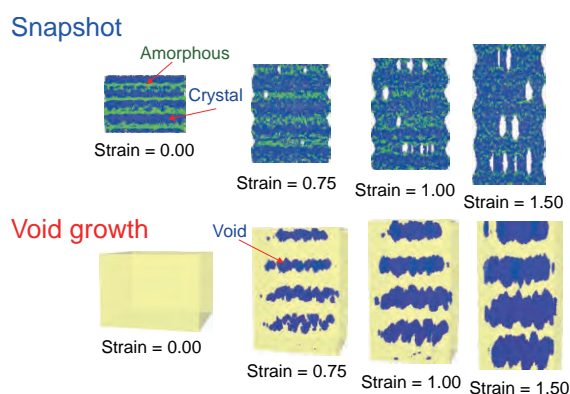


Figure 1: The deformation and fracture process of the lamellar structure. (a) Snapshot and (b) void generation and growth processes.

References

- [1] Y. Higuchi and M. Kubo: *Macromolecules* **50** (2017) 3690.
- [2] Y. Higuchi: *Polym. J.* **50** (2018) 579.
- [3] Y. Higuchi: *Macromolecules* **52** (2019) 6201.
- [4] Y. Higuchi, K. Saito, T. Sakai, J. P. Gong, and M. Kubo: *Macromolecules* **51** (2018) 3075.
- [5] S. Humbert, O. Lame, J. M. Chenal, C. Rochas, and G. Vigier: *Macromolecules* **43** (2010) 7212.

Topological Magnetization Plateau of Quantum Antiferromagnetic Spin Chain with Anisotropies

Tôru SAKAI^{1,2}, Hiroki NAKANO^{1,2}, and Tokuro SHIMOKAWA³,

¹*Graduate School of Material Science, University of Hyogo,
Kouto, Kamigori, Hyogo 678-1297, Japan*

²*Synchrotron Radiation Research Center, Kansai Photon Science Institute,
Quantum Beam Science Research Directorate,
National Institute for Quantum and Radiological Science and Technology (QST)
SPRING-8, Kouto, Sayo, Hyogo 679-5148, Japan*

³*Okinawa Institute of Science and Technology Graduate University, Onna,
Okinawa 904-0945, Japan*

The symmetry protected topological phase[1, 2] is one of interesting topics in the strongly correlated electron systems. The recent study[3, 4] using the numerical diagonalization of finite-size clusters and the level spectroscopy analysis revealed that the symmetry protected topological phase appears in the $S = 2$ antiferromagnetic chain with the single-ion anisotropy D and the coupling anisotropy Δ . However, the region of this phase is quite small in the ground state phase diagram. Thus it would be difficult to discover in some real experiments. In the present study we focused on the symmetry protected topological phase in the magnetization plateau of the $S = 2$ antiferromagnetic chain, using the same numerical diagonalization and level spectroscopy analysis. As a result, it is successfully found that the symmetry protected topological phase appears in much larger region of the phase diagram of the $1/2$ magnetization plateau. In addition the biquadratic interaction is revealed to enhance this phase[5].

The $1/3$ magnetization plateau of the distorted diamond spin chain was also investigated using the numerical diagonalization and the finite-size scaling analysis. As a result it

is found that the magnetization plateau vanishes for sufficiently large XY -like coupling anisotropy. The phase diagram of the $1/3$ magnetization plateau was also obtained[6, 7].

As related topics to the magnetization plateau, we investigated the spin gap of the kagome-lattice antiferromagnet. We performed the large-scale numerical diagonalization of the spin gap and the magnetization curve of the system and tried to compare them with the recent experimental results[8, 9]

References

- [1] F. Pollmann, A. M. Turner, E. Berg and M. Oshikawa, Phys. Rev. B **81**, 064439 (2010).
- [2] F. Pollmann, E. Berg, A. M. Turner and M. Oshikawa, Phys. Rev. B **85**, 075125 (2012).
- [3] T. Tonegawa, K. Okamoto, H. Nakano, T. Sakai, K. Nomura and M. Kaburagi, J. Phys. Soc. Jpn. **80**, 043001 (2011).
- [4] K. Okamoto, T. Tonegawa and T. Sakai, J. Phys. Soc. Jpn. **85**, 063704 (2016).

- [5] T. Sakai, K. Okamoto and T. Tonegawa, Phys. Rev. B **100**, 054407 (2019).
- [6] Y. Ueno, T. Zenda, Y. Tachibana, K. Okamoto and T. Sakai, JPS Conference Proceedings **30**, 011085 (2020).
- [7] T. Zenda, Y. Tachibana, Y. Ueno, K. Okamoto and T. Sakai, JPS Conference Proceedings **30**, 011084 (2020).
- [8] H. O. Jeschke, H. Nakano and T. Sakai, Phys. Rev. B **99**, 140410(R) (2019).
- [9] R. Shirakami, H. Ueda, H. O. Jeschke, H. Nakano, S. Kobayashi, A. Matsuo, T. Sakai, N. Katayama, H. Sawa, K. Kindo, C. Michioka and K. Yoshimura, Phys. Rev. B **100**, 8722674 (2019).

Numerical Diagonalization Study on Spin Nematic Phase of Low-Dimensional System

Tôru SAKAI^{1,2}, Hiroki NAKANO^{1,2}, and Tokuro SHIMOKAWA³,

¹*Graduate School of Material Science, University of Hyogo,
Kouto, Kamigori, Hyogo 678-1297, Japan*

²*Synchrotron Radiation Research Center, Kansai Photon Science Institute,
Quantum Beam Science Research Directorate,
National Institute for Quantum and Radiological Science and Technology (QST)
SPring-8, Kouto, Sayo, Hyogo 679-5148, Japan*

³*Okinawa Institute of Science and Technology Graduate University, Onna,
Okinawa 904-0945, Japan*

The spin nematic phase has attracted a lot of interests in the field of the quantum spin systems. It was theoretically predicted to appear around the saturation magnetization in the magnetization process of the frustrated spin chain[1]. Our present study using the numerical diagonalization and the finite-size scaling analysis revealed that the spin nematic liquid phase appears in the $S = 1$ spin ladder system with the easy-axis single-ion anisotropy D even for a small magnetic field H . The phase diagram in the DH plane and the DH plane were obtained[2, 3].

The research of the three-leg spin tube with the ring-exchange interaction J_4 using the numerical diagonalization and the finite-size scaling analysis[4] indicated that the spin nematic liquid phase appears for sufficiently large J_4 . In addition the spin nematic liquid phase was also revealed to appear in the spin ladder system with the antiferromagnetic leg and the ferromagnetic rung exchange interaction in the present of the XXZ anisotropy[5].

References

- [1] T. Hikihara, L. Kecke, T. Momoi and A. Furusaki, Phys. Rev. B **78**, 144404 (2008).
- [2] R. Yamanokuchi, K. Okamoto and T. Sakai, Proceedings of 2018 16th International Conference on Megagauss Magnetic Field Generation and Related Topics (MEGAGAUSS) (2019) 8722674.
- [3] T. Sakai and K. Okamoto, JPS Conference Proceedings **30**, 011083 (2020).
- [4] T. Sakai, JPS Conference Proceedings **29**, 014004 (2020).
- [5] K. Okamoto, T. Tonegawa, M. Kaburagi and T. Sakai, JPS Conference Proceedings **30**, 011024 (2020).

Aggregation process of full-length amyloid-beta peptides studied by molecular dynamics simulations

Hisashi Okumura

*Exploratory Research Center on Life and Living Systems,
Institute for Molecular Science, Okazaki, Aichi 444-8585*

Alzheimer's disease is thought to be caused by aggregates of amyloid-beta peptides, such as oligomers and amyloid fibrils. Amyloid-beta peptide is a peptide consisting of 39-43 amino acid residues. The oligomer structure of the amyloid-beta peptides is not clear. We investigated the aggregation process of full-length amyloid-beta peptides by molecular dynamics simulations. Several amyloid-beta peptides were placed in explicit water, and their dynamics and structural changes were observed. As a result, aggregates with intermolecular beta-sheet structure was generated. During this oligomerization process, A β peptides are first aggregated by electrostatic force. Then, they are aggregated by hydrophobic interaction.

We also developed an improvement of the replica-exchange [1, 2] and replica-permutation methods [3], which we call the replica sub-permutation method (RSPM) [4]. Instead of considering all permutations, this method uses a new algorithm referred to as sub-permutation that contains transitions only to the adjacent temperatures. The RSPM can reduce the

number of combinations between replicas and parameters without the loss of sampling efficiency. For comparison, we applied the replica sub-permutation, replica-permutation, and replica-exchange methods to a β -hairpin mini protein, chignolin, in explicit water. We calculated the transition ratio and number of tunneling events in the parameter space, the number of folding–unfolding events, and the autocorrelation function to compare sampling efficiency. The results indicate that among the three methods, the RSPM is the most efficient in both parameter and conformational spaces.

References

- [1] K. Hukushima, K. Nemoto, *J. Phys. Soc. Jpn.* **65** (1996) 1604.
- [2] Y. Sugita, Y. Okamoto, *Chem. Phys. Lett.* **314** (1999) 141.
- [3] S. G. Itoh, H. Okumura, *J. Chem. Theor. Comput.* **9** (2013) 570.
- [4] M. Yamauchi and H. Okumura: *J. Comput. Chem. B* **40** (2019) 2694.

Monte Carlo study of the critical properties of noncollinear Heisenberg magnets: $O(3) \times O(2)$ universality class

Yoshihiro Nagano, Kazuki Uematsu and Hikaru Kawamura
Graduate School of Science, Osaka University, Toyonaka 560-0043

The critical properties of the antiferromagnetic Heisenberg model on the three-dimensional stacked-triangular lattice [1] are studied by means of a large-scale Monte Carlo simulation in order to get insight into the controversial issue of the criticality of the noncollinear magnets with the $O(3) \times O(2)$ symmetry [2]. The maximum size studied is 384^3 , considerably larger than the sizes studied by the previous numerical works on the model. Availability of such large-size data enables us to examine the detailed critical properties including the effect of corrections to the leading scaling. Strong numerical evidence of the continuous nature of the transition is obtained. Our data indicates the existence of significant corrections to the leading scaling. Careful analysis by taking account of the possible corrections yield critical exponents estimates, $\alpha = 0.44(3)$, $\beta = 0.26(2)$, $\gamma = 1.03(5)$, $\nu = 0.52(1)$, $\eta = 0.02(5)$, and the chirality exponents $\beta_k = 0.40(3)$ and $\gamma_k = 0.77(6)$, supporting the existence of the $O(3)$ chiral (or $O(3) \times O(2)$) universality class governed by a new 'chiral' fixed point [3,4]. We also obtain an indication that the underlying fixed point is of the focus-

type, characterized by the complex-valued correction-to-scaling exponent, $\omega = 0.1^{+0.4}_{-0.05} + i 0.7^{+0.1}_{-0.4}$. The focus-like nature of the chiral fixed point accompanied by the spiral-like renormalization-group (RG) flow [5] is likely to be the origin of the apparently complicated critical behavior. The results are compared and discussed in conjunction with the results of other numerical simulations, several distinct types of RG calculations including the higher-order perturbative massive and massless RG calculations and the nonperturbative functional RG calculation, and the conformal-bootstrap program.

References

- [1] H. Kawamura, *J. Phys. Condens. Matter* **10**, 4707 (1998).
- [2] Y. Nagano, K. Uematsu and H. Kawamura, *Phys. Rev. B* **83**, 103704 (2019).
- [3] H. Kawamura, *Phys. Rev. B* **8**, 4916 (1988).
- [4] A. Pelissetto, P. Rossi and E. Vicari, *Phys. Rev. B* **63**, 140414(R) (2001); **65**, 020403(R) (2001).hi
- [5] P. Calabrese, P. Parruccini and A.I. Sokolov, *Phys. Rev. B* **66**, 180403(R) (2002).

Multiscale analysis of polymeric fluids and solids

Takahiro MURASHIMA

*Department of Physics, Graduate School of Science,
Tohoku University, Aramaki-Aza-Aoba, Aoba-Ward, Sendai, Miyagi 980-8578*

Polymeric materials are used in many products and are now an integral part of our lives. In recent years, however, the use of microplastics has tended to be discouraged due to concerns about the damage they can cause to ecosystems. The development of new materials with less impact on ecosystems, such as biodegradable plastics, is expected.

In order to develop more functional materials, it is essential to control the physical properties on the molecular scale and to control the formability on the macro scale. The micro-scale properties of polymer materials and macro-scale mechanical properties are strongly correlated and cannot be treated independently, making their understanding difficult. Therefore, we have been developing multi-scale simulations that simultaneously combine micro-scale molecular simulations and macro-scale continuum simulations. In this project, we have developed a multi-scale simulation that combines molecular dynamics simulation and finite element simulation, and the results have been published in several papers[1-3].

The method of multi-scale simulation is as follows. The macro-scale cube is divided into

100 tetrahedral elements and the deformation of each element is calculated using the finite element method. Each element has a molecular simulation system and molecular simulation is carried out according to the deformation. The stresses are then obtained from the molecular simulation system and passed on to the macroscopic system. On the macro-scale side, the deformation occurs according to the determined stress field. The entire system is developed in time by alternating these macro- and micro-scale calculations. Multiscale simulations are now possible to include molecular features that are difficult to handle in conventional macro-scale simulations, and to calculate large deformations that are difficult to handle in conventional micro-scale simulations.

References

- [1] T. Murashima, S. Urata, S. Li: Euro. Phys. J. B **92** (2019) 221.
- [2] T. Murashima: CICSJ Bulletin **37** (2019) 87.
- [3] S. Li, S. Urata, T. Murashima: IACM Express. **46** (2020) 10.

Dynamical simulation of spin-orbit insulators

Hidemaro Suwa

*Department of Physics, University of Tokyo
7-3-1 Hongo Bunkyo, Tokyo 113-0033*

Dynamics of correlated quantum materials is a long-standing problem in condensed matter physics. The recent development of experimental techniques such as inelastic neutron and x-ray scattering has revealed dynamical properties and excitations with unprecedented precision. In particular, resonant inelastic X-ray scattering has revealed a lot of hidden features of high- T_c superconductors and spin-orbit insulators. It is of great interest to find novel quasi-particles and understand complex excitations in correlated materials.

Spin-orbit insulators emerge from $5d$ electron systems with strong spin-orbit coupling. Coulomb repulsion between electrons in $5d$ atomic orbitals is not strong enough to suppress charge degrees of freedom completely. As a result, the charge gap can be comparable to the magnon-band width, as experimentally measured in strontium iridates. Such electron systems can be described by the Hubbard model with an intermediate Coulomb repulsion, which is parameterized by U .

Strontium iridates, which can be approximated by a half-filled $J = 1/2$ single-band Hubbard model, provide an excellent playground of charge-spin-orbital entanglement. The dimensionality drastically changes the electronic property: the single layer material Sr_2IrO_4 is a Mott insulator with 400 meV charge gap, the bilayer material $\text{Sr}_3\text{Ir}_2\text{O}_7$ is an insulator in the intermediate coupling regime with 130 meV charge gap, and the three-dimensional material SrIrO_3 is a correlated metal. These systems provide one of the best opportunities to study the metal-insulator

transition. Particularly, the bilayer system is expected to show a characteristic excitation emerging in the crossover regime. Moreover, in the view of engineering, the magnetic energy scale enhanced in the crossover regime would be crucial to realistic devices.

To understand the dynamics of spin-orbit insulators, we have developed an efficient numerical approach that enables large-scale calculation of dynamical quantities at finite temperatures in a broad- U region of the Hubbard model. In our approach, sampling of the auxiliary vector fields from the Boltzmann distribution is combined with real time evolution of the self-consistent density matrix.

We used ISSP System B through class C projects (ID: H31-Ca-0057, H31-Cb-0047). Our code is implemented with MPI parallelization using GPUs. In particular, GPU programming is crucial to fast matrix-vector multiplication and diagonalization. Applying our approach to the bilayer iridate $\text{Sr}_3\text{Ir}_2\text{O}_7$, we have clarified excitonic excitations of the longitudinal or Higgs mode appearing in the dynamical spin structure factor. Interestingly, excitons exhibit a significant softening as the temperature approaches the magnetic transition temperature, while transverse magnons do not.

Our approach is applicable to a broad range of the Hubbard model without restrictions of the lattice, hopping parameters, and electron filling. The developed method is expected to push the boundary of dynamical simulation of correlated electron systems and lead to the identification of hidden excitations emerging from charge-spin-orbital entanglement.

Computational design of enzymes and ligand-binding proteins

Kazuhisa OHARA¹, Mio SANNO¹, Shunji SUETAKA¹, Nao SATO¹, Yoshiki OKA¹,
Koji OOKA², Yuuki HAYASHI¹, and Munehito ARAI^{1,2}

¹*Department of Life Sciences, Graduate School of Arts and Sciences, and*

²*Department of Physics, Graduate School of Science,*

The University of Tokyo, Komaba, Meguro, Tokyo 153-8902

Proteins have various functions, including binding and catalysis. Thus, proteins are potentially useful for industry and medicine if their functions are sufficiently improved or modified. However, because the protein folding problem remains unsolved, development of computational protein design strategies has been a great challenge. To solve this issue, here we attempted to use the Rosetta software suite to computationally design various proteins, including enzymes and ligand-binding proteins. The static version of the Rosetta 3.8 suite was used in the following calculations [1,2]. In addition, to solve the protein folding problem, we developed a statistical mechanical model of protein folding that can explain the folding pathways of multi-domain proteins.

(1) First, we aimed to rationally improve a catalytic activity of an enzyme. By optimizing the interactions between an enzyme, dihydrofolate reductase [3], and its ligands, we computationally designed many mutants of the enzyme that were expected to improve its catalytic activity. Subsequently, we selected 34

top mutants, created the mutant proteins experimentally, and measured their activities. We found that 20 out of 34 mutants had the activity higher than the wild-type protein. Moreover, for the top 2 mutants, we succeeded in improving the activity ~4-fold compared with the wild type. Thus, our strategies for rationally improving activity of an enzyme will be applicable to industrial use.

(2) Second, to develop a protein that can be used as an anti-allergy drug, we designed two types of proteins that inhibit the interaction of interleukin-33 (IL-33) with the ST2 receptor of type 2 innate lymphoid cells [4]. One template for the inhibitor design was a fragment of the ST2 protein. Rosetta calculation was used to reduce the number of disulfide bonds in the fragment, to make it easier to purify the protein that was expressed in *Escherichia coli*. As expected, we could obtain the mutant of the ST2 fragment having a reduced number of disulfide bonds as well as the ability to bind IL-33. Another strategy to design the IL-33–ST2 inhibitors was to make mutants of IL-33 that

binds tightly to one of the two IL-33 binding sites on ST2 but does not bind to another site. The calculations were already done, and the experimental verification is now under way.

(3) Third, we rationally designed inhibitors for the interactions between the KIX domain of a transcriptional coactivator CBP and transcriptional activators [5]. We designed and created the mutant fragments of the transcription activator MLL, which bind more tightly than the wild type. We also designed the KIX mutant that can bind more tightly to the transcription activator c-Myb than the wild-type KIX. Since the protein-protein interaction between KIX and c-Myb is responsible for the blood cancer, leukemia, our results may be useful for developing anti-cancer drugs.

(4) Fourth, we attempted to modify a substrate specificity of a ligand-binding protein using the Rosetta software. Here, an ATP-binding protein was designed to bind GTP instead of ATP. For experimental verification, we selected more than 20 mutants that were predicted by Rosetta to bind GTP more tightly than ATP. However, the experimental results showed that none of the mutants acquired a new function to bind a different ligand. It might be possible that dynamics of both the protein and ligand should be taken into account more extensively to accommodate the difference in the size and shape of ligands, although it requires much more calculations.

(5) Finally, to solve the protein folding problem, we developed a statistical mechanical model of protein folding. The WSME model has been known to be able to explain the folding pathways of small proteins and is considered to be a promising model to solve the protein folding problem [6]. However, the model could not be applicable to large, multi-domain proteins, and this problem has been unsolved for more than 20 years. By introducing a new Hamiltonian in the WSME model and computationally calculating the closed form of the partition function, we succeeded in predicting the folding pathways of multi-domain proteins. Thus, our model is promising for a unified theoretical description of protein folding mechanisms.

References

- [1] B.J. Bender, et al.: *Biochemistry*, **55** (2016) 4748-4763.
- [2] R. F. Alford, et al.: *J Chem Theory Comput.* **13** (2017) 3031-3048.
- [3] M. Arai, et al.: *J Mol Biol.* **410** (2011) 329-342.
- [4] X. Liu, et al.: *Proc Natl Acad Sci USA.* **110** (2013) 14918-14923.
- [5] R. N. De Guzman, et al.: *J Mol Biol.* **355** (2006) 1005-1013.
- [6] M. Sasai, et al.: *Biophys Physicobiol.* **13** (2016) 281-293.

Event-chain Monte Carlo method applied to non-equilibrium relaxation analysis

Y. Ozeki and Y. Osada

Graduate School of Informatics and Engineering, The University of Electro-Communications

The event-chain algorithm is investigated for its applicability to the nonequilibrium relaxation (NER) method and the estimation of the dynamical exponent z , which indicates an efficiency to perform Monte Carlo (MC) simulations. The event-chain method has introduced for the MC simulation with a multi-spin-flip algorithm [1,2]. It shows an efficient performance for the relaxation even in frustrated systems and gives estimation of the dynamical critical exponent $z \sim 1$ [1], which indicates a faster dynamics as compared with those with a single-spin-flip algorithm such as the the Metropolis one.

The NER method is an efficient numerical technique for analyzing equilibrium phase transition [3]. It provides the critical temperature and critical exponents accurately for second-order transition systems, and has been used successfully to study various problems, including frustrated and/or random systems. In the NER analysis, the equilibration step is not necessary. Simulation is made only up to steps when the asymptotic behavior indicates the equilibrium state. Thus, one can analyze large systems as compared with equilibrium simulations. This advantage becomes more effective for slow-relaxation systems.

We analyze the classical XY model in three dimensions;

$$\mathcal{H} = -J \sum_{\langle ij \rangle} \mathbf{S}_i \cdot \mathbf{S}_j, \quad (1)$$

where summation for $\langle ij \rangle$ is taken over all nearest-neighbor sites on a simple cubic lattice. The initial state of relaxation is prepared as the all-aligned state $(1, 0)$. Since the relaxation is much fast in the simulation with the event chain analysis, we cannot use the magnetization $\langle S_i^x \rangle$ as the dynamical order parameter, which is used in the NER analysis with the Metropolis algorithm. Thus, we estimate the relaxation of the absolute value of the magnetization,

$$|m(t)| = (\langle S_i^x \rangle^2 + \langle S_i^y \rangle^2)^{1/2}. \quad (2)$$

In the standard NER analysis, the asymptotic behaviors of relaxations are used to analyze the phase transition, and are necessary to be regarded

as those in the thermodynamic limit. In other words, the finite size effect must be avoided in the observed regime of relaxations. Thus, first, we check the size-dependence for the relaxation of $|m(t)|$. Calculations are carried out at around the expected transition temperature $T/ = 2.202$ on 4^3 to $350 - 3$ simple cubic lattices up to the observation time of 200 MCSs. Note that the temperature is measured in the unit of J/k_B hereafter. About 840 samples are taken for statistical averaging. The result is plotted in Fig. 1. It is confirmed that the size dependence disappears for $L \geq 300$ up to 200 MCSs. It is remarked that the relaxation simulated by the event-chain algorithm is much faster than that by the Metropolis one, which is an advantage. Furthermore, the appearance of the size dependence also becomes faster. In the Metropolis case, it does not appear at least in 10^4 MCSs for $L = 200$ lattice, while it does at 100 MCSs in the event-chain case. The latter property is an disadvantage, since we must simulate on larger lattices. Anyway, in the present study, we will use $L = 300$ lattice for the analysis of phase transition.

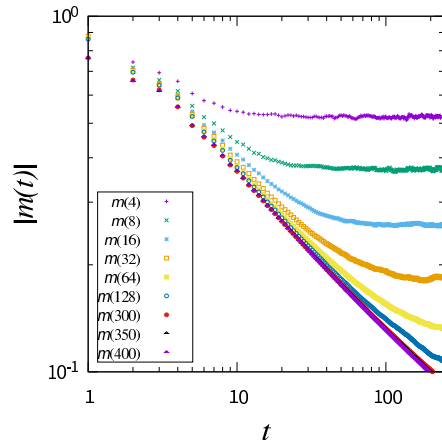


Figure 1: Size dependence for the relaxation of $|m(t)|$ at $T = 2.202$ for the 3D XY model.

The relaxation of the order parameter $|m(t)|$ are calculated for $2.182 \leq T \leq 2.222$ on the 300^3 simple cubic lattice up to an observation time of 200

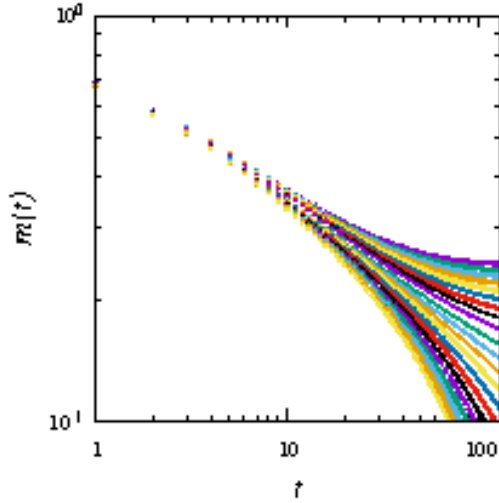


Figure 2: Relaxation of $|m(t)$ for the 3D XY model in $2.182 \leq T \leq 2.222$ with the interval $\Delta T = 0.002$.

MCSs. About 864 samples are taken for statistical averaging. The estimations are plotted in Fig. 2. Using the improved dynamical scaling analysis for the NER data [4], we analyze the dynamical scaling form,

$$|m(t, T)| = \tau^{-\lambda} Y[t/\tau], \quad (3)$$

where $\tau(T)$ is the relaxation time and λ is a dynamical critical exponent. In Fig. 2, the relaxation curves show downward trend in $2.204 \leq T \leq 2.222$, which indicates the paramagnetic phase. Thus, applying the scaling form (3), the data for these temperatures collapse as in Fig. 3 with $T_c = 2.20216$ and $z = 1.461$. Furthermore in Fig. 2, the relaxation curves show upward trend in $2.182 \leq T \leq 2.200$, which indicates the ferromagnetic phase. Thus, applying the scaling form (3), the data for these temperatures collapse as in Fig. 4 with $T_c = 2.20183$ and $z = 1.478$.

The estimated transition temperature $T_c = 2.202$ is consistent with $T_c = 2016$ obtained previously [5]. The estimated dynamical exponent $z \sim 1.47$ is greater than $z \sim 1$ estimated previously for the event-chain algorithm [1], while it keeps still a smaller value than $z \sim 2$ which is expected for the short-range algorithm such as the Metropolis one. Consequently, the event-chain algorithm can be used in the NER analysis with an efficient relaxation performance, and would be applicable to various slowly relaxing problems such as frustrated and/or random systems.

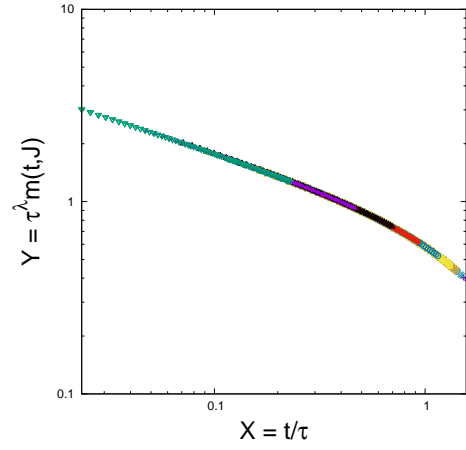


Figure 3: Scaling plot for the data in $2.204 \leq T \leq 2.222$ in Fig. 2

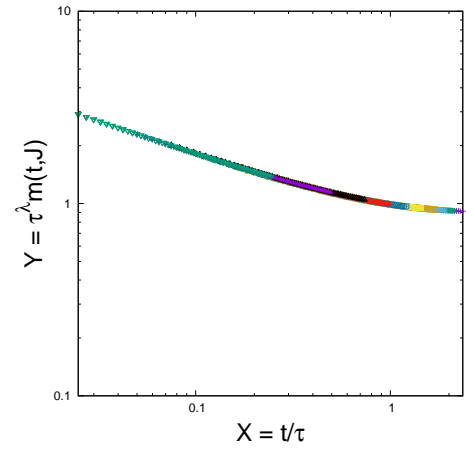


Figure 4: Scaling plot for the data $2.182 \leq T \leq 2.200$ in Fig. 2

References

- [1] Y. Nishikawa *et. al.*, *Phys. Rev.* **E92** 063306 (2015)
- [2] M. Michel *et. al.*, *Europhys. Lett.* **112** 20003 (2015)
- [3] Y. Ozeki and N. Ito, *J. Phys.: Math. Theor.* **40** R149 (2007).
- [4] Y. Echinaka and Y. Ozeki, *Phys. Rev.* **E94** 043312 (2016).
- [5] A. P. Aloysius and M. Harsenbusch, *Physica* **A201** 593 (1993)

Entanglement, Quantum Phase Transition, and Quantum Dynamics in Quantum Many-body Systems

Syngé Todo

Department of Physics, University of Tokyo, Tokyo 113-0033, Japan
Institute for Solid State Physics, University of Tokyo, Kashiwa, 277-8581, Japan

We have developed various novel numerical methods for quantum/classical many-body systems with strong correlations. An efficient quantum Monte Carlo method has been developed to calculate the entanglement entropy of quantum spin systems. The entanglement entropy is an essential index that characterizes quantum correlations and the topological order in quantum many-body systems. Our method works directly at absolutely zero temperature, and thus it is entirely free from systematic errors coming from extrapolation to the zero-temperature limit, unlike the previous methods.

We also have developed a nonlocal-update quantum Monte Carlo method for quantum dimer models on general lattices. By implementing the technique recently suggested for quantum Monte Carlo simulation on quantum dimer model with the help of priority queue, which can help find the next operator for updating efficiently, we can simulate on the finite temperature region of the quantum dimer model. By the finite-size scaling, the phase boundary between low-temperature columnar phase with the maximum number of parallel neighboring dimers, and disordered phase at high temperatures can be decided in a broad region of dimer-dimer interaction potential, and the value of which is both consistent of the classical limit, where a KT phase transition is known, and also tends to a constant slope near the RK-point.

In the meantime, the real-space renormalization group methods based on the tensor networks have been widely used in recent years.

The tensor renormalization group method can efficiently calculate physical quantities of large-scale classical/quantum systems. However, the existing methods, such as the tensor renormalization group (TRG) and the higher-order tensor renormalization group (HOTRG), suffer from the huge computational cost in higher dimensions. To solve this problem, we have developed the anisotropic tensor renormalization group (ATRG) that can dramatically reduce the computational complexity in high-dimensional systems such as three-dimensional quantum systems. In addition, we further improve the accuracy of ATRG by combining with techniques such as the tensor renormalization group method that incorporates bond weights, etc.

Spins coupled with photon degrees of freedom in the cavity exhibit a non-equilibrium phase transition with bistability in the number of photons. We have performed simulation based on the quantum master equations. From the eigenvalues and eigenstates of the time evolution operator, we discussed the correspondence to the first-order phase transition in the equilibrium system. We have calculated the hysteresis loop under the periodic modulation of laser intensity, from the viewpoint of the Floquet operator, and clarified that a dynamical phase transition phenomenon appears with respect to the period of laser intensity.

Superconducting dome in electron doped FeSe intercalates

Harald JESCHKE

*Research Institute for Interdisciplinary Science, Okayama University
3-1-1 Tsushima-naka, Kita-ku, Okayama 700-8530*

The van-der-Waals gap of iron chalcogenide superconductors can be intercalated with a variety of inorganic and organic compounds that modify the electron doping level of the iron layers. In $\text{Li}_x(\text{C}_3\text{N}_2\text{H}_{10})_{0.37}\text{FeSe}$, a dome in the superconducting transition temperature T_c has been reported to occur in the doping range of $x = 0.06$ to $x = 0.68$ [1]. We used massive parallel computer simulations to address magnetic and superconducting properties of $\text{Li}_x(\text{C}_3\text{N}_2\text{H}_{10})_{0.37}\text{FeSe}$ [2]. With a combination of density functional theory and spin fluctuation theory, we capture the evolution of superconducting transition temperatures theoretically. We clearly demonstrate how the changing electronic structure supports an increasing superconducting T_c (Figure 1). The suppression of T_c at high doping levels can, however, only be understood by analyzing the magnetic tendencies. We determine the Heisenberg exchange couplings between the iron moments; superconductivity is realized out of these underlying interactions. We can show that with doping, they evolve from stripe-type at low doping to bicollinear at high doping. With increasing carrier density, magnetic interactions mutate from FeSe-like to FeTe-like, explaining a T_c suppression at high doping.

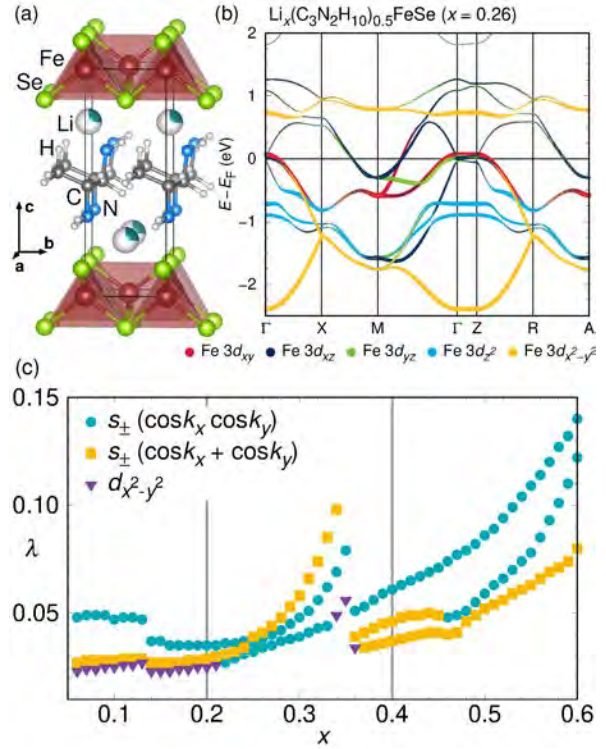


Figure 1: Structure, band structure and leading eigenvalues of the gap equation for $\text{Li}_x(\text{C}_3\text{N}_2\text{H}_{10})_{0.37}\text{FeSe}$.

- [2] M. Shimizu, N. Takemori, D. Guterding and H. O. Jeschke, Importance of Fermi surface and magnetic interactions for the superconducting dome in electron doped FeSe intercalates, under review (2020).

References

- [1] R. J. Sun *et al.*, Phys. Rev. B **98**, 214508 (2018).

Properties of electron doped iron based superconductor LaFe_2As_2

Harald JESCHKE

*Research Institute for Interdisciplinary Science, Okayama University
3-1-1 Tsushima-naka, Kita-ku, Okayama 700-8530*

For more than a decade after the discovery of Fe-based superconducting pnictides it seemed that superconductivity existed in a relatively narrow range of dopings away from the nominal Fe^{2+} valency. One of the few examples of strongly overdoped (up to $\text{Fe}^{2.5+}$ valency) pnictides was provided by the 1111 material LaFeOAs , with up to 50% of O^{2-} replaced by H^- . Recently, another compound with formally $\text{Fe}^{2.5+}$ has been synthesized [1], LaFe_2As_2 . It was found experimentally that the material can exist in two distinctly different crystallographic phases, “collapsed-tetragonal” (CT) and “uncollapsed-tetragonal” (UT). We used massive parallel computer simulations to address structural, magnetic, and electronic properties of LaFe_2As_2 [2]. We show that the UT phase, as opposed to the CT one, bears a strong short-range magnetism of the stripe type driven by the next-nearest-neighbor exchange. The structural changes are triggered by magnetic collapse, as in CaFe_2As_2 . Even though the orbitals relevant for the low-energy physics are not the usual d_{xz} and d_{yz} , the electron pockets do not exclude the usual spin-fluctuation driven mechanism with an overall s symmetry (Figure 1). Importantly, La in this compound assumes a non-integer valence closer to $2.7+$ than to $3+$, corresponding to doping of $\sim 0.35e$, rather than $0.5e$. It is thus overdoped, but not dramatically.

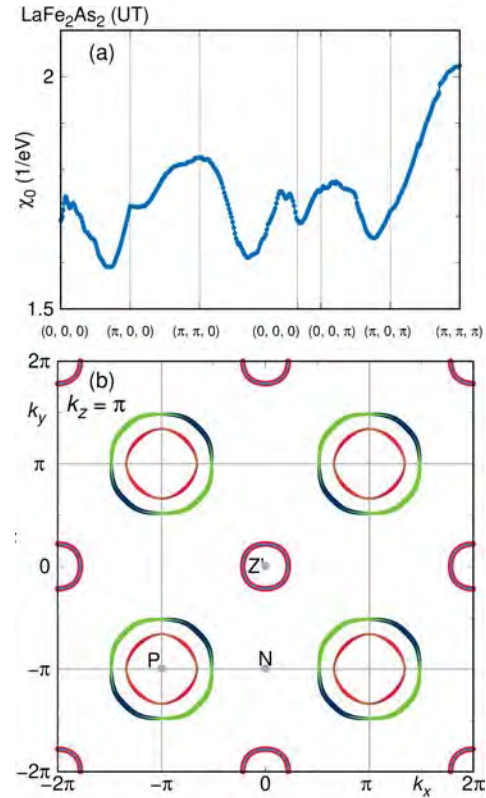


Figure 1: Susceptibility and Fermi surface of LaFe_2As_2 .

References

- [1] A. Iyo *et al.*, J. Phys. Chem. Lett. **10**, 1018 (2019).
- [2] I. I. Mazin, M. Shimizu, N. Takemori, and H. O. Jeschke, Novel Fe-Based Superconductor LaFe_2As_2 in Comparison with Traditional Pnictides, Phys. Rev. Lett. **123**, 267001 (2019).

Novel phases and dynamics in frustrated spin systems

Tsuyoshi OKUBO

*Department of Physics, The University of Tokyo
7-3-1 Hongo, Bunkyo-ku, Tokyo 113-0033*

Frustrated interactions in spin systems often induce novel phenomena, *e.g.*, non-magnetic ground states including spin liquid and topological orders. Conventionally, geometrically frustrated spin systems, such as the kagomé lattice and the pyrochlore lattice Heisenberg antiferromagnets have been investigated actively. Recently, a different kind of frustrated interaction introduced by the strong spin-orbit coupling has attracted much interest. For example, in Na_2IrO_3 and $\alpha\text{-RuCl}_3$, the dominant magnetic interaction induced by the strong spin-orbit coupling is considered to be the Kitaev interaction: it is an Ising like anisotropic interaction with different spin component depending on the bonds. When we consider the $S = 1/2$ quantum spin model on the honeycomb lattice with only the Kitaev interaction (Kitaev model), its ground state is a spin liquid state without any spontaneous symmetry breakings [1]. This fact indicate real compounds might have a spin liquid ground states. However, real compounds contain other interactions such as the Heisenberg interaction, further neighbor interactions, or the off-diagonal interactions, and they can induce magnetic long range orders at low temperature.

In this year, in order to clarify effects of additional interactions in the Kitaev materials, we numerically investigated the ground state and finite temperature properties of the models with the Kitaev interaction and the Γ interactions (the Kitaev- Γ model) by means of tensor network methods. The Γ term is an off-diagonal interaction and the Hamiltonian

of the model is given by

$$\mathcal{H} = \sum_{\gamma \in x, y, z} \mathcal{H}_\gamma, \quad (1)$$

where for $\gamma = z$,

$$\mathcal{H}_z = \sum_{\langle i, j \rangle_z} [K S_i^z S_j^z + \Gamma (S_i^x S_j^y + S_i^y S_j^x)]. \quad (2)$$

For $\gamma = x, y$, we consider similar interaction with cyclic rotation of x, y, z components. We consider the honeycomb lattice and $\gamma = x, y, z$ corresponds to three directions of the bonds. This model is considered to be an effective model for $\alpha\text{-RuCl}_3$ [2, 3].

Firstly, we investigated the phase diagram of the Kitaev- Γ model by using a two-dimensional infinite tensor network approach. We represented the ground state wave function as products of small tensors, and optimize each tensor element so that the energy expectation value becomes smaller. By assuming several transnational symmetries of the ground state, we can represent infinitely large system by using finite numbers of tensors. As a network of tensors, we used the infinite tensor product states (iTPS), which is also called as the infinite projected entangled-pair states (iPEPS). As the optimization algorithm, previously, we have used the imaginary time evolution. However, it have become clear that the imaginary time evolution often trapped at local minima and it was very hard to obtain novel spin liquid state from random initial states. Thus, this year, we used a different type of optimization, so called variational optimization [4]. We confirmed that by using the variational optimization

tion, we correctly obtained the Kitaev spin liquid state at the pure Kitaev model ($\Gamma = 0$) even from the random initial states. Then we applied the variational optimization to finite Γ and draw the phase diagram. Although the obtained variational energies were largely improved from those obtained by the imaginary time evolution, the phase diagram was almost unchanged; except for the vicinity of the pure Kitaev model, the ground states were magnetically ordered states. This observation was contrasted with the phase diagrams obtained by the exact diagonalization (ED) [2] or by the infinite density matrix renormalization group (iDMRG) [3]; they concluded much wider spin liquid phases. In order to clarify nature of the phase diagram further, we might need larger scale calculation with iTPS.

Secondly, we investigated finite temperature properties of the model. In order to calculate physical quantities at a finite temperature, we represented the density matrix of the system in tensor network representations. We employed two types of the tensor network representations: the local purification, *e.g.*, Ref. [5], and the direct tensor product operator (TPO) [6]. By applying them to the pure Kitaev model, we found that the former representation failed to reproduce the expected lower temperature specific heat peak [7], while the latter TPO representation reproduced it, at least qualitatively. This observation indicated that the direct TPO representation was more efficient than the local purification. The applications of the developed technique to the model with finite Γ is on going.

References

- [1] A. Kitaev: *Ann. Phys.* **321** (2006) 2.
- [2] A. Catuneanu, Y. Yamaji, G. Wachtel, H.-Y. Kee, and Y. B. Kim: *npj Quantum Materials* **3** (2018) 23.
- [3] M. Gohlke, G. Wachtel, Y. Yamaji, F. Pollmann, and Y. B. Kim: *Phys. Rev. B* **97** (2018) 075126.
- [4] P. Corboz: *Phys. Rev. B* **94** (2016) 035133.
- [5] P. Czarnik, J. Dziamaga, and P. Corboz: *Phys. Rev. B* **99** (2019) 035115.
- [6] A. Kshetrimayum, M. Rizzi, J. Eisert, and R. Orús: *Phys. Rev. Lett.* **122** (2019) 070502.
- [7] J. Nasu, M. Udagawa, and Y. Motome: *Phys. Rev. B* **92** (2015) 115122.

Thermal effects on quantum frustrated magnetisms

Tokuro Shimokawa

*Okinawa Institute of Science and Technology Graduate University,
Tancha, Onna-son, Kunigami-gun, Okinawa 904-0495*

We know well that quantum frustrated magnetisms often exhibit rich many-body physics, but we also know difficulties to investigate the effects of the thermal fluctuations numerically, hence thermally induced novel phases still remain unexplored.

We use a state of art numerical method, quantum typicality method [1-2] for investigating the finite-temperature properties of $S=1/2$ bilayer-breathing-kagome (BBK) Heisenberg model for $\text{Ca}_{10}\text{Cr}_7\text{O}_{28}$ and $S=1/2$ Shastry-Surtherland (SS) Heisenberg model for $\text{SrCu}_2(\text{BO}_3)_2$. The former magnet joined recently the family of quantum spin liquid candidates [3] in spite of the complexity of its Hamiltonian. The latter magnet has been known well, but recent experiments under high pressures [4] could reveal successfully the existence of the intermediate plaquette state, so the theoretical studies at finite temperatures are required.

The BBK model: We computed the several physical quantities such as specific heat, magnetization curve, and equal-time spin structure factor at finite-temperature with the quantum typicality method and found the possible existence of a spiral spin liquid state at

moderate temperatures exhibiting a characteristic ring-like structure in the equal-time spin structure factor. These obtained results are reasonable for explaining qualitatively the nature of the $\text{Ca}_{10}\text{Cr}_7\text{O}_{28}$. [5]

The SS model: Owing to the Ising degrees of freedom in the intermediate plaquette ground state, we found the signature of the finite-temperature phase transition associated with the breaking of the mirror symmetry at moderate temperatures via specific heat and correlation functions calculations. We also investigate the relationship the transition and the existence of the degenerated excited states by the exact diagonalization method. [6]

References

- [1] A. Hams and H. De Raedt, Phys. Rev. E **62**, 4365 (2000).
- [2] S. Sugiura and A. Shimizu, Phys. Rev. Lett. **111**, 010401 (2013).
- [3] C. Balz, et al, Nat. Phys. **12**, 942 (2016).
- [4] M. E. Zayed et al, Nat. Phys. **13**, 962 (2017).
- [5] T. Shimokawa, R. Pohle, N. Shannon, in preparation.
- [6] T. Shimokawa, in preparation.

Numerical studies on magnetization process of the Kitaev spin liquid

Kota IDO

*Institute for Solid State Physics, University of Tokyo
Kashiwa-no-ha, Kashiwa, Chiba 277-8581*

The Kitaev model is one of the prominent examples of quantum many-body systems where quantum spin liquids emerge[1]. In the Kitaev model, the nearest-neighbor spins interact with each other via bond-dependent Ising-type interactions. Although the Kitaev model seems to be an artificial model, it has been proposed that the Kitaev model can be realized in real materials[2]. Inspired by the proposal, it is now one of the hot topics in the condensed matter physics how to synthesize and characterize the Kitaev-like materials.

The Kitaev model under a magnetic field has been intensively studied, because the magnetization processes offer useful information for characterizing the nature of the quantum spin liquid in the Kitaev model. Recently, it was reported that an intermediate gapless state appears in the antiferromagnetic coupling Kitaev honeycomb model under a magnetic field. For example, exact diagonalization (ED) calculations showed that the magnetization curve has two abruptly changes by increasing the field[3, 4]. This feature was observed by other numerical methods such as the density matrix renormalization group (DMRG)[5] and Majorana mean-field (MF) theory[6]. However, ED and DMRG studies were done in small system size and quasi-one-dimensional system on cylindrical boundary condition, respectively. It is desired to perform accurate analysis based on a numerical calculation method applicable to the large two-dimensional system.

In this study[7], by using the variational

Monte Carlo (VMC) method, we investigate whether the intermediate state exists as the ground state of the Kitaev model in two dimensions in a [001] magnetic field. We used a generalized Bardeen-Cooper-Schrieffer trial wavefunction with Jastrow factor, which can exactly represent the ground state of the pure Kitaev model fermionized by the Jordan-Wigner transformation[8, 9]. Our benchmark for a small system show that this trial wavefunction well reproduces the exact magnetization process. In applications to the antiferromagnetic Kitaev model with large system sizes, a double-peaked structure is found in the magnetic susceptibility, which signals the existence of the intermediate phase. In the intermediate strength of the magnetic field, we find that the local Z_2 gauge field takes non-integer values, which is consistent with the spin liquid phase with fluctuating flux for [111] case. Our results also show that the momentum distribution of the complex fermions changes topologically at the first transition point, suggesting that this is a topological phase transition resembling the Lifshitz transition. We cannot find these properties in the ferromagnetic Kitaev model. Our results show that in the antiferromagnetic Kitaev model, the intermediate state is stable against many-body correlations beyond the MF approximation.

Our VMC results also suggest that it is a useful and accurate way to analyze the Kitaev model in a magnetic field by using fermionization of the localized spin different from the

spinon representation. Using other types of the fermionizations, it would be possible to accurately analyze the magnetization process of the Kitaev model with additional interactions such as the Heisenberg term and the Γ term within the framework of VMC. Our study offers a firm basis for such extended treatments.

In addition, we have proposed how to calculate the charge (density) dynamical structure factors for the ground states of correlated electron systems based on the VMC method[10]. It is a future issue to study complex fermion dynamics of quantum spin liquids by using our proposed method.

References

- [1] A. Kitaev: *Ann. Phys.* **321** (2006) 2.
- [2] G. Jackeli and G. Khaliullin: *Phys. Rev. Lett.* **102** (2009) 017205.
- [3] Z. Zhu, I. Kimchi, D. N. Sheng, and L. Fu: *Phys. Rev. B* **97** (2018) 241110(R).
- [4] C. Hickey and S. Trebst: *Nat. Commun.* **10** (2019) 530.
- [5] M. Gohlke, R. Moessner, and F. Pollmann: *Phys. Rev. B* **98** (2018) 014418.
- [6] J. Nasu, Y. Kato, Y. Kamiya, and Y. Motome: *Phys. Rev. B* **98** (2018) 060416(R).
- [7] K. Ido, and T. Misawa: *Phys. Rev. B* **101** (2020) 045121.
- [8] H.-D. Chen and Z. Nussinov: *J. Phys. A* **41** (2008) 075001.
- [9] X.-Y. Feng, G.-M. Zhang, and T. Xiang: *Phys. Rev. Lett.* **98** (2007) 087204.
- [10] K. Ido, M. Imada, and T. Misawa: *Phys. Rev. B* **101** (2020) 075124.

A new block-spin transformation in Potts models

Yusuke TOMITA

*College of Engineering, Shibaura Institute of Technology
Saitama, Saitama 337-8570*

In usual block-spin transformation, the majority rule is mainly used as a renormalization scheme. Many studies using the block-spin transformation have shown that spin configurations are well renormalized well by the majority rule. But the legitimacy of the majority rule has not been understood. In this study, I propose a block-spin transformation rule, which utilizes the fractality of the Kasteleyn-Fortuin cluster on the critical point. The new block-spin transformation is constructed to conform Kasteleyn-Fortuin clusters to the usual finite-size scaling form, $L^{-\beta/\nu}$.

Magnetic susceptibilities for 2D Potts models through the new block-spin transformation are shown in Fig. 1. The original system size is 8192. Slopes of lines in Fig. 1 are drawn by using exact critical exponents, γ/ν 's. The result indicates the new transformation rule works well for each q -state Potts model. While the newly proposed transformation utilizes the fractal property of Kasteleyn-Fortuin cluster on critical points, I also examined the renormalization properties at off-critical points. Figure 2 shows numbers of clusters for the 2D Ising model for $T = 0.95 \times T_c, T_c$, and $1.05 \times T_c$. At the critical point, the number of clusters is well fitted by a power function with exponent $4/(2 - \beta/\nu)$. On the other hand, the numbers of clusters at off-critical points suddenly drop at some block-spin transformation steps. A renormalized cluster expands almost whole the system at a some finite renormalized step when the temperature is lower than the critical temperature, while all of the clusters disappear at a some finite renormalized step

when the temperature is higher than the critical temperature. Therefore, we can estimate critical points by the linearity of the number of clusters.

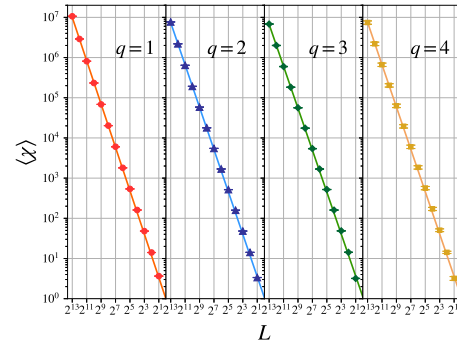


Figure 1: Plot of the susceptibilities for the 2D Potts models. Slopes of lines are drawn by using exact critical exponents, γ/ν

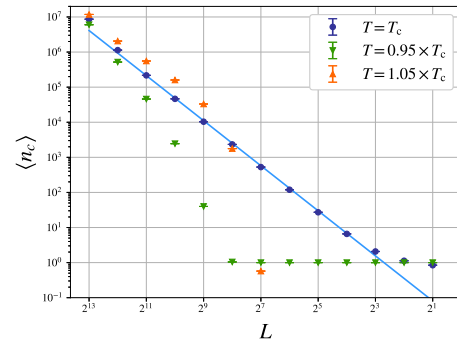


Figure 2: Plot of the numbers of clusters for the 2D Ising ($q = 2$) models. A slope of line is drawn by using exact critical exponents, $4/(2 - \beta/\nu)$

Screening for Thermal Functional Materials using Materials Informatics

Junichiro SHIOMI

7-3-1, Hongo, Bunkyo-kun, The University of Tokyo, Tokyo 113-8656

Controlling the thermal boundary conductance (TBC) between copper and carbon crystals is important since it can bottleneck the thermal conductivity when reinforcing copper with carbon-crystals fillers, namely diamond or graphite, to develop heat sinks and spreaders needed for the thermal management. In the work of this year [1], we demonstrate the spectral control of TBC between copper and carbon crystal by self-assembled monolayers (SAMs) using the non-equilibrium molecular dynamics simulation.

The resultant values of TBC for copper/diamond and copper/graphite interfaces are 9.06 ± 0.16 MW/m²K and 81.76 ± 14.85 MW/m²K, respectively. The result indicates the TBC at copper/graphite interfaces is almost an order of magnitude greater than that at copper/diamond interface. In order to interpret the behavior, the vibrational density of states (VDOS) of copper/diamond and copper/graphite interfaces are calculated, as shown in Fig. 1. The result indicates the out-of-plane VDOS of graphite surface provides the overlap in phonon vibrational modes with that of copper surface. In view of elastic energy transport, which is usually the main contribution to interfacial heat

conduction, the overlap results in the higher value in TBC compared with the copper/diamond interface.

To improve the TBC at the copper/diamond interface, the covalently bonded SAMs with different chain lengths are installed at the interface. The resultant values of TBC with SAMs of various chain lengths are plotted in Fig. 2. The data at $n=0$ refers to the TBC at copper/diamond and copper/graphite interfaces without SAMs. For the chain length studied in this work, the value of TBC increases monotonically with the chain length for chain length shorter than C15 and reaches a plateau afterward. The highest value of TBC approaches to that of bare copper/graphite interface.

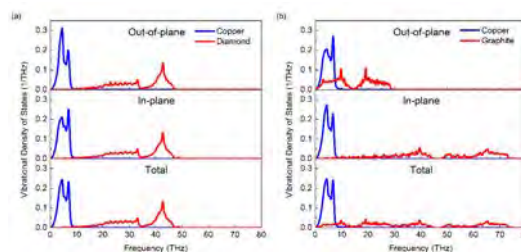


Fig. 1: Vibrational density of states of various components of (a) copper/diamond and (b) copper/graphite interfaces.

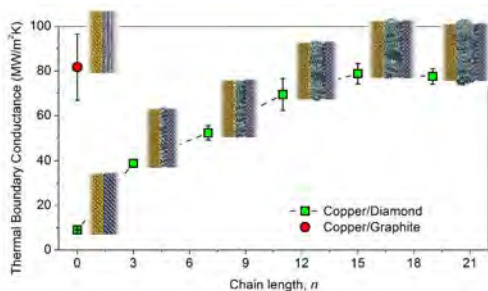


Fig. 2: Thermal boundary conductance as a function of chain length of SAMs. $n=0$ refer to the interfaces without SAMs.

Both the spectral and structural analysis are implemented to further understand the underlying mechanism. The analysis identifies that this is because the SAMs becomes softer with increasing chain length due to disordering of the collective SAMs structure, enhancing the spectral overlap with copper at low frequency vibrational modes. In the future, the materials informatics techniques can be conducted to find out the optimum design of SAMs to enhance the interfacial heat transfer. The obtained results are

useful to improve the thermal conductivity of metal/carbon-crystal composite materials in the industry applications.

In summary, we have demonstrated (1) the poor TBC at copper/diamond interface is mainly due to the mismatch of VDOS between copper and diamond (2) the installation of SAMs at copper/diamond interface can improve the TBC significantly. The TBC shows a strong dependence on chain length that the TBC increases with the increasing chain length for chain length shorter than C15 and reaches a plateau afterward. The materials informatics technique will be helpful for the design of SAMs to enhance the thermal conductivity of metal/carbon-crystal composite materials.

References

- [1] S.-W. Hung, S. Hu, and J. Shiomi, *ACS Appl. Electron. Mater.* **1** (2019) 2594.

Wave function analyses in disordered electron systems

TOMI OHTSUKI¹
 TOHRU KAWARABAYASHI²
 KEITH SLEVIN³
 KOJI KOBAYASHI⁴
 TOMOHIRO MANO¹

- 1) Dept. Phys., Sophia University, Chiyoda-ku, Tokyo 102-8554, Japan
 2) Dept. Phys., Toho University, Miyama 2-2-1, Funabashi 274-8510, Japan
 3) Dept. Phys., Osaka University, Toyonaka, Osaka 560-0043, Japan
 4) IMR, Tohoku University, Sendai 980-8577, Japan

Recent discoveries of Weyl semimetal (WSM) have inspired extensive research of these novel topological materials, especially from the point of the new universality classes, which has discrete symmetries such as particle-hole symmetry. Here we have studied the Anderson transition in chiral orthogonal class as well as class BDI, the latter showing the nodal line Weyl semimetal phase[1]. We have also studied the various quantum phase transitions by analyzing the wave functions via convolutional neural network (CNN) [2]. The typical wave functions in disordered quantum systems are shown in Fig. 1. The method is especially powerful when analyzing the quantum percolation, where the transfer matrix method breaks down due to the irregular lattice structure. We have trained CNN to capture the features of wave functions in topological as well as nontopological phases, and let CNN draw the phase diagram (Fig.2) [3]. In addition, we have calculated the distribution of Kondo temperature at the Anderson transition from the local density of states obtained by kernel polynomial method[4].

References

1. X. Luo, B. Xu, T. Ohtsuki, R. Shindou: Physical Review B **101**, 020202(R), (2020).
2. T. Ohtsuki, T. Mano: Journal of the Physical Society of Japan **89**, 022001 (2020).
3. T. Mano, T. Ohtsuki: Journal of the Physical Society of Japan **88**, 123704 (2019).

4. K. Slevin, S. Kettemann, T. Ohtsuki: The European Physical Journal B **92**, 281 (2019).

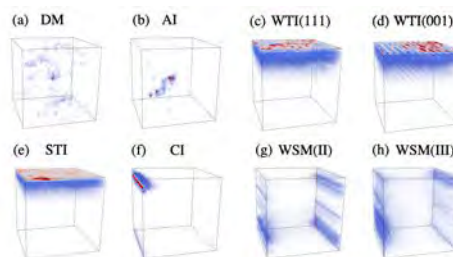


Figure 1: Typical 3D wave functions in real space in various phases. Taken from [2].

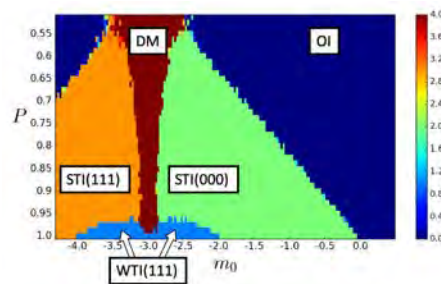


Figure 2: Phase diagram of quantum percolation in 3D topological insulator. OI (ordinary insulator), WTI (weak topological insulator), STI (strong topological insulator), and DM (diffusive metal). (ijk) indicates the weak indices.

Numerical study on low-energy states of quantum spin systems

Hiroki NAKANO

*Graduate School of Material Science, University of Hyogo
3-2-1 Kouto, Kamigori-cho, Ako-gun, Hyogo 678-1297, Japan*

It is difficult to precisely estimate physical quantities for many-body problems. Particularly, we often have to tackle such many-body problems in condensed matter physics. Quantum spin systems are typical many-body problems. Under circumstances, numerical approaches have widely and effectively been employed to examine the systems. Many computational investigations have been carried out and provided us with useful information and deeper understanding of the target systems.

It is well known that within the field of quantum spin systems, three methods are effectively used; the numerical diagonalizations, the quantum Monte Carlo (QMC) simulations, and the density matrix renormalization group (DMRG) calculations. Each of them has advantages and disadvantages at the same time. In the QMC simulations, large systems can be treated irrespective of their spatial dimensions although it is difficult to obtain precise evaluations due to the negative sign problem when the systems include frustrations. On the other hand, the DMRG method is very useful when spatial dimension of a target system is one irrespective of whether frustrations is present or absent in the system. However, this method is still under development for the cases when the spatial dimension is larger than one. The numerical diagonalization method can be applied irrespective of the spatial dimension and the presence of frustrations. Unfortunately, this method has a serious weak point that it can treat only very small system sizes. As one way to overcome this disadvantage, we successfully developed a hybrid-type parallelized code of Lanczos diagonalization[1]. If we use this Lanczos-diagonalization code, it

is possible to treat various large systems that have not been previously treated yet within this method. Therefore, we investigate various quantum spin systems by this method as a primary approach.

In the project in 2019, we tackled two systems. The first one is the $S = 1/2$ Heisenberg antiferromagnet on the kagome lattice with a specific distortion[2, 3]. We investigated a family of materials with Ti^{3+} $S = 1/2$ ions forming distorted kagome lattices. Employing all electron density functional theory technique, the Heisenberg Hamiltonian was established for each material; finite-size clusters for the Hamiltonians were numerically diagonalized. Our calculations successfully provided us with the magnetization processes, which enable us to analyze experimental measurements. The comparisons were quite good; our theoretical calculations succeeded in predicting the behavior in fields higher than the maximum field which the present experiments can reach presently.

The second one is the large- S Heisenberg antiferromagnet in one dimension[4]. Particularly, we focused our attention on the cases of $S = 5$ and $S = 6$. The case of $S = 5$ had been studied before in Ref. [1] where systems up to 10 sites were treated. We successfully carried out our huge-scale parallel calculation in the K computer using approximately 97% of the total computational nodes without any troubles and obtained novel results up to 14 sites of the target system. Note also that the Hilbert space dimension of 14-site cluster for the $S = 5$ chain is larger than the case of 20-site cluster for the $S = 2$ chain[5]. From the new results, our analysis gave a more precise estimation of

the $S = 5$ Haldane gap. In this study, we also attempted to estimate the Haldane gap for the case of $S = 6$, which had not been examined before. From our new estimates of the Haldane gaps for large S , the asymptotic formula of the Haldane gap was examined; we successfully determined the coefficient in the formula more precisely.

Our studies contribute to our deeper understandings of the various antiferromagnets and the nontrivial effect of quantum nature and frustration in magnetic materials.

References

- [1] H. Nakano and A. Terai: J. Phys. Soc. Jpn. **78** (2009) 014003.
- [2] H. O. Jeschke, H. Nakano, and T. Sakai: Phys. Rev. B **99** (2019) 140410(R)(1-6)
- [3] R. Shirakami, H. Ueda, H. O. Jeschke, H. Nakano, S. Kobayashi, A. Matsuo, T. Sakai, N. Katayama, H. Sawa, K. Kindo, C. Michioka, and K. Yoshimura: Phys. Rev. B **100** (2019) 174401(1-7)
- [4] H. Nakano, N. Todoroki, and T. Sakai: J. Phys. Soc. Jpn. **88** (2019) 114702(1-4)
- [5] H. Nakano and T. Sakai: J. Phys. Soc. Jpn. **87** (2018) 105002(1-2)

Efficient Sampling Simulation of the Soft Modes Significantly Contribute to Protein Properties

Kazuhiro TAKEMURA, Duy TRAN, Hiroaki HATA, Kenichiro TAKABA,
Mohamed Marzouk SOBEH, and Akio KITAO

School of Life Science and Technology, Tokyo Institute of Technology

Ookayama, Meguro, Tokyo 152-8550

We have developed a method to evaluate binding free energy differences of complex models generated by docking prediction using the all-atom molecular dynamics simulation and solution theory in the energy representation (ER), termed evERdock (evaluation with ER method of docking generated decoys)[1]. By evaluating binding free energy difference with the method, we previously showed that “near-native” models similar to crystal structure are successfully selected as the lowest energy structures in several complex systems. The method requires relatively short MD simulations (2 ns) and can calculate binding free energy difference among several hundreds of complex models. We also reported that refinements of docking generated decoys by relatively long MD simulation and averaging the binding free energies obtained from multiple snapshots further improved the evaluation of evERdock[2]. However, such treatments required additional computational costs. To address this problem, we propose a method

for efficiently selecting near-native decoys using Best Arm Identification (BAI), called evERDock BAI[3].

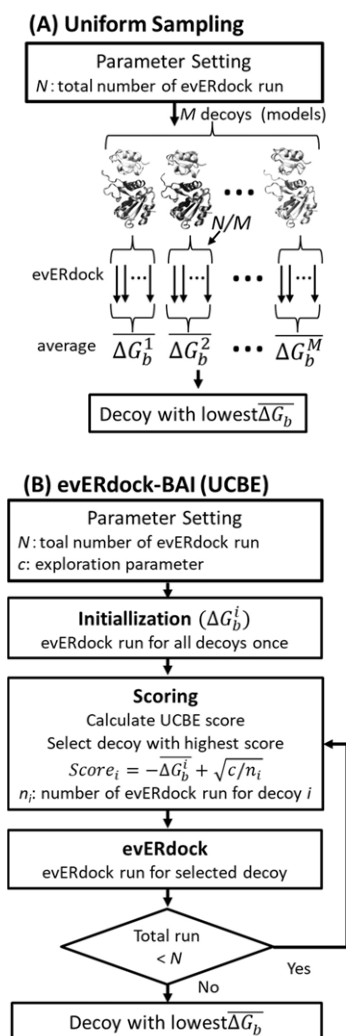


Fig. 1 Flows of (A) uniform sampling and (B) BAI (UCBE) based evaluation.

Let the number of evERdock runs decoys are N be M , respectively. If we conduct evERdock runs for all decoys equally (uniform sampling, US), all decoys are evaluated M/N times (Fig.1A). Fig. 1B shows the flow chart of evERdock-BAI using UCBE as a BAI algorithm. After all decoys are evaluated once, the algorithm repeatedly calculates UCBE scores, selects the decoy with the highest score, and conducts evERdock run for the selected decoy. Promising decoys for exploitation are evaluated by the first term of the score (binding free energy, $-\overline{\Delta G_b^i}$). The second term of the score contains the number of evERdock runs for the decoy i (n_i) in its denominator. Thus, the score decreases as the number of evERdock runs for a decoy i increases. As a result, unpromising decoys are sometimes selected, and exploration is realized. Such a balance between exploitation and exploration is essential to achieve an efficient and accurate prediction of the correct decoy.

We applied evERdock-BAI to three protein-protein complex systems (Fig. 2). Decoys are generated by rigid-body dockings. The number of decoys (N_{decoys}), the number of near-native decoys ($N_{\text{near-native}}$), and the number of total evERdock runs to achieve a prediction accuracy 95 % ($N_{95\%}$) using US and UCBE are shown in Table 1. For all three cases, $N_{95\%}$ using UCBE were smaller than those using US. The UCBE algorithm

successfully reduced computational cost by a factor of 2.20, 1.22, and 4.05 (values in parentheses in Table 1) for 1AY7, 1PPE, and 3SIC, respectively.

As shown above, we successfully improved the computational efficiency of the evERdock evaluation of protein-protein complex models by combining with BAI algorithm.

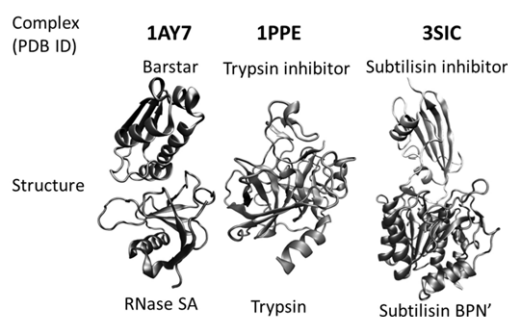


Fig. 2 Structures of target complexes

Table 1 Summary of results

Complex	1AY7	1PPE	3SIC
N_{decoys}	11	11	21
$N_{\text{near-native}}$	2	4	1
$N_{95\%}$ (US)	33	33	336
$N_{95\%}$ (UCBE)	15 (2.20)	27 (1.22)	83 (4.05)

References

- [1] K. Takemura, N. Matubayasi, and A. Kitao, J. Chem. Phys. 148, 105101 (2018).
- [2] A. Shinobu, K. Takemura, N. Matubayasi, and A. Kitao, J. Chem. Phys. 149, 195101 (2018).
- [3] K. Terayama, A. Shinobu, K. Tsuda, K. Takemura, and A. Kitao. J. Chem. Phys. 151, 215104 (2019).

Pseudo-fermion functional renormalization group approach for frustrated quantum spin systems

Kiyu FUKUI, Yukitoshi MOTOME, and Yusuke KATO

Department of Physics, The University of Tokyo, Bunkyo, Tokyo 113-0033

Department of Applied Physics, The University of Tokyo, Bunkyo, Tokyo 113-8656

Department of Basic Science, The University of Tokyo, Meguro, Tokyo 153-8902

Frustrated quantum spin systems have been studied intensively for very long time [1, 2]. It is impossible to solve them exactly mathematically in general. Therefore, numerical approaches to investigate frustrated quantum spin systems are indispensable. Numerical approaches used widely to study them are, for example, exact diagonalization (ED), quantum Monte Carlo (QMC), density matrix renormalization group (DMRG). Each method has pros and cons, of course. Since 2010s, a new method called pseudo-fermion functional renormalization group (PFFRG or pf-FRG) has been used gradually [3]. Although PFFRG overestimates ordering tendencies to magnetic orders [4], it can treat large-size systems and strongly-frustrated systems and detect quantum paramagnetism due to strong frustration.

In order to study quantum paramagnetism, particularly quantum spin liquid, we made up a PFFRG numerical code and tested it by reproducing previous studies. At first, we made PFFRG codes for SU(2) symmetrical systems (i.e. systems with Heisenberg-type interactions) [3] and benchmarked it. Then we extended our codes to systems with XXZ-type [4] and Kitaev-type [5] interactions.

Computational complexity of PFFRG calculation is scaled by $\mathcal{O}(N_L^2 \cdot N_\omega^4 \cdot N_\Lambda \cdot N_\sigma)$. N_L , N_ω , N_Λ , and N_σ are symmetry-reduced system size, the number of frequency mesh points, the number of energy cut-off grid points, and relative complexity due to symmetry of Hamilto-

nian (1 = Heisenberg Hamiltonian with time-reversal symmetry), respectively. Typically, $N_L = 10-20$, $N_\omega = 50-100$, and $N_\Lambda = 200-500$. Therefore, it is necessary to exploit parallelization. We submitted jobs parallelized by openMP+MPI to F144cpu queue using 64-144 nodes and $\mathcal{O}(1000)$ MPI processes. One PFFRG calculation with spin susceptibility calculation with vertices obtained by PFFRG takes one to several days. In addition, we tried to use GPU nodes by openACC directives in order to accelerate our PFFRG calculation.

References

- [1] C. Lacroix, P. Mendels, and F. Mila, *Introduction to Frustrated Magnetism* (Springer, New York, 2011).
- [2] H. T. Diep, *Frustrated Spin Systems* (World Scientific, Singapore, 2013) 2nd ed.
- [3] J. Reuther and P. Wölfle, Phys. Rev. B **81**, 144410 (2010).
- [4] S. Göttel, S. Andergassen, C. Honerkamp, D. Schuricht, and S. Wessel, Phys. Rev. B **85**, 214406 (2012).
- [5] J. Reuther, R. Thomale, and S. Trebst, Phys. Rev. B **84**, 100406(R) (2011).

Precise measurement of crystal nucleation rate in a hard-sphere colloidal system

Michio Tateno and Hajime Tanaka

*Department of Fundamental Engineering, Institute of Industrial Science, University of Tokyo
4-6-1 Komaba, Meguro-ku, Tokyo 153-8505*

Hard-sphere colloids have been intensively studied as one of the most fundamental systems that show a liquid-crystal transition [1]. In 2001, Auer and Frenkel pointed out [2] a huge mismatch in the crystal nucleation rate between results of light scattering experiments and numerical prediction based on Monte Carlo simulations using the Umbrella Sampling method. Revealing the physical origin behind this huge discrepancy is one of the central issues in this field [1]. Hydrodynamic interactions (HI) among colloids are viewed as one of the possible factors to cause the discrepancy since simulation results used for the comparison completely neglect HI. So far, two simulation studies based on different models incorporating HI have been performed to address this problem. However, these studies reported conflicting results: one concluded that HI might speed up crystal nucleation [3], whereas the other claimed that HI slows down it [4].

In this project, we study the crystallization kinetics of hard-sphere colloids by two simulation methods with HI (Fluid Particle Dynamics method: FPD [5]) and without (Brownian Dynamics method: BD). By comparing two results, we can investigate the impact of HI on the crystal nucleation process. By combining the FPD method with fluctuating hydrodynamics, we have shown that FPD simulations can almost perfectly reproduce the motion of colloids under thermal noise at low volume fractions while retaining statistical mechanical consistency between colloids and a

solvent. Furthermore, we have confirmed that this simulation approach can precisely reproduce the phase separation process of colloidal suspensions observed by confocal microscopy measurements without any adjustable parameters [6]. However, crystal nucleation is a rare event, and thus, the resulting computational cost is quite high. We have overcome this problem by speeding up our code, utilizing ISSP's GPGPU implementation services [7].

According to Ref. [2], the theoretical values of I change mainly by a small change in the volume fraction ϕ : for example, I at $\phi = 52.8\%$ differs from that at 53.4% by at least 4 orders of magnitude. Thus, in order to study the nucleation rate accurately, we need to estimate the volume fraction ϕ precisely. To realize this, we first check the volume fraction dependence of the virial pressure. In Fig. 1a, we show the results obtained by BD and FPD together with theoretical predictions (the Carnahan-Starling equation of a state in the liquid phase and the Speedy equation of a state in the solid phase). Here we can see almost perfect agreement between them, supporting the validity of our numerical simulation methods from the thermodynamic point of view.

Now we turn our attention to a dynamic aspect. Here we examine the volume-fraction dependence of the long-time self-diffusion constant, D_L as one of the most fundamental quantities to characterize colloidal dynamics. Figure 1b shows the results for FPD and BD, where we can see that D_L deviates from the diffusion coefficient for a free isolated particle

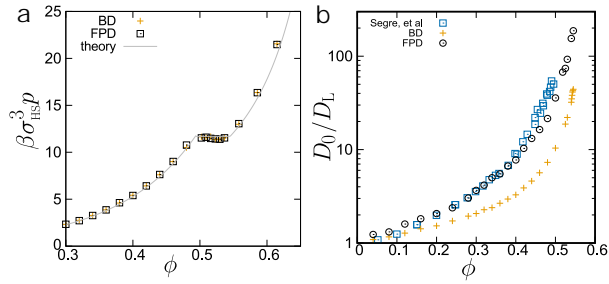


Figure 1: (a) Virial pressure in equilibrium states. Cross and square symbols represent the results obtained by BD and FPD simulations, respectively. Gary curve is the theoretical prediction for a hard-sphere system. (b) Volume fraction dependence of the long-time diffusion constant D_L scaled by that in the dilute limit D_0 . Cross and circle symbols represent the results obtained by BD and FPD simulation, respectively. The light blue square symbols are experimental data obtained by dynamic light scattering measurements for hard-sphere-like colloids with 5 % polydispersity [8].

D_0 for large ϕ , but the deviation is more significant for FPD than for BD, which depends on the presence or absence of hydrodynamic interactions. For example, we can see that D_L in BD is approximately four times larger than that in FPD at $\phi = 0.54$. In the figure, we also compare the simulation results with experimental data obtained by dynamic light scattering measurements for hard-sphere-like colloids with 5 % polydispersity [8]. Here we can see that there is a mismatch between FPD and BD, but there is a good agreement between FPD and the experimental results at least at intermediate volume fractions. To determine the nucleation rate I , we used an approach to monitor the temporal change of a cluster with the largest size. We compare I at $0.54 \leq \phi \leq 0.545$ between BD and FPD, by using D_L and the diameter of colloids as spatiotemporal units, and find that all nucleation rates collapse onto a single curve.

In summary, to examine the influence of HI on crystallization kinetics of hard-sphere colloids, we precisely compare simulation results with and without HI. We show that the long-

time diffusive dynamics of the colloids is more rapidly slowed down by HI with increasing volume fraction. We find that this long-time diffusion controls the nucleation rate and that it is possible to account for most of the effects of HI by rescaling with this time scale. The research results are summarized in Ref. [9].

References

- [1] T. Palberg: J. Phys. Cond. Matt. **33** (2014) 333101
- [2] S. Auer and D. Frenkel: Nature **409** (2001) 1020
- [3] M. Radu and T. Schilling: EPL **105** (2014) 26001
- [4] D. Roehm, S. Kesselheim and A. Arnold: Soft matter **10** (2014) 30
- [5] H. Tanaka and T. Araki: Phys. Rev. Lett. **85**, (1999) 1338; A. Furukawa and H. Tanaka: Phys. Rev. Lett. **104**, (2010) 245702; A. Furukawa, M. Tateno and H. Tanaka: Soft Matter **14** (2018) 3738
- [6] M. Tateno and H. Tanaka: npj Comput. Mater. **5** (2019) 40
- [7] M. Tateno, K. Takae and H. Tanaka, “GPGPU implementation of Fluid Particle Dynamics method”, Activity Report in 2017
- [8] P. N. Segre and S. P. Meeker, P.N. Pusey and W. C. K. Poon: Phys. Rev. Lett. **75** (1995) 958
- [9] M. Tateno, T. Yanagishima, J. Russo, and H. Tanaka: Phys. Rev. Lett. **123**, (2019) 258002

Impact of hydrodynamic interactions on colloidal dynamics near a critical point

Michio Tateno and Hajime Tanaka

*Department of Fundamental Engineering, Institute of Industrial Science, University of Tokyo
4-6-1 Komaba, Meguro-ku, Tokyo 153-8505*

The behaviors of simple liquids near a critical point are well-understood both from a theoretical and experimental point of view. The density fluctuation decays exponentially with single relaxation time. Contrary to this knowledge, several studies on colloidal suspensions using light scattering experiments report that time correlation function of concentration fluctuations in the vicinity of the critical point show nonexponential decay [1].

The central aim of this project is to reveal the physical mechanism underlying the non-exponential decay. As a possible candidate to bring about this unconventional dynamical behavior in colloidal suspensions, we focus on hydrodynamic interactions (HI), which is an essential difference between simple liquids and colloidal suspensions. We use two different simulation methods; the Brownian dynamics (BD) method neglecting HI and Fluid particle dynamics (FPD) method incorporating HI [2]. We compare the results from two simulation methods and aim to examine the effect of HI on dynamical critical phenomena.

In order to capture dynamical critical phenomena numerically, a long time simulation is required, since the relaxation time for density fluctuation grows dramatically as approaching to a critical point. However, FPD method is numerically costly because it is based on the direct computation of Navier-Stokes equations. To overcome this, we implemented GPU on our FPD codes utilizing a service provided by ISSP. To further suppress numerical cost, we

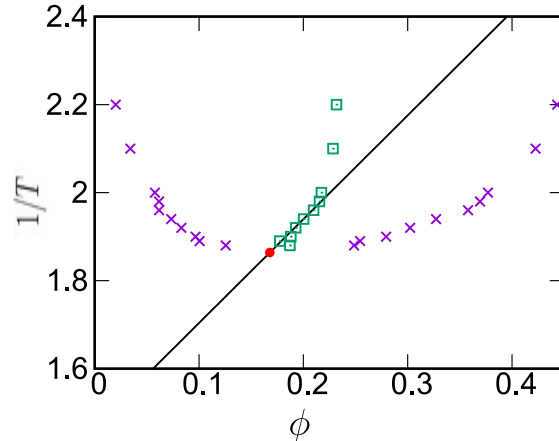


Figure 1: Temperature-volume fraction phase diagram. The cross symbols show the gas and liquid phases. The black line represents the tieline, which is obtained from asymptotic behavior of median between two phases (square) towards the vertex of binodal line. We fit a parabolic function to the cross symbols with volume fraction and tieline as two axis, and determine the critical point (circle).

adopt a rather short-range interaction. More specifically, we use the modified Lennard-Jones potential with cutoff length $r_c = 1.7\sigma$: $U(r) = 4\epsilon((\sigma/r)^{24} - (\sigma/r)^{12} + c_2(r/\sigma)^2 + c_0)$ for $r < r_c$ and $U(r) = 0$ for otherwise. Here c_2 and c_0 are constants to satisfy $U(r_c) = 0$ and $U'(r_c) = 0$. This short-range nature of intercolloid potential suppresses the correlation length of density fluctuations and allows us to perform simulations with a rather small system size ($L = 17.3\sigma$).

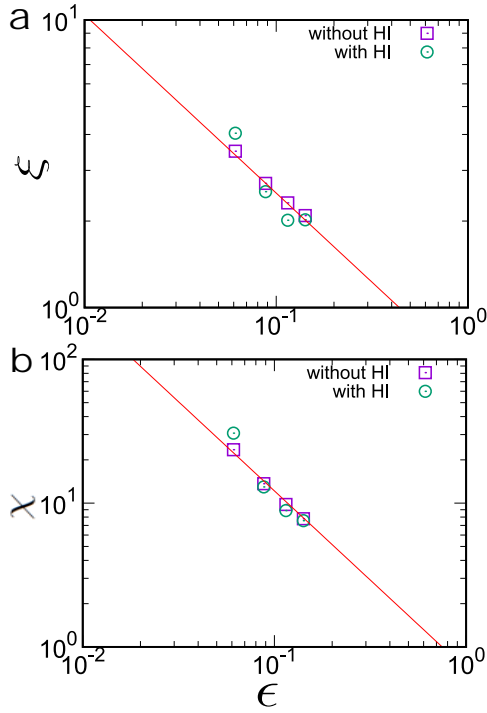


Figure 2: The correlation length ξ (a) and susceptibility χ (b) as a function of critical parameter $\epsilon := T_c/(T - T_c)$. The red line represents a power-law function with critical exponent (approximately 0.62 and 1.24 for ξ and χ , respectively)

We study the static behavior of colloidal suspensions near a critical point. We perform simulations for states on tieline (see the black line in Fig. 1) approaching to a critical point (red circle point). Figure 2 shows the correlation length ξ and susceptibility χ , which is determined by fitting the static structure factor with the Ornstein-Zernike form. Here we can see that the two results obtained from BD and FPD show an excellent agreement with each other, and both follow to power-law function with the critical exponent. These trends are consistent with a well-known fact that HI does not influence the thermodynamic behaviors of colloidal suspensions. Next, we compute the auto-correlation function of density fluctuation and evaluate the dependence of lifetime on the critical parameter ϵ . We find that the auto-

correlation function decays exponentially with a single time τ_ξ scale, and τ_ξ is proportional to the cube of ξ , which coincides with the case of dynamical critical phenomena for simple liquids.

In summary, we performed numerical simulations for colloidal suspensions with and without HI and examined the effect of HI on the dynamical critical phenomena. We obtained the results that HI does not influence both static and dynamical behaviors. However, due to the constraint by numerical cost, the critical parameter that we accessed is limited ($0.05 < \epsilon$), and the anomaly in the time correlation function of concentration fluctuations is reported in a smaller ϵ . To make a definitive conclusion for this phenomenon, we realize a much larger simulation.

References

- [1] J. Rouch, et al.: Phys. Rev. Lett. **71**, (1993) 1947; B. M. Fine, et al.: Phys. Rev. Lett. **74**, (1995) 198; B. M. Fine, et al.: J. Chem. Phys., **104**, (1996) 326
- [2] H. Tanaka and T. Araki: Phys. Rev. Lett. **85**, (1999) 1338

Coarsening mechanism of network-forming phase separation in colloidal suspensions

Michio Tateno and Hajime Tanaka

*Department of Fundamental Engineering, Institute of Industrial Science, University of Tokyo
4-6-1 Komaba, Meguro-ku, Tokyo 153-8505*

Phase separation is one of the most fundamental physical phenomena in nature to form a spatially inhomogeneous structure, whose basic coarsening laws were well-established in the 20th century. However, the conventional mechanisms are valid only near the critical point, and the coarsening behavior under deep quench remains elusive. We noticed that for network-forming deeply-quenched phase separation, unusual coarsening behavior of network structures had been reported in experiments for various soft matter such as colloidal suspensions [1], protein solutions [2] and lyotropic liquid crystal [3]: their characteristic network size ℓ commonly grows as $\ell \sim t^{1/2}$ while retaining their connectivity. The goal of this project is to reveal the physical principle behind the growth exponent 1/2.

To address this problem, we used a hydrodynamic simulation model for colloidal suspensions, Fluid Particle Dynamics (FPD) method [5], which is based on the direct computation of the Navier-Stokes equation, and studied network-forming process during gas-liquid phase demixing. To capture the coarsening of network structure without suffering from a finite-size effect, we developed GPU-MPI hybrid codes utilizing a service provided by ISSP and realized a large scale simulation. Since our interest is in phase separation dynamics under a deep quench, we neglect thermal noise.

We show in Fig. 1 the time evolution of phase-separation structures in the colloidal suspension. Here we can clearly see that a

space-spanning network structure is spontaneously formed in the early stage, and its characteristic length scale grows afterward. By computing the temporal change of the first moment of the structure factor, we confirmed that the characteristic length of network structure ℓ follows a power-law growth with exponent 1/2 while retaining self-similarity.

In the absence of thermal noise at zero temperature, the coarsening cannot be due to thermal activation but should be of purely mechanical nature. Then, we focus on the slow elastic dynamics of dense colloidal aggregates and analyze the strain field ϵ by coarse-graining the displacements of colloidal particles. Here in particular, we consider the time evolution of the distribution function, $P(\epsilon)$, from a reference time t_0 to an arbitrary time $t_0 + t'$. We find that the distribution functions are collapsed onto a master curve after scaling the argument ϵ by t'/t_0 (see Fig. 2), indicating that the elastic relaxation of network structure controls the speed to the coarsening process.

Here we note that the exponent 1/2 is observed only in the presence of solvent component: for example, the Brownian dynamics method completely neglecting the motion of a solvent does not reproduce the exponent 1/2 (see, e.g., Ref. [4]). This fact implies that dynamic coupling between densely-packed colloid and a solvent saturated in the colloid-rich domain plays a crucial role. Biot's poroelastic theory is known as a model to describe the motion of fluid saturated elastic materials. By

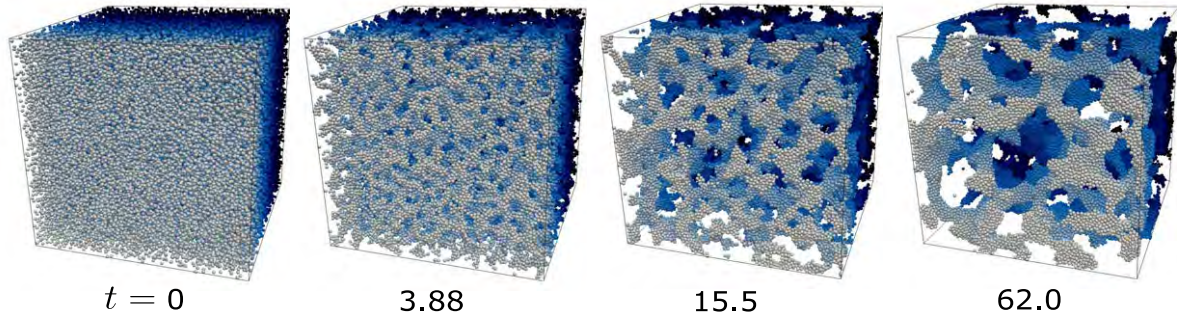


Figure 1: Coarsening behavior of network-forming phase separation of colloidal suspensions. Particles are colored to distinguish front particles from back ones.

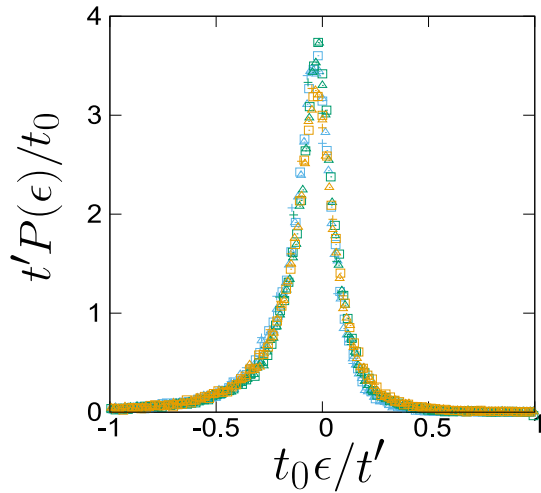


Figure 2: $P(\epsilon)$ after scaling ϵ by t'/t_0 . The data are sampled from the data whose reference time is $t_0 = 31.0$ (blue), 46.5 (green), 62.0 (brown). Then, cross, triangle and square symbols represent the data at $t'/t_0 = 0.001, 0.01, 0.02$, respectively.

performing a scaling analysis on this theory, we obtain a coarsening law, $\ell \sim (D_p t)^{1/2}$, where D_p is a poroelastic diffusibility. See Ref. [6] for further discussion on the validity of the coarsening law.

In summary, we performed a large-scale hydrodynamic simulation for colloidal suspensions and studied the dynamic process of network-forming phase demixing. We found that the coarsening process has self-similarity,

and the domain grows with the growth exponent of $1/2$. We revealed that the exponent is a consequence of slow elastic relaxation of the network-forming dense phase, whose limiting process is permeation flow of the solvent.

References

- [1] H. Tanaka, et al., J. Phys.: Condens. Matter, **17**, (2005) L143; A. Bailey, et al.: Phys. Rev. Lett. **99**, (2007) 205701; M. Tateno and H. Tanaka, npj Comput. Mater., **5**, (2019) 40
- [2] H. Tanaka and Y. Nishikawa: Phys. Rev. Lett., **95**, (2005) 078103
- [3] Y. Iwashita and H. Tanaka: Nat. Phys., **5**, (2006) 147
- [4] A. Furukawa and H. Tanaka: Phys. Rev. Lett. **104**, (2010) 245702.
- [5] H. Tanaka and T. Araki: Phys. Rev. Lett. **85**, (1999) 1338
- [6] M. Tateno and H. Tanaka: Nat. Commun., under review.

Structural origin of glassy slow dynamics

Hua Tong and Hajime Tanaka

*Department of Fundamental Engineering, Institute of Industrial Science, University of Tokyo
4-6-1 Komaba, Meguro-ku, Tokyo 153-8505*

Despite the use of glasses for thousands of years, the nature of glass and the glass transition remains probably “the deepest and most interesting unsolved problem” in condensed matter physics and materials science. In contrast to crystallization where the solidity emerges as a result of the formation of long-range periodic order, the drastic dynamical slowing down toward the glass transition is accompanied by little change in the geometric structure, as measured by two-point correlators accessible through diffraction and scattering experiments [1, 2]. Therefore, glasses are widely thought as the epitome of completely disordered state of materials and the glass transition is described as a purely dynamical phenomenon in kinetically constrained models. The physical scenarios which posit a growing static order and hence a thermodynamic origin behind the slowing down of glassy dynamics have regained popularity since the discovery of the so-called dynamic heterogeneity in 1990s. The spatially correlated domains which move significantly faster or slower than the average are proposed to be the long sought-after cooperatively relaxing regions (CRRs), which is the core concept of Adam-Gibbs theory of glass transition and its modern version, i.e., the random first-order transition (RFOT) theory. Meanwhile, a growing correlation length characterizing the extent of heterogeneous dynamics is also suggestive of a similarity between glass transition and the critical phenomena [3–5]. However, since the dynamic heterogeneity is only accessible through dynamic variables [6, 7], the crucial physical mechanism is still not established, namely a quantitative characterization of the glassy structural order and its link to dynamics, which precludes a decisive

underpinning to the (thermodynamic) nature of the glass transition.

To look for key structural features responsible for glassy dynamics, one typical approach is to consider specific physical aspects of the local atomic environment, e.g., free volume, potential energy, and symmetry. The free volume approach [8, 9] and the inherent potential energy based on the potential energy landscape (PEL) formalism enjoyed early success showing a clear macroscopic correlation (that is, for globally averaged quantities) with dynamics, but not microscopically at a particle level [10–12]. Therefore, more efforts have been devoted to the identification of locally favored structures (LFSs) based on symmetry considerations. For instance, icosahedral [13, 14], crystal-like orders [3, 4, 15], or more complicated topological clusters [16] are identified and suggested as the origin of slow dynamics in different glass-forming liquids. However, the general relevance of LFSs in glassy slow dynamics remains controversial due to its strong and sensitive system dependence. This may arise from the system-dependent nature of locally low free-energy configurations [4]. Another approach developed by Cubuk *et al.* recently is to define some structural quantity, “softness”, based on machine-learning methods [17, 18]. The strong correlation observed between softness and structure relaxation suggests that important structural features are captured. However, softness is defined in a high-dimensional space with more than 100 structure functions, prohibiting a clear identification of glassy structural order. It is desirable to unveil the structural characteristics of glass-forming liquids from a physically inspired perspective.

Recently in ref. [12], we constructed a set of structural order parameters, namely Θ in 2D and Ω in 3D, to capture sterically favored structures with high local packing capability in hard-sphere-like glass formers. In the absence of obvious density fluctuations beyond the particle scale, such sterically favored structures provide more room for particle motions through better arrangement, and hence higher correlational (or, vibrational) entropy and lower free energy [4]. This is analogous to the crystallization process of hard spheres. We showed at a picture level that the mobility develops systematically following the structural order parameter field and confirmed a common structural origin for both fast β and slow α dynamics.

In this study, we move a crucial step forward to study *quantitatively* the formation of

structural order and its relation to slow glassy dynamics. We find that the degree of glassy structural order follows a linear scaling law with temperature, which initiates around the onset temperature T_{on} of the super-Arrhenius dynamics and is ceased by the dynamical glass transition T_g . This provides us with a direct quantitative relation between structural order and structure relaxation time τ_α , and therefore represents a key thermodynamic characteristic of the glass transition. More interestingly, based on a nonlocal excitation scenario, we confirm that such an intimate structure-dynamics correlation is valid even microscopically at a particle level. Therefore, our results may provide an essential piece in the microscopic theoretical description of the long-standing glass transition problem from a structural perspective.

-
- [1] J. C. Dyre, Rev. Mod. Phys. **78**, 953 (2006).
 [2] K. Binder and W. Kob, *Glassy materials and disordered solids: An introduction to their statistical mechanics* (World Scientific, 2011).
 [3] H. Tanaka, T. Kawasaki, H. Shintani, and K. Watanabe, Nature Mater. **9**, 324 (2010).
 [4] H. Tanaka, Eur. Phys. J. E **35**, 113 (2012).
 [5] J. S. Langer, Phys. Rev. E **88**, 012122 (2013).
 [6] M. D. Ediger, Annu. Rev. Phys. Chem. **51**, 99 (2000).
 [7] L. Berthier and G. Biroli, Rev. Mod. Phys. **83**, 587 (2011).
 [8] M. H. Cohen and G. S. Grest, Phys. Rev. B **20**, 1077 (1979).
 [9] F. W. Starr, S. Sastry, J. F. Douglas, and S. C. Glotzer, Phys. Rev. Lett. **89**, 125501 (2002).
 [10] A. Widmer-Cooper and P. Harrowell, Phys. Rev. Lett. **96**, 185701 (2006).
 [11] A. Widmer-Cooper and P. Harrowell, J. Non-Cryst. Solids **352**, 5098 (2006).
 [12] H. Tong and H. Tanaka, Phys. Rev. X **8**, 011041 (2018).
 [13] F. C. Frank, Proc. R. Soc. Lond. A **215**, 43 (1952).
 [14] P. J. Steinhardt, D. R. Nelson, and M. Ronchetti, Phys. Rev. B **28**, 784 (1983).
 [15] M. Leocmach, J. Russo, and H. Tanaka, J. Chem. Phys. **138**, 12A536 (2013).
 [16] C. P. Royall and S. R. Williams, Phys. Rep. **560**, 1 (2015).
 [17] E. D. Cubuk, S. S. Schoenholz, J. M. Rieser, B. D. Malone, J. Rottler, D. J. Durian, E. Kaxiras, and A. J. Liu, Phys. Rev. Lett. **114**, 108001 (2015).
 [18] S. S. Schoenholz, E. D. Cubuk, D. M. Sussman, E. Kaxiras, and A. J. Liu, Nature Phys. **12**, 469 (2016).

Universality of bulk-edge correspondence by numerical methods

Y. Hatsugai

*Department of Physics, University of Tsukuba
1-1-1 Tennodai, Tsukuba 305-8571, Ibaraki, Japan*

One of the key concepts of the topological phases is the bulk-edge correspondence, that relates non-trivial topology of the bulk to the low energy physics near boundaries or impurities[1]. Non-trivial bulk topology is hidden for low energy physics of the bulk and most of the characteristic and experimental features appear as generalized edge states living near the boundaries. Although its historical example is a quantum phenomenon (quantum Hall effect), its validity is much more universal and the concept is applicable even for non-quantum phenomena such as photonic crystals of classical electromagnetic field and even classical mechanics of periodic systems. Using a formal analogy among the various systems, one can define a Berry connection for the bulk (even for the classical systems). Although there is no physical, at least, direct meaning for the topological quantities based on the Berry connection, the edges states predicted by the bulk-edge correspondence are physical observables. Such a hidden Berry connection of the bulk and topological numbers support the edge states of various physical phenomena. This is the universality of the bulk-edge correspondence, which we numerically try to establish in the project.

The corner states of the higher order topological phases are such generalized edge states which characterize the specific bulk topology reversely. We have shown such examples supported by the quantized Z_N ($n \in \mathbb{Z}$) Berry phases as a bulk topological invariants for a quantum three dimensional model [2] and classical mechanics on a Kagome lattice[3]. We have further proposed a higher order topological Mott insulator that hosts spin-charge separated corner states and demonstrated its validity numerically[4].

We also performed a topological characterization of the $J_1 - J_2$ spin ladder for higher integer spins using a quantized Berry phases[5]. It justifies a generalized valence bond solid state as the adiabatic limit of the ground state obtained numerically. Then sequential topological phase transitions associated with the valence bond reconstruction are clearly demonstrated.

We further discussed several other topics related such as non hermitian topological phenomena[6, 7, 8, 9] and obtained new insight for the adiabatic heuristic argument[10] that is a conceptual/historical background of topological characterization.

References

- [1] Yasuhiro Hatsugai, Phys. Rev. Lett. **71**, 3697 (1993).
- [2] Hiromu Araki, Tomonari Mizoguchi and Yasuhiro Hatsugai: Phys. Rev. Research **2**, 012009(R) (2020).
- [3] Hiromasa Wakao, Tsuneya Yoshida, Hiromu Araki, Tomonari Mizoguchi, and Yasuhiro Hatsugai: Phys. Rev. **101**, 094107 (2020).
- [4] Koji Kudo, Tsuneya Yoshida, and Yasuhiro Hatsugai : Phys. Rev. Lett. **123**, 196402 (2019).

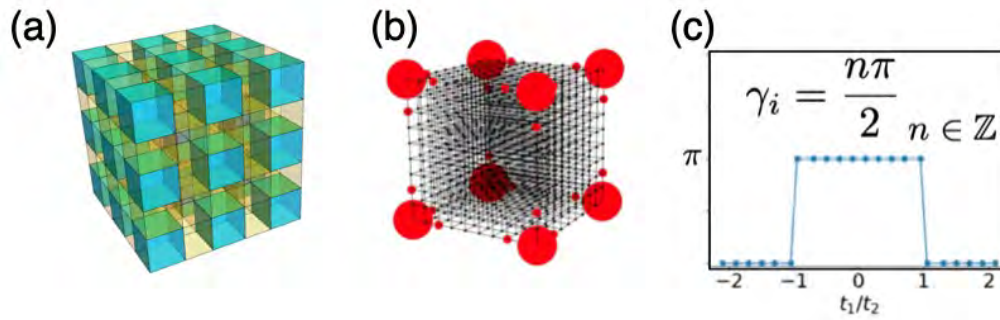


Figure 1: (a) Schematic lattice structure of the three dimensional BBH model, (b) corner states and (c) Z_4 Berry phases (See. Ref.[2])

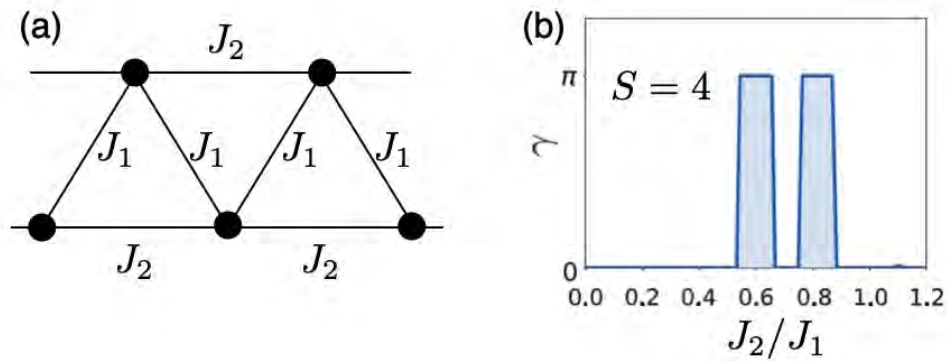


Figure 2: (a) $J_1 - J_2$ Heisenberg spin chain of integer $S(\geq 1)$ and (b) Z_2 Berry phase of $S = 4$ (8 site system with periodic boundary condition) (See Ref. [5])

- [5] Shota Fubasami, Tomonari Mizoguchi and Yasuhiro Hatsugai: Phys. Rev. B **100**, 014438 (2019).
- [6] Tsuneya Yoshida, Koji Kudo, and Yasuhiro Hatsugai: Scientific Reports **9**, 16895 (2019).
- [7] Tsuneya Yoshida and Yasuhiro Hatsugai: Phys. Rev. B **100**, 054109 (2019).
- [8] Tsuneya Yoshida, Robert Peters, Norio Kawakami, Yasuhiro Hatsugai: arXiv:2002.11265
- [9] Tsuneya Yoshida, Tomonari Mizoguchi, and Yasuhiro Hatsugai: arXiv:1912.12022
- [10] Koji Kudo and Yasuhiro Hatsugai : arXiv:2004.00859.

Kinetics of phase transition and polyamorphism

Kazuhiro Fuchizaki, Kei Watanabe, and Hiroki Naruta

Department of Physics, Ehime University, Matsuyama 790-8577

In FY2019, we have undertaken two subjects, as reported briefly below. The first task has been almost completed, and its full report will soon be submitted elsewhere. The second one is still at a preliminary stage and will be ongoing in FY2020.

Growth of density fluctuations at the beginning of a phase separation

The concept of spinodal has been examined for an Ising system [1]. However, no explicit discussion has been found for a fluid system, which is believed to belong to the same unitary class. Ushcats has suggested [3], extending the equation of state beyond the thermodynamically stable region, that the spinodal line of the modified Lennard-Jones (mLJ) system [2] approaches the liquid-gas coexistence (binodal) line. Our prediction based on the coarse-graining limit for the coarse-grained free energy, estimated by applying the block-spin coarsening technique, supports Ushcats' conjecture [4]. It is then highly anticipated that the "dynamics" of a system also depends on a coarsening level.

We conducted isothermal–isobaric molecular dynamics (MD) simulations for an mLJ system consisting of 4×10^6 particles to examine the dynamical process of liquid–gas phase separation. Length, time, and temperature are expressed in units of σ , $\sqrt{m\sigma^2/\epsilon}$, and ϵ/k_B [5], respectively, where σ and ϵ are the fundamental length and energy scales of the mLJ potential function and k_B denotes Boltzmann's constant. The critical temperature, pressure, and density of the mLJ system are $T_c = 1.0762(2)$, $p_c = 0.09394(17)$, and $\rho_c = 0.331(3)$, respectively. We treated two systems with differ-

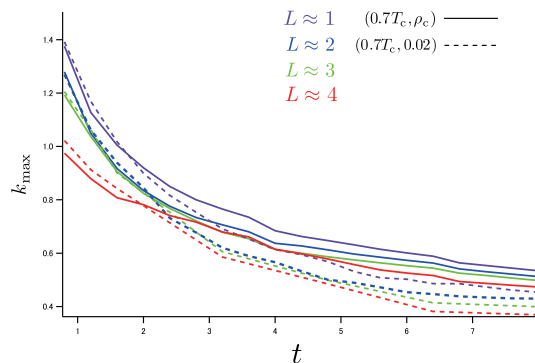


Figure 1: The peak position of S_L is plotted against time with the same color for every coarsening scale of L . Those at ρ_c (0.02) are delineated by solid (dotted) lines.

ent density; 0.02 and ρ_c . The fluid system well-equilibrated at $20T_c$ was instantaneously brought to $0.7T_c$ to undergo phase separation. The lower- and critical-density systems were expected to be quenched in the metastable and unstable regions, respectively, judging from the shape of the coarse-grained free energy.

The term, "local density," has been quite often used in mesoscopic descriptions. However, it has been far unclear what is meant by "local." In this case, we can define the local density unambiguously using the length L , the coarse-graining scale based on which the coarse-grained free energy was defined [4].

Based on this well-defined "local" density and its fluctuations around the average density, we defined the structure factor S_L . Figure 1 shows the time evolution of S_L after quenching. On the short-time side ($t < 2$), L predominantly determines the peak position of S_L , whereas it approaches the value determined by the average density on the long-time side ($t > 2$).

To examine in detail the L -dependence of the wavelength at which structural destabilization occurs, S_L was scaled by its peak position and height. The dynamical process in another state, obtained by quenching the critical-density system to $0.97T_c$, was also examined. We could identify in the short-time region the new universal process (Figure 2), in which phase separation proceeds in a statistically self-similar fashion irrespective of the average density, quenching temperature as well as the coarsening length. We name this stage a “super-early” stage.

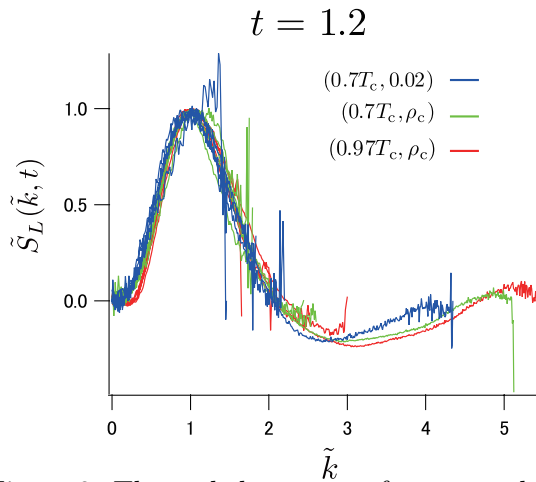


Figure 2: The scaled structure factors at three different states fall into a single curve when plotted against scaled wavelength, implying the existence of universality in a phase separation process right after a quench.

Estimating entropy of a fluid

A method proposed by Goddard *et al.* [6] has been widely used for evaluating entropy of a disordered system even with such a kind of network structure. The entropy is generally estimated from the density of states (DOS), which is obtainable through Fourier inversion of the velocity autocorrelation. Goddard *et al.* have claimed that a DOS of a fluid state can be constructed from those of solid and gas states [6]. This claim does not have any physical basis. Although an LJ fluid was used to testify their claim [6], we employ as another simple liquid an mLJ system to thoroughly examine their

assertion.

An isochoric–isothermal MD simulation generated an equilibrated mLJ fluid consisting of 2048 particles. We employed such a small number of particles because Goddard *et al.* used for a similar size for an LJ fluid [6]. Similar finite-size effects would then be involved in the results. We chose for this purpose three states with density 5.00×10^{-2} , ρ_c , and 0.600 along the isotherm $1.001T_c$, where T_c is the aforementioned critical temperature of the mLJ system [6]. The density is again expressed in terms of the mLJ units.

The entropy of the three states was also calculated using the λ -integration [7], which is too costly but can give the numerically exact result. The entropies based on the method of Goddard *et al.* could not well reproduce the λ -integration based ones. We should undertake a critical review of their basic idea.

References

- [1] K. Kaski, K. Binder, and J. D. Gunton, *Phys. Rev. B* **29**, 3996 (1984).
- [2] Y. Asano and K. Fuchizaki, *J. Chem. Phys.* **137**, 174502 (2012).
- [3] M. V. Ushcats, *J. Chem. Phys.* **141**, 101103 (2014).
- [4] K. Fuchizaki and K. Watanabe, *J. Phys. Soc. Jpn.* **87**, 114006 (2018).
- [5] K. Okamoto and K. Fuchizaki, *J. Phys. Soc. Jpn.* **86**, 034003 (2017).
- [6] S. Lin, M. Blanco, and W. A. Goddard, *J. Chem. Phys.* **119**, 11792 (2003).
- [7] J. Q. Broughton and G. H. Gilmer, *J. Chem. Phys.* **79**, 5095 (1983).

Ground-State Phase Diagram of the $S=1/2$ Kitaev- Γ model on a Honeycomb Lattice

Takafumi SUZUKI

Graduate School of Engineering,

University of Hyogo, Shosha, Himeji, Hyogo 670-2280

We have studied the ground-state phase diagram of the $S=1/2$ Kitaev- Γ model on a honeycomb lattice [1] and quantized $\Delta S=2$ excitation spectra by confinement in an $S=1$ spin chain [2].

First, we have investigated the ground-state phase diagram of the $S=1/2$ Kitaev- Γ model on a honeycomb lattice with the numerical exact diagonalization method, DMRG and cluster-series expansion method [3]. By changing the magnitude of interactions on each bond, the model connects with three characteristic points, where the model is described by spin chains, isolated dimers, or an isotropic honeycomb-lattice model. The obtained results have clarified that in the spin chain limit, two Tomonaga-Luttinger (TL) liquid phases and three non-TL liquid phases appear when the ratio of the Kitaev interaction and the Γ interaction changes. In the dimer limit, the dimerized state with the lowest energy is $|t_x\rangle = (|\uparrow\uparrow\rangle - |\downarrow\downarrow\rangle) / \sqrt{2}$, when the positive Γ interaction and the negative Kitaev interaction are considered. We have found that this $|t_x\rangle$ state can survive up to the isotropic point.

Next, we have studied low-energy excitations of an $S=1$ Ising spin chain with the negative single-ion anisotropy in magnetic fields. We have calculated the dynamical structure factor with the infinite time-evolving block decimation (iTEBD) method [4]. We have found that when the transverse magnetic field is absent, both a $\Delta S=2$ excitation continuum and one-magnon isolated mode appear in the low-lying excitation. This $\Delta S=2$ excitation continuum is quantized by the weak longitudinal magnetic field. The quantized $\Delta S=2$ excitation spectra originate from the confinement of two domain walls and the excitation energies of the quantized $\Delta S=2$ spectra are well explained the negative zeros in the Airy function.

References

- [1] Y. Yamada, et al., in preparation.
- [2] T. Suzuki and S. Suga, *J. Phys. Soc. Jpn.* **88** (2019) 053702.
- [3] J. Oitmaa, et al., *Series Expansion Methods for Strongly Interacting Lattice Models*, Cambridge University Press, 2006.
- [4] H. N. Phien, et al., *Phys. Rev. B* **86** (2012) 245107.

Macroscopic properties characterized by an extended thermodynamic functions to nonequilibrium

Naoko NAKAGAWA

*Department of Physics, Ibaraki University
2-1-1 Bunkyo, Mito, Ibaraki 310-8512*

Thermodynamic functions such as entropy and free energy play an essential role in equilibrium systems. In order to extend these powerful functions to various non-equilibrium systems, such as thermal conduction systems and external force-driven systems, we have performed numerical experiments on the systems shown in Figs. 1 and 2.

Figure 1 shows a one-dimensional system of particles under thermal conduction that interact with each other at the Leonard-Jones potential, and each particle is subjected to a constant external force (gravity). Various local thermodynamic quantities such as temperature, density, pressure, and chemical potential were determined by molecular dynamics simulations, and from these quantities the free energy and entropy of the whole system were estimated. The thermodynamic relation is found to give the free energy change of the whole system when the temperature equivalent to the total kinetic energy of the system and the spatial average pressure are adopted as temperature and pressure for the system, respectively. The equation of state has an additional effect from the second order of the external force, implying a limit to the global view of the thermodynamic system under the external force.

Figure 2 shows a two-component fluid under thermal conduction separated by a semi-permeable membrane. The osmotic pressure is determined from the balance of the chemical potentials in the isothermal state, but the

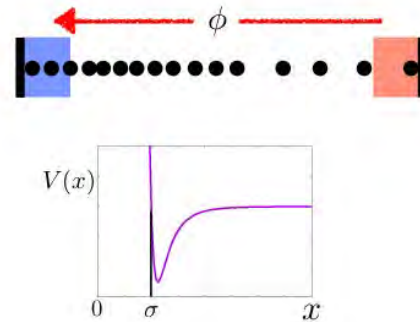


Figure 1: Heat conduction system under an external force.

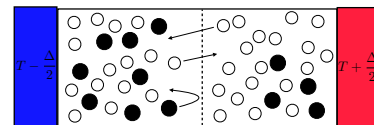


Figure 2: Two component fluid separated by a semi-permeable membrane.

chemical potentials are not spatially uniform in the thermal conduction state. In order to explore the principle of determining the osmotic pressure under thermal conduction, molecular dynamics simulations are performed and the dependence of the osmotic pressure on various parameters is investigated. We used the LAMMPS in order to achieve efficient results.

References

- [1] N. Nakagawa and S.-i. Sasa: J. Stat. Phys. **177** (2019) 825.

Development of data-driven science to materials science

Koji HUKUSHIMA

*Department of Basic Science, University of Tokyo
3-8-1 Komaba, Meguro-ku, Tokyo 153-8902*

In recent years, data-driven science methods have been attracting attention and have been applied to condensed matter physics and materials sciences. There are two main purposes to analyze the data obtained as a result of experiments and numerical experiments. One would be to extract the mathematical structure behind the data, and the other would be to make predictions to get the next data.

In this project, we carried out the tasks corresponding to the above-mentioned two purposes as actual problems. As the former problem, the model Hamiltonian was estimated from experimental data with a magnetic compound. As an example of the latter problem, we have conducted research on data-driven scientific methodologies in crystal structure search.

First, we proposed a data-driven methods to extract the spin Hamiltonian with uncertainty from multiple experiments. Using our method, an effective model of $\text{KCu}_4\text{P}_3\text{O}_{12}$ is determined from the experimentally observed magnetic susceptibility and magnetization curves with various temperatures under high magnetic fields. An effective model is the quantum Heisenberg model on a zigzag chain with eight spins in which four independent parameters are contained. Based on Bayesian statistics, these four parameters were estimated using MCMC sampling from the posterior distribution with experimental data as input. Our method yields that $J_1 = 8.54 \pm 0.51$ meV, $J_2 = -2.67 \pm 1.13$ meV, $J_3 = -3.90 \pm 0.15$ meV, and $J_4 = 6.24 \pm 0.95$ meV, describes these measured results well. Evaluation of these error bars is possible only by evaluating noise. The relations among the estimated magnetic

interactions or physical quantities are also discussed. These are the advantages of sampling from the posterior distribution. The obtained effective model is useful to predict hard-to-measure properties such as spin gap, spin configuration at the ground state, magnetic specific heat, and magnetic entropy.

Next, we studied the efficiency of Bayesian optimization as a method of selecting the next candidate when searching for a crystal structure. Bayesian optimization is a global optimization machine learning technique for a black-box function that requires a large amount of computation to be evaluated. A crystal structure is represented by a numerical vector called a descriptor that is used to quantify how similar structures are. This descriptor is an input of the crystal structure search with Bayesian optimization. The efficiency of the optimization significantly depends on the choice of the descriptor. We evaluated its efficiency with a varying parameter value in the descriptor[1]. Applying the crystal structure search to crystalline silicon shows that the efficiency of the search depends heavily on the parameter value. We find that the efficiency is linked to the distribution of the descriptor. Therefore, we introduce an information measure of the distribution to estimate an appropriate parameter value for performing the crystal structure search efficiently. The measure can also be used to predetermine an appropriate parameter value. The validity of the measure is confirmed with its applications to silicon oxide and yttrium cobalt alloy.

[1] N. Sato, *et al.* Phys. Rev. Materials **4**, (2020) 033801.

Unified understanding of early-time nonequilibrium relaxation in Monte Carlo simulations

Yoshihiko NONOMURA

MANA, National Institute for Materials Science

Namiki 1-1, Tsukuba, Ibaraki 305-0044

Recently we numerically revealed that the critical nonequilibrium relaxation (NER) behaviors in cluster algorithms are described by the stretched-exponential simulation-time dependence of physical quantities in various spin systems [1], and we derived such a relaxation formula phenomenologically [2].

Quite recently, we found a general derivation of a scaling for off-critical relaxation in local- and cluster-update algorithms. As an example, we consider the magnetic susceptibility in cluster-update algorithms. From the initial-time critical relaxation $\chi(t; T_c) \sim \exp(ct^\sigma)$ and the temperature dependence in equilibrium $\chi(t = \infty, T) \sim (T - T_c)^{-\gamma}$, we have $\chi(t, T)(T - T_c)^\gamma \sim \exp[ct^\sigma + \ln(T - T_c)^\gamma]$, or

$$\chi(t, T) \sim (T - T_c)^{-\gamma} f_{sc}[ct^\sigma + \ln(T - T_c)^\gamma], \quad (1)$$

which means that all the off-critical relaxation data near T_c are scaled on a single curve.

Here we assume that the relaxation process along the Kibble-Zurek mechanism [3], namely the controlled annealing process in accordance with critical relaxation, is expressed by the above scaling curve, and try to reconstruct the annealing process from the NER data in the two-dimensional (2D) Ising model. Although various attempts within the standard power-law annealing are not successful, the following stretched-exponential modified KZ process,

$$T(t) = T_0 + T_d \exp[-C(t/\tau)^\sigma], \quad (2)$$

$$T_0 = \frac{T_f - aT_i}{1 - a}, \quad T_d = \frac{T_i - T_f}{1 - a}; \quad a = e^{-C}, \quad (3)$$

gives consistent results for $L = 4096$ with the

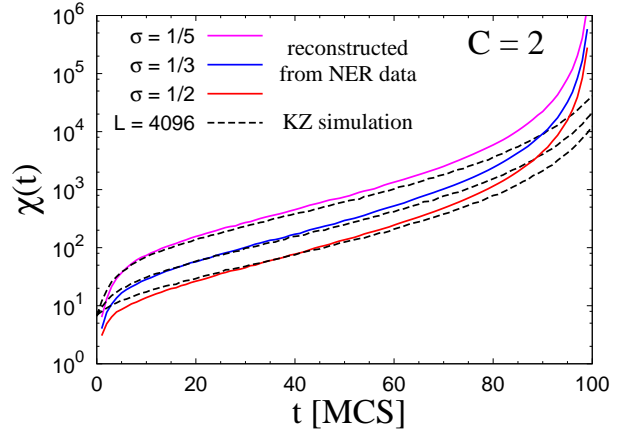


Figure 1: Simulation-time dependence of the magnetic susceptibility in the 2D Ising model in the SW algorithm for the modified KZ process explained in the main text. The dashed and solid lines are the simulated and reconstructed data based on Eq. (1), respectively.

relaxation process in the Swendsen-Wang algorithm with a set of parameters for a rather slow relaxation: $T_i = 1.5T_c$, $T_f = T_c$, $\tau = 100$, $C = 2$, and $\sigma = 1/5, 1/3, 1/2$ with the exact critical temperature T_c as shown in Fig. 1.

References

- [1] Y. Nonomura, *JPSJ* **83**, 113001 (2014); YN & Y. Tomita, *PRE* **92**, 062121 (2015), **93**, 012101 (2016), **101**, 032105 (2020).
- [2] YT & YN, *PRE* **98**, 052110 (2018).
- [3] C.-W. Liu et al., *PRB* **89**, 054307 (2014); Refs. therein (including originals by KZ).

Generalization of temperature scaling in early-time nonequilibrium relaxation

Yoshihiko NONOMURA

*MANA, National Institute for Materials Science
Namiki 1-1, Tsukuba, Ibaraki 305-0044*

Recently we numerically revealed that the critical nonequilibrium relaxation (NER) behaviors in cluster algorithms are described by the stretched-exponential simulation-time dependence of physical quantities in various classical spin systems [1, 2, 3] and in a quantum phase transition [4], and derived such a relaxation formula phenomenologically [5]. There we utilized the nonequilibrium-to-equilibrium scaling (NE-ES) which connects initial-time and equilibrium relaxation behaviors.

Here we generalize this derivation to off-critical behaviors. As an example, we consider the magnetic susceptibility. From the initial-time critical relaxation $\chi(t; T_c) \sim \exp(ct^\sigma)$ and the temperature dependence in equilibrium $\chi(t = \infty, T) \sim (T - T_c)^{-\gamma}$, we have $\chi(t, T)(T - T_c)^\gamma \sim \exp[ct^\sigma + \ln(T - T_c)^\gamma]$, or

$$\chi(t, T) \sim (T - T_c)^{-\gamma} f_{sc}[ct^\sigma + \ln(T - T_c)^\gamma]. \quad (1)$$

We confirm this temperature scaling by analyzing the NER process of the three-dimensional Heisenberg model in the Swendsen-Wang algorithm from the perfectly-disordered states [3].

Here we take the $L \times L \times L$ system with the periodic boundary condition for $L = 560$, the largest size used in Ref. [3]. The data up to 225 Monte Carlo steps are scaled with Eq. (1) in Fig. 1. Minimizing the mutual residuals using our previous estimates with the NE-ES, $T_c = 1.442987(2)J/k_B$ and $\sigma = 0.47(1)$ [3], we have

$$\gamma = 1.3945 \pm 0.0019, \quad c = 1.2593 \pm 0.0043, \quad (2)$$

which is consistent with the previous estimate from detailed simulations, $\gamma = 1.3960(9)$ [6].

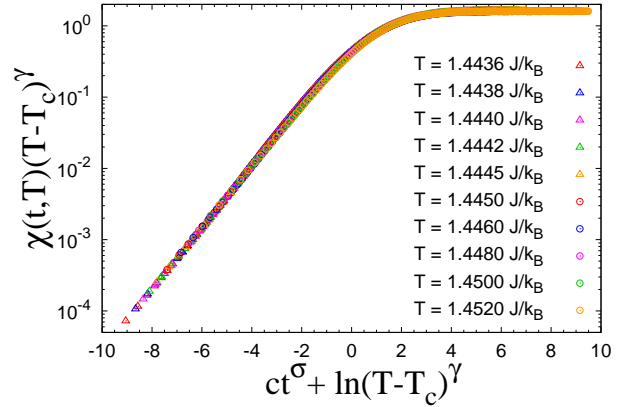


Figure 1: Temperature scaling plot of the magnetic susceptibility in the 3D Heisenberg model for various temperatures in a semi-log scale using the estimates of T_c and σ in Ref. [3].

References

- [1] Y. Nonomura, J. Phys. Soc. Jpn. **83**, 113001 (2014).
- [2] Y. Nonomura and Y. Tomita, Phys. Rev. E **92**, 062121 (2015).
- [3] Y. Nonomura and Y. Tomita, Phys. Rev. E **93**, 012101 (2016).
- [4] Y. Nonomura and Y. Tomita, Phys. Rev. E **101**, 032105 (2020).
- [5] Y. Tomita and Y. Nonomura, Phys. Rev. E **98**, 052110 (2018).
- [6] M. Campostrini, M. Hasenbusch, A. Pelissetto, P. Rossi, and E. Vicari, Phys. Rev. B **65**, 144520 (2002).

Finite-temperature properties of the Kitaev-Heisenberg models on kagome and triangular lattices

Takami TOHYAMA

Department of Applied Physics, Tokyo University of Science, Tokyo 125-8585

Frustrated quantum spin systems such as the Heisenberg and Kitaev models on various lattices have been known to exhibit various exotic properties not only at zero temperature but also for finite temperatures. Inspired by the remarkable development of the quantum frustrated spin systems in recent years, we decided to investigate the finite-temperature properties of the $S = 1/2$ Kitaev-Heisenberg models on kagome and triangular lattices.

For calculating accurate low-temperature properties, we developed two types of improved version for finite-temperature Lanczos method (FTLM) [1]: replaced FTLM and orthogonalized FTLM. In standard FTLM [2], a very large number of samplings of initial vector is required to obtain good accuracy at low temperatures. The low-temperature FTLM [2] is known as one of the solutions to this problem. However, this method has a difficulty for large-scale calculations because it requires huge random access memory to keep all vectors in the Krylov subspace. In RFTLM, low-lying eigenstates obtained by the ground-state Lanczos method are used in the partition function and other thermodynamic quantities. In OFTLM, initial random vectors are prepared to be orthogonal to the low-lying eigenstates. We also developed a Lanczos code that equips a technique to save the memory for the Hamiltonian by dividing H into two subsystems. These techniques lead us to calculate finite-temperature properties up to 36 lattice sites with good accuracy even at low temperatures.

The newly developed RFTLM was also used in the calculation of specific heat and magnetic susceptibility for $S = 1/2$ frustrated J_1 - J_2 Heisenberg model on kagome, triangular, and square lattice up to 36 sites [3].

In both kagome and triangular lattices for the Kitaev-Heisenberg model, multiple peaks are confirmed in the specific heat. To find the origin of the multiple peaks, we calculate the static spin structure factor. The origin of the high-temperature peak of the specific heat is attributed to a crossover from the paramagnetic state to a short-range ordered state whose static spin structure factor has zigzag or linear intensity distributions in momentum space. In the triangular Kitaev model, the order by disorder due to quantum fluctuation occurs. On the other hand, in the kagome Kitaev model it does not occur even with both quantum and thermal fluctuations [1].

References

- [1] K. Morita and T. Tohyama: Phys. Rev. Research **2** (2020) 013205.
- [2] P. Prelovsek and J. Bonca: Ground state and finite-temperature Lanczos methods, in *Strongly Correlated Systems, Numerical Methods*, Vol. 176 of Springer Series in Solid-State Sciences (Springer, 2013).
- [3] P. Prelovsek, K. Morita, T. Tohyama, and J. Herbrych: Phys. Rev. Research **2** (2020) 023024.

Constructing the electronic structure database for the molecular design of pigments utilizing near infrared light

Yu KOMATSU

National Institutes of Natural Sciences Astrobiology Center

National Astronomical Observatory of Japan

2-21-1 Osawa, Mitaka, Tokyo 181-8588

Novel dye molecules absorbing NIR radiation are being anticipated for dye-sensitized solar cells and imaging. Moreover, cyanobacteria, oxygenic photosynthetic bacteria, turn to utilize chlorophyll *f*, which is the reddest chlorophyll, for photochemistry after growing under the far-red light [1]. Thus, the red limit of photosynthesis has been updated. In this study, in order to explore redder molecules with possibly working as photosynthetic pigments, the database has been constructed using ab initio calculations for ring molecules like porphyrins with certain properties, combined with high-throughput methods.

The physical-chemical quantities of molecules, were estimated at DFT level as follows: *[total energies in ground and excited states, orbital energies, ionization potentials (IPs), electronic affinities (EAs), binding energies for central metals, electronic structures for each orbital, ...]*. Dye molecules are calculated with different central metals (Mg, Ca, Ni, Zn, Sr, Pd, Cd, Ba, Pt, Hg, Pb and H₂) in vacuum and water, methanol and benzene with PCM. In Fig.1, IPs and EAs for three pigments

are shown with 12 kinds of metals in four solvents. The data will be combined with an existing dataset like QM9 for further analysis to search for functional molecules effectively.

The computation in related work has been done using supercomputers of Tokyo Institute of Technology and National Astronomical Observatory of Japan, as well.

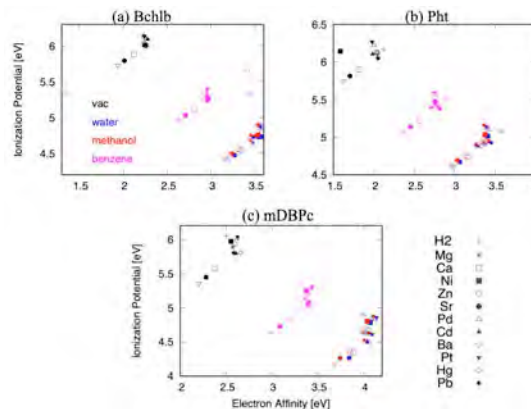


Fig. 1: Estimated ionization potentials and electronic affinities for (a) bacteriochlorophylls *b*, (b) phthalocyanines and (c) meso-dibenzoporphycenes with different central metals in 4 kinds of solvent conditions (CAM-B3LYP/Def2tzvp//B3LYP-D3/Def2tzvp).

References

[1] D. J. Nürnberg *et al.*: Science 360 (2018) 1210.

Application of numerical renormalization group method in condensed- matter physics

Kenji HARADA

Graduate School of Informatics, Kyoto University, Kyoto 606-8501, Japan

We have applied the tensor renormalization group (TRG) methods [1-4] to various condensed matter systems. We tried to use them for the non-equilibrium systems.

The directed percolation (DP) show a continuous phase transition in the phase diagram in the long-time limit. We have studied the phase diagram through the Renyi entropy by using a TEBD method on the matrix product states representation of a state-probability distribution [5]. In the case of one-dimensional DP, we have found a critical relaxation at the critical point and a new phase transition point in the active phase of the one-dim. DP.

The state-probability distribution of the d -dim. DP can be written as a $(d+1)$ -dim. tensor network. In the case of one-dim. DP, the TRG shows better accuracy than the TEBD method.

To check the existence of the new transition point in the activity phase of higher dim. DP, we tried to apply the TRG method on the two-dim. DP by a massively parallel computer on the ISSP.

In the case of the $(2+1)$ -dim. tensor network, the performance of the TRG method is not stable. The average density of active objects is not consistent with the Monte Carlo results, not near a critical point. The accuracy of the oblique projection in the TRG method is bad. However, due to the higher complexity of the TRG method, we could not increase the bond-dimension of tensors even using the system B. The reduction of the complexity of the TRG method is a future work to improve the accuracy of the TRG method.

Reference

- [1] M. Levin and C. P. Nave, Phys. Rev. Lett. **99**, 120601 (2007).
- [2] Z. Y. Xie, J. Chen, M. P. Qin, J. W. Zhu, L. P. Yang, and T. Xiang, Phys. Rev. B **86**, 045139 (2012).
- [3] G. Evenbly and G. Vidal, Phys. Rev. Lett. **115**, 180405 (2015).
- [4] S. Yang, Z.-C. Gu, and X.-G. Wen, Phys. Rev. Lett. **118**, 110504 (2017).
- [5] K. Harada and N. Kawashima, Phys. Rev. Lett., **123**, 090601, (2019).

Clarification of thermal transport spectra in hierarchical structured organic bulk materials

Takuma Shiga

Department of Mechanical Engineering,

The University of Tokyo, Hongo, Bunkyo, Tokyo 113-8656

Material design of cellulose nanostructure has been recently paid much attention because cellulose structure was identified by X-ray and neutron scattering spectroscopies. Cellulose nanomaterial is expected as candidates such as transparent conductive film and thermal insulator since it has high degree of self-organization and high mechanical property. Turning to thermal insulation, thermal conductivity of cellulose thermal insulators such as aerogel and foam is around $15\text{--}18\text{ mWm}^{-1}\text{K}^{-1}$, and it is lower than widely-used glass wool and urethane foam. However investigation of microscopic heat conduction mechanism of cellulose nanomaterial is very limited. In order to further improve thermal insulation performance, it is necessary to get insight into the knowledge on cellulose nanocrystal and fibrils.

We have evaluated heat conduction and its size effect of I- β type cellulose nanocrystal and single chain by performing non-equilibrium molecular dynamics (NEMD) simulation. In the NEMD calculation, we employed the GLYCAM06 [1] force field which reproduces thermal expansion coefficient of cellulose well.

This force field is composed of bond stretching, bond angle, dihedral angle, van der Waals, and Coulombic interaction. For non-bonding, we used the combination of particle-particle particle mesh and cutoff methods [2]. In the calculation, we applied periodic boundary conditions along all directions. After equilibration with $T=300\text{ K}$, hot and cold thermostats with $T=330\text{ K}$ and $T=270\text{ K}$ were attached to the simulation cell as illustrated in Fig. 1. Heat flux and temperature gradient were evaluated after the system reaches non-equilibrium steady-state, and then thermal conductivity was evaluated through the Fourier's law. All calculations were done by LAMMPS package.

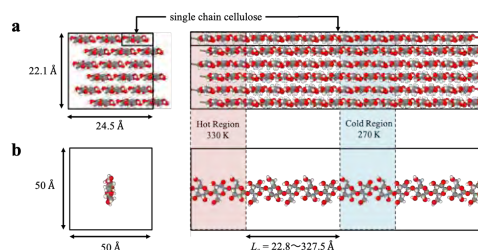


Fig. 1 Schematics for (a)cellulose nanocrystal (CNC) and (b)single chain cellulose.

Size effect of thermal conductivity of cellulose nanocrystal is shown in Fig. 2. As thermal conductivity increases with long-axis length increasing, we found that phonon

transport inside cellulose nanocrystal is quasi-ballistic. This feature is attributed to strong covalent bond of intra-interaction. From the obtained results and linear-relationship between an inverse of thermal conductivity and an inverse of long-axis length (L_c), we estimated the thermal conductivity of bulk cellulose nanocrystal as $4.50 \pm 0.60 \text{ Wm}^{-1}\text{K}^{-1}$, which is similar with reported literatures.

As for single cellulose chain, it was expected that thermal conductivity of single chain is larger than that of nanocrystal however these two thermal conductivities are actually quite similar with each other, which is different with the reported works on polyethylene [3]. Similar to the results of poly-dimethylpolysiloxane [4], this result can be understood because non-linear vibration of side structure arising from thermal fluctuation impedes phonon transport along long-axis direction. The non-linear vibration of side structure is strongly dependent on dihedral angle interaction and then we calculated thermal conductivity by strengthening or softening spring constant of dihedral angle, which are shown in Fig. 3 denoted as stiff and soft chains. While strength of dihedral interaction increases thermal conductivity, heat conduction along long-axis direction is found to be insensitive to the softening of dihedral interaction.

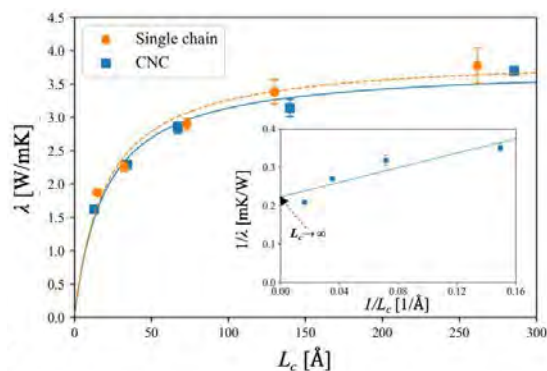


Fig. 2 Thermal conductivity of CNC (solid line) and cellulose single chain (dashed line) as a function of the conduction region length. The inset shows extrapolation of inverse of thermal conductivity in infinite conduction region length.

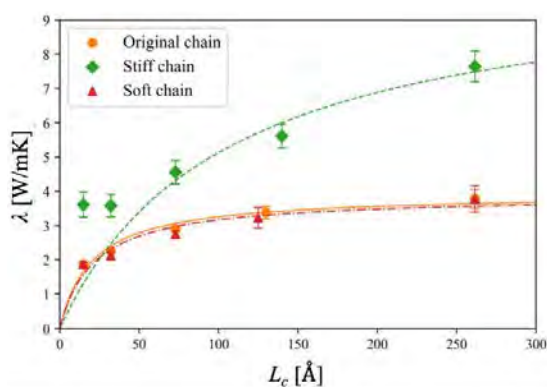


Fig. 3 Thermal conductivity of original single cellulose chain (solid line), stiff chain (dashed line) and soft chain (dash-dotted).

References

- [1] S. Hashmi, et al., *Int. J. Clin. Exp. Pathol.*, **8** (2015), 8786.
- [2] R.W.Hockney, et al., “Computer simulation using particles”, Adam Hilger, NY,(1989).
- [3] A. Henry, et al., *Phys. Rev. Lett.*, **101**-23(2008), 235502.
- [4] T. Luo, et al., *J. Appl. Phys.*, **109**-7(2011), 074321.

Heat conduction analysis for phononic crystal

Takuma Shiga

Department of Mechanical Engineering,

The University of Tokyo, Hongo, Bunkyo, Tokyo 113-8656

It has been known that phononic crystal (PnC) such as superlattice and thin-film with air-holes leads to significant modulation of phonon dispersion relation, which finally results in large reduction of thermal conductivity while crystallinity remains. In order to qualitatively evaluate a thermal conductivity reduction, we need to directly calculate thermal conductivity of PnC by means of microscopic simulation.

Before considering actual PnCs, we have considered heat conduction of silicon thin films with a thickness of an order of nanometer by performing anharmonic lattice dynamics (ALD) simulation. For interatomic force constants which are needed in ALD calculation, we employed the optimized Stillinger-Weber potential [1]. Surface orientation of silicon film is set to (001) and 20×20 sampling mech for two-dimensional Brillouin zone is chosen for the calculation of scattering rate [2].

Figure 1(a) shows phonon dispersion relation of silicon thin-film with the thickness of 10 nm. Because of the presence of surface, there are surface phonon modes labeled by S_1 - S_5 . From the analysis of eigenvectors, we identified S_1 and S_2 are Love and Rayleigh waves, respectively.

Figure 1(b) shows thickness-dependent in-plane thermal conductivity of silicon thin-films at $T=300$ K. We found that the thickness dependence is largely different with the convectional theory considering size effect.

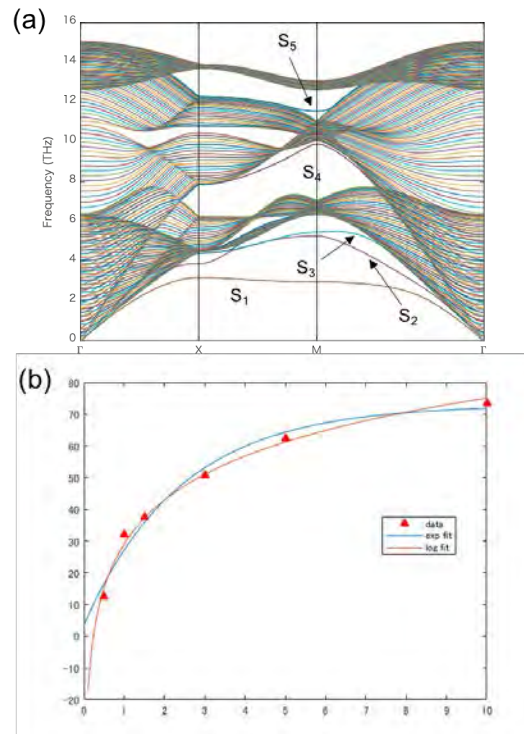


Fig. 1 (a) phonon dispersion relation of silicon thin film with 10 nm thickness. (b) thickness-dependent thermal conductivity at $T=300$ K.

References

- [1] Y. Lee, et al., Phys. Rev. B **85**, 125204 (2012).
- [2] T. Tadano, et al., J. Phys. Condens. Mater **26**, 225402 (2014).

Comprehensive study on transition between heat conduction and radiative heat transfer

Takuma Shiga

Department of Mechanical Engineering,

The University of Tokyo, Hongo, Bunkyo, Tokyo 113-8656

It has been so far revealed that thermal transport across two substrates with nanogap is known to be attributed by phonon-polariton resonance and tunneling of acoustic phonons and therefore such a near-field heat transfer can exceed black-body limit. In order to explore thermally-functionalized devices utilizing near-field heat transfer such as thermal switch, thermal rectifier, and so on, microscopic mechanism of transport regime changing from near-field heat transfer to heat conduction is needed to be investigated.

In order to realize such investigation, we chose a combination of spectral heat current and non-equilibrium molecular dynamics (NEMD) simulations. Figure 1 shows frequency-dependent spectral thermal boundary conductance at the interface across solid argon and heavy-mass argon crystals for different temperatures. As temperature increases, inelastic terms of interfacial scattering contribute to overall heat conduction. In addition, we calculated dielectric function of β -cristobalite SiO_2 on the basis of fluctuation-dissipation theorem. These two results are in good agreement with previous works [1,2], and

we realized the framework for investigating transition between heat conduction and near-field radiation.

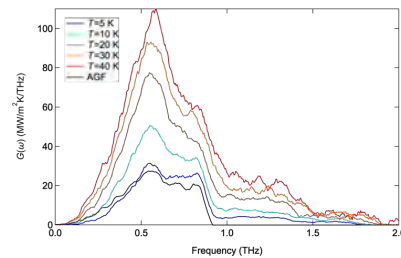


Fig. 1 Spectral thermal boundary conductance across the interface between Ar and heavy-Ar solids at different temperatures.

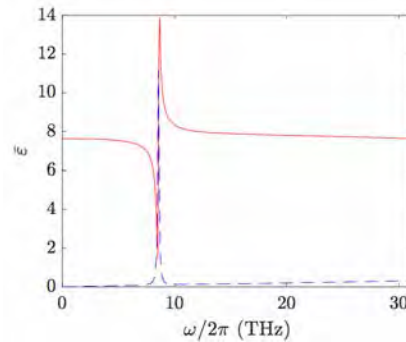


Fig. 2 Frequency-dependent dielectric function of β -cristobalite SiO_2 at $T=300$ K.

References

- [1] K. Sääskilähti, et al., Phys. Rev. B **90**, 134312 (2014).
- [2] Y. Chalopin, et al., Appl. Phys. Lett. **104**, 011905 (2014).

Ground-State Phase Diagram of an Anisotropic $S=1/2$ Two-Leg Ladder

Takashi Tonegawa

Professor Emeritus, Kobe Univ. and Visiting Professor, Osaka Prefecture Univ.

The purpose of this report is to explore the ground-state phase diagram of an anisotropic $S=1/2$ two-leg ladder by using mainly numerical methods. We express the Hamiltonian which describes this system as

$$\mathcal{H} = \sum_{j=1}^L \sum_{\ell=1,2} [\vec{S}_{j,\ell}, \vec{S}_{j+1,\ell}]_{\Delta} + J_r \sum_{j=1}^L [\vec{S}_{j,1}, \vec{S}_{j,2}]_{\Delta} \quad (1)$$

with

$$[\vec{S}_{j,\ell}, \vec{S}_{j',\ell'}]_{\Delta} \equiv S_{j,\ell}^x S_{j',\ell'}^x + S_{j,\ell}^y S_{j',\ell'}^y + \Delta S_{j,\ell}^z S_{j',\ell'}^z. \quad (2)$$

Here, $\vec{S}_{j,\ell} = (S_{j,\ell}^x, S_{j,\ell}^y, S_{j,\ell}^z)$ is the $S=1/2$ operator acting at the (j, ℓ) site assigned by rung j and leg $\ell (=1 \text{ or } 2)$; J_r denotes the magnitude of the rung interactions; Δ is the parameter which controls the the XXZ -type anisotropy of both the leg and rung interactions; L is the total number of rungs, which is assumed to be even. It is noted that the magnitude of the leg interactions is set to be unity as the unit of energy.

The phase diagrams on the Δ versus J_r plane have already been discussed by Li *et al.* [1] who have used the tensor network representation of quantum many-body states, and also and by Roy *et al.* [2] who have analyzed the variation of bipartite and multipartite entanglements. Unfortunately, however, their phase diagrams contain some unphysical results. Firstly, the XY phase region extends to the $\Delta > 0$ region, but this is physically unreasonable. Secondly, in Roy *et al.*'s phase diagram, the ferromagnetic phase does not exist, but this is also unreasonable since the ground state is the ferromagnetic state at least when $\Delta \ll -1$ and $J_r \gg 1$. Finally, the term ' $XY2$ ' in Li *et al.*'s phase diagram is misleading, because the $XY2$ state proposed originally by Schulz [3] is characterized not only by the formation of two-magnon bound state or, almost equivalently, the exponential-decay behavior of the transverse two-spin correlation function $\langle S_{j,\ell}^+ S_{j+j',\ell}^- \rangle$, but also by the fact that the nematic four-spin correlation function (with power-decay behavior) $\langle S_{j,1}^+ S_{j,2}^+ S_{j+j',1}^- S_{j+j',2}^- \rangle$ is more dominant

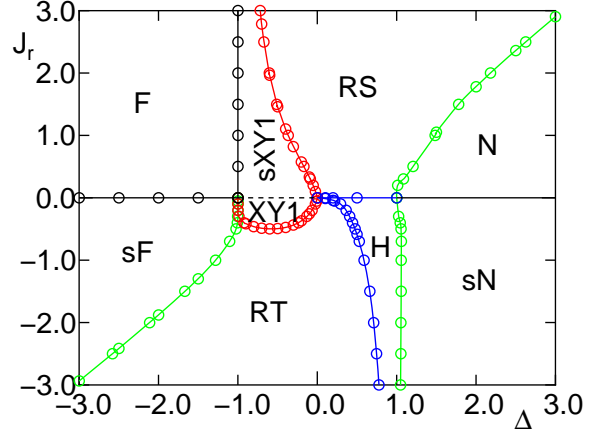


Figure 1: Ground-state phase diagram on the Δ versus J_r plane obtained in the present work.

than the longitudinal two-spin correlation function (with power-decay behavior) $\langle S_{j,\ell}^z S_{j+j',\ell}^z \rangle$. This is not the case for the $XY2$ state in Li *et al.*'s paper, and in our opinion the term ' $staggered XY1$ ' should be used (for details, see the last sentence of the next paragraph).

In this report we numerically determine the ground-state phase diagram as accurately as possible. Estimating the phase boundary lines, we make a variety of analyses such as the level spectroscopy (LS) analysis, the phenomenological renormalization-group (PRG) analysis, and so on, of the numerical data obtained by the exact diagonalization (ED) method. The resultant phase diagram is shown in Fig. 1. Here, the solid and dotted black lines are the first-order and second-order phase transition lines, respectively. In spite of the present simple system, this phase diagram is rather rich and consists of nine kinds of phases; these are the ferromagnetic (F), stripe ferromagnetic (sF), staggered $XY1$ (s $XY1$), $XY1$ ($XY1$), rung triplet (RT), rung singlet (RS), Haldane (H), Néel (N), and stripe Néel (sN) phases. The schematic picture of the sF, N, and sN states are given in Fig. 3 of Hiji *et al.*'s paper [4], which treats the case of isotropic rung interactions. (Also in this paper, the term ' $XY2$ ' is misleadingly used.) It

is noted that the sF state is essentially the N state. We note also that both the XY1 and sXY1 states are the usual Tomonaga-Luttinger liquid states, but in the former state the relation $(-1)^{j'} \langle S_{j,\ell}^+ S_{j+j',\ell'}^- \rangle > 0$ holds, while in the latter state $(-1)^{j'} (-1)^{\ell+\ell'} \langle S_{j,\ell}^+ S_{j+j',\ell'}^- \rangle > 0$ holds [4].

Let us now discuss how to numerically determine the phase boundary lines shown in Fig. 1. We denote, respectively, by $E_0^P(L, M)$ and $E_1^P(L, M)$, the lowest and second-lowest energy eigenvalues of the Hamiltonian \mathcal{H} under the periodic boundary condition within the subspace of L and M , where M is the total magnetization ($M=0, \pm 1, \dots, \pm L$). We also denote by $E_0^T(L, M, P)$ the lowest energy eigenvalue of \mathcal{H} under the twisted boundary condition within the subspace of L, M , and P , where $P(=\pm 1)$ is the eigenvalue of the space inversion operator with respect to the twisted bond. We have numerically calculated these energies for finite-size systems with up to $L=12$ spins by means of the ED method. The ground-state energy of the finite- L system is given by $E_0^P(L, L)$ in the F region and by $E_0^P(L, 0)$ in the other regions.

In the following way, we estimate the finite-size critical values of J_r (or Δ) for various values of Δ (or J_r), for each phase transition. Then, the phase boundary line for the transition is obtained by connecting the results for the $L \rightarrow \infty$ extrapolation of the finite-size critical values.

The phase transition between the H and RS phases as well as that between the H and RT phases is the Gaussian transition. In this case, the Kitazawa's LS method [5] is very powerful to determine the phase boundary lines. That is to say, we numerically solve the equation

$$E_0^T(L, 0, +1) = E_0^T(L, 0, -1) \quad (3)$$

to calculate the finite-size critical values. The results of our calculations show that, for the transition between the H and RS phases, the finite-critical value of J_r for a given value of Δ ($0.0 < \Delta < 1.0$) is equal to 0.0, independently of L .

Since the phase transition between the RS and sXY1 phases and that between the RT and XY1 phases are of the Berezinskii-Kosterlitz-Thouless type [6], the phase transition line can be very accurately estimated by using the LS method developed by Nomura and Kitazawa [7]. Then, the finite-size critical values are calculated from

$$E_0^P(L, 2) = E_0^T(L, 0, +1). \quad (4)$$

The three phase transitions between the RS and N phases, between the H and sN phases, and between the RT and sF phases are the 2D Ising-type transitions. Then, it is well known that the phase transition lines are determined by the PRG

method [8]. Then, to estimate the finite-size critical values, we solve the PRG equation,

$$L \Delta E^P(L, 0) = (L+2) \Delta E^P(L+2, 0), \quad (5)$$

where

$$\Delta E^P(L, 0) = E_1^P(L, 0) - E_0^P(L, 0). \quad (6)$$

It is apparent that the finite-size critical values for the phase transitions between the F and sXY1 phases and between the F and sF phases are calculated from

$$E_0^P(L, L) = E_0^P(L, 0). \quad (7)$$

The results show that, for the transition between the F and sXY1 phases, the finite-critical value of Δ for a given value of J_r ($0.0 < J_r$) is equal to -1.0 , independently of L . Furthermore, for the transition between the F and sF phases, the finite-size critical value of J_r for a given value of Δ ($\Delta < -1.0$) is equal to 0.0, independently of L .

Lastly, we note that the phase transition between the sN and N phases is of the first-order, while that between the XY1 and sXY1 phase is of the second-order. These have been discussed in detail in Hijii *et al.*'s paper [4].

Invaluable discussions with K. Okamoto, K. Nomura, and T. Sakai are gratefully acknowledged.

[1] S.-H. Li, Q.-Q. Shi, M. T. Batchelor, and H.-Q. Zhou: *New J. Phys.* **19** (2017) 113027.

[2] S. S. Roy, H. S. Dhar, D. Rakshit, A. Sen(De), and U. Sen: *J. Magn. Magn. Mater.* **444** (2017) 227.

[3] H. J. Schulz: *Phys. Rev. B* **34** (1986) 6372.

[4] K. Hijii, A. Kitazawa, and K. Nomura: *Phys. Rev. B* **72** (2005) 014449.

[5] A. Kitazawa: *J. Phys. A* **30** (1997) L285.

[6] Z. L. Berezinskii: *Sov. Phys.-JETP* **34** (1971) 610; J. M. Kosterlitz and D. J. Thouless: *J. Phys. C: Solid State Phys.* **6** (1973) 1181.

[7] K. Nomura and A. Kitazawa: *J. Phys. A: Math. Gen.* **31** (1998) 7341.

[8] M. P. Nightingale: *Physica A* **83** (1976) 561.

Spin multipole dynamics and spin transport in frustrated magnets

Hiroaki ONISHI

*Advanced Science Research Center, Japan Atomic Energy Agency
Tokai, Ibaraki 319-1195*

In a spin-1/2 J_1 - J_2 Heisenberg chain with ferromagnetic J_1 and antiferromagnetic J_2 in a magnetic field, there appear a series of spin multipole liquid ground states, i.e., quadrupole, octupole, hexadecapole, etc. To clarify magnetic and transport properties in the quadrupole state, we have studied spin and quadrupole excitation spectra [1] and spin Drude weight [2] by numerical methods. We have argued that low-energy excitations are governed by bound two-magnon pairs, so that magnon pairs would carry spin current.

Here, we extend our focus to the octupole regime. By using a dynamical DMRG method, we examine the dynamical octupole structure factor at zero temperature, given by

$$O^{---}(q, \omega) = -\text{Im} \frac{1}{\pi} \langle 0 | O_q^{---\dagger} \frac{1}{\omega + E_0 - H + i\eta} O_q^{---} | 0 \rangle,$$

where O_q^{---} is the Fourier transform of $O_i^{---} = S_i^- S_{i+1}^- S_{i+2}^-$. Note that we perform one DMRG run to obtain the spectral weight for a set of q and ω , so that we need to do many runs to scan a wide range of the q - ω space. The computations are accelerated by parallel simulations using the system B of the ISSP supercomputer.

We present intensity plots of $O^{---}(q, \omega)$ in Fig. 1. We find a finite gap in the quadrupole regime [Fig. 1(a)], while we observe a gapless mode at $q = \pi$ in the octupole regime in accordance with quasi-long-range antiferro-octupole correlations [Fig. 1(b)]. Since a bound three-magnon cluster is excited with zero energy in

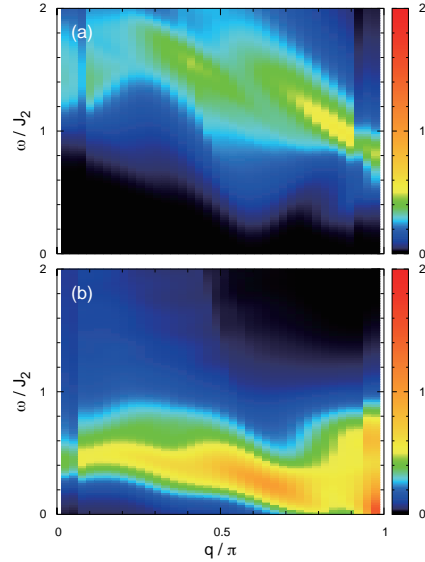


Figure 1: $O^{---}(q, \omega)$ at (a) $J_1/J_2 = -2$ and $M = 0.35$ and (b) $J_1/J_2 = -3$ and $M = 0.35$, where M is the magnetization. DMRG results with 40 sites.

the octupole state, we envisage that magnon clusters would contribute to the spin transport. The analyses of current correlation functions and wavepacket dynamics are also on going to clarify the relationship between magnetic and transport properties.

References

- [1] H. Onishi, J. Phys. Soc. Jpn. **84**, 083702 (2015); J. Phys.: Conf. Ser. **592**, 012109 (2015); Physica B **536**, 346 (2018).
- [2] H. Onishi, J. Magn. Magn. Mater. **479**, 88 (2019).

Molecular Dynamics Simulation of Ferroelectrics Using a Shell Model V

T. Hashimoto

*Research Center for Computational Design of Advanced Functional Materials (CD-FMat),
National Institute of Advanced Industrial Science and Technology (AIST),
Tsukuba Central 2, 1-1-1 Umezono, Tsukuba, Ibaraki 305-8568, Japan*

Amorphous BaTiO₃ can be formed by sputtering. Its structure is assumed to be a random network of TiO_{*n*} local bonding units (LBUs). By X-ray absorption fine-structure (XAFS) spectroscopy, *n* was found to be 6[1]. But, due to the experimental difficulty, the LBU linkage for amorphous BaTiO₃ is not clear. We have developed a classical molecular dynamics (MD) simulation code that can handle shell models that reproduce physical properties of BaTiO₃[2], and applied it to the study of amorphous BaTiO₃.

In the shell model, each atom is composed of a core and a shell. The intra-atomic core-shell interaction is expressed by $V(r) = c_2 r^2/2 + c_4 r^4/24$, where r is the core-shell distance and c_2 and c_4 are parameters. The inter-atomic interaction is through the Coulomb interaction and the Buckingham type shell-shell interaction $V(r) = A \exp(-r/\rho) - C/r^6$, where r is the inter-atomic shell-shell distance and A , ρ , and C are parameters. The computations were carried out in constant temperature and constant pressure (NPT) ensembles. The pressure and the temperature were controlled by the Parrinello-Rahman method and the massive Nose-Hoover chain method, respectively. The externally applied pressure was set to 0 Pa. Because we cooled the system slow enough, the densities were very close to each other, and the susceptibilities were also very close to each other, both in agreement with experiments[3].

As shown in Fig. 1, the probability of TiO₆

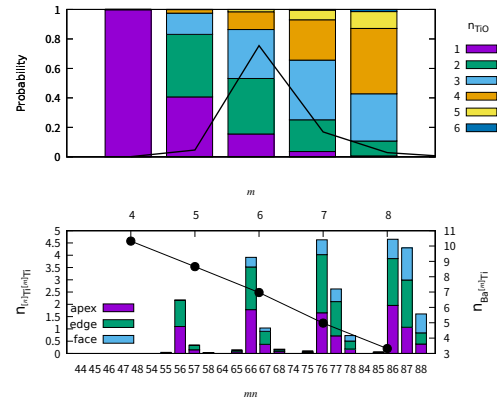


Figure 1: The probability of $[m]$ Ti and the number of Ti around O (n_{TiO}) (upper panel), and $n_{[m]\text{Ti}[m]\text{Ti}}$ and $n_{\text{Ba}^{[m]\text{Ti}}}$ (lower panel).

was the largest, and the probability of NBOs (purple) was larger for smaller m . The number of Ti (Ba) around $[m]$ Ti was larger (smaller) for larger m . $[7]$ Ti and $[8]$ Ti were in an O rich, Ti rich, and Ba poor environment with fewer NBOs and many edge or face-sharings, while $[5]$ Ti was in an O poor, Ti poor, and Ba rich environment with many NBOs.

- [1] A. I. Frenkel *et al.*: Phys. Rev. B **71** (2005) 024116.
- [2] S. Tinte *et al.*: J. Phys.: Condens. Matter **16** (2004) 3495.
- [3] T. Hashimoto and H. Moriwake: Physica B: Condens. Matter **579** (2020) 411799.

Transport properties of the antiferromagnetic classical XXZ model in two dimensions

Kazushi AOYAMA

*Department of Earth and Space Science, Graduate School of Science, Osaka University
Machikaneyama-cho, Toyonaka-shi, Osaka 560-0043*

Transport phenomena in magnetic systems reflect dynamical properties of interacting spins, such as magnetic excitations and fluctuations. In this work, we theoretically investigate transport properties of two-dimensional antiferromagnetic insulators, putting emphasis on how the occurrence of a phase transition is reflected in spin and thermal transports. In the classical nearest-neighbor (NN) antiferromagnetic XXZ model on the square lattice,

$$\mathcal{H} = -J \sum_{\langle i,j \rangle} (S_i^x S_j^x + S_i^y S_j^y + \Delta S_i^z S_j^z), \quad (1)$$

the anisotropy Δ plays a role to control the universality class of the transition, i.e., either a second-order transition at T_N into a magnetically ordered state or the Kosterlitz-Thouless (KT) transition at T_{KT} , which respectively occur for the Ising-type ($\Delta > 1$) and XY -type ($\Delta < 1$) anisotropies, while for the isotropic Heisenberg case of $\Delta = 1$, a phase transition does not occur at any finite temperature. The dynamics of the spins \mathbf{S}_i is determined by the following semiclassical equation of motion:

$$\begin{aligned} \frac{d\mathbf{S}_i}{dt} &= \mathbf{S}_i \times \mathbf{H}_i^{\text{eff}}, \\ \mathbf{H}_i^{\text{eff}} &= J \sum_{j \in N(i)} (S_j^x, S_j^y, \Delta S_j^z), \end{aligned} \quad (2)$$

where $N(i)$ denotes all the NN sites of i .

The spin current and the associated spin conductivity $\sigma_{\mu\nu}^s$ are respectively given by

$$\begin{aligned} \mathbf{J}_s^z(t) &= J \sum_{\langle i,j \rangle} \mathbf{r}_{ij} (\mathbf{S}_i \times \mathbf{S}_j)^z, \\ \sigma_{\mu\nu}^s &= \frac{1}{T L^2} \int_0^\infty dt \langle J_{s,\nu}^z(0) J_{s,\mu}^z(t) \rangle, \end{aligned} \quad (3)$$

where \mathbf{r}_{ij} and L denote a vector connecting two sites i and j and the linear system size, respectively. We numerically integrate Eq. (2) with initial equilibrium spin configurations generated by Monte Carlo simulations and calculate the time correlations $\langle J_{s,\nu}^z(0) J_{s,\mu}^z(t) \rangle$ at each time step. By using the second order symplectic method, we perform long-time integrations typically up to $t = 100|J|^{-1} - 800|J|^{-1}$ with the time step $\delta t = 0.01|J|^{-1}$ until the time correlations $\langle J_{s,\nu}^z(0) J_{s,\mu}^z(t) \rangle$ is completely lost. The thermal conductivity $\kappa_{\mu\nu}$ can also be calculated in a similar way.

It is found that the spin current probes the difference in the ordering properties, while the thermal current does not. Figure 1 shows the temperature dependence of the longitudinal spin conductivity σ_{xx}^s for the Ising-type ($\Delta = 1.05$), XY -type ($\Delta = 0.95$), and Heisenberg-type ($\Delta = 1$) spin systems. For the XY -type anisotropy, σ_{xx}^s exhibits a divergence at T_{KT} of the exponential form, $\sigma_{xx}^s \propto \exp[B/\sqrt{T/T_{KT} - 1}]$ with $B = \mathcal{O}(1)$, while for the Ising-type anisotropy, the temperature dependence of σ_{xx}^s is almost monotonic without showing a clear anomaly at T_N and such a monotonic behavior is also the case in the Heisenberg-type spin system [see the dashed curve in Fig. 1 (c)] [1]. Noting that in the XY -type spin system, the inter-free-vortex distance ξ_s diverges toward T_{KT} in the form of $\xi_s \sim \exp[(\pi/2)/\sqrt{T/T_{KT} - 1}]$, the significant enhancement of σ_{xx}^s at T_{KT} can be understood as a manifestation of the topological nature of

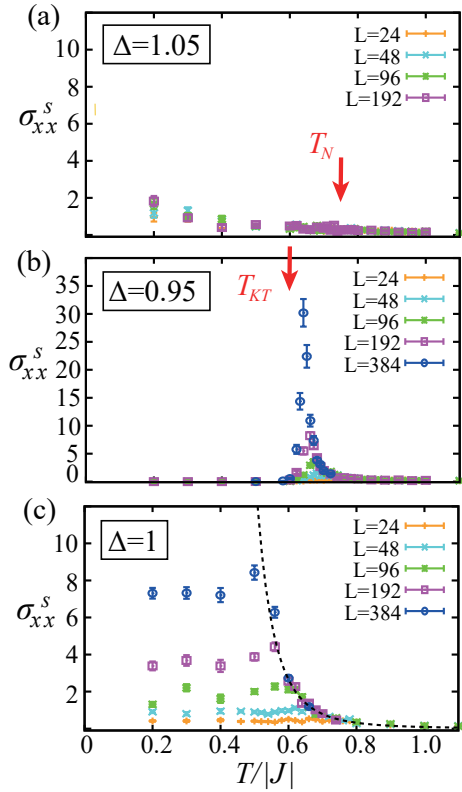


Figure 1: The temperature dependence of the longitudinal spin-current conductivity $\sigma_{\mu\mu}^s$ in the (a) Ising-type ($\Delta = 1.05$), (b) XY-type ($\Delta = 0.95$), and (c) Heisenberg-type ($\Delta = 1$) spin systems. In (a) and (b), red arrows indicate the magnetic and KT transition temperatures, $T_N/|J| \simeq 0.75$ and $T_{KT}/|J| \simeq 0.6$, respectively. In (c), a dashed curve represents the $\sigma_{xx}^s(T)$ curve extrapolated to the thermodynamic limit of $L \rightarrow \infty$.

a vortex whose lifetime τ_v gets longer toward T_{KT} due to the diffusive vortex motion characterized by the relation $\tau_v \propto \xi_s^2$.

Such an anomalous spin transport is also found in the NN antiferromagnetic Heisenberg model on the triangular lattice. In contrast to the XXZ antiferromagnets on the square lattice, the triangular-lattice antiferromagnet is a frustrated system. In the latter frustrated system, a KT-type binding-unbinding topological transition of \mathbb{Z}_2 vortices is predicted to occur at T_v , although spins do not order except at $T = 0$ with the spin correlation length ξ_s be-

ing finite at any finite temperature. It is found that the longitudinal spin-current conductivity exhibits a divergence at the \mathbb{Z}_2 -vortex transition temperature T_v , while the thermal conductivity only shows a monotonic temperature dependence with no clear anomaly at T_v [2].

Our results suggest the strong association between the spin transport and the binding-unbinding topological transition of vortex excitations.

References

- [1] K. Aoyama and H. Kawamura, Phys. Rev. B **100**, 144416 (2019).
- [2] K. Aoyama and H. Kawamura, Phys. Rev. Lett. **124**, 047202 (2020).

Study on Dynamic Mechanical Properties of Slide-Ring Gels using Coarse-Grained MD Simulations

Koichi Mayumi

Material Innovation Research Center (MIRC) and Department of Advanced Materials Science, Graduate School of Frontier Sciences, The University of Tokyo, 5-1-5 Kashiwanoha, Kashiwa, Chiba 277-8561, Japan

Polyrotaxane (PR) is a supramolecular polymer composed of many ring molecules, α -cyclodextrins (CDs) and one linear polymer, poly (ethylene glycol) (PEG), threading on these rings. By cross-linking rings belonging to PRs, Okumura and Ito succeeded in fabricating supramolecular polymer gels called slide-ring gels (SR gels)[1]. SR gels do not have direct cross-links between polymer chains, but topological interlock by figure-of-eight shaped cross-links composed of two ring molecules. Because SR gels have slidable cross-links, they show unique mechanical properties. For example, SR gels show lower Young's moduli than conventional fixed cross-linking polymer gels. So far, no molecular models have succeeded in representing the quantitative relationship between the sliding motion of the cross-linking points and the low Young's moduli of SR gels. In this study, we investigate the relationship between the sliding of figure-of-eight cross-links and Young's moduli by means of coarse-grained molecular dynamics simulations.

For the modeling of SR gels, we fabricated

a coarse-grained model of PR with 7-membered rings which can slide freely along the axial chain[2]. By cross-linking rings of the PRs, we prepared SR gels. We conducted uniaxial elongation simulations of the SR gels, and obtained Young's moduli E_{SR} , which were lower than theoretical values by the classical affine network model. Then, we analyzed the partial chain length distribution in SR gels under uniaxial deformation. While the distribution was described by a single exponential function in un-deformed state, while it became bimodal by stretching: longer and shorter chains appeared.

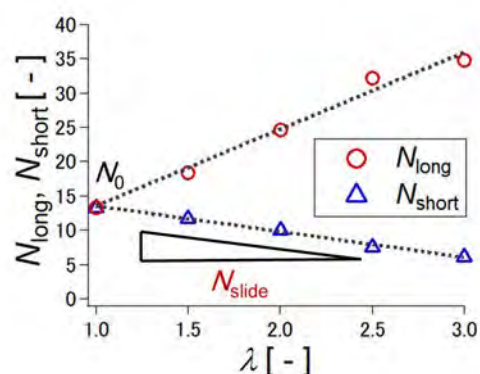


Fig. 1. λ dependence of the average length of long and short chain.

The average length of short and long chains

change linearly with λ (Fig.1). We defined this decay rate of the segment number of the shorter partial chain length as N_{slide} . By considering the chain movement through the slidable cross-links, we have succeeded in establishing a molecular model for SR gels based on the classical three chain model [3] (Fig. 2.), and obtained the simple equation :

$$E_{SR} = E_{Affine} \left(1 - \frac{N_{slide}}{N_0}\right)^2$$

Where E_{Affine} is the theoretical prediction by classical three-chain model, N_0 is the average partial chain length in undeformed state.

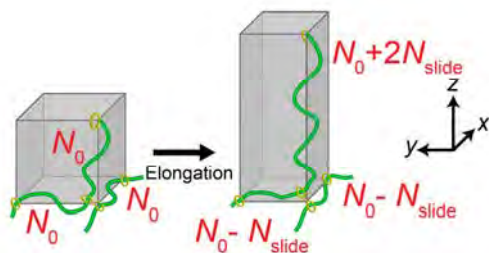


Fig. 2. Schematic illustration of the proposed

In order to verify this equation, we compare the Young's moduli obtained from the simulation results and theoretical estimation. We found that this estimation is realistic enough to reproduce the simulation results. Thus we succeeded in quantitatively evaluating the effect of the sliding on the elasticity of the slide-ring gels.

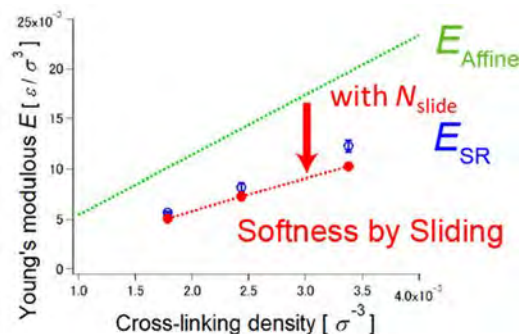


Fig. 3. The Young's moduli of SR gels plotted against the cross-linking density.

References

1. Okumura Y.; Ito K. *Adv. Mater.*, **2001**, *13*, 485
2. Y. Yasuda et al., *Macromolecules*, **2019**, *52*, 3787.
3. James, H. M.; Guth, E. *J. Chem. Phys.* **1943**, *11*, 455.
4. Y. Yasuda et al., *ACS Macro Letters*, under review.

Study on Microscopic Dynamics of Polyrotaxanes using Full-Atomistic MD Simulations

Koichi Mayumi

Material Innovation Research Center (MIRC) and Department of Advanced Materials Science, Graduate School of Frontier Sciences, The University of Tokyo, 5-1-5 Kashiwanoha, Kashiwa, Chiba 277-8561, Japan

Polyrotaxane (PR) is a supramolecular polymer which consists of an axial linear polymer and multiple ring-shaped molecules threaded on the chain. A unique feature of PR is that the rings can slide and rotate along the axial polymer, and this feature has been utilized for fabricating biomaterials[1] and topological gels[2]. However, the internal dynamics such as the sliding and rotation have not been disclosed yet. In this study, we investigated the internal molecular dynamics of PR composed of α -cyclodextrins (CDs) and poly (ethylene glycol) (PEG) chain in solution by means of full-atomistic molecular dynamics (MD) simulations [3].

We measured the mean squared displacement and estimated the diffusion coefficient of free PEG, free CD, and CD in PR. The simulation results agree well with the diffusion coefficients measured by the quasi-elastic neutron scattering experiment (Table 1). From this result, we consider that our model is realistic enough. Then we tried the analysis of intramolecular motion: the sliding dynamics.

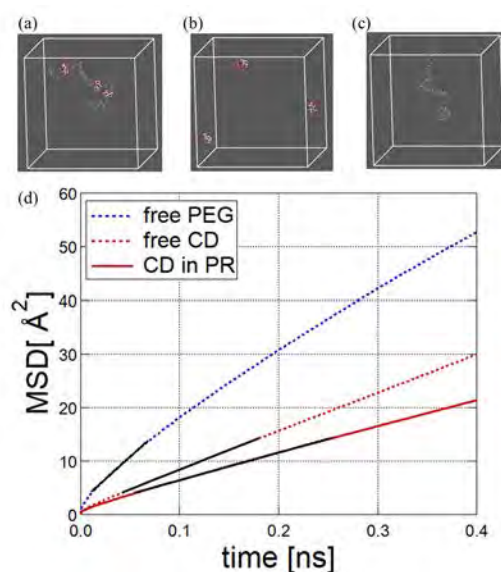


Figure 1. Simulation snapshot of the full-atomistic model for (a) PRs, (b) free CD, (c) free PEG, and (d) MSD for translational diffusion of CD in PR (red solid line), free CD (red dotted line), and free PEG (blue dotted line)

Table 1. Diffusion coefficients of CD in PR, free CD, and free PEG from the quasi-elastic neutron scattering (QENS) experiment and MD simulation.

Sample	Free PEG	Free CD	CD in PR
$D_{\text{QENS}} [10^{-7} \text{ cm}^2/\text{s}]$	40	13	11
$D_{\text{MD}} [10^{-7} \text{ cm}^2/\text{s}]$	27	12	8.6

In order to evaluate the sliding dynamics in PR, we tracked the one-dimensional trajectory of CD along PEG. The mean squared displacement corresponding to the sliding motion ($\text{MSD}_{\text{slide}}$) increased linearly with time, which suggests that the sliding motion is diffusive (Fig. 2.). From the time dependence of $\text{MSD}_{\text{slide}}$, we calculated from the diffusion coefficient for the sliding motion D_{slide} at 300 K as $1.42 \text{ \AA}^2/\text{ns}$, which is quite smaller value than that of the translational diffusion of CD in PR.

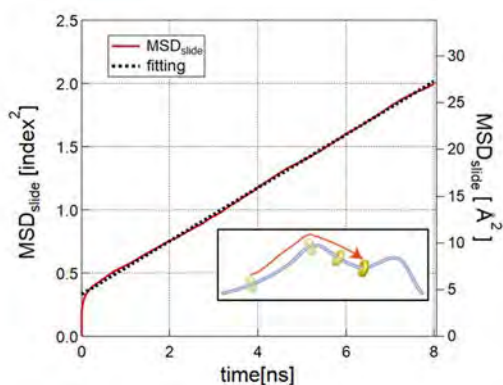


Fig. 2. $\text{MSD}_{\text{slide}}$ of CD along the PEG chain.

In order to clarify the molecular origin of this slow sliding dynamics, we analyzed the temperature dependence of D_{slide} (Fig. 3). We found that the diffusion coefficients of the sliding dynamics was dominated by the energy barrier between CD and PEG. This energy barrier was 8.92 kJ/mol , which corresponds to the energy potential barrier for CD on PEG, $2 \text{ kcal/mol} = 8.37 \text{ kJ/mol}$ [4].

In conclusion, we succeeded in representing the diffusion coefficient for the sliding motion of PR by the combination of the jump diffusion term with the Einstein-Stokes equation:

$$D_{\text{slide}} \propto \frac{k_B T}{\eta} \exp\left(-\frac{E_a}{k_B T}\right)$$

This relationship is valuable for controlling the sliding speed in polyrotaxanes.

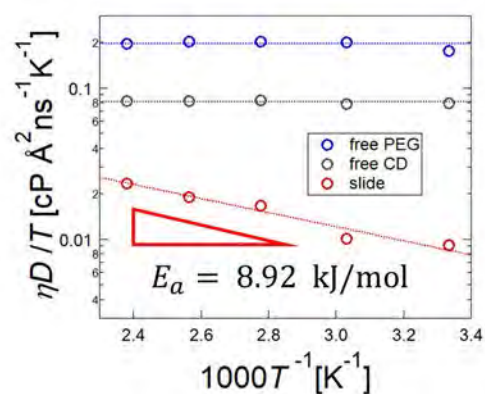


Fig. 3 Temperature dependence of the diffusion coefficient of free CD, free PEG and sliding motion.

References

- (1). Yui, N. et al., *Chem. Eur. J.* **2006**, *12*, 6730
- (2). Okumura, Y. et al., *Adv. Mater.* **2001**, *13*, 485
- (3). Yasuda, Y. et al., *J. Am. Chem. Soc.* **2019**, *141* (24), 9655.
- (4). Liu, P. et al., *J. Phys. Chem. C* **2012**, *116*, 17913.

Comparison of X-ray pinhole topographs experimentally obtained and computer-simulated based on the Ewald-Laue and Takagi dynamical theories

Kouhei OKITSU

*Institute of Engineering Innovation, School of Engineering,
The University of Tokyo, 2-11-16 Yayoi Bunkyo-ku Tokyo 113-8656*

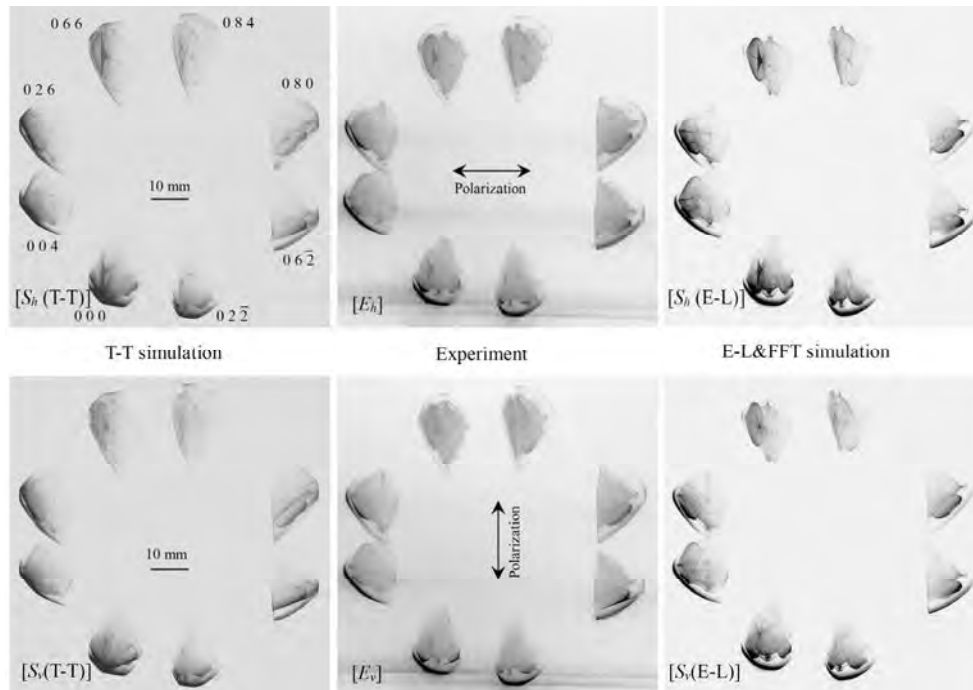


Fig.1 $[S_x(\text{T-T})]$, $[E_x]$ and $[S_x(\text{E-L})]$ ($x \in \{h, v\}$) show T-T simulated, experimentally obtained and E-L&FFT simulated eight-beam pinhole topographs for horizontally ($x = h$) and vertically ($x = v$) polarized incident X-rays [2].

The present author verified the simple relation between the n -beam Ewald-Laue (E-L) and Takagi (T-T) X-ray dynamical theories explicitly [1-4] for the first time. It can be described with Fourier transformation. Then, the behavior of diffracted X-rays in a perfect crystal can be described by both the E-L and T-T dynamical theories.

Figs. 1 $[S_x(\text{T-T})]$, $[E_x]$ and $[S_x(\text{E-L})]$ ($x \in \{h, v\}$) show T-T simulated, experimentally obtained and E-L&FFT simulated eight-beam pinhole topographs for horizontally ($x = h$) and vertically

($x = v$) polarized incident X-rays whose photon energy was adjusted or assumed to be 18.245 keV. The experiment was performed with the polarization state of the monochromated synchrotron radiation by using the four-quadrant phase retarder system [1, 2, 4] at the BL09XU of SPring-8. A $[1 \ -1 \ 1]$ -oriented floating zone silicon crystal with a thickness of 9.6 mm was used as the sample. The indices of reflections are as described in Fig. 1 $[S_h(\text{T-T})]$. The T-T simulated topographs were computed by integrating the T-T equation

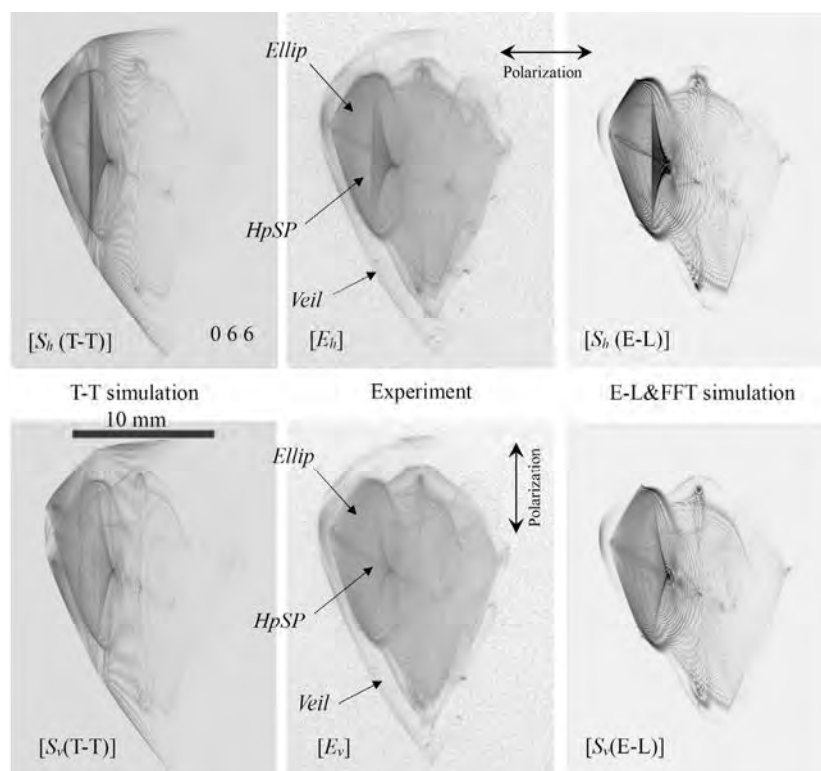


Fig. 2 Enlargement of the 0 6 6 transmitted-reflected images in Fig. 1 [2].

with the finite-difference method. However, the E-L&FFT topographs were obtained by fast Fourier transforming the solution of the E-L dynamical theory.

Figs. 2 $[S_x(T-T)]$, $[E_x]$ and $[S_x(E-L)]$ are enlargements of the 0 6 6 transmitted-reflected images in Figs. 1 $[S_x(T-T)]$, $[E_x]$ and $[S_x(E-L)]$. Good agreements among Figs. 2 $[S_x(T-T)]$, $[E_x]$ and $[S_x(E-L)]$ are found both for $x=h$ and for $x=v$, respectively. However, evident discrepancies are also found between the cases of $x=h$ and $x=v$.

The present author has a hypothesis that too large R factors for protein crystals is caused by interferences of multiple-reflected wave fields and bankruptcy of the two-beam approximation that has been used for over 100 years. The present author has prepared to verify this hypothesis

concerning the too large R factors in protein crystallography by estimating them with n -beam approximation in place of the conventional two-beam approximation.

References

- [1] K. Okitsu, Y. Imai, and Y. Yoda: *Recent Advances in Crystallography*, (2012) pp. 67-86. InTech Open. <http://dx.doi.org/10.5772/47846>.
- [2] K. Okitsu, Y. Imai, Y. Yoda and Y. Ueji: *Acta Cryst.* **A75** (2019) 474-482; <https://doi.org/10.1107/S2053273319001499>.
- [3] K. Okitsu, Y. Imai, and Y. Yoda: *Acta Cryst.* **A75** (2019) 483-488; <https://doi.org/10.1107/S2053273319002936>.
- [4] K. Okitsu: *J. Jpn. Soc. Synchrotron Rad. Res.* **33** (2020) 61-80 [Invited].

Numerical verification of the higher-order ETH in quantum XXZ spin ladder

Eiki IYODA

*Department of Physics, Tokai University
Kitakaname, Hiratsuka-shi, Kanagawa 259-1292*

Recently, isolated quantum many-body systems, which are realized in artificial systems such as cold-atoms or superconducting qubits, have attracted much attention, because they are useful to study fundamental problems in statistical mechanics. Especially, it has been shown that even an isolated quantum many-body system exhibits thermalization. The eigenstate thermalization hypothesis (ETH) [1] is a promising mechanism of thermalization, which is closely related to quantum chaos. Many numerical studies have shown that ETH holds in non-integrable systems.

We propose a higher-order generalization of the ETH, to which we refer as the k -ETH ($k = 1, 2, \dots$) [3]. The lowest order ETH ($k = 1$) is the conventional ETH. The k -ETH gives many conditions which are obtained by comparing Hamiltonian dynamics with the Haar-random unitary of the k -fold channel. As a non-trivial contribution of the higher-order ETH, we show that the Page correction of the k th Renyi entanglement entropy of individual energy eigenstates originates from the k -ETH.

In this study, we numerically investigated 2-ETH for the one-dimensional spin-1/2 Heisenberg XXZ ladder model, which is composed by two chains whose lengths are p and $p + 1$ respectively. In order to numerically investigate 2-ETH, we should discuss finite size scaling of indicators of 2-ETH by changing the system size. The 2-ETH gives many conditions. For example, 2-ETH states that diagonal and off-diagonal matrix elements such as

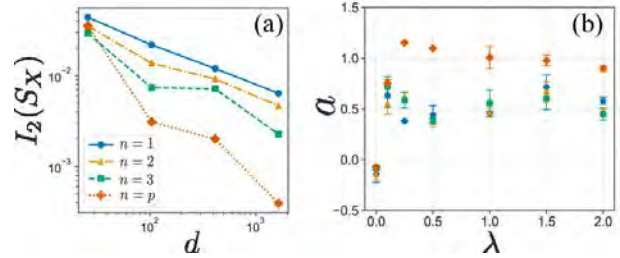


Figure 1: (a) d -dependence of $I_2(S_X)$. (b) λ -dependence of a .

$\langle E_i E_j | O | E_i E_j \rangle$ equal some value. There are totally d^2 equalities, where d is the dimension of the energy shell. We adopt $I_2(O)$ as an indicator of 2-ETH, which is defined as the maximum value of the deviation of the d^2 equalities. $I_2(O)$ is a straightforward extension of the indicator of strong 1-ETH [2]. By numerically exact diagonalization, we calculate $I_2(O)$ by changing parameters about energy shell and the Hamiltonian.

We numerically calculated $I_2(S_X)$, where S_X is the partial swap operator which swaps the region X between the original system and a replicated system. Figure 1(a) shows the d -dependence of $I_2(S_X)$ with $\lambda = 1$, where λ is the coupling constant in the rungs and tunes the integrability of the model. In non-integrable systems, the indicator $I_2(S_X)$ decays polynomially with d , which implies the 2-ETH for S_X holds in non-integrable systems.

We fit the numerical data of $\log I_2$ against a fitting function $f(d) := -a \log d + b$. Figure 1(b) shows the λ -dependence of the exponent

a . In the non-integrable cases ($\lambda \neq 0$), the exponent a takes a sufficiently large value. Especially, when the size of the region X equals p , the exponent $a \sim 1$, which is consistent with the typicality prediction.

In this report, we have numerically shown that the higher-order ETH holds by using the indicator $I_2(O)$. Numerical studies about finite size scaling with other indicators and the weaker version of higher-order ETH are left as future issues.

References

- [1] M. Rigol, V. Dunjko, and M. Olshanii, Nature **452**, 854 (2008).
- [2] H. Kim, T. N. Ikeda, and D. A. Huse, Phys. Rev. E **90**, 052105 (2014).
- [3] K. Kazuya, E. Iyoda, T. Sagawa, arXiv:1911.10755.

Analysis on Structuring and Dynamics of Ionic Liquid Forming Electric Double Layer as a Local Interfacial Field

Ken-ichi FUKUI

Department of Materials Engineering Science, Graduate School of Engineering Science,
Osaka University, Machikaneyama, Toyonaka, Osaka 560-8531

The interfacial ionic-liquid (IL) behavior causing bias stress in the electric double layer organic field effect transistor (EDL-OFET) (Fig. 1) has been investigated in the molecular scale using MD simulations combined with experimental techniques [1].

The MD simulations were performed with GROMACS-5.0.7. The rubrene substrate was of linear dimensions $7.2165 \times 7.1930 \times 2.7760$ nm. EMIM-FSI ion pairs were sandwiched between the rubrene substrate (2.7760 nm) and vacuum layer (~9.5 nm). Simulations were performed for the uncharged rubrene surface ($\sigma = 0$) and for the positively charged surfaces ($\sigma = 0.6, 1.2,$ and $1.8 \mu\text{C cm}^{-2}$). Single point charges were placed on each carbon atom consisting of a tetracene backbone of a rubrene molecule corresponding to the HOMO of rubrene, and its magnitude was determined by the overall surface charge density σ . The systems were equilibrated at a constant volume for 100 ps, followed by a constant volume simulation for 20 ns.

Fig. 2 shows the plane-averaged charge density profiles with respect to the amount of injected charge into rubrene electrode and number density profiles of atoms in EMIM cation and FSI anion, respectively, at the charge density of $1.8 \mu\text{C cm}^{-2}$. At this potential, EMIM cations and FSI anions form a checkerboard structure with their major molecular axis perpendicular to the surface. Thus, negative atoms of $-\text{SO}_2\text{F}$ of FSI anions are pointing the rubrene surface ($\text{O} \times 2$ and F). This configuration probably causes the bias stress by efficiently trap the hole carrier at the interface with structured interfacial IL as observed by force curve measurements with EC-FM-AFM [1].

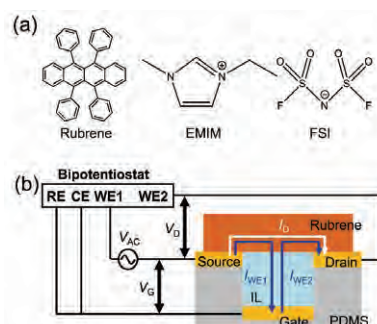


Fig. 1: (a) Molecular structures of rubrene and EMIM-FSI. (b) Schematic of EDL-OFET using rubrene semiconductor and IL gate dielectrics.

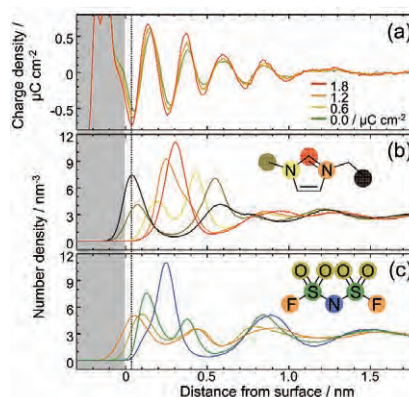


Fig. 2: (a) Plane-averaged charge density profiles with respect to the amount of injected charge into rubrene electrode. (b),(c) Number density profiles of atoms in the EMIM cation and the FSI anion, respectively, at the charge density of $1.8 \mu\text{C cm}^{-2}$. Each line corresponds to the shaded atom with the same color. Gray-shaded area is the rubrene-electrode region. Dotted line at $z = 0.04$ nm suggests the position of negative charge density next to the rubrene electrode surface.

Reference

- [1] D. Okaue, I. Tanabe, S. Ono, K. Sakamoto, T. Sato, A. Imanishi, Y. Morikawa, J. Takeya, K. Fukui, *J. Phys. Chem. C* **124** (2020) 2543.

Calculation of ordered structures and their optical properties of soft materials

Jun-ichi FUKUDA

Department of Physics, Kyushu University, Motoooka 744, Nishi-ku, Fukuoka 819-0395

This year we have studied how a topological defect in a thin cell of a nematic liquid crystal look under optical microscope. Such defects are commonly observed in experimental labs studying liquid crystals. However, usual identifications of topological defects in a nematic liquid crystal relies on the observation of the orientation profile *around* the topological defects. How the image should be *at the center* of topological defects has given little attention so far. It is because the length characterizing the defect core is $\sim 10\text{nm}$, much smaller than the resolution of optical imaging.

We have made use of the technique developed previously [1] which reproduced excellently the microscope images of a thin cell of a chiral liquid crystal. We solve the full Maxwell equations for the electromagnetic wave to investigate the response of the liquid crystal to monochromatic incident light with given wavevector. By doing calculations for different incident wavevectors, one can construct a microscope image, whose details are presented in Ref. [1].

Calculations have been done to investigate

the effect of the variation of the numerical aperture. We have found that the core of a topological defect appears as a dark spot, and also that the spot becomes sharper as the numerical aperture increases. More details will be presented in a manuscript in preparation.

Another subject is the lattice orientation of a cubic lattice of cholesteric blue phase liquid crystal in contact with unidirectionally orienting surfaces. Previous experiments found that the cubic lattice exhibits specific orientation with respect to the direction of the surface orientation. We have simulated the structures of cholesteric blue phases in such a setup using the Landau-de Gennes theory describing the orientational order of the liquid crystal by a second-rank tensor. This study is now under way.

References

- [1] A. Nych, J. Fukuda, U. Ognysta, S. Žumer and I Mušević, *Nature Phys.* **13**, 1215 (2017).
- [2] M. Takahashi *et al.* *J. Phys. D: Appl. Phys.* **51**, 104003 (2018)

Ultrafast relaxation of inhomogeneous electron distribution around the Dirac cone in graphene

Shota ONO

*Department of Electrical, Electronic and Computer Engineering, Gifu University
Gifu 501-1193*

It has been known that the inhomogeneous electron distribution can be created around the Dirac cone of monolayer graphene after photon absorption [1]. Motivated by recent experiment using ultrafast laser pulse [2], we simulate the ultrafast dynamics of the photoexcited Dirac electrons coupled with the optical phonons by solving the Boltzmann equation: $\partial f_{\mathbf{k}s}^{(\nu)}/\partial t = (\partial f/\partial t)_{e-e} + (\partial f/\partial t)_{e-ph}$ and $\partial n_{\mathbf{q}}^{(\beta)}/\partial t = (\partial n/\partial t)_{ph-e}$, where $f_{\mathbf{k}s}^{(\nu)}$ is the electron distribution function with the wavevector $\mathbf{k} = (k_x, k_y)$, the valleys $\nu = K$ and K' , and the band index $s = \pm 1$. $n_{\mathbf{q}}^{(\beta)}$ is the phonon distribution function, where β and \mathbf{q} denote the phonon mode and wavevector, respectively. The collision terms include the electron-electron (e-e) and the electron-phonon (e-ph) scattering contributions. The e-e interaction matrix element is calculated by using the expression given in Ref. [3]. The expression for the e-ph interaction matrix elements given in Ref. [4] were used to compute the scattering rates, while different e-ph coupling strengths [5] were used for the coupling with the Γ and K phonons, respectively. The initial condition for the electron distribution is imposed to show the inhomogeneous population around the Dirac cones [6].

Figure 1 (upper) shows the time-evolution of $f_{\mathbf{k},+1}^{(\nu)}$: The excited electrons inhomogeneously populated around the Dirac cone initially go to the K point due to the e-e scattering mainly, followed by electron thermalization due to both the e-e and e-ph scattering. The electron relaxation is slowed down from ~ 50 fs to more longer when the e-e scattering is neglected (lower). Using the electron distribution, the time-evolution of absorption

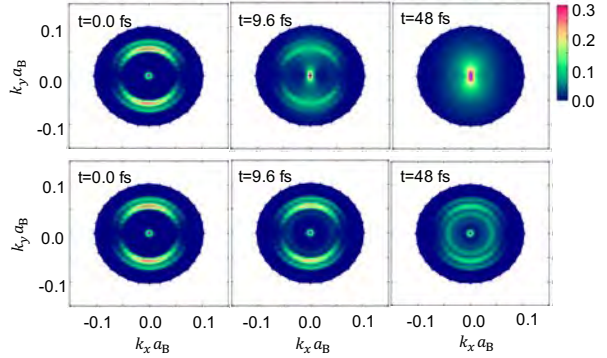


Figure 1: The time-evolution of the electron distribution around the Dirac cone: In upper figure, both the e-e and e-ph scattering are considered, while in lower figure the e-ph scattering is considered only.

spectra can also be calculated. We expect that the present study will stimulate further experimental work on this system.

The author thank I. Katayama (Yokohama National University) for useful discussions.

References

- [1] A. Grüneis *et al.*: Phys. Rev. B **67** (2003) 165402.
- [2] S. Nara *et al.*: JPS 2018 Autumn, 11aPS-20.
- [3] T. Ando: J. Phys. Soc. Jpn. **75** (2006) 074716.
- [4] S. Piscanec *et al.*: Phys. Rev. Lett. **93** (2004) 185503.
- [5] M. Lazzeri *et al.*: Phys. Rev. B **78** (2008) 081406(R).
- [6] M. Trushin *et al.*: Phys. Rev. B **92** (2015) 165429.

Boltzmann equation solver for nonequilibrium electrons and phonons in solids

Shota ONO

*Department of Electrical, Electronic and Computer Engineering, Gifu University
Gifu 501-1193*

It is of importance to establish a theoretical scheme for studying the ultrafast electron dynamics of laser-excited solids, where the nonequilibrium electron distribution approaches thermal distribution within a picosecond time scale through the electron-electron (e-e) and electron-phonon (e-ph) scattering. Recently the author has developed the Boltzmann equation solver to calculate the time-evolution of the electron and phonon distribution [1], where the free-electron, the Debye phonon, and the deformation potential models are used to describe the electron density-of-states (DOS), the phonon DOS, and the Eliashberg function (the e-ph coupling function), respectively. In the present study, based on *ab initio* approach to calculate these three functions, we develop the Boltzmann Equation solver for Nonequilibrium Electrons and Phonons, BENEP, which enables us to study the ultrafast electron and phonon dynamics of realistic materials absorbing a femtosecond laser pulse. It would be useful to analyze the pump-probe experimental data beyond the well-known two-temperature model [2].

By taking the wavevector average of the distribution functions, we calculate the time-evolution of the electron distribution $f(\varepsilon)$ and the phonon distribution $n(\omega)$, where ε and ω are the electron energy and the phonon frequency, respectively. The time-evolution of $f(\varepsilon)$ and $n(\omega)$ is regulated by the Boltzmann equation $\partial f(\varepsilon)/\partial t = (\partial f/\partial t)_{e-e} + (\partial f/\partial t)_{e-ph} + (\partial f/\partial t)_{laser}$ and $\partial n(\omega)/\partial t = (\partial n/\partial t)_{ph-e}$, where the laser excitation as well as the e-e and e-ph collision terms are considered.

We apply our BENEP code to the calculation of the femtosecond infrared photolumi-

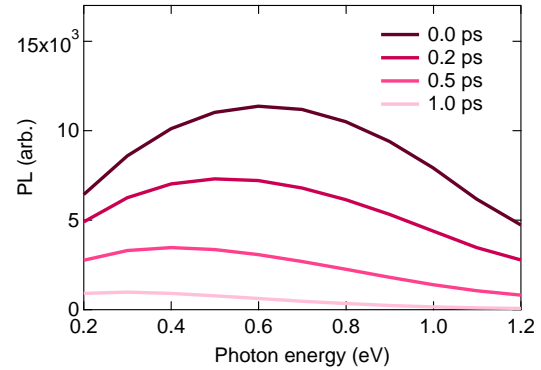


Figure 1: The time-evolution of PL in silver: The excitation density, the effective Coulomb interaction strength, and the electron diffusion time are assumed to be 460 J/cm^3 , 0.37 eV , and 0.5 ps , respectively.

nescence (PL) of metals. Figure 1 shows the time-evolution of PL spectra in silver: The PL spectra changes with time because the electron distribution thermalizes through the e-e scattering and because the electron energy is transferred to phonons. We find that the agreement between the numerical simulation and the experimental data is good, which will be demonstrated in our future paper [3].

The author thank T. Suemoto (Toyota Physical and Chemical Research Institute) for useful discussions.

References

- [1] S. Ono: Phys. Rev. B **97** (2018) 054310.
- [2] P. B. Allen: Phys. Rev. Lett. **59** (1987) 1460.
- [3] S. Ono and T. Suemoto, arXiv:2004.09000.

Entanglement in Remote Electron-phonon Systems Created by Photoirradiation

Kunio ISHIDA

School of Engineering and Center for Optics Research and Education

Utsunomiya University, Yoto, Utsunomiya, Tochigi 321-8585

Recent experiments on quantum entanglement between remote systems has revealed that the irradiated photons mediates quantum correlation between noninteracting material systems[1,2]. Since, however, its mechanism and/or dynamical behavior has not been understood theoretically, we study the dynamics of entanglement generation between remote systems by irradiation of a quantized light pulse. We employed a model of coupled electron-phonon-photon systems described by[3]

$$\mathcal{H} = \sum_{i=1}^3 \Omega_i c_i^\dagger c_i + \sum_{j=1}^2 \left[\omega a_j^\dagger a_j + \{ \mu (a_j^\dagger + a_j) + \varepsilon \} \frac{\sigma_z^{j+1}}{2} + \{ \sum_{i=1}^3 v_i (c_i^\dagger + c_i) + \lambda \} \sigma_x^j \right].$$

Solving the time-dependent Schrödinger equation by numerical calculation on the System B at ISSP, we found that the quantum mutual information for phonons reveals the dynamics of phonon entanglement generation.

Detection methods of entanglement generation dynamics are also studied and we showed that the scattered light, e.g., Stokes light, carries information on the phonon entanglement.

We derived relevant composite modes obtained by the Heisenberg equation of motion for c_i , and found that the heterodyne detection of it will help us distill the information on phonon correlation which slowly increases after a certain number of phonons is created. As shown in the previous study on phonon entanglement between remote diamond crystals[1], the entanglement is generated as a result of measurement on the scattered light, i.e., measurement corresponds to a disentanglement process between photons and phonons. Under the projection hypothesis, this means that the quantum correlation before measurement is also important to find appropriate methods for entanglement control. These results will help us design a method of coherent control of entanglement generation.

References

- [1] K. C. Lee, et al., *Science* **334**, 1253(2011).
- [2] F. Borjans, et al., *Nature* **577**, 195 (2020).
- [3] K. Ishida, *Eur. Phys. J.* **D73**, 117 (2019).

Molecular simulation of patchy particles

Takamichi TERAO

*Department of Electrical, Electronic, and Computer Engineering,
Gifu University, Yanagido 1-1, Gifu, 501-1193*

In colloidal systems, many studies have been performed to clarify the properties of spherical particles with isotropic interactions. Recently, there has been much interest in the studies of patchy particles with anisotropic interactions. It is of interest to create novel functional materials using these particles. In this study, the structural formation of patchy particles was studied by molecular simulations using cluster Monte Carlo method. To describe the effective interaction between patchy particles, the Kern-Frenkel model has been employed [1].

First, computer simulations are performed for 2-patch particles. Each particle has degrees of freedom of rotation in three-dimensional space, and its motion was constrained in a plane. In order to clarify the phase diagram, we analyzed the structure of the system using the generalized local bond order parameter that we have developed in previous studies [2]. As a result, a fluid phase, a hexagonal phase, a Kagome phase, and their coexistence phase have been observed.

Next, we studied tetrahedral patchy particles in a three-dimensional system (Figure 1), and the stability with diamond structure was numerically investigated. The photonic band

structures of colloidal crystals have been analyzed for various crystal structures. It has been revealed that a wide photonic bandgap exists in a colloidal crystal with diamond structure. Melting transition of such crystals have been studied by Monte Carlo simulations, and it was confirmed that the crystals with diamond structure becomes thermodynamically stable if the attractive interaction energy between patchy particles is about $10k_B T$.

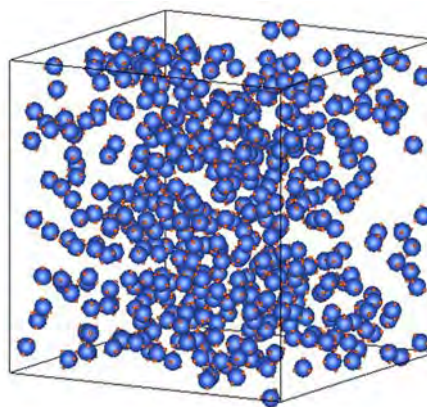


Fig. 1: Snapshot of tetrahedral patchy particles.

References

- [1] F. Romano, E. Sanz, P. Tartaglia, and F. Sciortino: *J. Phys.: Condens. Matter* **24** (2012) 064113.
- [2] R. Mizuno, K. Okumura, J. Oguri, and T. Terao: *Mol. Simul.* **45** (2019) 743.

Effects of Dzyaloshinskii-Moriya interactions and exchange randomness on low-temperature specific heats of spherical-kagome spin-systems

Yoshiyuki Fukumoto

*Department of Physics, Faculty of Science and Technology, Tokyo University of Science
2641 Yamazaki, Noda, Chiba 278-8510*

For cluster magnets described by Heisenberg models, in general, stepwise structures are expected in zero-temperature magnetization curves. However, for a spherical-kagome system $\{W_{72}V_{30}\}$ [1], which contains 30 vanadium ions with $S = 1/2$, it was reported that there is no such structure up to 50 T in a magnetization measurement at 0.5 K [2]. So far, the effects of (i) a distribution in the strength of the exchange interaction [2] and (ii) the Dzyaloshinskii-Moriya (DM) interaction [3] have been investigated. If in (i) the distribution width is about 30% of the average exchange interaction, or if in (ii) the DM interaction strength is about 10% of the exchange interaction, it has been shown that the low temperature magnetization process of $\{W_{72}V_{30}\}$ can be explained.

In this study, we focus on the effects of (i) and (ii) on the specific heat. To be specific, we first notice the fact that the recently reported experimental results for the low-temperature specific heat of $\{W_{72}V_{30}\}$ in several magnetic fields do not match the calculated results in the Heisenberg model; (a) the peak at about 2K in the calculated result is not seen in the experimental result, and (b) the observed magnetic-field dependence is very smaller than the calculation [4]. In order to resolve these two discrepancies, (a) and (b), we use the method of thermal quantum pure state [5] to calculate the specific heat, taking (i) and (ii) into account. As a result, regarding (a), we conclude that

the distribution of low-energy singlet states is affected by the distribution of exchange interactions to wipe out the low-temperature peak. The important finding is that the lowest singlet excitation-energy in the Heisenberg model is a fraction of the lowest triplet excitation-energy, which leads to the distribution width of exchange interaction being about 10% of the average exchange interaction (a fraction of the previous study [2]). Regarding (b), we found that the DM interaction can have the effect of suppressing the magnetic-field dependence of the energy eigenvalues, whose mechanism can also be illustrated by the two-spin model.

In conclusion, the specific heat of the 30-site system has been quantitatively evaluated up to sufficiently low temperatures, and we have qualitatively discussed the differences and similarities between the effects of two types of perturbations (i) and (ii) on the specific heat in magnetic fields and the magnetization process.

References

- [1] N. Kunisada *et al.*, PTEP 2014, 41I01 (2014).
- [2] J. Schnack *et al.*, arXiv:cond-mat/1304.2603v1.
- [3] Y. Fukumoto *et al.*, J. Phys. Soc. Jpn. 87, 124710, 2018.
- [4] T. Kihara *et al.*, PRB 99, 064430 (2019).
- [5] S. Sugiura and A. Shimizu, Phys. Rev. Lett. 108, 240401(2012).

Data-driven determination of a spin Hamiltonian of $\text{KCu}_4\text{P}_3\text{O}_{12}$

Ryo TAMURA

*International Center for Materials Nanoarchitectonics,
National Institute for Materials Science,
1-1 Namiki, Tsukuba, Ibaraki, 305-0044*

The origin of physical properties in materials is often understood through an effective model in materials science. Many methods have been developed in order to construct the effective model for a target material and they are mainly divided into two groups. One is ab initio calculations which determine the model parameters in an assumed effective model only by giving basic information of the target material. The other is a data-driven approach in which model parameters are determined so as to fit the experimentally measured data in the target material. In the latter case, from a view point of effective model estimations, data-driven techniques are considered to be efficient for the acceleration of automatic search for appropriate model parameters[1] and the extraction of relevant model parameters[2, 3, 4].

Here, by a data-driven approach, a spin Hamiltonian as an effective model of $\text{KCu}_4\text{P}_3\text{O}_{12}$ is determined. The crystal structure of $\text{KCu}_4\text{P}_3\text{O}_{12}$ is defined by $a = 7.433 \text{ \AA}$, $b = 7.839 \text{ \AA}$, $c = 9.464 \text{ \AA}$, $\alpha = 108.28^\circ$, $\beta = 112.68^\circ$, $\gamma = 92.73^\circ$, and space group: $\text{P}\bar{1}$ [5]. Cu(II) ions have $S = 1/2$ isotropic Heisenberg spin, but magnetic properties of this compound have not been reported yet. The lattice structure of Cu ions can be regarded as a zigzag chain consisting of eight Cu ions. Thus, a quantum Heisenberg model on a zigzag chain is targeted for a spin Hamiltonian of $\text{KCu}_4\text{P}_3\text{O}_{12}$ to be estimated. We estimate superexchange interactions between Cu

ions in this target model by a data-driven approach with susceptibility and magnetization curves experimentally measured. The estimated model parameters are $J_1 = -8.54 \text{ meV}$, $J_2 = -2.67 \text{ meV}$, $J_3 = -3.90 \text{ meV}$, and $J_4 = 6.24 \text{ meV}$, which describe the measured results well.

Once an estimated spin Hamiltonian is established, we predict, through theoretical analysis of the Hamiltonian, various magnetic properties which cannot be or have not been measured, such as magnetic specific heat, magnetic entropy, spin configuration, and spin gap. These predictions are helpful to propose a further experimental plan and design.

This work is the collaboration work with Koji Hukushima, Akira Matsuo, Koichi Kindo, and Masashi Hase.

References

- [1] R. Tamura and K. Hukushima, PLoS ONE **13**, e0193785 (2018).
- [2] H. Takenaka, K. Nagata, T. Mizokawa, and M. Okada, J. Phys. Soc. Jpn. **83**, 124706 (2014).
- [3] R. Tamura and K. Hukushima, Phys. Rev. B **95**, 064407 (2017).
- [4] H. Fujita, Y. O. Nakagawa, S. Sugiyama, and M. Oshikawa, Phys. Rev. B **97**, 075114 (2018).

- [5] H. Effenberger, *Zeitschrift für Kristallographie* **180**, 43 (1987).

Establishment of new analysis method for extend X-ray absorption fine structure with sparse modeling

Hiroyuki KUMAZOE

*Institute of Industrial Nanomaterials, Kumamoto University
Kurokami, Chuo-ku, Kumamoto, 860-8555*

Measurement of extended X-ray absorption fine structure (EXAFS) is one of the primary methods to obtain local structure information around a specific element with atomic scale. We are building a new method for the analysis of EXAFS by the sparse modeling. This year, we focused on Bayes free energy as an information criteria for choosing the regularization parameter.

To perform the sparse modeling on the EXAFS signals, we employed a simplified model of the EXAFS formalism based on the single-scattering approximation [1]:

$$\begin{aligned}
 y(k) &= \chi(k) \cdot k^3 \\
 &= \sum_{j=1}^N \frac{k^2}{R_j^2} \exp[-2k^2\sigma_j^2] \exp\left[-2\frac{R_j}{\Lambda}\right] \\
 &\quad \times (a_j \sin 2kR_j + b_j \cos 2kR_j), \quad (1)
 \end{aligned}$$

where, $y(k)$ is the k^3 weighted EXAFS signal, $\chi(k)$ as a function of the photoelectron wavenumber, k . R_j is the distance from the focused atom, j . σ_j is the Debye–Waller factor for atom, j . Λ is the mean free path. To obtain the local structure information, we convert Eq. (1) to a linear regression problem and solve it with L_1 regularization.

$$\hat{\mathbf{w}} = \arg \min_{\mathbf{w}} \left[\frac{1}{2} \|\mathbf{y} - \mathbf{X}\mathbf{w}\|_2^2 + \lambda \|\mathbf{w}\|_1 \right], \quad (2)$$

where the regression coefficient is $\mathbf{w} = (\dots, a_j, b_j, \dots)^T$. The response vector, \mathbf{y} comes from the target data and the predictor

matrix, \mathbf{X} incorporates other terms in Eq. (1). In this method, some elements of the coefficient, \mathbf{w} is are suppressed to exactly zero with the moderate value of λ .

Let us consider the sparse regression problem for the LASSO estimations within Bayesian inference to choose the regression parameter, λ . In Bayesian inference, this linear regression problem is optimized by maximizing the posterior probability. Here, we introduce the Bayesian free energy [2, 3] as an information criterion to optimize a regularization parameter and to extract the physical model appropriately. As a result, we estimated the radial distribution function with fewer bases than in previous studies [1].

This work was supported by JST CREST Grant Number JPMJCR 1861, Japan.

References

- [1] I. Akai, K. Iwamitsu, Y. Igarashi, M. Okada, H. Setoyama, T. Okajima, and Y. Hirai, *J. Phys. Soc. Jpn.* **87**, 074003 (2018).
- [2] Y. Igarashi, H. Takenaka, Y. Nakanishi-Ohno, M. Uemura, S. Ikeda, and M. Okada, *J. Phys. Soc. Jpn.* **87**, 044802 (2018).
- [3] Y. Mototake, Y. Igarashi, H. Takenaka, K. Nagata, and M. Okada, *J. Phys. Soc. Jpn.* **87**, 114004 (2018).

Competition between dipolar and short-range interactions on the magnetic thin films

Hisato KOMATSU, Yoshihiko NONOMURA, and Masamichi NISHINO
National Institute for Materials Science, Namiki, Tsukuba, Ibaraki 305-0044

Magnetic thin films are known to exhibit a variety of orderings when the exchange and the dipolar interactions compete with each other [1]. These systems are described by the following Hamiltonian:

$$\begin{aligned} \mathcal{H} = & -J \sum_{\langle i,j \rangle} \mathbf{S}_i \cdot \mathbf{S}_j \\ & + D' \sum_{i < j} \left\{ \frac{\mathbf{S}_i \cdot \mathbf{S}_j}{r_{ij}^3} - \frac{3(\mathbf{S}_i \cdot \mathbf{r}_{ij})(\mathbf{S}_j \cdot \mathbf{r}_{ij})}{r_{ij}^5} \right\} \\ & - \eta \sum_i (S_i^z)^2 - H \sum_i S_i^z. \end{aligned} \quad (1)$$

Here, $\mathbf{r}_{ij} = {}^t(x_{ij}, y_{ij}, 0) \equiv \mathbf{j} - \mathbf{i}$ means the difference between the position i and j . Previous studies revealed that this system has the spin-reorientation(SR) transition between the stripe and the planar ferromagnetic phase [2, 3] driven by the anisotropy η . However, these studies are limited to the cases when the magnetic field H does not exist.

We investigate the relation between the structure of the ordered phase and the parameters η and H using the Monte-Carlo(MC) simulation. In the simulation, naive MC algorithm require $O(N^2)$ simulation time, and thus we adopt the $O(N)$ SCO algorithm [4]. The coupling constant of interactions are fixed as $J = D' = 1$. Figures 1 and 2 show the snapshots and the $\eta - T$ phase diagrams given by our investigation, respectively. These figures show that the SR transition exists no matter whether H is zero or nonzero.

The numerical calculations of this study were mainly performed on the Numerical Materials Simulator at National Institute for Ma-

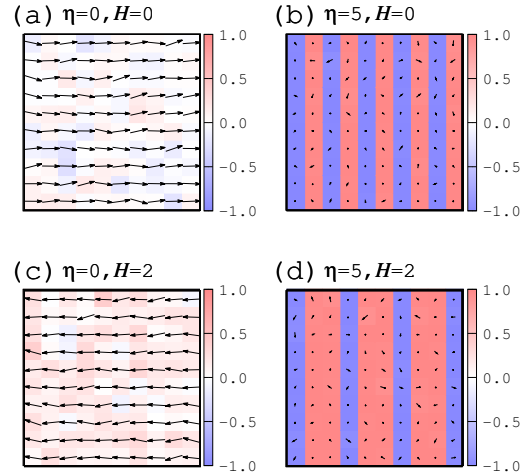


Figure 1: Snapshots of the system at several cases. The vectors and color mean the values of (S^x, S^y) and S^z , respectively. The parameters η and H are fixed at (a) $\eta = 0, H = 0$, (b) $\eta = 5, H = 0$, (c) $\eta = 0, H = 2$, and (d) $\eta = 5, H = 2$, and the temperature $T = 0.1$. Note that the widths of the stripes depend on H .

terials Science. We applied for the uage of the ISSP Supercomputer in preparation for the maintenance period of this simulator. However, we have ended this period without need for the new large-scale simulation, and do not have used the ISSP Supercomputer.

References

- [1] K. De’Bell, A. B. MacIsaac, and J. P. Whitehead, *Rev. Mod. Phys.* **72**, 225 (2000).

[2] J. P. Whitehead, A. B. MacIsaac, and K. De'Bell, Phys. Rev. B **77**, 174415 (2008)

[3] M. Carubelli, O. V. Billoni, S. A. Pighin, S. A. Cannas, D. A. Stariolo, and F. A. Tamarit, Phys. Rev. B **77**, 134417 (2008).

[4] M. Sasaki and F. Matsubara, J. Phys. Soc. Jpn. **77**, 024004 (2008).

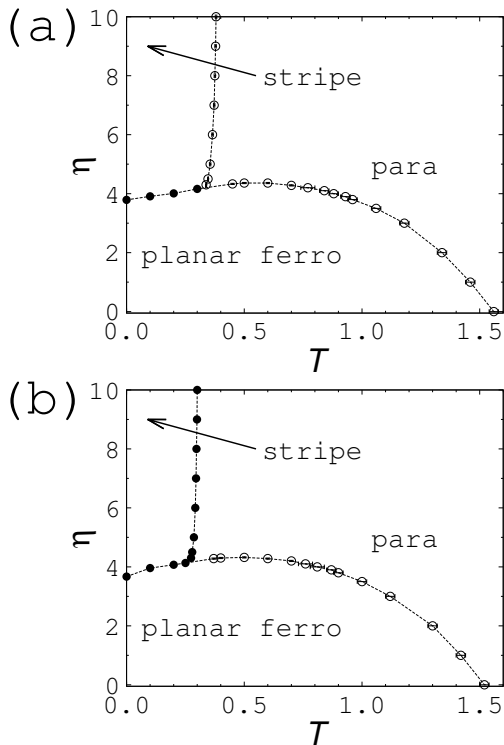


Figure 2: The $\eta - T$ phase diagrams at (a) $H = 0$ and (b) $H = 2$. The closed and open circles mean the first- and the second-order phase transition.

Competition between dipolar and Dzyaloshinskii-Moriya interactions on the magnetic thin films

Hisato KOMATSU, Yoshihiko NONOMURA, and Masamichi NISHINO
National Institute for Materials Science, Namiki, Tsukuba, Ibaraki 305-0044

Studies in recent years revealed that the spin systems with the Dzyaloshinskii-Moriya(DM) interaction have various types of magnetic structures such as the skyrmion lattice or the chiral magnetism [1]. Most of these studies does not consider the effect of the dipolar interaction between the magnetic moments of the spins, although it can not be removed. We investigate the two-dimensional square lattice where the DM, the nearest-neighbor ferromagnetic, and the dipolar interactions compete with each other, by the Monte-Carlo(MC) simulation.

The Hamiltonian we consider in this study is given as follows:

$$\begin{aligned} \mathcal{H} = & -J \sum_{\langle i,j \rangle} \mathbf{S}_i \cdot \mathbf{S}_j \\ & -D \sum_i \left\{ (\mathbf{S}_i \times \mathbf{S}_{i+e_x})_x + (\mathbf{S}_i \times \mathbf{S}_{i+e_y})_y \right\} \\ & +D' \sum_{i<j} \left\{ \frac{\mathbf{S}_i \cdot \mathbf{S}_j}{r_{ij}^3} - \frac{3(\mathbf{S}_i \cdot \mathbf{r}_{ij})(\mathbf{S}_j \cdot \mathbf{r}_{ij})}{r_{ij}^5} \right\} \\ & -\eta \sum_i (S_i^z)^2 - H \sum_i S_i^z. \end{aligned} \quad (1)$$

Here, $\mathbf{r}_{ij} = {}^t(x_{ij}, y_{ij}, 0) \equiv \mathbf{j} - \mathbf{i}$ means the difference between the position \mathbf{i} and \mathbf{j} . We fixed the coupling constant of short range interaction as $J = D = 1$. In the simulation, naive MC algorithm require $O(N^2)$ simulation time, and thus we adopt the $O(N)$ SCO algorithm [3].

As we can see in the figure 1, the skyrmion lattice changes its structure depending mainly

on the value of D' and η . It makes the triangular lattice under certain conditions, and the square lattice under the others. Furthermore, the chiral magnetic phase also shows the change of the direction of the structure depending on the parameters. We calculate the orientational order parameter of these phases, and investigated the condition under which each structure appear.

The numerical calculations of this study were mainly performed on the Numerical Materials Simulator at National Institute for Materials Science. We applied for the uage of the ISSP Supercomputer in preparation for the maintenance period of this simulator. However, we have ended this period without need for the new large-scale simulation, and do not have used the ISSP Supercomputer.

References

- [1] S. D. Yi, S. Onoda, N. Nishikawa, and J. H. Han, Phys. Rev. B **80**, 054416 (2009).
- [2] M. Sasaki and F. Matsubara, J. Phys. Soc. Jpn. **77**, 024004 (2008).

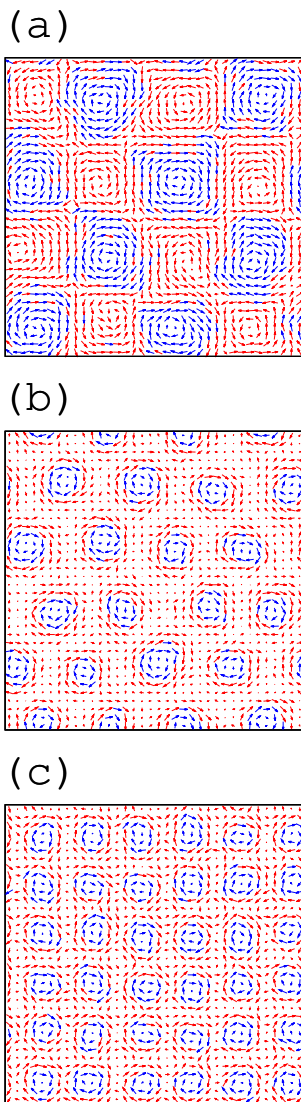


Figure 1: Snapshots of the skyrmion lattice phase at (a) $D' = 0.0$, $\eta = -1.2$, $H = 0.2$, (b) $D' = 0.0$, $\eta = 0.0$, $H = 0.5$, and (c) $D' = 0.6$, $\eta = 2.0$, $H = 1.5$. The temperature of each one is fixed at $T = 0.1$. The skyrmions make the square lattice at the cases (a) and (c), whereas they make the triangular lattice at (b). Note that direction of the square lattice is different in (a) and (c).

Investigation of Dynamics of a Supercooled Liquid and Proteins using the Free-Energy Landscape

Takashi YOSHIDOME

*Department of Applied Physics, Graduate School of Engineering, Tohoku University, Sendai
980-8579*

Free-energy landscape (FEL) picture has been used for understanding the properties of glass transition and protein folding [1,2]. The free-energy landscape is defined as a function of a particle configuration [2]. In the present study, we have investigated the dynamics of a Lennard-Jones system in a supercooled state and the dynamics of two proteins upon unfolding process from the viewpoint of the FEL.

We first computed the FEL for a crystallization process in a supercooled state. The computation of free-energy landscape was conducted using the protocol we have proposed [3]. The initial configuration was prepared using a Monte-Carlo (MC) simulation at a temperature above the freezing temperature. We have successfully obtained a FEL upon crystallization.

As for the protein dynamics upon unfolding process, we focused on the two proteins (goat alpha-lactalbumin and human lysozyme). It has experimentally shown that they have quite similar native structures but different structures at the transition state. We first performed all-atom molecular dynamics (MD) simulations of

the two proteins at 400 K to observe unfolding process. Then the trajectories were analyzed. It was found that the experimental result was successfully reproduced.

The calculations were performed using the L4cpu and F18acc in the system B, and L4cpu in the system C. We used our custom-made program [3] for computing the free-energy landscape of a Lennard-Jones system and for MC simulations. As for the study of protein unfolding, MD simulations were performed using the program GROMACS [5]. The MD trajectories were analyzed using our custom-made programs.

References

- [1] D. Wales: *Energy Landscapes: Applications to Clusters, Biomolecules and Glasses* (Cambridge University Press, 2004).
- [2] T. Odagaki: J. Phys. Soc. Jpn. **86** (2017) 082001.
- [3] T. Yoshidome, A. Yoshimori, and T. Odagaki: Phys. Rev. E **76** (2007) 021506.
- [4] H.J.C. Berendsen, D. Van der Spoel, and R. van Drunen, Comput. Phys. Commu. **91** (1995) 43.

Non-monotonic Behavior of the Binder Parameter in Potts Models

Hiroshi WATANABE

*Department of Applied Physics and Physico-Informatics, Keio University
Yokohama, Kanagawa 223-8522, Japan*

Satoshi MORITA, Yuichi MOTOYAMA, and Naoki KAWASHIMA
*Institute for Solid State Physics, University of Tokyo
Kashiwa-no-ha, Kashiwa, Chiba 277-8581*

The Binder parameter, *a.k.a.*, the forth-order cumulant, is a useful tool for analyzing the critical phenomena [1]. Since the scaling dimension of the Binder parameter is zero, its value does not depend on the system size at the criticality. While the Binder parameter usually a monotonic function for the systems involving continuous phase transition, it sometimes exhibits non-monotonic behavior. For example, a hump appears in the Binder parameter near the criticality of the Potts model. It exhibit system size dependence, and therefore, it is not trivial whether the universal scaling function itself has a hump or not. Additionally, it is known that the amplitude of the hump depends on the definition of the order parameter. However, the reason has not been clarified yet.

To study the peculiar behavior of the Binder parameter, we investigate the Fortuin-Kastelyen graph representation. We find that the graph representation of the Binder parameter consists of two parts, namely, the low- and high-temperature components, and the peculiar behavior of the Binder parameter is caused by the low-temperature one. We also find the spin representation of the high-temperature components of the Binder parameter, which is a monotonic function. We study the $J_1 - -J_2$ frustrated Ising model [2] and find that the non-monotonic behavior of the Binder parameter can be removed.

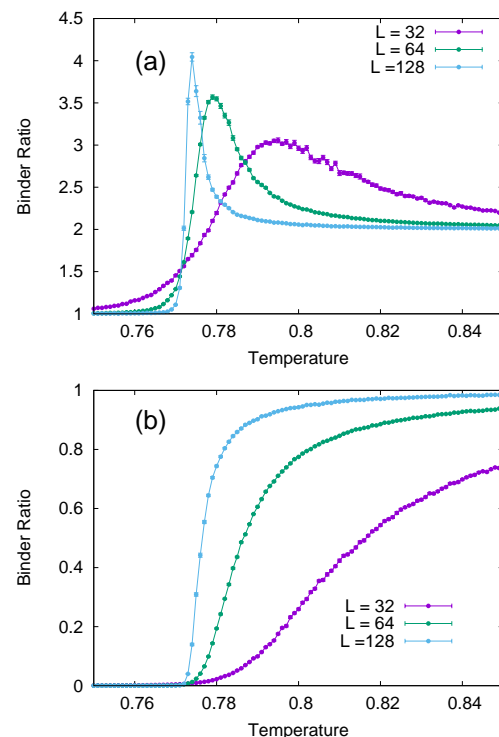


Figure 1: The Binder parameters of the $J_1 - -J_2$ frustrated Ising model with (a) the conventional and (b) the proposed definitions. The former exhibits humps while the latter does not.

[1] K. Binder, Z. Phys. B Cond. Matt. , vol. 43, pp. 119-140 (1981).

[2] S. Jin, A. Sen, and A. W. Sandvik, Phys. Rev. Lett. vol. 108, pp. 2-6 (2012).

Simulating phonon cross section using density functional theory

Naoki Murai

*Materials and Life Science Division, J-PARC Center, Japan Atomic Energy Agency
Tokai, Ibaraki 319-1195, Japan*

The studies of lattice dynamics, phonons, in crystalline materials are of fundamental importance as they provide key insights into the understanding of some relevant physical properties such as superconductivity and thermal conductivity. Historically, the direct observation of phonon dispersion using inelastic neutron scattering (INS) by Brockhouse opened the field of phonon spectroscopy as an energy- and momentum-resolved technique[1]. Since then, especially with the development of modern time-of-flight spectrometers at spallation neutron sources[2], INS has emerged as a powerful tool that allows efficient determination of phonon dispersion. Meanwhile, as an alternative method, inelastic x-ray scattering (IXS) has demonstrated its potential to precisely measure phonon dispersion[3]. Thus, the field of phonon spectroscopy has grown quickly over the past few decades, and the development of new instruments offers a unique opportunity to explore lattice dynamics in novel materials.

So far, we have been working on phonon dispersion measurements using the state-of-the-art INS spectrometers at J-PARC. The present project was carried out as a joint experimental and numerical study of lattice dynamics properties in novel materials. In particular, thanks to recent advances in density functional theory (DFT) calculations, it is now possible to perform *ab initio* phonon calculations whose only input information is the chemical composition of the materials.

In the present research project, we per-

formed *ab initio* phonon calculations, with a particular focus on unconventional superconductors and thermoelectric materials. Phonon calculations were performed using the density functional perturbation theory (DFPT)[4], as implemented in QUANTUM ESPRESSO code[5, 6]. Figure. 1 shows representative results obtained for SnS, which is predicted to be an attractive thermoelectric candidate. Here, all calculations were performed using the plane-wave pseudopotential method and the generalized gradient approximation (GGA) for the exchange correlation functional in the Perdew-Burke-Ernzerhof (PBE) parametrization[7]. Pseudopotentials and energy cutoffs of plane-wave basis were chosen according to the results of convergence tests provided in the standard solid-state pseudopotential (SSSP) library[8], in which the precision and performance of publicly available pseudopotential libraries are extensively tested to facilitate the optimal choice of pseudopotentials. In the present work, we used ultrasoft pseudopotentials from the GBRV library[9] with cutoffs of 70 Ry and 560 Ry for the expansion of the wave functions and charge densities, respectively. The Brillouin zone integration was performed over a $12 \times 12 \times 12$ \mathbf{k} mesh. Dynamical matrices were computed on $6 \times 6 \times 6$ meshes in \mathbf{q} space, which were then interpolated to determine the full phonon dispersion. Comparing the experimental phonon dispersion of SnS with DFPT calculations, we found that DFPT calculations are quite successful in

predicting the experimental phonon frequencies. From the calculated phonon eigenvalues and eigenvectors, we also computed the dynamical structure factor $S(\mathbf{Q}, \omega)$, which provides an estimation of the phonon intensity. A comparison with the neutron scattering data revealed that the experimental phonon intensities of SnS were perfectly reproduced by this simulation.

The present work thus serves to highlight the potential to use DFPT phonon calculations to simulate phonon cross sections as well as phonon frequencies. A more detailed report is now in course of preparation and will be published elsewhere.

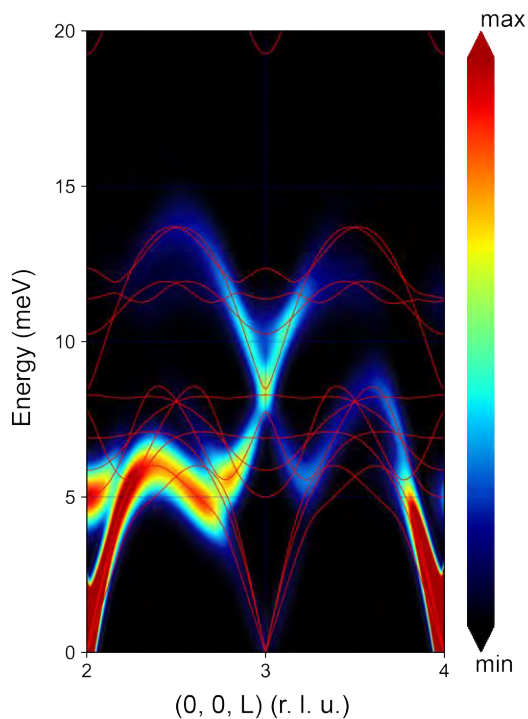


Figure 1: Calculated phonon dispersion of SnS. To facilitate the comparison between theory and experiment, the dynamical structure factor, $S(\mathbf{Q}, \omega)$, is weighted on the calculated phonon dispersion curves.

References

- [1] B. N. Brockhouse and A. T. Stewart Phys. Rev. **100**, 756 (1995).
- [2] K. Nakajima *et al.*, Quantum Beam Sci. **1**, 9 (2017).
- [3] A. Q. R. Baron, High-Resolution Inelastic X-Ray Scattering, in *Synchrotron Light Sources and Free-Electron Lasers: Accelerator Physics, Instrumentation and Science Applications*, edited by E. J. Jaeschke, S. Khan, J. R. Schneider, and J. B. Hastings (Springer International Publishing, Cham, 2016) pp. 1643–1719, (see also arXiv:1504.01098).
- [4] S. Baroni *et al.*, Rev. Mod. Phys. **73**, 515 (2001).
- [5] P. Giannozzi *et al.*, J. Phys. Condens. Matter **21**, 395502 (2009).
- [6] P. Giannozzi *et al.*, J. Phys. Condens. Matter **29**, 465901 (2017).
- [7] J. P. Perdew, K. Burke, and M. Ernzerhof, Phys. Rev. Lett. **77**, 3865 (1996).
- [8] G. Prandini *et al.*, npj Computational Materials **4**, 72 (2018).
- [9] K. F. Garrity *et al.*, Computational Materials Science **81**, 446 (2014).

Molecular dynamics simulations of water confined in carbon structures with the reactive force field

Tomoko MIZUGUCHI

*Faculty of Materials Science and Engineering, Kyoto Institute of Technology
Matsugasaki, Sakyo-ku, Kyoto 606-8585*

Many studies have been done on water in confinement by both theoretical and experimental techniques and revealed that the properties of confined water may strongly differ from that of bulk water. It is clearly important to properly evaluate the influence of confinement on water for various applications such as ion channels or drug delivery. Until last year, we had performed molecular dynamics (MD) simulations of confined water in nanoporous silica with the reactive force field (ReaxFF) using the supercomputer at ISSP. We examined the influence of hydrophilic surface on the physical properties of water, specifically, the hydrogen bond structure and dynamics [1]. This year, I embarked on MD simulations using ReaxFF for water in a carbon nanotube as a model of a hydrophobic pore to clarify the influence of interface on water.

ReaxFF allows us to incorporate bond breakage and formation, which are particularly important on interface, in MD simulations with a lower computational cost than quantum-mechanics-level calculations. I used four ReaxFF parameter sets: (i) developed by Monti *et al.* for biomolecules (protein-2013) [2], (ii) by Zhang and van Duin to improve the weak interaction between hydrocarbon and water from protein-2013 force field (CHON-2017_weak) [3], (iii) by Yeon and van Duin to simulate hydrolysis reactions at silica/water interface (Yeon2015) [4], and (iv) by Pitman and van Duin for clayzeolite com-

posites (Pitman2012) [5]. I prepared a single-walled carbon nanotube solvated in water and observed the inflow and outflow of water into the nanotube. The diameter of the carbon nanotube (CNT) was set 2.7 nm for comparison with our previous results in the silica/water system. All simulations were conducted in the NPT ensemble ($T = 300$ K and $P = 1$ atm) using the Nosé-Hoover thermostat and barostat with LAMMPS pre-installed in the supercomputer at ISSP. The ReaxFF MD simulations were carried out with a time step of 0.25 fs through the USER-REAXC package of LAMMPS.

When the protein-2013 and Pitman2012 force fields were used, water flowed into the CNT and filled it in 250 ps. In the 250-ps simulation using the Yeon2015 force field, water flowed into the CNT somewhat. It seems to need more time to fill in the CNT with water. In fact, when I started the simulation with a structure where the CNT was filled with water, the CNT remained filled with water. On the other hand, water went out of the CNT using the CHON-2017_weak force field. Some experiments show that water spontaneously flows inside the CNT, thus the CHON-2017_weak force field seems not to be suitable for the CNT/water system. But we should carefully verify the result. I am now planning to carry out DFT calculations to compare with the simulation results using ReaxFF.

References

- [1] T. Mizuguchi, K. Hagita, S. Fujiwara and T. Yamada: *Mo. Sim.* **45** (2019) 1437.
- [2] S. Monti, A. Corozzi, P. Fristrup, K. L. Joshi, Y. K. Shin, P. Oelschlager, A. C. T. van Duin, and V. Barone: *Phys. Chem. Chem. Phys.* **15** (2013) 15062.
- [3] W. Zhang and A. C. T. van Duin: *J. Phys. Chem. B* **122** (2018) 4083.
- [4] J. Yeon and A. C. T. van Duin: *J. Phys. Chem. C* **120** (2016) 305.
- [5] M. C. Pitman and A. C. T. van Duin: *J. Am. Chem. Soc.* **134** (2012) 3042.

Manipulation of electronic states with nanostructures: model construction and its application

Toshikaze KARIYADO

International Center for Materials Nanoarchitectonics,

National Institute for Materials Science, Namiki, Tsukuba, Ibaraki 305-0044

We focus on computing orbital magnetic susceptibility, which is relatively easy to measure in experiment, to characterize novel band structure such as Dirac/Weyl fermions. There are some situations in which computation of orbital magnetic susceptibility requires large computing resources. One example of such a situation is when we deal with (i) nanostructured system, which is the main topic of this project. Nanostructures lead to large number of sites in a unit cell, which in turn makes the computation hard. Another situation is when we handle with (ii) real materials. Generically, taking more orbitals into account gives better precision at the cost of computing power. Furthermore, in order to characterize singular band structures like Dirac/Weyl cones, fine sampling of k-points is inevitable.

A useful strategy to improve the efficiency of computation is applying massive parallelization on k-point sampling, which had been done in the preceding project last year. This year, we have made some corrections in memory handling to push up the maximum system size allowed in the same facility.

The improved program has been used to calculate the orbital magnetic susceptibility of Sr₃PbO, a Dirac material with antiperovskite crystalline structure. Temperature and carrier number dependence of the susceptibility is obtained using a tight-binding model derived from the ab-initio calculation. The improved program enables us to have better results in low temperature. It turned out that the susceptibility at low temperature is affected mainly by the change in the temperature dependence of the chemical potential associated with the change in the density of states.

Another topic in this project is the investigation on the bilayers of atomically thin materials with some mismatch showing moire pattern. A generic theory on the symmetry-based constraints on the interlayer coupling is proposed [1], which is inspired by data sets of the interlayer coupling in bilayer graphene obtained by systematic ab-initio calculations.

References

- [1] T. Kariyado and A. Vishwanath, Phys. Rev. Research 1 (2019) 033076.

Statistical Properties in a Branching Network

Satoshi YUKAWA, Kei TAKAYA, and Takeru WATANABE
Department of Earth and Space Science, Osaka University
Machikaneyama, Toyonaka, Osaka 560-0043

In a river network, there are many interesting statistical laws, such as Hack's law and Horton's law. Recently another statistical law was found in the distribution of bifurcation angle.[1, 2] The distribution has a universal characteristic angle depending on the aridity of the climate:[3] For the humid area, the angle is $2\pi/5 = 72^\circ$ and, on the other hand, for the highly arid area, it takes a smaller angle of almost 45° . The angle $2\pi/5$ is theoretically explained for the Laplacian growth network, but the smaller angle is not.

In this supercomputer project, we develop a theoretical model to understand the aridity dependence of the network based on the coupled map lattice model.[4] The model is constructed on a square lattice with water and soil variables. Dynamical rules are too complicated to be expressed here. The resultant networks generated by computer simulation are shown in Figs. 1.

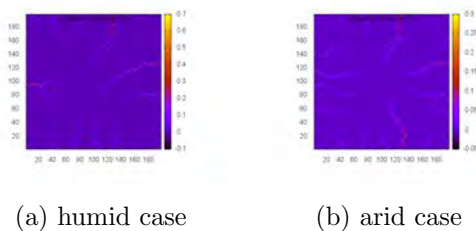


Figure 1: Simulated network structures

Distribution of the bifurcation angle can be obtained from the simulated network. The result is presented in Fig. 2. We observe slight aridity dependence in the figure. Increasing aridity index, the peak at the characteristic angle becomes much larger. Besides the lower tail

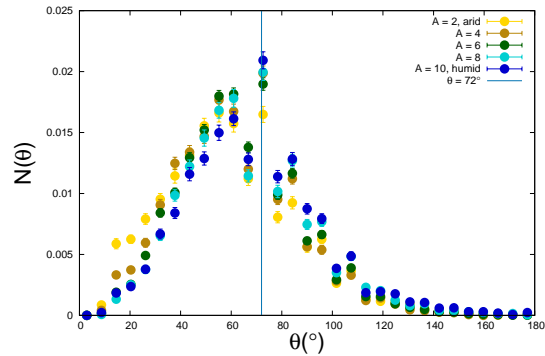


Figure 2: Bifurcation angle distribution for several aridity parameters A .

of the distribution decreases. There is, however, discontinuous behavior around the characteristic angle in the distribution. The origin of such behavior is unclear. We need additional computer simulations.

References

- [1] O. Devauchelle, A. P. Petroff, H. F. Seybold, and D. H. Rothman: *Proceedings of the National Academy of Sciences* **109** (2012) 20832.
- [2] S. Yukawa, T. Watanabe, and K. Hara: *Journal of the Physical Society of Japan* **88** (2019) 024901.
- [3] H. Seybold, D. H. Rothman, and J. W. Kirchner: *Geophysical Research Letters* **44** (2017) 2272.
- [4] B. Murray and C. Paola: *Earth Surface Processes and Landforms* **22** (1997) 1001.

Numerical Study of Cell Guiding Mechanism in Cellular Tissue

Katsuyoshi Matsushita

*Department of Biological Science, Osaka University
Toyonaka, Osaka 563-0043*

Cells have function in the organisms. In the development of organisms, cells are not always born in the suitable place which the cells function. In these cases, cell migration play a significant role to transport the cells to the suitable place. As a prominent observation, there is a case that the transport length of the cell migration reaches mm scales much larger than the cell's typical scale of $10\mu\text{m}$ [1]. In such cases, the migration should be properly guided by surrounding tissues to transport the cell for its suitable position. The guiding mechanism is still unclear and is expected to utilize chemical signals.

As a candidate of the chemical signal, the chemical cell-cell adhesion is one of most powerful candidate. The possibility of the cell-cell adhesion on the explanation of the long distance transport of cells is not sufficiently examined. In this work, we have investigated the cell migration on tissue which is guided by the cell-cell adhesion. We employed the Cellular Potts model and examine cell-cell adhesion effect on the cell migration in tissue [2].

We consider the model consists of suspended transported cells on cellular tissue on the Cellular Potts model[3] and one dimensional transport of the cells. The cells and tissue interacts with the heterophilic cell-cell adhesion, As a guiding mechanism of the cell migration direction, we consider the polarity of the cell-cell l adhesion. The polarity is a hypothetical factor for guiding collective cell migrations with long distance [4, 5] and is expected to be

effective in the case of cell transport on tissue.

We show that the migration direction of cells on the tissue aligns in the same direction even when the cells are suspended. The order in cell migration is induced as a polarity memory effect [6, 7]. The net transport velocity exhibits a non-linear transport and becomes a finite value above a threshold adhesion strength. Furthermore, the transport distance is longer than 10^2 times of the cell scale. This result show potential of the heterophilic adhesion with polarity as the guiding mechanism of cell transports.

References

- [1] C. Lois and A. Alvarez-Buylla, *Science* **264**, 1145 (1994).
- [2] K. Matsushita: submitted to PRE.
- [3] F. Graner and J. Glazier, *Phys. Rev. Lett.* **69**, 2013 (1992).
- [4] K. Matsushita: *Phys. Rev. E* **97**, 042413 (2018).
- [5] K. Matsushita: *Phys. Rev. E* **95**, 032415 (2017).
- [6] K Matsushita, K Horibe, N Kamamoto, S Yabunaka, K Fujimoto, *Proc. Sympo. Simul. Traffic Flow* **25**, 21 (2019).
- [7] Matsushita, K Horibe, N Kamamoto, K Fujimoto, *J. Phys. Soc. Jpn.* **88**, 103801 (2019).

Magnetism in the System with the Multiple-Spin Exchange Interactions

Chitoshi YASUDA

*Department of Physics and Earth Sciences, Faculty of Science,
University of the Ryukyus, Okinawa 903-0213, Japan*

Helium-3 (^3He) atoms adsorbed on graphite form the commensurate solid layer regarded as the spin-1/2 quantum spin system on a triangular lattice at certain density of ^3He . In the exchange process of ^3He atoms, there are not only an exchange between two neighbor atoms but also that among three or more neighbor atoms. The exchange integrals of three- and four-spin cyclic exchange interactions are larger than that of two-spin exchange interaction. Furthermore, the comparison between the theoretical and experimental studies shows that effects of the five- and six-spin exchange interactions are not negligible. Thus, in relation to the solid ^3He , the multiple-spin exchange (MSE) model on the triangular lattice has been extensively studied. Ground states and thermodynamic properties of the MSE model on the triangular lattice have been investigated using various methods, e.g., the mean-field approximation[1,2], the Monte Carlo simulations, the exact diagonalization, and the spin-wave theory[3,4]. In particular, the model has attracted attention owing to the existence of novel states such as the quantum spin liquid and the spin-nematic state and the effects of fluctuations on ordered phases with chirality. However, the study becomes difficult for the complexity of the system with the various interactions on the triangular lattice.

Recently, a new quantum spin liquid is experimentally observed in the solid ^3He layer. This layer is a monolayer ^3He adsorbed on graphite preplated with atomic layers of deuterium hydride. At low density of ^3He , it was suggested that there exists the quantum spin liquid with novel dependences of

the heat capacity and the magnetic susceptibility on temperature. In particular, the low-temperature heat capacity is proportional to $2/3$ power of temperature, which is an unprecedented behavior in the quantum spin system. The details of this experimental work are not yet clear, however, it is suggested that the solid ^3He layer is a honeycomb lattice.

We investigate the MSE model on the honeycomb lattice using numerical methods, which were applied in works of the MSE model on the triangular lattice. In the present project, we concentrate the classical MSE model with the two-spin interaction and the six-body ring exchange interaction. The ground state is investigated using the conjugate gradient method. In this method, we need to prepare many random spin states as the initial states because of avoidance of the trap to a metastable state. For large six-body ring exchange interactions, we found the classical ground state with the multi-sublattice structure. We also advance research on thermodynamic properties using the exchange Monte Carlo simulations.

References

- [1] C. Yasuda, Y. Uchihira, K. Kubo, J. Mag. Mag. Mater. **310**, 1285 (2007).
- [2] C. Yasuda, Y. Uchihira, S. Taira, K. Kubo, J. Phys. Soc. Jpn. **87** 104704 (2018).
- [3] C. Yasuda, D. Kinouchi, K. Kubo, J. Phys. Soc. Jpn. **75**, 104705 (2006).
- [4] S. Taira, C. Yasuda, T. Momoi, K. Kubo, J. Phys. Soc. Jpn. **88**, 014701 (2019).

Simulation Analysis of Collision of Two Filaments Driven by Protein Molecular Motors

Kazuo SASAKI

*Department of Applied Physics, Graduate School of Engineering, Tohoku University,
Sendai, 980-8579*

It is known that protein filaments driven by protein motors distributed on the glass surface form vortices when the density of filaments is high [1]. We studied this collective motion by computer simulation. In this year, we focused on the following two systems. One is the system consisting of two filaments and a lot of protein motors [2]. The other is the system in which the filaments were simplified as point particles.

In the first system, we studied the collision between two protein filaments, which is closely related to the emergence of the vortices. Four types of collisions were found experimentally [1]: parallel, anti-parallel, stop, and crossing; the probability of which type was observed strongly depended on the incident angle between two filaments. We simulated the collision of the two filaments for various incident angles. We have successfully reproduced the dependences of the probabilities on collision angle for parallel, anti-parallel, and stop of collision types.

In the second system, we simplified the model of protein filaments in accordance with the previous study [3]: The filaments were modeled as self-propelled particles; and they moved on a lattice. We performed Monte-Carlo

simulations of the particles for several particle densities and parameters of the model, and their collective motion was analyzed from the viewpoint of percolation theory [4]. A percolation transition was found to occur as the particle density was increased if the interaction between particles was weak, while a new phenomenon, the character of which is to be clarified, was observed in the case of strong interaction. Formation of vortices was not observed, probably due to the simplicity of the model.

The calculations were performed using the L4cpu in both the systems B and C. We used our custom-made program for the calculations.

References

- [1] Y. Sumino, *et al.*: *Nature* **483** (2012) 448.
- [2] Y. Ishigure and T. Nitta: *Langmuir* **30** (2014) 12089.
- [3] F. Peruani, T. Klaus, A. Deutsch, and A. Voss-Boehm: *Phys. Rev. Lett.* **106** (2011) 128101.
- [4] D. Stauffer and A. Aharony: *Introduction To Percolation Theory*, 2nd ed. (Taylor & Francis, London, 1992).

Elucidation of the coercivity mechanism by statistical physical approaches

Masamichi Nishino
*National Institute for Materials Science,
 Tsukuba, Ibaraki 305-0044, Japan*

The neodymium (Nd) permanent magnet, $\text{Nd}_2\text{Fe}_{14}\text{B}$, which has strong coercivity, is an indispensable material in modern technologies, applied to information-storage devices, hybrid and electric vehicles, generators, etc. [1] This magnet has also another interesting feature. It exhibits a temperature-induced spin-reorientation (SR) transition. The spin dynamics on the SR transition in the magnet has not been clarified. The temperature dependence of the ferromagnetic resonance (FMR) frequency is an open question.

In the present work we studied the temperature dependence of the FMR frequency at zero external field. [2] The FMR spectrum $I(f)$ is calculated by the auto-correlation function of spins (power spectrum) for an atomistic model of the Nd magnet. The temperature dependence of the FMR frequency f_R is plotted by blue diamonds in Fig. 1.

We find that f_R exhibits a drastic change around T_R (SR transition temperature) and non monotonic temperature dependence. In particular, it is found that $f_R \sim 0$ below T_R .

This is totally different from the dependence of conventional magnets with a single uniaxial anisotropy energy, in which a monotonic decrease of the FMR frequency is observed. We clarified the mechanism for $f_R \sim 0$ below T_R . At zero temperature the state of the tilted spin alignment is stable, and the precession around the ground-state (GS) easy axis (parallel to the GS magnetic moments) does not occur. We also derived the formula for the FMR fre-

quency above T_R in connection to the temperature, magnetization along to the easy axis, and the fluctuation of the magnetization along to the hard axis (hard plane). We found that this formula is a good description for overall temperature region, and the last factor (fluctuation of transverse magnetization) in the formula is important for the qualitative nature of the FMR frequency.

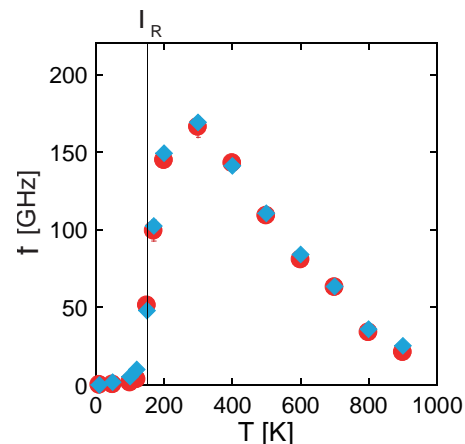


Figure 1: Temperature dependences of f_R (blue diamonds) for the atomistic Nd magnet model..

References

- [1] S. Hirosawa, M. Nishino, and S. Miyashita, *Adv. Nat. Sci: Nanosci. Nanotechnol.* **8** (2017) 013002.
- [2] M. Nishino, and S. Miyashita, *Phys. Rev. B* **100** (2019) 020403(R).

Transition in the memory effect of paste

Akio NAKAHARA

College of Science and Technology, Nihon University

7-24-1 Narashino-dai, Funabashi, Chiba 274-8501

A dense colloidal suspension, called a paste, remembers the direction of its motion, such as vibration and shear, and these memories in paste dominate the preferential direction for cracks to propagate. When a paste remembers vibration, cracks propagate in the direction perpendicular to the direction of the vibration, while, when a paste remembers shear, cracks propagate along the shear as is shown in Fig. 1 [1-2].

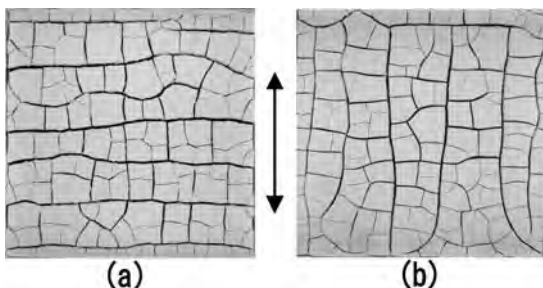


Fig. 1: Crack patterns induced by memory effect. (a) Memory of vibration (b) Memory of shear.

To explain the formation of striped crack pattern, we performed numerical simulations of shear motion of colloidal suspension using LAMMPS. Colloidal particles attract each other via Lennard-Jones potential and receives Stokes’s drag force from surrounding fluid. When we assume a simple shear as shown in Fig. 2, we obtain formation of elongated clusters along shear, as shown in Fig. 3, which dominates preferential direction for cracks to propagate. To

reproduce the transition from memory of shear to vibration, we find that we have to abandon the assumption of simple shear flow and solve more realistic flow motion under vibration.

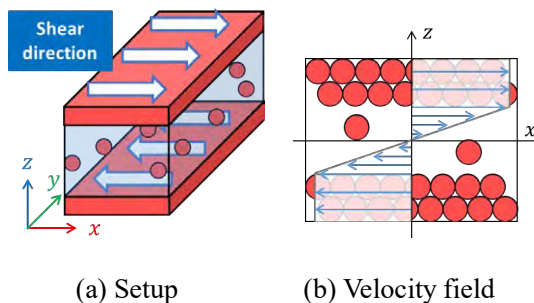


Fig. 2: Direction of a simple shear applied to a paste in numerical simulations.

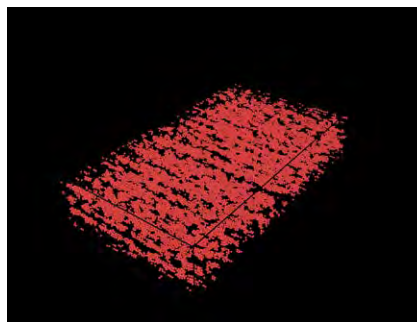


Fig. 3: Elongated clusters along shear flow with its solid volume fraction of paste 3.3%.

References

[1] L. Goehring, A. Nakahara, T. Dutta, S. Kitsunezaki and S. Tarafdar, *Desiccation Cracks and their Patterns* (Wiley, 2015).
 [2] Japan patent JP 6565067, Material Mixing Method, A. Nakahara, Y. Matsuo, M. Ito and R. Yoneyama (2019)

Numerical Study of One Dimensional Frustrated Quantum Spin Systems

Kazuo HIDA

*Professor Emeritus, Division of Material Science,
Graduate School of Science and Engineering,
Saitama University, Saitama, Saitama 338-8570*

We investigate the ground-state phases of spin-1 alternating-bond diamond chains described by the following Hamiltonian [1]:

$$\begin{aligned} \mathcal{H} = & \sum_{l=1}^N \left[(1 + \delta) \mathbf{S}_l \boldsymbol{\tau}_l^{(1)} + (1 - \delta) \boldsymbol{\tau}_l^{(1)} \mathbf{S}_{l+1} \right. \\ & + (1 + \delta) \mathbf{S}_l \boldsymbol{\tau}_l^{(2)} + (1 - \delta) \boldsymbol{\tau}_l^{(2)} \mathbf{S}_{l+1} \\ & \left. + \lambda \boldsymbol{\tau}_l^{(1)} \boldsymbol{\tau}_l^{(2)} \right], \end{aligned} \quad (1)$$

where \mathbf{S}_l , $\boldsymbol{\tau}_l^{(1)}$, $\boldsymbol{\tau}_l^{(2)}$ are spin-1 operators. The lattice structure is depicted in Fig. 1.

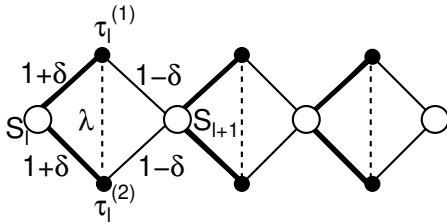


Figure 1: Structure of a spin-1 alternating-bond diamond chain. $S = \tau^{(1)} = \tau^{(2)} = 1$. The exchange parameters are denoted by λ , $1 + \delta$, and $1 - \delta$, where λ and δ control the strengths of frustration and bond alternation, respectively.

Each ground state consists of an array of spin clusters separated by singlet dimers owing to an infinite number of local conservation law,

$$\forall l \quad [\mathbf{T}_l^2, \mathcal{H}] = 0, \quad (\mathbf{T}_l \equiv \boldsymbol{\tau}_l^{(1)} + \boldsymbol{\tau}_l^{(2)}). \quad (2)$$

A pair of spins with $T_l = 0$ is a singlet dimer. For $\lambda > 2$, the state with $T_l = 2$ is not allowed.

Hence, each ground state consists of an array of n successive $T_l = 1$ pairs separated by singlet dimers. This phase is called a DC n phase. If no singlet dimers are present, the ground state is equivalent to that of a mixed spin chain,

$$\begin{aligned} \mathcal{H} = & \sum_{l=1}^N \left[(1 + \delta) \mathbf{S}_l \mathbf{T}_l + (1 - \delta) \mathbf{T}_l \mathbf{S}_{l+1} \right. \\ & \left. + \lambda (T_l (T_l + 1) - 4) \right] \quad (T_l = 1 \text{ or } 2) \end{aligned} \quad (3)$$

with infinite length. For strong frustration, we find a series of quantum phase transitions as in the case of alternating-bond mixed diamond chains with spins 1 and 1/2[2]. For intermediate frustration, we find the nonmagnetic Haldane or dimer phases according to whether the bond alternation is weak or strong. For weak frustration and weak bond alternation, we find the ferrimagnetic states with spontaneous magnetizations $m = 1/6$ ($F_{1/6}$ phase) and $1/3$ ($F_{1/3}$ phase) per site. The $F_{1/6}$ phase is accompanied by a spontaneous translational symmetry breakdown. This phase vanishes for strong bond alternation[1]. The presence of a narrow partial ferrimagnetic phase is suggested near the point $(\lambda, \delta) = (\lambda_c, \delta_c) \simeq (1.0832, 0.2598)$. The phase diagram determined by the numerical calculation for the Hamiltonian (3) using finite-size DMRG and infinite-size DMRG methods is shown in Fig. 2 except for the partial ferrimagnetic phase whose width is estimated to be so narrow that it is invisible in this scale.

References

- [1] K. Hida, J. Phys. Soc. Jpn. **89**, 024709 (2020)
 [2] K. Hida, K. Takano, and H. Suzuki, J. Phys. Soc. Jpn. **79**, 044702 (2010).

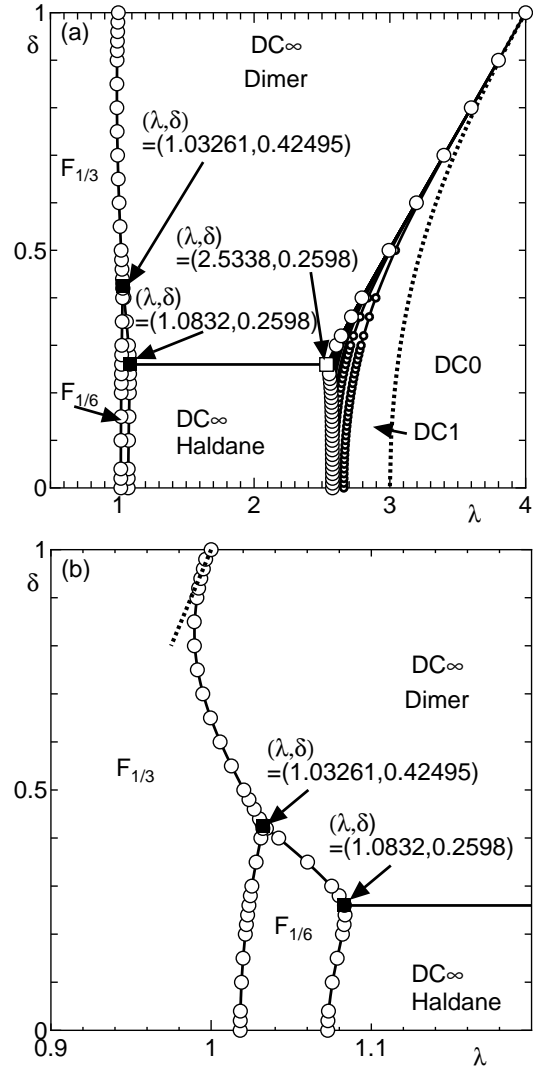


Figure 2: (a) Overall ground-state phase diagram. Small open circles are the phase boundaries between DCn and $DC(n-1)$ phases. For $n \geq 4$, these phase boundaries are only shown by solid lines to avoid complications. Other phase boundaries are shown by the large open circles and solid lines. The exact $DC0$ - $DC1$ phase boundary is shown by the thick dotted line. The open square is the accumulation point of infinite series of critical points at $\delta = \delta_c (\simeq 0.2598)$. The filled squares are triple points. (b) The enlarged phase diagram in the small λ region. The thick dotted line is the approximate relation for $\delta \simeq 1$. (from Ref. [1])

Construction of A New Method for Analysis of Crystallization Mechanism from Amorphous Precursor Using Molecular Dynamics Simulation Method and Unsupervised Machine Learning

Hiroki NADA

National Institute of Advanced Industrial Science and Technology (AIST),

16-1 Onogawa, Tsukuba, Ibaraki 305-8569

The control of crystallization from disordered systems, such as amorphous and melt, is essential to crystal engineering. However, our understanding of the mechanism of crystallization from disordered systems is still poor. This is because the structure of disordered systems can hardly be elucidated by experimental means.

Molecular dynamics (MD) are often helpful to elucidate the structure of disordered systems. A question is how to evaluate the time-evolution of the structure in disordered systems during crystallization properly.

Recently, a new methodology for evaluation of the structural similarity between different phases using the dimensional reduction, which has been developed as a method of unsupervised machine learning, is proposed [1]. The purpose of this project is to demonstrate that this methodology contributes to elucidating the mechanism of

crystallization from disordered systems in MD simulation studies.

An MD simulation of a supercooled Lennard-Jones melt was performed using ISSP supercomputer. The methodology was utilized to evaluate the structural similarity between the melt and its crystalline form, which was regarded as the geometrical similarity of the pair-distribution function between them, at each period during crystallization. An abrupt change of the structural similarity, which corresponded to crystal nucleation, was successfully detected. It is anticipated this methodology contributes to elucidation of the mechanism of crystallization, even for multicomponent systems, such as crystallization of calcium carbonate from its amorphous precursor.

References

[1] H. Nada: ACS Omega **3** (2018) 578.

The analysis of the dynamical response to the optical bistability

Tatsuhiko SHIRAI

*Green Computing Systems Research Organization, Waseda University
Waseda-chou, Shinjuku-ku, Tokyo 162-0042*

We have studied a dynamical response of an optical bistable system to a time-periodic driving field. The optical bistability has been found in cavity systems with an external driving field. As a function of laser intensity, there is a finite interval with bistability of a high transmission state (HTS) and a low transmission state (LTS). When the intensity of the input laser is time-periodically modulated beyond the bistable regime, the system shows a dynamical phase transition when the period of the modulation changes. At large period, the system stays in a different stable state depending on whether the laser intensity is increasing or decreasing. On the other hand, at small period, the system is kept in either the HTS or the LTS. Here, we show that the Floquet dissipative map is useful to characterize the dynamical phase transition. The Floquet dissipative map is given by a time-evolution operator of a quantum master equation, and it characterizes the limit cycle and the decay rate of the relaxation dynamics. We found that the decay rate exhibits qualitatively different system-size dependence before and after the phase transition, and it shows a finite-size scaling of spinodal phenomena around the transition point. This work was published to Physical Review A [1].

In this work, we develop a numerical algorithm to efficiently solve the dynamics governed by the quantum master equation consisting of many spins. To do it numerically, it is necessary to express the time evolution

operator L as a matrix. Naively, the number of elements in L increases exponentially with the number of spins N , which gives a strong restriction on N in the numerical simulation. However, we made use of the fact that the present model has a symmetry under exchange of spins. This symmetry reduces the number of non-zero elements in L to the order of N^3 [2, 3, 4]. We have used this property and performed simulations up to $N = 100$.

This research was supported by MEXT as the “Exploratory Challenge on Post-K Computer” project (Challenge of Basic Science-Exploring Extremes through Multi-Physics and Multi-Scale Simulations).

References

- [1] T. Shirai, S. Todo, and S. Miyashita: Phys. Rev. A **101** (2020) 013809.
- [2] S. Sarkar, and J. S. Satchell: EPL **3** (1987) 797.
- [3] M. Gegg, and M. Richter: New J. Phys **18** (2016) 043037.
- [4] T. Shirai, S. Todo, H. de Raedt, and S. Miyashita: Phys. Rev. A **98** (2018) 043802.

Theoretical study for superconductivity in superstructured strongly correlated materials with two-particle self-consistent approach

Kazutaka NISHIGUCHI

*Graduate School of Science, Technology, and Innovation, Kobe University
1-1 Rokkodai-cho, Nada-ku, Kobe 657-8501, Japan*

– *High- T_c superconductivity in multi-layer cuprates* –

We have theoretically studied superconductivity in multi-layer cuprate, which is a series of superstructured strongly correlated materials. Here 1–5-layer Hubbard model has been considered as an effective model for multi-layer cuprate superconductors. Then we have investigated the multi-layer superconductivity by solving the linearized Eliashberg equation for the superconducting gap function within the two-particle self-consistent (TPSC) approach. We have also developed the TPSC approach so as to treat the multi-layer systems. Many degrees of freedom arising from the multi-layer properties have been treated by the massive parallelization in ISSP Supercomputer Systems.

– *Possible superconductivity induced by spin-orbit coupling in carrier doped Sr_2IrO_4* –

Possible superconductivity in carrier-doped iridium oxide insulator Sr_2IrO_4 have studied by a weak-coupling approach[1]. We have treated t_{2g} 3-orbital Hubbard model with a large spin-orbit coupling (SOC) as an effective model for carrier-doped Sr_2IrO_4 . Numerically solving the linearized Eliashberg equation for the superconducting (SC) gap function with the random phase approximation (RPA), we have systematically examined both singlet and triplet SC gap functions with possible pairing symmetries and their parameter dependence. For the realistic SOC λ and Hund's coupling

J/U relevant to Sr_2IrO_4 , namely, for a large λ and small J/U region, we find that the intra-band antiferromagnetic (AF) pseudospin $j_{\text{eff}} = -l + s$ fluctuations favor a $d_{x^2-y^2}$ -wave pseudospin $j_{\text{eff}} = 1/2$ singlet pairing in the electron-doping (Figure 1). We also find that the $d_{x^2-y^2}$ -wave pairing is more stabilized with increasing the SOC and decreasing the Hund's coupling. Furthermore, we show for a small λ and large J/U region that an s_{\pm} -wave singlet pairing is favored in the hole-doped region (Figure 2). The origin of the s_{\pm} -wave pairing is due to the interband pair scattering arising from the intra-orbital AF spin s fluctuations. Although the possibility of a pseudospin triplet pairing is considered, we find it always unfavorable for all parameters studied here. We have also developed the multi-orbital and spin-dependent RPA so as to treat the multi-orbital systems with spin-orbit coupling. Many degrees of freedom arising from the multi-orbital and spin properties, namely, spin-orbit coupling, have been treated by the massive parallelization in ISSP Supercomputer Systems.

– *Electronic structures of doped $SrTiO_3$ as H_2 -generation semiconductor photocatalyst* –

We have performed the first-principles calculations based on the density functional theory to obtain electronic structures of doped $SrTiO_3$ as a H_2 -generation semiconductor photocatalyst. We have set the dopants to be a Rh and Sb atom and replaced the Ti sites with them in the $3 \times 3 \times 3$ $SrTiO_3$ supercell. The

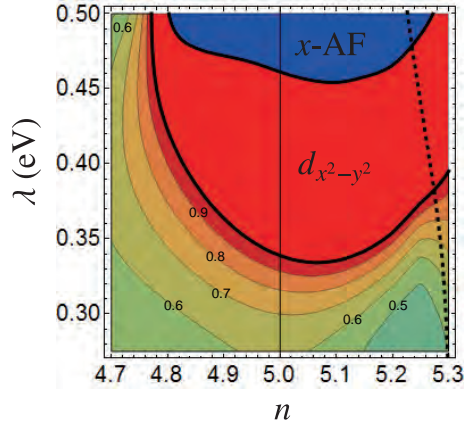


Figure 1: Contour plot of the largest eigenvalue of the linearized Eliashberg equation for the $d_{x^2-y^2}$ -wave pseudospin singlet pairing in the parameter space of the electron density n and the SOC λ for $U = 0.8$ eV, and $J/U = 0.05$. The red (blue) region represents the $d_{x^2-y^2}$ -wave pseudospin singlet SC (x -AF) phase.

O-vacancies have also been considered as the intrinsic defect in the realistic experimental situations. The first-principles calculations have been performed by using VASP (The Vienna Ab initio Simulation Package)[2], in which the hybrid functionals (HSE06) are adopted to reproduce the accurate band gap of SrTiO₃, and the massive band and k-point parallelization are used in ISSP Supercomputer Systems. The numerical calculations have shown from the density of states that the Rh-doping produces the impurity levels within the band gap as both donor and acceptor levels. We have also observed that the Sb-doping works as electron-doping and then removes the acceptors in the Rh+Sb-doping systems. In addition, the O-vacancies also works as electron-doping, which leads SrTiO₃ to the n-type semiconductors.

References

- [1] K. Nishiguchi, T. Shirakawa, H. Watanabe, R. Arita, and S. Yunoki: *J. Phys. Soc. Jpn.* **88** (2019) 094701.

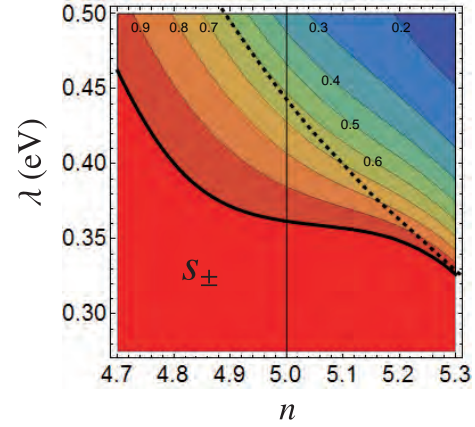


Figure 2: Contour plots of largest eigenvalue of the linearized Eliashberg equation for the s_{\pm} -wave pseudospin singlet pairing in the parameter space of n and λ for $U = 0.9$ eV and $J/U = 0.3$. The red region represents the s_{\pm} -wave pseudospin singlet SC phase.

- [2] VASP (The Vienna Ab initio Simulation Package): <https://www.vasp.at>

Study on Ising machines from a viewpoint of statistical mechanics

Shu TANAKA

*Green Computing Systems Research Organization, Waseda University
27 Wasedacho, Shinjuku, Tokyo 162-0042*

We have studied the performance of Ising machines from a viewpoint of statistical mechanics. The Ising machines have been attracting attention in recent years as a computer that has the potential to solve combinatorial optimization problems with high speed and accuracy. Very recently, quantum annealing machines, simulated annealing machines, and various other types of Ising machines have been developed. In order to draw out the potential of the Ising machine, it is more important to develop not only the hardware of the Ising machine but also the algorithm and software in accordance with the established mathematical framework. We conducted research on the following two topics on the basis of this trend.

(A) A guiding principle for embedding in simulated-annealing based Ising machines

When we use the Ising machine, the cost function and constraints of the combinatorial optimization problem are first expressed in the Hamiltonian of the Ising model or equivalent form. Herein, we refer to the Ising model as the logical Ising model. Next, we represent the logical Ising model on the limitations of the network of spins in an Ising machine. The operation is called embedding. In embedding algorithms, there are hyperparameters that should be adjusted to improve the computational performance, and how to adjust them is still unknown. In order to solve this question, we have succeeded in constructing a method of embedding algorithm based on the calculation

of the correlation function by the transfer matrix. The results suggest an improvement in the computational performance of simulated annealing-based Ising machines against typical existing embedding algorithms [1].

This work was done in collaboration with Dr. Tatsuhiko Shirai (Waseda University).

(B) The performance of black-box optimization using Ising machines from a viewpoint of statistical mechanical informatics

We have previously proposed a new method of black-box optimization using the Ising machine [2]. The results suggest that this method is superior to existing methods in the search for metamaterials with excellent thermal radiation characteristics. The theoretical basis for the superiority of this method is clarified from the perspective of statistical mechanical information.

This work was done in collaboration with Dr. Ryo Tamura (National Institute for Materials Science, The University of Tokyo).

References

- [1] T. Shirai, S. Tanaka, and N. Togawa, submitted. preprint version is available via https://www.dropbox.com/s/o8alkr8ch05ahtr/bare_jrnl_compsoc.pdf
- [2] K. Kitai, J. Guo, S. Ju, S. Tanaka, K. Tsuda, J. Shiomi, and R. Tamura: Phys. Rev. Research **2** (2020) 013319.

Nonequilibrium phase transition and slow dynamics in the dense hard sphere systems

Masaharu ISOBE

Nagoya Institute of Technology
Gokiso-cho, Showa-ku, Nagoya, 466-8555

The hard disk/sphere systems are one of the simplest models, which have been actively investigated in both equilibrium and non-equilibrium statistical physics. In this project, we investigated non-equilibrium phenomena in the hard disk/sphere model system with modern algorithms, especially for Event-Chain Monte Carlo(ECMC) [1] and Event-Driven Molecular Dynamics(EDMD) [2], where we propose the “Hybrid Scheme”, namely, ECMC for equilibration and EDMD for calculation of dynamical properties [3, 4].

Dynamic facilitation and direct evidence of void induced structural relaxations in glass formers:

On approaching glass transition, the viscosity of the supercooled liquid would be increased rapidly. It often behaves as solid with disorder structure within observation timescale. One of the challenging issues is to understand whether the essential properties of glass-forming materials are fundamentally thermodynamic or dynamic in origin. However, the microscopic origin of structural (so-called α) slow relaxation in deeply supercooled liquids at an atomic scale has remained elusive due to the limitation of both electron microscopy experiments and computer simulation. Although many theoretical models have been proposed and debated actively, one of a perspective that favors a dynamic origin is called Dynamic Facilitation (DF) theory [5, 6, 7]. DF theory was known to explain a wide range of empirically observed dynamical features of thermal super-

cooled liquids and glasses. The applicability of DF theory to athermal systems, i.e., systems of hard particles where the relevant control parameter is pressure rather than temperature, under “super-compressed” conditions was investigated by employing novel efficient algorithms [1, 2, 3]. The novel methodologies allowed studying in detail the true equilibrium dynamics of high-density systems, which is consistent with the predictions of DF theory. In such athermal molecular systems under “super-compressed” conditions — where what is facilitated is the ability of the constituent particles to structurally relax — giving rise to correlated and cooperative dynamics, in a manner predicted by theory [8].

In collaboration with the experimental group in Hong Kong, we resolve the coarse-grained trajectories obtained by colloidal experiments to confirm DF theory. The results undergo a transition from collective “creeping” to the string-like “hopping” motion on approaching the glass transition, where mobile of particles can be rearranged in string-like manners or compact geometries. Still, the compact ones decomposed into connected sequences of string-like hopping motion. Furthermore, such a string-like motion has an ultra-high returning hopping probability, which is proved to be the leading contributor to the kinetic arrest for slow relaxation. One of the paradoxical issues in DF theory is how a starter of string-like hopping has sufficient room for the first hop in highly dense packing fraction. A void as a

defect in the crystal structure can diffuse one after another on the crystal lattice positions in case of dense mono-disperse systems. However, in a dense amorphous structure, there are few voids with a size of particle diameter. Instead, we found the quasi-voids distributed within a few neighboring shells. The sufficient free volumes come from accumulated quasi-voids within a local area as a soft spot might induce the origin of string motion, where free volumes transport along to the string-like hopping motions. These hypotheses are now carefully investigated by molecular dynamics simulation, where the results would show direct evidence of the scenario based on DF theory [9].

[9] C.-T. Yip, M. Isobe et al.: in preparation.

References

- [1] E. P. Bernard, W. Krauth, and D. B. Wilson: *Phys. Rev. E* **80** (2009) 056704.
- [2] M. Isobe: *Int. J. Mod. Phys. C* **10** (1999) 1281.
- [3] M. Isobe: *Mol. Sim.* **42** (2016) 1317.
- [4] M. Isobe: “Advances in the Computational Sciences — Proceedings of the Symposium in Honor of Dr Berni Alder’s 90th Birthday”, edited by Eric Shwegerl, Brenda M. Rubenstein, and Stephen B. Libby, World Scientific, **Chapter 6** (2017) 83.
- [5] D. Chandler and J. P. Garrahan: *Annu. Rev. Phys. Chem.* **61** (2010) 191.
- [6] L. O. Hedges, R. L. Jack, J. P. Garrahan and D. Chandler: *Science* **323** (2009) 1309.
- [7] A. S. Keys, L. O. Hedges, J. P. Garrahan, S. C. Glotzer, and D. Chandler, *Phys. Rev. X*, **1** (2011) 021013.
- [8] M. Isobe, A. S. Keys, D. Chandler, and J. P. Garrahan: *Phys. Rev. Lett.* **117** (2016) 145701.

Glass phases induced by correlations

Chisa Hotta

*Department of Basic Science, University of Tokyo
Meguro-ku, Komaba, Tokyo 153-8902*

We studied the possibility of having a finite temperature glass phases driven by the correlation effect. Conventional spin glasses in realistic spatial dimensions, $d = 2, 3$ are realized in a series of Edwards-Anderson models with classical interactions between spins, J_{ij} , which distribute at around $\overline{J_{ij}} = 0$. There, the degree of disorder the only energy scale that competes with the thermal fluctuation. Even in such case the spin glass phases breaking the time reversal symmetry is allowed to exist at finite temperature only when $d \geq 3$. We studied two different types of models [1,2].

One is the classical vector spin Heisenberg model on a pyrochlore lattice with additional Ising-like lattice degrees of freedom, σ_i [1]; $\sigma_i = \pm 1$ indicate the displacement of the lattice site at each vertex, in and out of the tetrahedra, and the exchange interaction J_{σ_i, σ_j} between Heisenberg spins depends on the location of displacements of sites that the spins live on. Although there is no quenched randomness in the system, the elastic energy term $\propto \sigma_i \sigma_j$ and the spin exchange energy term $J_{\sigma_i, \sigma_j} \mathbf{S}_i \cdot \mathbf{S}_j$ are correlated with each other via J_{σ_i, σ_j} and work as dynamical randomness to each other. The two degrees of freedom finally undergo a simultaneous glass transition, which is detected by the scaling analysis on the auto-correlation functions[1].

The other one is the quantum transverse Ising model on a triangular lattice with very small quenched bond randomness[2]. This time, the transverse field first works on the spin degrees of freedom and drives the system to a KT phase, and successively to the clock-

phase, where the three-sublattice magnetic ordering appears. Introducing a very small bond randomness breaks the regular three-sublattice structure of the clock phase into pieces of domains, cooperatively with the emergent glass behavior of the spin degrees of freedom. The spins and lattices(bond order) work to each other as an emergent random fictitious field, which is the origin of the finite temperature spin glass in $d = 2$ system.

There are two common aspects between these two cases. First, the model has a finite spin coupling constant J , and energy scale representing the quenched disorder is either absent or very small, which is contradictory to the case of conventional spin glass whose energy is scaled by the quenched disorder. However, since these J 's are defined on frustrated lattices, the interactions themselves are not enough to stabilize any kind of magnetic orderings. This allows the emergent energy scale of disorder to dominate the low energy properties of the system. Second point is that the interplay of the two different species of degrees of freedom can stabilize the glass phase much more easily than had been considered before. Each of the degrees of freedom have a tendency to order and are on the verge of transition. The correlation with other degrees of freedom would not allow them to have a regular order, and both cooperatively goes into the glass phase.

References

- [1] K. Mitsumoto, C. Hotta, and H. Yoshino, Phys. Rev. Lett. **124**, 087201, (2020).
- [2] C. Hotta, K. Ueda and M. Imada, in preparation.

Magnetic structures of multiple-Q states in frustrated itinerant magnets

Takashi UCHIDA

Hokkaido University of Science

4-1, 7-15, Maeda, Teine-ku, Sapporo 006-8585

Recently, the magnetic structures of multiple-Q states have attracted attention since the topologically protected vortex-like magnetic structures such as magnetic skyrmions emerge as 3Q multiple helical spin density waves in the Dzyaloshinskii-Moriya (DM) interaction driven systems under magnetic field. In addition to these systems, the frustrated systems without the DM interaction have been found to reveal magnetic skyrmions [1, 2]. In the present work, we have applied the molecular spin dynamics (MSD) method [3] to the triangular-lattice single-band Hubbard model without the DM interaction to investigate the magnetic structures of multiple-Q states realized around the antiferromagnetic-ferromagnetic phase boundary.

The MSD method is based on the functional integral method with the static approximation for the spin fluctuation theories and the isothermal molecular dynamics method. The method allows us to find automatically the magnetic structures of a large system with thousands of atoms in a unit cell at finite temperatures.

In the numerical calculations the most time-consuming process is the magnetic force calculation at each time step, where the local electronic structures are calculated in real space by means of the recursion method. We have adopted the automatic parallel calculation scheme and found it to be effective in saving both computing time and CPU resources.

We have performed the magnetic structure calculations on the supercell with 20×20 triangular lattice, which is embedded in a large cluster consisting of 3×3 supercells, each of which are connected by the periodic boundary condition and are subject to the self-consistent uniform effective medium. Under zero magnetic field and the fixed value of the temperature $T/t = 0.0005$, we have changed the Coulomb interaction strength $U/t = 5 \sim 8$ and the electron number $n = 1.29 \sim 1.36$. The various multiple-Q states such as 2Q, 4Q, 2Q+1Q were found to be realized near the ferromagnetic boundary. Of these, the 2Q states are accompanied by small spontaneous magnetization. It is not clear, however, whether the calculated multiple-Q states are topologically protected structures or not. This is partly because that the main Q state is often accompanied by small satellite components, which make the whole magnetic structure complex. In order to make clear the magnetic structures of the multiple-Q states, the magnetic structure calculations with the site-dependent self-consistent effective medium are now in progress.

References

- [1] T. Okubo, S. Chung, and H. Kawamura: Phys. Rev. Lett. **108** (2012) 017206
- [2] Y. Takehashi, D. Kojima, T. Otonari, and H. Miyagi: J. Phys. Soc. Jpn. **87** (2018) 094712.
- [3] Y. Takehashi, S. Akbar, and N. Kimura: Phys. Rev. B **57** (1998) 8354.

Magnetization reversal process in classical spin systems

Taichi Hinokihara

Institute for Solid State Physics,

The University of Tokyo, Kashiwa-no-ha, Kashiwa, Chiba 277-8581

We studied a reveal the magnetization reversal process by using the classical spin Heisenberg model with the dipole-dipole interactions (DDI).

Recently, theoretical studies for the coercivity based on the atomistic-scale spin model are increasing due to the development of the first-principles calculations.

While these studies enable us to obtain material-dependent properties, the computational cost also increases to simulate such the model.

The problem becomes severe for studying the coercivity of magnet because it strongly depends on the long-range interaction, DDI [1,2].

In this project, we focused on the following two subjects: (i) develop efficient methods to simulate this system. (ii) propose a coarse-graining method to construct a macro spin model from the atomistic scale system obtained from the first-principles calculations.

For the subject (i), we recently developed the novel efficient method for the simulation of the dynamics of spins, called time quantified Monte Carlo with the stochastic cutoff method (TQMC+SCO).

As an example, the computational cost for the spin update is for the three-dimensional DDI system even when the system consists of the complicated lattice structure.

We analytically prove that the TQMC+SCO gives the same Fokker-Planck equation with the stochastic Landau-Lifshitz-Gilbert (s-LLG) equation, which is widely used for the simulation of spin dynamics.

Namely, the ensemble average of the magnetization trajectory calculated by the TQMC+SCO is the same as that by the s-LLG.

We also evaluated the validity of the present method by demonstrating the magnetization reversal process and comparing it to the result obtained by the s-LLG.

Figure 1 shows three magnetization-trajectories of the total magnetization along z-axis: s-LLG without DDI, s-LLG with DDI, and TQMC+SCO with DDI.

This simulation is performed in the $10 \times 10 \times 10$ spin system with exchange coupling J , the

anisotropy $K = 0.1J$, the DDI $D = 0.05J$, and the temperature $T = 0.2J$.

We performed the magnetic field $= 0.085J$ to drive the magnetization reversal process.

This figure clearly shows two results: (a) the DDI plays an essential role in the system with DDI, and (b) both s-LLG and TQMC+SCO gives the almost same magnetization trajectory.

We have submitted our paper, and it is now under review [3].

Besides, we recently found the other way of the bond-update process, which is suitable for the GPU calculation.

We are now preparing this paper.

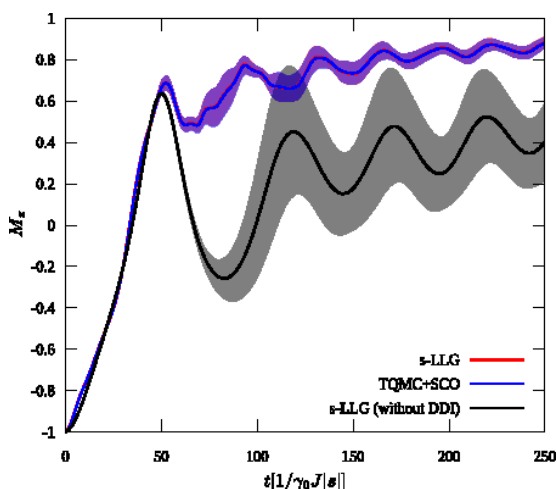


Fig. 1: Magnetization reversal process calculated by s-LLG without DDI (black), s-LLG with DDI (red), and TQMC+SCO with DDI (blue).

For the subject (ii), we constructed the macro-spin Hamiltonian from the atomistic-scale spin model of Nd₂Fe₁₄B in the following procedure. First, we construct the free-energy landscape for the single macro spin from the atomistic-scale spin model.

Each macro spin motion follows this landscape.

Next, the exchange coupling between the macro spins is selected to optimize the physical properties such as domain-all width.

We study the validity of our model by comparing it to other physical properties such as the total-magnetization and the susceptibility.

We are now preparing this paper.

References

- [1] Taichi Hinokihara, Masamichi Nishino, Yuta Toga, and Seiji Miyashita: Phys. Rev. B **97** 104427 (2018).
- [2] Yuta Toga, Masamichi Nihino, Seiji Miyashita, Takashi Miyake, and Akimasa Sakuma: Phys. Rev. B **98** 054418 (2018)
- [3] Taichi Hinokihara, Yuta Okuyama, Munetaka Sasaki, and Seiji Miyashita, arXiv: 1811.00237v2 (2019)

Quantum simulation for quantum many body systems using noisy-intermediate-scale quantum computers

Keisuke Fujii

Graduate School of Engineering Science,

Osaka University, 1-3 Machikaneyama, Toyonaka, Osaka 560-8531

Noisy Intermediate-Scale Quantum (NISQ) devices, or medium-scale quantum computers whose qubits are not fault-tolerant, are expected to be realized within a few years. As Google showed in 2019 [1], NISQ devices may be able to perform some tasks faster than the state-of-the-art classical computer. Such tasks should be sufficiently simple and suitable for a quantum computer, because of its incapability to remove errors in the computation process. Particularly, calculations for quantum many-body systems and quantum chemical systems are expected to be promising applications of NISQ devices.

In this project, we have developed a method to compute properties of quantum many-body systems, especially molecules in quantum chemistry, with NISQ devices and performed numerical simulations of them by using the ISSP supercomputer. Concretely, we invented a perturbative approach based on the variational quantum eigensolver (VQE) algorithm [2], which is a quantum-classical hybrid algorithm to compute the ground state energy of a system. One of the obstacles to utilize NISQ devices in quantum chemistry is that the number of available qubits is limited and often not enough

to describe molecular electronic wavefunctions quantitatively. Our method mitigates the problem by decomposing VQE calculation for a large system into a lot of VQE calculations for small systems. We applied this method to various molecules to verify accuracy and efficiency by numerically simulating the outputs of quantum circuits. The largest system we investigated was the Benzene molecule with the cc-pVDZ basis sets. We note that it is unfeasible to perform the simulation of the original VQE algorithm on classical computers as it requires 228 qubits for this system.

Our numerical simulation is based on the following programs: a fast quantum circuit simulator Qulacs [3] developed by our group; OpenFermion library [4] which can handle mapping fermionic Hamiltonians to qubit Hamiltonian; a quantum chemistry library PySCF [5]. Our code was highly parallelized using MPI, as our perturbative VQE method can be performed in an embarrassingly parallel fashion owing to its additive scheme.

K.F. would like to thank Wataru Mizukami for his help and collaboration throughout this project.

References

- [1] F. Arute et al., Nature **574**, 505-510 (2019).
- [2] A. Peruzzo et al., Nat. Commun. **5**, 4213 (2014).
- [3] Qulacs, <https://github.com/qulacs/qulacs>
- [4] J. McClean et al., arXiv:1710.07629
- [5] Q. Sun et al., WIREs Comput. Mol. Sci. **8**, e1340 (2017).

Study on Complex Systems by Generalized-Ensemble Algorithms

Takuya HAYASHI, Daiki MATSUBARA, and Yuko OKAMOTO

Department of Physics, Graduate School of Science, Nagoya University

Furo-cho, Chikusa-ku, Nagoya, Aichi 464-8602

We had two projects regarding generalized-ensemble algorithms applied to complex systems.

The density of states (DOS) is one of the most important physical values in statistical mechanics. Recently, we proposed a simulation protocol, REWL-MUCAREM [1], in order to obtain the DOS with high accuracy even in large systems by combining the *Replica-Exchange Wang-Landau* (REWL) method [2] and the *Multicanonical Replica-Exchange Method* (MUCAREM) [3]. The effectiveness of REWL-MUCAREM was demonstrated by using the 2-dimensional Ising model in [1].

We also applied the REWL-MUCAREM protocol to the ice Ih system in order to estimate the residual entropy with high accuracy. The residual entropy of ice has become one of good examples to test the efficiency of sampling algorithms. However, it seems that there is slight disagreement among the estimates by various calculation methods (see Fig.1). In this work, we give our latest estimate of the residual entropy by REWL-MUCAREM protocol.

Our latest estimate of residual entropy

per one water molecule [4] is

$$S = 0.815533 \pm 0.000066.$$

This estimate is in good agreement with the results of several other research groups. The results also imply that we need to develop a new simulation model in order to estimate the residual entropy with more accuracy.

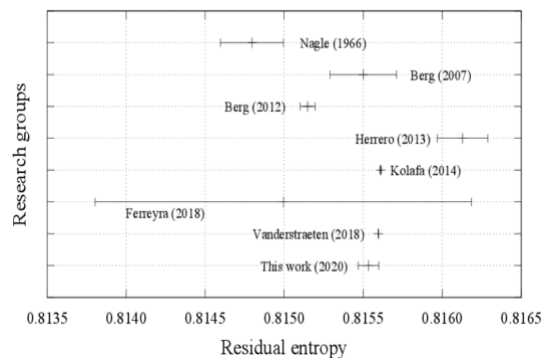


Figure 1: The estimates of residual entropy of ice Ih by several research groups.

In the second project, we have proposed the Grand Canonical Replica-Exchange Method (GCREM) [5], which is one of the multidimensional replica-exchange methods [6]. This method achieves a random walk in the temperature and chemical potential space, i.e., variables of grand canonical ensemble, in one simulation. In this study, we applied GCREM to the LJ potential system and succeeded in drawing a phase diagram

including gas-liquid first-order phase transition, second-order phase transition, and supercritical fluid (see Fig.2). We also calculated the critical point as $(T_c^*, \mu_c^*) = (1.18 \pm 0.01, -3.34 \pm 0.01)$. This is in good agreement with the results of previous study [7].

GCREM could sample various structural phases in one simulation run (see Fig.3): It was possible to sample the states of different numbers of particles such as gas, liquid, supercritical fluid, because the number of particles in the grand canonical ensemble varies. By using the structure that defines each of these states, structural analysis based on, e.g., radial distribution functions and cluster formation, became possible.

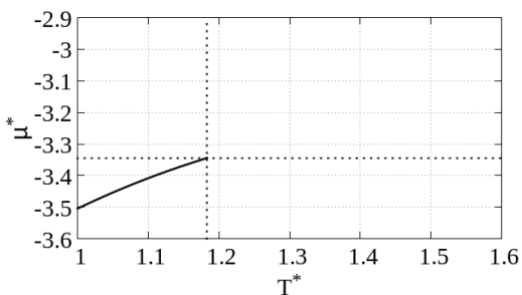


Figure 2: The phase diagram on reduced temperature and chemical potential space. The black line indicate 1st order phase transition points and the edge is the 2nd order phase transition point, i.e., critical point. Dotted lines indicate the critical temperature and chemical potential.

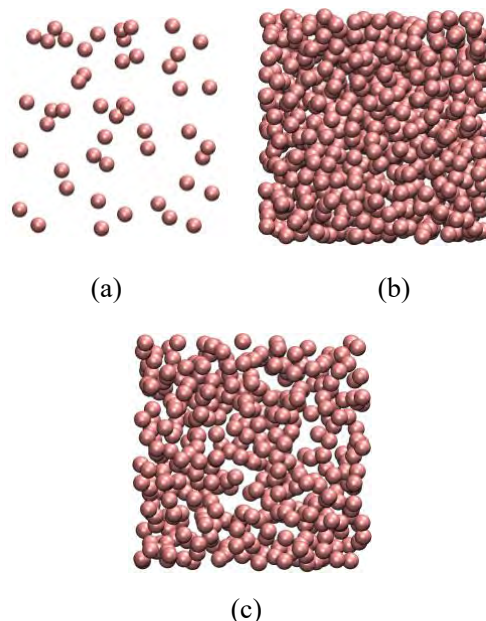


Figure 3: Snapshots of the LJ particle system obtained from a single GCREM run. Fig.3 (a) corresponds to Gas phase, (b) corresponds to Liquid phase, and (c) corresponds to supercritical phase.

References

- [1] T. Hayashi and Y. Okamoto, Phys. Rev. E. **100**, 043304 (2019).
- [2] T. Vogel, Y. W. Li, T. Wüst and D. P. Landau, Phys. Rev. Lett. **110**, 210603 (2013).
- [3] Y. Sugita and Y. Okamoto, Chem. Phys. Lett. **329**, 261 (2000).
- [4] T. Hayashi, C. Muguruma, and Y. Okamoto, in preparation.
- [5] D. Matsubara and Y. Okamoto, J. Chem. Phys. **152**, 194108 (2020).
- [6] Y. Sugita, A. Kitao, and Y. Okamoto, J. Chem. Phys. **113**, 6042–6051 (2000).
- [7] N. B. Wilding, Am. J. Phys. **69**, 1147-1155 (2001).

Development of a Coarse-Grained Force Field Designed with a Polar Water Model

Wataru Shinoda

*Department of Materials Chemistry, Nagoya University
Furo-cho, Chikusa-ku, Nagoya 464-8653*

Coarse-grained (CG) approaches have been adopted to investigate biological events relevant to the mesoscale. Many models have been proposed and used for various target systems, depending on the level of accuracy required in the CG description. One of the promising CG FFs, recently renamed as SPICA FF [1, 2, 3], accurately reproduces the experimental thermodynamic properties and structure (distribution function) obtained from AA-MD simulations using the CHARMM FF [4]. However, the ability of the SPICA FF to predict the morphology of highly charged molecular complexes in aqueous solution is still limited due to the lack of the polarity with the CG water model and to the assumption of a high (background) dielectric constant. To overcome this problem, we developed a CG FF, pSPICA, that is based on a polar CG water model in order to precisely describe the molecular events that are difficult to simulate using the SPICA FF with non-polar water in lipid membrane systems, such as water defects, membrane electroporation, and morphological changes in the charged lipid self-assemblies. We follow the parameter-optimization scheme used in the SPICA FF, namely, the parameters are optimized to reproduce several thermodynamic quantities measured experimentally [1, 2, 3].

In this study, we used the LAMMPS for CG-MD simulations, and the simulations were significantly accelerated by GPU. In the pSPICA FF, the polar CG water particle is composed of a pair of interacting sites, WO and WH

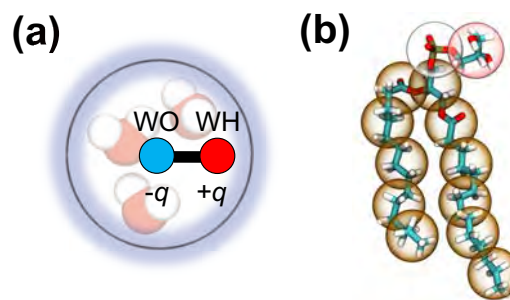


Figure 1: (a) Polar CG water, representing three water molecules, developed in this study. The blue bead, WO, has a van der Waals radius shown with a black circle. The red bead, WH, is connected to WO via a rigid bond and is positioned within the van der Waals radius of WO. (b) The CG mapping of a DMPG lipid. All-atom representation is given in stick and CG representation is given in transparent particle.

(Fig. 1 (a)), and was designed to represent three neighboring water molecules in aqueous solution. The two sites, WO and WH, are connected by a rigid bond, and have positive and negative partial charges, respectively. The choice of the CG sites for lipid molecules is the same as that in SPICA FF (Fig. 1). The parameters of the CG sites were systematically optimized to reproduce surface/interfacial tension, density, solvation or transfer free energy, as well as distribution functions obtained from all-atom molecular dynamics trajectory generated with the CHARMM FF, following the

scheme used in the SPICA FF. Lipid membranes simulated using the present CG FF demonstrate reasonable membrane area and thickness, elasticity, and line tension, which ensure that the simulated lipid membranes exhibit proper mesoscopic morphology. Using the pSPICA FF with the supercomputer at ISSP, we performed a large scale simulation to investigate the morphology of aggregates of the lipids dimyristoylphosphatidylglycerol (DMPG) in dilute solution. Thanks to the reasonable variation of line tension and elastic moduli of the lipid membranes depending on salt concentrations in the pSPICA FF, the morphological changes in the lipid aggregates showed good agreement with those observed in experiments (Fig. 2 (a)). CG-MD simulations of the membrane electroporation processes of flat lipid bilayers and vesicles were successfully performed by the pSPICA FF. A water channel bridging the lipid bilayer was formed spontaneously in the presence of an electric field generated by an imbalanced NaCl salt distribution, allowing ion transport across the lipid bilayer (Fig. 2 (b)). The results were similar to the pore opening process observed using AA-MD. Thus, the new CG FF enabled us to quantitatively investigate biological events, especially those involving water strings and defects in lipid membranes and ionic molecules.

References

- [1] W. Shinoda, R. DeVane, and M. L. Klein: *Mol. Simul.* **33** (2007) 27.
- [2] W. Shinoda, R. DeVane, and M. L. Klein: *J. Phys. Chem. B* **114** (2010) 6836.
- [3] S. Seo, W. Shinoda: *J. Chem. Theory Comput.* **15** (2019) 762.
- [4] J. B. Klauda, R. M. Venable, J. A. Freites, J. W. O' Connor, D. J. Tobias, C. Mondragon-Ramirez, I. Vorobyov, A. D. MacKerell, R. W. Pastor: *J. Chem. Phys. B* **114** (2010) 7830.

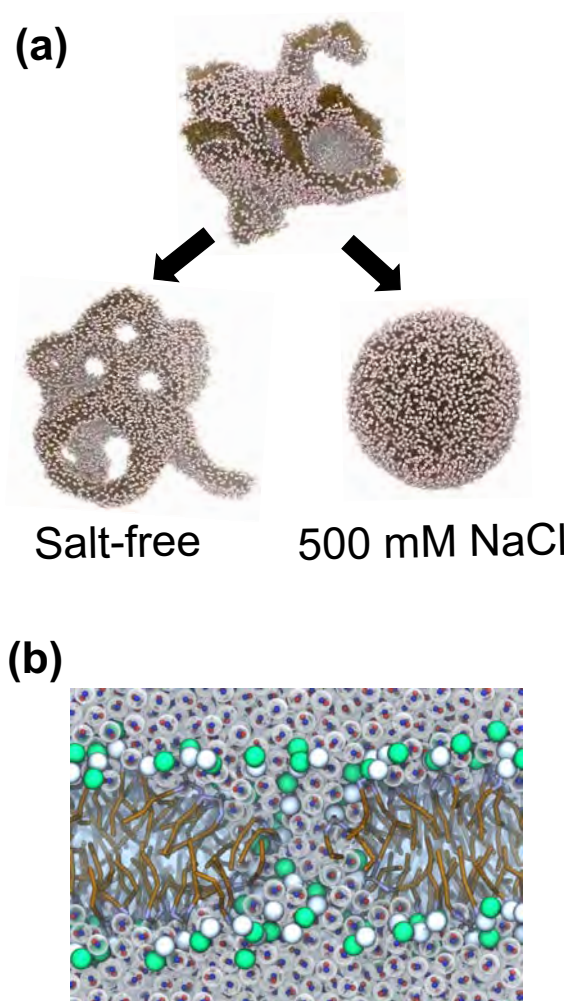


Figure 2: (a) Snapshots of the initial aggregate composed of 5000 DMPG units and the finally obtained aggregate in salt-free and 500 mM NaCl solution. (b) Snapshot of the electroporation process found in the simulation for a planar membrane system.

Screening of Substitutable Element in Rare-earth Inter-metallic Compounds

Riki KOBAYASHI

*Department of Physics and Earth Sciences, Faculty of Science
University of the Ryukyus, Nakagami, Okinawa 903-0213, Japan*

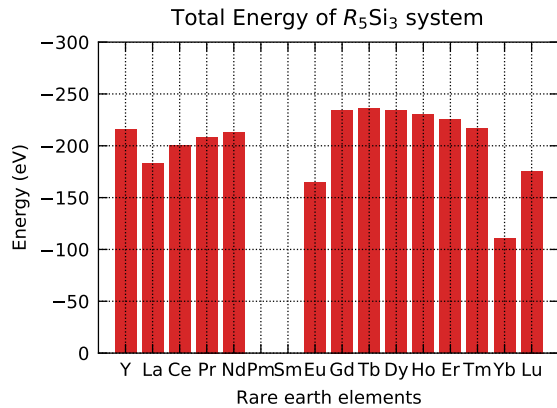


Figure 1: Total energy of R_5Si_3 ($R = \text{REEs}$) system after structure relaxation.

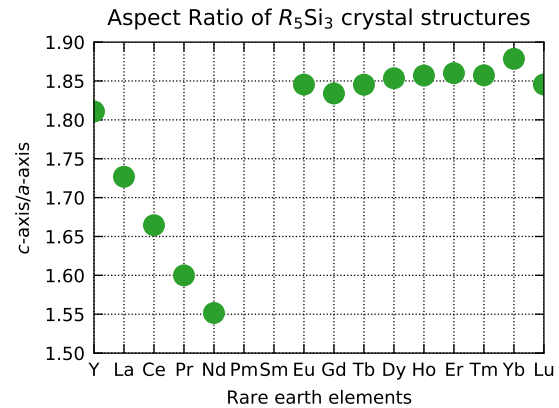


Figure 2: Aspect ratio of R_5Si_3 ($R = \text{REEs}$) crystal structures.

Recently, we have succeeded in growing single crystals of Ce_5Si_3 and Ce_5Ga_2Ge with the tetragonal Cr_5B_3 -type crystal structure and found that the Cr2-sites in the Cr_5B_3 -type crystal structure form the Shastry-Sutherland-Tetrahedral-Lattice (SSTL). SSTL has four geometrically frustrated two-dimensional layers in a unit cell, called orthogonal-dimer systems, and the ground state of Ce2-sites in Ce_5Si_3 and Ce_5Ga_2Ge is a spin-dimer due to this geometric frustration. There are no other Ce compounds showing spin-dimers at the ground state other than Ce_5Si_3 and Ce_5Ga_2Ge , which are important targets for the study of heavy fermion systems with geometric frustration. However, few rare-earth compounds with the Cr_5B_3 -type crystal structure have been reported, and this lack of targets is a bottle-

neck for the above research. In this study, the structural stability of R_5Si_3 ($R = \text{Rare earth elements}$) is investigated by comparing the total energy of R_5Si_3 obtained by first-principles calculations to find new Cr_5B_3 -type materials.

The calculations were performed using the Vienna Ab-initio Simulation Package (VASP), which is capable of generalized gradient density approximation (GGA), and the K-points and energy cut-off values were based on the $8 \times 8 \times 4$ mesh and VASP recommendations, respectively[1]. In this study, both quasi-Newtonian and conjugate gradient algorithms are used to calculate the structural relaxation, and it is confirmed that there is no significant difference in the results between the two algorithms.

Figure 1 shows the total energy of R_5Si_3

from first-principles calculations. Pm_5Si_3 and Sm_5Si_3 were excluded from the graphs because Pm is a radioactive isotope with a short half-life, and Sm_5Si_3 did not converge in the SCF calculation. The present calculations revealed that the total energy is lower in the compounds containing Eu and Yb elements than in the others, and it may be difficult to obtain a Cr_5B_3 -type crystal structure in these compounds.

Figure 2 shows the aspect ratio of the lattice parameter of $R_5\text{Si}_3$. Systematic changes in the aspect ratios were observed for compounds containing light REE from Y to Nd. This indicates that a specific axis of the unit cell may shrink due to lanthanide contraction.

References

- [1] G. Kresse and J. Furthmuller, Phys. Rev. B **54**, 11 169 (1996).

3.5 SCCMS Projects

First-Principles Phase Field Mapping

Kaoru Ohno

Department of Physics, Faculty of Engineering Science,

Yokohama National University, Tokiwadai, Hodogaya-ku, Yokohama 240-8501

In order to predict microstructures of alloys without relying on any empirical or experimental parameter, we have developed the first-principles phase field method by combining cluster expansion theory, potential renormalization theory and density functional theory and applied it to NiAl alloys that are used for example in jet engine turbine blades at high temperature [1]. This year, we focused on Ti-6wt%Al-4wt%V (Ti64) alloy, which is one of the most used Ti alloys in industry in a broad range from aerospace to medical applications. The mechanical properties and the phase transformation of Ti64 are strongly influenced by the microstructure, which is reliant on the history of processing, thermal treatment procedures and alloying element partitioning

effects. We succeeded in applying the first-principles phase field method to this system without using any thermodynamic parameter and identifying the element partitioning effect, i.e., enrichment of V in the β grain boundary and Al in the α phase at 977 °C. Figs. 1(a) and (b) show the resulting V and Al concentrations, while Figs. 1(c) and (d) show the corresponding experimental images [3], which look very similar to each other. As a conclusion, the present method has an ability to predict complex microstructure of alloys.

References

- [1] S. Bhattacharyya, R. Sahara, and K. Ohno, Nature Communications **10**, 3451;1-10 (2019).
- [2] T. N. Pham, K. Ohno, R. Kuwahara, and S. Bhattacharyya, J. Phys.: Cond. Mat. **32**, 264001;1-9 (2020).
- [3] S. Huang, et al. J. Alloys Compounds. **791**, 575-585 (2019).

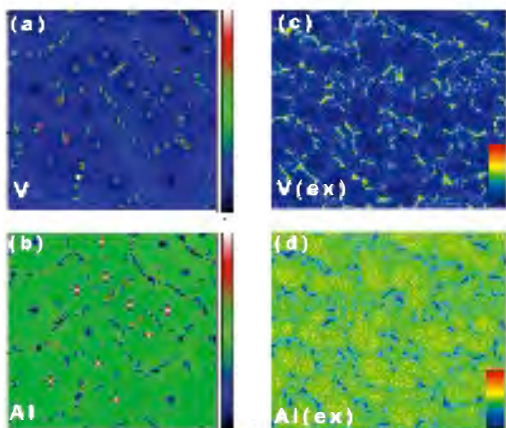


Fig. 1: (a) V and (b) Al concentrations obtained by the present method [2], and (c), (d) the corresponding experimental images [3].

Energy conversion --chemical energy--

Osamu SUGINO

Institute for Solid State Physics,

The University of Tokyo, Kashiwa-no-ha, Kashiwa, Chiba 277-8581

Challenge of electrochemical interface study is to establish a quantum theory of electrode and to predict an ultimately efficient energy conversion. To this end we studied two topics, manifestation of nuclear quantum effect on H/Pt(111) and environmental effect on the oxygen reduction reaction (ORR) on transition metal oxides. The nuclear quantum effect was investigated by applying the first-principles path integral molecular dynamics (PIMD) under different coverage conditions [1]. The hydrogen atoms are known to be delocalized quantum mechanically under low coverage but, with increasing coverage, the interatomic repulsion is found to induce localization within an adsorption site; atop, fcc, or hcp. The interaction induced localization, which had been shown to exist in a low index noble metal surfaces, was captured on platinum and this phenomenon is found to

provide a hint to the hitherto unexplained structure of H/Pt(111).

It is also important to utilize the simulation for electrocatalyst design. Platinum alloys are used in the existing fuel cells, but they are not active enough. For better electrocatalysts, transition metal oxides are attracting attention, but the mechanism has not been understood. In collaboration with experimental groups, we calculated the correlation of the adsorption energies of the ORR intermediates, O_2H , OH , and O ; the correlation is known to be a descriptor of the activity. For most materials, the correlation curve does not cross the point for ideal activity, but TiO_2 and ZrO_2 are found to cross it when doped with some noble metal dopants [2]. The activity versus defects relation is consistent with experimental findings. From these results, the joint research group is now planning to realize an ideal

catalyst.

C123 19486 (2019).

References

- [1] L. Yan et al. Phys. Rev. B101, 165414 (2020).
- [2] Y. Yamamoto et al. J. Phys. Chem.

Molecular Dynamics Simulation Studies of Electrochemical Properties of Ionic Liquid Electrolytes

Hayato SHIBA^{1,2} and Patrick A. BONNAUD¹

¹*Institute for Materials Research, Tohoku University, Katahira, Aoba-ku, Sendai 980-8577*

²*Information Technology Center, The University of Tokyo, Kashiwa-no-ha, Kashiwa, Chiba 277-8589*

Ionic liquids (ILs) are salts that are liquid at the good reason that they are composed only of ions, they are expected to be good candidates for electrolytes in supercapacitors. They may exhibit fast charging times, excellent power performances, and good aging properties. In this project, we focused on capacitors based on properties of Electrical Double Layer Capacitors (EDLC), in which ionic liquid are confined between a pair of planar electrodes.

We employed molecular simulation to study underlying molecular mechanisms of electrical properties in EDLC. we selected an ionic pair widely studied experimentally: 1-butyl-3-methylimidazolium / bis[(trifluoromethyl) sulfonyl] imide. Then, we inserted those ions in a simulation box made of two electrodes separated by a slit-shape gap of 4 and 6 nm up to a mass density corresponding to given thermodynamics conditions ($300 < T < 400$ K and $p \sim 1$ atm). We employed LAMMPS in combination with the constant potential method to simulate EDLC at the molecular scale, by using a subroutine by Zhenxing Wang *et al.*¹

We have observed that ions migrate toward electrodes of opposite charge upon an applied voltage. The fluid structure in vicinal layers that span over roughly 1 nm with respect to the electrode surface is more pronounced than in the neutral state. In the core of the gap between electrodes, the higher the applied voltage, the more structured the fluid. Ions formed alternative layers of cations and anions. From the average total charge sampled on one of the electrodes, we computed the total gravimetric capacitance and observed a fast increase at low applied voltages before reaching a nearly constant behavior beyond 1V. Those results set a cornerstone for the understanding of molecular mechanisms underlying electrical properties of EDLC.

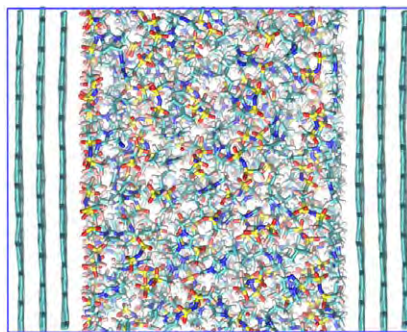


Fig. 1: Snapshot of a molecular model for simulations at constant potential.

¹ <https://github.com/zhenxingwang/lammps-conp>

Development of accuracy verification method on analytic continuation results using cross validation

Kazuyoshi YOSHIMI¹, Yuichi MOTOYAMA¹, Yoshinori NAKANISHI-OHNO²

¹*Institute for Solid State Physics, University of Tokyo, Kashiwa 277-8581*

²*Graduate School of Arts and Sciences, University of Tokyo, Tokyo, 153-8902*

Recent developments in computational sciences have made it possible to construct and analyze effective models for realistic materials. Quantum Monte Carlo (QMC) calculations are one of powerful methods for finite temperature analysis of effective models. To compare with experimental results such as excitation spectra, it is necessary to connect the results of imaginary time simulations in QMC method to real time by means of a numerical analytic continuation. However, there is a problem that small statistical noise of the input data has a great influence on the results of the analytic continuation, and there has been no decisive method to enable high-precision spectral analysis until now.

Recently, we have proposed a method to automatically select bases which are insensitive to noise using sparse modeling and to achieve a numerically stable analytic continuation against noise (SpM) [1-3]. In addition, SpM can easily add physically required conditions as constraints, such as spectral non-negativity and sum rule. In this work, we have developed a new method to improve the validity of the results obtained by SpM. We also developed software to enable the

verification on the results obtained by SpM using cross-validation.

In SpM, artificial oscillations appear in the low frequency range due to the cutoff of the bases. To solve this problem, we focused on the Pade approximation, which gives high-precise analytic continuation in the low-frequency region. In our method (SpM-Pade), the cost function which becomes large when the difference between the spectrum and that by Pade becomes large in the region where the spectrum by Pade is stable to noise. We

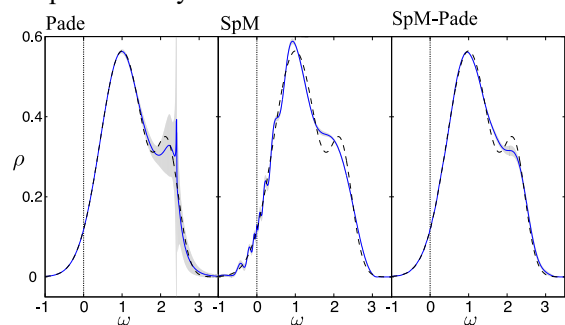


Figure 1 Reconstructed spectrum by the Pade (left), the SpM (center), and the SpM-Pade (right) method. The line denotes the mean value and the shaded region denotes the standard deviation from 30 independent samples. The exact spectrum is shown as the black dashed line.

examined the validity of SpM-Pade using the test data obtained by adding noise to the artificially given spectrum and performing an inverse transformation of the analytic continuation. In order to see the sensitivity to noise, the simulations were done for 30 independent samples. In Fig. 1, we show the reconstructed spectrum by the Pade (left), the SpM (center), and the SpM-Pade (right) methods, respectively. It is seen that using Pade approximation, the spectrum (solid line) is almost same as the exact one (dashed line) around $\omega=0$ and the standard deviation (shaded area) is small. With increasing ω , both the difference between the spectrum and the exact one and the deviation become large toward the second peak around $\omega=2$ as expected. In the case of SpM, the oscillations appear around $\omega=0$ and the second peak becomes broad compared to the exact one. However, the small variance indicates that this method is insensitive to noise. In the case of SpM-Pade, due to introducing the cost function, the oscillations around $\omega=0$ is suppressed. On the other hand, the noise tolerance is still strong as seen from the small

deviation. Actual data, such as QMC data, have a correlation between imaginary time data. In the current simulation, we have ignored these effects. We plan to apply SpM-Pade to the QMC data and investigate its applicability.

For the cross-validation program, we develop a program for large-scale parallel computers so that it is designed not only to be used for analytic continuation but also for various methods. Now, we confirmed that it worked on the ISSP supercomputer for the analysis in which the reduction of the noise of the image was done using sparse modeling. We plan to release this program as open source software when it can be used for various solvers, including the program of SpM [2].

References

- [1] J. Otsuki, M. Ohzeki, H. Shinaoka, and K. Yoshimi: Phys. Rev. E **95** (2017) 061302.
- [2] K. Yoshimi J. Otsuki, Y. Motoyama, M. Ohzeki, and H. Shinaoka: Comput. Phys. Commun. **244** (2019) 319.
- [3] J. Otsuki, M. Ohzeki, H. Shinaoka, and K. Yoshimi: J. Phys. Soc. Jpn. **89** (2020) 2061.

Ab initio study of quantum spin liquid in molecular conductors

Takahiro Misawa

Institute for Solid State Physics, University of Tokyo
Kashiwa-no-ha, Kashiwa, Chiba 277-8581

It has been experimentally reported that the $X[\text{Pd}(\text{dmit})_2]_2$ molecular conductors exhibit various phases such as antiferromagnetic, spin-liquid, and charge-ordered states depending on the choice of cation (X) [1]. In order to elucidate the origin of this variety of phenomena, detailed analyzes of band structures and transfer integrals based on the extended Hückel method and first-principles calculations have been performed to quantitatively evaluate the material dependence of electronic states [2]. On the other hand, systematic analyses incorporating the electron correlation effect, which plays an important role in the emergence of various phases, have not been carried out due to the lack of efficient tools and the need for large computational resources for analysis in molecular conductors. We note that the derivation of the low-energy effective Hamiltonian including the interaction parameters is carried out only for $\text{EtMe}_3\text{Sb}[\text{Pd}(\text{dmit})_2]_2$ [3], which has the quantum spin liquid ground state.

In this project, using the open-source software package RESPACK [4, 5], we systematically derive effective Hamiltonians for all available nine β' - $X[\text{Pd}(\text{dmit})_2]_2$ ($X = \text{Me}_4\text{Y}$, EtMe_3Y , $\text{Et}_2\text{Me}_2\text{Y}$ and , $Y = \text{As}$, Sb , and P) [6]. In the part of obtaining the global band structures, we use Quantum ESPRESSO [7]. Furthermore, using the quantum lattice model solver $\mathcal{H}\Phi$ [8, 9], we perform the numerically exact analyzes for the obtained low-energy effective Hamiltonians and show that the mag-

netic properties are well reproduced including the quantum spin liquid behavior observed in $X=\text{EtMe}_3\text{Sb}$. We also show that both the geometrical frustration and the off-site interactions play key role in stabilizing the quantum spin liquid.

In addition to the *ab initio* study for the molecular conductors, we perform the *ab initio* calculations for the high- T_c cuprates [10, 11]. We also analyze the quantum transport phenomena in the Weyl semimetals [12] and the topological semimetals [13] using the real-time evolution of the quantum systems. Furthermore, using the many-variable variational Monte Carlo method [14, 15], we analyze the quantum spin-nematic phase [16], the Kitaev model under magnetic fields [17], and the dynamical properties of the correlated electron systems [18].

References

- [1] R. Kato, Chem. Rev. **104**, 5319 (2004).
- [2] K. Kanoda, R. Kato, Annu. Rev. Condens. Matter Phys. **2**, 167 (2011).
- [3] K. Nakamura, Y. Yoshimoto, M. Imada, Phys. Rev. B **86**, 205117 (2012).
- [4] <https://sites.google.com/view/kazuma7k6r>
- [5] K. Nakamura, Y. Yoshimoto, Y. Nomura, T. Tadano, M. Kawamura, T. Kosugi,

- K. Yoshimi, T. Misawa, Y. Motoyama,
arXiv preprint arXiv:2001.02351.
- [6] T. Misawa, K. Yoshimi, T. Tsumuraya,
arXiv preprint arXiv:2004.00970.
- [7] P. Giannozzi, O. Andreussi, T. Brumme,
O. Bunau, M. B. Nardelli, M. Calandra,
R. Car, C. Cavazzoni, D. Ceresoli, M. Co-
coccioni, et al., *Journal of Physics: Con-
densed Matter* **29**, 465901 (2017).
- [8] M. Kawamura, K. Yoshimi, T. Misawa,
Y. Yamaji, S. Todo, N. Kawashima, *Com-
put. Phys. Commun.* **217**, 180 (2017).
- [9] [https://www.pasums.issp.u-tokyo.
ac.jp/HPhi/en/](https://www.pasums.issp.u-tokyo.ac.jp/HPhi/en/)
- [10] M. Hirayama, T. Misawa, T. Ohgoe,
Y. Yamaji, M. Imada, *Phys. Rev. B* **99**,
245155 (2019).
- [11] T. Ohgoe, M. Hirayama, T. Misawa,
K. Ido, Y. Yamaji, M. Imada, *Phys. Rev.
B* **101**, 045124 (2020).
- [12] T. Misawa, R. Nakai, K. Nomura, *Phys.
Rev. B* **100**, 155123 (2019).
- [13] T. Misawa, K. Nomura, *Scientific Reports*
9, 19659 (2019).
- [14] T. Misawa, S. Morita, K. Yoshimi,
M. Kawamura, Y. Motoyama, K. Ido,
T. Ohgoe, M. Imada, T. Kato, *Comput.
Phys. Commun.* **235**, 447 (2019).
- [15] [https://www.pasums.issp.u-tokyo.
ac.jp/mvmc/en/](https://www.pasums.issp.u-tokyo.ac.jp/mvmc/en/)
- [16] T. Hikihara, T. Misawa, T. Momoi, *Phys.
Rev. B* **100**, 214414 (2019).
- [17] K. Ido, T. Misawa, *Phys. Rev. B* **101**,
045121 (2020).
- [18] K. Ido, M. Imada, T. Misawa, *Phys. Rev.
B* **101**, 075124 (2020).

Unified Photonic-Electronic Devices

Kazuhiro YABANA

*Center for Computational Sciences,
University of Tsukuba, Tsukuba 305-8577*

We develop a first-principles computational method to investigate electron dynamics induced by ultrashort laser pulses based on time-dependent density functional theory (TDDFT) in real time. We develop the code SALMON (Scalable Ab-initio Light-Matter simulator for Optics and Nanoscience) [1] and make it open to the public at our website, <http://salmon-tddft.jp>.

SALMON is developed as a unified software that include traditional computational methods of light-matter interaction, the electromagnetism analysis using finite-difference time-domain (FDTD) method, and linear response calculation for susceptibilities based on TDDFT. There are two options for the coupling: macroscopic[2] and microscopic [3]. In addition, Ehrenfest molecular dynamics can be combined in the multiscale simulation [4].

This year, we have concentrated on the development of ver. 2 of SALMON. In the new version, we intended to improve the readability and extensibility of the code by using structures of Fortran extensively. We also paid much effort to improve the efficiency and scalability for large-scale calculations. Using the code, it is

now possible to calculate the ground state and electron dynamics of systems of more than a few thousand atoms. We intend to make the new version public in early fiscal year of 2020.

References

- [1] M. Noda, et.al, “SALMON: Scalable Ab-initio Light–Matter simulator for Optics and Nanoscience”, *Comp. Phys. Comm.* 235, 356 (2019).
- [2] K. Yabana, T. Sugiyama, Y. Shinohara, T. Otobe, G.F. Bertsch, “Time-dependent density functional theory for strong electromagnetic fields in crystalline solids”, *Phys. Rev. B* 85, 045134 (2012).
- [3] S. Yamada, M. Noda, K. Nobusada, K. Yabana, “Time-dependent density functional theory for interaction of ultrashort light pulse with thin materials”, *Phys. Rev. B* 98, 245147 (2018).
- [4] A. Yamada, K. Yabana, “Multiscale time-dependent density functional theory for a unified description of ultrafast dynamics: Pulsed light, electron, and lattice motion in crystalline solids”, *Phys. Rev. B* 99, 245103 (2019).

Dynamical DMRG study of magnetic excitations in magnetization plateaus of a frustrated spin ladder

Takami TOHYAMA

Department of Applied Physics, Tokyo University of Science, Tokyo 125-8585

Magnetization plateau (MP) emerges in quantum spin systems due to spontaneously breaking of translational symmetry. The broken symmetry can induce reconstruction of elementary excitations, but its microscopic mechanism and reconstructed quasiparticle in MP phases have remained unclear. We theoretically study magnetic excitations in the MP phases of a frustrated spin ladder (FSL) by using the dynamical density-matrix renormalization-group (DDMRG) method [1].

The Hamiltonian of FSL is defined as $H = H_{\perp} + H_{\parallel} + H_Z$ with $H_{\perp} = J_{\perp} \sum_{i=1}^N \mathbf{S}_{i,1} \cdot \mathbf{S}_{i,2}$, $H_{\parallel} = \sum_{\eta=1}^2 J_{\eta} \sum_i \sum_{j=1}^2 \mathbf{S}_{i,j} \cdot \mathbf{S}_{i+\eta,j}$, and $H_Z = -h \sum_{i,j} S_{i,j}^z$, where $\mathbf{S}_{i,1}$ ($\mathbf{S}_{i,2}$) is the $S = 1/2$ spin operator on i th rung in the upper (lower) chain. Exchange energies of the first-neighbor bond in a leg, the second-neighbor bond in a leg, and the first-neighbor bond in a rung, are denoted by J_1 , J_2 , and J_{\perp} , respectively. We set $J_1/J_{\perp} = 0.2$ and $J_2/J_{\perp} = 0.65$. Changing magnetic field h , we obtain MPs at $m = M/M_s = 1/3, 1/2$, and $2/3$, where M (M_s) is magnetization (saturation magnetization).

We calculate dynamical spin structure factor (DSSF) using DDMRG, where the correction vector is expanded by the Legendre polynomial with a Gaussian averaging [2] and a broadening factor is replaced by the width of the Gaussian, for which we set $0.02J_{\perp}$. The system size, $N = 48$ rungs, is sufficient to discuss dynamical behaviors. The number of states kept in the DDMRG is $m = 600$, leading to truncation error less than 1×10^{-4} .

Figure 1 shows DSSF for momentum along

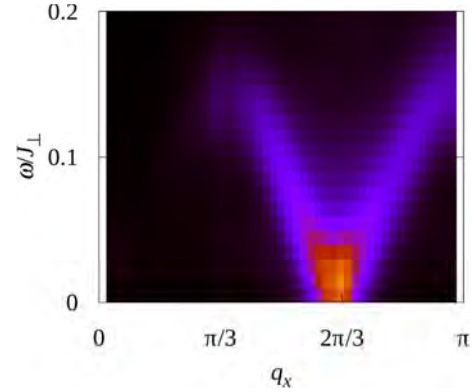


Figure 1: DSSF for $q_y = \pi$ in the $m = 1/3$ MP.

rung $q_y = \pi$ as a function of momentum along leg q_x in the case of $m = 1/3$ [1]. A dispersive feature with zero-energy excitation at $q_x = 2\pi/3$, indicating a period with three times the original unit-cell length in real space.

We also perform analytical approaches with the perturbation theory to obtain an intuitive view of magnetic excitations. A comparison between numerical and analytical results indicates the presence of a reconstructed quasiparticle originating from spontaneously broken translational symmetry, which is realized as a collective mode of the spin trimer called a trimeron [1].

References

- [1] K. Sasaki, T. Sugimoto, T. Tohyama, and S. Sota: Phys. Rev. B **101** (2020) 144407.
- [2] S. Sota and T. Tohyama: Phys. Rev. B **82** (2010) 195130.

Conversion and storage of energy—fuel cells and secondary batteries: Research and development of fundamental technologies of battery simulators.

Susumu OKAZAKI

*Department of Materials Chemistry, Nagoya University
Furo-cho, Chikusa-ku, Nagoya 464-8603*

The goal of our project is to develop the basic technology of the whole battery simulator. One of the key techniques is molecular-level design of polymer membranes controlling transportation of protons and ions across the membrane with proper stiffness resistant to mechanical deformation under external stress. Such membranes are widely applicable to the fuel cells used in the industrial products.

We previously performed fully atomistic molecular dynamics (MD) calculations of hydrated perfluorosulfonic acid (PFSA) ionomers composed of a hydrophobic polytetrafluoroethylene backbone with hydrophilic side chains terminated by sulfonic acid, as a model of proton exchange polymer electrolyte membrane of fuel cells[1, 2, 3]. On the system B and C, we further performed a series of MD calculations of different equivalent weight PFSA membranes containing H₂ molecules at different water uptakes[4] (examples are shown in Figs. 1 (A)–(C)). They explored atomistic detail of H₂ permeation through the membranes. The local semicrystalline structure of the PFSA polymer and the morphology of the water clusters in the membrane were found to affect H₂ permeation.

Moreover, new algorithms relating to the fast multipole method which enable to treat two dimensional periodic boundary conditions (slab geometry)[5] and rectangular unit cell with an anisotropic cell-partitioning[6] were developed. They make it possible to perform

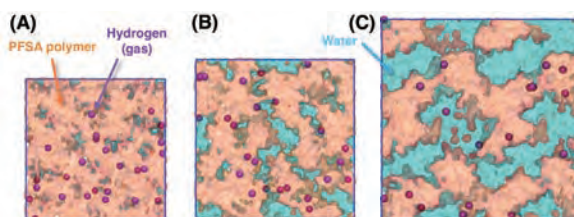


Figure 1: Schematic images of hydrated equivalent weight PFSA membranes with (A) 6, (B) 16, and (C) 30 wt % of water uptakes[4].

MD calculations for more general calculation systems by the software MODYLAS.

These results will contribute to the development of higher performance fuel-cells and secondary batteries and to the realization of the entire battery simulator in the near future.

References

- [1] A. T. Kuo, W. Shinoda, S. Okazaki : *J. Phys. Chem. C* **120** (2016) 25832.
- [2] A. T. Kuo, S. Okazaki, W. Shinoda : *J. Chem. Phys.* **147** (2017) 094904.
- [3] A. T. Kuo, K. Takeuchi, A. Tanaka, S. Urata, S. Okazaki, and W. Shinoda : *Polymer* **146** (2018) 53.
- [4] K. Takeuchi, A. Kuo, T. Hirai, T. Miyajima, S. Urata, S. Terazono, S. Okazaki, and W. Shinoda: *J. Phys. Chem. C*, **123** (2019) 20628.
- [5] N. Yoshii, Y. Andoh, S. Okazaki: *J. Comput. Chem.*, **41** (2020) 940.
- [6] Y. Andoh, N. Yoshii, S. Okazaki: *J. Comput. Chem.*, **41** (2020) 1353.

Development of Fragment-Based GW/BSE Method and Application to Organic Optoelectronic Materials

Takatoshi Fujita

Institute for Molecular Science

Myodaiji, Okazaki, Aichi 444-8585

Accurate calculations of electronic states are essential for computational studies of organic materials which are directed toward understanding of fundamental processes in organic electronic devices. Many fundamental processes governing the device operation take place at the variety of interfaces, such as metal-organic and organic donor-acceptor interfaces. Although developments of quantum chemistry or ab initio program packages have enabled one to routinely run a calculation for an isolated molecule or a molecular crystal, performing such a calculation for interface systems is still a challenging issue.

We have recently developed the large-scale GW method [1, 2] which can be applied to large and disordered molecular systems. Our implementation is based on the fragment molecular orbital (FMO) method, in which an entire system is first divided into many subsystems referred as fragments, and total energy or physical properties are approximated from molecular orbital calculations for fragment monomers, dimers, and optionally, trimmers. In the FMO-GW method, the polarization function of an entire system is approximated from molecular orbital localized within fragment monomer or dimers. In addition, the Δ COHSEX approximation is employed, in which dynamically-screened Coulomb potential is explicitly evaluated for a target fragment, while the statically-screened Coulomb potential of entire system is evaluated at the static COHSEX level. Based

on these development, we have performed the large-scale GW calculation for systems which contain more than 1,000 atoms, such as the organic semiconductor thin film [1] and the donor/acceptor interface [2]. In addition, we have also developed the GW/Bethe-Salpeter equation method which reasonably describes excited states in polarizable molecular environments.

As applications of the FMO-GW, we have explored the energy levels and charge-transfer excited states in pentacene/C₆₀ bilayer heterojunctions. In particular, we have investigated the dependence of interfacial morphologies on the electronic states and the effects of polarization and delocalization effects. Calculated energy levels and the excitation energies of charge-transfer states are in reasonable agreement with those estimated from ultraviolet photoelectron spectroscopy and from external quantum efficiency measurements. We have found that the electrostatic contribution of polarization energies, which arises from pentacene quadrupole moments, governs dependence of interfacial morphologies on the electronic states.

References

- [1] T. Fujita, Y. Noguchi, *Phys. Rev. B* **98** (2018) 205140.
- [2] T. Fujita, Y. Noguchi, T. Hoshi, *J. Chem. Phys.* **151** (2019) 114109.

Data-driven materials design for new functional high entropy alloys

Tetsuya Fukushima

*Institute for Solid State Physics, University of Tokyo
Kashiwa-no-ha, Kashiwa, Chiba 277-8581*

Recently, the constructions of materials databases using first-principles calculations have been actively carried out. Combining such materials databases and data-mining technique, one can not only analyze the mechanisms of physical phenomena, but also design new functional materials. Actually, there are several large materials databases, such as Materials Project, Open Quantum Materials Database (OQMD), and Novel Materials Discovery (NOMAD), which researchers can freely access. However, these inorganic materials databases are only for compounds with stoichiometric compositions and do not contain information about configurational disordered systems

In this year, in order to construct the materials databases for configurational disordered systems, we have developed an automatic high-throughput calculation method on the basis of the Korringa-Kohn-Rostoker (KKR) Green's function method. There are several merits in the KKR Green's function method, compared to other first-principles approaches. The most important advantage is the ability to perform the calculations of alloys and impurity doped systems, combining with the coherent potential approximation (CPA). Additionally, since the Green's function is directory calculated in this method, physical quantities, e.g., magnetic exchange interactions and transport properties, can be efficiently calculated by the linear response theory.

Automatic high-throughput calculations by

first-principles approaches are not easy tasks, because we need to appropriately control many numerical parameters and self-consistent procedures. For example, in the KKR Green's function method, the energy integration of the Green's function is performed in the complex energy plane to obtain the electron density. This complex energy contour must cover the valence bands and depends on systems. Our python interface for the high-throughput calculations enable to determine the numerical parameters and to manage the self-consistent procedures completely automatically. For the electronic structure calculations, the AkaiKKR program package is employed.

The automatic high-throughput calculations have been demonstrated for quaternary high entropy alloys with BCC and FCC solid solution phases, where 4 principal elements have the same atomic concentration and are randomly distributed in the crystals. The number of the target elements are 38 as follows: Al, Si, Sc, Ti, V, Cr, Mn, Fe, Co, Ni, Cu, Zn, Ga, Ge, Y, Zr, Nb, Mo, Tc, Ru, Rh, Pd, Ag, Cd, In, Sn, Hf, Ta, W, Re, Os, Ir, Pt, Au, Hg, Tl, Pb and Bi. We randomly choose the 4 elements from the above target elements and construct a quaternary high entropy alloy. Since both the BCC and FCC cases are considered, the total number of the systems is 147,630. All calculations are done by the ISSP supercomputer, system B.

We succeeded in automatically converging 99.99% of the systems, i.e., 147614/147630.

Figure 1 shows a part of our high-throughput calculations, in which the magnetic moments and Curie temperatures for the quaternary high entropy alloys with the BCC phase are plotted. The Curie temperatures are calculated by the magnetic exchange interactions and mean-field approximation. Such database is quite useful for the design of new functional materials. For example, in the cases of high-performance soft magnets, the high magnet moments and Curie temperatures are needed. Using the database, we can screen the candidate systems immediately. Here, it is concluded that FeCoXY, FeCoNiY, and MnFeCoY systems are good candidates for the high-performance soft magnets

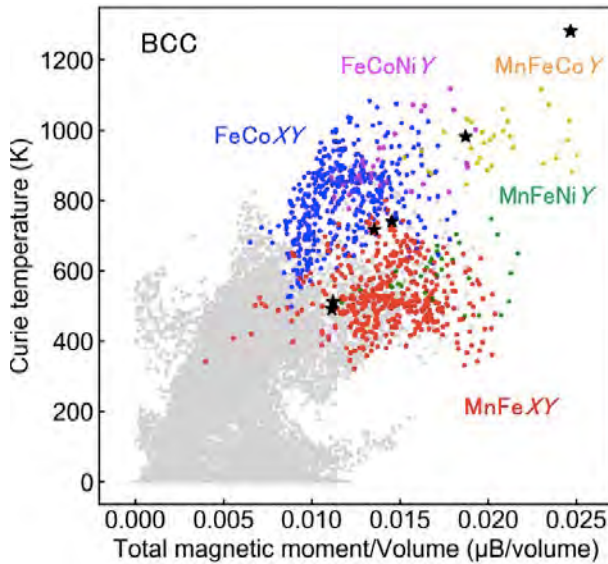


Figure 1: Automatic high-throughput calculations for quaternary high entropy alloys with the BCC phase.

References

- [1] T. Fukushima, H. Shinya, A. Masago, K. Sato and H. Katayama-Yoshida: Appl. Phys. Exp. **12** (2019) 063006.
- [2] S. Yamada, S. Kobayashi, A. Masago, L. S. R. Kumara, H. Tajiri, T. Fukushima, S. Abo, Y. Sakuraba, K. Hono, T. Oguchi,

and K. Hamaya: Phys. Rev. B **100** (2019) 195137.

- [3] A. Masago, H. Shinya, T. Fukushima, K. Sato, and H. Katayama-Yoshida: AIP Advances **10** (2020) 025216.
- [4] T. Nunokawa, Y. Fujiwara, Y. Miyata, N. Fujimura, T. Sakurai, H. Ohta, A. Masago, H. Shinya, T. Fukushima, K. Sato, and H. Katayama-Yoshida: J. Appl. Phys. **127** (2020) 083901.

Electron Theory on Secondary-Battery Materials

Hiroki KOTAKA¹, Motoyuki HAMAGUCHI², Huu Duc LUONG²,
Hiroyoshi MOMIDA^{1,2}, Tamio OGUCHI^{1,2}

¹*ESICB, Kyoto University, Katsuragoryo, Kyoto, Kyoto 615-8245*

²*ISIR, Osaka University, Mihogaoka, Ibaraki, Osaka 567-0047*

Microscopic mechanism of charging and discharging reactions in several battery systems is studied by first-principles calculations to explore novel secondary battery materials. In this year, we further extended our previous studies on Na/NaFeSO₄F and Li/Li_{2+2x}Mn_{1-x}Ti_{1-x}O₄ systems.

Recently NaFeSO₄F has been expected to be a candidate cathode material for the next-generation Na secondary batteries. In this first-principles study [1], the structural stability and voltage-capacity profiles of Na/NaFeSO₄F system are investigated. Calculated total energy of NaFeSO₄F is compared with those of NaF and FeSO₄ and found to be slightly stable to the phase separation. X-ray absorption spectroscopy (XAS) spectra at the K-edges of Fe, Na, and F for NaFeSO₄F and FeSO₄F in the fully discharged and charged states and of NaF and FeSO₄ are computed with the Fermi golden rule within the electric dipole and quadrupole approximation. The XAS spectra at Fe K-edge reveal that the discharged state in NaFeSO₄F and the charged state in FeSO₄F are dominated by Fe²⁺ (*d*⁶) and Fe³⁺ (*d*⁵), respectively. It is also found that the XAS spectra near K-edge of F in addition to Fe provide crucial information concerning the local structure in the relevant phases existing during the reaction processes.

Li-excess cation-disordered rock-salt oxides Li_{2+2x}Mn_{1-x}Ti_{1-x}O₄ have recently attracted much interests as high-capacity cathodes associated with two-electron reactions. In these oxides, cations are disordered on the octahedral

sites coordinated by six oxygen ions and the octahedra are expected to be stable during discharging and charging reactions. To clarify the mechanism of the reactions, cathode properties of the oxides with the Li-excess of $0 \leq x \leq 0.3$ are investigated by using first-principles calculations [2]. To evaluate the structure stability and reaction equations of the cathode materials for each *x*, formation enthalpies of Li_{2+2x-y}Mn_{1-x}Ti_{1-x}O₄ are calculated as a function of Li-removal amounts *y* considering several Li configurations. To model the oxides with disordered cations and several Li concentrations *x* and *y*, supercells including 80 atoms of rock-salt lattice are assumed with the special quasi-random structure method. Based on the estimated reaction equations, voltage-capacity profiles are obtained for each *x* and compared with experiments. By analyzing the electronic structures, roles of cation and anion redox reactions depending on *y* as well as *x* are discussed in detail. We discuss energy stability of O₂-release from the cathode during charging/discharging processes by calculating vacancy formation energies of O and Li. The best *x* values in terms of voltages, capacities, and stability against the O₂-releases are proposed.

References

- [1] H. Momida *et al.*, *J. Phys. Soc. Jpn.* **88**, 124709 (2019).
- [2] M. Hamaguchi, *et al.*, *Electrochimica Acta* **330**, 135286 (2020).

Ab initio studies toward functional nanomaterials based on abundant elements

Tetsuya TAKETSUGU

Faculty of Science, Hokkaido University

N10W8, Sapporo, Hokkaido 060-0810

Ab initio studies on various nano materials are important to understand and design new functional materials with abundant elements for reducing costs and dependences on precious metals used in many important aspects in our daily lives and therefore toward sustainable society. Heterogeneous catalysts rely mostly on the expensive and rare metals such as Pt, Rh, Pd, or Ru in automotive gas exhausts control, water gas shifts, fuel cells, as well as combusitive decomposition of ammonia. Platinum and palladium are also used for hydrogen based energy strategies. Due to their high cost and limited amounts, to reduce or even replace these metals is emergent issues in industry. To that end, we perform density functional theory (DFT) computations under the periodic boundary conditions together with projector augmented wave method with VASP using ISSP supercomputers to gain chemical insights to understand the chemical mechanisms in conventional catalysts as well as to design novel catalysts with abundant elements.

We have developed a surface adsorption model calculation database toward application to activity prediction of heterogeneous catalysts [1], where band calculations with SIESTA are performed for various pure and alloy metal surfaces adsorbed with molecules and atoms relevant to important catalysis such as water gas shift. As a new functional nanomaterial, we have studied structural and electronic properties of borophene, an artificial two-dimensional materials, whose structural

and electronic properties are not typical for their bulk counterparts [2]. Scanning tunneling microscopy and density functional theory calculations show that this structure forms as a single phase on iridium substrate in a wide range of experimental conditions and maybe then decoupled from the substrate via intercalation. We foresee that the adjacent borophene sites with opposite electron doping might exhibit catalytic activity or facilitate highly regular adsorption of large molecules, metal clusters, and other objects interesting for catalysis, sensors, and nanotechnology.

The excited states dynamics and spectroscopy are also important for the study on functional nanomaterials. For spectroscopy, the roles of silver nanocluster and plasmonic nanocavity for surface- and tip-enhanced Raman spectroscopies, respectively, are investigated [3,4]. We are further studying electronic excitations of small molecule excited by spatially nonuniform electric field, namely the near-field, by using the real-time time-dependent density functional theory codes such as SALMON.

References [1] M. Kobayashi, H. Onoda, Y. Kuroda, and T. Taketsugu, *J. Comput. Chem. Jap.*, 18, 251-253 (2019). [2] N. A. Vinogradov, et al, *ACS Nano*, 13, 14511-14518 (2019). [3] T. Tsuneda, T. Iwasa, and T. Taketsugu, *J. Chem. Phys.*, 151, 094102 (2019). [4] R. B. Jaculbia et al., *Nature Nanotechnology*, 15, 105-110 (2020).

Development of high-performance permanent magnets by large-scale simulation and data-driven approach

Takashi MIYAKE

CD-FMat, AIST

Umezono, Tsukuba, Ibaraki 305-8568

We have studied magnetic properties and stability of rare-earth magnet compounds using first-principles calculation combined with machine-learning techniques. The $R\text{Fe}_{12}$ -type compounds having the ThMn_{12} structure have attracted attention in recent years, because high saturation magnetization can be expected from their high iron concentration. $\text{NdFe}_{12}\text{N}_x$ and $\text{Sm}(\text{Fe},\text{Co})_{12}$ films have successfully synthesized a few years ago, and it was reported experimentally that these compounds have higher saturation magnetization, higher anisotropy field and higher Curie temperature than $\text{Nd}_2\text{Fe}_{14}\text{B}$ which is the main phase of the neodymium magnet. However, they are thermodynamically unstable, and partial substitution of Fe sites are necessary to stabilize a bulk phase. The choice of rare-earth element also affects stability [1].

We calculated the magnetization, Curie temperature and formation energy of $(R_{1-\alpha}Z_\alpha)(\text{Fe}_{(1-\beta)(1-\gamma)}\text{Co}_{\beta(1-\gamma)}\text{Ti}_\gamma)_{12}$ ($R=\text{Nd}, \text{Sm}, \text{Y}, Z=\text{Zr}, \text{Dy}$) based on density functional theory using Akai-KKR code. Non-stoichiometric composition is treated by the coherent potential approximation. Intersite magnetic exchange couplings are calculated by Liechtenstein's method, from which the Curie temperature is evaluated by solving the derived Heisenberg model in the mean-field approximation. To reduce the systematic error in the formation energy obtained by the KKR-CPA, data integration method (Fig.1)

is adopted, where the formation energies of stoichiometric systems calculated by QMAS are used to reduce the systematic error.

In order to determine the optimal composition efficiently, we adopt Bayesian optimization. We performed 1000 independent runs to evaluate the success rate statistically. Figure 2 shows the success rate of finding top 10 systems out of 3630 chemical compositions within 50 trials. The target variables are saturation magnetization, Curie temperature and formation energy. The success rate is over 95 % if we appropriately chose the descriptor, which is much higher than that by the random sampling (12.9%).

References

- [1] Yosuke Harashima, Taro Fukazawa, and Takashi Miyake: *Scripta Materialia* **179** (2020) 12.
- [2] Taro Fukazawa, Yosuke Harashima, Zhufeng Hou and Takashi Miyake: *Phys. Rev. Mater.* **3** (2019) 053807.

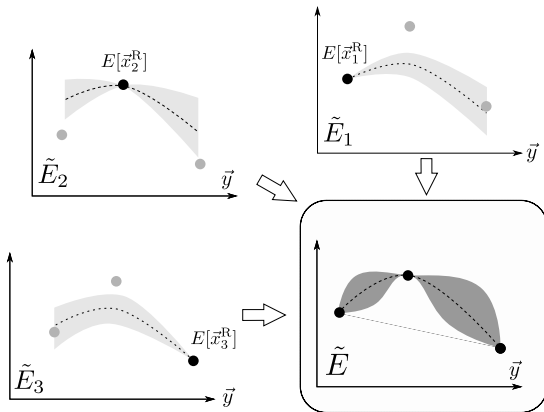


Figure 1: Data integration method, where systematic errors contained in a large number of data for non-stoichiometric compositions are corrected by a small number of more accurate data for stoichiometric compositions. [2].

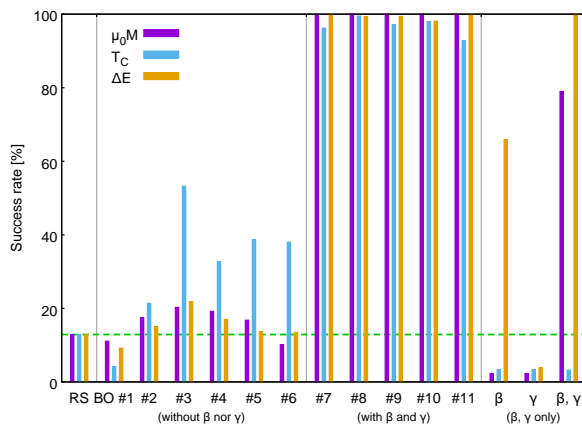


Figure 2: Success rate of finding the system with the top 10 values of magnetization, Curie temperature and formation energy out of 3630 candidates within 50 trials [2].

Multiscale simulations on complex multiphase flows

Youhei Morii, Takahiro Murashima, and Toshihiro Kawakatsu

Department of Physics, Graduate School of Science, Tohoku University, Sendai 980-8578

We developed multiscale simulation techniques (MSS) [1] and a multiscale simulation platform for complex fluids (MSSP) [2,3], under the support from Post-K project and HPCI. These MSS and MSSP are aimed to apply for complex flow phenomena such as multiphase flows and viscoelastic flows whose constitutive equations are not a priori known. In such systems, a simple model constitutive equation is not in general available, and therefore one must obtain the stress tensor from the flow history of the fluid. As such a flow is often non-Markovian, Lagrangian description is quite suitable to trace the flow history. Smoothed particle hydrodynamics (SPH) is a typical simulation technique of fluid flows based on Lagrangian description. Our MSSP is based on this SPH method, where each SPH particle contains a microscopic simulator inside

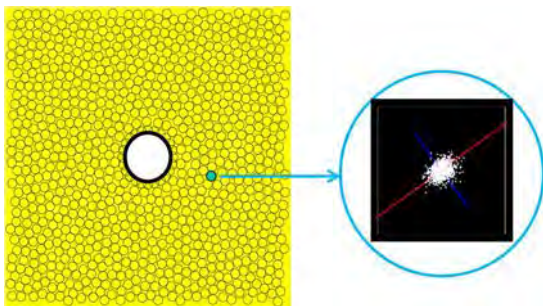


Fig.1 A schematic illustration of MSSP.

it (See Fig.1). The instantaneous stress that drives the macroscopic flow is calculated using this microscopic simulator.

We applied this technique to a viscoelastic polymeric fluid flowing around a cylindrical obstacle that generates Karman's vortex street. Figure 2 shows a comparison between (a) a Newtonian fluid and (b) a Maxwellian fluid that contains set of dumbbells as a model of polymer solution. One can confirm the effect of viscoelasticity coming from the polymer component on the Karman's vortex street.

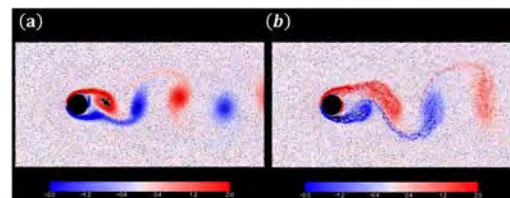


Fig.2 Karman vortex street for (a) a Newtonian fluid and (b) a Maxwellian fluid.

References

- [1] T. Murashima, S. Urata, S. Li, *Eur. Phys. J. B*, 92, 211 (2019).
- [2] 森井洋平, 川勝年洋, 第 68 回高分子討論会, 福井大学 文京キャンパス, 2019/9/25.
- [3] Youhei Morii, Toshihiro Kawakatsu, 10th International Conference of the Asian Consortium on Computational Materials Science (ACCMS-10), Hong Kong, 2019/7/24.

Order-disorder transition in the superhigh-pressure phase of Mg_2SiO_4

Koichiro UMEMOTO

Earth-Life Science Institute,

Tokyo Institute of Technology, 2-12-1 Meguro-ku, Ookayama, Tokyo 152-8550

MgSiO_3 bridgmanite with the orthorhombic perovskite structure is a major constituent of the lower mantle of the Earth. It takes the post-perovskite (PPV) structure near the core-mantle boundary pressure (~ 125 GPa). The PPV phase is the final form of MgSiO_3 in the Earth. However, at much higher pressures in “super-Earths” which are exoplanets expected to be terrestrial with masses much larger than the Earth, MgSiO_3 PPV should undergo “post-PPV” transitions. So far, first principles studies have predicted the three-stage dissociation of MgSiO_3 PPV: MgSiO_3 PPV \rightarrow I-42d-type Mg_2SiO_4 + P2₁/c-type MgSi_2O_5 \rightarrow Mg_2SiO_4 + Fe₂P-type SiO_2 \rightarrow CsCl-type MgO + SiO_2 [1,2]. When MgSiO_3 coexists with NaCl-type MgO or pyrite-type SiO_2 , they were predicted to recombine into Mg_2SiO_4 or MgSi_2O_5 [3]. Transition pressures of these post-PPV transitions are extremely high, $> \sim 500$ GPa, and have been still difficult to be achieved experimentally. These predictions were based on the lowest-enthalpy phases under ultrahigh pressures. Temperature effects by phonon were taken into account by using the quasi-harmonic approximation (QHA). These post-PPV

transitions and thermodynamic quantities calculated for these phases have been already used in numerical modeling of mantle dynamics of super-Earths [5].

In this study, we predicted order-disorder transition in the cation sublattice of tetragonal Mg_2GeO_4 by first principles [4]. Mg_2GeO_4 is a candidate of low-pressure analog of Mg_2SiO_4 . The dissociation of MgGeO_3 PPV into pyrite-type GeO_2 and I-42d-type Mg_2GeO_4 was predicted to occur at ~ 170 GPa [5]. Therefore, Mg_2GeO_4 is a useful system to study the post-PPV transitions experimentally. In Mg_2GeO_4 and Mg_2SiO_4 , local oxygen arrangements around Mg and Ge atoms are very close to each other. Therefore, configuration entropy is expected to induce the order-disorder transition at high temperature.

The order-disorder transition temperature (T_c) is given by the peak temperature of the heat capacity which is calculated from the partition function with respect to cation configurations. For Mg_2GeO_4 , we constructed a supercell consisting of 56 atoms and generated cation configurations until the convergence of T_c was achieved. Then we predicted that the

order-disorder transition should occur at ~ 3000 K and 200 GPa; this pressure-temperature condition is now achievable by the diamond-anvil-cell experiments. We found that T_c increases with pressure. Across the transition, the symmetry of Mg_2GeO_4 increases from tetragonal (I-42d) in the ordered phase to cubic (I-43d) in disordered one. In fact, the crystal structure of the disordered cubic phase is identical to that of Th_3P_4 . We also clarified that the effect of phonon on this transition is very small within the QHA.

Since Mg_2GeO_4 is the low-pressure analog of Mg_2SiO_4 , the order-disorder transition predicted in this study is expected to occur also in Mg_2SiO_4 and will play an important role in modeling interiors of super-Earths.

The first principles calculations in this study were performed using the Quantum-Espresso package (<https://www.quantum-espresso.org>) on the supercomputer (system B) at the

Institute for Solid State Physics. This research was supported by MEXT as “Exploratory Challenge on Post-K computer” (Challenge of Basic Science – Exploring Extremes through Multi-Physics and Multi-Scale Simulations)

References

- [1] S. Q. Wu, et al.: J. Phys.: Condens. Matter **26** (2014) 035402.
- [2] H. Niu et al.: Sci. Rep. **5** (2015) 18347.
- [3] K. Umemoto et al.: Earth Planet. Sci. Lett. **478** (2017) 40.
- [4] K. Umemoto and R. M. Wentzcovitch: in preparation.
- [5] A. P. van den Berg, et al.: Icarus **317** (2019) 412.
- [6] K. Umemoto and R. M. Wentzcovitch: Phys. Rev. Mat. **3** (2019) 123601.

Chain-Increment Method for Approaching the Chemical Potential of a Polymer with All-Atom Model

Kazuo YAMADA and Nobuyuki MATUBAYASI

Division of Chemical Engineering, Graduate School of Engineering Science,

Osaka University, Toyonaka, Osaka 560-8531

We have computed the free energy of the dissolution of the polymer in polymer binary systems [1] using all-atom molecular dynamics simulations. An atomistic computation of free energy is a challenging task, however, when a polymer molecule is treated simultaneously as a whole. This is because a polymer is highly flexible and structurally diverse due to large number of intramolecular degrees of freedom. Given the fundamental and practical importance of the chemical-potential calculation of polymer, therefore, an elaborate scheme needs to be established which exploits a specific nature of the polymeric structure.

We develop a chain-increment method to approach the chemical potential of a polymer with all-atom model. The intermolecular interaction of a polymer of interest with the surrounding molecules is introduced sequentially for the monomers, and the free energy for turning on the interaction is treated within the framework of the energy-representation theory of solutions. In our method, we compute the free energy of chain increment $\Delta\mu_i^{\text{incr}}$ along the monomers in the tagged polymer as well as the total free energy $\Delta\mu$ of the

polymer as a sum of $\Delta\mu_i^{\text{incr}}$ over the monomers in the tagged polymer. In the present report, we focus on the computation of the incremental free energy in polymer-melt systems [1].

The polymer species treated are polyethylene (PE), polypropylene (PP), poly(methyl methacrylate) (PMMA), and polyvinylidene difluoride (PVDF) in their linear forms. All-atom molecular dynamics simulations and free-energy calculations have been implemented on the supercomputer system at ISSP. The free energy of chain increment is shown in Fig. 1 at the number of monomer units of 100. The incremental free energy $\Delta\mu_i^{\text{incr}}$ is obtained for each monomer by using the scheme in [1], and it is found that the incremental free energy stays constant within 0.1 kcal/mol except at terminals. The standard deviation is within 0.2 kcal/mol in the inner part of the polymer, and the averaged free energy of chain increment is insensitive to the chain length. All-atom computation is thus feasible for the free-energy analysis of a polymer system at the degree of polymerization of several tens or more. It is also seen that the preference order of $\Delta\mu_i^{\text{incr}}$ agrees with that of the average interaction energy $\langle u \rangle_i$ of the

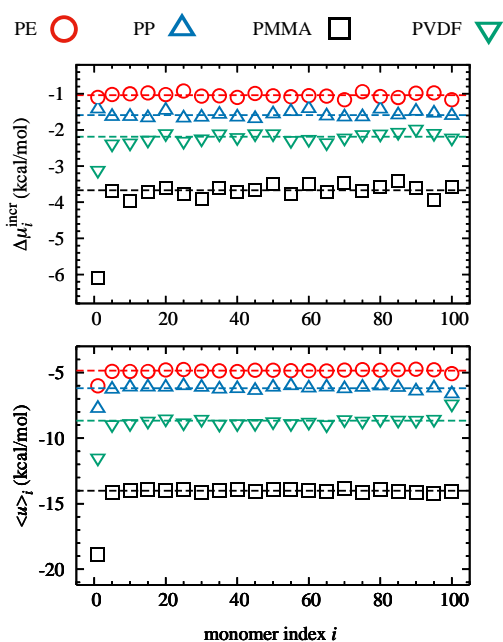


Fig 1: Incremental free energy and the average interaction energy against the index i of the incremented monomer in the tagged polymer. The degree of polymerization is 100 in this figure, and $\Delta\mu_i^{\text{incr}}$ and $\langle u \rangle_i$ are plotted against the monomer index at $i = 1, 5, 10, 15, \dots, 90, 95, \text{ and } 100$. The horizontal, dashed line is the averaged value of $\Delta\mu_i^{\text{incr}}$ or $\langle u \rangle_i$ over $i = 5, 10, 15, \dots, 90, \text{ and } 95$.

incremented monomer with the surroundings.

We further compute the total solvation free energy $\Delta\mu$ as a function of the degree of the polymerization N for PE and PMMA, by using the incremental free energy of solvation $\Delta\mu_i^{\text{incr}}$ at $i = 1, 5, 10, \dots, (N-10), (N-5), \text{ and } N$. In Fig. 2, a good linearity of $\Delta\mu$ to N is observed. The free energetics of a long polymer is thus determined by the chain-increment contribution $\Delta\mu_i^{\text{incr}}$, and Figs. 1 and 2 demonstrate that $\Delta\mu_i^{\text{incr}}$ can be assessed from an all-atom simulation with the

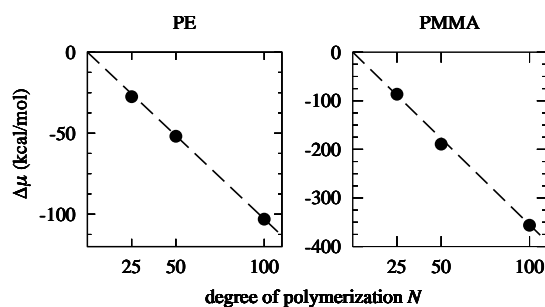


Fig 2: Total solvation free energy $\Delta\mu$ against the degree of polymerization N at 25, 50, and 100 for PE and PMMA. $\Delta\mu$ is estimated from $\Delta\mu_i^{\text{incr}}$ at $i = 1, 5, 10, \dots, (N-10), (N-5), \text{ and } N$. The dashed line is the least-square fit to the form of $\Delta\mu \propto N$, and the slope is -1.0 and -3.6 kcal/mol for PE and PMMA, respectively.

degree of polymerization of several tens or more.

Atomistic computation of the chemical potential is of much computational demand for a polymer when the interaction with the solvent is turned on simultaneously throughout the whole polymer. The method of chain increment is an alternative scheme that introduces the interactions sequentially along the polymer chain. This work formulates an all-atom method for chain increment by combining molecular simulation with the energy-representation theory of solutions, and it is demonstrated that the free energy of chain increment can be obtained at a precision of a few tenths of kcal/mol.

References

- [1] K. Yamada and N. Matubayasi: Macromol. **53** (2020) 775-788.

Study on thermodynamic properties and NO_x redox reactions of ternary alloy nanoclusters by O(N) density functional calculations

Shih-Hsuan Hung and Taisuke Ozaki

Institute for Solid State Physics, University of Tokyo

Kashiwa-no-ha, Kashiwa, Chiba 277-8581

We perform first-principles calculations and Monte Carlo sampling to investigate the structures of ternary PdRuM (M=Pt, Rh, or Ir) nanoparticles (NPs) with respect to three different spherical shapes. The calculation is carried out using OpenMX (Open source package for Material eXplorer) software package.

1 Introduction

Metallic nanoparticles (NPs) are a promising functional material in many aspects, such as energy conservation, catalyst, and elements storage. [1] To achieve better performance of particular functions, many experiments synthesize modified NPs to adjust their properties physically and chemically. Bimetallic PdRu NPs have been reported for providing better catalytic reactions, but the drawback is suffered from the loss of metal element during catalytic cycles. [1, 2] Therefore, PdRuPt, PdRuRh, and PdRuIr NPs or alloy have been studied and demonstrate their promising ability of NO reaction. [4, 3] Therefore, we would like to investigate these NPs and provide deeper insight in atomistic aspect.

2 Result

To compare different morphology influencing different composition ternary NP, we select three different spherical shapes for the NPs. There are hexagonal close-packed (hcp),

truncated-octahedral (fcc), and icosahedral (fcc) shapes with 57, 55, and 55 atoms, respectively. To achieve higher coverage of energy survey, each nanoparticle is sampled 30 times using Monte Carlo sampling method, thus there is 270 sampling in total. The statistical characteristic implies the position trend of individual atom for respective nanoparticles (detail is in published paper). By following the trend, we manually construct the bare ternary NPs and find the most stable one. Figure 1 shows the most stable ternary NPs in our calculation. The calculation shows that the atomic arrangements depend on the surface formation energy of individual elements. In other words, the element possesses smaller surface formation energy dominating the surface sites. The species have greater surface formation energy immerse in the NPs as bulk-like state. Figure 1 demonstrates Ru atoms are always as a core in NPs due to its larger surface formation energy ($\gamma = 1.31$ eV/atom) of fcc (111) surface. In addition, there are two particular shells are found in the investigation. One configuration is binary solid solution alloy and the other one represents that two elements segregate from each other on the shell. The reason of these two particular arrangements is because the NPs tend to minimize its surface strain, compared to lattice constant of Pd fcc bulk (3.79 Å). For the NPs with solid solution shell, the Pd-M bond length decreases by 3.8 % in average. Meanwhile, the bond reduc-

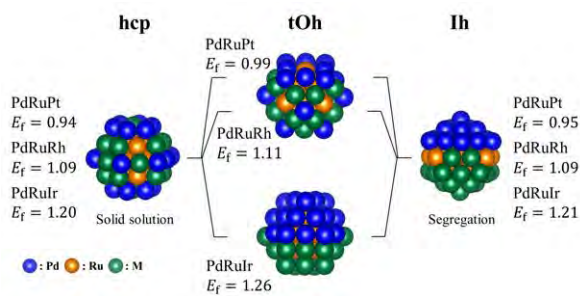


Figure 1: The most energetically stable ternary PdRuM NPs in the calculations. The unit of E_f is eV/atom.

tion of 3.0 % in average has been found for the configurations with segregation shell. In addition, the Ir-Ir bond length shows a significant reduction of 6.2 %. By modeling the single layer hexagonal as shell structure, the calculation shows a good agreement with our NPs calculation. The reduced bond length of alloy decreases the total calculated energy.

Oxidized NPs is an other problematic issue of catalyst. Due to the oxidation formation energy variance, the elements of the NPs may migrate from site to site. The oxygen adsorption on surface calculation demonstrates that the preference of oxygen adsorption (eV/atom) on fcc hollow site is found to be Ru (-3.65) \rightarrow Rh (-2.78) \rightarrow Ir (-2.47) \rightarrow Pd (-2.06) \rightarrow Pt (-1.84). Besides the single oxygen adsorption on cleaved surface, we examine the oxygen molecule adsorption on pure Pd NPs. The calculation demonstrate that the oxidation energy is as a function of O-O distances. The increasing O-O distance up to 5.0 Å decreases the oxidation formation energy. Figure 2 demonstrates the most stable oxidized ternary NPs and their oxidation formation energy what we can find. The result shows that the Ru atoms migrate outward to the surfaces of NPs to be oxide. Pt, Pd and Pd atoms penetrate inwards as a core of the ternary PdRuPt, PdRuRh, and PdRuIr NPs, respectively. By calculating the NPs formation energy with respect to chemical potential of oxygen molecule, the free energy indicates hcp ternary NP is thermodynamically

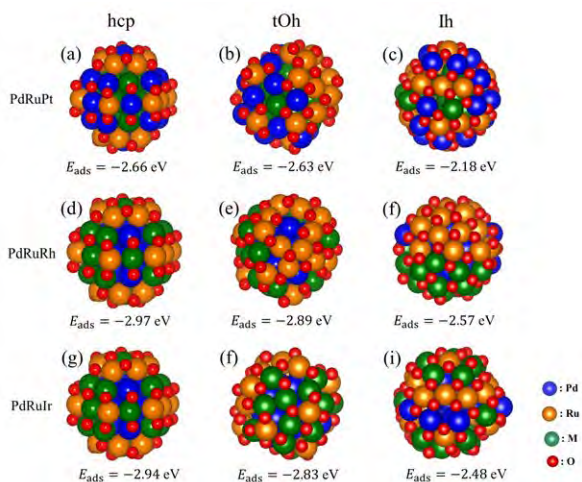


Figure 2: The most energetically stable structures of high oxygen coverage on hcp, tOh, and Ih ternary NPs.

cally unstable under oxygen-rich condition.

3 Conclusion and Discussion

In summary, we have provide deeper insight into the most stable structures with three different morphologies and two oxidation statuses. The investigation shows the atoms are organized in specific arrangement instead of solid solution alloy. In addition, the oxidation condition can facilitate the atomic migration in the ternary NPs. Although the scale of the study is not satisfying to interpret real situation, it can be a pilot investigation for real scale NPs calculation and provide some possible configurations in advance.

References

- [1] Kusada Kohei et al.: *J. Am. Chem. Soc.* **136** (2014) 1864–1871
- [2] Wu Dongshuang et al.: *Phys. Chem. Chem. Phys.* **14** (2012) 8051–8057
- [3] Sarker Md Samiul et al.: *J. Mater. Res.* **29** (2014) 856–864
- [4] Shang Changshuai et al.: *Nano Res.* **11** 2018 4348–4355

3.6 Software Advancement Projects, GPGPU Implementation, and Workshop Support

Development of ab-initio configuration sampling toolkit (abICS) for combining first-principles calculations with extended ensemble methods

Shusuke KASAMATSU¹, Yuichi MOTOYAMA², Kazuyoshi YOSHIMI²,
Yoshiyuki YAMAMOTO², Osamu SUGINO², Taisuke OZAKI²

¹*Faculty of Science, Academic Assembly, Yamagata University,
Yamagata 990-8560*

²*Institute for Solid State Physics, University of Tokyo, Kashiwa 277-8581*

In functional materials, varying types of configurational disorder are often employed to obtain favorable properties for a given application. The ability to simulate such disorder as a function of temperature should be immensely helpful for comparing with experiment. It would also enable prediction and design of properties in materials with realistic levels of disorder. To achieve this, a natural way may be to combine first-principles calculations with the Metropolis Monte Carlo algorithm. However, this is quite costly in terms of computational power, so many workers have opted to first derive lightweight models from first-principles calculations, then use that model for Monte Carlo sampling. The problem is that deriving lightweight *and* reliable models becomes increasingly difficult with increasing complexity of the system (various dopants, charged defects, interfaces, etc.).

In last year's ISSP joint-use project, SK proposed to bypass such fitting and instead rely

on efficient parallel algorithms for thermodynamic sampling. Figure 1 shows our computational scheme. There are N_{rep} Metropolis samplers running in parallel at different temperatures. Each of the samplers spawns parallel DFT processes (we used VASP [1]) to perform local structural relaxation and energy calculation at every Metropolis step. The temperatures are swapped according to the replica exchange algorithm [2] to speed up the sampling. We successfully demonstrated that sufficient sampling can be performed on meaningfully large supercells by calculating the degree of disorder in MgAl_2O_4 [3].

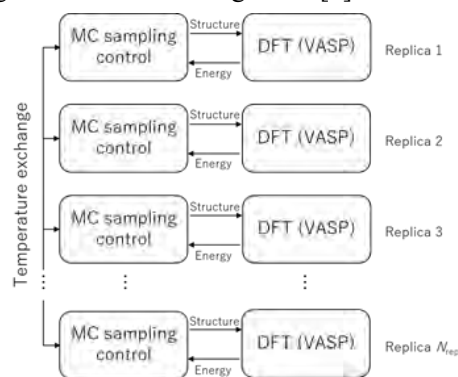


Figure 1 Our scheme for parallel configuration sampling. Reproduced from Ref. [3].

As this year's Software Advancement Project, we proposed to develop an easy-to-use interface for this computational scheme. The result has been released as ab-Initio Configuration Sampling toolkit, or *abICS* for short. It is written in Python 3 and is registered at PyPI (Python Package Index; pypi.org). It can thus be installed in most environments rather easily through the command "`pip install --user abics`". Now, abICS can sample using the replica exchange Monte Carlo algorithm, and we are planning to add support for other extended ensemble methods soon. The parameters for the sampling are controlled by an input file in TOML format, which is a minimal and easy-to-read configuration format that is being used in many software projects [4]. The parameters for the DFT calculations such as k-point sampling, basis set specification, convergence parameters, etc. are controlled by input formats of the specified solver. As the solver, abICS supports the use of DFT codes VASP, Quantum Espresso [5], and OpenMX [6] as of May 2020. It also has experimental support for aenet [7], which uses neural network potentials. Preprocessing scripts are provided for converting structure

files to abICS input.

We believe that abICS will be immensely useful for making efficient use of next-generation supercomputers due to its multi-layered parallelism. We are also aiming to bring together information science, materials simulation, and statistical physics using abICS as a hub. Because of modular coding practices employed in our project, it should be relatively easy to implement interfaces for other solvers, or to implement new sampling schemes. Please have a look at our homepage [8] and do not refrain from contacting us if you are interested in using or extending this software.

References

- [1] <https://vasp.at/>
- [2] K. Hukushima and K. Nemoto: J. Phys. Soc. Jpn. **65** (1996) 1604.
- [3] S. Kasamatsu and O. Sugino: J. Phys.: Condens. Matter **31** (2019) 085901.
- [4] <https://github.com/toml-lang/toml>
- [5] <https://www.quantum-espresso.org/>
- [6] <http://www.openmx-square.org/>
- [7] <http://ann.atomistic.net/>
- [8] <https://www.pasums.issp.u-tokyo.ac.jp/abics/en>

GPU acceleration for solving Bethe-Salpeter equation

Junya Otsuki¹ and Kazuyoshi Yoshimi²

¹*Research Institute for Interdisciplinary Science, Okayama University, Okayama 700-8530*

²*Institute for Solid State Physics, University of Tokyo, Chiba 277-8581*

The Bethe-Salpeter equation (BSE) provides two-particle responses in interacting many-body systems. In the context of dynamical mean-field theory (DMFT), for example, the momentum-dependent dynamical susceptibility $\chi(\mathbf{q}, i\nu_n)$ is obtained by solving the BSE.

The BSE is symbolically written as

$$\tilde{\chi}(\mathbf{q}, i\nu_n) = [\tilde{\chi}_0^{-1}(\mathbf{q}, i\nu_n) - \mathbf{\Gamma}(i\nu_n)]^{-1}, \quad (1)$$

where the bold symbols indicate matrices of size $M = N_{\text{sp}}^2 N_{\text{orb}}^2 N_{\omega}$. Here, N_{sp} is the number of spin components, N_{orb} is the number of orbitals, and N_{ω} is the number of the fermionic Matsubara frequencies. Solving Eq. (1) requires computations of matrix multiplications and the inverse of a matrix. Therefore, the computational cost is $\mathcal{O}(M^3)$.

The matrix size M for typical models is shown in Table 1. Here, the value of N_{ω} is fixed at 20, but a larger value is necessary to address low-temperature properties. Namely, M in Table 1 should be regarded as a minimum estimation. We see that d -orbital systems require $M = 500$ without spin-orbit coupling (SOC) and $M = 2,000$ with SOC. For the f -orbital, we need $M \approx 4,000$.

Table 1: The matrix size M for typical models.

Model	N_{sp}	N_{orb}	N_{ω}	M
1 orbital	1	1	20	20
2 orbital	1	2	20	80
3 orbital	1	3	20	180
5 orbital	1	5	20	500
5 orbital (SOC)	2	5	20	2,000
7 orbital (SOC)	2	7	20	3,920

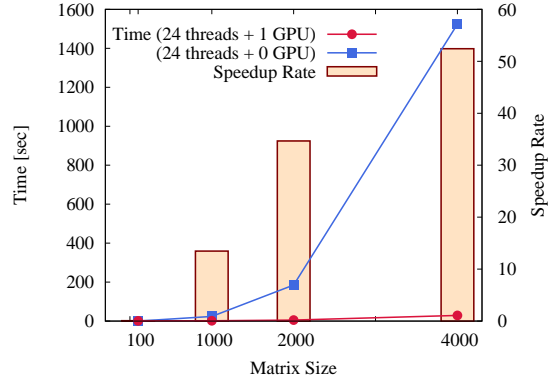


Figure 1: Computation time for solving the BSE (left axis) and the speedup rate achieved by the use of GPU (right axis).

Figure 1 shows a benchmark. We used 1 node (24 thread) of System B in ISSP supercomputer center. Without GPU, the computational time grows in proportion to M^3 as expected (filled squares). Use of GPU suppresses the growth of the time (filled circles). A significant speedup is achieved for $M \gtrsim 100$: The speedup rate (the time without GPU divided by the time with GPU) is 13 and 52 for $M = 1,000$ and $4,000$, respectively. This benchmark indicates that the GPU acceleration is highly beneficial for d and f orbitals especially on the existence of SOC.

As a future work, our BSE code will be integrated into the open-source DMFT software **DCore** developed under the support of ISSP [1]. **Acknowledgment:** This work was supported by support service of program portability to GPGPU.

Reference:

[1] <https://github.com/issp-center-dev/DCore>

Report of CCMS hands-on sessions in the 2019 fiscal year

Takahiro Misawa

*Institute for Solid State Physics, University of Tokyo
Kashiwa-no-ha, Kashiwa, Chiba 277-8581*

In the 2019 fiscal year, center for computational materials science (CCMS) in institute for solid state physics (ISSP) held two hands-on sessions by using supercomputer (sekirei) of ISSP. A list of the hands-on sessions is shown in Table 1. In this report, we briefly summarize the hands-on sessions in the order of date.

DSQSS [1] is an open-source software package for solving quantum many-body problems using the quantum Monte Carlo method that sample the Feynman path integral using the worm update. Development of DSQSS was supported by “Project for advancement of software usability in materials science”(PASUMS) [2] in the 2018 fiscal year. In the hands-on session, Naoki Kawashima and co-developers explained the basics of the quantum Monte Carlo method and gave a tutorial of DSQSS [3].

DCore [4] is a tool for performing quantum many-body simulations based on the dynamical mean-field theory (DMFT). Development of DCore was also supported by PASUMUS in the 2017 fiscal year. In the hands-on session, Hiroshi Shinaoka and co-developers explained the basics of the DMFT and gave a tutorial of DCore [5].

Date	Software	Main lecturer
Jun. 6	DSQSS	N. Kawashima
Dec. 26	DCore	H. Shinaoka

Table 1: List of software packages used in CCMS hands-on sessions.

References

- [1] <https://ma.issp.u-tokyo.ac.jp/en/app/180>
- [2] <https://www.pasums.issp.u-tokyo.ac.jp>
- [3] <https://ccms.issp.u-tokyo.ac.jp/event/1942>
- [4] <https://ma.issp.u-tokyo.ac.jp/en/app/1004>
- [5] <https://ccms.issp.u-tokyo.ac.jp/event/2486>

Supercomputer course of Computational Materials Design (CMD[®]) workshop

Masaaki GESHI¹, Yoshitada MORIKAWA², Tomoya ONO³

¹*Institute for NanoScience Design,*

Osaka University, 1-2 Machikaneyama, Toyonaka, Osaka 560-0043

²*Department of Precision Engineering, Graduate School of Engineering,*

Osaka University, 2-1 Yamadaoka, Suita, Osaka 565-0871

³*Department of Electrical and Electronic Engineering, Graduate School of Engineering,*

Kobe University, 1-1 Rokkodaicho, Nada, Kobe 657-8501

The 35rd Computational Materials Design (CMD[®]) workshop (CMD35) has been held from September 2nd to September 6th and the 36th CMD[®] workshop (CMD36) has been done from February 17th to February 21st at Graduate School of Engineering Science, Osaka University. In this workshop we have the supercomputer course to train up human resources to advance researches by using system B supercomputer of ISSP, the University of Tokyo.

In CMD35 eight participants took the supercomputer course and got a tutorial on STATE-Senri developed by Y. Morikawa. After giving the introductory lecture of large-scale computing by M. Geshi and explaining how to use the supercomputer of ISSP and explaining how to use STATE-Senri, calculation models on each research subject of the participants were built and their calculations were carried out. Specific subjects include oxidation of solid surfaces, chemical reactions on two-dimensional

materials, atomic diffusion on solid surfaces, dry reforming of methane, chemical reactions in solid oxide fuel cell, and so on. The participants performed the calculations and examined the results.

In CMD36 two participants took the supercomputer course and used the supercomputer of ISSP. They got a tutorial on RSPACE developed by T. Ono. After giving the introductory lecture of large-scale computing by M. Geshi and describing the calculation method of electronic states and electron conduction property using RSPACE, exercises published in the manual were carried out by Y. Egami. Then, electronic state calculations were carried out for several molecules, and the electronic density distribution was visualized. Finally, the atomic structure optimization of the defects in GaAs bulks was carried out, and the calculation of carrier scattering property by the defects was investigated.

4 PUBLICATION LIST

Example:

LASTNAME, Firstname [project class; # points (B), # points (C)] (Page #)

— *Project title*

1. First paper
Names of Authors, etc.
2. Second paper
- ...

□ ISSP Joint Research Projects

AKAGI, Kazuto [C class; 5000 (B), 0 (C)] (104)

— *Elucidation of diffusion process of ionic species in organic solvent*

AKAGI, Yutaka [B class; 900 (B), 100 (C)] ()

— *Novel Topological Excitation in Magnet*

AKAI, Hisazumi [B class; 1800 (B), 100 (C)] (146, 147)

— *Data accumulation of magnetic properties of rare earth mixed crystal*

— *Data accumulation of magnetic properties of rare earth mixed crystal magnetic materials*

1. Calculating Curie temperatures for rare-earth permanent magnets: Ab initio inspection of localized magnetic moments in d-electron ferromagnetism
M.Matsumoto and H.Akai : Phys. Rev. B **101**, 1444402 (2020).
2. Curie temperature of $\text{Sm}_2\text{Fe}_{17}$ and $\text{Nd}_2\text{Fe}_{14}\text{B}$: a first-principles study
T. Fukazawa, H.Akai, Y. Harashima, and T. Miyake : IEEE Trans. Magn. **55**,2101305 (2019).
3. Ab initio Study of High-field NMR Shift of ^{59}Co in the Ferromagnetic Heusler Alloy Co_2TiGa
H.Nishihara, H.Akai, K.Sato, T.Kanomata, M.Geshi, T.Sakon, and T.Wada : J. Phys. Soc. Jpn. **88**, 034712 (2019).
4. First-principles study of spin-wave dispersion in $\text{Sm}(\text{Fe}_{1-x}\text{Co}_x)_{12}$
T. Fukazawa, H.Akai, Y. Harashima, and T. Miyake : J. Magn. Magn. Mater. **469**, 296 (2019).

AKASHI, Ryosuke [C class; 5000 (B), 850 (C)] (89)

— *Ab initio study on the metallization and superconductivity in metallic superhydrides*

1. Superconductivity of LaH_{10} and LaH_{16} polyhydrides
I. A. Kruglov, D. V. Semenov, H. Song, R. Szcześniak, I. A. Wrona, R. Akashi, M. M. D. Esfahani, D. Duan, T. Cui, A. G. Kvashnin, and A. R. Oganov: Phys. Rev. B **101** (2020) 024508.
2. Archetypical "push the band critical point" mechanism for peaking of the density of states in three-dimensional crystals: Theory and case study of cubic H_3S
Phys. Rev. B **101** (2020) 075126.

AOYAMA, Kazushi [B class; 1500 (B), 190 (C)] (301)

— *Effects of a magnetic field on spin-lattice-coupled orders in breathing pyrochlore antiferromagnets*

— *Transport properties of the antiferromagnetic classical XXZ model in two dimensions*

1. Effects of magnetic anisotropy on spin and thermal transport in classical antiferromagnets on the square lattice
K. Aoyama and H. Kawamura: Phys. Rev. B **100** (2019) 144416.
2. Spin Current as a Probe of the \mathbf{Z}_2 -Vortex Topological Transition in the Classical Heisenberg Antiferromagnet on the Triangular Lattice

K. Aoyama and H. Kawamura: Phys. Rev. Lett. **124** (2020) 047202.

ARAI, Munehito [C class; 9000 (B), 0 (C)] (252)

— *Computational rational design of novel proteins for industrial and pharmaceutical applications*
— *Protein design toward the development of anti-allergy drugs*

ARAI, Toyoko [C class; 2000 (B), 600 (C)] (135)

— *DFT calculation of atomic displacement captured by energy dissipation channel of noncontact atomic force microscope*

ARIMA, Kenta [B class; 700 (B), 90 (C)] (178)

— *Simulation of STM images of graphene sheet after chemical reduction*

ASANO, Yuta [E class; 30000 (B), 4600 (C)] (241)

— *Karman-Vortex Cavitation in a Complex Fluid*

— *Molecular Dynamics Simulation of Cavitating Flow in a Complex Fluid*

1. Effects of cavitation on Kármán vortex behind circular-cylinder arrays: A molecular dynamics study
Y. Aasno, H. Watanabe, and H. Noguchi: J. Chem. Phys. **152** (2020) 034501.
2. 分子動力学計算による複雑流体中のカルマン渦の解析
浅野 優太, 渡辺 宙志, 野口 博司: 分子シミュレーション研究会会誌 “アンサンブル” **22**, 157 (2020).

DEKURA, Haruhiko [B class; 800 (B), 0 (C)] (173)

— *First-principles calculation of the higher-order phonon-phonon scattering strength*

EGAMI, Yoshiyuki [C class; 2500 (B), 800 (C)] (119)

— *First-principles study on controlling of electronic structures and electron-transport properties of 2-D materials*

— *First-principles study on controlling of electronic structures and electron-transport properties of atomic layered materials*

1. Efficient calculation of the self-energy matrices for electron-transport simulations
Y. Egami, S. Tsukamoto and T. Ono: Phys. Rev. B. **100** (2019) 075413.
2. Efficient calculation of the Green's function in scattering region for electron-transport simulations
Y. Egami, S. Tsukamoto and T. Ono: submitted to Phys. Rev. Lett.

FUCHIZAKI, Kazuhiro [C class; 4500 (B), 200 (C)] (283)

— *Kinetics of phase transition and polyamorphism*

1. Predicting the Melting Curve of MgO: An Essential Update
K. Fuchizaki: J. Phys. Soc. Jpn. **88** (2019) 065003.

FUJII, Keisuke [B class; 400 (B), 0 (C)] (351)

— *Quantum simulation for quantum many body systems using noisy-intermediate-scale quantum computers*

FUJIMOTO, Yoshitaka [C class; 1500 (B), 0 (C)] (155)

— *First-principles investigation of electronic properties of carbon nanotubes and graphene*

1. STM visualization of carbon impurities in sandwich structures consisting of hexagonal boron nitride and graphene
T. Haga, Y. Fujimoto, and S. Saito: Jpn. J. Appl. Phys. **58**, SIIB03 (2019).
2. Electronic structures and scanning tunneling microscopy images of heterostructures consisting of graphene and carbon-doped hexagonal boron nitride layers
T. Haga, Y. Fujimoto, and S. Saito: Phys. Rev. B **100**, 125403 (2019).
3. Atomic structures and scanning tunneling microscopy of nitrogen-doped carbon nanotubes
Y. Fujimoto and S. Saito: IOP Conf. Ser.: Mater. Sci. Eng. **744**, 012032 (2020).
4. First-Principles Materials Design for Graphene-based Sensor Devices

Y. Fujimoto: Sustainable Materials for Next Generation Energy Devices (Elsevier 2020), Accepted.

FUJISHIRO, Hiroki [C class; 1500 (B), 0 (C)] (153)

— *Strained Band-Structure Engineering for Antimonide-Based Terahertz Transistors*

FUKUDA, Jun-ichi [B class; 1500 (B), 0 (C)] (312)

— *Calculation of ordered structures and their optical properties of soft materials*

FUKUDA, Masahiro [B class; 800 (B), 100 (C)] (169)

— *Local physical quantities analysis based on the quantum field theory in material surface*

FUKUDA, Tuneo [B class; 700 (B), 0 (C)] (181)

— *First Principles Calculation of 2-Dimensional Silicides Formed on Nickel Surfaces*

1. Formation of two-dimensional silicide on the Ni(100) surface
T. Fukuda, I. Kishida and K. Umezawa: Jpn. J. Appl. Phys., in press.

FUKUI, Ken-ichi [C class; 1500 (B), 0 (C)] (311)

— *Analysis on Structuring and Dynamics of Ionic Liquid Forming Electric Double Layer as a Local Interfacial Field*

1. Correlation between Mobility and Hydrogen Bonding Network of Water at Electrified-Graphite Electrode Using Molecular Dynamics Simulation
M. Imai, Y. Yokota, I. Tanabe, K. Inagaki, Y. Morikawa, K. Fukui : Phys. Chem. Chem. Phys. **22** (2020) 1767
2. Ionic-Liquid-Originated Carrier Trapping Dynamics at the Interface in Electric Double-Layer Organic FET Revealed by Operando Interfacial Analyses
D. Okaue, I. Tanabe, S. Ono, K. Sakamoto, T. Sato, A. Imanishi, Y. Morikawa, J. Takeya, K. Fukui: J. Phys. Chem. C, **124** (2020) 2543

FUKUMOTO, Yoshiyuki [B class; 1300 (B), 0 (C)] (317)

— *Effects of Dzyaloshinskii–Moriya interactions and structural distortions on magnetic susceptibilities of spherical-kagome spin-systems*

— *Effects of Dzyaloshinskii–Moriya interactions and exchange randomness on low-temperature specific heats of spherical-kagome spin-systems*

GOHDA, Yoshihiro [C class; 4500 (B), 700 (C)] (99)

— *First-principles calculations of multiferroic interfaces*

1. First-principles study on surface stability and interface magnetic properties of SmFe₁₂
Y. Ainai, T. Shiozawa, Y. Tatetsu, and Y. Gohda: Appl. Phys. Express **13**, 045502 (2020).
2. First-principles study of crystalline Nd-Fe alloys
Y. Ainai, Y. Tatetsu, A. Terasawa, and Y. Gohda: Appl. Phys. Express **13**, 017006 (2020).
3. Enhancement of magnetoelectric coupling by insertion of Co atomic layer into Fe₃Si/BaTiO₃(001) interfaces identified by first-principles calculations
Y. Hamazaki and Y. Gohda: J. Appl. Phys. **126**, 233902 (2019).
4. Great Differences between Low-Temperature Grown Co₂FeSi and Co₂MnSi Films on Single-Crystalline Oxides
K. Kudo, Y. Hamazaki, S. Yamada, S. Abo, Y. Gohda, and K. Hamaya: ACS Appl. Electron. Mater. **1**, 2371 (2019).
5. Efficient Algorithm Based on Liechtenstein Method for Computing Exchange Coupling Constants Using Localized Basis Set
A. Terasawa, M. Matsumoto, T. Ozaki, and Y. Gohda: J. Phys. Soc. Jpn. **88**, 114706 (2019).

HAGIWARA, Satoshi [B class; 800 (B), 0 (C)] ()

— *Real-time propagated simulation for electron-positron scattering at the surface*

HAMADA, Ikutaro [C class; 5500 (B), 800 (C)] (82)

— *van der Waals density functional study of molecules adsorbed on metal surfaces*

HAMAGUCHI, Satoshi [C class; 4000 (B), 650 (C)] ()

— *Analyses of Surface Reactions in Atomic Layer Etching Processes*

HAMAMOTO, Yuji [C class; 2000 (B), 0 (C)] (141)

— *van der Waals density functional study of image potential states at organic-metal interfaces*

HARADA, KENJI [C class; 2000 (B), 500 (C)] (292)

— *Application of numerical renormalization group method in condensed-matter physics*

1. Entropy Governed by the Absorbing State of Directed Percolation
K. Harada and N. Kawashima: Phys. Rev. Lett. **123** (2019) 090601.

HARASHIMA, Yosuke [C class; 1500 (B), 0 (C)] (151)

— *First principles study on leaking current at a dislocation in doped semiconductors*

1. Screw dislocation that converts p-type GaN to n-type: Microscopic study on the Mg condensation and the leakage current in p-n diodes
T. Nakano, Y. Harashima, K. Chokawa, K. Shiraishi, A. Oshiyama, Y. Kangawa, S. Usami, N. Mayama, K. Toda, A. Tanaka, Y. Honda, and H. Amano: arXiv, 2004.06876 (2020).

HARUYAMA, Jun [C class; 5500 (B), 800 (C)] (80)

— *Electrochemical reaction analysis using density functional calculation + implicit solvation model*

HASHIMOTO, Tamotsu [C class; 1500 (B), 450 (C)] (300)

— *Molecular dynamics simulation of ferroelectrics using a shell model V*

1. Structure of Amorphous BaTiO₃ by Molecular Dynamics Simulations Using a Shell Model
T. Hashimoto and H. Moriwake: Physica B: Condens. Matter **579** (2020) 411799.

HASHMI, Arqum [C class; 1000 (B), 0 (C)] (168)

— *2D materials based symmetric and non-symmetric magnetoresistive junctions*

1. Graphene-based Symmetric and Non-Symmetric Magnetoresistive Junctions
A. Hashmi, K. Nakanishi, T. Ono: J. Phys. Soc. Jpn. **89**, 034708 (2020).

HATSUGAI, Yasuhiro [C class; 4000 (B), 700 (C)] (281)

— *Universality of bulk-edge correspondence by numerical methods*

1. Sequential quantum phase transitions in $J_1 - J_2$ Heisenberg chains with integer spins ($S > 1$): Quantized Berry phase and valence
Shota Fubasami, Tomonari Mizoguchi and Yasuhiro Hatsugai: Phys. Rev. B **100**, 014438 (2019)
2. Many-Body Chern Number without Integration
Koji Kudo, Haruki Watanabe, Toshikaze Kariyado, and Yasuhiro Hatsugai: Phys. Rev. Lett. **122**, 146601 (2019)
3. Higher-order Topological Mott Insulators
Koji Kudo, Tsuneya Yoshida, and Yasuhiro Hatsugai : Phys. Rev. Lett. **123**, 196402 (2019)
4. Non-Hermitian fractional quantum Hall states
Tsuneya Yoshida, Koji Kudo, and Yasuhiro Hatsugai: Scientific Reports **9**, 16895 (2019)
5. Exceptional rings protected by emergent symmetry for mechanical systems
Tsuneya Yoshida and Yasuhiro Hatsugai: Phys. Rev. B **100**, 054109 (2019)
6. Phase diagram of a disordered higher-order topological insulator: A machine learning study
H. Araki, T. Mizoguchi, and Y. Hatsugai: Phys. Rev. B **99**, 085406 (2019)
7. Z_Q Berry Phase for Higher-Order Symmetry-Protected Topological Phases
Hiromu Araki, Tomonari Mizoguchi and Yasuhiro Hatsugai: Phys. Rev. Research **2**, 012009(R) (2020)
8. Higher-order topological phases in a spring-mass model on a breathing kagome lattice
Hiromasa Wakao, Tsuneya Yoshida, Hiromu Araki, Tomonari Mizoguchi, and Yasuhiro Hatsugai:

Phys. Rev. **101**, 094107 (2020)

9. Exceptional band touching for strongly correlated systems in equilibrium
Tsuneya Yoshida, Robert Peters, Norio Kawakami, Yasuhiro Hatsugai: arXiv:2002.11265
10. Mirror skin effect and its electric circuit simulation
Tsuneya Yoshida, Tomonari Mizoguchi, and Yasuhiro Hatsugai: arXiv:1912.12022
11. Non-Analytic Adiabatic Principle for Anyons
Koji Kudo and Yasuhiro Hatsugai : arXiv:2004.00859.

HATTORI, Ken [C class; 1500 (B), 450 (C)] (143)

— *Atomic structure and electronic states for silicide films*

HAYAMI, Satoru [C class; 5500 (B), 0 (C)] (221)

— *Search for new types of skyrmion crystals based on point group symmetry*

1. Magnetic Vortex induced by Nonmagnetic Impurity in Ferromagnets: Magnetic Multipole and Toroidal around the Vacancy
S. Hayami, H.Kusunose, and Y. Motome: J. Phys. Soc. Jpn. **88**, 063702 (2019).
2. Double- Q Chiral Stripe in the d - p Model with Strong Spin-Charge Coupling
R. Yambe and S. Hayami: J. Phys. Soc. Jpn. **89**, 013702 (2020).
3. Electric Toroidal Quadrupoles in Spin-Orbit-Coupled Metal $\text{Cd}_2\text{Re}_2\text{O}_7$
S. Hayami, Y. Yanagi, H. Kusunose, and Y. Motome: Phys. Rev. Lett. **122**, 147602 (2019).
4. Atomic-Scale Magnetic Toroidal Dipole under Odd-Parity Hybridization
M. Yatsushiro and S. Hayami: J. Phys. Soc. Jpn. **88**, 054708 (2019).
5. Multipole expansion for magnetic structures: A generation scheme for symmetry-adapted orthonormal basis set in crystallographic point group
M.-T. Suzuki, T. Nomoto, R. Arita, Y. Yanagi, S. Hayami, and H. Kusunose: Phys. Rev. B **99**, 174407 (2019).
6. Momentum-Dependent Spin Splitting by Collinear Antiferromagnetic Ordering
M. Naka, S. Hayami, H. Kusunose, Y. Yanagi, Y. Motome, and H. Seo: Nat. Commun. **10**, 4305 (2019).
7. Momentum-Dependent Spin Splitting by Collinear Antiferromagnetic Ordering
S. Hayami, Y. Yanagi, and H. Kusunose: J. Phys. Soc. Jpn. **88**, 123702 (2019).
8. Odd-Parity Multipoles by Staggered Magnetic Dipole and Electric Quadrupole Orderings in Ce-CoSi
M. Yatsushiro and S. Hayami: J. Phys. Soc. Jpn. **89**, 013705 (2020).
9. Dimension transcendence and anomalous charge transport in magnets with moving multiple- Q spin textures
Y. Su, S. Hayami, and S.-Z. Lin: Phys. Rev. Research **2**, 013160 (2020).

HIDA, Kazuo [B class; 700 (B), 90 (C)] (338)

— *Numerical Study of One Dimensional Frustrated Quantum Spin Systems*

1. Ground State Phases of Distorted $S=1$ Diamond Chains
K. Hida: J. Phys. Soc. Jpn. **88**, 074705 (2019)
2. Exact Thermodynamic Properties of Mixed Diamond Chains with Strong Single-Site Anisotropy
R. Iwazaki and K. Hida: J. Phys. Soc. Jpn. **88**, 095001 (2019)
3. Ground-State Phases of Alternating-Bond $S=1$ Diamond Chains
K. Hida: J. Phys. Soc. Jpn. **89**, 024709 (2020)

HIGUCHI, Yuji [C class; 9500 (B), 1650 (C)] (244)

— *Brittle structure of crystalline polymers by large-scale coarse-grained molecular dynamics simulation*

— *Creep fracture process of crystalline polymers by large-scale molecular dynamics simulation*

1. Stress Transmitters at the Molecular Level in the Deformation and Fracture Processes of the Lamellar Structure of Polyethylene via Coarse-Grained Molecular Dynamics Simulations
Y. Higuchi: Macromolecules **52** (2019) 6201.

HINOKIHARA, Taichi [C class; 500 (B), 0 (C)] (349)

— *Magnetization reversal process in classical spin systems*

1. Time Quantified Monte Carlo method for Long-range Interacting Systems
Taichi Hinokihara, Yuta Okuyama, Munetaka Sasaki, and Seiji Miyashita: *Journal of Computational Physics*, in review

HINUMA, Yoyo [B class; 600 (B), 0 (C)] (188)

— *Calculation of multication oxide surface properties for catalyst informatics*

1. Band alignment at surfaces and heterointerfaces of Al₂O₃, Ga₂O₃, In₂O₃, and related group-III oxide polymorphs: A first-principles study
Y. Hinuma, T. Gake, and F. Oba: *Phys. Rev. Mater.*, **3** (2019) 084605.

HIRATSUKA, Masaki [B class; 800 (B), 100 (C)] ()

— *Effect of van der Waals interaction on vibrational spectra from ab initio molecular dynamics simulation*

HIYAMA, Miyabi [B class; 600 (B), 80 (C)] (186)

— *Analysis of absorption spectra for caged compounds in aqueous solution*

1. Theoretical study of the wavelength selection for the photocleavage of coumarin-caged D-luciferin
J. Usukura, M. Hiyama, M. Kurata, Y. Hazama, X-P. Qiu, F. M. Winnik, H. Akiyama, and N. Koga: *Photochem. Photobiol.* (2020) in press.
2. Photoabsorption Spectra of Aqueous Oxyluciferin Anions Elucidated by Explicit Quantum Solvent
Y. Noguchi, M. Hiyama, M. Shiga, H. Akiyama, and O. Sugino: *J. Chem. Theo. Comput.*, **15** (2019) 5474.

HOSHI, Takeo [C class; 6500 (B), 900 (C)] (76)

— *Unification of massively parallel quantum material simulation and data-driven science*

1. $K\omega$ - Open-source library for the shifted Krylov subspace method
Takeo Hoshi, Mitsuaki Kawamura, Kazuyoshi Yoshimi, Yuichi Motoyama, Takahiro Misawa, Youhei Yamaji, Synge Todo, Naoki Kawashima, Tomohiro Sogabe: arXiv:2001.08707
2. Two-stage data-analysis method for total-reflection high-energy positron diffraction (TRHEPD)
Kazuyuki Tanaka, Izumi Mochizuki, Takashi Hanada, Ayahiko Ichimiya, Toshio Hyodo, and Takeo Hoshi: Submitted; Preprint: <https://arxiv.org/abs/2002.12165>
3. Development of data-analysis software for total-reflection high-energy positron diffraction (TRHEPD)
Kazuyuki Tanaka, Takeo Hoshi, Izumi Mochizuki, Takashi Hanada, Ayahiko Ichimiya, Toshio Hyodo: *Acta. Phys. Pol. A* **137**, 188-192 (2020).
4. An a posteriori verification method for generalized Hermitian eigenvalue problems in large-scale electronic state calculations
Takeo Hoshi, Takeshi Ogita, Katsuhisa Ozaki, Takeshi Terao: *J. Comp. Appl. Math.* **376**, 112830/1-13 (2020).
5. Charge-Transfer Excited States in the Donor/Acceptor Interface from Large-Scale GW Calculations
Takatoshi Fujita, Yoshifumi Noguchi, Takeo Hoshi: *J. Chem. Phys.* **151**, 114109/1-8 (2019).
6. EigenKernel - A middleware for parallel generalized eigenvalue solvers to attain high scalability and usability
Kazuyuki Tanaka, Hiroto Imachi, Tomoya Fukumoto, Akiyoshi Kuwata, Yuki Harada, Takeshi Fukaya, Yusaku Yamamoto, Takeo Hoshi: *Japan J. Indust. Appl. Math* **36**, 719-742 (2019).
7. Numerical aspect of large-scale electronic state calculation for flexible device material
Takeo Hoshi, Hiroto Imachi, Akiyoshi Kuwata, Kohsuke Kakuda, Takatoshi Fujita, Hiroyuki Matsui: *Japan J. Indust. Appl. Math* **36**, 685-698 (2019).
8. Recent progress in large-scale electronic state calculations and data-driven sciences
Takeo Hoshi and Satoshi Ito: Chap. 14 of *Handbook of Silicon Based MEMS Materials and Technologies* 3rd Ed., Elsevier (2020).
9. Numerical methods for large scale electronic state calculation on supercomputer
Takeo Hoshi, Yusaku Yamamoto, Tomohiro Sogabe, Kohei Shimamura, Fuyuki Shimojo, Aiichiro

Nakano, Rajiv Kalia, Priya Vashishta: Chap. 15 of 21st Century Nanoscience - A Handbook: Nanophysics Sourcebook (Volume One), CRC Press (2019).

HOSHINO, Shintaro [B class; 900 (B), 0 (C)] (230)

— *Dynamical mean-field theory + quantum Monte Carlo approach to strongly correlated electron systems with multi-orbitals*

1. Nickelate superconductors: Multiorbital nature and spin freezing
P. Werner and S. Hoshino, Phys. Rev. B 101, 041104(R) (2020).
2. Magnetic Field Induced Phase Transition in Superconducting State of Non-Kramers Doublet Kondo Lattice Systems with Semi-Metallic Conduction Bands
S. Imura, M. Hirayama, and S. Hoshino: JPS Conf. Proc. 30, 011048 (2020).
3. Fermi-surface anisotropy effects on full-gap superconductivity in non-Kramers doublets coupled to compensated metals
S. Imura, M. Hirayama, and S. Hoshino: JPS Conf. Proc. 29, 011003 (2020).

HOTTA, Chisa [B class; 600 (B), 0 (C)] (347)

— *Numerical studies on some new phases of the transverse Ising model*

1. Spin-orbital glass transition in a model of frustrated pyrochlore magnet without quenched disorder
Kouta Mitsumoto, Chisa Hotta, and Hajime Yoshino: Phys. Rev. Lett. **124** (2020) 087201.
2. Multiple quadrupolar or nematic phases driven by the Heisenberg interactions in a spin-1 dimer system forming a bilayer
Katsuhiko Tanaka, Chisa Hotta: Phys. Rev. B **101** (2020) 094422.
3. Discovering momentum-dependent magnon spin texture in insulating antiferromagnets: Role of the Kitaev interaction
Masataka Kawano, Chisa Hotta: Phys. Rev. B **100** (2019) 174402.

HOTTA, Takashi [C class; 7500 (B), 0 (C)] (215, 217)

— *Research of Two-Channel Kondo Effect in Transuranium Systems*

— *Two-Channel Kondo Effect Emerging in a Multiorbital Anderson Model Hybridized with Γ_7 and Γ_8 Conduction Bands*

1. Two-Channel Kondo Effect Emerging from Np and Pu Ions
Dai Matsui and Takashi Hotta, JPS Conf. Proc. **30**, 011125 (2020).

HU, Shiqian [C class; 2500 (B), 650 (C)] (125)

— *manipulation of the cross-plane thermal conductivity on the 2D hetero-junction materials*

HUKUSHIMA, Koji [C class; 3500 (B), 0 (C)] (287)

— *Development of data-driven science to materials science*

1. Adjusting the descriptor for a crystal structure search using Bayesian optimization
Nobuya Sato, Tomoki Yamashita, Tamio Oguchi, Koji Hukushima, and Takashi Miyake: Phys. Rev. Materials **4**, (2020) 033801.

IDO, Kota [C class; 5000 (B), 750 (C)] (262)

— *Numerical studies on magnetization process of the Kitaev spin liquid*

1. Correlation effects on the magnetization process of the Kitaev model
K. Ido, and T. Misawa: Phys. Rev. B **101** (2020) 045121.
2. Charge dynamics of correlated electrons: Variational description with inclusion of composite fermions
K. Ido, M. Imada, and T. Misawa: Phys. Rev. B **101** (2020) 075124.

IGARASHI, Ryo [C class; 1000 (B), 500 (C)] ()

— *Full diagonalization using low-rank approximation to Hamiltonian matrices and its application to quantum spin models*

IKEDA, Hiroaki [B class; 400 (B), 0 (C)] (195)

— *Development and application of the first-principles approach*

IKUHARA, Yuichi [C class; 4500 (B), 0 (C)] (111)

— *Ab initio calculations of atomic and electronic structures for functional oxide materials*

— *Study of atomic and electronic structure of hetero interface by first-principles molecular dynamics simulations*

1. Strong metalmetal interaction and bonding nature in metal/oxide interfaces with large mismatches
H. Li, M. Saito, C. Chen, K. Inoue, K. Akagi, Y. Ikuhara: *Acta Mater.* **179** (2019) 237.

IMADA, Masatoshi [E class; 34000 (B), 4950 (C)] (197)

— *Development of methodology for analysis of nonequilibrium superconductivity in strongly correlated systems via integration of electronic state theory and time-resolved experimental data*

— *Mechanism of quantum spin liquid and high-Tc superconductivity studied by excitation spectra and nonequilibrium dynamics calculation by variational Monte Carlo methods*

1. Charge dynamics of correlated electrons: Variational description with inclusion of composite fermions
Kota Ido, Masatoshi Imada, Takahiro Misawa: *Phys. Rev. B* **101** (2020) 075124.
2. *Ab initio* study of superconductivity and inhomogeneity in a Hg-based cuprate superconductor
Takahiro Ohgoe, Motoaki Hirayama, Takahiro Misawa, Kota Ido, Youhei Yamaji, Masatoshi Imada: *Phys. Rev. B* **101** (2020) 045124.
3. Effective Hamiltonian for cuprate superconductors derived from multiscale ab initio scheme with level renormalization
Motoaki Hirayama, Takahiro Misawa, Takahiro Ohgoe, Youhei Yamaji, Masatoshi Imada: *Phys. Rev. B* **99** (2019) 245155.
4. *Ab initio* derivation of an effective Hamiltonian for the $\text{La}_2\text{CuO}_4/\text{La}_{1.55}\text{Sr}_{0.45}\text{CuO}_4$ heterostructure
Terumasa Tadano, Yusuke Nomura, Masatoshi Imada: *Phys. Rev. B* **99** (2019) 155148.

INAGAKI, Kouji [C class; 2000 (B), 600 (C)] ()

— *Analysis and Design of reaction process and catalyst material for CARE machining*

INAOKA, Takeshi [B,C class; 1000 (B), 200 (C)] (160)

— *Search and realization of novel electronic properties of solid surfaces and interfaces and of small particles*

— *Search and realization of novel electronic properties of solid surfaces and interfaces and of small particles II*

1. Finite-difference time-domain analysis of scanning tunneling microscope light emission from vibrating molecules
Y. Uehara, W. Iida, T. Inaoka, S. Iwaoka, H. Aoyagi, and S. Katano: to be submitted.

ISHIBASHI, Shoji [C class; 4500 (B), 0 (C)] (110)

— *Prediction of properties of organic ferroelectrics and piezoelectrics by first-principles calculation*

1. Coexistence of normal and inverse deuterium isotope effects in a phase-transition sequence of organic ferroelectrics
S. Horiuchi, S. Ishibashi, K. Kobayashi, and R. Kumai: *RSC Adv.* **9** (2019) 39662.

ISHIDA, Kunio [B class; 1200 (B), 170 (C)] (315)

— *Entanglement in remote electron-phonon systems created by photoirradiation*

— *Ultrafast nonadiabatic dynamics of electron-phonon-photon system*

1. Interplay of electron-phonon nonadiabaticity and Raman scattering in the wavepacket dynamics of electron-phonon-photon systems
Kunio Ishida: *Eur. Phys. J. D73*, 117 (2019)
2. Coherent control of nonadiabatic dynamics of electron-phonon systems by quantized light field
Kunio Ishida: *Progress in Ultrafast Intense Laser Science XV*, 10.1007/978-3-030-47098-2_6

ISHIHARA, Sumio [B class; 800 (B), 0 (C)] (234)— *Photoinduced dynamics and high harmonic generation in magnetism*

1. Nonequilibrium susceptibility in photoinduced Floquet states
Atsushi Ono and Sumio Ishihara, *Phys. Rev. B* **100**, 075127 (2019).
2. Optical Response in Excitonic Insulating State: Variational Cluster Approach
Hengyue Li, Junya Otsuki, Makoto Naka, Sumio Ishihara, *Phys. Rev. B* **101**, 125117 (2020).
3. Photoinduced Ultrafast Phenomena in Correlated Electron Magnets
Sumio Ishihara, *J. Phys. Soc. Jpn.* **88**, 023703 (2019).

ISHII, Fumiya [C class; 8500 (B), 0 (C)] (70)— *First-Principles Crystal Structure Prediction of Magnetic Thermoelectric Materials*— *First-principles study of electric-field effect on magnetic insulator*

1. Realization of Spin-dependent Functionality by Covering a Metal Surface with a Single Layer of Molecules
H. Isshiki, K. Kondou, S. Takizawa, K. Shimose, T. Kawabe, E. Minamitani, N. Yamaguchi, F. Ishii, A. Shiotari, Y. Sugimoto, S. Miwa and Y. Otani: *Nano Lett.* **197** (2019) 7119.
2. First-principles Study of Spiral Spin Density Waves in Monolayer MnCl₂ Using Generalized Bloch Theorem
T.B. Prayitno and F. Ishii: *J. Phys. Soc. Jpn.* **88** (2019) 104705.
3. Intrinsic persistent spin helix state in two-dimensional group-IV monochalcogenide MX monolayers (M=Sn or Ge and X=S, Se, or Te)
M.A.U. Absor and F. Ishii: *Phys. Rev. B.* **100** (2019) 115104.
4. Photoinduced Rashba Spin-to-Charge Conversion via an Interfacial Unoccupied State
J. Puebla, F. Auvray, N. Yamaguchi, M. Xu, S.Z. Bisri, Y. Iwasa, F. Ishii, and Y. Otani: *Phys. Rev. Lett.* **122** (2019) 256401.
5. Electric-field-induced Z₂ topological phase transition in strained single bilayer Bi(111)
H. Sawahata, Y. Yamaguchi, and F. Ishii: *Appl. Phys. Express* **12** (2019) 075009.

ISHIZUKA, Jun [C class; 4500 (B), 750 (C)] (223)— *Multipole and anisotropic superconductivity from first principles*

1. Insulator-Metal Transition and Topological Superconductivity in UTe₂ from a First-Principles Calculation
Jun Ishizuka, Shuntaro Sumita, Akito Daido, and Youichi Yanase: *Phys. Rev. Lett.* **123**, 217001 (2019).
2. Observation of superconducting diode effect
Fuyuki Ando, Yuta Miyasaka, Tian Li, Jun Ishizuka, Yoichi Shiota, Takahiro Moriyama, Yoichi Yanase, and Teruo Ono: submitted to *Nature*.

ISOBE, Masaharu [B class; 600 (B), 0 (C)] (345)— *Nonequilibrium phase transition and slow dynamics in the dense hard sphere systems***IYODA, Eiki** [C class; 1500 (B), 0 (C)] (309)— *Numerical analysis on the off-diagonal eigenstate thermalization hypothesis*

1. Characterizing complexity of many-body quantum dynamics by higher-order eigenstate thermalization
K. Kaneko, E. Iyoda, and T. Sagawa: *Phys. Rev. A*, in press.

JESCHKE, Harald [C class; 6500 (B), 0 (C)] (257, 258)— *Doping dependence of electronic structure and superconductivity in FeSe intercalated by organic molecules*— *Stability of the superconductor LaFe₂As₂*

1. Novel Fe-Based Superconductor LaFe₂As₂ in Comparison with Traditional Pnictides
I. I. Mazin, M. Shimizu, N. Takemori, and H. O. Jeschke: *Phys. Rev. Lett.* **123** (2019), 267001.
2. Unusual non-valence-skipping electronic state of Sn in AgSnSe₂

Y. Naijo, K. Hada, T. Furukawa, T. Itou, T. Ueno, K. Kobayashi, I. I. Mazin, H. O. Jeschke, and J. Akimitsu: *Phys. Rev. B* **101** (2020), 075134.

JOUTSUKA, Tatsuya [B class; 1300 (B), 0 (C)] (158, 159)

— *Ab Initio Calculation of High-Rate Deposition of Copper Film by Low-Pressure Chemical Vapor Deposition with CuI on Ru Substrate*

— *Molecular Science at Solid/Liquid Interfaces using Molecular Dynamics Simulation and Ab Initio Calculation*

1. Low-pressure chemical vapor deposition of Cu on Ru substrate using CuI: Ab initio calculations
T. Joutsuka, S. Yamauchi: *Chem. Phys. Lett.* **741** (2020) 137108.

JU, Shenghong [C class; 5000 (B), 1200 (C)] (83)

— *Energy Transport in Hybrid Organic-Inorganic Thermoelectric Materials*

KAGESHIMA, Hiroyuki [C class; 500 (B), 0 (C)] (189)

— *Study on structural elementary excitations at semiconductor surfaces and interfaces*

1. First-principles Study of pressure and SiO-incorporation effect on dynamical properties of silicon oxide
H. Kageshima, Y. Yajima, K. Shiraishi, and T. Endoh: *Jpn. J. Appl. Phys.* **58** (2019) 111004 (11pages).

KARIYADO, Toshikaze [B class; 1000 (B), 0 (C)] (331)

— *Manipulation of electronic states with nanostructures: model construction and its application*

1. Flat band in twisted bilayer Bravais lattices
T. Kariyado and A. Vishwanath, *Phys. Rev. Research* **1** (2019) 033076.

KASAMATSU, Shusuke [C class; 11000 (B), 1750 (C)] (57, 386)

— *Designing doping schemes for BaZrO₃-based ion conductors*

— *First-principles configurational sampling of highly-doped ionic conductors*

1. Insights Into Defect Arrangements in Y-Doped BaZrO₃ From Large-Scale First-Principles Thermodynamic Sampling: Association, Repulsion, Percolation, and Trapping
Chemrxiv. Preprint.

KATO, Takeo [D class; 10000 (B), 1000 (C)] (210)

— *Variational Monte Carlo calculation of two-dimensional Wigner crystal under lattice commensurability*

KATO, Yusuke [C class; 5000 (B), 0 (C)] (272)

— *Functional Renormalization Group Study of Quantum Spin Liquids*

KAWAKAMI, Norio [C class; 9500 (B), 1700 (C)] (206)

— *Study of magnetism and superconductivity in strongly correlated quantum systems using approaches including non-equilibrium methods*

— *Study of magnetism topology and transport phenomena in strongly correlated quantum systems*

1. Spin-caloritronic transport in hexagonal graphene nanoflakes
Thi. Thu Phung, Robert Peters, Andreas Honecker, Guy Trambly de Laissardiere, and Javad Vahedi: arXiv:2003.01139.
2. Equivalence of the effective non-hermitian Hamiltonians in the context of open quantum systems and strongly-correlated electron systems
Yoshihiro Michishita and Robert Peters: arXiv:2001.09045.
3. Hubbard model on the honeycomb lattice: From static and dynamical mean-field theories to lattice quantum Monte Carlo simulations
Marcin Raczkowski, Robert Peters, Thi. Thu Phng, Nayuta Takemori, Fakher F. Assaad, Andreas Honecker, and Javad Vahedi: *Phys. Rev. B* **101** (2020) 125103.
4. Relationship between exceptional points and the Kondo effect in f-electron materials

- Yoshihiro Michishita, Tsuneya Yoshida, and Robert Peters: Phys. Rev. B **101** (2020) 085122.
5. Chiral-symmetry protected exceptional torus in correlated nodal-line semimetals
Kazuhiro Kimura, Tsuneya Yoshida, and Norio Kawakami: Phys. Rev. B **100** (2019) 115124.
 6. Quantum oscillations in strongly correlated topological Kondo insulators
Robert Peters, Tsuneya Yoshida, and Norio Kawakami: Phys. Rev. B **100** (2019) 085104.
 7. Impact of the Rashba Spin Orbit Coupling on f-electron Materials
Yoshihiro Michishita and Robert Peters: Phys. Rev. B **99** (2019) 155141.

KAWAMURA, Hikaru [C class; 11000 (B), 0 (C)] (249)— *Novel order in frustrated magnets*

1. Spin ordering induced by lattice distortions in classical Heisenberg antiferromagnets on the breathing pyrochlore lattice
K. Aoyama and H. Kawamura, Phys. Rev., B 99, 1444062-(1-14) (2019)
2. Ripple state in the frustrated honeycomb-lattice antiferromagnet
T. Shimokawa and H. Kawamura, Phys. Rev. Letters 123, 057202(1-6) (2019)
3. Nature of the randomness-induced quantum spin liquids in two dimensions
H. Kawamura and K. Uematsu, J. Phys. Condens. Matter 31, 504003(1-18) (2019)
4. Randomness-induced quantum spin liquid behavior in the $s=1/2$ random-bond Heisenberg antiferromagnet on the pyrochlore lattice
K. Uematsu and H. Kawamura, Phys. Rev. Letters 123, 087201-(1-6) (2019)
5. Effects of magnetic anisotropy on spin and thermal transport in classical antiferromagnets on the square lattice
K. Aoyama and H. Kawamura, Phys. Rev. B 100, 144416-(1-19) (2019)
6. Multiple-q states of the J1-J2 classical honeycomb-lattice Heisenberg antiferromagnet under a magnetic field
T. Shimokawa and H. Kawamura, Phys. Rev. B 100, 224404-(1-15) (2019)
7. Monte Carlo study of the critical properties of noncollinear Heisenberg magnets: $O(3) \times O(2)$ universality class
Y. Nagano, K. Uematsu, and H. Kawamura, Phys. Rev. B 100, 224430(1-15) (2019)
8. Monte Carlo studies of the spin-chirality decoupling in the three-dimensional Heisenberg spin glass
T. Ogawa, K. Uematsu, and H. Kawamura, Phys. Rev. B 101, 014434(1-16) (2020)
9. Spin Current as a Probe of the Z2-Vortex Topological Transition in the Classical Heisenberg Antiferromagnet on the Triangular Lattice
K. Aoyama and H. Kawamura, Phys. Rev. Letters 124, 047202-(1-6) (2020)

KAWAMURA, Mitsuaki [B class; 700 (B), 90 (C)] (176)— *Benchmark of density functional theory for superconductors*

1. Benchmark of density functional theory for superconductors in elemental materials
M. Kawamura, Y. Hizume, and T. Ozaki Phys. Rev. B **101**, (2020) 134511.

KAWASHIMA, Naoki [E class; 39000 (B), 5450 (C)] (239)— *Tensor-Ring Decomposition Based on HOSVD and Its Application*— *Variational calculation of Kitaev and related models with tensor-network representation*

1. Tensor network wavefunction of $S = 1$ Kitaev spin liquids
Hyun-Yong Lee, Naoki Kawashima, and Yong Baek Kim:arXiv:1911.07714
2. Boundary conformal spectrum and surface critical behavior of classical spin systems:A tensor network renormalization study
Shumpei Iino, Satoshi Morita, and Naoki Kawashima: Phys. Rev. B **101**, 155418 (2020)
3. Magnetic field induced quantum phases in a tensor network study of Kitaev magnets
Hyun-Yong Lee, Ryui Kaneko, Li Ern Chern, Tsuyoshi Okubo, Youhei Yamaji, Naoki Kawashima and Yong Baek Kim: Nature Communications **11**, 1639 (2020)
4. Abelian and non-Abelian chiral spin liquids in a compact tensor network
Hyun-Yong Lee, Ryui Kaneko, Tsuyoshi Okubo, Naoki Kawashima: Phys. Rev. B **101**, 035140 (2020)
5. Thermal-transport studies of kagom antiferromagnets

Minoru Yamashita, Masatoshi Akazawa, Masaaki Shimozawa, Takasada Shibauchi, Yuji Matsuda, Hajime Ishikawa, Takeshi Yajima, Zenji Hiroi, Migaku Oda, Hiroyuki Yoshida, Hyun-Yong Lee, Jung Hoon Han and Naoki Kawashima: *J. Phys: Condens. Matter* **32**, 074001(11pp) (2019)

6. Entropy Governed by the Absorbing State of Directed Percolation
Kenji Harada and Naoki Kawashima: *Phys. Rev. Lett.* **123**, 090601 (2019)
7. Boundary Tensor Renormalization Group
Shumpei Iino, Satoshi Morita, and Naoki Kawashima: *Phys. Rev. B* **100**, 035449 (2019)
8. Gapless Kitaev Spin Liquid to Classical String Gas through Tensor Networks
Hyun-Yong Lee, Ryui Kaneko, Tsuyoshi Okubo, and Naoki Kawashima: *Phys. Rev. Lett.* **123**, 087203 (2019)
9. Tensor-Ring Decomposition with Index-Splitting
Hyun-Yong Lee and Naoki Kawashima: *J. Phys. Soc. Jpn.* **89**, 054003 (2020)

KITA, Takafumi [C class; 1000 (B), 0 (C)] ()

— *studying the enhancement of the thermal Hall angle in d-wave superconductors*

KITAO, Akio [C class; 5000 (B), 0 (C)] (270)

— *Efficient sampling simulation of the soft modes significantly contribute to protein properties*

1. Kinetic selection and relaxation of the Intrinsically Disordered Region of a Protein upon Binding.
D.P. Tran and A Kitao: *J. Chem. Theory Comput*, in press (2020) doi: 10.1021/acs.jctc.9b01203.
2. High pressure inhibits signaling protein binding to the flagellar motor and bacterial chemotaxis through enhanced hydration.
H. Hata, Y. Nishihara, M. Nishiyama, Y. Sowa, I. Kawagishi, A. Kitao: *Sci. rep.* **10** (2020) 2351.
3. Molecular dynamics simulation of proteins under high pressure: Structure, function and thermodynamics.
H. Hata, M. Nishiyama, A. Kitao: *Biochimica et Biophysica Acta* **1864** (2020) 7.
4. evERdock BAI: Machine-learning-guided selection of protein-protein complex structure.
K. Terayama, A. Shinobu, K. Tsuda, K. Takemura, and A. Kitao: *J. Chem. Phys.* **151** (2019) 215104.
5. Impact of key residues within chloroplast thioredoxin-f on recognition for reduction and oxidation of target proteins.
Y. Yokochi et. al.: *J. Biol. Chem.* **294** (2019) 17437.
6. Phagocytosis is mediated by two-dimensional assemblies of the F-BAR protein GAS7.
K. Hanawa-Suetsugu et. al.: *Nat. Commun.* **10** (2019) 10.
7. Enhancing Biomolecular Sampling with Reinforcement Learning: A Tree Search Molecular Dynamics Simulation Method.
K. Shin, D.P. Tran, K. Takemura, A. Kitao, K. Terayama, and K. Tsuda: *ACS omega* **4** (2019) 13853.
8. Cancellation between auto-and mutual correlation contributions of protein/water dynamics in terahertz time-domain spectra.
Y. Joti and A. Kitao: *Biophys. Physicobiol.* **16** (2019) 240.
9. More efficient screening of protein-protein complex model structures for reducing the number of candidates.
K. Takemura and A. Kitao: *Biophys. Physicobiol.* **16** (2019) 295.

KOBAYASHI, Akito [B class; 1500 (B), 200 (C)] (228)

— *Spin-Charge Separation in Charge Order Phase of Organic Dirac Electron System α -(BEDT-TTF)₂I₃*

1. Domain wall conductivity with strong Coulomb interaction of two-dimensional massive Dirac electrons in the organic conductor α -(BEDT-TTF)₂I₃
D. Ohki, Y. Omori, and A. Kobayashi, *Phys. Rev. B* **100**, 075206 (2019).

KOBAYASHI, Katsuyoshi [B class; 400 (B), 50 (C)] (190)

— *Theoretical study on electronic properties of new nanoscale surfaces and interfaces*

KOBAYASHI, Nobuhiko [C class; 4000 (B), 650 (C)] (108)— *First-principles study of quantum transport in nanostructures*

1. Second highest occupied molecular orbital effects on the valence band structure of organic semiconductors
Y. Kuroda, H. Ishii, S. Yoshino, N. Kobayashi, Jpn. J. Appl. Phys. 58 SIIB27 (2019).
2. Carrier transport calculations of organic semiconductors with static and dynamic disorder
H. Ishii, N. Kobayashi, and K. Hirose, Jpn. J. Appl. Physics 58, 110501 (2019).
3. Electronic Band Structure of TiN/MgO- 4×4 and 5×5 Nanostructures
K. Kobayashi, H. Takaki, M. Shimono, N. Kobayashi, and K. Hirose, Jpn. J. Appl. Phys. 58 SBBH06 (2019).
4. Seebeck coefficients in CuFeS₂ thin films by first-principles calculations
H. Takaki, K. Kobayashi, M. Shimono, N. Kobayashi, K. Hirose, N. Tsujii, and T. Mori Jpn. J. Appl. Phys. 58 SIIB01 (2019).
5. Magnetism-mediated thermoelectric performance of the Cr-doped bismuth telluride tetradymite
J. B. Vaney, S. A. Yamini, H. Takaki, K. Kobayashi, N. Kobayashi, T. Mori, Mater. Today Phys. 8 (2019) 100090.
6. Sub-molecular structural relaxation at a physisorbed interface with monolayer organic single-crystal semiconductors
A. Yamamura, H. Fujii, H. Ogasawara, D. Nordlund, O. Takahashi, Y. Kishi, H. Ishii, N. Kobayashi, N. Niitsu, B. Blulle, T. Okamoto, Y. Wakabayashi, S. Watanabe, and J. Takeya, Commun. Phys. 3 20 (2020)
7. Charge mobility calculation of organic semiconductors without use of experimental single-crystal data
H. Ishii, S. Obata, N. Niitsu, S. Watanabe, H. Goto, K. Hirose, N. Kobayashi, T. Okamoto, and J. Takeya, Sci Rep 10, 2524 (2020)

KOBAYASHI, Riki [B class; 300 (B), 0 (C)] (357)— *Screening of substitutable non-magnetic element in rare-earth inter-metallic compounds***KOGA, Akihisa** [C class; 9500 (B), 650 (C)] (211, 212)— *Magnetic and transport properties in double-exchange systems with quasiperiodicity*— *Numerical analysis for nonequilibrium dynamics in correlated electron systems with orbital degrees of freedom*

1. Majorana-mediated spin transport without spin polarization in Kitaev quantum spin liquids
T. Minakawa, Y. Murakami, A. Koga and J. Nasu: submitted to PRL.
2. Spin transport in the Quantum Spin Liquid State in the $S = 1$ Kitaev model: role of the fractionalized quasiparticles
A. Koga, T. Minakawa, Y. Murakami and J. Nasu: J. Phys. Soc. Jpn. **89** (2020) 033701.
3. Excitonic condensation reflecting electronic states in two-band Penrose-Hubbard model
K. Inayoshi, Y. Murakami and A. Koga: submitted to JPSJ.

KOMATSU, Hisato [B class; 1100 (B), 150 (C)] (321, 323)— *Competition between dipolar and Dzyaloshinskii-Moriya interactions on the magnetic thin films*— *Competition between dipolar and short-range interactions on the magnetic thin films*

1. Anisotropy-temperature phase diagram for the two-dimensional dipolar Heisenberg model with and without magnetic field
H. Komatsu, Y. Nonomura, and M. Nishino, Phys. Rev. B **100**, 094407 (2019).

KOMATSU, Yu [C class; 2500 (B), 500 (C)] (291)— *Constructing the electronic structure database for the molecular design of pigments utilizing near infrared light***KOTA, Yohei** [B class; 400 (B), 0 (C)] (193)— *Analysis of magnetic properties in Cr and Mn alloys*— *Analysis of strain effect on magnetism in chromium metals*

1. Perpendicularly magnetized Cu_2Sb type (Mn-Cr)AlGe films onto amorphous SiO_2
T. Kubota, Y. Kota, K. Ito, R. Y. Umetsu, M. Sun, M. Mizuguchi, and K. Takahashi: Appl. Phys. Express **12** (2019) 103002.

KOU, Sonju [B class; 400 (B), 0 (C)] (191)

— *Development of First-principles calculations method of Seebeck coefficient in the framework of linear response theory*

KOURA, Akihide [C class; 1000 (B), 0 (C)] (167)

— *First principles study on static structure of glass materials*

1. Guidelines for creating artificial neural network empirical interatomic potential from first-principles molecular dynamics data under specific conditions and its application to $\alpha\text{-Ag}_2\text{Se}$
K. Shimamura, S. Fukushima, A. Koura, F. Shimojo, M. Misawa, R. K. Kalia, A. Nakano, P. Vashishta et al.: J. Chem. Phys. **151**, (2019) 124303.
2. GGA+U Molecular Dynamics Study of Structural and Dynamic Properties of Superionic Conductor Ag_2Se
S. Fukushima, M. Misawa, A. Koura, and F. Shimojo: J. Phys. Soc. Jpn. **88**, (2019) 115002.
3. Thermodynamic Integration by Neural Network Potentials Based on First-principles Dynamic Calculations
S. Fukushima, E. Ushijima, H. Kumazoe, A. Koura, F. Shimojo, K. Shimamura, M. Misawa, R. K. Kalia, A. Nakano, and P. Vashishta: Phys. Rev. B **100**, (2019) 214108.
4. コンピュータシミュレーションによる永久高密度化ガラスの構造計算
高良明英, 若林大佑, 下條冬樹: NEW GLASS **35**, (2020) 12.
5. Intermediate range structure of amorphous Cu_2GeTe_3 : *ab initio* molecular dynamics study
A. Koura, and F. Shimojo: J. Phys.: Condens. Matter **32**, (2020) 244001.
6. Molecular-Dynamics Study of Thermal Conductivity of Silver Chalcogenides
S. Fukushima, A. Koura, and F. Shimojo: submitted to Phys. Status Solidi B
7. Pressure Dependence of Static Structure of Liquid V_2O_5 : *ab initio* Molecular Dynamics Study
A. Koura, and F. Shimojo: submitted to Phys. Status Solidi B

KUMAZOE, Hiroyuki [C class; 1000 (B), 250 (C)] (320)

— *Establishment of new analysis method for extend X-ray absorption fine structure with sparse modeling*

KUNISADA, Yuji [C class; 8000 (B), 0 (C)] (72)

— *Reduction of Rare Metals in Formic Acid Decomposition Catalysts and Oxygen Storage Materials*

1. グラフェン上での金属原子吸着状態の理論的研究
長谷川瞬, 國貞雄治, 坂口紀史: 表面と真空 **62** (2019) 344.
2. Extraordinarily Large Kinetic Isotope Effect on Alkene Hydrogenation over Rh-based Intermetallic Compounds
S. Furukawa, P. Yi, Y. Kunisada, K. Shimizu: Science and Technology of Advanced Materials **20** (2019) 805.
3. Co-appearance of superconductivity and ferromagnetism in a Ca_2RuO_4 nanofilm crystal
SH. Nobukane, K. Yanagihara, Y. Kunisada, Y. Ogasawara, K. Nomura, Y. Asano, S. Tanda: Scientific Reports **10** (2020) 3462.

KUROKI, Kazuhiko [C class; 10500 (B), 1600 (C)] (204)

— *Study on electron correlation and possible superconductivity in mixed-anion systems*

— *Study on the possibility of superconductivity in ladder-type electronic structures constructed from multiple anions*

1. Comparative first-principles study of antiperovskite oxides and nitrides as thermoelectric material: multiple dirac cones, low-dimensional band dispersion, and high valley degeneracy
M. Ochi, K. Kuroki: Phys. Rev. Applied. **12** (2019) 034009.
2. Strongly enhanced superconductivity due to finite energy spin fluctuations induced by an incipient band : a FLEX study on the bilayer Hubbard model with vertical and diagonal interlayer hoppings
K. Matsumoto, D. Ogura, and K. Kuroki: J. Phys. Soc. Jpn. **89** (2020) 044709.

3. Many-variable variational Monte-Carlo study of superconductivity in two-band Hubbard models with an incipient band
D. Kato and K. Kuroki: Phys. Rev. Research, in press (2020) (arXiv:1912.11983)

KUSAKABE, Koichi [C class; 2000 (B), 300 (C)] (140)

— *Transport and reaction properties of nanographene*

1. Spin-current control by induced electric-polarization reversal in Ni/hBN/Ni: A cross-correlation material
H. Harfah, Y. Wicaksono, M.A. Majidi, and K. Kusakabe: ACS Appl. Elect. Materials, in press.
2. Interplanar stiffness in defect-free monocrystalline graphite
K. Kusakabe, A. Wake, A. Nagakubo, K. Murashima, M. Murakami, K. Adachi, H. Ogi: Phys. Rev. Materials **4** (2020) 043603.
3. アルカン脱水素触媒、及びこれを用いる水素製造方法
草部浩一, 高井和之, 西川正浩, 劉明, 特願 2019-135780.
4. Counting the Zero Modes and Magnetic Moment by Topology of a Phenalenyl-Tessellation Molecule with Vacancies
N. Morishita, K. Kusakabe: J. Phys. Soc. Jpn. **88** (2019) 124707.

MAKINO, Takayuki [B class; 1500 (B), 210 (C)] (149)

— *Ab-initio calculation of phonon density-of-states spectra in cuprous oxides*

— *Calculation of electron-phonon interaction in delafossite-type cuprates*

— *Electronic structure calculation in strongly-correlated electron oxides under presence of static electric field*

1. Temperature dependence of dielectric functions in Yb₂O₃ and Lu₂O₃ epitaxial thin films on sapphire (0001)
T. Makino et al.: Jpn. J. Appl. Phys. (2020) .

MASUDA, Keisuke [B class; 600 (B), 90 (C)] (184)

— *First-principles study of magnetoresistance ratios and magnetic anisotropy in magnetic tunnel junctions*

1. Mechanism of strong enhancement of anomalous Nernst effect in Fe by Ga substitution
H. Nakayama, K. Masuda, J. Wang, A. Miura, K. Uchida, M. Murata, and Yuya Sakuraba: Phys. Rev. Materials **3** (2019) 114412.
2. Observation of anomalous Ettingshausen effect and large transverse thermoelectric conductivity in permanent magnets
A. Miura, H. Sepehri-Amin, K. Masuda, H. Tsuchiura, Y. Miura, R. Iguchi, Y. Sakuraba, J. Shiomi, K. Hono, and K. Uchida: Appl. Phys. Lett. **115** (2019) 222403.
3. Contributions of magnetic structure and nitrogen to perpendicular magnetocrystalline anisotropy in antiperovskite $\epsilon - \text{Mn}_4\text{N}$
S. Isogami, K. Masuda, and Y. Miura: Phys. Rev. Materials **4** (2020) 014406.
4. Strain-induced enhancement of the Seebeck effect in magnetic tunneling junctions via interface resonant tunneling: *Abinitio* study
K. Yamamoto, K. Masuda, K. Uchida, and Y. Miura: Phys. Rev. B **101** (2020) 094430.
5. Interface-driven giant tunnel magnetoresistance in (111)-oriented junctions
K. Masuda, H. Itoh, and Y. Miura: Phys. Rev. B **101** (2020) 144404.

MATSUDA, Yasuhiro [B,C class; 3700 (B), 640 (C)] (227)

— *Estimation of the density of states using Maximum entropy method and Sparse modeling*

— *Study on the high-field-induced phases of low dimensional frustrated quantum spin system*

MATSUKAWA, Hiroshi [C class; 1500 (B), 400 (C)] ()

— *Physics of Friction*

MATSUMOTO, Munehisa [C,D class; 17000 (B), 1350 (C)] (49, 51)

— *Ab initio optimization of the champion rare earth magnet compound (Nd R)₂(Fe Co)₁₄B (R=rare earth)*

— *Multiscale data assimilation between ab initio theory at finite temperatures and experiments for rare-earth permanent magnets*

— *Self-consistent analysis between microscopic electronic structure calculations and macroscopic data analysis for experimental measurements*

1. Calculating Curie temperatures for rare-earth permanent magnets: Ab initio inspection of localized magnetic moments in d-electron ferromagnetism
Munehisa Matsumoto and Hisazumi Akai: Phys. Rev. B **101** (2020) 144402.
2. Magnetism trends in doped Ce-Cu intermetallics in the vicinity of quantum criticality: realistic Kondo lattice models based on dynamical mean-field theory
Munehisa Matsumoto: Phys. Rev. Materials **4** (2020) 054401.
3. (Sm,Zr)Fe_{12-x}M_x (M=Zr,Ti,Co) for permanent-magnet applications: Ab initio material design integrated with experimental characterization
Munehisa Matsumoto, Takafumi Hawaii, and Kanta Ono: Phys. Rev. Applied **13** (2020) 064028.

MATSUNAKA, Daisuke [B class; 700 (B), 0 (C)] (183)

— *First-principles Study of Defects of Magnesium Alloys*

1. Molecular Dynamics Study of Influences of Non-Glide Stress on Slips in Magnesium
So Yoshikawa, Daisuke Matsunaka: Materials Transactions **61** (2019) 127-135.
2. Molecular Dynamics Simulation on Defect Nucleation from Pre-existing I1 Stacking Fault in Magnesium
S. Yoshikawa and D. Matsunaka: Computational Materials Science, **179** (2020) 109644.

MATSUSHITA, Katsuyoshi [C class; 0 (B), 800 (C)] (333)

— *Adhesion Inducing Cell Dynamics in Tissue*

— *Numerical Study of Cell Guiding Mechanism in Cellular Tissue*

1. Crowding-Boosting Polarity and Motion Order of Cells
K Matsushita, K Horibe, N Kamamoto, S Yabunaka, K Fujimoto Proceedings of the Symposium on Simulation of Traffic Flow **25**, 21
2. Curved surface geometry-induced topological change of an excitable planar wavefront
K Horibe, K Hironaka, K Matsushita, K Fujimoto Chaos: An Interdisciplinary Journal of Non-linear Science **29** (9), 093120
3. Cell Motion Alignment as a Polarity Memory Effect
Matsushita, K Horibe, N Kamamoto, K Fujimoto Journal of the Physical Society of Japan **88** (10), 103801

MATSUSHITA, Yu-ichiro [C class; 11500 (B), 1800 (C)] (56)

— *Identification of interface-state defects in power semiconductors: Approach from ab-initio calculations*

— *Relation between defect structures and electronic properties in power semiconductors: Approach from ab-initio calculations*

1. Native point defects and carbon clusters in 4H-SiC: A hybrid functional study
T. Kobayashi, K. Harada, Y. Kumagai, F. Oba, and Y. Matsushita: J. Appl. Phys. **125** (2019) 125701.
2. Energetics and electronic structure of native point defects in α -Ga₂O₃
T. Kobayashi, T. Gake, Y. Kumagai, F. Oba, and Y. Matsushita: Appl. Phys. Expr. **12** (2019) 091001.
3. Structure and energetics of carbon-related defects in SiC(0001)/SiO₂ systems revealed by first-principles calculations: Defects in SiC, SiO₂, and just at their interface
T. Kobayashi and Y. Matsushita: J. Appl. Phys. **126** (2019) 145302.
4. Carbon dangling-bond center (carbon P_b center) at 4H-SiC(0001)/SiO₂ interface
T. Umeda, T. Kobayashi, M. Sometani, H. Yano, Y. Matsushita, and S. Harada: Appl. Phys. Lett. **116** (2020) 071604.

MAYUMI, Koichi [B class; 1400 (B), 180 (C)] (303, 305)

— *Study on Dynamic Mechanical Properties of Slide-Ring Gels using Coarse-Grained MD Simulations*

— *Study on Microscopic Dynamics of Polyrotaxanes using Full-Atomistic MD Simulations*

1. Sliding Dynamics of Ring on Polymer in Rotaxane: A Coarse-Grained Molecular Dynamics Simulation Study
Y. Yasuda, M. Toda, K. Mayumi, H. Yokoyama, H. Morita, K. Ito: *Macromolecules*, 2019, 52, 3787.
2. Molecular Dynamics of Polyrotaxane in Solution Investigated by Quasi-Elastic Neutron Scattering and Molecular Dynamics Simulation: Sliding Motion of Rings on Polymer
Y. Yasuda, Y. Hidaka, K. Mayumi, H. Yokoyama, T. Yamada, K. Fujimoto, S. Okazaki, H. Yokoyama, K. Ito: *J. Am. Chem. Soc.*, 2019, 141, 9655.

MINAMITANI, Emi [C class; 6500 (B), 450 (C)] (79)

— *Ab-initio analysis of electron-phonon interaction*

1. Simulating lattice thermal conductivity in semiconducting materials using high-dimensional neural network potential
E. Minamitani, M. Ogura, S. Watanabe: *Appl. Phys. Express*, 12 (2019) 095001

MISAWA, Masaaki [B class; 400 (B), 0 (C)] ()

— *First-principles study on the structures and electronic properties of silicates under high pressure*

MISAWA, Takahiro [E class; 19500 (B), 2750 (C)] ()

— *Numerical analysis of quantum transport phenomena in topological materials*

MIURA, Yoshio [B class; 800 (B), 100 (C)] ()

— *A first-principles calculation on finite temperature effects of half-metallic ferromagnets*

MIZUGUCHI, Tomoko [C class; 1000 (B), 0 (C)] (329)

— *Molecular dynamics simulations of water confined in carbon structures with the reactive force field*

1. Hydrogen bond analysis of confined water in mesoporous silica using the reactive force field
T. Mizuguchi, K. Hagita, S. Fujiwara and T. Yamada: *Mol. Sim.* **45** (2019) 1437.
2. Icosahedral order in liquid and glassy phases of cyclohexane
T. Mizuguchi, S. Tatsumi and S. Fujiwara: *Mol. Sim.* in press.

MIZUKAMI, Wataru [C class; 2500 (B), 150 (C)] (134)

— *Exploration of surface reactions on model real catalyst II*

1. Orbital optimized unitary coupled cluster theory for quantum computer
W. Mizukami, K. Mitarai, Y.O. Nakagawa, T. Yamamoto, T. Yan, Y.y. Ohnishi: arXiv:1910:11526 (2019)

MOMIDA, Hiroyoshi [C class; 4000 (B), 650 (C)] (106)

— *Electrode properties of novel lithium-ion secondary battery materials: First-principles calculations*

1. First-Principles Study of Na-Ion Battery Performance and Reaction Mechanism of Tin Sulfide as Negative Electrode
H. Kotaka, H. Momida, A. Kitajou, S. Okada and T. Oguchi: *Chem. Rec.* **19**, 811 (2019).
2. Spectral Dependence of the Third-Order Optical Susceptibility of Au Nanostructures: Experiments and First-Principles Calculations
B. Zhang, R. Sato, H. Momida, T. Ohno, M. Chundak, M. Naito, M. Yoshitake and Y. Takeda: *Phys. Rev. B* **100**, 035446 (2019).
3. Amorphous $x\text{NaF-FeSO}_4$ Systems ($1 \leq x \leq 2$) with Excellent Cathode Properties for Sodium-Ion Batteries
A. Kitajou, H. Momida, T. Yamashita, T. Oguchi and S. Okada: *ACS Appl. Energy Mater.* **2**, 5968 (2019).
4. First-Principles Study of X-Ray Absorption Spectra in NaFeSO_4F for Exploring Na-Ion Battery Reactions

H. Momida, A. Kitajou, S. Okada and T. Oguchi: J. Phys. Soc. Jpn. **88**, 124709 (2019).

5. Significant Role of Oxygen Redox Reaction with O₂-Release in Li-Excess Cation-Disordered Rock-Salt Cathodes Li_{2+2x}Mn_{1-x}Ti_{1-x}O₄: First-Principles Calculations
M. Hamaguchi, H. Momida and T. Oguchi: Electrochim. Acta **330**, 135286 (2020).

MORIKAWA, Yoshitada [C class; 5000 (B), 750 (C)] (95)

— *First-principles Theoretical Study of Chemical Reactions in Heterogeneous Catalysts*

1. Van der Waals Density Functional Study of Formic Acid Adsorption and Decomposition on Cu(111)
S. E. M. Putra, F. Muttaqien, Y. Hamamoto, K. Inagaki, I. Hamada, and Y. Morikawa: J. Chem. Phys. **150** (2019) 154707.
2. Vibration-driven reaction of CO₂ on Cu surfaces via EleyRideal-type mechanism
J. Quan, F. Muttaqien, T. Kondo, T. Kozarashi, T. Mogi, T. Imabayashi, Y. Hamamoto, K. Inagaki, I. Hamada, Y. Morikawa, and J. Nakamura: Nature Chem. **11** (2019) 722.
3. Development of Co supported on Co- Al spinel catalysts from exsolution of amorphous Co- Al oxides for carbon dioxide reforming of methane
Y. J. Wong, M. K. Koh, N. F. Khairudin, S. Ichikawa, Y. Morikawa, and A. R. Mohamed: Chem. Cat. Chem. **11** (2019) 5593.
4. First-principles theoretical study on carrier doping effects induced by Zn vacancies in Mn-doped in ZnSnAs₂
H. Kizaki and Y. Morikawa: Jpn. J. Appl. Phys. **58** (2019) 110601.
5. Analyses of three-dimensional atomic arrangements of impurities doped in Si relating to electrical activity by spectro-photoelectron holography
K. Tsutsui and Y. Morikawa: Jpn. J. Appl. Phys. **59** (2020) 010503.
6. Insight into Trimeric Formation of Nitric Oxide on Cu(111): A Density Functional Theory Study
T. N. Pham, Y. Hamamoto, K. Inagaki, D. N. Son, I. Hamada, and Y. Morikawa: J. Phys. Chem. C **124** (2020) 2968.
7. Atomic and Molecular Adsorption on Single Platinum Atom at the Graphene Edge: A Density Functional Theory Study
S. A. Wella, Y. Hamamoto, F. Iskandar, Suprijadi, Y. Morikawa, and I. Hamada: J. Chem. Phys. **152** (2020) 104707.

MORITA, Satoshi [B class; 800 (B), 100 (C)] (25)

— *Improvement of higher-order tensor renormalization group method and its applications*

MOTOME, Yukitoshi [C class; 13500 (B), 1900 (C)] (202)

— *Theoretical study of novel quantum properties induced by strong spin-orbit coupling*

— *Theoretical study of quantum properties induced by spin-orbit coupling and electron correlation*

1. Magnetic Vortex Induced by Nonmagnetic Impurity in Ferromagnets: Magnetic Multipole and Toroidal around the Vacancy
S. Hayami, H. Kusunose, and Y. Motome, J. Phys. Soc. Jpn. **88**, 063702 (2019).
2. Antiferromagnetic Kitaev interaction in f-electron based honeycomb magnets
S.-H. Jang, R. Sano, Y. Kato, and Y. Motome, Phys. Rev. B **99**, 241106(R) (2019).
3. Nonequilibrium Majorana dynamics by quenching a magnetic field in Kitaev spin liquids
J. Nasu and Y. Motome, Phys. Rev. Research **1**, 033007 (2019).
4. Hunting Majorana Fermions in Kitaev Magnets
Y. Motome and J. Nasu, J. Phys. Soc. Jpn. **89**, 012002 (2020).
5. Chiral spin liquids with crystalline **Z**₂ gauge order in a three-dimensional Kitaev model
P. A. Mishchenko, Y. Kato, K. O'Brien, T. A. Bojesen, T. Eschmann, M. Hermanns, S. Trebst, and Y. Motome, Phys. Rev. B **101**, 045118 (2020).
6. The range of non-Kitaev terms and fractional particles in α -RuCl₃
Y. Wang, G. B. Osterhoudt, Y. Tian, P. Lampen-Kelley, A. Banerjee, T. Goldstein, J. Yan, J. Knolle, H. Ji, J. Cava, J. Nasu, Y. Motome, S. Nagler, D. Mandrus, and K. S. Burch, npj Quant. Mat. **5**, 14 (2020).
7. Majorana-magnon crossover by a magnetic field in the Kitaev model: Continuous-time quantum

Monte Carlo study

J. Yoshitake, J. Nasu, Y. Kato, and Y. Motome, Phys. Rev. B **101**, 100408(R) (2020).

8. Antiferromagnetic Kitaev interactions in polar spin-orbit Mott insulators
Y. Sugita, Y. Kato, and Y. Motome, Phys. Rev. B **101**, 100410(R) (2020).
9. Spin-current diode with a monoaxial chiral magnet
S.-H. Jang, R. Sano, Y. Kato, and Y. Motome, preprint (arXiv:1912.03422), submitted to Phys. Rev. Materials

MURAGUCHI, Masakazu [B class; 600 (B), 80 (C)] (185)

— *Study on carrier dynamics in nano scale semiconductor devices with machine learning*

MURAI, Naoki [B class; 900 (B), 100 (C)] (327)

— *Lattice dynamics investigation of a charge-density-wave phase in transition metal chalcogenides*

MURASHIMA, Takahiro [E class; 8500 (B), 2100 (C)] (250)

— *Multiscale analysis of polymeric fluids and solids*

1. Coupling Finite Element Method with Large Scale Atomic/Molecular Massively Parallel Simulator(LAMMPS) for Hierarchical Multiscale Simulations
T. Murashima, S. Urata, S. Li: Euro. Phys. J. B **92** (2019) 211.
2. ミクロスケールとマクロスケールのシミュレーション連成による高分子材料系のマルチスケールシミュレーション
村島隆浩: CICSJ Bulletin (日本化学情報化学部会誌) **37** (2019) 87.
3. Multiscale Modeling of Plasticity in Amorphous & Polymeric Materials
S. Li, S. Urata, T. Murashima: IACM Express. **46** (2020) 10.

NADA, Hiroki [C class; 0 (B), 750 (C)] (340)

— *Construction of A New Method for Analysis of Crystallization Mechanism from Amorphous Precursor Using Molecular Dynamics Simulation Method and Unsupervised Machine Learning*

1. Shock Growth of Ice Crystals Near Equilibrium Melting Pressure Under Dynamic Compression
Y.-J. Kim, Y.-H. Lee, S. Lee, H. Nada and G. W. Lee: Proc. Natl. Acad. Sci. U.S.A., **116** (2019) 8679.
2. Anisotropy in Stable Conformations of Hydroxylate Ions Between the 001 and 110 Planes of TiO₂ Rutile Crystals for Glycolate, Lactate, and 2-Hydroxybutyrate Ions Studied by Metadynamics Method
H. Nada, M. Kobayashi and M. Kakihana: ACS Omega, **4** (2019) 11014.
3. Transport Mechanisms of Water Molecules and Ions in Sub-Nano Channels of Nanostructured Water Treatment Liquid-Crystalline Membranes: A Molecular Dynamics Simulation Study
H. Nada, T. Sakamoto, M. Henmi, T. Ogawa, M. Kimura and T. Kato: Environ. Sci.: Water Res. & Technol., **6** (2020) 604.
4. Pathways for the Formation of Ice Polymorphs from Water Predicted by a Metadynamics Method
H. Nada: Sci. Rep., **10** (2020) 4708.

NAKAGAWA, Naoko [C class; 3500 (B), 600 (C)] (286)

— *Macroscopic properties characterized by an extended thermodynamic functions to nonequilibrium*

1. Global thermodynamics for heat conduction systems
N. Nakagawa and S.-i. Sasa: J. Stat. Phys. **177** (2019) 825.
2. Multiplicative Langevin Equation to Reproduce Long-time Properties of Nonequilibrium Brownian Motion
Atsumasa Seya, Tatsuya Aoyagi, Masato Itami, Yohei Nakayama and Naoko Nakagawa: J. Stat. Mech. **2020** (2020) 013201

NAKAHARA, Akio [B class; 700 (B), 90 (C)] (337)

— *Transition in the memory effect of paste*

NAKAMURA, Kazuma [C,D class; 8500 (B), 0 (C)] (66, 68)— *Ab initio calculation for thermodynamic phase diagram*— *Ab initio calculations for Sr₂IrO₄ and Ca₅Ir₃O₁₂*— *Ab initio phonon calculation for Ca₅Ir₃O₁₂*

1. GW calculation of plasmon excitations in the quasi-one-dimensional organic compound (TMTSF)₂PF₆
Kazuma Nakamura, Shiro Sakai, Ryotaro Arita, and Kazuhiko Kuroki: *Physical Review B* **88** (2013) 125128.
2. Effect of Electron-Phonon Interactions on Orbital Fluctuations in Iron-Based Superconductors
Yusuke Nomura, Kazuma Nakamura, and Ryotaro Arita: *Phys. Rev. Lett.* **112** (2014) 027002.
3. Ab initio GW plus cumulant calculation for isolated band systems: Application to organic conductor (TMTSF)₂PF₆ and transition-metal oxide
Kazuma Nakamura, Yoshiro Nohara, Yoshihide Yoshimoto, and Yusuke Nomura: *Phys. Rev. B* **93** (2016) 085124.
4. Large enhancement of superconducting transition temperature in single-element superconducting rhenium by shear strain
M. Mito, H. Matsui, K. Tsuruta, T. Yamaguchi, K. Nakamura, H. Deguchi, N. Shirakawa, H. Adachi, T. Yamasaki, H. Iwaoka, Y. Ikoma, and Z. Horita: *Scientific reports* **6**, (2016) 36337.
5. Uniaxial strain effects on superconducting transition in Re-doped Hg-1223 cuprate superconductors
M. Mito, K. Ogata, H. Goto, K. Tsuruta, K. Nakamura, H. Deguchi, T. Horide, K. Matsumoto, T. Tajiri, H. Hara, T. Ozaki, H. Takeya, and Y. Takano: *Phys. Rev. B* **95**, (2017) 064503.
6. Nonlinear Conductivity of Geometrically Frustrated Iridate Ca₅Ir₃O₁₂
K. Matsuhira, K. Nakamura, Y. Yasukuni, Y. Yoshimoto, D. Hirai, Z. Hiroi: *J. Phys. Soc. Jpn.* **87**, (2018) 013703.
7. Hydrostatic pressure effects on superconducting transition of nanostructured niobium highly strained by high-pressure torsion
M. Mito, Y. Kitamura, T. Tajiri, K. Nakamura, R. Shiraishi, K. Ogata, H. Deguchi, T. Yamaguchi, N. Takeshita, T. Nishizaki, K. Edalati, Z. Horita: *J. Appl. Phys.* **125**, (2019) 125901.
8. Hydrostatic Compression Effects on Fifth-Group Element Superconductors V, Nb, and Ta Subjected to High-Pressure Torsion
M. Mito, S. Shigeoka, H. Kondo, N. Noumi, Y. Kitamura, K. Irie, K. Nakamura, S. Takagi, H. Deguchi, T. Tajiri, M. Ishizuka, T. Nishizaki, K. Edalati, Z. Horita: *Mater. Trans. (Overview)*, **60**, (2019) 1472-1483.
9. Anisotropic compression effects on nanocrystalline crystals of nickel oxide
M. Mito, T. Tajiri, S. Saisho, H. Deguch, A. Kohno, K. Nakamura: *Journal of Magnetism and Magnetic Materials* **489**, (2019) 165407.
10. Harmonic voltage response to AC current in the nonlinear conductivity of iridium oxide Ca₅Ir₃O₁₂
H. Hanate, K. Nakamura, K. Matsuhira: *J. Magn. Magn. Mater.* **498**, (2020) 166203.
11. Formation of a two-dimensional single-component correlated electron system and band engineering in the nickelate superconductor NdNiO₂
Y. Nomura, M. Hirayama, T. Tadano, Y. Yoshimoto, K. Nakamura, R. Arita: *Phys. Rev. B* **100**, (2019) 205138(1-11). [Editors' Suggestion]
12. Raman Scattering Investigation of Structural Transition in Ca₅Ir₃O₁₂
T. Hasegawa, W. Yoshida, K. Nakamura, N. Ogita, K. Matsuhira: *J. Phys. Soc. Jpn* **89** (2020) 054602/1-11.
13. Study of Phonon Dispersion of Iridium Oxide Ca₅Ir₃O₁₂ with Strong Spin-Orbit Interaction
H. Hanate, T. Hasegawa, S. Tsutsui, K. Nakamura, Y. Yoshimoto, N. Kishigami, S. Haneta, K. Matsuhira: *J. Phys. Soc. Jpn* **89** (2020) 053601/1-5.

NAKANO, Hiroki [C class; 4000 (B), 1050 (C)] (268)— *Numerical study on low-energy states of quantum spin systems*

1. Haldane Gaps of Large-S Heisenberg Antiferromagnetic Chains and Asymptotic Behavior
H. Nakano, N. Todoroki, and T. Sakai: *J. Phys. Soc. Jpn.* **88** (2019) 114702.
2. From kagome strip to kagome lattice: Realizations of frustrated $S = 1/2$ antiferromagnets in Ti(III) fluorides

H. O. Jeschke, H. Nakano, and T. Sakai: Phys. Rev. B **99** (2019) 140410(R).

- Two magnetization plateaus in the kagome fluoride $\text{Cs}_2\text{LiTi}_3\text{F}_{12}$
R. Shirakami, H. Ueda, H. O. Jeschke, H. Nakano, S. Kobayashi, A. Matsuo, T. Sakai, N. Katayama, H. Sawa, K. Kindo, C. Michioka, and K. Yoshimura: Phys. Rev. B **100** (2019) 174401.

NAKAYAMA, Takashi [C class; 5000 (B), 800 (C)] (92)

— *First-principles study on physics of gap-state control at metal/semiconductor interfaces*

- Effect of electric field on formation energies of point defects around metal/SiC and metal/GaN interfaces: First-principles study
R. Nagasawa, T. Nakayama: Jpn. J. Appl. Phys. **58** (2019) 091006.
- Origin of Fermi-level depinning at TiN/Ge(001) interfaces: first-principles study
T. Nishimoto, T. Nakayama: Jpn. J. Appl. Phys. **58** (2019) 061007.
- Origin of Fermi-level depinning at metal/Ge interfaces: first-principles study on effect of segregation
T. Nishimoto, T. Nakayama: Jpn. J. Appl. Phys. **58** (2019) SIIB11.
- Resonance-enhanced tunneling current through Si-p/n junction with additional dopants; theoretical study
S. Cho, S. Iizuka, T. Nakayama: Jpn. J. Appl. Phys. **58** (2019) 061004.
- Theoretical studies on the switching mechanism of VMCO memories
T. Nakanishi, K. Chokawa, M. Araidai, T. Nakayama, K. Shiraishi: Microelectronic Engineering **215** (2019) 110997.

NASU, Joji [C class; 3500 (B), 1500 (C)] (226)

— *Magnetic state of Kitaev spin liquid under time-dependent field*

— *Time evolution by magnetic-field quench in Kitaev spin liquid*

- Low temperature properties in the Bilayer Kitaev model
H. Tomishige, J. Nasu, A. Koga: Phys. Rev. B **99**, 174424 (2019).
- Ferromagnetic instability for the single-band Hubbard model in the strong-coupling regime
Y. Kamogawa, J. Nasu, and A. Koga: Phys. Rev. B **99**, 235107 (2019).
- Residual Entropy and Spin Fractionalizations in the Mixed-Spin Kitaev Model
A. Koga and J. Nasu: Phys. Rev. B **100**, 100404(R) (2019).
- Nonequilibrium Majorana Dynamics by Quenching a Magnetic Field in Kitaev Spin Liquids
J. Nasu, and Y. Motome: Phys. Rev. Research **1**, 033007 (2019).
- Hunting Majorana Fermions in Kitaev Magnets
Y. Motome and J. Nasu: J. Phys. Soc. Jpn. **89**, 012002 (2020).
- Two-step gap opening across the quantum critical point in the Kitaev honeycomb magnet $\alpha\text{-RuCl}_3$
Y. Nagai, T. Jinno, Y. Yoshitake, J. Nasu, Y. Motome, M. Itoh, and Y. Shimizu: Phys. Rev. B **101**, 020414(R) (2020).
- Spin Transport in the Quantum Spin Liquid State in the $S = 1$ Kitaev Model: Role of the Fractionalized Quasiparticles
A. Koga, T. Minakawa, Y. Murakami, and J. Nasu: J. Phys. Soc. Jpn. **89**, 033701 (2020).
- The range of non-Kitaev terms and fractional particles in $\alpha\text{-RuCl}_3$
Y. Wang, G. B. Osterhoudt, Y. Tian, P. Lampen-Kelley, A. Banerjee, T. Goldstein, J. Yan, J. Knolle, H. Ji, R. J. Cava, J. Nasu, Y. Motome, S. Nagler, D. Mandrus, and K. S. Burch: npj Quantum Materials **5**, 14 (2020).
- Majorana-Magnon Crossover by a Magnetic Field in the Kitaev Model: Continuous-Time Quantum Monte Carlo Study
J. Yoshitake, J. Nasu, Y. Kato, and Y. Motome: Phys. Rev. B **101**, 100408(R) (2020).

NISHIDATE, Kazume [C class; 3000 (B), 0 (C)] (131)

— *Computational physics and chemistry approach to develop the artificial photosynthesis and fuel cell catalysts*

- Electronic Properties and Crystal Structures of Double-Perovskites, $\text{Ba}_2\text{Bi}^{\text{III}}\text{Bi}^{\text{V}}\text{O}_6$, $\text{Ba}_2\text{PrBiO}_6$, and $\text{Ba}_2\text{PrSbO}_6$: First-principles study

K. Nishidate et al.: submitted.

NISHIGUCHI, Kazutaka [B class; 700 (B), 0 (C)] (342)

— *Theoretical study for superconductivity in superstructured strongly correlated materials with two-particle self-consistent approach*

1. Possible Superconductivity Induced by a Large Spin-Orbit Coupling in Carrier Doped Iridium Oxide Insulators: A Weak Coupling Approach
Kazutaka Nishiguchi, Tomonori Shirakawa, Hiroshi Watanabe, Ryotaro Arita, and Seiji Yunoki: J. Phys. Soc. Jpn. **88** (2019) 094701

NISHINO, Masamichi [B class; 700 (B), 90 (C)] (336)

— *Elucidation of coercivity mechanism by statistical physical approaches*

1. Nontrivial temperature dependence of ferromagnetic resonance frequency for spin reorientation transitions
M. Nishino, and S. Miyashita: Phys. Rev. B **100** (2019) 020403(R).
2. Multistep spin-crossover transitions induced by the interplay between short- and long-range interactions with frustration on a triangular lattice
M. Nishino, C. Enachescu, and S. Miyashita: Phys. Rev. B **100** (2019) 134414
3. Anisotropy-temperature phase diagram for the two-dimensional dipolar Heisenberg model with and without magnetic field
H. Komatsu, Y. Nonomura, and M. Nishino: Phys. Rev. B **100**, (2019) 094407

NOGUCHI, Hiroshi [C class; 11000 (B), 1800 (C)] (243)

— *structure formation of biomembrane*

1. Shape transition from elliptical to cylindrical membrane tubes induced by chiral crescent-shaped protein rods
H. Noguchi: Sci. Rep. **9**, 11721 (2019).
2. Cup-to-vesicle transition of a fluid membrane with spontaneous curvature
H. Noguchi: J. Chem. Phys. **51**, 094903 (2019).
3. Detachment of fluid membrane from substrate and vesiculation
H. Noguchi: Soft Matter **15**, 8741 (2019).
4. Curvature induction and sensing of the F-BAR protein Pacsin1 on lipid membranes via molecular dynamics simulations
M. I. Mahmood, H. Noguchi, and K. Okazaki: Sci. Rep. **9**, 14557 (2019).
5. Effects of Cavitation on Karman Vortex Behind Circular-Cylinder Arrays: A Molecular Dynamics Study
Y. Asano, H. Watanabe, and H. Noguchi: J. Chem. Phys. **152**, 034501 (2020).
6. 分子動力学計算による複雑流体中のカルマン渦の解析
浅野 優太, 渡辺 宙志, 野口 博司: 分子シミュレーション研究会会誌 “アンサンブル” **22**, 157 (2020).

NOGUCHI, Yoshifumi [C class; 3500 (B), 600 (C)] (112)

— *GW method without GPP model*

1. Photoabsorption Spectra of Aqueous Oxyluciferin Anions Elucidated by Explicit Quantum Solvent
Y. Noguchi, M. Hiyama, M. Shiga, H. Akiyama, and O. Sugino: J. Chem. Theory Compt., **15** (2019) 5474.

NOMURA, Yusuke [C class; 9500 (B), 1600 (C)] (207, 209)

— *Study on frustrated magnetism using machine learning*

— *Study on metal-insulator transition in nickel oxides*

1. Strong-coupling formula for momentum-dependent susceptibilities in dynamical mean-field theory
Junya Otsuki, Kazuyoshi Yoshimi, Hiroshi Shinaoka, and Yusuke Nomura: Phys. Rev. B **99** (2019) 165134.
2. Ab initio derivation of an effective Hamiltonian for the La₂CuO₄/La_{1.55}Sr_{0.45}CuO₄ heterostructure
Terumasa Tadano, Yusuke Nomura, and Masatoshi Imada: Phys. Rev. B **99** (2019) 155148.

3. Formation of a two-dimensional single-component correlated electron system and band engineering in the nickelate superconductor NdNiO₂
Yusuke Nomura, Motoaki Hirayama, Terumasa Tadano, Yoshihide Yoshimoto, Kazuma Nakamura, and Ryotaro Arita: *Phys. Rev. B* **100** (2019) 205138.
4. Wannier90 as a community code: new features and applications
Giovanni Pizzi *et. al.*: *J. Phys.: Condens. Matter* **32** (2020) 165902.
5. Materials design of dynamically stable d9 layered nickelates
Motoaki Hirayama, Terumasa Tadano, Yusuke Nomura, and Ryotaro Arita: *Phys. Rev. B* **101** (2020) 075107.

NONOMURA, Yoshihiko [B,C class; 2700 (B), 490 (C)] (288, 289)

— *Generalization of temperature scaling in early-time nonequilibrium relaxation*

— *Unified understanding of early-time nonequilibrium relaxation in Monte Carlo simulations*

NOZAWA, Kazuki [C class; 1000 (B), 100 (C)] (162)

— *Atomic and electronic structures of intermetallic compound catalysts*

OBATA, Masao [B,C class; 1800 (B), 100 (C)] (145)

— *Analysis on atomic and magnetic structure in magnetic molecular complex crystal and interface and investigation of external electric and magnetic field effect*

1. Noncollinear magnetic structure with spin-dependent van der Waals density functional approach: β -phase solid oxygen
M. Christivana, M. Obata, and T. Oda: *J. Phys. Soc. Jpn.* **88** (2019) 104601
2. Density Functional Approach under External Magnetic Field
A. R. Rio, I. Pardede, A. M. Gani, M. Christivana, M. Obata, T. Oda: *J. Phys. Soc. Jpn.* **89**, (2020) 035002

ODA, Tatsuki [E class; 25500 (B), 2650 (C)] (47)

— *Analyses on electronic structure and magnetic property in high-performance spintronics and magnetic materials*

1. Noncollinear magnetic structure with spin-dependent van der Waals density functional approach: β -phase solid oxygen
Mega Christivana, Masao Obata, and Tatsuki Oda: *Journal of the Physical Society of Japan*, **88** (2019) 104601.
2. Large nonvolatile control of interfacial magnetic anisotropy in CoPt by a ferroelectric ZnO-based tunneling barrier
Muftah Al-Mahdawi, Mohamed Belmoubarik, Masao Obata, Daiki Yoshikawa, Hideyuki Sato, Tomohiro Nozaki, Tatsuki Oda, Masashi Sahashi: *Phys. Rev. B*, **100** (2019) 054423.
3. Anatomy of large perpendicular magnetic anisotropy in free-standing Co/Ni (111) multilayer, *Journal of Magnetism and Magnetic Materials*
Indra Pardede, Daiki Yoshikawa, Tomosato Kanagawa, Nurul Ikhsan, Itsuki Murata, Masao Obata, Tatsuki Oda: *Journal of Magnetism and Magnetic Materials* **500**(2020)166357.
4. Density functional approach under external magnetic field
Afrioni Roma Rio, Indra Pardede, Achmad Maulana Gani, Mega Christivana, Masao Obata, and Tatsuki Oda: *Journal of the Physical Society of Japan*, **89**,(2020) 035002.
5. Finite electric-field approach to evaluate the vertex correction for the screened Coulomb interaction in the quasiparticle self-consistent GW method
Hirofumi Sakakibara, Takao Kotani, Masao Obata, and Tatsuki Oda: submitted to *Physical Review B*.

OHGOE, Takahiro [C class; 4500 (B), 700 (C)] (225)

— *Development and applications of continuous-time quantum Monte Carlo method in the thermodynamic limit*

OHMURA, Satoshi [B,C class; 3200 (B), 0 (C)] (122, 123)— *Ab initio molecular dynamics study of stability of artificial retina molecule*— *Ab initio molecular dynamics study of structural properties and immiscibility in liquid Fe-Si-O mixtures under high pressure*

1. Selective Reduction Mechanism of Graphene Oxide Driven by the Photon Mode versus the Thermal Mode
M. Hada, K. Miyata, S. Ohmura, Y. Arashida, K. Ichianagi, I. Katayama, T. Suzuki, W. Chen, S. Mizote, T. Sawa, T. Yokoya, T. Seki, J. Matsuo, T. Tokunaga, C. Itoh, K. Tsuruta, R. Fukaya, S. Nozawa, S. Adachi, J. Takeda, K. Onda, S. Koshihara, Y. Hayashi, Y. Nishina: ACS NANO, **13** (2019) 10103.
2. 共有結合にとらわれた原子が液体中でどのように動くのか——共有結合性液体の高圧物性
大村訓史, 下條冬樹, 土屋卓久: 日本物理学会誌, **74** (2019) 621.
3. Structures of liquid iron-light-element mixtures under high pressure
S. Ohmura, T. Tsuchiya, and F. Shimojo: Physica Status Solidi B. in press

OHNISHI, Masato [C class; 4500 (B), 700 (C)] (98)— *Analysis of Thermoelectric Properties of Clathrate Compounds with Ab Initio Calculations*

1. Enhancing thermal boundary conductance of graphite- metal interface by triazine-based molecular bonding
Aun Ota, Masato Ohnishi, Hisayoshi Oshima, Hisayoshi, Takuma Shiga, Takashi Kodama, Junichiro Shiomi :ACS Applied Materials & Interfaces, **11**, 37295-37301 (2019).
2. Spectral control of thermal boundary conductance between copper and carbon crystals by self-assembled monolayers
Shih-Wei Hung, Shiqian Hu, Junichiro Shiomi: ACS Applied Electronic Materials, **1**, 2594-2601 (2019).
3. Disorder Limits the Coherent Phonon Transport in Two- Dimensional Phononic Crystal Structure
Shiqian Hu, Zhongwei Zhang, Pengfei Jiang, Weijun Ren, Cuiqian Yu, Junichiro Shiomi, Jie Chen: Nanoscale, **11**, 11839-11846 (2019).

OHSAWA, Kazuhito [C class; 1000 (B), 0 (C)] (165)— *Study of interaction between radiation damage and interstitial atom***OHTO, Tatsuhiko** [C class; 9500 (B), 0 (C)] (60, 61)— *First-principles molecular dynamics simulation of electron-doped graphene/water interfaces*— *First-principles molecular dynamics simulation of the water/air interface using hybrid functionals*

1. Hydrogen-Bonds and Molecular Orientations of Supramolecular Structure between Barbituric Acid and Melamine Derivative at the Air/Water Interface Revealed by Heterodyne-Detected Vibrational Sum Frequency Generation Spectroscopy
Masanari Okuno, Shuhei Yamada, Tatsuhiko Ohto, Hirokazu Tada, Waka Nakanishi, Katsuhiko Ariga, and Taka-aki Ishibashi: J. Phys. Chem. Lett. **11**, 2422 (2020).
2. Mechanical switching of current-voltage characteristics in spiropyran single-molecule junctions
Takashi Tamaki, Keigo Minode, Yuichi Numai, Tatsuhiko Ohto, Ryo Yamada, Hiroshi Masai, Hirokazu Tada, and Jun Terao: Nanoscale, in press.
3. Molecular Structure and Modeling of Water-Air and Ice-Air Interfaces Monitored by Sum-Frequency Generation
Fujie Tang, Tatsuhiko Ohto, Shumei Sun, Jeremy Rouxel, Sho Imoto, Ellen H. G. Backus, Shaul Mukamel, Mischa Bonn, and Yuki Nagata: Chem. Rev. in press.
4. Effect of Graphene Encapsulation of NiMo Alloys on Oxygen Evolution Reaction
Samuel Jeong, Kailong Hu, Tatsuhiko Ohto, Yuki Nagata, Hideki Masuda, Jun-ichi Fujita, and Yoshikazu Ito: ACS Catal. **10**, 792 (2020).
5. Three Sites Molecular Orbital Controlled Single-Molecule Rectifier based on Perpendicularly Linked Porphyrin-Imide Dyads
Murni Handayani, Hirofumi Tanaka, Shinichi Katayose, Tatsuhiko Ohto, Zhijin Chen, Ryo Yamada, Hirokazu Tada, and Takuji Ogawa: Nanoscale, **11**, 22724 (2019).
6. Effects of cis-trans Conformation Between Thiophene Rings on Conductance of Oligothiophenes

- Tatsuhiko Ohto, Takuya Inoue, Helen Stewart, Yuichi Numai, Yoshio Aso, Yutaka Ie, Ryo Yamada, and Hirokazu Tada: *J. Phys. Chem. Lett.* **10**, 5292 (2019).
7. Accessing the Accuracy of Density Functional Theory through Structure and Dynamics of the Water-Air Interface
Tatsuhiko Ohto, Mayank Dodia, Jianhang Xu, Sho Imoto, Fujie Tang, Frederik Zysk, Thomas D. Kuhne, Yasuteru Shigeta, Mischa Bonn, Xifan Wu, and Yuki Nagata: *J. Phys. Chem. Lett.* **10**, 4914 (2019).
 8. Impact of intermolecular vibrational coupling effects on the sum-frequency generation spectra of the water/air interface
Naveen Kumar Kaliannan, Andres Henao Aristizabal, Hendrik Wiebeler, Frederik Zysk, Tatsuhiko Ohto, Yuki Nagata, and Thomas D. Kuhne: *Mol. Phys.* in press.
 9. Highly Planar and Completely Insulated Oligothiophenes: Effects of π -Conjugation on Hopping Charge Transport
Yutaka Ie, Yuji Okamoto, Takuya Inoue, Saori Tone, Takuji Seo, Yasushi Honda, Shoji Tanaka, See Kei Lee, Tatsuhiko Ohto, Ryo Yamada, Hirokazu Tada, and Yoshio Aso: *J. Phys. Chem. Lett.* **10**, 3197 (2019).
 10. Structure and Dynamics of Water at the Water?Air Interface Using First Principles Molecular Dynamics Simulations II: Non-Local vs Empirical van der Waals Corrections
Mayank Dodia, Tatsuhiko Ohto, Sho Imoto, and Yuki Nagata: *J. Chem. Theory Comput.* **15**, 3836 (2019).
 11. Chemical dopants on edge of holey graphene accelerate electrochemical hydrogen evolution reaction
Akichika Kumatani, Chiho Miura, Hirotaka Kuramochi, Tatsuhiko Ohto, Mitsuru Wakisaka, Yuki Nagata, Hiroki Ida, Yasufumi Takahashi, Kailong Hu, Samuel Jeong, Jun-ichi Fujita, Tomokazu Matsue, Yoshikazu Ito: *Adv. Sci.* **6**, 1900119 (2019).

OHTSUKI, Tomi [C class; 4500 (B), 750 (C)] (267)— *Wave function analyses in disordered electron systems*

1. Ballistic transport in disordered Dirac and Weyl semimetals
K. Kobayashi, M. Wada, T. Ohtsuki: arXiv:2003.01929
2. Drawing Phase Diagrams of Random Quantum Systems by Deep Learning the Wave Functions
T. Ohtsuki, T. Mano: *Journal of the Physical Society of Japan* **89**, 022001 (2020)
3. Critical behavior of Anderson transitions in three-dimensional orthogonal classes with particle-hole symmetries
X. Luo, B. Xu, T. Ohtsuki, R. Shindou: *Physical Review B* **101**, 020202(R), (2020)
4. Application of Convolutional Neural Network to Quantum Percolation in Topological Insulators
T. Mano, T. Ohtsuki: *Journal of the Physical Society of Japan* **88**, 123704 (2019)
5. Multifractality and the distribution of the Kondo temperature at the Anderson transition
K. Slevin, S. Kettemann, T. Ohtsuki: *The European Physical Journal B* **92**, 281, (2019)

OKAMOTO, Yuko [C,E class; 2000 (B), 0 (C)] (353)— *Study on complex systems by generalized-ensemble algorithms*— *Study on phase transitions of Lennard-Jones fluid systems by generalized-ensemble algorithms*

1. Efficient simulation protocol for determining the density of states: Combination of replica-exchange Wang-Landau method and multicanonical replica-exchange method
T. Hayashi and Y. Okamoto: *Phys. Rev. E* **100** (2019) 043304.
2. Analysis of liquids, gases, and supercritical fluids by a two-dimensional replica-exchange Monte Carlo method in temperature and chemical potential space
D. Matsubara and Y. Okamoto: *J. Chem. Phys.* **152** (2020) 194108.

OKITSU, Kouhei [C class; 1500 (B), 0 (C)] (307)— *Study on an X-ray n-beam method to solve protein crystal structure*— *Study on crystal structure analysis using the X-ray multiple-beam diffraction theory*

1. Experimentally obtained and computer-simulated X-ray asymmetric eight-beam pinhole topographs for a silicon crystal

- K. Okitsu, Y. Imai, Y. Yoda and Y. Ueji: Acta Cryst. **A75** (2019) 474-482. <https://doi.org/10.1107/S205327331900>
- Experimentally obtained and computer-simulated X-ray non-coplanar 18-beam pinhole topographs for a silicon crystal
K. Okitsu, Y. Imai and Y. Yoda: Acta Cryst. **A75** (2019) 483-488. <https://doi.org/10.1107/S2053273319002936>.
 - X線多波 (n波) 動力学理論とその数値解法および放射光実験による検証 (X-ray n-beam dynamical diffraction theories, numerical method to solve them and experimental verification)
沖津康平: 日本結晶学会誌 **33** (2020) K. Okitsu: J. Jpn. Soc. Synchrotron Rad. Res. **33** (2020) 61-80 [Invited].

OKUBO, Tsuyoshi [C class; 5500 (B), 800 (C)] (259)— *Novel phases and dynamics in frustrated spin systems*

- Anisotropic Tensor Renormalization Group
D. Adachi, T. Okubo and S. Todo: arXiv:1906.02007.
- Gapless Kitaev Spin Liquid to Classical String Gas through Tensor Networks
H.-Y. Lee, R. Kaneko, T. Okubo and N. Kawashima: Phys. Rev. Lett. **123** (2019) 087203.
- Multiple- q states of the J_1 - J_2 classical honeycomb-lattice Heisenberg antiferromagnet under magnetic fields
T. Shimokawa, T. Okubo and H. Kawamura: Phys. Rev. B **100** (2019) 224404.
- Abelian and Non-Abelian Chiral Spin Liquids in a Compact Tensor Network Representation
H.-Y. Lee, R. Kaneko, T. Okubo and N. Kawashima: Phys. Rev. B **101** (2020) 035140.
- Magnetic-field Induced Quantum Phases in Tensor Network Study of Kitaev Magnets
H.-Y. Lee, R. Kaneko, L.-E. Chern, T. Okubo, Y. Yamaji, N. Kawashima, and Y.-B. Kim: Nat. Commun. **11** (2020) 1639.

OKUMURA, Hisashi [C class; 11000 (B), 0 (C)] (248)— *Aggregation process of full-length amyloid-beta peptides studied by molecular dynamics simulations*

- Conformational change of amyloid- β 40 in associated with binding to GM1-glycan cluster
Y. Tachi, Y. Okamoto, and H. Okumura: Sci. Rep. **9** (2019) 6853 (11 pages).
- Dynamic views of the Fc region of immunoglobulin G provided by experimental and computational observations
S. Yanaka, R. Yogo, R. Inoue, M. Sugiyama, S. G. Itoh, H. Okumura, Y. Miyanoiri, H. Yagi, T. Satoh, T. Yamaguchi, and K. Kato: Antibodies **8** (2019) 39 (13pages).
- Replica sub-permutation method for molecular dynamics and Monte Carlo simulations
M. Yamauchi and H. Okumura: J. Comput. Chem. **40** (2019) 2694-2711.
- Structural characterization of HypX responsible for CO biosynthesis in the maturation of NiFe-hydrogenase
N. Muraki, K. Ishii, S. Uchiyama, S. G. Itoh, H. Okumura, S. Aono: Commun. Biol. **2** (2019) 385 (12 pages).
- Molecular dynamics simulations of amyloid- β (16-22) peptide aggregation at air-water interfaces
H. Okumura and S. G. Itoh: J. Chem. Phys. **151** (2020) 095101 (12 pages).

ONISHI, Hiroaki [C class; 2000 (B), 0 (C)] (299)— *Spin multipole dynamics and spin transport in frustrated magnets*

- Magnetic excitations and transport properties in frustrated ferromagnetic chain
H. Onishi, J. Magn. Magn. Mater. **479**, 88 (2019).

ONO, Shota [B class; 1200 (B), 170 (C)] (313, 314)— *Femtosecond luminescence dynamics of metals*— *Ultrafast relaxation of inhomogeneous electron distribution around the Dirac cone in graphene*

- Ultrafast photoluminescence in metals: Theory and its application to silver
S. Ono and T. Suemoto: submitted to Phys. Rev. B

ONO, Tomoya [C class; 8500 (B), 750 (C)] (62)— *Development of first-principles electronic-structure and transport calculation code RSPACE and simulations for device*

1. Highly Reproducible Formation of a Polymer Single-Molecule Junction for a Well-Defined Current Signal
T. Harashima, Y. Hasegawa, S. Kaneko, M. Kiguchi, T. Ono, and T. Nishino: *Angewandte Chem. Int. Ed.* **58** (2019) 9109.
2. Efficient calculation of self-energy matrices for electron-transport simulations
Y. Egami, S. Tsukamoto, and T. Ono: *Phys. Rev. B*, **100** (2019) 075413.
3. Graphene-based Symmetric and Non-Symmetric Magnetoresistive Junctions
A. Hashmi, K. Nakanishi, and T. Ono: *J. Phys. Soc. Jpn.* **89** (2019) 034708.
4. DFT calculation for oxidation reaction of SiC(0001)
T. Ono: *Materials Science Forum, Materials Science Forum* **963** (2019) 208.a

ONO, Yoshiaki [C class; 5000 (B), 750 (C)] (219)

— *First-principles and quantum many-body calculations for electronic states and superconductivity in the multi-band systems*

1. First-Principles Study and Orbital-Fluctuation Effect on the Superconductivity in Tungsten Bronze A_xWO_3
Takuya Sekikawa, Rai Watabe, Jun Ishizuka, Yoshihiro Nitta, Kazuhiro Sano and Yoshiaki Ōno: *JPS Conf. Proc.* **30**, 011043 (2020)
2. RKKY Interaction and Quadrupole Order in PrT_2Al_{20} ($T=Ti, V$) Based on Effective 196 Orbital Model Extracted from First-Principles Calculation
Yuto Iizuka, Takemi Yamada, Katsuro Hanzawa and Yoshiaki Ōno: *JPS Conf. Proc.* **30**, 011152 (2020)
3. Dynamical Mean-Field Study of Excitonic Phase in the Spinless Two-Band Hubbard Model for Electron-Hole System
Kento Sasaki, Takemi Yamada, Kaoru Domon and Yoshiaki Ōno: *JPS Conf. Proc.* **30**, 011070 (2020)
4. FFLO Superconductivity Mediated by Excitonic Fluctuation in Semimetallic Ta_2NiSe_5
Takemi Yamada, Kaoru Domon and Yoshiaki Ōno: *Journal of the Physical Society of Japan* **88**, 064701 (2019)

OSHIKAWA, Masaki [B class; 700 (B), 0 (C)] (180)

— *A data-driven investigation of topological materials based on symmetry*

OSHIYAMA, Atsushi [E class; 43500 (B), 5550 (C)] (44)

— *Mechanisms of Semiconductor Interface Formation and its Electronic Properties based on Quantum Theory*

1. Microscopic Identification of Surface Steps on SiC by Density-Functional Calculations
K. Seino and A. Oshiyama: *Proc. ICSRM2019*
2. Energetics of the surface step and its morphology on the 3C-SiC(111) surface clarified by the density-functional theory
K. Seino and A. Oshiyama: *Appl. Phys. Exp.* **13** (2020) 015506.
3. Density-Functional Calculations for Structures and Energetics of Atomic Steps and their Implication for Surface Morphology on Si-face SiC Polar Surfaces
K. Seino and A. Oshiyama: *Phys. Rev. B* (2020) to be published
4. A two-dimensional liquid-like phase on Ga-rich GaN (0001) surfaces evidenced by first principles molecular dynamics
K. M. Bui, M. Boero, K. Shiraishi and A. Oshiyama: *Jpn. J. Appl. Phys.* **59** (2020) SGGK04.
5. Computational study of oxygen stability in vicinal m(10-10)-GaN growth by MOVPE
F. Shintaku, D. Yoshio, Y. Kangawa, J.-I. Iwata, A. Oshiyama, K. Shiraishi, A. Tanaka and H. Amano: *Appl. Phys. Exp.* **13** (2020) 055507.
6. Oxygen incorporation kinetics in vicinal m(10-10)-GaN growth by MOVPE
D. Yoshio, F. Shintaku, Y. Inatomi, Y. Kangawa, J.-I. Iwata, A. Oshiyama, K. Shiraishi, A. Tanaka and H. Amano: *Phys. Sta. Solidi - Rapid Res. Lett.* (2020) 2000142.

OTOMO, Junichiro [C class; 1500 (B), 950 (C)] (138)

— *Analysis of ion conduction in materials of proton-conducting solid electrolyte and application to catalytic surface reaction with proton conductors*

OZEKI, Yukiyasu [C class; 8000 (B), 0 (C)] (254)

— *Dynamical scaling analysis applied to studies on critical universality for topological phase transitions*

— *Dynamical scaling analysis applied to studies on critical universality for topological phase transitions II*

1. Dynamical scaling analysis on critical universality class for fully frustrated XY models in two dimensions

Y. Ozeki, Y. Yajima and Y. Nakamura: Phys. Rev B **101** (2020) 094437

RAEBIGER, Hannes [C class; 6000 (B), 0 (C)] (87)

— *First principles calculation of quantum phase transitions*

1. Supercomputer System at ISSP
S. Tsuneyuki: J. Phys. Soc. Jpn. **32** (1996) 41.
2. First principles methods for defects: state of the art and emerging methods
E. Ertekin and H. Raebiger: Characterisation and Control of Defects in Semiconductors, ed. F. Tuomisto (IET, United Kingdom 2019) pp. 289–343; ISBN-10: 1-78561-655-2, ISBN-13: 978-1-78561-655-6
3. Electronic mechanism for resistive Switching in metal/insulator/metal nanodevices
H. Raebiger, A. C. M. Padilha, A. R. Rocha, and G. M. Dalpian: Journal of Physics D: Applied Physics, accepted (2020); DOI: 10.1088/1361-6463/ab7a58
4. Modulation of the optical absorption edge of ϵ - and κ -Ga₂O₃ due to Co impurities caused by band structure changes: Work function measurements and first-principle calculations
K. Yamanaka, H. Raebiger, K. Mukai, and K. Shudo: Journal of Applied Physics **127** (2020) 065701.
5. Carrier mediated ferromagnetism in Ga₂O₃:Cr
K. Ichihashi, H. Shinya, and H. Raebiger: Applied Physics Express **13** (2020) 021002.

SAITO, Mineo [C class; 7500 (B), 0 (C)] (75)

— *First-principles study for widening the potential of spin-polarized positron experiments*

1. First-principles calculation of anomalous muonium in silicon: origin of the negative Fermi contact interaction constant
Muhamad Nasruddin Manaf, Susumu Minami, Fumiyuki Ishii and Mineo Saito: J. J. Appl. Phys. **58** (2019) 081008.

SAKAGUCHI, Norihito [C class; 7000 (B), 0 (C)] (78)

— *Reduction of Rare Metals in Fuel Cell Catalysts and Hydrogen Permeable Membrane*

1. グラフェン上での金属原子吸着状態の理論的研究
長谷川瞬, 國貞雄治, 坂口紀史: 表面と真空 **62** (2019) 344.
2. Extraordinarily Large Kinetic Isotope Effect on Alkene Hydrogenation over Rh-based Intermetallic Compounds
S. Furukawa, P. Yi, Y. Kunisada, K. Shimizu: Science and Technology of Advanced Materials **20** (2019) 805.
3. Co-appearance of superconductivity and ferromagnetism in a Ca₂RuO₄ nanofilm crystal
SH. Nobukane, K. Yanagihara, Y. Kunisada, Y. Ogasawara, K. Nomura, Y. Asano, S. Tanda: Scientific Reports **10** (2020) 3462.

SAKAI, Toru [C class; 9500 (B), 1600 (C)] (245, 247)

— *Numerical Diagonalization Study on Spin Nematic Phase of Low-Dimensional Systems*

— *Topological Magnetization Plateau of Quantum Antiferromagnetic Spin Chain with Anisotropies*

1. Analysis of Rashba Effect on Au(111) Model Surface
M. Fujiwara, N. Shima, K. Makoshi and T. Sakai: J. Phys. Soc. Jpn. **88** (2019), 034604.
2. From kagome strip to kagome lattice: Realizations of frustrated S=1/2 antiferromagnets in Ti(III)

fluorides

- H. O. Jeschke, H. Nakano and T. Sakai: Phys. Rev. B 99 (2019) 140410(R).
3. Magnetization plateau of the S=2 antiferromagnetic Heisenberg chain with anisotropies
T. Sakai, K. Okamoto and T. Tonegawa: Phys. Rev. B 100 (2019) 054407.
 4. Two magnetization plateaus in the kagome fluoride $Ce_2LiTi_3F_{12}$
R. Shirakami, H. Ueda, H. O. Jeschke, H. Nakano, S. Kobayashi, A. Matsuo, T. Sakai, N. Katayama, H. Sawa, K. Kindo, C. Michioka and K. Yoshimura: Phys. Rev. B 100 (2019) 174401.
 5. Properties of the H-T phase diagram of the 3-K phase in eutectic Sr_2RuO_4 -Ru: Evidence for chiral superconductivity
H. Kaneyasu, Y. Enokida, T. Nomura, Y. Hasegawa, T. Sakai and M. Sigrist: Phys. Rev. B 100 (2019) 21451.
 6. Spin Nematic Phase of the Quantum Spin Nanotube
T. Sakai: JPS Conference Proceedings 29 (2020) 014004.
 7. Field-Induced Spin Nematic Phase in the S=1 Anisotropic Spin Ladder
R. Yamanokuchi, K. Okamoto and T. Sakai: Proceedings of 2018 16th International Conference on Megagauss Magnetic Field Generation and Related Topics (MEGAGAUSS) (2019) 8722674.
 8. Haldane Gaps of Large-S Heisenberg Antiferromagnetic Chains and Asymptotic Behavior
H. Nakano, N. Todoroki and T. Sakai: J. Phys. Soc. Jpn. 88 (2019) 114702.
 9. Spin Nematic Liquids of the S = 1 Spin Ladder in Magnetic Field
T. Sakai and K. Okamoto: JPS Conference Proceedings 30 (2020) 011083.
 10. Ground-State Phase Diagram of an Anisotropic S = 1 Ferromagnetic-Antiferromagnetic Bond-Alternating Chain
K. Okamoto, T. Tonegawa, M. Kaburagi and T. Sakai: JPS Conference Proceedings 30 (2020) 011024.
 11. Quantum Phase Transition of the Twisted Spin Tube
Y. Tachibana, Y. Ueno, T. Zenda, K. Okamoto and T. Sakai: JPS Conference Proceedings 30 (2020) 011082.
 12. Quantum Phase Transitions of the Distorted Diamond Spin Chain
T. Zenda, Y. Tachibana, Y. Ueno, K. Okamoto and T. Sakai: JPS Conference Proceedings 30 (2020) 011084.
 13. Magnetization Plateau of the Distorted Diamond Spin Chain
Y. Ueno, T. Zenda, Y. Tachibana, K. Okamoto and T. Sakai: JPS Conference Proceedings 30 (2020) 011085.
 14. Features of Chirality Generated by Paramagnetic Coupling to Magnetic Fields in the 3K-Phase of Sr_2RuO_4
H. Kaneyasu, Y. Enokida, T. Nomura, Y. Hasegawa, T. Sakai and M. Sigrist: JPS Conference Proceedings 30 (2020) 011039.

SAKAKIBARA, Hirofumi [B class; 800 (B), 0 (C)] (171)

— *Developments of a derivation method of a low-energy models in first-principles*

1. Model-mapped random phase approximation to evaluate superconductivity in the fluctuation exchange approximation from first principles
H. Sakakibara, T. Kotani: Phys. Rev. B **99**, 195141(2019).
2. Finite electric-field approach to evaluate the vertex correction for the screened Coulomb interaction in the quasiparticle self-consistent GW method
H. Sakakibara, T. Kotani, M. Obata, T. Oda: Phys. Rev. B (2020) in press.

SAKURAGI, Shunsuke [C class; 1000 (B), 0 (C)] (163)

— *Controlling of magnetism in Pd(100) ultrathin films by modification of quantum-well states via adsorption of transition metals*

1. Switching of magnetism via modifying phase shift of quantum-well states by tailoring the interface electronic structure
S. Sakuragi, H. Kageshima, and T. Sato: Phys. Rev. B **101** (2020) 014410.

SASAKI, Kazuo [B class; 700 (B), 90 (C)] (335)

— *Simulation analysis of collision of two filaments driven by protein molecular motors*

SASAKI, Takehiko [C class; 3000 (B), 200 (C)] (120)

— *Reaction processes of polyalcohols in high temperature water by First Principles Calculations*

SATO, Tetsuya [C class; 1000 (B), 350 (C)] (157)

— *Study of appearance of ferromagnetism by electric field application to Pt thin film*

SHAO, Cheng [C class; 2000 (B), 650 (C)] (132)

— *Multiscale computational design of thermoelectric materials*

SHIGA, Takuma [B,C class; 2200 (B), 0 (C)] (293, 295, 296)

— *Clarification of thermal transport spectra in hierarchical structured organic bulk materials*

— *Comprehensive study on transition between heat conduction and radiative heat transfer*

— *Heat conduction analysis for phononic crystal*

SHIMADA, Toshihiro [B class; 800 (B), 0 (C)] (170)

— *First principle simulation on ultrahigh pressure synthesis of new material from organic molecules*

1. Sugar-assisted Mechanochemical Exfoliation of Graphitic Carbon Nitride for Enhanced Visible-light Photocatalytic Performance
Wei Liu, Takashi Yanase, Nobuhiro Iwasa, Hitoshi Koizumi, Shin Mukai, Shinichiro Iwamura, Taro Nagahama, and Toshihiro Shimada: *International J. of Hydrogen Energy* **44** (2020) 8444.
2. Porous Graphitic Carbon Nitride Nanoplates Obtained by A Combined Exfoliation Strategy for Enhanced Visible Light Photocatalytic Activity
Wei Liu, Nobuhiro Iwasa, Shinichiro Fujita, Hitoshi Koizumi, Makoto Yamaguchi and Toshihiro Shimada: *Applied Surface Science* **499** (2020) 143901.
3. Synthesis and Enhanced Room-temperature Ferromagnetic Properties of Carbon-doped Boron Nitride Nanosheets
Wei Liu, Takashi Yanase, Taro Nagahama and Toshihiro Shimada: *J. Alloys and Compounds* **792** (2019) 1206.

SHIMAMURA, Kohei [C class; 2500 (B), 650 (C)] (124)

— *Construction of neural network force field for molecular dynamics simulation in multicomponent system*

1. Guidelines for Creating Artificial Neural Network Empirical Interatomic Potential from First-Principles Molecular Dynamics Data under Specific Conditions and Its Application to α -Ag₂Se
K. Shimamura, S. Fukushima, A. Koura, F. Shimojo, M. Misawa, R. K. Kalia, A. Nakano, P. Vashishta, T. Matsubara, and S. Tanaka: *J. Chem. Phys.* **151** (2019) 124303.

SHIMOJO, Fuyuki [C class; 5000 (B), 0 (C)] (103)

— *First-Principles Molecular-Dynamics Study of Structural and Electronic Properties of Covalent Liquids and Glasses under Pressure*

1. Structural studies on fluid sulfur at high temperatures and high pressures: II. Molecular structure obtained by *ab initio* molecular dynamics simulations
S. Munejiri, F. Shimojo, K. Hoshino, and M. Inui: *J. Non-Cryst. Solids* **510**, 15 (2019).
2. Structural change in liquid sulphur from chain polymeric liquid to atomic simple liquid under high pressure
S. Ohmura and F. Shimojo,: *J. Phys.: Condens. Matter* **31**, 215101 (2019).
3. Guidelines for Creating Artificial Neural Network Empirical Interatomic Potential from First-Principles Molecular Dynamics Data under Specific Conditions and Its Application to α -Ag₂Se
K. Shimamura, S. Fukushima, A. Koura, F. Shimojo, M. Misawa, R. K. Kalia, A. Nakano, P. Vashishta, T. Matsubara, and S. Tanaka: *J. Chem. Phys.* **151**, 124303 (2019).
4. GGA+U Molecular Dynamics Study of Structural and Dynamic Properties of Superionic Conductor Ag₂Se

S. Fukushima, M. Misawa, A. Koura and F. Shimojo: J. Phys. Soc. Jpn. **88**, 115002 (2019).

5. Thermodynamic Integration by Neural Network Potentials Based on First-principles Dynamic Calculations

S. Fukushima, E. Ushijima, H. Kumazoe, A. Koura, F. Shimojo, K. Shimamura, M. Misawa, R. K. Kalia, A. Nakano, and P. Vashishta: Phys. Rev. B **100**, 214108 (2019).

SHIMOKAWA, Tokuro [C class; 4500 (B), 1250 (C)] (261)

— *Thermal effect on the quantum frustrated magnetism*

SHINAOKA, Hiroshi [B class; 800 (B), 0 (C)] (232)

— *Exploring low-rank tensor representation of Matsubara Green's functions*

1. Sparse sampling and tensor network representation of two-particle Green's functions
H. Shinaoka, D. Geffroy, M. Wallerberger, J. Otsuki, K. Yoshimi, E. Gull, J. Kuneš, SciPost Phys. **8**, (2020) 012 .

SHINODA, Wataru [E class; 24000 (B), 3000 (C)] (355)

— *Molecular basis analysis of Soft Materials using All-Atom and Coarse-Grained Molecular Dynamics Simulations*

1. Free energy analysis of membrane pore formation process in the presence of multiple melittin peptides
Y. Miyazaki, S. Okazaki, and W. Shinodai: BBA - Biomembranes **1861** (2019) 1409-1419.
2. Cholesterol-Induced Conformational Change in the Sphingomyelin Headgroup
S. Hanashima, K. Murakami, M. Yura, Y. Yano, Y. Umegawa, H. Tsuchikawa, N. Matsumori, S. Seo, W. Shinoda, and M. Murata: Biophys. J. **117** (2019) 307-318.
3. Hydrogen Permeation in Hydrated Perfluorosulfonic Acid Polymer Membranes: Effect of Polymer Crystallinity and Equivalent Weight
K. Takeuchi, A. Kuo, T. Hirai, T. Miyajima, S. Urata, S. Terazono, S. Okazaki, and W. Shinoda: J. Phys. Chem. C **123**, (2019) 20628-20638.
4. Average Conformation of Branched Chain Lipid PGP-Me That Accounts for the Thermal Stability and High-Salinity Resistance of Archaeal Membranes
M. Yamagami, H. Tsuchikawa, J. Cui, Y. Umegawa, Y. Miyazaki, S. Seo, W. Shinoda, and M. Murata: Biochemistry **58**, (2019) 3869-3879.
5. Effects of Packing Density and Chain Length on the Surface Hydrophobicity of Thin Films Composed of Perfluoroalkyl Acrylate Chains: A Molecular Dynamics Study
H. O. S. Yadav, A. Kuo, S. Urata, and W. Shinoda: Langmuir **35**, (2019) 14316-14323.
6. Large-scale molecular dynamics simulation of perfluorosulfonic acid T membranes: Remapping coarse-grained to all-atomistic simulations
A. Kuo, Y. Miyazaki, C. Jang, T. Miyajima, S. Urata, S. O. Nielsen, S. Okazaki, and W. Shinoda: Polymer **181**, (2019) 121766.
7. Heteroaryldihydropyrimidines Alter Capsid Assembly By Adjusting the Binding Affinity and Pattern of the Hepatitis B Virus Core Protein
H. Liu, S. Okazaki, and W. Shinoda: J. Chem. Inf. Model. **59**, (2019) 5104-5110.
8. pSPICA: A Coarse-Grained Force Field for Lipid Membranes Based on a Polar Water Model
Y. Miyazaki, S. Okazaki, and W. Shinoda: J. Chem. Theory Comput. **16**, (2020) 782-793.

SHINOHARA, Yasushi [C class; 4000 (B), 0 (C)] (113)

— *First-principles calculations for nonlinear light absorption of insulators*

1. Asymmetric nonlinear optics of a polar chemical bond
Yuya Morimoto, Yasushi Shinohara, Mizuki Tani, Bo-Han Chen, Kenichi L. Ishikawa, Peter Baum: arXiv:1910.11821, submitted.
2. Detecting electron-phonon couplings during photo-induced phase transition
Takeshi Suzuki, Yasushi Shinohara, Yangfan Lu, Mari Watanabe, Jiadi Xu, Kenichi L. Ishikawa, Hide Takagi, Minoru Nohara, Naoyuki Katayama, Hiroshi Sawa, Masami Fujisawa, Teruto Kanai, Jiro Itatani, Takashi Mizokawa, Shik Shin, Kozo Okazaki: arXiv:2002.10037, submitted.
3. Strong-Field Electron Dynamics in Solids

Kenichi L. Ishikawa, Yasushi Shinohara, Takeshi Sato, Tomohito Otobe: arXiv:2003.14090, appeared as a chapter in a book.

SHIOMI, Junichiro [C class; 4500 (B), 750 (C)] (265)

— *Screening for Thermal Functional Materials using Materials Informatics*

1. Design of highly-selective radiative-cooling structure accelerated by materials informatics
Jiang Guo, Shenghong Ju, Junichiro Shiomi: *Optics Letters*, 45, 343-346(2020).
2. Enhancing thermal boundary conductance of graphite- metal interface by triazine-based molecular bonding
Aun Ota, Masato Ohnishi, Hisayoshi Oshima, Hisayoshi, Takuma Shiga, Takashi Kodama, Junichiro Shiomi: *ACS Applied Materials & Interfaces*, 11, 37295-37301 (2019).
3. Spectral control of thermal boundary conductance between copper and carbon crystals by self-assembled monolayers
Shih-Wei Hung, Shiqian Hu, Junichiro Shiomi: *ACS Applied Electronic Materials*, 1, 2594-2601 (2019).
4. Scalable multi- nanostructured silicon for room-temperature thermoelectrics
Makoto Kashiwagi, Yuxuan Liao, Shenghong Ju, Asuka Miura, Shota Konishi, Takuma Shiga, Takashi Kodama, and Junichiro Shiomi: *ACS Applied Energy Materials*, 2, 7083-7091 (2019).
5. Disorder Limits the Coherent Phonon Transport in Two- Dimensional Phononic Crystal Structure
Shiqian Hu, Zhongwei Zhang, Pengfei Jiang, Weijun Ren, Cuiqian Yu, Junichiro Shiomi, Jie Chen: *Nanoscale*, 11, 11839-11846 (2019).
6. Monte Carlo tree search for materials design and discovery
Thaer Dieb, Shenghong Ju, Junichiro Shiomi, Koji Tsuda: *MRS Communications*, 9, 532-536 (2019).
7. Anomalously low thermal conductivity in superhard cubic-Si₃N₄
Jing Liu, Shenghong Ju, Norimasa Nishiyama, Junichiro Shiomi: *Physical Review B*, 100, 064303 (2019).
8. Materials informatics for heat transfer: Recent progresses and perspectives
Shenghong Ju, Junichiro Shiomi: *Nanoscale and Microscale Thermophysical Engineering*, 23, 157172 (2019).
9. Quantifying phonon particle and wave transport in nanostructures—The unexpectedly strong particle effect in silicon nanophononic metamaterial with cross junction, *Materials Today Physics*, 8, 56-61 (2019). cooling structure accelerated by materials informatics
Dengke Ma, Anuj Arora, Shichen Deng, Junichiro Shiomi, Nuo Yang: *Optics Letters*, 45, 343-346 (2020).

SHIRAI, Tatsuhiko [B class; 700 (B), 0 (C)] (341)

— *The analysis of the dynamical response to the optical bistability*

1. Dynamical phase transition in Floquet optical bistable systems: An approach from finite-size quantum systems
T. Shirai, S. Todo, and S. Miyashita: *Phys. Rev. A* **101** (2020) 013809.
2. Thermalization in open many-body systems based on eigenstate thermalization hypothesis
T. Shirai and T. Mori: *Phys. Rev. E* **101** (2020) 042116.
3. A guiding principle for embedding in simulated-annealing based Ising machines
T. Shirai, S. Tanaka and N. Togawa: Submitted to *IEEE Transactions on Computers: Special Issue of Quantum Computing*

SHIRAISHI, Kenji [C class; 5500 (B), 0 (C)] (97)

— *Theoretical Design of Gate Dielectrics of Future GaN Power Devices*

SHUDO, Ken-ichi [C class; 500 (B), 50 (C)] ()

— *Impurity effects on electronic states of PbS nano-particles*

SUGINO, Osamu [E class; 13000 (B), 2000 (C)] (52)

— *Physics of electrode interfaces*

1. Nuclear quantum effect for hydrogen adsorption on Pt(111)
L. Yan, Y. Yamamoto, M. Shiga, and O. Sugino: Phys. Rev. B **101**, 165414 (2020).
2. Scaling Relation of Oxygen Reduction Reaction Intermediates at Defective TiO₂ Surfaces
Y. Yamamoto, S. Kasamatsu, and O. Sugino: J. Phys. Chem. C **123**, 19486-19492 (2019).

SUWA, Hidemaro [C class; 9500 (B), 0 (C)] (251)

— *Dynamical spin structure factor of spin-orbit insulator*

— *Dynamics of Slater-Mott crossover materials*

SUZUKI, Takafumi [C class; 4000 (B), 650 (C)] (285)

— *Quantum spin liquids in extended Kitaev models on a honeycomb lattice*

1. Quantized $\Delta S=2$ Excitation Spectra by Confinement in an S=1 Spin Chain
Takafumi Suzuki and Seiichiro Suga: J. Phys. Soc. Jpn. **88**, 053702 (2019).
2. Temperature Dependence of Heat Capacity in the Kitaev-Heisenberg Model on a Honeycomb Lattice
Takafumi Suzuki and Youhei Yamaji: J. Phys. Soc. Jpn. **88**, 115001 (2019).

SUZUKI, Yuji [C class; 6000 (B), 0 (C)] (85)

— *Development of High-performance Polymer Electret*

— *Development of High-performance Polymer Electret Using Quantum Chemical Analysis*

1. Solid State Quantum Chemical Investigation of a High-performance Fluorinated Amorphous Polymer Electret
S. Kim, K. Suzuki, and Y. Suzuki: Invited talk, IEEE 17th Int. Symp. Electrets (ISE17), Limerick, p.23 (2019)
2. Investigation of Charge Stability in Amorphous Fluorinated Polymer Using Quantum Chemical Analysis
S. Kim, Y. Zhang, K. Suzuki, and Y. Suzuki: IEEE Conf. on Electr. Insul. Dielectr. Phenom. (CEIDP), Richland, 8-1 (2019)

TADANO, Terumasa [C class; 6000 (B), 1000 (C)] (15)

— *Predicting and understanding structural phase transition of solids from finite-temperature phonon calculations*

1. First-principles study of phonon anharmonicity and negative thermal expansion in ScF₃
Y. Oba, T. Tadano, R. Akashi and S. Tsuneyuki: Phys. Rev. Mater. **3** (2019) 033601.
2. Quantum crystal structure in the 250-kelvin superconducting lanthanum hydride
I. Errea, F. Belli, L. Monacelli, A. Sanna, T. Koretsune, T. Tadano, R. Bianco, M. Calandra, R. Arita, F. Mauri and J. A. Flores-Livas: Nature **578** (2020) 66.
3. Materials design of dynamically stable d9 layered nickelates
M. Hirayama, T. Tadano, Y. Nomura and R. Arita: Phys. Rev. B **101** (2020) 075107.
4. Anharmonicity Explains Temperature Renormalization Effects of the Band Gap in SrTiO₃.
Y. Wu, W. A. Saidi, J. K. Wuenschell, T. Tadano, P. Ohodnicki, B. Chorpene and Y. Duan: J. Phys. Chem. Lett. **11** (2020) 2518.
5. Enargite Cu₃PS₄: A CuS-Based Thermoelectric Material with a Wurtzite-Derivative Structure
T. Tanimoto, K. Suekuni, T. Tanishita, H. Usui, T. Tadano, T. Kamei, H. Saito, H. Nishiate, C. H. Lee, K. Kuroki and M. Ohtaki: Adv. Funct. Mater. **2020** (2020) 2000973.

TAKAHASHI, Osamu [C,D class; 1000 (B), 750 (C)] (148)

— *Electronic state of water and ethanol in aqueous solution*

— *Electronic state of water under various environments*

1. Si 1s⁻¹, 2s⁻¹ and 2p⁻¹ lifetime broadening of SiX₄ (X = F, Cl, Br, CH₃) molecules: SiF₄ anomalous behaviour reassessed
R. Pttner, T. Marchenko, R. Guillemin, L. Journal, G. Goldsztejn, D. Colin, O. Takahashi, K. Ueda, A. F. Lago, M. N. Piancastelli, and M. Simon: Phys. Chem. Chem. Phys., **21**(17), 8827 -

8836 (2019)

2. Electronic States of Acetic Acid in a Binary Mixture of Acetic Acid and 1-Methylimidazole Depend on the Environment
N. Yoshimura, O. Takahashi, M. Oura, and Y. Horikawa: *J. Phys. Chem. B* **123** (6), 1332 - 1339(2019)
3. pH dependence of aqueous oxalic acid observed by X-ray absorption and emission spectroscopy
R. Yamamura, T. Suenaga, M. Oura, T. Tokushima, and O. Takahashi, *Chem. Phys. Lett.* **738**, 136895 (2020).

TAKETSUGU, Tetsuya [C class; 3500 (B), 600 (C)] ()— *Ab initio study on the structure and functions of nanomaterials***TAMURA, Ryo** [C class; 1000 (B), 250 (C)] (318)

Effective model estimation using experimental results

1. Efficient recommendation tool of materials by an executable file based on machine learning
K. Terayama, K. Tsuda, and R. Tamura: *Japanese Journal of Applied Physics* **58** (2019) 098001.
2. Quantum Phase Transition in Fully Connected Quantum WajnflaszPick Model
Y. Seki, S. Tanaka, and S. Kawabata: *J. Phys. Soc. Jpn.* **88** (2019) 054006.
3. Application of Ising Machines and a Software Development for Ising Machines
K. Tanahashi, S. Takayanagi, T. Motohashi, and S. Tanaka: *J. Phys. Soc. Jpn.* **88** (2019) 061010.
4. A Fully-Connected Ising Model Embedding Method and Its Evaluation for CMOS Annealing Machines
D. Oku, K. Terada, M. Hayashi, M. Yamaoka, S. Tanaka, and N. Togawa: *IEICE Transactions on Information and Systems*, **E102.D** (2019) 1696.
5. Designing metamaterials with quantum annealing and factorization machines
K. Kitai, J. Guo, S. Ju, S. Tanaka, K. Tsuda, J. Shiomi, and R. Tamura: *Physical Review Research* **2** (2019) 013319.
6. Data Integration for Accelerated Materials Design via Preference Learning
X. Sun, Z. Hou, M. Sumita, S. Ishihara, R. Tamura, and K. Tsuda: *New Journal of Physics* in press.
7. A guiding principle for embedding in simulated-annealing based Ising machines
T. Shirai, S. Tanaka, and N. Togawa: submitted to *IEEE Journal*
8. Data-driven determination of a spin Hamiltonian of $\text{KCu}_4\text{P}_3\text{O}_{12}$ with uncertainty
R. Tamura, K. Hukushima, A. Matsuo, K. Kindo, and M. Hase: submitted.

TANAKA, Hajime [B,D class; 4900 (B), 0 (C)] (273, 275, 277, 279)— *Coarsening mechanism of network-forming phase separation in colloidal suspensions*

1. Influence of Hydrodynamic Interactions on Colloidal Crystallization
M. Tateno, T. Yanagishima, J. Russo and H. Tanaka: *Phys. Rev. Lett.* **123** (2019) 258002.

TANAKA, Shu [C class; 500 (B), 100 (C)] (344)— *Study on Ising machines from a viewpoint of statistical mechanics*

1. Quantum Phase Transition in Fully Connected Quantum WajnflaszPick Model
Y. Seki, S. Tanaka, and S. Kawabata: *J. Phys. Soc. Jpn.* **88** (2019) 054006.
2. Application of Ising Machines and a Software Development for Ising Machines
K. Tanahashi, S. Takayanagi, T. Motohashi, and S. Tanaka: *J. Phys. Soc. Jpn.* **88** (2019) 061010.
3. A Fully-Connected Ising Model Embedding Method and Its Evaluation for CMOS Annealing Machines
D. Oku, K. Terada, M. Hayashi, M. Yamaoka, S. Tanaka, and N. Togawa: *IEICE Transactions on Information and Systems*, **E102.D** (2019) 1696.
4. Efficient recommendation tool of materials by an executable file based on machine learning
K. Terayama, K. Tsuda, and R. Tamura: *Japanese Journal of Applied Physics* **58** (2019) 098001.
5. Designing Metamaterials with Quantum Annealing and Factorization Machines
K. Kitai, J. Guo, S. Ju, S. Tanaka, K. Tsuda, J. Shiomi, and R. Tamura: *Phys. Rev. Research* **2** (2020) 013319.

6. Data Integration for Accelerated Materials Design via Preference Learning
X. Sun, Z. Hou, M. Sumita, S. Ishihara, R. Tamura, and K. Tsuda: *New Journal of Physics* in press.
7. A guiding principle for embedding in simulated-annealing based Ising machines
T. Shirai, S. Tanaka, and N. Togawa: submitted to *IEEE Journal*.
8. Data-driven determination of a spin Hamiltonian of $\text{KCu}_4\text{P}_3\text{O}_{12}$ with uncertainty
R. Tamura, K. Hukushima, A. Matsuo, K. Kindo, and M. Hase: submitted.

TATENNO, Masaru [C class; 5000 (B), 0 (C)] ()

— *Multi-scale Hybrid Molecular Dynamics Simulations of Biological Catalysis*

TATETSU, Yasutomi [C class; 4000 (B), 750 (C)] (105)

— *First-principles study on grain boundaries of permanent magnets*

1. First-principles study on surface stability and interface magnetic properties of SmFe_{12}
Y. Aina, T. Shiozawa, Y. Tatetsu, and Y. Gohda: *Appl. Phys. Exp.* **13** (2020) 045502.
2. First-principles study of crystalline NdFe alloys
Y. Aina, Y. Tatetsu, A. Terasawa, and Y. Gohda, *Appl. Phys. Exp.* **13** (2020) 017006.

TATEYAMA, Yoshitaka [C class; 12500 (B), 900 (C)] (54)

— *DFT sampling analysis of interfaces and electrolytes in novel batteries*

— *DFT-MD sampling analysis of interfaces and electrolytes in novel batteries*

1. Li⁺ Transport Mechanism at Heterogeneous Cathode / Solid Electrolyte Interface in All-Solid-State Battery via First-Principles Structure Prediction Scheme
B. Gao, R. Jalem, Y. Ma, Y. Tateyama, *Chem. Mater.* **32** (2020) 85.
2. Reaction Energy Benchmarks of Hydrocarbon Combustion by Gaussian Basis and Plane Wave Basis Approaches
A. Ishikawa, Y. Tateyama, *J. Comp. Chem.* **40** (2019) 1866.
3. Electrochemical properties of fluorinated boron-doped diamond electrodes via fluorine-containing plasma treatment
C. Yamaguchi, K. Natsui, S. Iizuka, Y. Tateyama, Y. Einaga, *Phys. Chem. Chem. Phys.* **21** (2019) 13788.
4. Theoretical picture of positive electrode / solid electrolyte interface in all-solid-state battery from electrochemistry and semiconductor physics viewpoints
Y. Tateyama, B. Gao, R. Jalem, J. Haruyama, *Curr. Opin. Electrochem.* **17** (2019) 149.
5. Surface-Dependent Stability of Interface between the Garnet $\text{Li}_7\text{La}_3\text{Zr}_2\text{O}_{12}$ and the Li Metal in the All-Solid-State Battery from First-Principles Calculations
B. Gao, R. Jalem, Y. Tateyama, *ACS Appl. Mater. Interfaces*, **12** (2020) 16350.
6. Possible high-potential ilmenite type Na_1MO_3 ($\text{M} = \text{VNi}$) cathodes realized by dominant oxygen redox reaction
M. H. N. Assadi, M. Okubo, A. Yamada, Y. Tateyama, *Phys. Rev. Mater.* **4** (2020) 015401.
7. Machine learning prediction of coordination energies for alkali group elements in battery electrolyte solvents
A. Ishikawa, K. Sodeyama, Y. Igarashi, T. Nakayama, Y. Tateyama, M. Okada, *Phys. Chem. Chem. Phys.* **21** (2019) 26339.
8. What Is the Active Site for the Oxidative Coupling of Methane Catalyzed by MgO? A Metadynamics-Biased Ab Initio Molecular Dynamics Study
A. Ishikawa, Y. Tateyama, *J. Phys. Chem. C* **124** (2020) 6054.

TERAO, Takamichi [B class; 1200 (B), 160 (C)] (316)

— *Molecular simulation of patchy particles*

1. Numerical method to study three-dimensional metamaterial composites
T. Terao: *Proceedings of 13th international congress on artificial materials for novel wave phenomena* (2019) X426.

TERASAWA, Asako [C class; 3000 (B), 550 (C)] (115)

— *First principles calculations and analysis on relationship between exchange coupling constants and local structures for magnetic alloys and amorphous grain boundary phases in permanent magnets*

1. Efficient Algorithm Based on Liechtenstein Method for Computing Exchange Coupling Constants Using Localized Basis Set

A. Terasawa, M. Matsumoto, T. Ozaki, and Y. Gohda: J. Phys. Soc. Jpn., vol. 88, no. 11, p. 114706, Oct. 2019, doi: 10.7566/JPSJ.88.114706.

TODO, Syngé [C class; 6000 (B), 850 (C)] (256)

— *Entanglement Quantum Phase Transition and Quantum Dynamics in Quantum Many-body Systems*

1. Machine learning for molecular dynamics with strongly correlated electrons
Hidemaro Suwa, Justin S. Smith, Nicholas Lubbers, Cristian D. Batista, Gia-Wei Chern, Kipton Barros, Phys. Rev. B **99**, 161107 (5pp) (2019)
2. Gapless Kitaev Spin Liquid to Classical String Gas through Tensor Networks
Hyun-Yong Lee, Ryui Kaneko, Tsuyoshi Okubo, Naoki Kawashima, Phys. Rev. Lett. **123**, 087203 (6pp) (2019)
3. Subspace-search variational quantum eigensolver for excited states
Ken M. Nakanishi, Kosuke Mitarai, Keisuke Fujii, Phys. Rev. Research **1**, 033062 (7pp) (2019)
4. Characterization of localized effective spins in gapped quantum spin chains
Hayate Nakano, Seiji Miyashita, Phys. Rev. B **100**, 195105 (11pp) (2019)
5. Multiple- q states of the J_1 - J_2 classical honeycomb-lattice Heisenberg antiferromagnet under magnetic fields
Tokuro Shimokawa, Tsuyoshi Okubo, Hikaru Kawamura, Phys. Rev. B **100**, 224404 (15pp) (2019)
6. Dynamical phase transition in Floquet optical bistable systems: An approach from finite-size quantum systems
Tatsuhiko Shirai, Syngé Todo, Seiji Miyashita, Phys. Rev. A **101**, 013809 (7pp) (2020)
7. Abelian and Non-Abelian Chiral Spin Liquids in a Compact Tensor Network Representation
Hyun-Yong Lee, Ryui Kaneko, Tsuyoshi Okubo, Naoki Kawashima, Phys. Rev. B **101**, 035140 (9pp) (2020)
8. Spin-lattice coupling in a ferrimagnetic spinel: Exotic $H - T$ phase diagram of MnCr_2S_4 up to 110 T
A. Miyata, H. Suwa, T. Nomura, L. Prodan, V. Felea, Y. Skourski, J. Deisenhofer, H.-A. Krug von Nidda, O. Portugall, S. Zherlitsyn, V. Tsurkan, J. Wosnitza, A. Loidl, Phys. Rev. B **101**, 054432 (8pp) (2020)

TOHYAMA, Takami [C class; 2500 (B), 550 (C)] (290)

— *Finite-Temperature Properties and Spin Dynamics in Kagome Kitaev-Heisenberg Model*

1. Finite-temperature properties of the Kitaev-Heisenberg models on kagome and triangular lattices studied by improved finite-temperature Lanczos methods
K. Morita and T. Tohyama: Phys. Rev. Research **2**, (2020) 013205.
2. Magnetic orders induced by RKKY interaction in Tsai-type quasicrystalline approximant Au-Al-Gd
H. Miyazaki, T. Sugimoto, K. Morita, and T. Tohyama: Phys. Rev. Materials **4**, (2020) 024417.
3. Vanishing Wilson ratio as the hallmark of quantum spin-liquid models
P. Prelovsek, K. Morita, T. Tohyama, and J. Herbrych: Phys. Rev. Research **2**, (2020) 023024.

TOMITA, Yusuke [C class; 5500 (B), 0 (C)] (264)

— *Study of relaxor ferroelectrics by using a minimal model*

TONEGAWA, Takashi [B,C class; 2100 (B), 0 (C)] (297)

— *Numerical Study of the One-Dimensional Quantum Spin Systems with Spatial Structures*

— *Numerical Study of the One-Dimensional Quantum Spin Systems with Spatial Studies*

1. Magnetization Plateau of the $S = 2$ Antiferromagnetic Heisenberg Chain with Anisotropies
T. Sakai, K. Okamoto, and T. Tonegawa: Phys. Rev. B **100**, 054407 (2019).
2. Ground-State Phase Diagram of an Anisotropic $S = 1$ Ferromagnetic-Antiferromagnetic Bond-

Alternating Chain

K. Okamoto, T. Tonegawa, M. Kaburagi, and T. Sakai: JPS Conf. Proc. **30**, 011024 (2020).**TSUKAHARA, Noriyuki** [B class; 400 (B), 0 (C)] ()— *Theoretical study of spin detection in lanthanoid atoms and molecules by adsorption on superconducting substrate***TSUNEYUKI, Shinji** [C class; 7000 (B), 950 (C)] (73)— *Material exploration by advanced first-principles simulation*

1. Ab initio prediction of structural phase-transition temperature of SrTiO₃ from finite-temperature phonon calculation
T. Tadano and S. Tsuneyuki: J. Ceram. Soc. Jpn., **127** (2019) 404.
2. Search for common minima in joint optimization of multiple cost functions
D. Adachi, N. Tsujimoto, R. Akashi, S. Todo and S. Tsuneyuki: Comp. Phys. Commun. **241** (2019) 92.
3. X線回折実験とシミュレーションのデータ同化による結晶構造解析
藤堂 真治, 常行 真司, 日本結晶学会誌 **62** (2020) 51.

TSURUTA, Kenji [C class; 2500 (B), 0 (C)] (137)— *Hybrid Ab-Initio/Machine-Learning Computation for Designing Dynamical Properties of Nano/Molecular Structures*

1. First-principles Study on Water Dissociation in Grain Boundary of MAPbI₃ Perovskite
M.A.A. Asad, K. Sato, and K. Tsuruta: MRS Adv. **4** (2019) 1965.
2. Optimization of Molecular Characteristics via Machine Learning based on Continuous Representation of Molecules
K. Sato and K. Tsuruta: Mater. Sci. Forum, in press.

UCHIDA, Takashi [B class; 500 (B), 90 (C)] (348)— *Magnetic structures of multiple-Q states in frustrated itinerant magnets***WAKABAYASHI, Daisuke** [B class; 700 (B), 0 (C)] ()— *Inhomogeneous structure of silica glass during the structural transformations under high pressure***WATANABE, Hiroshi** [B class; 900 (B), 100 (C)] (326)— *Molecular dynamics study of the properties of near-critical fluids***WATANABE, Hiroshi** [B class; 700 (B), 0 (C)] (236)— *Calculation for ground and excited states in strongly-correlated electron systems by variational Monte Carlo method*

1. Mechanism of superconductivity and electron-hole doping asymmetry in κ -type molecular conductors
H. Watanabe, H. Seo, and S. Yunoki: Nat. Commun. **10** (2019) 3167.

WATANABE, Kazuyuki [C class; 8000 (B), 700 (C)] (64)— *First-Principles Study of Excited Electron Positron and Atom Dynamics and Optical and Thermoelectric Properties of Nanostructures*

1. Angle-resolved photoemission spectroscopy in low-dimensional periodic structures: a real-time first-principles simulation
K. Uchida, Y. Akimoto, K. Einaga, and K. Watanabe, Jpn. J. Appl. Phys. **58**, 128001 (2019).
2. Excitons in two-dimensional atomic layer materials from time-dependent density functional theory : mono-layer and bi-layer hexagonal boron nitride and transition-metal dichalcogenides
Y. Suzuki and K. Watanabe, Phys. Chem. Chem. Phys. **22**, 2908 (2020).
3. Simulation of a hydrogen atom in a laser field using the time-dependent variational principle
K. Rowan, L. Schatzki, T. Zaklana, Y. Suzuki, K. Watanabe, and K. Varga, Phys. Rev. E **101**, 023313 (2020).

- Stationary-state electron scattering using a complex injecting potential
T. Yamaguchi, K. Uchida, K. Varga, and K. Watanabe, *J. Phys. Soc. Jpn.* **89**,044002(2020).

WATANABE, Satoshi [C class; 10500 (B), 1700 (C)] (58)

— *Analyses of atomic structures and atom dynamics at surfaces interfaces and defects*

- A Comparative Study on the Diffusion Behaviors of Metal and Oxygen Ions in Metal-Oxide Based Resistance Switches via Ab Initio Molecular Dynamics Simulations
B. Xiao, X.-F. Yu, and S. Watanabe: *ACS Appl. Electronic Mater.* **1** (2019) 585.
- Simulating lattice thermal conductivity in semiconducting materials using high-dimensional neural network potential
E Minamitani, M Ogura, and S Watanabe: *Appl. Phys. Express* **12** (2019) 095001.
- Low-Energy-Consumption Three-Valued Memory Device Inspired by Solid-State Batteries
Y. Watanabe, S. Kobayashi, I. Sugiyama, K. Nishio, W. Liu, S. Watanabe, R. Shimizu, and T. Hitosugi: *ACS Appl. Mater. interfaces* **11** (2019) 45150.
- Mechanically Tunable Spontaneous Vertical Charge Redistribution in Few-Layer WTe₂
Z. Ni, E. Minamitani, K. Kawahara, R. Arafune, C.-L. Lin, N. Takagi, and S. Watanabe: *J. Phys. Chem. C* **124** (2019) 2008.
- Moisture effect on the diffusion of Cu ions in Cu/Ta₂O₅/Pt and Cu/SiO₂/Pt resistance switches: a first-principles study
B. Xiao and S. Watanabe: *Sci. Technol. Adv. Mater.* **20** (2019) 580.
- First-principles study of Li-ion distribution at γ -Li₃PO₄/metal interfaces
K. Shimizu, W. Liu, W. Li, S. Kasamatsu, Y. Ando, E. Minamitani, and S. Watanabe: *Phys. Rev. Mater.* **4** (2020) 015402.
- The effect of phonon anharmonicity on the lattice thermal conductivity of rare-earth pyrochlores: A first-principles study
Z. Li, Y. Xing, S. Watanabe, and W. Pan: *Ceram. Int'l* **46** (2020) 9947.
- Atomistic Simulations for Understanding Microscopic Mechanism of Resistive Switches
S. Watanabe and B. Xiao: in M. Aono (Ed.) "Atomic Switch: From Invention to Practical Use and Future Prospects" (Springer, 2020), p. 95.

YAMADA, Atsuo [C class; 5000 (B), 750 (C)] (94)

— *First-principles analyses on the cathode materials for rechargeable batteries*

- Sodium- and Potassium- Hydrate Melts Containing Asymmetric Imide Anions for High- Voltage Aqueous Batteries
Q. Zheng, S. Miura, K. Miyazaki, S. Ko, E. Watanabe, M. Okoshi, C.- P. Chou, Y. Nishimura, H. Nakai, T. Kamiya, T. Honda, J. Akikusa, Y. Yamada, A. Yamada: *Angew. Chem. Int. Ed.* **58** (2019) 2358.

YAMADA, Atsushi [C class; 500 (B), 300 (C)] (231)

— *Superconductivity and magnetic properties of the Hubbard model*

YAMAJI, Youhei [E class; 15000 (B), 2300 (C)] (200)

— *Numerical studies on energy current correlations in frustrated quantum spin systems*

- Possible Kitaev Quantum Spin Liquid State in 2D Materials with S=3/2
C. Xu, J. Feng, M. Kawamura, Y. Yamaji, Yousra Nahas, S. Prokhorenko, Y. Qi, H. Xiang, L. Bellaiche: *Phys. Rev. Lett.* **124**(2020) 087205.

YAMAMOTO, Kaoru [B class; 500 (B), 80 (C)] ()

— *First-principles calculation of thermoelectric properties for magnetic tunneling junctions and giant magneto-resistance devices*

YAMAMOTO, Norifumi [B class; 700 (B), 90 (C)] (175)

— *Theoretical Study on the Aggregation-Induced Emission*

YAMASHITA, Koichi [C class; 3000 (B), 0 (C)] (129)

— *Large scale ab initio calculations on the fundamental processes of solar energy convergence devices and on designing principles for new materials*

1. Simulation of Conductive Atomic Force Microscopy of Organic Photovoltaics by Dynamic Monte Carlo Method
E. Kawashima, M. Fujii, and K. Yamashita: Chem. Lett. **48** (2019) 513.
2. Laser-induced fluorescence of the CHFCHO radical and reaction of OH radicals with halogenated ethylenes
I. Masumoto, N. Washida, S. Inomata, A. Muraoka, and K. Yamashita: J. Chem. Phys. **150** (2019) 174302.
3. A route for minimizing emissions: sun-mediated processes & clean batteries
G. Giorgi, K. Yamashita, M. Palumbo, and S. Fabris: Curr. Opin. Green. Sustain. Chem. **17** (2019) A1.
4. Entropy Promotes Charge Separation in Bulk Heterojunction Organic Photovoltaics
E. Kawashima, M. Fujii, and K. Yamashita: J. Photochem. Photobiol. A: Chem. **382** (2019) 111875.
5. Importance of Side-Chains on Molecular Characteristics of Interacting Organic Molecules
K. Mishima, K. Yamashita: ACS Omega **4** (2019) 10396.
6. Application of accelerated long-range corrected exchange functional [LC-DFT(2Gau)] to periodic boundary condition systems: CO adsorption on Cu(111) surface
K. Mishima, M. Kaneko, J.-W. Song, H. Kawai, K. Yamashita, and K. Hirao: J. Chem. Phys. **152** (2020) 104105.

YAMASHITA, Tomoki [C class; 2500 (B), 600 (C)] (127)

— *Development of algorithms in crystal structure prediction*

YAMAUCHI, Kunihiko [C class; 5000 (B), 0 (C)] (102)

— *First-principles density functional calculations of transition-metal magnetic oxides*

1. Bulk Rashba effect in multiferroics: A theoretical prediction for BiCoO₃
Kunihiko Yamauchi, Paolo Barone, Silvia Picozzi: Phys. Rev. B **100** (2019) 245115.
2. Conversion of a conventional superconductor into a topological superconductor by topological proximity effect
C.X. Trang, N. Shimamura, K. Nakayama, S. Souma, K. Sugawara, I. Watanabe, K. Yamauchi, T. Oguchi, K. Segawa, T. Takahashi, Yoichi Ando, and T. Sato: Nat. Commun. **11** (2020) 159.
3. Dimensionality reduction and band quantization induced by potassium intercalation in 1T-HfTe₂
Y. Nakata, K. Sugawara, A. Chainani, K. Yamauchi, K. Nakayama, S. Souma, P.-Y. Chuang, C.-M. Cheng, T. Oguchi, K. Ueno, T. Takahashi, and T. Sato: Phys. Rev. Materials **3** (2019) 071001(R).
4. Evidence for bulk nodal loops and universality of Dirac-node arc surface states in ZrGeXc (Xc = S, Se, Te)
Takechika Nakamura, Seigo Souma, Zhiwei Wang, Kunihiko Yamauchi, Daichi Takane, Hikaru Oinuma, Kosuke Nakayama, Koji Horiba, Hiroshi Kumigashira, Tamio Oguchi, Takashi Takahashi, Yoichi Ando, and Takafumi Sato: Phys. Rev. B **99** (2019) 245105.
5. Topology analysis for anomalous Hall effect in the noncollinear antiferromagnetic states of Mn₃AN (A = Ni, Cu, Zn, Ga, Ge, Pd, In, Sn, Ir, Pt)
Vu Thi Ngoc Huyen, Michi-To Suzuki, Kunihiko Yamauchi, and Tamio Oguchi: Phys. Rev. B **100** (2019) 094426.
6. Possible emergence of a skyrmion phase in ferroelectric GaMo₄S₈
Hui-Min Zhang, Jun Chen, Paolo Barone, Kunihiko Yamauchi, Shuai Dong, and Silvia Picozzi: Phys. Rev. B **99** (2019) 214427.

YANAGISAWA, Susumu [C class; 5000 (B), 0 (C)] (100)

— *Implementation of the phonon analysis for organic semiconductor crystals*

— *Structural distortion or defect in organic molecular thin film: theoretical study*

1. Determination of the ionization energy and the electron affinity of organic molecular crystals from

first-principles: dependence on the molecular orientation at the surface

S. Yanagisawa: Jpn. J. Appl. Phys. **59** (2020) 031002.

2. Nanoscale First-Principles Electronic Structure Simulations of Materials Relevant to Organic Electronics
S. Yanagisawa and I. Hamada: In: T. Onishi (eds) Theoretical Chemistry for Advanced Nanomaterials. Springer, Singapore (2020) 89.
3. Enhancement of the GW space-time program code for accurate prediction of the electronic properties of organic electronics materials
S. Yanagisawa, T. Yamashita, and R. Egawa: Sustained Simulation Performance 2018 and 2019. Springer (2020) 225.

YANAGISAWA, Takashi [B class; 1100 (B), 150 (C)] (229)

— *Study of strongly correlated electron systems based on optimization Monte Carlo method and first-principles calculations*

1. Antiferromagnetism, Superconductivity and phase diagram in the two-dimensional Hubbard model
T. Yanagisawa: J. Phys. Soc. Jpn. **88** (2019) 054702.a
2. Mechanism of high-temperature superconductivity in correlated electron systems
T. Yanagisawa: Condensed Matter 2019 (2019) 57.a
3. Fractional Skyrmion and Absence of Low-lying Andreev Bound States in a Micro Fractional-flux Quantum Vortex
T. Yanagisawa: J. Phys. Soc. Jpn. **88** (2019) 104704.
4. Flat-band in Pyrochlore Oxides: A First-Principles Study
I. Hase, T. Yanagisawa, K. Kawashima: Nanomaterials 2019 (2019) 876.
5. Renormalization group analysis of the hyperbolic sine-Gordon model
T. Yanagisawa: Prog. Theor. Exp. Phys. **2019** (2019) 023A01.
6. Antiferromagnetism, Superconductivity and phase diagram in the three-band model of high-temperature superconductors
T. Yanagisawa: J. Phys. Conf. Ser. **1293** (2019) 012027.a
7. Electronic Structure of Novel Non-centrosymmetric Superconductor $\text{Mg}_2\text{Rh}_3\text{P}$
I. Hase, T. Yanagisawa, A. Iyo, H. Fujihisa, Y. Goto, H. Eisaki, K. Kawashima: J. Phys. Conf. Ser. **1293** (2019) 012028.
8. Flattened remnant-field distribution in superconducting bilayer
Y. Tanaka, H. Yamamori, T. Yanagisawa, S. ooi, M. Tachiki, S. Arisawa: Physica C **567** (2019) 1253489.
9. Phase diagram of cuprate high-temperature superconductors based on the optimization Monte Carlo method
T. Yanagisawa, M. Miyazaki, K. Yamaji: Modern Phys. Lett. (2019) in press.a
10. Phase diagram and mechanism of superconductivity in strongly correlated electrons
T. Yanagisawa, M. Miyazaki, K. Yamaji: J. Super. Novel Magne. (2019) in press.a
11. Electronic structure of novel superconductor doped ZrPSe
I. Hase, T. Yanagisawa, H. Kito et al.: J. Phys. Conf. Ser. (2019) in press.

YASUDA, Chitoshi [B class; 700 (B), 90 (C)] (334)

— *Magnetism in the system with the multiple-spin exchange interactions*

YOKO, Akira [B class; 1400 (B), 180 (C)] (150)

— *Theoretical calculation of solvation and reaction in supercritical fluids*

— *Theoretical study for structure and property of organic modified metal oxide nanoparticles*

YOKOI, Tatsuya [C class; 3000 (B), 500 (C)] (117)

— *Machine-learning-driven molecular simulations for grain-boundary atomic dynamics*

YOSHIDA, Tsuneya [C class; 7500 (B), 0 (C)] (213)

— *Non-Hermitian topological phenomena in strongly correlated systems*

— *Novel topological phenomena induced by strongly correlated dynamics*

1. Exceptional band touching for strongly correlated systems in equilibrium
Tsuneya Yoshida, Robert Peters, Norio Kawakami, Yasuhiro Hatsugai: arXiv:2002.11265
2. Antiferromagnetic Topological Insulator in Three-Dimensional Heavy-Fermion Systems
Kazuhiro Kimura, Tsuneya Yoshida, and Norio Kawakami: JPS Conf. Proc. **30**, 011012 (2020).
3. Relationship between exceptional points and the Kondo effect in f-electron materials
Yoshihiro Michishita, Tsuneya Yoshida, and Robert Peters: Phys. Rev. B **101**, 085122 (2020).
4. Mirror skin effect and its electric circuit simulation
Tsuneya Yoshida, Tomonari Mizoguchi, and Yasuhiro Hatsugai: arXiv:1912.12022
5. Non-Hermitian fractional quantum Hall states
Tsuneya Yoshida, Koji Kudo, and Yasuhiro Hatsugai: Scientific Reports **9**, 16895 (2019).
6. Higher-Order Topological Mott Insulators
Koji Kudo, Tsuneya Yoshida, and Yasuhiro Hatsugai: Phys. Rev. Lett. **123**, 196402(2019).
7. Chiral-symmetry protected exceptional torus in correlated nodal-line semimetals
Kazuhiro Kimura, Tsuneya Yoshida, and Norio Kawakami: Phys. Rev. B **100**, 115124 (2019)
8. Efficient method to compute Z_4 -indices with glide symmetry and applications to Möbius materials, CeNiSn and UCoGe
Tsuneya Yoshida, Akito Daido, Norio Kawakami, and Youichi Yanase: Phys. Rev. B **99**, 235105 (2019).
9. Exceptional rings protected by emergent symmetry for mechanical systems
Tsuneya Yoshida and Yasuhiro Hatsugai: Phys. Rev. B **100**, 054109 (2019).

YOSHIDOME, Takashi [C class; 500 (B), 550 (C)] (325)

— *Investigation of dynamics of a supercooled liquid and proteins using the free-energy landscape*

1. Effects of a Low-Pass Filter on the Classification of Protein Electron-Density Maps in terms of Structural Polymorphism using Manifold Learning: A Simulation Study for Cryo-Electron Microscopy Experiments
N. Takano and T. Yoshidome: J. Phys. Soc. Jpn. **88** (2019) 094801.

YOSHINO, Hajime [C class; 9000 (B), 0 (C)] (35)

— *Phase transitions of an antiferromagnetic Heisenberg spin model with a dynamical Jahn-Teller effect on a pyrochlore lattice*

— *Simultaneous spin and Jahn-Teller glass transitions in a model frustrated system on pyrochlore lattice*

1. Spin-Orbital Glass Transition in a Model of a Frustrated Pyrochlore Magnet without Quenched Disorder
Kota Mitsumoto, Chisa Hotta and Hajime Yoshino: Phys. Rev. Lett. **124**, 087201 (2020).

YUKAWA, Satoshi [B class; 800 (B), 100 (C)] (332)

— *Statistical Properties in a Branching Network*

□ SCCMS Projects

FUJITA, Takatoshi [7000 (B), 0 (C)] (371)— *Development of Fragment-Based GW/BSE Method and Application to Organic Optoelectronic Materials*— *Large-scale GW+BSE excited-state calculations for organic optoelectronic materials*

1. Charge-transfer excited states in the donor/acceptor interface from large-scale GW calculations
T. Fujita, Y. Noguchi, T. Hoshi, J. Chem. Phys. **151** (2019) 114109.
2. Numerical aspect of large-scale electronic state calculation for flexible device material
T. Hoshi, H. Imachi, A. Kuwata, K. Kakuda, T. Fujita, H. Matsui, Japan J. Indust. Appl. Math. **36** (2019) 685.

FUKUSHIMA, Tetsuya [5000 (B), 500 (C)] (372)— *Data-driven materials design for new functional high entropy alloys*

1. Theoretical prediction of maximum Curie temperatures of Fe-based dilute magnetic semiconductors by first-principles calculations
T. Fukushima, H. Shinya, A. Masago, K. Sato and H. Katayama-Yoshida: Appl. Phys. Exp. **12** (2019) 063006
2. Experimental verification of the origin of positive linear magnetoresistance in CoFe(V1 - xMnx)Si Heusler alloys
S. Yamada, S. Kobayashi, A. Masago, L. S. R. Kumara, H. Tajiri, T. Fukushima, S. Abo, Y. Sakuraba, K. Hono, T. Oguchi, and K. Hamaya: Phys. Rev. B **100** (2019) 195137
3. High Curie temperature in Eu-doped GaN caused by volume-compensated Ga-vacancy
A. Masago, H. Shinya, T. Fukushima, K. Sato, and H. Katayama-Yoshida: AIP Advances **10** (2020) 025216
4. Valence states and the magnetism of Eu ions in Eu-doped GaN
T. Nunokawa, Y. Fujiwara, Y. Miyata, N. Fujimura, T. Sakurai, H. Ohta, A. Masago, H. Shinya, T. Fukushima, K. Sato, and H. Katayama-Yoshida: J. Appl. Phys. **127** (2020) 083901

GOHDA, Yoshihiro [5000 (B), 500 (C)] (99)— *First-principles study of magnetic-material interfaces*

1. First-principles study on surface stability and interface magnetic properties of SmFe₁₂
Y. Ainai, T. Shiozawa, Y. Tatetsu, and Y. Gohda: Appl. Phys. Express **13**, 045502 (2020).
2. First-principles study of crystalline Nd-Fe alloys
Y. Ainai, Y. Tatetsu, A. Terasawa, and Y. Gohda: Appl. Phys. Express **13**, 017006 (2020).
3. Enhancement of magnetoelectric coupling by insertion of Co atomic layer into Fe₃Si/BaTiO₃(001) interfaces identified by first-principles calculations
Y. Hamazaki and Y. Gohda: J. Appl. Phys. **126**, 233902 (2019).
4. Great Differences between Low-Temperature Grown Co₂FeSi and Co₂MnSi Films on Single-Crystalline Oxides
K. Kudo, Y. Hamazaki, S. Yamada, S. Abo, Y. Gohda, and K. Hamaya: ACS Appl. Electron. Mater. **1**, 2371 (2019).
5. Efficient Algorithm Based on Liechtenstein Method for Computing Exchange Coupling Constants Using Localized Basis Set
A. Terasawa, M. Matsumoto, T. Ozaki, and Y. Gohda: J. Phys. Soc. Jpn. **88**, 114706 (2019).

HOSHI, Takeo [10000 (B), 1000 (C)] (76)— *Massively parallel electronic structure calculation and data-driven science for next-generation supercomputers*

1. K ω -Open-source library for the shifted Krylov subspace method
Takeo Hoshi, Mitsuaki Kawamura, Kazuyoshi Yoshimi, Yuichi Motoyama, Takahiro Misawa, Youhei Yamaji, Synge Todo, Naoki Kawashima, Tomohiro Sogabe: arXiv:2001.08707
2. Two-stage data-analysis method for total-reflection high-energy positron diffraction (TRHEPD)

- Kazuyuki Tanaka, Izumi Mochizuki, Takashi Hanada, Ayahiko Ichimiya, Toshio Hyodo, and Takeo Hoshi: Submitted; Preprint: <https://arxiv.org/abs/2002.12165>
3. Development of data-analysis software for total-reflection high-energy positron diffraction (TRHEPD)
Kazuyuki Tanaka, Takeo Hoshi, Izumi Mochizuki, Takashi Hanada, Ayahiko Ichimiya, Toshio Hyodo: *Acta. Phys. Pol. A* **137**, 188-192 (2020).
 4. An a posteriori verification method for generalized Hermitian eigenvalue problems in large-scale electronic state calculations
Takeo Hoshi, Takeshi Ogita, Katsuhisa Ozaki, Takeshi Terao: *J. Comp. Appl. Math.* **376**, 112830/1-13 (2020).
 5. Charge-Transfer Excited States in the Donor/Acceptor Interface from Large-Scale GW Calculations
Takatoshi Fujita, Yoshifumi Noguchi, Takeo Hoshi: *J. Chem. Phys.* **151**, 114109/1-8 (2019).
 6. EigenKernel - A middleware for parallel generalized eigenvalue solvers to attain high scalability and usability
Kazuyuki Tanaka, Hiroto Imachi, Tomoya Fukumoto, Akiyoshi Kuwata, Yuki Harada, Takeshi Fukaya, Yusaku Yamamoto, Takeo Hoshi: *Japan J. Indust. Appl. Math* **36**, 719-742 (2019).
 7. Numerical aspect of large-scale electronic state calculation for flexible device material
Takeo Hoshi, Hiroto Imachi, Akiyoshi Kuwata, Kohsuke Kakuda, Takatoshi Fujita, Hiroyuki Matsui: *Japan J. Indust. Appl. Math* **36**, 685-698 (2019).
 8. Recent progress in large-scale electronic state calculations and data-driven sciences
Takeo Hoshi and Satoshi Ito: Chap. 14 of *Handbook of Silicon Based MEMS Materials and Technologies 3rd Ed.*, Elsevier (2020).
 9. Numerical methods for large scale electronic state calculation on supercomputer
Takeo Hoshi, Yusaku Yamamoto, Tomohiro Sogabe, Kohei Shimamura, Fuyuki Shimojo, Aiichiro Nakano, Rajiv Kalia, Priya Vashishta: Chap. 15 of *21st Century Nanoscience - A Handbook: Nanophysics Sourcebook (Volume One)*, CRC Press (2019).

IITAKA, Toshiaki [10000 (B), 1000 (C)] (379)— *Order-disorder transition in the superhigh-pressure phase of Mg₂SiO₄***IMADA, Masatoshi** [20000 (B), 2000 (C)] (197)— *Studies on Quantum Spin Liquids in Materials with Strong Spin-Orbit Interaction*— *Studies on quantum spin liquids in molecular conductors based on first-principles Hamiltonian*

1. Charge dynamics of correlated electrons: Variational description with inclusion of composite fermions
Kota Ido, Masatoshi Imada, Takahiro Misawa: *Phys. Rev. B* **101** (2020) 075124.
2. *Ab initio* study of superconductivity and inhomogeneity in a Hg-based cuprate superconductor
Takahiro Ohgoe, Motoaki Hirayama, Takahiro Misawa, Kota Ido, Youhei Yamaji, Masatoshi Imada: *Phys. Rev. B* **101** (2020) 045124.
3. Effective Hamiltonian for cuprate superconductors derived from multiscale *ab initio* scheme with level renormalization
Motoaki Hirayama, Takahiro Misawa, Takahiro Ohgoe, Youhei Yamaji, Masatoshi Imada: *Phys. Rev. B* **99** (2019) 245155.
4. *Ab initio* derivation of an effective Hamiltonian for the La₂CuO₄/La_{1.55}Sr_{0.45}CuO₄ heterostructure
Terumasa Tadano, Yusuke Nomura, Masatoshi Imada: *Phys. Rev. B* **99** (2019) 155148.

KAWAKATSU, Toshihiro [20000 (B), 2000 (C)] (378)— *Multiscale simulations on complex multiphase flows*

1. Coupling Finite Element Method with Large Scale Atomic/Molecular Massively Parallel Simulator (LAMMPS) for Hierarchical Multiscale Simulations
T. Murashima, S. Urata, S. Li: *Euro. Phys. J. B* **92** (2019) 211.
2. ミクロスケールとマクロスケールのシミュレーション連成による高分子材料系のマルチスケールシミュレーション
村島隆浩: *日本化学会情報化学部会誌* **37** (2019) 87.

3. Multiscale Modeling of Plasticity in Amorphous & Polymeric Materials
S. Li, S. Urata, T. Murashima: IACM Expressions **46** (2020) 10.
4. Lagrangian Multiscale SIMulation of Complex Fluids. I.
Y. Morii, T. Kawakatsu: to be submitted.

KAWASHIMA, Naoki [20000 (B), 2000 (C)] (239)— *Application of Tensor Network Method to Condensed Matter Physics*

1. Tensor network wavefunction of $S = 1$ Kitaev spin liquids
Hyun-Yong Lee, Naoki Kawashima, and Yong Baek Kim: arXiv:1911.07714
2. Boundary conformal spectrum and surface critical behavior of classical spin systems: A tensor network renormalization study
Shumpei Iino, Satoshi Morita, and Naoki Kawashima: Phys. Rev. B **101**, 155418 (2020)
3. Magnetic field induced quantum phases in a tensor network study of Kitaev magnets
Hyun-Yong Lee, Ryui Kaneko, Li Ern Chern, Tsuyoshi Okubo, Youhei Yamaji, Naoki Kawashima and Yong Baek Kim: Nature Communications **11**, 1639 (2020)
4. Abelian and non-Abelian chiral spin liquids in a compact tensor network
Hyun-Yong Lee, Ryui Kaneko, Tsuyoshi Okubo, Naoki Kawashima: Phys. Rev. B **101**, 035140 (2020)
5. Thermal-transport studies of kagom antiferromagnets
Minoru Yamashita, Masatoshi Akazawa, Masaaki Shimozawa, Takasada Shibauchi, Yuji Matsuda, Hajime Ishikawa, Takeshi Yajima, Zenji Hiroi, Migaku Oda, Hiroyuki Yoshida, Hyun-Yong Lee, Jung Hoon Han and Naoki Kawashima: J. Phys: Condens. Matter **32**, 074001(11pp) (2019)
6. Entropy Governed by the Absorbing State of Directed Percolation
Kenji Harada and Naoki Kawashima: Phys. Rev. Lett. **123**, 090601 (2019)
7. Boundary Tensor Renormalization Group
Shumpei Iino, Satoshi Morita, and Naoki Kawashima: Phys. Rev. B **100**, 035449 (2019)
8. Gapless Kitaev Spin Liquid to Classical String Gas through Tensor Networks
Hyun-Yong Lee, Ryui Kaneko, Tsuyoshi Okubo, and Naoki Kawashima: Phys. Rev. Lett. **123**, 087203 (2019)
9. Tensor-Ring Decomposition with Index-Splitting
Hyun-Yong Lee and Naoki Kawashima: J. Phys. Soc. Jpn. **89**, 054003 (2020)

KOHYAMA, Masanori [20000 (B), 2000 (C)] (360)— *First-Principles Phase Field Mapping*

1. A first-principles phase field method for quantitatively predicting multi-composition phase separation without thermodynamic empirical parameter
Swastibrata Bhattacharyya, Ryoji Sahara, and Kaoru Ohno: Nature Communications **10** (2019) 3451.
2. Clear evidence of element partitioning effects in a Ti-6Al-4V alloy by the first-principles phase field method
Thi Nu Pham, Kaoru Ohno, Riichi Kuwahara, and Swastibrata Bhattacharyya: J. Phys.: Cond. Mat. **32** (2020) 264001.

MATUBAYASI, Nobuyuki [5000 (B), 500 (C)] (381)— *Development of calculation method of chemical potential for long-chain polymer melt using all-atom molecular dynamics simulation*

1. Chain-Increment Method for Approaching the Chemical Potential of a Polymer with All-Atom Model
K. Yamada and N. Matubayasi: Macromolecules **53** (2020) 775.

MISAWA, Takahiro [10000 (B), 1000 (C)] (366)— *Numerical Study of Quantum Spin Liquid in Organic Conductors using Ab initio Calculation*— *Development of numerical method for calculating dynamical structure factors based on many-variable variational Monte Carlo method*

1. Effective Hamiltonian for cuprate superconductors derived from multi-scale ab initio scheme with

level renormalization

Motoaki Hirayama, Takahiro Misawa, Takahiro Ohgoe, Youhei Yamaji, and Masatoshi Imada: Phys. Rev. B **99**, 245155 (2019).

2. Real-time evolution and quantized charge pumping in magnetic Weyl semimetals
Takahiro Misawa, Ryota Nakai, and Kentaro Nomura : Phys. Rev. B **100**, 155123 (2019).
3. Spin nematics in frustrated spin-dimer systems with bilayer structure
Toshiya Hikihara, Takahiro Misawa, and Tsutomu Momoi : Phys. Rev. B **100**, 214414 (2019).
4. Semi-quantized Spin pumping and Spin-orbit torques in topological Dirac Semimetals
Takahiro Misawa and Kentaro Nomura : Scientific Reports **9**, 19659 (2019).
5. Ab initio study of superconductivity and inhomogeneity in a Hg-based cuprate superconductor
Takahiro Ohgoe, Motoaki Hirayama, Takahiro Misawa, Kota Ido, Youhei Yamaji and Masatoshi Imada : Phys. Rev. B **101**, 045124 (2020).
6. Charge dynamics of correlated electrons: Variational description with inclusion of composite fermions
Kota Ido, Masatoshi Imada, and Takahiro Misawa : Phys. Rev. B **101**, 075124 (2020).
7. Correlation effects on the magnetization process of the Kitaev model
Kota Ido and Takahiro Misawa : Phys. Rev. B **101**, 045121 (2020).

MIYAKE, Takashi [6000 (B), 0 (C)] (376)

— *High performance permanent magnets and magnetic materials*

1. Cerium as a possible stabilizer of ThMn₁₂-type iron-based compounds: A first-principles study
Yosuke Harashima, Taro Fukazawa, and Takashi Miyake: Scripta Materialia **179** (2020) 12.
2. Adjusting the descriptor for a crystal structure search using Bayesian optimization
Nobuya Sato, Tomoki Yamashita, Tamio Oguchi, Koji Hukushima and Takashi Miyake: Phys. Rev. Mater. **4** (2020) 033801.
3. Thermal decomposition of ThMn₁₂-type phase and its optimum stabilizing elements in SmFe₁₂-based alloys I. Dirba, Y. Harashima, H. Sepehri-Amin, T. Ohkubo, T. Miyake, S. Hirose, K. Hono: J. Alloy Compounds **813** (2020) 152224.
4. Bayesian optimization of chemical composition: a comprehensive framework and its application to RFe₁₂-type magnet compounds
Taro Fukazawa, Yosuke Harashima, Zhufeng Hou and Takashi Miyake: Phys. Rev. Mater. **3** (2019) 053807.
5. Ensemble learning reveals dissimilarity between rare-earth transition-metal binary alloys with respect to the Curie temperature
Duong-Nguyen Nguyen, Tien-Lam Pham, Viet-Cuong Nguyen, Hiori Kino, Takashi Miyake, Hieu-Chi Dam: J. Phys. Materials **2** (2019) 034009.

NOGUCHI, Hiroshi [10000 (B), 1000 (C)] (241)

— *Molecular Dynamics Simulation of Complex Fluids*

1. Effects of Cavitation on Karman Vortex Behind Circular-Cylinder Arrays: A Molecular Dynamics Study
Y. Asano, H. Watanabe, and H. Noguchi: J. Chem. Phys. **152**, 034501 (2020).
2. 分子動力学計算による複雑流体中のカルマン渦の解析
浅野 優太, 渡辺 宙志, 野口 博司: 分子シミュレーション研究会会誌 “アンサンブル” **22**, 157 (2020).

OGUCHI, Tamio [5000 (B), 0 (C)] (374)

— *Electron Theory on Secondary-Battery Materials*

1. First-Principles Study of Na-Ion Battery Performance and Reaction Mechanism of Tin Sulfide as Negative Electrode
Hiroki Kotaka, Hiroyoshi Momida, Ayuko Kitajou, Shigeto Okada, and Tamio Oguchi, Chem. Rec. **19**, 811 (2019).
2. First-Principles Study of X-Ray Absorption Spectra in NaFeSO₄F for Exploring Na-Ion Battery Reactions
Hiroyoshi Momida, Ayuko Kitajou, Shigeto Okada, and Tamio Oguchi, J. Phys. Soc. Jpn. **88**, 124709 (2019).

3. Amorphous $x\text{NaF-FeSO}_4$ Systems ($1 \leq x \leq 2$) with Excellent Cathode Properties for Sodium Ion Batteries
A. Kitajou, H. Momida, T. Yamashita, T. Oguchi, and S. Okada, *ACS Appl. Energy Mater.* **2**, 5968 (2019).
4. Significant Role of Oxygen Redox Reaction with O_2 -Release in Li-Excess Cation-Disordered Rock-Salt Cathodes $\text{Li}_{2+2x}\text{Mn}_{1-x}\text{Ti}_{1-x}\text{O}_4$: First-Principles Calculations
Motoyuki Hamaguchi, Hiroyoshi Momida, and Tamio Oguchi, *Electrochimica Acta* **330**, 135286 (2020).

OKAZAKI, Susumu [10000 (B), 1000 (C)] (370)

— *Conversion and storage of energy - Fuel cells and secondary batteries: Research and development of fundamental technologies of battery simulators*

1. Hydrogen Permeation in Hydrated Perfluorosulfonic Acid Polymer Membranes: Effect of Polymer Crystallinity and Equivalent Weight
K. Takeuchi, A. Kuo, T. Hirai, T. Miyajima, S. Urata, S. Terazono, S. Okazaki, and W. Shinoda: *J. Phys. Chem. C*, **123**, 20628-20638 (2019)
2. Structure of Hydrated Crystal (Lc), Tilted Gel ($\text{L}\beta'$), and Liquid Crystal ($\text{L}\alpha$) Phases of Linear Alkylbenzene Sulfonate (LAS) Studied by X-ray Diffraction and Molecular Dynamics Simulation
K. Takeda, Y. Andoh, S. Shinoda, and S. Okazaki: *Langmuir*, **35**, 9011-9019 (2019).
3. Molecular Behavior of Linear Alkylbenzene Sulfonate in Hydrated Crystal, Tilted Gel, and Liquid Crystal Phases Studied by Molecular Dynamics Simulation
K. Takeda, Y. Andoh, S. Shinoda, and S. Okazaki: *Langmuir*, **35**, 10877-10884 (2019).
4. Molecular dynamics study of solubilization of cyclohexane, benzene, and phenol into mixed micelles composed of sodium dodecyl sulfate and octaethylene glycol monododecyl ether
K. Takeda, K. Fujimoto, N. Yoshii, and S. Okazaki: *J. Comput. Chem.*, **40**, 2722-2729 (2019).
5. Fast multipole method for three dimensional systems with periodic boundary condition in two directions
N. Yoshii, Y. Andoh, S. Okazaki: *J. Comput. Chem.*, **41**, 940-948 (2020).
6. Extension of the fast multipole method for the rectangular cells with an anisotropic partition tree structure
Y. Andoh, N. Yoshii, S. Okazaki: *J. Comput. Chem.*, **41**, 1353-1367 (2020).

OSHIYAMA, Atsushi [20000 (B), 2000 (C)] (44)

— *Exploration of new-functionality and high-performance semiconductor devices*

1. Microscopic Identification of Surface Steps on SiC by Density-Functional Calculations
K. Seino and A. Oshiyama: *Proc. ICSRM2019*
2. Energetics of the surface step and its morphology on the 3C-SiC(111) surface clarified by the density-functional theory
K. Seino and A. Oshiyama: *Appl. Phys. Exp.* **13** (2020) 015506
3. Density-Functional Calculations for Structures and Energetics of Atomic Steps and their Implication for Surface Morphology on Si-face SiC Polar Surfaces
K. Seino and A. Oshiyama: *Phys. Rev. B* (2020) to be published
4. A two-dimensional liquid-like phase on Ga-rich GaN (0001) surfaces evidenced by first principles molecular dynamics
K. M. Bui, M. Boero, K. Shiraishi and A. Oshiyama: *Jpn. J. Appl. Phys.* **59** (2020) SGGK04
5. Computational study of oxygen stability in vicinal $m(10\text{-}10)$ -GaN growth by MOVPE
F. Shintaku, D. Yoshio, Y. Kangawa, J.-I. Iwata, A. Oshiyama, K. Shiraishi, A. Tanaka and H. Amano: *Appl. Phys. Exp.* **13** (2020) 055507
6. Oxygen incorporation kinetics in vicinal $m(10\text{-}10)$ -GaN growth by MOVPE
D. Yoshio, F. Shintaku, Y. Inatomi, Y. Kangawa, J.-I. Iwata, A. Oshiyama, K. Shiraishi, A. Tanaka and H. Amano: *Phys. Sta. Solidi - Rapid Res. Lett.* (2020) 2000142

OZAKI, Taisuke [10000 (B), 1000 (C)] (383)

— *Study on thermodynamic properties and NO_x redox reactions of ternary alloy nanoclusters by $O(N)$ density functional calculations*

1. Study on thermodynamic properties and NO_x redox reactions of ternary alloy nanoclusters by O(N) density functional calculations
S.-H. Hung, A. Hiroshi, Y. Osamu, and T. Ozaki, RSC Advances, in press.

SAITO, Susumu [5000 (B), 500 (C)] ()

— *Materials design using B, C, and N for next-generation device*

SHIBA, Hayato [10000 (B), 1000 (C)] (363)

— *Molecular dynamics study of long-ranged fluctuation and transport properties of electrolyte and glassy liquids*

— *Simulation of electrolyte liquids under constant potential bias*

1. Local Density Fluctuation Governs the Divergence of Viscosity Underlying Elastic and Hydrodynamic Anomalies in a 2D Glass-Forming Liquid
H. Shiba, T. Kawasaki, and K. Kim: Phys. Rev. Lett. **123**, 2655 (2019).

SUGINO, Osamu [10000 (B), 1000 (C)] (361)

— *Priority project 5— energy conversion (chemical energy)*

1. Nuclear quantum effect for hydrogen adsorption on Pt(111)
L. Yan, Y. Yamamoto, M. Shiga, and O. Sugino: Phys. Rev. B **101**, 165414 (2020)
2. Scaling Relation of Oxygen Reduction Reaction Intermediates at Defective TiO₂ Surfaces
Y. Yamamoto, S. Kasamatsu, and O. Sugino: J. Phys. Chem. C **123**, 19486 (2019)

TAKETSUGU, Tetsuya [5000 (B), 500 (C)] (375)

— *Ab initio study toward abundant element nanocatalysts with less precious metals*

1. Photo-Induced Pyramidal Inversion Behavior of Phosphines Involved with the Aggregation-Induced Emission (AIE) Behavior
T. Machida, T. Iwasa, T. Taketsugu, K. Sada, and K. Kokado, Chemistry – A European J., in press.
2. Single-molecule resonance Raman effect in a plasmonic nanocavity
R. B. Jacubia, H. Imada, K. Miwa, T. Iwasa, M. Takenaka, B. Yang, E. Kazuma, N. Hayazawa, T. Taketsugu, and Y. Kim, Nature Nanotechnology, **15**, (2020) 105.
3. Observations and theories of quantum effects in proton transfer electrode processes
K. Sakaushi, A. Lyalin, and T. Taketsugu, Current Opinion in Electrochemistry, **19**, (2020) 96.
4. Surface adsorption model calculation database and its application to activity prediction of heterogeneous catalysts
M. Kobayashi, H. Onoda, Y. Kuroda, and T. Taketsugu, J. Comput. Chem. Jap. **18**, (2019) 251.
5. Single-Phase Borophene on Ir(111): Formation, Structure and Decoupling from the Support
N. A. Vinogradov, A. Lyalin, T. Taketsugu, A. S. Vinogradov, and A. Preobrajenski, ACS Nano, **13**, (2019) 14511.
6. Roles of silver nanoclusters in surface-enhanced Raman spectroscopy
T. Tsuneda, T. Iwasa, and T. Taketsugu, J. Chem. Phys. **151**, (2019) 094102.
7. Anharmonic Vibrational Computations with a Quartic Force Field for Curvilinear Coordinates
Y. Harabuchi, R. Tani, N. DeSilva, B. Njagic, M. S. Gordon, and T. Taketsugu, J. Chem. Phys. **151**, (2019) 064104.
8. Additive-Dependent Iptycene Incorporation in Polyanilines: Insights into the Pentiptycene Clipping Effect and the Polymerization Mechanism
W. S. Tan, T.-Y. Lee, S.-F. Tseng, Y.-F. Hsu, M. Ebina, T. Taketsugu, S.-J. Huang, and J.-S. Yang, J. Chin. Chem. Soc. **66**, (2019) 1141.
9. Synthesis of polyaminophosphonic acid-functionalized poly(glycidyl methacrylate) for the efficient sorption of La(III) and Y(III)
A. A. Galhoum, E. A. Elshehy, D. A. Tolan, A. M. El-Nahas, T. Taketsugu, K. Nishikiori, T. Akashi, A. S. Morshedy, and E. Guibal, Chem. Eng. J. **375**, (2019) 121932.
10. Suppression of Pyrite Oxidation by Ferric-catecholate Complexes: An Electrochemical Study
X. Li, M. Gao, N. Hiroyoshi, C. B. Tabelin, T. Taketsugu, and M. Ito, Minerals Eng. **138**, (2019) 226.

TOHYAMA, Takami [5000 (B), 500 (C)] (369)

— *Cooperation Research with Big Experimental Facilities*

1. Magnetic excitations in magnetization plateaus of a frustrated spin ladder
K. Sasaki, T. Sugimoto, T. Tohyama, and S. Sota: Phys. Rev. B **101**, (2020) 144407.
2. Spin dynamics in the t - t' - J model: Dynamical density-matrix renormalization group study
T. Tohyama, S. Sota, and S. Yunoki: submitted to Phys. Rev. B

YABANA, Kazuhiro [10000 (B), 1000 (C)] (368)

— *Unified Photonic-Electronic Devices*

YAMADA, Atsuo [5000 (B), 500 (C)] (94)

— *Dynamical analyses on electrolytes for Na-ion batteries*

1. Sodium- and Potassium- Hydrate Melts Containing Asymmetric Imide Anions for High- Voltage Aqueous Batteries
Q. Zheng, S. Miura, K. Miyazaki, S. Ko, E. Watanabe, M. Okoshi, C.- P. Chou, Y. Nishimura, H. Nakai, T. Kamiya, T. Honda, J. Akikusa, Y. Yamada, A. Yamada: Angew. Chem. Int. Ed. **58** (2019) 2358.

YOSHIMI, Kazuyoshi [10000 (B), 1000 (C)] (364, 388)

— *Development of accuracy verification method on analytic continuation results using cross validation*

1. SpM: Sparse modeling tool for analytic continuation of imaginary-time Green ' s function
K. Yoshimi J. Otsuki, Y. Motoyama, M. Ohzeki, and H. Shinaoka: Comput. Phys. Commun. **244** (2019) 319.

□ Doctor Theses

1. **ADACHI, Daiki**
High-accuracy tensor renormalization group algorithms and their applications
The University of Tokyo, 2020-03
2. **ARAKI, Hiromu**
Numerical study of higher order topological insulators by machine learning and Berry phases
Tsukuba University, 2020-03
3. **DOMON, Kaoru**
Theory of novel excitonic order in the electron-hole systems with the multiple bands
Niigata University, 2020-03
4. **HAMAGUCHI, Motoyuki**
First-Principles Investigations of Cation-Disordered Rock-Salt Type Oxides for Li-Ion Battery Cathodes
Osaka University, 2020-03
5. **KANEKO, Kazuya**
Quantum information-theoretic study of complexity in chaotic many-body dynamics
The University of Tokyo, 2020-03
6. **KATO, Daichi**
Many-Variable Variational Monte Carlo Study of Unconventional Superconductivity in Multiband Systems
Osaka University, 2020-03
7. **MANAF, Muhamad Nasruddin**
Electronic Structure Calculation of Muonium in Silicon
Kanazawa University, 2019-09
8. **MINAMI, Susumu**
First-Principles Study of Magneto-Thermoelectric Properties in Ferromagnetic Heusler Alloys
Kanazawa University, 2020-03
9. **MISHCHENKO, Petr**
Quantum Monte Carlo study of the extended Kitaev models
The University of Tokyo, 2020-03
10. **MIYAZAKI, Kasumi**
Molecular simulation study on microscopic electrochemical stability of lithium-ion battery electrolyte
The University of Tokyo, 2020-03
11. **MIYAZAKI, Yusuke**
Molecular dynamics study of membrane pore formation induced by antimicrobial peptides
Nagoya University, 2020-03
12. **OKAUE, Daijiro**
Interfacial Polarization Effects of Ionic-Liquid Dielectrics on Carrier Transports in Electric Double Layer Organic Field Effect Transistors
Osaka University, 2020-03

13. **PARDEDE, Indra**
First-principles design of magnetic anisotropy in nanostructures by electric-field, strain, and metal alloying
Kanazawa University, 2019-09
14. **SAMPEI(UCHIDA), Kazuki**
Electron Emission and Atom Evaporation under Femtosecond Laser Pulses Studied by Time-Dependent Density Functional Theory
Tokyo University of Science, 2020-03
15. **UEMATSU, Kazuki**
Randomness-induced universal quantum spin liquids in frustrated magnets – Cooperation of frustration and randomness in quantum magnets –
Osaka University, 2020-03
16. **WELLA, Sasfan Arman**
DFT Study of the Adsorption States of an Organic Molecule Overlayer and a Single Platinum Atom on Graphene
Osaka University, 2019-09

□ Master Theses

1. **AINAI, Yuta**
First-principles study on structures of Nd-Fe alloys
Tokyo Institute of Technology, 2020-03
2. **BABA, Keita**
Electronic states of Si(111)-B surfaces with metallic adatoms
Tokyo Institute of Technology, 2020-03
3. **CHO, Sanghun**
Theory of tunneling currents at Si-p/n junctions with potential modulations
Chiba University, 2020-03
4. **KONDO, Chihiro**
Measurement of entanglement entropy by ground-state quantum Monte Carlo method
The University of Tokyo, 2020-03
5. **HAMAZAKI, Yasunari**
First-principles calculations of magnetoelectric effects at ferromagnetic-Heusler-alloy/BaTiO₃ interfaces
Tokyo Institute of Technology, 2020-03
6. **HARA, Soichiro**
Theoretical Calculations on Defect Properties of Two-Dimensional Topological Insulator W₂CO₂
The University of Tokyo, 2020-03
7. **HORI, Akihiro**
First-principles Study of Thermal Conductivity in Half-Heusler Thermoelectric Materials
Kanazawa University, 2020-03
8. **ICHIHASHI, Kodai**
Role of impurities in wide band-gap semiconductors: magnetism and optics
Yokohama National University, 2020-03
9. **INOUE, Kouki**
Theoretical study for thermodynamic properties of the spherical Kagome system {W₇₂V₃₀}
Tokyo University of Science, 2020-03
10. **KIKUCHI, Asuka**
Density Functional Theory Study on Water Clusters on Cu(110)
Osaka University, 2020-03
11. **KINOSHITA, Takahiro**
First-principles Theoretical Study of Graphene Adsorption on Metal Surfaces Including Van Der Waals Correction
Osaka University, 2020-03
12. **KIYOZAWA, Fumihito**
Theoretical prediction of crystal structure by energy regression utilizing sparse representation
The University of Tokyo, 2020-03
13. **KOSHINO, Koichi**
HCl gas sensing principle of porphyrin functionalized solid-state device

Yokohama National University, 2020-03

14. **MASAKI, Rina**
Calculation of photoelectron spectroscopy in Rashba systems
Ochanomizu University, 2020-03
15. **MIYAZAKI, Ryota**
Atomic Structures and Electronic States of Organic Semiconductors using Van Der Waals Density Functional
Osaka University, 2020-03
16. **MIZOO, Yoshiki**
Microscopic theory for superconductivity in plutonium compounds: Analysis on the basis of a two-orbital model
Tokyo Metropolitan University, 2020-03
17. **MORISHITA, Hirotaka**
Structural Analysis of Ag-Adsorbed Si(001) Surface Using Neural Network Potentials
The University of Tokyo, 2020-03
18. **MORIYAMA, Masaya**
Stacking Effect on Vacancy Stability of MoSe₂
Shimane University, 2020-03
19. **MURASE, Fumiya**
Theoretical investigation of electrochemical promotion effect in surface reaction of nitrogen
The University of Tokyo, 2020-03
20. **NAKANO, Takashi**
First-principles electronic structure calculations for the complexes of the screw dislocation and Mg impurity in GaN
Nagoya University, 2020-03
21. **NARUTA, Hiroki**
Evaluation of entropy change associated with a formation of molecular networks in a fluid
Ehime University, 2020-03
22. **OCHIAI, Kesuke**
appearing of ferromagnetism in Pt (100) ultra thin films dependent on film thickness
Keio University, 2020-03
23. **OGINO, Takuhiro**
Quantum phase transition in $S = 1$ two-leg XXZ spin-ladder systems with a four-spin interaction
The University of Tokyo, 2020-03
24. **OHARA, Kazuhisa**
Improving activity of dihydrofolate reductase by theoretical saturation mutagenesis
The University of Tokyo, 2020-03
25. **SAITOH, Rikio**
Oxygen storage property change of Ca₂AlMnO_{5+δ} by element substitution
Hokkaido University, 2020-03
26. **SANO, Mio**
Studies toward the development of an interleukin-33 responsible for allergic asthma

The University of Tokyo, 2020-03

27. **SASAKI, Shu**
First-principles study of magnetic structures in manganese hydride
The University of Tokyo, 2020-03
28. **SHIMIZU, Makoto**
Spin fluctuation theory for pressure and doping effects in iron-based superconductors
Okayama University, 2020-03
29. **SHIOZAWA, Tomoharu**
Development of first-principles method to evaluate magnetic refrigerants
Tokyo Institute of Technology, 2020-03
30. **SHIRAIISHI, Yuto**
Charging-induced formation of ferroelectric orthorhombic HfO₂: first-principles study
Chiba University, 2020-03
31. **SHIROTA, Riku**
Study of magnetic compounds doped with impurities using first principles calculations
Yokohama National University, 2020-03
32. **SUDO, Kaori**
Theoretical Study of Isotope Effects on the Elastic Constants of Diamond
Osaka University, 2020-03
33. **TACHI, Kyosuke**
Global thermodynamics for inhomogeneous systems under extend force and heat conduction
Ibaraki University, 2020-03
34. **TAKAMIZAWA, Taichi**
Theoretical study of electronic and magnetic properties in thin films of Weyl semimetals
The University of Tokyo, 2020-03
35. **TAKAYA, Kei**
Aridity dependence of the characteristic bifurcation angle in a model drainage network.
Osaka University, 2020-03
36. **TAKEUCHI, Yuki**
Magnetism in the double exchange model on the quasiperiodic lattice
Tokyo Institute of Technology, 2020-03
37. **TANAKA, Yoko**
Theoretical study on electrical conduction properties of higher-order topological insulators
Ochanomizu University, 2020-03
38. **TARUOKA, Yushi**
First-Principles Calculations on Defects in Fe Based Superconductor LiFeAs
The University of Tokyo, 2020-03
39. **TERASAKI, Tomoaki**
Density functional theory study of formic acid dehydrogenation reaction activity of metal clusters
on light-element doped graphene
Hokkaido University, 2020-03

40. **USHIKI, Ryota**
Theoretical analysis of diffusion mechanism of highly concentrated organic electrolytes for secondary batteries
The University of Tokyo, 2020-03
41. **WATANABE, Kei**
Growth of density fluctuations during phase separation toward nucleation or spinodal decomposition
Ehime University, 2020-03
42. **WATANABE, Takeru**
The characteristic bifurcation angle in a nonlinear growth network model.
Osaka University, 2020-03
43. **WICAKSONO, Yusuf**
Theory on controlling the opening and closing of gapped Dirac cone in Ni/Graphene/Ni nanostructure
Osaka University, 2019-09
44. **WU, Yan**
Study of Defects in GaN with High-Dimensional Neural Network Potential
The University of Tokyo, 2019-09
45. **YAMADE, Takufumi**
Femtosecond Carrier Dynamics in Rare-earth Monoxide Thin Films
University of Fukui, 2020-03
46. **YAMAGUCHI, Kotaro**
First-principles study of Ni₃Al surfaces
Kagoshima University, 2020-03
47. **YAMAUCHI, Takuya**
First-principles Theoretical Study on Oxygen Reduction Reaction over Pt(111)
Osaka University, 2020-03
48. **YASUDA, Hironori**
Theoretical study of spontaneous inversion symmetry breaking in a spin-orbital coupled metal Cd₂Re₂O₇
The University of Tokyo, 2020-03
49. **YATA, Kohei**
Study of V_O diffusion barrier in SiO₂ with lattice constant modulation
Shimane University, 2020-03
50. **ZHOU, Ling**
First-Principles Calculation of Electron and Phonon Properties of α -MoO₃
The University of Tokyo, 2019-09